Studies in Computational Intelligence 810

Huimin Lu *Editor*

Cognitive Internet of Things: Frameworks, Tools and Applications

Springer

Studies in Computational Intelligence

Volume 810

Series editor

Janusz Kacprzyk, Polish Academy of Sciences, Warsaw, Poland
e-mail: kacprzyk@ibspan.waw.pl

The series "Studies in Computational Intelligence" (SCI) publishes new developments and advances in the various areas of computational intelligence—quickly and with a high quality. The intent is to cover the theory, applications, and design methods of computational intelligence, as embedded in the fields of engineering, computer science, physics and life sciences, as well as the methodologies behind them. The series contains monographs, lecture notes and edited volumes in computational intelligence spanning the areas of neural networks, connectionist systems, genetic algorithms, evolutionary computation, artificial intelligence, cellular automata, self-organizing systems, soft computing, fuzzy systems, and hybrid intelligent systems. Of particular value to both the contributors and the readership are the short publication timeframe and the world-wide distribution, which enable both wide and rapid dissemination of research output.

The books of this series are submitted to indexing to Web of Science, EI-Compendex, DBLP, SCOPUS, Google Scholar and Springerlink.

More information about this series at http://www.springer.com/series/7092

Huimin Lu
Editor

Cognitive Internet of Things: Frameworks, Tools and Applications

Springer

Editor
Huimin Lu
Department of Mechanical and Control
Engineering
Kyushu Institute of Technology
Kitakyushu, Japan

ISSN 1860-949X ISSN 1860-9503 (electronic)
Studies in Computational Intelligence
ISBN 978-3-030-04945-4 ISBN 978-3-030-04946-1 (eBook)
https://doi.org/10.1007/978-3-030-04946-1

Library of Congress Control Number: 2018962755

This Springer imprint is published by the registered company Springer Nature Switzerland AG
The registered company address is: Gewerbestrasse 11, 6330 Cham, Switzerland

Preface

In recent years, Artificial Intelligence (AI) has attracted attention as a key for growth in developed countries and developing countries. The attention has been focused mainly on developing new deep learning-based Information Communication Technology (ICT) and Internet of Things (IoT) applications. Although recently developed deep learning technology certainly excels in extracting certain patterns, there are many limitations. Most of recent models are overly dependent on big data, lack a self-idea function, and are complicated. In order to overcome these limitations and to solve the real-world industrial problems, Cognitive Computing (CC) and Computational Neuroscience (CN) are driving as one of the best tools for future brain-inspired intelligence IoTs.

Rather than merely developing next-generation AI models, we are trying to provide a platform to share up-to-date scientific and industrial achievements of general-purpose intelligence cognition methods. These methods provide efficient tools to solve the issues of recent AI models, and capture remarkable human learning abilities, combining the strengths of CC/CN and deep generative neural networks.

The overall aim of this book is to collect the state-of-the-art contributions on the Computational Neuroscience, Computational Cognition and Perception, Computer Vision, Natural Language Processing, Human Action Analysis, and related applications.

We had received 206 submissions from over 10 countries in the world. After the careful review process, 50 papers were selected based on their originality, significance, technical soundness, and clarity of exposition. The papers of this book were chosen based on review scored submitted by members of the program committee and underwent further rigorous rounds of review.

It is our sincere hope that this volume provides stimulation and inspiration, and that it will be used as a foundation for works to come.

Kitakyushu, Japan — Huimin Lu
September 2018

Acknowledgements

This work was supported by Leading Initiative for Excellent Young Researcher (LEADER) of MEXT-Japan (16809746), Grants-in-Aid for Scientific Research of JSPS (17K14694), Research Fund of State Key Laboratory of Marine Geology at Tongji University (MGK1608), Research Fund of The Telecommunications Advancement Foundation, Open Collaborative Research Program at National Institute of Informatics Japan (NII), Japan–China Scientific Cooperation Program (6171101454), and International Exchange Program of National Institute of Information and Communications (NICT), and Fundamental Research Developing Association for Shipbuilding and Offshore and Strengthening Research Support Project of Kyushu Institute of Technology.

We would like to thank all authors for their contributions. The editors also wish to thank the referees who carefully reviewed the papers and gave useful suggestions and feedback to the authors. Finally, we would like to thank Prof. Changwen Chen, Prof. Xiaofang Zhou, Prof. Xiaoqing Wen, Prof. Ce Zhu, Prof. Chenglin Liu, Prof. Seiichi Serikawa, and all editors of Studies in Computational Intelligence for the cooperation in preparing the book.

Contents

MEG Signal Reconstruction via Low-Rank Matrix Recovery for Source Imaging in Simulations

Yegang Hu and Jicong Zhang

Abstract Source imaging with magnetoencephalography (MEG) has obtained good spatial accuracy on the shallow sources, and has been successfully applied in the brain cognition and the diagnosis of brain disease. However, its utility with locating deep sources may be more challenging. In this study, a new source imaging method was proposed to find real brain activity on deep locations. A sensor array with MEG measurements including 306 channels was represented as a low-rank matrix plus sparse noises. The low-rank matrix was used to reconstruct the MEG signal and remove interference. The source model was estimated using the reconstructed MEG signal and minimum variance beamforming. Simulations with a realistic head model indicated that the proposed method was effective.

Keywords Source imaging · Magnetoencephalography (MEG)
Low-rank matrix recovery · Beamforming · Signal reconstruction

Y. Hu · J. Zhang (✉)
School of Biological Science and Medical Engineering,
Beihang University, Beijing 100191, China
e-mail: jicongzhang@buaa.edu.cn

Y. Hu
e-mail: huyegang@buaa.edu.cn

Y. Hu · J. Zhang
Beijing Advanced Innovation Centre for Big Data-Based Precision Medicine,
Beihang University, Beijing 100191, China

Y. Hu · J. Zhang
Beijing Advanced Innovation Centre for Biomedical Engineering,
Beihang University, Beijing 100191, China

Y. Hu · J. Zhang
Hefei Innovation Research Institute, Beihang University, Hefei 230013, China

H. Lu (ed.), *Cognitive Internet of Things: Frameworks, Tools and Applications*, Studies in Computational Intelligence 810,
https://doi.org/10.1007/978-3-030-04946-1_1

1 Introduction

Magnetoencephalography (MEG) can capture neural activities with high spatiotemporal resolution, which are less affected by the skull and scalp than the electroencephalogram [1–3]. In recent years, MEG plays an important role in the field of neuroimaging, and is a worthful and noninvasive tool for finding epileptogenic zone with epilepsy patients [4–6]. Many source imaging methods have been proposed to find the real location of brain activity via a sensor array with MEG measurements [7–9]. Source modeling is common estimated by those existing techniques such as beamforming [10, 11], multiple signal classification [12], dipole fitting [13]. As a result, the inverse problem is expected to solve improved spatial accuracy on shallow sources. The shallow sources are then easily localized by solving inverse problem using the signal received by sensors [14]. However, the ability about localizing deep sources, such as those in mesial temporal structures, is doubtful [15]. An important reason is that signals received by MEG sensors from those deep sources are weak. Those signals are thus more susceptible to noises and artifacts than shallow sources [16]. The key issue about localizing deep sources is to remove the noise of the array signals and to extract intrinsic features of the signals.

In the past ten years, low-rank matrix recovery has emerged as an effective tool for face recognition, subspace representation, de-nosing, and image restoration [17–20]. This technique is robust to de-nosing and is suitable for recovering a low-rank matrix from a sparse corrupted data. The low-rank matrix then represents intrinsic features of the original data matrix. From the view of the computing times, low-rank matrix recovery can be solved in polynomial-time with performance guarantees [21]. Beamforming plays an important role in the fields of neuroimaging and signal processing. These methodologies make use of spatial filtering, and do not rely on one moment (i.e., snapshot) of the MEG measurements when solving inverse problem [22]. The source localization results using beamforming technique are stable, that is, may not "jump" (change abruptly and discontinuously) at adjacent time points [22]. However, the existing vector beamforming for MEG source localization is sensitive to noise, and poor at localizing deep sources [23]. The sensor array with MEG measurements could be regarded as a sparse corrupted data.

In this study, low-rank matrix recovery and beamforming were combined to localize deep sources with MEG measurements. The original sensor array was represented as a low-rank matrix plus sparse noises, where the sensor array removed the noises can be explained by the low-rank matrix. The low-rank matrix was used to reconstruct the MEG signal and remove interference. The source model was estimated using the reconstructed MEG signal and minimum variance beamforming. We assumed that the neuronal sources were uncorrelated, and that a single source could be isolated. The newly proposed method was validated on simulated data, and compared with three well-known methods, linearly constrained minimum variance (LCMV) [10], multiple signal classification (MUSIC) [12], and dipole fitting [13].

This paper is organized as follows. The materials and methods are covered in Sect. 2. A novel source imaging algorithm based on low-rank matrix recovery and minimum variance beamforming is described in Sect. 2. Experimental results are provided in Sect. 3. The significance of the results is discussed in Sect. 4.

2 Materials and Methods

2.1 Simulations

In this section, the simulated sensor array with MEG measurements was generated by the function ft_dipolesimulation in the FieldTrip toolbox. Since the cosine function has the characteristic of periodic oscillations, previous studies show that the cosine function is applied to generate the simulations with MEG measurements [23, 24], with a time-course as follows:

$$\mathrm{S}(t) = A\cos(2\pi ft + \tau) \tag{1}$$

where A is amplitude, f represents frequency, and τ represents phase. In this study, Gaussian noise was added to the time-course for verifying that the proposed method was insensitive to noise. A whole head MEG system (VectorView, Elekta Neuromag Oy, Finland) was then used and included 306 channels in total. We then applied a realistic head model for generating a grid matrix, and partitioned the brain space into a three-dimensional grid with millimeter resolution.

2.2 Low-Rank Matrix Recovery

A given data matrix $\boldsymbol{X}$ seeks to be decomposed into a low-rank matrix $\boldsymbol{L}$ plus the associated sparse error $\boldsymbol{E}$ using the technique of low-rank matrix recovery. In theory, the optimization process of the low-rank matrix recovery can then be formulated as:

$$\left(\hat{\boldsymbol{L}}, \hat{\boldsymbol{E}}\right) = \arg\min_{\boldsymbol{L},\boldsymbol{E}} (rank(\boldsymbol{L}) + \lambda \boldsymbol{E}_0)\ s.t.\ \boldsymbol{X} = \boldsymbol{L} + \boldsymbol{E} \tag{2}$$

where $\|\cdot\|_0$ represents l_0-norm operator, and $rank(\cdot)$ denotes rank operator of a matrix or vector. However, the optimization of this formula is NP-hard and hard to be solved approximately. Many studies have recently focused on how to obtain an approximate solution using convex surrogate, one of which is recognized and successfully applied in many fields [17–20, 25]. The convex surrogate is formulated as:

$$\left(\hat{\boldsymbol{L}}, \hat{\boldsymbol{E}}\right) = \arg\min_{\boldsymbol{L},\boldsymbol{E}} (\|\boldsymbol{L}\|_* + \lambda \|E\|_1)\ s.t.\ \boldsymbol{X} = \boldsymbol{L} + \boldsymbol{E} \tag{3}$$

where $\|\cdot\|_*$ indicates the nuclear norm (i.e., the sum of the singular values) operator, and $\|\cdot\|_1$ represents the l_1-norm operator. The technique of inexact augmented Lagrange multipliers (ALM) [21] is computational efficiency, and can then be used to solve the optimization problem of formula (3).

2.3 Source Imaging Using the Proposed Method

To realize the source imaging algorithm, two toolboxes were applied to analyze the simulated data with MEG measurements in this study, including FieldTrip [26] and MATLAB R2014a (The MathWorks Inc., Natick, MA, USA). Source imaging usually consists of four parts: head model construction, forward solution, inverse solution, and source display. In the forward solution, a volume conduction model was constructed by using a realistically shaped single-shell approximation based on the approach described by Nolte [27]. Individual anatomical MRIs (T1-weighted) and the digitized head shapes were co-registered to the MEG coordinate system using anatomical landmarks via an iterative closest point algorithm [28].

Figure 1 shows the flow chart of the inverse solution on source imaging using the proposed approach. In the inverse solution part, MEG data matrix was first preprocessed through three steps: filtering using a band-pass filter of 0.5–60 Hz, notch-filtering at 50 Hz, and detrending by removing the linear trend. Here, the data matrix including spikes was represented as a symbol $\boldsymbol{X}$. By performing low-rank matrix recovery, the data matrix $\boldsymbol{X}$ was then represented as a low-rank matrix $\boldsymbol{L}$ plus sparse noises $\boldsymbol{E}$ using the formula (3). Since the low-rank matrix $\boldsymbol{L}$ has a better representative ability than the data matrix $\boldsymbol{X}$ [17], $\boldsymbol{L}$ was then attempted to estimate the source model using a minimum variance beamforming. Its effectiveness was verified in simulation data.

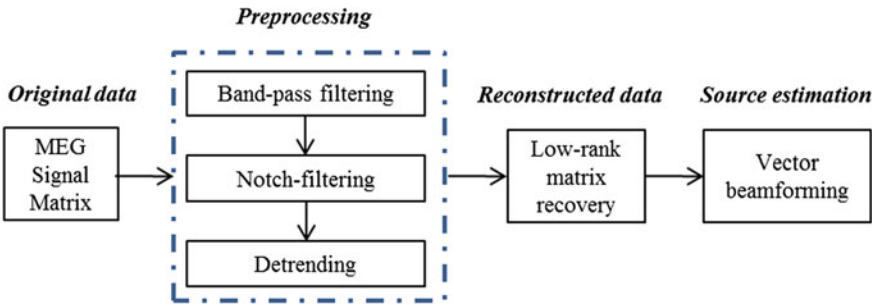

Fig. 1 The flow chart of the inverse solution on source imaging, and the inverse solution is estimated by low-rank matrix recovery and minimum variance beamforming

For an input matrix $\boldsymbol{L} = \left[\boldsymbol{l}^{(1)}, \boldsymbol{l}^{(2)}, \ldots, \boldsymbol{l}^{(N)}\right]$, the inverse solution model is described as:

$$\boldsymbol{L} = \boldsymbol{GD} + \boldsymbol{\varepsilon} \tag{4}$$

where $\boldsymbol{l}^{(i)}$ denotes an $M \times 1$ vector of the MEG measurements processed by the low-rank matrix recovery at the i-th time point, $\boldsymbol{G}$ is the $M \times J$ (lead-field) gain matrix, M is the number of MEG sensors, J is the number of unknown dipole moment parameters, $\boldsymbol{D}$ represents a $J \times N$ dipole moment matrix for a given time series, and $\boldsymbol{\varepsilon}$ denotes the $M \times N$ noise matrix. The objective function to be optimized is then posed mathematically as

$$\begin{aligned} &\min_{\boldsymbol{W}(r_0)} \; tr\left(\boldsymbol{W}^T(r_0)\hat{\boldsymbol{C}}\boldsymbol{W}(r_0)\right) \\ &subject\ to\ \boldsymbol{W}^T(r_0)G(r_0) = I \end{aligned} \tag{5}$$

where $\mathrm{tr}(\cdot)$ denotes the trace of a matrix, $\mathbf{I}$ is the unit matrix, and $\boldsymbol{W}(r_0)$ represents a spatial filter for the narrowband volume element centered on location r_0. The meaning of the constraint here is to allow the source activity at location r_0 to be passed with unit gain, while inhibiting contributions from all other sources. The minimizes interference (MinInf) algorithm [29] is then applied to optimize the objective function, yielding the optimal solution

$$\boldsymbol{W}(r_0) = \left[\boldsymbol{G}^T(r_0)\hat{\boldsymbol{C}}^{-1}\boldsymbol{G}(r_0)\right]^{-1}\boldsymbol{G}^T(r_0)\hat{\boldsymbol{C}}^{-1} \tag{6}$$

where $(\cdot)^{-1}$ represents the inverse operator of a matrix. The minimum variance can be regarded as the strength of the activity at grid point r_0. The variance or strength at all grid points in the brain can be calculated to perform source imaging, and the position corresponding to the maximum strength is assumed to be the source location.

3 Experimental Results

In this section, the proposed method was verified by two experiments with simulated data. To illustrate the effectiveness of the proposed method for deep sources, two locations were chosen to construct the simulations, which were represented as $\{(-29, 11, 38), (35, 11, 38)\}$ mm in the Neuromag coordinate system. These two locations are in near the center of left hippocampus and in near the center of right hippocampus. For evaluating the results of source imaging, the location error is then applied to describe the spatial accuracy, and is given as:

$$location\ error = \sqrt{\gamma - \hat{\gamma}_2} \tag{7}$$

Table 1 Comparison of the location error using the four methods

Source locations	Proposed method	Dipole fitting	LCMV	MUSIC
(−29, 11, 38)	3.9	4.9	4.7	6.7
(35, 11, 38)	3.4	4.0	4.1	5.8

The coordinates of the source locations are included in the Neuromag coordinate system, where (−29, 11, 38) is in near the center of left hippocampus, and (35, 11, 38) is in near the center of right hippocampus

where $\|\cdot\|_2$ denotes the two-norm operator, and $\hat{\gamma}$ represents the spatial location of the source generated by the source imaging algorithm, and γ represents the spatial location of the real source. Obviously, a smaller location error corresponds to a higher spatial accuracy. Table 1 shows the comparison of the spatial accuracy using the four approaches: dipole fitting, LCMV, MUSIC, and the proposed method. The proposed method had the lowest location error compared with the other three approaches in the two simulations generated by the two source locations. The new method is thus effective for the deep sources in simulation data.

4 Discussion and Conclusion

In this study, we proposed a new approach for finding deep sources in the brain with MEG recordings. By performing low-rank matrix recovery, the data matrix was represented as a low-rank matrix plus sparse noises. The low-rank matrix was used to reconstruct the MEG signal and remove interference. The sensor covariance matrix was then be estimated by the sample covariance matrix using a second-order statistic. Since the reconstructed MEG matrix has a better representative ability than the data matrix [17], it was attempted to estimate the source model using a minimum variance beamforming with a linear constraint. In MEG-simulated sensor data, the new method was superior to three classical methods (dipole fitting, LCMV and MUSIC) in spatial accuracy, and was thus effective for the deep sources.

However, this study was achieved based on the assumption that the neuronal sources were uncorrelated, and that a single source could be isolated. We are not sure whether the proposed method is still effective on multi-sources localization. In future work, we hope that the effective performance of the new method can be verified in practical applications, such as locating epileptogenic foci and locating functional areas, and also hope that this algorithm can play a role in the search for lesions involved in brain diseases.

Acknowledgements This work was supported by the National Key R&D Program of China (Grant Number: 2016YFF0201002), the National Natural Science Foundation of China (Grant Numbers: 61301005, 61572055), the Beihang University Hefei Innovation Research Institute, Project of 'The Thousand Talents Plan' for Young Professionals, and 'The Thousand Talents Plan' Workstation between Beihang University and Jiangsu Yuwell Medical Equipment and Supply Co. Ltd.

References

1. Barnes, G.R., Hillebrand, A.: Statistical flattening of MEG beamformer images. Hum. Brain Mapp. **18**, 1–12 (2003)
2. Zumer, J.M., Attias, H.T., Sekihara, K., Nagarajan, S.S.: A probabilistic algorithm integrating source localization and noise suppression for MEG and EEG data. Neuroimage **37**, 102–115 (2007)
3. Baillet, S.: Magnetoencephalography for brain electrophysiology and imaging. Nat. Neurosci. **20**, 327–339 (2017)
4. Nissen, I.A., Stam, C.J., Citroen, J., Reijneveldb, J.C., Hillebranda, A.: Preoperative evaluation using magnetoencephalography: experience in 382 epilepsy patients. Epilepsy Res. **124**, 23–33 (2016)
5. Wu, J.Y., et al.: Magnetic source imaging localizes epileptogenic zone in children with tuberous sclerosis complex. Neurology **66**, 1270–1272 (2006)
6. Nissen, I.A., et al.: Identifying the epileptogenic zone in interictal resting-state MEG source-space networks. Epilepsia **58**, 137–148 (2017)
7. Mattout, J., Phillips, C., Penny, W.D., et al.: MEG source localization under multiple constraints: an extended Bayesian framework. NeuroImage **30**, 753–767 (2006)
8. Grech, R., Cassar, T., Muscat, J., Camilleri, K.P., Fabri, S.G., Zervakis, M., Xanthopoulos, P., Sakkalis, V., Vanrumste, B.: Review on solving the inverse problem in EEG source analysis. J. NeuroEng. Rehabil. **5**, 25 (2008)
9. Lu, H., Li, Y., Mu, S., Wang, D., Kim, H., Serikawa, S.: Motor anomaly detection for unmanned aerial vehicles using reinforcement learning. IEEE Internet Things J. **5**(4), 2315–2322 (2018)
10. Van Veen, B.D., van Drongelen, W., Yuchtman, M., Suzuki, A.: Localization of brain electrical activity via linearly constrained minimum variance spatial filtering. IEEE Trans. Biomed. Eng. **44**, 867–880 (1997)
11. Oshino, S., Kato, A., Wakayama, A., et al.: Magnetoencephalographic analysis of cortical oscillatory activity in patients with brain tumors: synthetic aperture magnetometry (SAM) functional imaging of delta band activity. Neuroimage **34**, 957–964 (2007)
12. Mosher, J.C., Leahy, R.M.: Recursive MUSIC: a framework for EEG and MEG source localization. IEEE Trans. Biomed. Eng. **45**, 1342–1354 (1998)
13. Komssi, S., Huttunen, J., Aronen, H.J., et al.: EEG minimum-norm estimation compared with MEG dipole fitting in the localization of somatosensory sources at S1. Clin. Neurophysiol. **115**, 534–542 (2004)
14. Hillebrand, A., Singh, K.D., Holliday, I.E., Furlong, P.L., Barnes, G.R.: A new approach to neuroimaging with magnetoencephalography. Hum. Brain Mapp. **25**, 199–211 (2005)
15. Shigeto, H., Morioka, T., Hisada, K., Nishio, S., Ishibashi, H., Kira, D., Tobimatsu, S., Kato, M.: Feasibility and limitations of magnetoencephalographic detection of epileptic discharges: simultaneous recording of magnetic fields and electrocorticography. Neurol. Res. **24**, 531–536 (2002)
16. Lin, F.H., Witzel, T., Ahlfors, S.P., et al.: Assessing and improving the spatial accuracy in MEG source localization by depth-weighted minimum-norm estimates. Neuroimage **31**, 160–171 (2006)
17. Chen, C.F., Wei, C.P., Wang, Y.C.F.: Low-rank matrix recovery with structural incoherence for robust face recognition. IEEE Conf. Comput. Vis. Pattern Recogn. **CVPR**, 2618–2625 (2012)
18. Liu, G., Lin, Z., Yan, S., et al.: Robust recovery of subspace structures by low-rank representation. IEEE Trans. Pattern Anal. Mach. Intell. **35**, 171–184 (2013)
19. Shabalin, A.A., Nobel, A.B.: Reconstruction of a low-rank matrix in the presence of Gaussian noise. J. Multivar. Anal. **118**, 67–76 (2013)
20. Zhang, H., He, W., Zhang, L., et al.: Hyperspectral image restoration using low-rank matrix recovery. IEEE Trans. Geosci. Remote Sens. **52**, 4729–4743 (2014)
21. Candès, E.J., Li, X., Ma, Y., et al.: Robust principal component analysis? J. ACM **58**, 11 (2011)

22. Diwakar, M., Huang, M.X., Srinivasan, R., Harrington, D.L., Robb, A., Angeles, A., Muzzatti, L., Pakdaman, R., Song, T., Theilmann, R.J., et al.: Dual-core beamformer for obtaining highly correlated neuronal networks in MEG. Neuroimage **54**, 253–263 (2011)
23. Zhang, J., Liu, C.: On linearly constrained minimum variance beamforming. J. Mach. Learn. Res. **16**, 2099–2145 (2015)
24. Brookes, M.J., Stevenson, C.M., Barnes, G.R., et al.: Beamformer reconstruction of correlated sources using a modified source model. Neuroimage **34**, 1454–1465 (2007)
25. Wright, J., Ganesh, A., Rao, S., Ma, Y.: Robust principal component analysis: exact recovery of corrupted low-rank matrices. In: Proceedings of the Neural Information Processing Systems (NIPS), pp. 2080–2088 (2009)
26. Lu, H., Li, Y., Chen, M., Kim, H., Serikawa, S.: Brain intelligence: go beyond artificial intelligence. Mob. Netw. Appl. **23**, 368–375 (2018)
27. Nolte, G.: The magnetic lead field theorem in the quasi-static approximation and its use for magnetoencephalography forward calculation in realistic volume conductors. Phys. Med. Biol. **48**, 3637 (2003)
28. Besl, P.J., McKay, N.D.: A method for registration of 3-D shapes. IEEE Trans. Pattern Anal. Mach. **14**, 239–256 (1992)
29. Groß, J., Ioannides, A.A.: Linear transformations of data space in MEG. Phys. Med. Biol. **44**, 2081 (1999)

Silhouette Photo Style Transfer

Henan Li, Lili Wan and Shenghui Wang

Abstract Silhouette photography is popular among photographers. However, it is hard for ordinary users to shoot this kind of photos because of the limitations of cameras, weather and skills. In this work, we propose an automatic photo style transfer approach that can generate realistic silhouette images. First we present a sky segmentation method to divide an input image into an object foreground and a sky background. Then, for the background, we implement a statistic color transfer method using a specified sky photo. Finally, in order to generate natural results, we develop an adaptive approach to adjust the color of the object foreground considering the ambient color computed from the stylized background. The experimental results show that our methods can achieve satisfactory sky segmentation results and generate aesthetically pleasing silhouette photos.

Keywords Silhouette photography · Photo style transfer · Sky segmentation Color transfer

1 Introduction

Silhouette photos are attractive and inspiring, in which the intense contrast between the dark and light makes the photos more dramatic, mysterious, and expressive. However, silhouette photography highly depends on the weather and lighting conditions. The optimum time to shoot a silhouette is at dawn or dusk when the sun is low in the sky. Furthermore, professional shooting skills are also needed. Therefore, it is hard for ordinary users to take silhouette photos.

H. Li · L. Wan (✉) · S. Wang
Institute of Information Science, Beijing Jiaotong University, Beijing 100044, People's Republic of China
e-mail: llwan@bjtu.edu.cn

H. Li · L. Wan · S. Wang
Beijing Key Laboratory of Advanced Information Science and Network Technology, Beijing 100044, People's Republic of China

H. Lu (ed.), *Cognitive Internet of Things: Frameworks, Tools and Applications*, Studies in Computational Intelligence 810,
https://doi.org/10.1007/978-3-030-04946-1_2

For photo style transfer, some researchers use color transfer methods directly, such as the early work by Reinhard et al. [1] and some improved global color transfer methods [2–4]. These methods are suitable for the unitary lighting change of the landscape photo. Recently, some learning based methods are widely used in various fields [5, 6]. In common image stylization, some approaches based on deep learning [7, 8] have shown good performance. Nevertheless, silhouette photography is not just the variation of global lighting, and it demands special camera settings to highlight the contrast. To our knowledge, silhouette photo style transfer has not yet been studied in previous work.

To address this problem, we propose an automatic example-based photo style transfer approach that can transfer ordinary photos into realistic silhouette images. Our work is similar in spirit to these two papers [9, 10] which aim to overcome the limitations on taking photo with sky background. However, the sky image stylization is implemented by sky replacement in these two works. In contrast, we propose novel color transfer methods, which ensure the content of the original photo is not changed.

To achieve this goal, we divide this work into two parts. One part is sky segmentation, the other is color transfer. The overall framework of our approach is illustrated in Fig. 1. Specifically, considering that the background of a silhouette photo is sky in most cases, we first propose a critical background region extraction algorithm that is suitable for images of this semantic. And the critical foreground regions are extracted by the image saliency detection method. Then the automatic sky segmentation is realized by applying these two kinds of critical regions to the improved OneCut [11] algorithm. In addition, we implement a statistic color transfer method using a specified sky photo for the background. According to the optic artistry characteristics of the silhouette photos, we also develop an adaptive color correction approach considering the ambient color computed from the stylized background for the foreground to transfer the color naturally.

In summary, the main contributions of our work include:

- We propose a novel approach to transferring silhouette photo style for images. Based on the sky segmentation, different color transfer methods are adopted for the background and the foreground.
- We present an automatic OneCut based sky segmentation algorithm, which can be also applied to other scenes that require sky segmentation. A local regions similarities based critical background region extraction algorithm is proposed for images with sky as the backgrounds to realize the sky segmentation.
- We develop an adaptive foreground color correction method according to the ambient color. It calculates the ambient color based on the background color transfer results, which can not only make the stylization results coordinate with the backgrounds, but also produce the halo at the edge of the object.

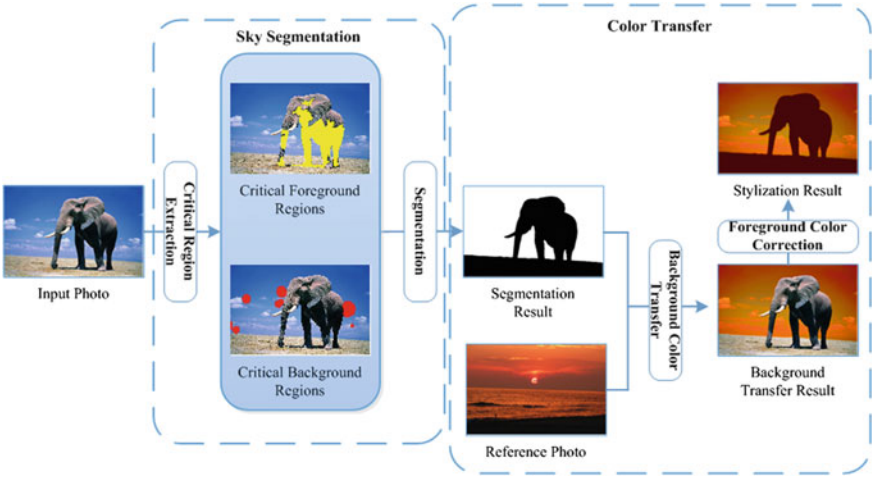

Fig. 1 Overview of the proposed silhouette photo style transfer algorithm

2 Algorithms

Given an input image, we aim to automatically generate a realistic silhouette stylization image. To achieve this, we first segment the input into the foreground and the background. See Sect. 2.1 for more details. In Sect. 2.2, our different color transfer methods of background and foreground are given respectively.

2.1 Sky Segmentation

The morphological features of the silhouette are obvious, details of the object are hidden in the dark while outlines are exposed. That's the glamour of the silhouette photography. Therefore, the extraction of the object outline is crucial for the effect of the silhouette. In this paper, the silhouette stylization algorithm is based on the segmentation.

Graph theory based segmentation method is one of the main methods of image foreground-background segmentation. Boykov et al. [12] propose the first graph cut based interactive image segmentation method in 2001. Since then, researchers have proposed a variety of segmentation methods [11, 13] based on this. Among them, OneCut [11] adopts a simply unary term that can guarantee a globally optimal solution in one graph cut and avoid the NP-hard problem in many applications. It is one of the best graph cut algorithms at present.

But all of the above methods require user interaction. In practical applications, the user interaction will bring a lot of trouble, and these methods are greatly influenced by the interaction. Deep learning based segmentation methods, e.g. [14, 15],

have been becoming quite popular recently. While these methods can produce good segmentation results, the heavy computational overhead makes them unsuitable for our simple segmentation mask. Therefore, we improve the OneCut by removing the user interaction for automatic segmentation.

There are three steps to segment. First, we need to extract the critical background regions. Then, the critical foreground regions are extracted in the second step. In the third step, we apply these critical regions to the sky segmentation.

Critical background region extraction. Due to the backgrounds of the silhouette images are almost skies, we propose a local regions similarities based critical background region extraction algorithm that is suitable for this semantic. The local regions are extracted by the improved BPLRs detector [16] firstly. And then, considering the obvious color features of the sky, we calculate the features of each local region by color histograms. Finally, the critical regions of the background are found by feature matching.

BPLRs detector is a dense local region detector that can produce repeatable shape-preserving regions. In our BPLR implementation, L_0 smoothing [17] is used to smooth the image firstly. It can effectively eliminate noise and unimportant details by removing small non-zero gradients, so as to facilitate the subsequent BPLRs detection. Then, we use [18] for fast edge detection to ensure that the detected local regions do not cross the edge. In addition, the areas of the detected regions can be automatically adjusted according to the resolution of the image in our method.

We detect BPLRs from images in the sky image set created by us, and extract the color histogram from the BPLRs thereafter. The BPLRs detection and features extraction of the images in the set are all processed in advance. Similarly, for each input image, we detect BPLRs of it and extract the color histogram features of the BPLRs. Then the features of the input image are matched with the pre-processed features in the sky image set by k-nearest neighbors algorithm. We find the 50 best matches, and use the corresponding local regions as the critical background regions.

Critical foreground region extraction. Since the foregrounds of the silhouette photos are often humans or animals with obvious outlines, we use the salient region detection algorithm [19] to obtain the high quality saliency map, and then the salient object regions can be obtained by threshold segmentation of the saliency map. These salient object regions are treated as the critical foreground regions in our sky segmentation method.

Segmentation. Instead of the cumbersome manual annotation, the critical regions automatically obtained by the above steps are used as the inputs of the OneCut, thereby the automatic sky segmentation based on OneCut is realized. In addition, considering the dependence of our silhouette stylization algorithm on the outline of the object, we optimize the segmentation result using dense CRFs [20]. Then we can get silhouette images by the color transfer method introduced in Sect. 2.2. The processes of sky segmentation are shown in Fig. 2.

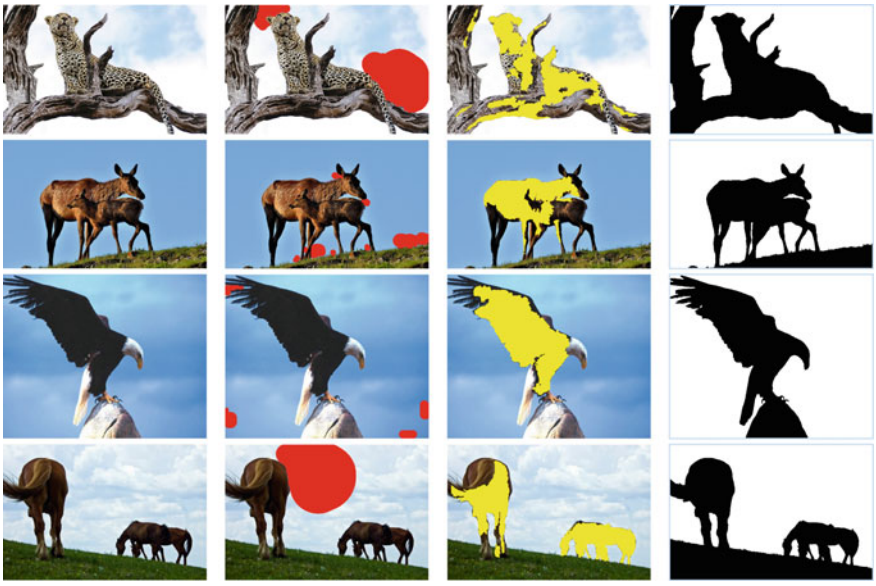

Fig. 2 The processes of sky segmentation

2.2 Color Transfer

In this subsection, we introduce the proposed color transfer algorithms. Initial segmentation results obtained by the previous steps are coarse around boundaries. In practice, smooth filter [21, 22] is widely used to ensure the smoothness of the image. We employ guided filter [22] to ensure the edge smooth.

Based on the human visual characteristic and the perception of image, the luminance and the chrominance are completely independent in the LAB color space. For natural scenes, the correlation between channels in LAB color space will be reduced to the minimum, which is more suitable for human visual systems. Therefore, the entire color transfer process is implemented in LAB color space.

Given an input image I, we first convert it from RGB to LAB color space. And then, the foreground and the background are transferred respectively. To generate a natural transition between the foreground and the background of the silhouette stylization image, we add the likelihood into the transferring process. We can obtain the likelihood value on pixel x for foreground/background based on the guided filter according to the equation:

$$P_b(x) = \boldsymbol{g}(x)/255, \tag{1}$$

$$P_f(x) = 1 - P_b(x), \tag{2}$$

where $g(x)$ denotes the gray value of the segmentation mask on pixel x after guided filtering, it ranges from 0 to 255. Among them, pixel whose gray value is neither 0 nor 255 belongs to the transition region and will participate in both the background color transfer and the foreground color correction. $P_b(x)$ and $P_f(x)$ are the likelihood values on pixel x for background/foreground.

Background Color Transfer. Considering the semantic consistency in the background color transfer process, we only transfer color statistics from a referred sky photo to the background of input. The referred sky photo should be shot at morning or evening with rich and colorful sun glow.

For luminance, we formulate the transfer process similar to [10] as follows:

$$L_b^O(x) = L_b^I(x) + P_b(x) \times \hat{L}, \tag{3}$$

where $L_b^I(x)$ and $L_b^O(x)$ are the background luminance of input/output at pixel x. Then the new desired mean of luminance can be computed as:

$$\hat{L} = \beta\left(L_b^R - L_b^I\right), \tag{4}$$

where L_b^I and L_b^R denote the means of background luminance of the input/reference. Here β is defined as:

$$\beta = \tanh\left(\left|C_b^I - C_b^R\right|\right), \tag{5}$$

where C_b^I and C_b^R are the means of background chrominance of the input/reference. It shows that we will retain the luminance of the input when the backgrounds are similar, and adjust more luminance to match the reference backgrounds when the input and reference backgrounds are significantly different.

For chrominance, the transfer algorithm is similar to the regularized matching method of [4]. It models the chrominance distributions using the multivariate Gaussian and maps the Gaussian statistics $\mathcal{N}_b^R\left(\mu_b^R, \Sigma_b^R\right)$ of the reference sky to $\mathcal{N}_b^I\left(\mu_b^I, \Sigma_b^I\right)$ of the input background as:

$$C_b^O(x) = P_b(x) \times \left(T\left(C_b^I(x) - \mu_b^I\right) + \mu_b^R\right) \quad s.t. \quad T\Sigma_b^I T^{\mathrm{T}} = \Sigma_b^R, \tag{6}$$

where $C_b^O(x)$ and $C_b^I(x)$ are the background chrominance of the output/input at pixel x. T is a linear transformation that maps chrominance between these two regions. To avoid color artifacts, the clipping diagonal elements of Σ_b^I are regularized as:

$$\Sigma_b^{I'} = \max\left(\Sigma_b^I, \lambda_r \mathbb{I}\right), \tag{7}$$

where $\mathbb{I}$ is an identity matrix and $\lambda_r = 7.5$. Then, the color transform can be solved by following [3] as:

$$T = \Sigma_b^{I'-1/2}\left(\Sigma_b^{I'1/2}\Sigma_b^R\Sigma_b^{I'1/2}\right)^{1/2}\Sigma_b^{I'-1/2} \tag{8}$$

Foreground Color Correction. Although using the segmentation mask as the foreground of the stylization image directly conform to the concept of silhouette, we find that it would lead to a stiff result. Therefore, considering the artistic features of silhouette photography, we take the following adaptive color correction method for the foreground according to the ambient color to make the result can not only coordinate with the background, but also produce the halo at the edge of the foreground.

After color transfer, we first find the background luminance and chrominance ranges and the foreground luminance and chrominance ranges of the input respectively. Then, the values in the ranges of the foreground are mapped by the curve $s = cr^{\gamma}$ to the ranges of the background. Here, in order to ensure that the foreground after color correction is as dark as possible, we set $c = 1$, $\gamma = 50$. Since the foreground of the silhouette images are usually omitted in the internal details, we take uniform values for the luminance and chrominance respectively. Thus, the foreground luminance and chrominance of output images at pixel x can be obtained by:

$$L_f^O(x) = P_f(x) \times L_f^{I'}/2, \tag{9}$$

$$C_f^O(x) = P_f(x) \times \left(C_b^O + C_f^{I'}\right)/2 \tag{10}$$

where $L_f^{I'}$ and $C_f^{I'}$ are the mean values of the input foreground luminance and chrominance after mapping, and C_b^O is the mean value of the output background chrominance, which is calculated from the above background color transfer. Finally, for each pixel in the transition region, we combine its color transfer result and color correction result together as shown in Sect. 3.2.

3 Results

In this section, we will firstly evaluate our sky segmentation method, and then test the effectiveness of the silhouette photo style transfer approach.

3.1 Evaluations of Sky Segmentation

Since the existing datasets do not meet our requirements, we built a small dataset containing 45 images of animals, characters, and scenery with skies as the backgrounds to verify the effectiveness of our sky segmentation algorithm. These images contain 34 images downloaded from the Internet and 11 images selected from the

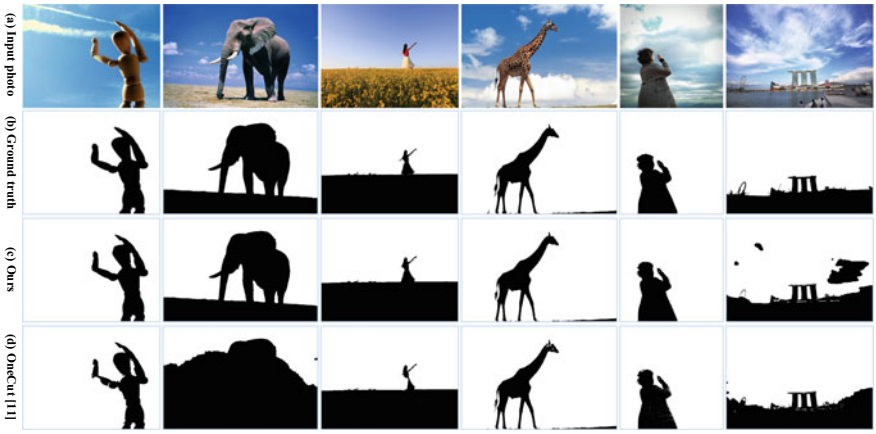

Fig. 3 Sky segmentation results

MSRA1K dataset [23] that meet our requirements. We manually marked the ground truth.

We compare our segmentation algorithm with OneCut [11] which is given enough annotations by us. In the stage of critical foreground region extraction, the pixel values of a saliency map obtained by [19] range from 0 to 255. The larger the pixel values are, the more salient the regions will be. In practice, we set the threshold as 220 empirically. Some sky segmentation results are visualized in Fig. 3. We can find that our segmentation method not only removes the artificial interaction, but also improves the segmentation results for most images.

Although the proposed segmentation algorithm usually performs better than the original OneCut, it will be influenced by the effects of the saliency detection. The segmentation results of some landscapes are not satisfactory resulting from the poor saliency detection (see the last column of Fig. 3). For future work, we intend to improve the robustness of our sky segmentation method.

3.2 Performance of Silhouette Photo Style Transfer

We test our silhouette photo style transfer method using sky photos shot at dawn or dusk, as shown in Fig. 4. For comparisons, we also provide the results without foreground color correction (see Fig. 4d) and results by other two style transfer methods [1, 2] (see Fig. 4e, f). Obviously, the results without foreground color correction are stiffly. From the visual effect, results in Fig. 4e are not realistic, and cannot show the effects of clouds. We can also find that each image in Fig. 4f has some distortions of details, which are sometimes unbearable for users. The results of our algorithm not only avoid the distortions, but also highlight the optic artistry characteristics of

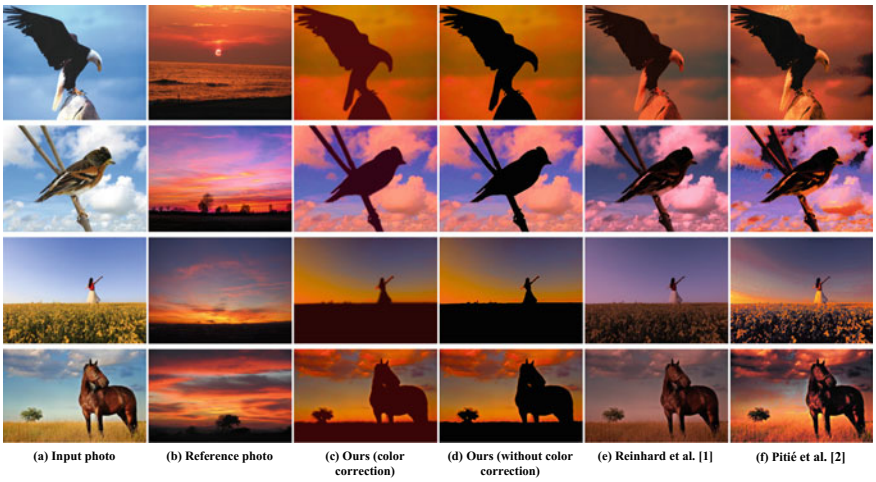

Fig. 4 Silhouette photo style transfer results

silhouette photography and produce soft effects on the edge of the foreground object. Since our algorithm is the first attempt in the computer simulation of silhouette photography style, there is no existing method to compare from the point of silhouette photo style.

4 Conclusion

In this paper, we propose a novel approach to transferring silhouette photo style for images. Differing from other photo style transfer methods, we emphasize the contrast of the foreground and background, which is characterized in silhouette photos. To achieve this, we present an automatic sky segmentation method and apply color transfer methods. We also develop an adaptive foreground color correction method to harmonize the foreground and background. Experiments show that our system can achieve good performance on generating images in silhouette photo style. For future work, we would like to further improve the sky segmentation method because our transfer approach demands accurate segmentation.

Acknowledgements This work is supported by National Natural Science Foundation of China (Grant No. 61572064 and 61672089).

References

1. Reinhard, E., Adhikhmin, M., Gooch, B., et al.: Color transfer between images. IEEE Comput. Graph. Appl. **21**(5), 34–41 (2001)
2. Pitié, F., Kokaram, A.C., Dahyot, R.: N-dimensional probability density function transfer and its application to color transfer. In: Tenth IEEE International Conference on Computer Vision, vol. 2, pp. 1434–1439 (2005)
3. Pitié, F., Kokaram, A.: The linear Monge-Kantorovitch linear color mapping for example-based color transfer. In: European Conference on Visual Media Production, pp. 1–9 (2008)
4. Lee, J.Y., Sunkavalli, K., Lin, Z., et al.: Automatic Content-aware color and tone stylization. In: IEEE Conference on Computer Vision and Pattern Recognition, pp. 2470–2478 (2016)
5. Lu, H., Li, Y., Mu, S., Wang, D., et al.: Motor anomaly detection for unmanned aerial vehicles using reinforcement learning. IEEE Internet Things J. **PP**(99), 1–1 (2017)
6. Lu, H., Li, Y., Chen, M., Kim, H., Serikawa, S.: Brain intelligence: go beyond artificial intelligence. In: Mobile Networks and Applications, pp. 1–8 (2017)
7. Gatys, L.A., Ecker, A.S., et al.: Image style transfer using convolutional neural networks. In: IEEE Conference on Computer Vision and Pattern Recognition, pp. 2414–2423 (2016)
8. Luan, F., Paris, S., Shechtman, E., Bala, K.: Deep photo style transfer. In: IEEE Conference on Computer Vision and Pattern Recognition, pp. 6997–7005 (2017)
9. Tao, L., Yuan, L., Sun, J.: SkyFinder: attribute-based sky image search. ACM Trans. Graph. **28**(3), 68 (2009)
10. Tsai, Y.H., Shen, H., Lin, Z., Sunkavalli, K., Yang, M.H.: Sky is not the limit: semantic-aware sky replacement. ACM Trans. Graph. **35**(4), 149 (2016)
11. Tang, M., Gorelick, L., Veksler, O., Boykov, Y.: GrabCut in One Cut. In: IEEE International Conference on Computer Vision, vol. 2013, pp. 1769–1776 (2013)
12. Boykov, Y.Y., Jolly, M.P.: Interactive graph cuts for optimal boundary & region segmentation of objects in N-D images. In: IEEE International Conference on Computer Vision, vol. 1, pp. 105–112 (2001)
13. Cheng, M.M., Prisacariu, V.A., Zheng, S., Torr, P.H.S., et al.: DenseCut: densely connected CRFs for realtime GrabCut. Comput. Graph. Forum **34**(7), 193–201 (2015)
14. He, K., Gkioxari, G., Dollár, P., Girshick, R.: Mask R-CNN. In: IEEE International Conference on Computer Vision, pp. 2980–2988 (2017)
15. Lu, H., Li, B., Zhu, J., Li, Y., Li, Y., Xu, X., et al.: Wound intensity correction and segmentation with convolutional neural networks. Concurr. Comput. Pract. Exp. **29**(6), e3927 (2017)
16. Kim, J., Grauman, K.: Boundary preserving dense local regions. In: IEEE Conference on Computer Vision and Pattern Recognition, vol. 37, pp. 1553–1560 (2011)
17. Xu, L., Lu, C., Xu, Y., Jia, J.: Image smoothing via L_0 gradient minimization. ACM Trans. Graph. **30**(6), 174 (2011)
18. Zitnick, C.L.: Structured forests for fast edge detection. In: IEEE International Conference on Computer Vision, pp. 1841–1848 (2014)
19. Cheng, M.M., Mitra, N.J., Huang, X., Torr, P.H.S.: Global contrast based salient region detection. IEEE Trans. Pattern Anal. Mach. Intell. **37**(3), 569–582 (2015)
20. Krähenbühl, P., Koltun, V.: Efficient inference in fully connected CRFs with Gaussian edge potentials. In: Advances in Neural Information Processing Systems, pp. 109–117 (2011)
21. Serikawa, S., Lu, H.: Underwater image dehazing using joint trilateral filter. Comput. Electr. Eng. **40**(1), 41–50 (2014)
22. He, K., Sun, J., Tang, X.: Guided image filtering. IEEE Trans. Pattern Anal. Mach. Intell. **37**(6), 1397–1409 (2013)
23. Achanta, R., Hemami, S., Estrada, F., Susstrunk, S.: Frequency-tuned salient region detection. In: IEEE Conference on Computer Vision and Pattern Recognition, pp. 1597–1604 (2009)

Improved Rao-Blackwellised Particle Filter Based on Randomly Weighted PSO

Ye Zhao, Ting Wang, Wen Qin and Xinghua Zhang

Abstract In this paper, a new RBPF-SLAM based on randomly weighted PSO (Particle Swarm Optimization) is proposed in order to solve some problems in the Rao-Blackwellised particle filter (RBPF), including the depletion of particles and loss of diversity in the process of resampling. PSO optimization strategy is introduced in the modified algorithm, inertia weight is randomly set. Modified PSO is utilized to optimize the particle set to avoid particle degenerating and keep diversity. The proposed algorithm is used in the Qt platform to do simulation and verified in ROS by turtlebot. Results show that the proposed RBPF outperform RBPF-SLAM and FastSLAM2.0.

Keywords Mobile robot · Particle swarm optimization · RBPF · FastSLAM Turtlebot

1 Introduction

Artificial intelligence (AI) becomes a vital technology that contributes to economy and social development. Huimin et al. [1] introduced the concept of Brain Intelligence (BI), BI model is a model fusing artificial intelligence and artificial life that can solve the issues of frame. Simultaneous Localization and Mapping means that a mobile robot calculates its own position with sensor information and builds surrounding

Y. Zhao · T. Wang (✉) · W. Qin · X. Zhang
College of Electrical Engineering and Control Science,
Nanjing Tech University, Nanjing, Jiangsu Province, China
e-mail: wangting0310@njtech.edu.cn

Y. Zhao
e-mail: zhaoye110@njtech.edu.cn

W. Qin
e-mail: qinwen.wts@njtech.edu.cn

X. Zhang
e-mail: zxhnjut@163.com

H. Lu (ed.), *Cognitive Internet of Things: Frameworks, Tools and Applications*, Studies in Computational Intelligence 810,
https://doi.org/10.1007/978-3-030-04946-1_3

environment model at the same time, without environment prior information [2]. For uncertain environment, SLAM can be described by probabilistic method and do state estimation [3]. SLAM problems based on probabilistic method can be divided into two types: Kalman Filter and Particle Filter. Extended Kalman Filter(EKF) is a linearization KF for nonlinear model. Unscented Kalman Filter (UKF) uses unscented transform to linearize motion and measurement model [4, 5], UKF does not need to calculate Jacobian matrix, but it has limitation in highly non-gaussian distribution.

Particle Filter (PF) is non-parametric implementation of Bayesian Filter. It uses finite parameters to approximate posterior probability density distribution [6]. To solve the problem of low efficiency and huge computation complexity, Murphy et al. proposed Rao-Blackwellised Particle Filter method to solve SLAM problem [7]. RBPF algorithm uses particle filter in robot pose estimation phase and uses Kalman Filter to estimate its probability in map estimation phase. RBPF-SLAM is also called FastSLAM.

Particle Swarm Optimization (PSO) is a kind of swarm intelligent algorithm [8]. This method uses two extremum values to update particle set. Moreover, the algorithm can converge to the global optimal solution with larger probability. To solve the problem of particle depletion, PSO is chosen to do optimization and genetic variation is introduced to guarantee the variety of particles [9–11].

In this works, we propose a new RBPF-SLAM algorithm based on modified particle swarm optimization. Randomly weighted PSO algorithm is added into original RBPF-SLAM framework where we set weight as random value in PSO. The new method can achieve the optimal initial particles and can randomly produce a small weight value to accelerate the convergence velocity of this algorithm. The experiment results show that the map of the improved algorithm is more accurate and smooth. Our main contributions include keeping the variety of particles, avoiding particles scarcity problem and improving the efficiency and precision of RBPF-SLAM.

The rest of the paper is organized as follows: Sect. 2 explain the structure of SLAM, Sect. 3 introduces our proposed method and explains details under four subsections. In Sect. 4, we are going to explain both our simulation and real- world experiments. Finally, we are going to conclude and talk about future work in Sect. 5.

2 Problem Statement

In this section, we briefly introduce the formulation and structure of SLAM problem. We illustrate the problem using the Fig. 1, as most systems did. It is natural to express our idea in the structure of SLAM. SLAM is a process that a mobile robot estimates its own position and builds a map of its surrounding environment at the same time [12].

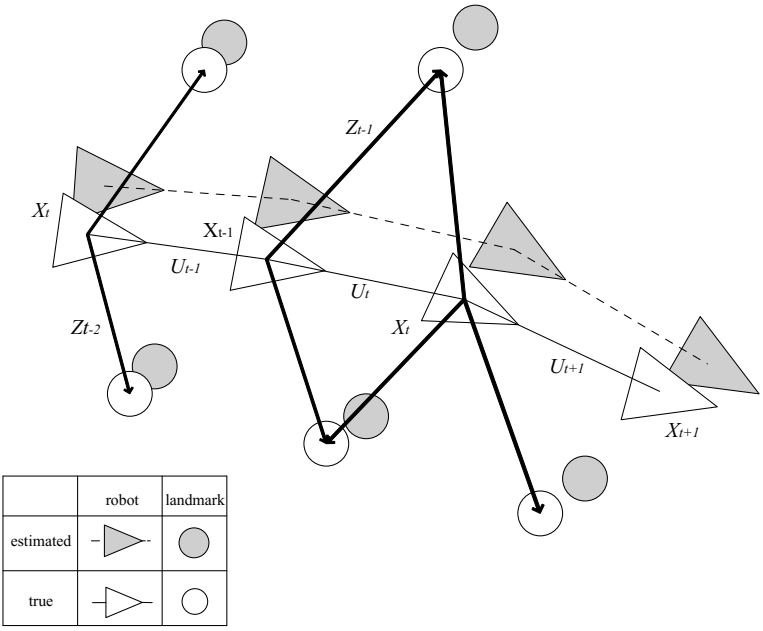

Fig. 1 The fundamental SLAM process

During the process of SLAM, the mobile robot estimates the position of all landmarks, using a sensor on the robot. At time instant t, some variables are defined as follows [13]:

X_t: The state vector describing the position of the robot.
U_t: The control vector, from the odometry, used at time $t-1$ to make the robot move to a state X_t at time t.
Z_{it}: Observation information got from the vehicle of the ith landmark at time t.

In addition, we can also define relative sets as follows:

$X_{0:t} = \{X_0, X_1, \ldots, X_t\} = \{X_{0:t-1}, x_t\}$: The set of robot locations.
$U_{0:t} = \{u_1, u_2, \ldots, u_k\} = \{U_{0:t-1}, u_t\}$: The set of control inputs.
$Z_{0:t} = \{z_1, z_2, \ldots, z_k\} = \{Z_{0:t-1}, z_t\}$: The set of all observation information.

3 Randomly Weighted PSO Based Rao-Blackwellised Particle Filter

3.1 Rao-Blackwellised Particle Filter Algorithm

3.1.1 Particle Filter

Particle filter is a nonparametric approach for approximating posterior probability distribution, using a group of random state samples, these samples of a posterior distribution are called particles, and they have corresponding non-negative importance weight, where M is the number of particles at time t in particle set S. Each particle represents one potential state the system might be in. The sum of particles' weights is 1.

$$S_t : \left\{ \left(x_t^{[1]}, \omega_t^{[1]} \right), \ldots, \left(x_t^{[M]}, \omega_t^{[M]} \right) \right\}$$

There are three steps in particle filter: prediction, likelihood weighting, and resampling. During predicting, particle filter will draw samples from the previous samples set with the probability given by importance weighting factor. The particle filter resamples the samples from the current sample set S_t. However, the Particle Filter still suffers from some deficiencies: 1. The resampling process removes these parts of particles and replace them with a high weight, and some important samples are lost, causing particle depletion problem. 2. In the high dimensional estimation, the computed complexity grows exponentially in the dimensions with the state space.

3.1.2 Rao-Blackwellised Particle Filter

Particle filter can be theoretically distributed by any probability. However, when facing high-dimensional state SLAM problem, particle filter method may be useless. Another method that can efficiently reduce the dimension of sample space is Rao-Blackwellised Particle Filter method. Rao-Blackwellised Particle Filter method has more accurate estimation than standard filter.

Map probability can be analytically calculated by robot path. The joint probability distribution can be decomposed into the following form:

$$p(x_{1:t}, m|z_{1:t}, u_{0:t-1}) = p(x_{1:t}|z_{1:t}, u_{0:t-1}) p(m|x_{1:t}, z_{1:t}) \tag{1}$$

where, $x_{1:t} = x_1, x_2, \ldots, x_t$, represents robot trajectory, m represents map, $z_{1:t} = z_1, z_2, \ldots, z_t$ are latest observation data, $u_0, u_1, \ldots, u_{t-1}$ are past information controlled by odometry. $p(x_{1:t}, m|z_{1:t}, u_{0:t-1})$ is the probability distribution that describes the joint posterior of the landmark and robot state at time t. $p(x_{1:t}|z_{1:t}, u_{0:t-1})$ is similar to probability in the Monte Carlo localization algorithm,

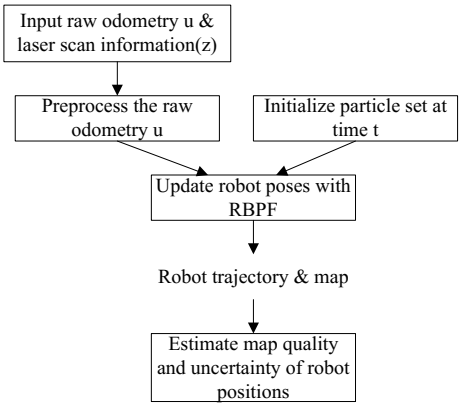

Fig. 2 The framework of RBPF-SLAM

it is the estimation of robot trajectory. In the Rao-Blackwellised Particle Filter, each particle owns a map. In $p(m|x_{1:t}, z_{1:t})$, map m uses observation information $z_{1:t}$ and robot trajectory $x_{1:t}$ to update. RBPF algorithm is divided into four steps: 1. prediction, 2. calculating likelihood weight, 3. resampling, 4. map estimation. Laser stabilized the odometry information after raw odometry information and laser scan measurement were input. In calculating likelihood weight, weight samples according to the importance function: $\omega_t^{(i)} = \omega_{t-1}^i \frac{P\left(x_{1:t}^{(i)}|z_{1:t},u_{1:t-1}\right)}{\pi\left(x_{1:t}^{(i)}|z_{1:t},u_{1:t-1}\right)}$. Resampling is completed by selecting particles with replacement, if efficient particles (N_{eff}) is less than threshold value ($N_{threshold}$), so particle with low weight will be replaced. Robot trajectory and map are achieved by RBPF-SLAM combined with particles set and corrected odometry and laser scan measurement. Finally, trajectory of particles ($x_{1:t}$) and observation information ($z_{1:t}$) are used for map updating, and we can estimate map quality and uncertainty of robot position. In fact, the approach for a robot SLAM based on Rao-Blackwellised particle filters is shown in the Fig. 2.

3.2 RBPF Based on Randomly Weighted PSO

3.2.1 Particle Swarm Optimization

Particle swarm filter algorithm is to simulate animal predation behavior. PSO starts from random solution, evaluates the quality of solution by fitness function, and follows optimal value which is currently searched to find the global optimal value. All particles have a fitness value decided by objective function. And each particle has velocity that can decide their direction and distance. PSO initializes a group of random particles, and finds optimal solution by iteration. In the iteration, particles achieve their own best value (pbest), this is an individual extremum. In addition, PSO can achieve the global best position information of all particles in the group, this extremum is a global extremum.

Assuming that in the N dimension target search space, position vector of particle i can be described as: $X_i = (x_{i1}, x_{i2}, \ldots, x_{iN})$, the local best position of particles for each iteration can be described as: $p_{best} = (p_{i1}, p_{i2}, \ldots, p_{iN})$, global best position of the whole particle swarm is described as: $g_{best} = \left(p_{g1}, p_{g2}, \ldots, p_{gN}\right)$. After k iteration, PSO can update its own velocity and position according to the equation in the below:

$$x_{id}^{k+1} = x_{id}^{k} + \omega_1 \cdot v_{id}^{k} + c_1 r_1 \left(p_{id} - x_{id}^{k}\right) + c_2 r_2 \left(p_{gd} - x_{id}^{k}\right) \tag{2}$$

3.2.2 RBPF Based on Randomly Weighted PSO

RBPF based on randomly weighting can be simply described as: for the nonlinear part of the state, this modified algorithm moves all sampling particles to the high likelihood region by utilizing PSO algorithm, for the linear part of the state, this algorithm still uses Kalman filter to deal with.

This paper uses a modified RBPF based on PSO, this method sets the inertia weight ω_1 in the standard PSO to a random number, so we call this method as random weighting particle swarm optimization method [15], n the following equation, $rand(0, 1)$ is a random distribution.

The method to update weight is:

$$\omega_1 = \mu + \sigma * N(0, 1) \tag{3}$$

$$\mu = \mu_{\min} + \left(\mu \max - \mu_{\min}\right) * rand(0, 1) \tag{4}$$

The details of RBPF based on random weight are shown below:

step 1: estimating robot state particle set $\left\{x_t^{(1)}, \ldots, x_t^{(i)}, \ldots, x_t^{(N)}\right\}$ according to robot pose $\left\{x_{t-1}^{(1)}, \ldots, x_{t-1}^{(i)}, \ldots, x_{t-1}^{(N)}\right\}$ and information controlled by odometry u_{t-1}.

step 2: doing particle swarm iteration, further adjusting and optimizing the state particle set, using Eq. (2) to adjust, updating weight ω_1 in the equation according to Eqs. (3) and (4), moving the particles toward the region of high likelihood functions.

step 3: executing step 2 until the co-variance is lower than a value we set, or iteration times are up to max times we set, executing step 4 next.

step 4: scanning match according to map $m_{t-1}^{(i)}$.

step 5: calculating weight of particles, $\omega_t^{(i)} = \omega_{t-1}^{(i)} \frac{P\left(x_{1:t}^{(i)} | z_{1:t}, u_{1:t-1}\right)}{\pi\left(x_{1:t}^{(i)} | z_{1:t}, u_{1:t-1}\right)}$.

step 6: replacing particles with small weight and improving particle scarcity phenomenon.

step 7: resampling, calculating N_{eff}, judging whether to do resampling, when N_{eff} is smaller than $N_{threshold}$, needing resampling.

step 8: calculating $p(m|x_{1:t}, z_{1:t})$ according to robot pose x_t^i and observation information z_t, and updating map m.

4 Experiments

We investigate the performances from the simulations and real-world experiments. Simulations are implemented by Qt that is a software for developing GUI program. The practical experiments are based on a turtlebot 2 mobile robot equipped with a laser range sensor (hokuyo URG-04LX-UG01) and pose odometry.

4.1 Simulation Experiments

To illustrate the effectiveness of the improved algorithm, we have done simulation experiments on Qt platform. We used the dataset from the Australian Centre for Field Robotics for simulation research. The size of environmental map in the simulation is 200 m $\times$ 160 m, including 50 waypoints. In the simulation, we configurate the robot speed as 3 m/s, the observation interval as 200 ms and control interval as 25 ms. Moreover, we set the initial position and the global target point.

In the simulation, we make the robot move at the speed of 3 m/s, the observation interval is 200 ms and control interval is 25 ms. The laptop parameters are as follows, memory 3 GB and CPU 2.4 GHz. After initialized, the robot moves according to the target point of the global setting, until it reaches the target point after a cycle.

In the simple simulation environment above, after initialized, the robot moves according to the target point of the global setting, until it reaches the target point after a cycle. The initial set up is shown in Fig. 3a, where "*" represents actual position of landmarks, "." represents estimation position of landmarks. Then we test RBPF algorithm and our method. The robot moves along the landmarks for two circles. Figure 3b shows that there are differences between estimated position and actual position of landmarks when RBPF algorithm is used. By contrast, estimated landmarks position based on improved RBPF coincides with actual landmarks very well as in Fig. 3c described. Thus it indicated that the estimated trajectories of the improved algorithm coincide very well with the true values, and are better than those of produced by Fast SLAM algorithm. From the Table 1, we can see that under the circumstance that same particles in the different experiment, improved RBPF has less running time, and its RMSE is relatively lower.

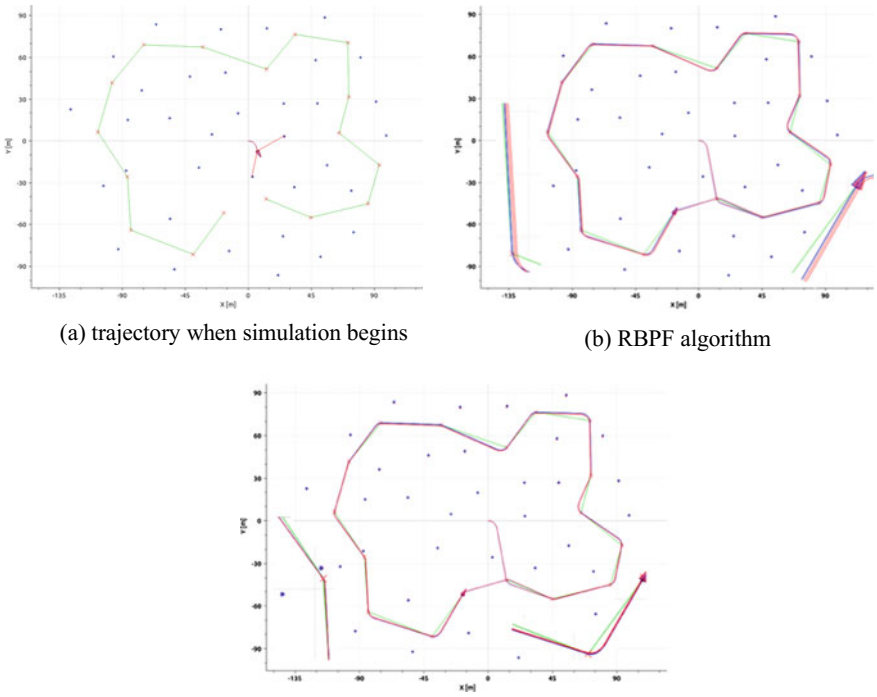

(a) trajectory when simulation begins

(b) RBPF algorithm

(c) improved RBPF

Fig. 3 Results of different algorithms in the simple environment

Table 1 Comparison of computation complexity of SLAM algorithm

Algorithm	Number of particles	RMSE	Running Time
RBPF	100	3.091	235.14
Improved RBPF	100	1.996	134.25

4.2 Field Experiments

To validate the validity of the algorithm above, we use turtlebot2 mobile robot to do actual verification in indoor environment and finish SLAM. There is a odometry to estimate its ego-motion. The laser (hokuyo URG-04LX-UG01) is installed to collect the 2D scan. ROS is installed on Ubuntu 14.04.

The real experiment was carried out in a scenario with the robot performing SLAM in the corridors of Nanjing Tech University. The selected area is 8.4 m * 2.4 m. The turtlebot moves at the speed of 2 m/s. Figure 4 shows the experimental device (Fig. 5).

We compare two algorithms in the field experiments. Figure 6a describes the map built by basic RBPF-SLAM method with 100 particles. The map is coarse and some points have flown out because of the scarcity of particles. Figure 6b describes the

Fig. 4 Experiment facility (turtlebot + hokuyo URG-04LX-UG01 + PC)

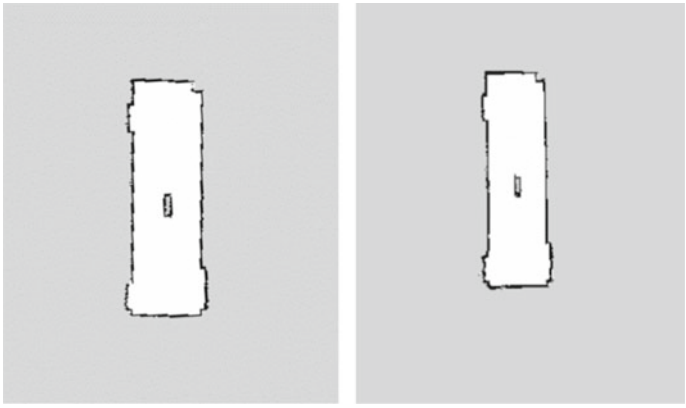

(a) original RBPF-SLAM **(b)** RBPF-SLAM based on PSO

Fig. 5 Results of different algorithms in the simple field environment

map in the same environment created by PSO based RBPF-SLAM algorithm. It can be seen that the map created by improved algorithm is more accurate. Experiment results show that the improved RBPF has more precise map.

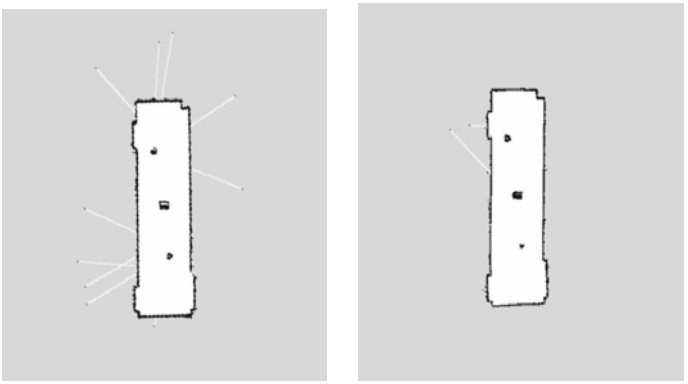

(a) original RBPF-SLAM **(b)** RBPF-SLAM based on PSO

Fig. 6 Results of different algorithms in the complex field environment

5 Conclusion

To solve the problem of particles degeneration and its diversity degradation in the RBPF algorithm, we proposed a modified RBPF-SLAM algorithm based on PSO. After initializing particles in the RBPF-SLAM, it iterates all particles in the swarm, adjusts and optimizes the particle set furtherly to make particles move towards area with high likelihood function. So it improves the phenomenon of particle scarcity. We compared two algorithms on Qt platform with simulation experiment and found that the improved algorithm can reduce errors in trajectories and landmarks estimation. Furthermore, we verified the two methods through field experiments which used turtlebot and ROS. The modified RBPF-SLAM algorithm can get more precise map. In the future work, we will do research on the efficiency of mapping and extend this new algorithm on multi-robot system.

References

1. Huimin, L., Yujie, L., Min, C., Hyoungseop, K., Seiichi, S.: Brain intelligence: go beyond artificial intelligence. Mob. Netw. Appl. **7553**, 1–8 (2017)
2. Andrew, J.D., Ian, D.R., Nicholas, D.M., Olivier, S.: MonoSLAM: real-time single camera SLAM. IEEE Trans. Pattern Anal. Mach. Intell. **29**(6), 1052–1067 (2007)
3. Sebastian, T., Wolfram, B., Dieter, F.: Probabilistic Robotics. MIT Press (2005)
4. Huimin, L., Yujie, L., Shenglin, M., Dong, W., Hyoungseop, K., Seiichi, S.: Motor anomaly detection for unmanned aerial vehicles using reinforcement learning. IEEE Internet Things J. **99**, 1–1 (2017)
5. Doucet, A., Johansen, A.M.: A tutorial on particle filtering and smoothing: fifteen years later. In: Handbook of Nonlinear Filtering, vol. 12, pp. 656–704 (2009)
6. Kim, C., Sakthivel, R., Chung, W.K.: Unscented FastSLAM: a robust and efficient solution to the SLAM problem. IEEE Trans. Robot. **24**(4), 808–820 (2008)

7. Kennedy, J.: Particle swarm optimization. In: Encyclopedia of Machine Learning, pp. 760–766 (2011)
8. Chatterjee, A., Matsuno, F.: A Geese PSO tuned fuzzy supervisor for EKF based solutions of simultaneous localization and mapping (SLAM) problems in mobile robots. Expert Syst. Appl. **37**(8), 5542–5548 (2010)
9. Seiichi, S., Huimin, L.: Underwater image dehazing using joint trilateral filter. Comput. Electr. Eng. **40**(1), 41–50 (2014)
10. Huimin, L., Bin, L., Junwu, Z., Yujie, L., Yun, L., Xing, X., Li, H., Xin, L., Jianru, L., Seiichi, S.: Wound intensity correction and segmentation with convolutional neural networks, Concurr. Comput. Pract. Exp. **29**(6) (2017)
11. Tim, B., Hugh, D.W.: Simultaneous localization and mapping (SLAM): part II. IEEE Robot. Autom. Mag. **13**(3), 108–117 (2006)
12. Jung-Suk, L., Chanki, K., Chung, W.K.: Robust RBPF-SLAM using sonar sensors in non-static environments. In: 2010 IEEE International Conference on Robotics and Automation(ICRA), pp. 250–256 (2010)
13. Pavithra, S., Bhuvaneswari, PTV.: PSO based obstacle detection for indoor cleaning robot, In: 2017 Third International Conference on Sensing, Signal Processing and Security (ICSSS), pp. 339–344 (2017)

Local Binary Pattern Metric-Based Multi-focus Image Fusion

Wenda Zhao, Weiling Yin, Di You and Dong Wang

Abstract Multi-focus image fusion is to integrate the partially focused images into one single image which is focused everywhere. Nowadays, it has become an important research topic due to the applications in more and more scientific fields. However, preserving more information of the low-contrast area in the focus area and maintaining the edge information are two challenges for existing approaches. In this paper, we address these two challenges with presenting a simple yet efficient multi-focus fusion method based on local binary pattern (LBP). In our algorithm, we measure the clarity using the LBP metric and construct the initial weight map. And then we use the connected area judgment strategy (CAJS) to reduce the noise in the initial map. Afterwards, the two source images are fused together by weighted arranging. The experimental results validate that the proposed algorithm outperforms state-of-the-art image fusion algorithms in both qualitative and quantitative evaluations, especially when dealing with low contrast regions and edge information.

Keywords Multi-focus image fusion · Local binary pattern
Connected area judgment strategy · Preserving the low-contrast area information
Maintaining the edge information

W. Zhao (✉) · W. Yin · D. You · D. Wang
School of Information and Communication Engineering,
Dalian University of Technology, Dalian, China
e-mail: zhaowenda@dlut.edu.cn

W. Yin
e-mail: weiling@mail.dlut.edu.cn

D. You
e-mail: 2461328309@mail.dlut.edu.cn

D. Wang
e-mail: wdice@dlut.edu.cn

H. Lu (ed.), *Cognitive Internet of Things: Frameworks, Tools and Applications*, Studies in Computational Intelligence 810,
https://doi.org/10.1007/978-3-030-04946-1_4

1 Introduction

Due to the limited depth of field of commonly used optical lenses, objects of different distances cannot be fully focused by the imaging device. However, an image with all the clear objects in the same scene is needed in application. Multi-focus image fusion, which combines the supplementary information of multiple images to form a visually perceived and high-quality image, is an effective way to solve this problem. Currently, multi-focus image fusion has been widely used in object recognition [1] and microscopic imaging [2], etc. also makes it a hot topic in the field of image processing.

In recent years, scholars have proposed many effective multi-focus image fusion algorithms. These methods can be roughly divided into two categories: transform domain-based and spatial domain-based multi-focus image fusion. Transform domain-based methods usually adopt the following strategy. The source images are firstly transformed into a sort of transform domain. Then, the fusion rules are structured to combine the transformed coefficients. Finally, the inverse transform is performed to obtain the fused image. The transformation strategy is important for achieving good multi-focus image fusion, and researchers have proposed many transformation strategies [3–13]. For instance, Yang et al. [6] proposed an image fusion method based on NSCT and focused area detection. Zhang et al. [8] introduced a multi-task robust sparse representation (MRSR) model to address the fusion of multi-focus images with misregistration. However, some flaws exist in these methods based on transform domain. One of them is that some information in low-contrast areas can be easily lost, because deviations are often generated when reconstructing a fused image.

The spatial domain-based multi-focus image fusion methods directly fuse the gray levels of image pixels. At present, the proposed methods include image matting-based method [14], steerable local frequency-based method [15], content adaptive blurring (CAB)-based method [16], the edge model and multi-matting (EMAM)-based method [17], convolutional neural network (CNN)-based methods [18, 19], and multi-scale morphological focus-measure-based method [20], and so on. Nejati et al. [21] proposed a focus measure based on the surface area of regions surrounded by intersection points of input source images. Li et al. [22] proposed a novel guided filtering-based weighted average technique to make full use of spatial consistency for fusion of the base and detail layers. The difference in their approaches is the sharpness measurement, which is the core issue in spatial domain-based image fusion algorithms.

To effectively fuse multi-focus images, the following two features of sharpness measurements are necessary. First, the metric should have good monotonicity, which makes metric value accurately reflect the clarity levels. And the estimation of sharpness affects the accuracy of the fusion. Second, the sensitivity of metrics for low contrast images is noteworthy. However, most of the current sharpness measurements have large deviations in the measurement of focused low-contrast regions [23–26], which results in a loss of information in the focused area when fusing images. In

this paper, we propose a simple but effective multi-focus image fusion method based on local binary patterns (LBP). To our knowledge, this is the first time to leverage LBP for multi-focus image fusion. LBP has the following two advantages for multi-focus image fusion. First, LBP-based sharpness metric has good monotonicity, which makes the fusion more accurate. Second, the metric we use have a more reliable response to blurred degree, even in low-contrast areas where deviations often occur. Both of the above advantages contribute to fewer errors when comparing and choosing sharper pixel values from source images. Undoubtedly, the recombination of these clear pixels gets better results. Therefore, the new multi-focus fusion method we proposed can be considered as a simple yet effective way.

2 Local Binary Pattern Metric-Based Multi-focus Image Fusion

In this section, our algorithm for multi-focus image fusion based on LBP-based sharpness metric is presented. Our framework is based on weighted average, as shown in Fig. 1. The algorithm is simple yet effect, which consists of three main steps: LBP sharpness map generation, weight map construction, and multi-focus image fusion. We will explain each step in details.

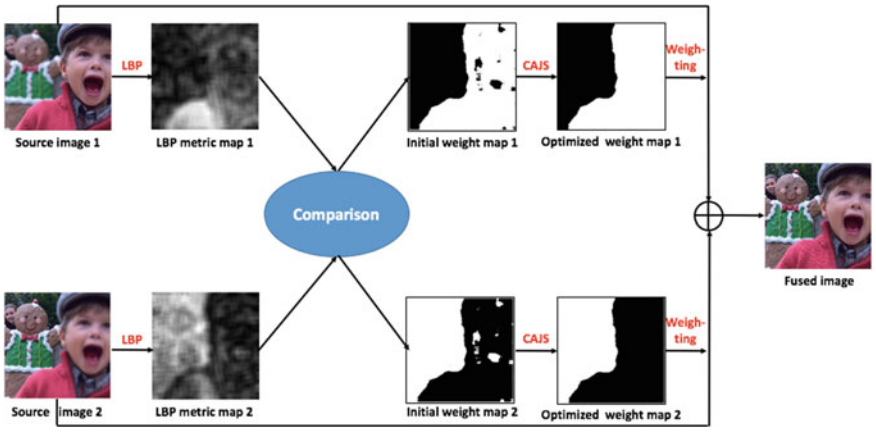

Fig. 1 Schematic diagram of the proposed multi-focus image fusion method

2.1 LBP Sharpness Map Generation

LBP. LBP [27] has been successfully used in various fields of image processing, such as face detection [28], target tracking [29], texture classification [30] and blur segmentation [31]. For a pixel (x_c, y_c), its LBP is defined as:

$$LBP(x_c, y_c) = \sum_{i=0}^{N-1} S(p_i - p_c) \times 2^i \tag{1}$$

$$S(p_i - p_c) = \begin{cases} 0, p_i - p_c < T_{LBP} \\ 1, p_i - p_c \geq T_{LBP} \end{cases} \tag{2}$$

where p_c is the intensity of the central pixel (x_c, y_c) in the window of N pixels, p_i indicates the intensity of the neighboring pixel of p_c, T_{LBP} is the threshold.

Dimension reduction. Due to the high dimensions of LBP (e.g., there are 256 types of LBP code for a $3 * 3$ window), the LBP can hardly be applied to focus-region estimation. Here, it is necessary to reduce the dimensions of LBP. The work of the reduction is divided into two steps. Taking a $3 * 3$ window as an example, we firstly use one code to represent 8 cases to obtain the rotation invariance [32]. The code is obtained by circular bitwise right shifting and then taking the minimum value. The dimension can be reduced to 36. Considering the transitions from one to zero and from zero to one, we divide the codes into 10 types including 9 types of rotation invariant uniform LBP (Fig. 2a–i) and 1 type of non-uniform LBP (Fig. 2j is an example).

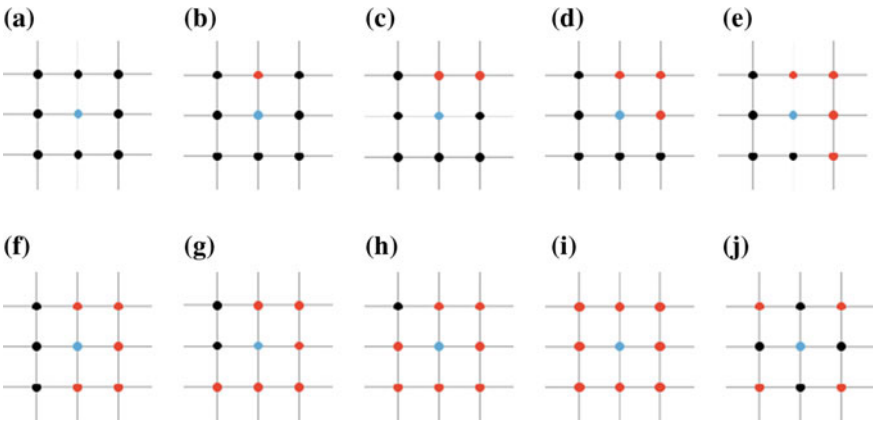

Fig. 2 9 types of rotation invariant uniform LBP and an example of non-uniform LBP

Fig. 3 The fusion image obtained based on different methods

LBP metric. For a region with M pixels, the LBP metric is achieved by follow:

$$m_{LBP} = \frac{1}{M}[\sum_{k=j}^{8} n\left(LBP^{riu2}k\right) + m] \tag{3}$$

where $n\left(LBP^{riu2}k\right)$ is the number of 8-bit LBP pattern with k triggered neighboring pixels, as shown in Fig. 3, j is a parameter deciding which types are chosen and m is the number of the 8-bit LBP pattern LBP^{riu2} when $U\,(LBP) \leq 2$. The m_{LBP} has been normalized, so $m_{LBP} \in [0, 1]$. The sharpness metric of each image pixel is computed for a local patch. The parameter j is taken to 5, which can achieve good performance. As shown in Fig. 1, the focused region is estimated accurately and shown in the LBP metric map (lighter areas are focused regions).

Applying the metric for focused region estimation has two advantages. First, the matric has good monotonicity and can accurately measure the focus area. Without a good monotonicity, two different clarity levels will map to the same metric value. This will result in inaccurate estimation of the clarity, which will cause the inaccuracy in the fusion task. Second, the metric has sensitivity for low contrast images. It can accurately reflect the sharpness of low-contrast area in the focus area, making the fusion image preserve more information of the low-contrast area in the focus area. The sharpness maps of two source images are generated by using LBP metric m_{LBP}, as shown in Fig. 1. When the value of j is 5, the detection error of the index to the background is relatively small, and the detection quality of the foreground is high.

2.2 Weight Map Construction

Initial weight map construction We construct the initial weight map by comparing two LBP sharpness maps, as shown in Fig. 1.

$$W_n^k = \begin{cases} 0, M_n^k = \min(M_1^k, M_2^k, \ldots, M_N^k) \\ 1, otherwise \end{cases} \tag{4}$$

where N is the number of source images, M_n^k is the m_{LBP} value of the pixel k in the nth image.

Weight map optimization Due to the complexity of the background and the foreground, the initial weight map contains noise and this will cause loss of information in the fused image. Li et al. used guided filtering [22, 33] to solve this problem. The source image is used to guide the filtering process. The filtering method can reduce the influence of noise, but the map is blurred, including the focus-region and the edge. In this paper, we use the connected area judgment strategy (CAJS) to reduce the noise in the initial map [18]. We observe that the size of the noise area is within a certain range. Therefore, CAJS is able to remove the noise as well as keep the edge information as follows.

$$W_n' = T(R(W_n), t) = \begin{cases} H(W_n), R(W_n) < t \\ W_n, R(W_n) > t \end{cases} \tag{5}$$

$$t = r \times H \times L \tag{6}$$

where H and L are the height and the wide of the source image, r is a scale parameter deciding the size of the threshold, $R(W_n)$ is the parameter of the size of region, t is the threshold of the image and W_n is the initial weight and $H(W_n)$ means swap the weight of the region. Specifically, a region in binary weight map which is smaller than the area threshold is reversed.

2.3 Multi-focus Image Fusion

The two source image are fused together by weighted arranging:

$$\mathrm{F} = \sum_{\mathrm{n}=1}^{\mathrm{N}} \mathrm{W}_{\mathrm{n}}^{'} \mathrm{I}_{\mathrm{n}} \tag{7}$$

where W_n' is the optimized weight map of the nth source image, I_n is the nth source image. Then the fusion image F is obtained. The fusion image F accurately inherits the low-contrast information of the focused area in source image. The edges of the focused area and the non-focused area are also fused effectively.

3 Experiment

3.1 Experiment Setup

Based on the multi-focus image dataset "Lytro" [34], we carry out our experiments. In this section, our LBP metric-based multi-focus image fusion method is compared with 3 representative fusion methods. Both subjective and objective comparison are explained in the next two subsections.

Parameter analysis. For our LBP sharpness map, the fusion process is effected by three parameters (T_{LBP}, j and r). The threshold T_{LBP} in Eq. (2) decides the metric's sensitivity for blur. The larger the T_{LBP} is, the less sensitive the metric is. To achieve a better focused-region estimation, we set the T_{LBP} to 0.0004. When using the CAJS to optimize the initial weight map, we introduce the variable r. It decides the threshold of the CAJS and its value is adjusted with the size of the focused-region in the source image.

3.2 Subjective Comparison

We compare our LBP metric-based fusion method with two transition domain methods (NSCT [35] and SR [7]) and one spatial domain method (GFF [22]). The fusion images based on four mentioned methods are shown in Fig. 3. Their source images are selected from the dataset "Lytro". Our LBP metric-based multi-focus image fusion method inherits the edge information and the focused region better than The GFF method, the NSCT method and the SR method.

3.3 Objective Comparison

In this subsection, we use fusion quality metrics, Q_{MI} [36] and $Q_{AB/F}$ [10], to evaluate the fusion performance of different methods objectively. The objective performances of the four methods are shown in Table 1. It can be obviously seen that the GFF method and our LBP metric-based method beat the other two transition domain methods on all the metric. Compared with the GFF method, our LBP metric-based method has larger quality indexes for Q_{MI} and $Q_{AB/F}$ for all image. The Q_{MI} quality index measures the similarity between source images and fused image. This means that our method can effectively preserve the focused information of sources images from different databases. The $Q_{AB/F}$ index reflects the retention ability of edge information. This means that our method can inherit the edge information effectively.

Table 1 Quantitative assessment of different image fusion methods. Fronts in red and green are the first and second best, respectively

Source images	Index	GFF	NSCT	SR	LBP
Child	Q_{MI}	7. 4059	6. 2245	6. 7763	7. 8689
	$Q_{AB/F}$	0. 7418	0. 7167	0. 7295	0. 7429
Wine	Q_{MI}	7. 2831	6. 0275	6. 4082	7. 6089
	$Q_{AB/F}$	0. 7989	0. 7833	0. 7901	0. 8007
Sidney	Q_{MI}	7. 7251	6. 9609	7. 2072	8. 2766
	$Q_{AB/F}$	0. 7716	0. 7581	0. 7653	0. 7733

4 Conclusion

We propose a simple yet efficient multi-focus fusion method based on LBP. The LBP metric is well applied in our image fusion framework, which is an innovation in this field. The accurate estimation of clarity due to the good monotony of the LBP metric optimizes the fusion effect. And the frequent loss of low-contrast area information in the current methods is also successfully avoided by using our improved fusion method, because the metric has sensitivity for low-contrast images. In addition, the preservation of the edge information is also one of our big advantages over many recent methods. Experimental results demonstrate that the fusion method we propose can be competitive with or even outperform some state-of-the-art methods.

References

1. Kaur, G., Kaur, P.: Survey on multifocus image fusion techniques. In: International Conference on Electrical, Electronics, and Optimization Techniques (ICEEOT), pp. 1420–1424 (2016)
2. Qu, Y., Yang, H.: Optical microscopy with flexible axial capabilities using a vari-focus liquid lens. J. Microsc. **258**(3), 212–222 (2015)
3. Abdipour, M., Nooshyar, M.: Multi-focus image fusion using sharpness criteria for visual sensor networks in wavelet domain. Comput. Electr. Eng. **51**, 74-88 (2016) (ISSN)
4. Liu, Y., Wang, Z.: Simultaneous image fusion and denoising with adaptive sparse representation. IET Image Proc. **9**(5), 347–357 (2015)
5. Yang, Y., Tong, S., Huang, S., Lin, P., Fang, Y.: A hybrid method for multi-focus image fusion based on fast discrete curvelet transform. IEEE Access **5**, 14898–14913 (2017)

6. Yang, Y., Tong, S., Huang, S., Lin, P.: Multifocus image fusion based on NSCT and focused area detection. IEEE Sens. J. **15**(5), 2824–2838 (2015)
7. Yang, Y., et al.: Multi-focus image fusion via clustering PCA based joint dictionary learning. IEEE Access **5**, 16985–16997 (2017)
8. Zhang, Q., Levine, M.D.: Robust multi-focus image fusion using multi-task sparse representation and spatial context. IEEE Trans. Image Process. **25**(5), 2045–2058 (2016)
9. Cao, L., Jin, L., Tao, H., Li, G., Zhuang, Z., Zhang, Y.: Multi-focus image fusion based on spatial frequency in discrete cosine transform domain. IEEE Signal Process. Lett. **22**(2), 220–224 (2015)
10. Jiang, Q., Jin, X., Lee, S.J., Yao, S.: A novel multi-focus image fusion method based on stationary wavelet transform and local features of fuzzy sets. IEEE Access **5**, 20286–20302 (2017)
11. Shreyamsha Kumar, B.K.: Multi-focus and multispectral image fusion based on pixel significance using discrete cosine harmonic wavelet transform. Signal Image Video Process. **7**(6), 125–1143 (2013)
12. Shreyamsha Kumar, B.K.: Image fusion based on pixel significance using cross bilateral filter. Signal Image Video Process. **9**(5), 1193–1204 (2015)
13. Liu, Y., Chen, X., Ward, R.K., Jane Wang, Z.: Image fusion with convolutional sparse representation. IEEE Signal Process. Lett. **23**(12), 1882–1886 (2016)
14. Guo, D., Yan, J., Xiaobo, Q.: High quality multi-focus image fusion using self-similarity and depth information. Opt. Commun. **338**, 138–144 (2015)
15. Gangapure, V.N., Banerjee, S., Chowdhury, A.S.: Steerable local frequency based multispectral multifocus image fusion. Inf. Fusion **23**, 99–115 (2015)
16. Farid, M.S., Mahmood, A., Al-Maadeed, S.A.: Multi-focus image fusion using content adaptive blurring. Inf. Fusion (2018)
17. Chen, Y., Guan, J., Cham, W.K.: Robust multi-focus image fusion using edge model and multi-matting. IEEE Trans. Image Process. **27**(3), 1526–1541 (2018)
18. Liu, Y., Chen, X., Peng, H., Wang, Z.: Multi-focus image fusion with a deep convolutional neural network. Inf. Fusion **36**, 191–207 (2017)
19. Du, C., Gao, S.: Image segmentation-based multi-focus image fusion through multi-scale convolutional neural network. IEEE Access **5**, 15750–15761 (2017)
20. Zhang, Y., Bai, X., Wang, T.: Boundary finding based multi-focus image fusion through multi-scale morphological focus-measure. Inf. Fusion **35**, 81–101 (2017)
21. Nejati, M., Samavi, S., Karimi, N., Reza Soroushmehr, S.M., Shirani, S., Roosta, I., Najarian, K.: Surface area-based focus criterion for multi-focus image fusion. Inf. Fusion **36**, 284–295 (2017)
22. Li, S., Kang, X., Hu, J.: Image Fusion With Guided Filtering. IEEE Trans. Image Process. **22**(7), 2864–2875 (2013)
23. Zhao, J., Feng, H., Xu, Z., Li, Q., Tao, X.: Automatic blur region segmentation approach using image matting. Signal Image Video Process. **7**(6), 1173–1181 (2013)
24. Shi, J., Xu, L., Jia, J.: Discriminative blur detection features. In: Proceedings of the IEEE Conference on Computer Vision and Pattern Recognition (CVPR), pp. 2965–2972 (2014)
25. Liu, R., Li, Z., Jia, J.: Image partial blur detection and classification. In: Proceedings of the IEEE Conference on Computer Vision and Pattern Recognition (CVPR), pp. 1–8 (2008)
26. Vu, C.T., Phan, T.D., Chandler, D.M.: S_3: a spectral and spatial measure of local perceived sharpness in natural images. IEEE Trans. Image Process. **21**(3), 934–945 (2012)
27. Ojala, T., Pietikäinen, M., Harwood, D.: A comparative study of texture measures with classification based on featured distributions. Pattern Recognit. **29**(1), 51–59 (1996)
28. Jun, Z., Jizhao, H., Zhenglan, T., Feng, W.: Face detection based on LBP. In: IEEE International Conference on Electronic Measurement & Instruments (ICEMI), pp. 421–425 (2017)
29. Shu, Z., Liu, G., Xie, Z.: Real time target tracking scale adaptive based on LBP operator and nonlinear meanshift. In: International Conference on Cyber-Enabled Distributed Computing and Knowledge Discovery (CyberC), pp. 130–133 (2017)

30. Guo, Z., Zhang, L., Zhang, D.: A completed modeling of local binary pattern operator for texture classification. IEEE Trans. Image Process. **19**(6), 1657–1663 (2010)
31. Yi, X., Eramian, M.: LBP-based segmentation of defocus blur [J]. IEEE transactions on image processing. **25**(4), 1626–1638 (2016)
32. Ojala, T., Pietikainen, M., Maenpaa, T.: Multiresolution gray-scale and rotation invariant texture classification with local binary patterns. IEEE Trans. Pattern Anal. Mach. Intell. **24**(7), 971–987 (2002)
33. Seiichi, S., Lu, H.: Underwater image dehazing using joint trilateral filter. Comput. Electr. Eng. **40**(1), 41–50 (2014)
34. http://mansournejati.ece.iut.ac.ir/content/lytro-multi-focus-dataset
35. Zhang, Q., Guo, B.: Multifocus image fusion using the non-subsampled contourlet transform. Signal Process. **89**(7), 1334–1346 (2009)
36. Hossny, M., Nahavandi, S., Creighton, D.: Comments on 'information measure for performance of image fusion'. Electron. Lett. **44**(18), 1066–1067 (2008)

Photo Aesthetic Scoring Through Spatial Aggregation Perception DCNN on a New IDEA Dataset

Xin Jin, Le Wu, Geng Zhao, Xinghui Zhou, Xiaokun Zhang and Xiaodong Li

Abstract The aesthetic quality assessment of image is a challenging work in computer vision field. The recent research work used the deep convolutional neural network to evaluate the aesthetic quality of images. However, the score of image data sets has a strongly normal distribution, which makes the training of neural network easy to be over-fitting. In addition, traditional deep learning methods usually preprocess images, which destroy the original aesthetic features of the picture, so that the network can only learn some superficial aesthetic features. This paper presents a new data set what images distributed evenly for aesthetics (IDEA). This data set has less statistical characteristics, which is helpful for the neural network to learn the deeper features. We propose a new spatial aggregation perception neural network architecture which can control channel weights automatically. The advantages and effectiveness of our method are proved by experiments in different data sets.

Keywords Aesthetic assessment · Neural network · Computer vision

1 Introduction

Recently, deep convolutional neural network technology has made great progress in computer image object recognition and semantic recognition. However, the aesthetic quality of using computer to identify or evaluate images is far from practical. Subjective Image Aesthetic Quality Assessment (IAQA) is still a challenging task [1].

X. Jin · L. Wu · G. Zhao · X. Zhou · X. Zhang · X. Li (✉)
Department of Cyber Security, Beijing Electronic Science and Technology Institute, 100070 Beijing, China
e-mail: lxd@besti.edu.cn

X. Jin
CETC Big Data Research Institute Co., Ltd., 550018, Guiyang, Guizhou, China

H. Lu (ed.), *Cognitive Internet of Things: Frameworks, Tools and Applications*, Studies in Computational Intelligence 810,
https://doi.org/10.1007/978-3-030-04946-1_5

1.1 Related Work

As summarized by [2], the early work of image aesthetic quality evaluation mainly focuses on the manual design of various image aesthetic features, and connected with a machine classification or regression method. Another line is to use generic image description features. Recently, the powerful deep feature representation learned from large amount of data has shown an ever-increased performance on this task, surpassing the capability of conventional hand-crafted features [3–15]. Most of the above research work follows the following methods to predict the quality of image aesthetics:

- Image preprocessing;
- Convolutional neural networks.

The quality evaluation of image aesthetics is ambiguous [16]. Figure 1 shows the effect of data augmentation on image aesthetic semantics. Obviously, just changing the position of an image can have such a huge impact. In the field of object detection, He et al. [17] proposed to increase the spatial pyramid pooling layer in the neural network to deal with images of different sizes. In the field of aesthetics, some work has begun to use modified or generated evaluation score distribution to train and give the binary classification results of aesthetic image quality or one-dimensional numerical evaluation [18–20]. Wu et al. [21] training on small data sets. Mai et al. [1] used adaptive convolution to process the original image, retained the original aesthetic image features.

On aesthetic data set, Murray et al. [22] the first puts forward a large-scale database for aesthetic visual analysis (AVA). Then, in view of the imbalance of AVA samples,

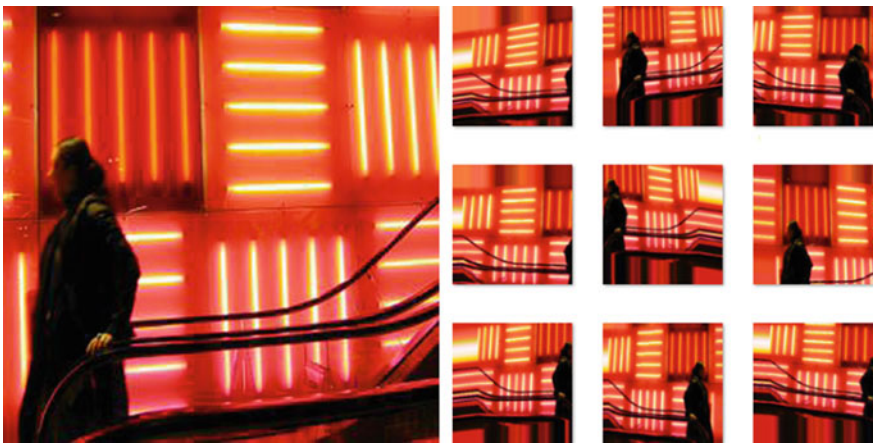

Fig. 1 The original and preprocessed images. The left image represents the original image, and the right image is produced by the random combination of translation, cropping and left-right flips. Images are from the AVA dataset [22]

Kong et al. [12] proposed the AADB data set to make the aesthetic data set more balanced and better fit in the normal distribution [23–27].

1.2 Our Approach

The new data set what images distributed evenly for aesthetics (IDEA) is presented in our paper. The IDEA data set contains 9191 images, 0–8 points with 1000 images per score, and 9 point has 191 pictures. The obvious distribution features of the data set make the network output keep approaching the bigger weight of the training set's distribution.

This paper presents a new spatial aggregation awareness neural network architecture (SAP-Net). We used the squeeze-and-excitation structure proposed by Hu et al. [28] to perceptually learn characteristics of different channels. At the end of the network, the spatial aggregation of these channel characteristics is carried out so that the local information of the network can be merged to form a complete picture aesthetic semantic feature. Behind the network part, we use parallel tasks through divide score on a scale of different particle size and finally formed the global characteristics. The main contributions of this paper are as follows:

- This is the first time to propose a completely balanced aesthetic data set;
- The first work that channel sensing technology was applied to aesthetic mission, put forward a new space fusion strategy to dynamic control channel weighting flow to extract aesthetic characteristics and combine all of local characteristics;
- A multi-task network learning strategy based on fractional granularity is proposed.

2 IDEA Data Set

To create a more balanced set of aesthetic images, we collected several images and score tags from the professional photography website: *dpchallenge* and *Flickr*. Website's scores are ranging from 0 to 9, we selected 1000 images for each segment as far as possible (Flickr's label come from AADB). Finally, the data set, which is almost balance distributed, is named as the IDEA dataset. The IDEA data set has 9191 images, of which 9-points's number are 191 and the rest are 1,000. In the training, 8191 pictures were used for the training set and randomly selected 1000 images for testing.

Figures 2 and 3 show that the IDEA dataset is more evenly distributed and have less statistical characteristics than the AVA and AADB data sets. The AVA data set has the highest kurtosis due to the serious unbalance of each score segment. The relative mitigation kurtosis of the AADB dataset is centered. IDEA distribution is more balanced, kurtosis is the smallest. However, the normal distribution cannot fit all AVA data, the aesthetic score cannot simply be regarded as normal distribution. In

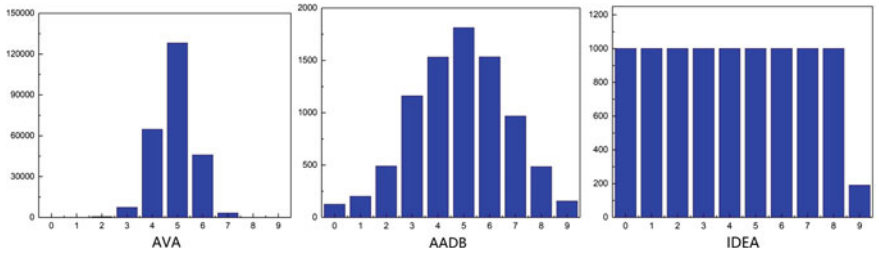

Fig. 2 From left to right: AVA, AADB, and IDEA data sets. X-axis is the fraction, Y-axis is the number of pictures. The intermediate fraction of the AVA dataset accounts for the most of total, and the number of images in other segments is seriously unbalanced. The AADB data set is closer to the normal distribution, and the distribution is relatively smooth. The IDEA distribution is almost completely balance

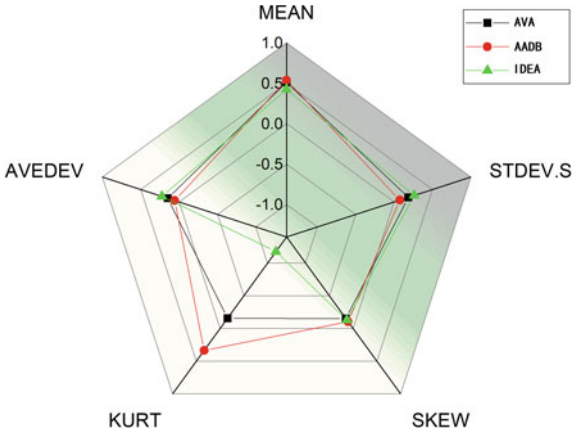

Fig. 3 The relative radar maps of the statistics of AVA, AADB, and IDEA. Counterclockwise from the top represent the mean, absolute mean variance, kurtosis, skewness, standard deviation. The mean, absolute mean deviation, skewness and standard deviation of the three data sets are almost the same standard

addition, the obvious distribution features of AADB make neural network learning only remember those simple statistical features and shallow aesthetic features, so that the network cannot learn deeper features. In this regard, we propose to remove the statistical features that the neural network can easily remember in the IDEA dataset, and let the network directly learn the semantic features and abstract features of the images so that the performance of the network can be concentrated in the purest aesthetic tasks.

3 Spatial Aggregation Perception Network

3.1 Perception Polymerization

In neural networks, the information of different channels in the convolution kernel can be regarded as different perspectives. In this paper, we use the Squeeze-and-Excitation block proposed by Hu et al. [28] to realize channel dimension perception.

As shown in Fig. 4, the Squeeze-and-Excitation block module was applied to the ResNet-50 [29] in this article and added to each Residual unit. Here we use global average pooling as the Squeeze operation. The two Fully Connected layers form a Bottleneck structure to model the correlation between the channels and to output the same number of weights as the input features. The function of this module can be expressed by the following formula:

$$u_c = v_c * X = \sum_{s=1}^{C'} v_c^s * x^s \tag{1}$$

Among them, u_c represents the output, C represents the output dimension, C' represents the input dimension. Here is v_c^s a 2D spatial kernel, and therefore represents a single channel of v_c which acts on the corresponding channel of X. Since the output is produced by a summation through all channels, the channel dependencies are implicitly embedded in v_c, but these dependencies are entangled with the spatial correlation captured by the filters.

3.2 Spatial Aggregation

Traditional neural networks often feature fusion directly through the full connectivity layer, but the relative position of the image cannot be maintained due to the complex combination of the full connectivity layers. In addition, since the number of nodes in the final full connection layer is often fixed in the neural network, which destroys the

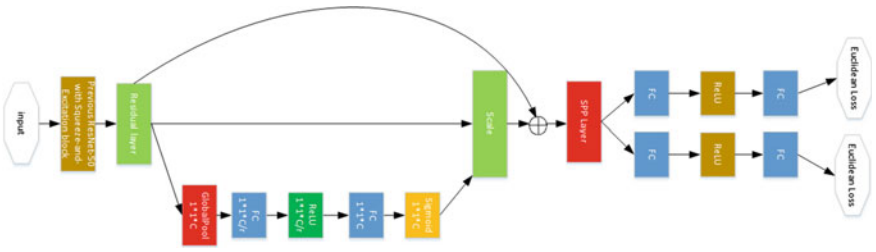

Fig. 4 The architecture of the SAP-net

composition information of the pictures and has an impact on the aesthetic judgment. In response to this problem, He et al. [17] proposed to increase the spatial pyramid pooling layer in neural networks to deal with different size feature maps.

The spatial pyramid pooling layer is to perform three convolution operations on each image of the previous volumetric feature maps. The left image is the original image, the middle one is the size of the image is divided into 9 characteristics of the map, the right one is the image is divided into 49 size characteristics.

3.3 Multi-task Learning

We put the results of aggregation into different fully connected structures for spatial information fusion. After a ReLU activation, the output of different dimensions is fully connected according to different tasks.

$$\begin{aligned} \text{Loss} &= \text{Loss}_{\text{RegLoss}} + \text{Loss}_{\text{SoftmaxLoss}} \\ &= \frac{1}{2N}\sum_{i=1}^{N} ||\hat{y}_i - y_i||_2^2 + \frac{1}{N}\sum_{i=1}^{N} -log\frac{e^{f(w,x,b)}}{\sum_{c=1}^{C} f(w,x,b)} \end{aligned} \tag{2}$$

The above formula represents the loss calculation formula for multitasking learning used in this paper. The formula consists of two parts, namely, regression loss and classification, that is, $\text{Loss}_{\text{RegLoss}}$ and $\text{Loss}_{\text{SoftmaxLoss}}$ in the formula. Where N represents the batch size, regression loss is calculated by the Euclidean distance, $\hat{y}_i$ represents the predicted aesthetic score, y_i represents the true aesthetic score, and $f(w, x, b)$ represents the output of the upper layer of the category loss layer (Fig. 5).

4 Experiments

4.1 Implementation Details

We fix the parameters of the layers before SPP layer of a pre-trained ResNet-50 model on the ImageNet [2] and fine tune all of the full connected layers on the training set of the AADB dataset and IDEA dataset. We use the Caffe framework [30] to train and test our models. The learning policy is set to step, The momentum of 0.9, a gamma of 0.5 and a weight decay of 0.0005. The training time is about four hours using Titan X Pascal GPU. We show some experimental results in Fig. 5.

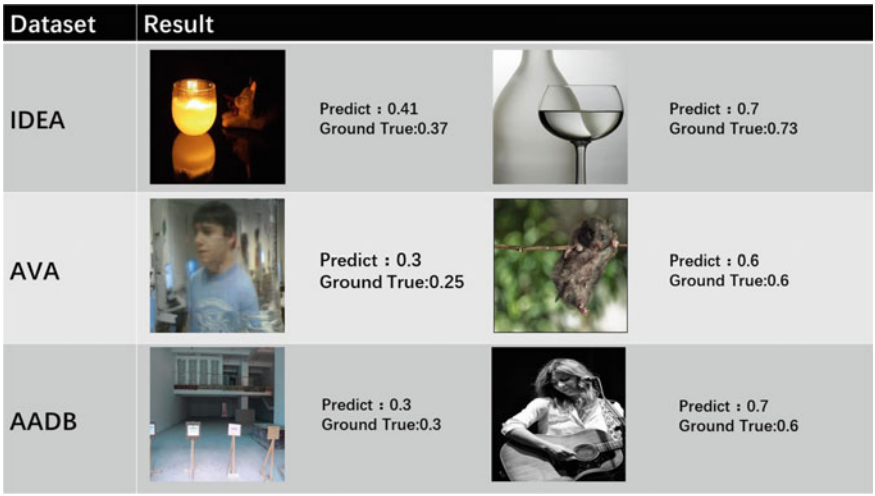

Fig. 5 Some experimental results. Here we are on the IDEA data set for training, and test on the three data sets of validation set

4.2 The Performance of SAP-Net on AADB

To evaluate the aesthetic scores predicted by our model, we use the mean residual sum of squares error (MRSSE)and the ranking correlation measured by Spearman's ρ between the estimated aesthetics scores and the ground-truth scores in the test set [12].

By comparison of Tables 1 and 2, it can be found that through the training of the AADB data set (the second-to-last row in the table), in the test of AVA's 20,000 test sets, the SAP-net can perform better performance. The performance of the SAP-net in MRSSE and the ρ performance was significantly better than the previous methods. In addition, in the AADB verification set, Kong et al. [12] has the best performance of $\rho = 0.6782$, and the SAP-net on the AADB validation set is equal to 0.6850, which is better than the previous method.

4.3 The Performance of SAP-Net on IDEA

The AADB data set is better distributed than the AVA data set, and SAP-Net's learning ability is more fully developed in the IDEA data set. In the training of the IDEA training set (the last line in the Table 2), the performance of the SAP-Net in MRSSE and the ρ performance was the best.

Table 1 Performance comparison of aesthetic quality assessment on validation set of the AVA dataset using MRSSE

Methods	MRSSE
Always predicting 5 as aesthetic score	0.5700
BOV-SIFT + rbfSVR ([31] adapted in [5])	0.5515
BOV-SIFT + linSVR ([31] adapted in [5])	0.5401
GIST + rbfSVR ([31] adapted in [5])	0.5307
GIST + linSVR ([31] adapted in [5])	0.5222
Aest-CNN [5]	0.4501
DeepIA [32]	0.3727
SAP-Net (Training using AADB)	0.3146
SAP-Net (Training using IDEA)	0.2856

Table 2 Performance comparison of aesthetic quality assessment on validation set of the AVA dataset using ρ

Methods	ρ
Murray et al. [22]	–
SPP [17]	–
AlexNet FT Conf [12]	0.4807
DCNN [4]	–
RDCNN [4]	–
RDCNN semantic [7]	–
DMA [6]	–
DMA AlexNet FT [6]	–
Reg + Rank + Att + Cont [12]	0.5581
SAP-Net (Training using AADB)	0.5834
SAP-Net (Training using IDEA)	0.6159

5 Conclusions

In this dissertation, a new data set what images distributed evenly for aesthetics (IDEA) is constructed and a new architecture of spatial aggregation perception deep convolution neural network is proposed. The statistical properties of IDEA datasets make neural network learning images can effectively learn deeper aesthetics. Compared with traditional convolution, SAP-net has no restriction on the input size of the network, reduces the loss of resize to aesthetics, and learns different channels after convolution to extract features, effectively preserving more deep aesthetics feature. Finally, the network spatially aggregates the features of these channels and optimizes the final result through the multitask goal, lets the network have better performance in the experiment.

Acknowledgements We thank all the reviewers and ACs. This work is partially supported by the National Natural Science Foundation of China (Grant Nos. 61772047, 61772513), the Science and Technology Project of the State Archives Administrator (Grant No. 2015-B-10), the open funding project of State Key Laboratory of Virtual Reality Technology and Systems, Beihang University (Grant No. BUAA-VR-16KF-09), the Fundamental Research Funds for the Central Universities (Grant No. 3122014C017), the China Postdoctoral Science Foundation (Grant No. 2015M581841), and the Postdoctoral Science Foundation of Jiangsu Province (Grant No. 1501019A).

References

1. Mai, L., Jin, H., Liu, F.: Composition-preserving deep photo aesthetics assessment. In: Proceedings of the IEEE Conference on Computer Vision and Pattern Recognition, pp. 497–506 (2016)
2. Deng, J., Dong, W., Socher, R., et al.: Imagenet: a large-scale hierarchical image database. In: IEEE Conference on Computer Vision and Pattern Recognition, 2009. CVPR 2009, pp. 248–255. IEEE (2009)
3. Karayev, S., Trentacoste, M., Han, H., et al.: Recognizing image style (2013). arXiv:1311.3715
4. Lu, X., Lin, Z., Jin, H., et al.: Rapid: rating pictorial aesthetics using deep learning. In: Proceedings of the 22nd ACM International Conference on Multimedia, pp. 457–466. ACM (2014)
5. Kao, Y., Wang, C., Huang, K.: Visual aesthetic quality assessment with a regression model. In: 2015 IEEE International Conference on Image Processing (ICIP), pp. 1583–1587. IEEE (2015)
6. Lu, X., Lin, Z., Shen, X., et al.: Deep multi-patch aggregation network for image style, aesthetics, and quality estimation. In: Proceedings of the IEEE International Conference on Computer Vision, pp. 990–998 (2015)
7. Lu, X., Lin, Z., Jin, H., et al.: Rating image aesthetics using deep learning. IEEE Trans. Multimed. **17**(11), 2021–2034 (2015)
8. Dong, Z., Tian, X.: Multi-level photo quality assessment with multi-view features. Neurocomputing **168**, 308–319 (2015)
9. Kao, Y., Huang, K., Maybank, S.: Hierarchical aesthetic quality assessment using deep convolutional neural networks. Signal Process. Image Commun. **47**, 500–510 (2016)
10. Wang, W., Zhao, M., Wang, L., et al.: A multi-scene deep learning model for image aesthetic evaluation. Signal Process. Image Commun. **47**, 511–518 (2016)
11. Ma, S., Liu, J., Chen, C.W.: A-lamp: Adaptive layout-aware multi-patch deep convolutional neural network for photo aesthetic assessment (2017). CoRR abs/1704.00248. http://arxiv.org/abs/1704.00248
12. Kong, S., Shen, X., Lin, Z., et al.: Photo aesthetics ranking network with attributes and content adaptation. In: European Conference on Computer Vision, pp. 662–679. Springer, Cham (2016)
13. Jin, X., Chi, J., Peng, S., et al.: Deep image aesthetics classification using inception modules and fine-tuning connected layer. In: 2016 8th International Conference on Wireless Communications & Signal Processing (WCSP), pp. 1–6. IEEE (2016)
14. Jin, X., Wu, L., Song, C., et al.: Predicting aesthetic score distribution through cumulative Jensen-Shannon divergence. In: Proceedings of the 32th international conference of the America Association for Artificial Intelligence (AAAI18), New Orleans, Louisiana, 2–7 Feb 2018 (2017)
15. Kao, Y., He, R., Huang, K.: Deep aesthetic quality assessment with semantic information. IEEE Trans. Image Process. **26**(3), 1482–1495 (2017)
16. Ke, Y., Tang, X., Jing, F.: The design of high-level features for photo quality assessment. In: 2006 IEEE Computer Society Conference on Computer Vision and Pattern Recognition, vol. 1, pp. 419–426. IEEE (2006)

17. He, K., Zhang, X., Ren, S., et al.: Spatial pyramid pooling in deep convolutional networks for visual recognition. In: European Conference on Computer Vision, pp. 346–361. Springer, Cham (2014)
18. Wang, Z., Liu, D., Chang, S., et al.: Image aesthetics assessment using Deep Chatterjee's machine. In: 2017 International Joint Conference on Neural Networks (IJCNN), pp. 941–948. IEEE (2017)
19. Jin, B., Segovia, M.V.O., Süsstrunk, S.: Image aesthetic predictors based on weighted CNNs. In: 2016 IEEE International Conference on Image Processing (ICIP), pp. 2291–2295. IEEE (2016)
20. Hou, L., Yu, C.P., Samaras, D.: Squared Earth Mover's Distance-based Loss for Training Deep Neural Networks (2016). arXiv:1611.05916
21. Wu, O., Hu, W., Gao, J.: Learning to predict the perceived visual quality of photos. In: 2011 IEEE International Conference on Computer Vision (ICCV), pp. 225–232. IEEE (2011)
22. Murray, N., Marchesotti, L., Perronnin, F.: AVA: a large-scale database for aesthetic visual analysis. In: 2012 IEEE Conference on Computer Vision and Pattern Recognition (CVPR), pp. 2408–2415. IEEE (2012)
23. Serikawa, S., Lu, H.: Underwater image dehazing using joint trilateral filter. Comput. Electr. Eng. **40**(1), 41–50 (2014)
24. Lu, H., Li, Y., Mu, S., et al.: Motor anomaly detection for unmanned aerial vehicles using reinforcement learning. IEEE Internet Things J. (2017)
25. Lu, H., Li, Y., Chen, M., et al.: Brain intelligence: go beyond artificial intelligence. In: Mobile Networks and Applications, pp. 1–8 (2017)
26. Lu, H., Li, B., Zhu, J., et al.: Wound intensity correction and segmentation with convolutional neural networks. Concurr. Comput. Pract. Exp. **29**(6) (2017)
27. Lu, H., Li, Y., Uemura, T., et al.: Low illumination underwater light field images reconstruction using deep convolutional neural networks. Future Gener. Comput. Syst. (2018)
28. Hu, J., Shen, L., Sun, G.: Squeeze-and-excitation networks (2017). arXiv:1709.01507
29. He, K., Zhang, X., Ren, S., et al.: Deep residual learning for image recognition. In: Proceedings of the IEEE Conference on Computer Vision and Pattern Recognition, pp. 770–778 (2016)
30. Jia, Y., Shelhamer, E., Donahue, J., et al.: Caffe: convolutional architecture for fast feature embedding. In: Proceedings of the 22nd ACM international conference on Multimedia, pp. 675–678. ACM (2014)
31. Marchesotti, L., Perronnin, F., Larlus, D., et al.: Assessing the aesthetic quality of photographs using generic image descriptors. In: 2011 IEEE International Conference on Computer Vision (ICCV), pp. 1784–1791. IEEE (2011)
32. Bianco, S., Celona, L., Napoletano, P., et al.: Predicting image aesthetics with deep learning. In: International Conference on Advanced Concepts for Intelligent Vision Systems, pp. 117–125. Springer, Cham (2016)

Synthesizing Virtual-Real Artworks Using Sun Orientation Estimation

Xin Jin, Xing Sun, Xiaokun Zhang, Hongbo Sun, Ri Xu, Xiaodong Li and Nan Sun

Abstract The illumination effect is essential for the realistic results in images which are created by inserting virtual objects into real scene. For outdoor scenes, automatic estimation of sun orientation condition from a single outdoor image is fundamental for inserting 3D models to a single image. Traditional methods for outdoor sun orientation estimation often use handcraft illumination features or cues. These cues heavily rely on the experiences of human and pre-processing progresses using other image understanding technologies such as shadow and sky detection, geometry recovery and intrinsic image decomposition, which limit their performances. We propose an end to end way of outdoor sun orientation estimation via a novel deep convolutional neural network (DCNN), which directly outputs the orientation of the sun from an outdoor image. Our proposed SunOriNet contains a contact layer that directly contacts the intermediate feature maps to the high-level ones and learns hierarchical features automatically from a large-scale image dataset with annotated sun orientations. The experiments reveal that our DCNN can well estimate sun orientation from a single outdoor image. The estimation accuracy of our method outperforms model state-of-the-art DCNN based methods.

Keywords Sun orientation estimation · Inserting 3D models
Single outdoor image · Augmented reality

1 Introduction

Images which contain both virtual objects and real scene are new patterns of image artworks. When rendering a 3D model into a real scene, the illumination effect is

X. Jin · X. Sun · X. Zhang · H. Sun · R. Xu · X. Li (✉) · N. Sun
Department of Cyber Security, Beijing Electronic
Science and Technology Institute, 100070 Beijing, China
e-mail: lxd@besti.edu.cn

X. Jin
CETC Big Data Research Institute Co., Ltd., 550018 Guiyang, Guizhou, China

H. Lu (ed.), *Cognitive Internet of Things: Frameworks, Tools and Applications*, Studies in Computational Intelligence 810,
https://doi.org/10.1007/978-3-030-04946-1_6

essential for the realistic results. The fundamental step is to estimate the illumination condition from an image or video. Then the estimated illumination condition can be used to render 3D models.

Illumination estimation from a single outdoor image is a hot topic in computer vision. From the technology view, it can be used for illumination invariant object recognition, inserting virtual objects into real scene images etc. From the application view, it can be used for many applications such as film industry, graphics design and digital entertainments.

However, illumination estimation from a single outdoor image is very a challenging issue. Human can easily estimate the approximate sun orientation from a non-cloudy outdoor image. The illumination cues or features used by human mainly rely on shadow directions, highlight positions etc. The extractions of these high-level illumination cues are non-trivial issues themselves.

Traditional methods [1–8] for illumination estimation rely on handcraft features. Both low level image features and high-level illumination features have been studied. High level illumination cues rely on shadow and sky detection, geometry recovery or intrinsic image decomposition. The performance of the illumination estimation is determined by the above pre-processing progresses using other image understanding technologies.

We propose an end to end way of outdoor illumination estimation via a novel multiscale deep convolutional neural network (DCNN), which directly outputs the orientation of the sun from a non-cloudy outdoor image. Our DCNN learns both low and high-level features automatically from a large-scale image dataset with annotated sun orientations. The experiments reveal that our DCNN can well estimate sun orientation from a single outdoor image. The estimation accuracy of our method outperforms both traditional handcraft feature-based method and a baseline deep convolutional neural network called AlexNet [9].

To the best of knowledge, beside our method, there exists other methods that have already use DCNN for sun orientation estimation such as SUN-CNN [13]. Their method and ours are different in the network architectures, the loss functions, the datasets for training, and the training processes. The most important difference is that they do not consider connecting an intermediate layer to high-level layer, which is quite important for sun orientation estimation [11–19].

2 Sun Orientation Estimation

2.1 Preliminaries

The sun orientation is relative to the position of the camera. It is influenced by the Latitude and longitude, the shooting time, the pose of the camera and the focal length etc. Thus, quantitatively analyzing the sun orientation is a non-trivial task. We use the azimuth and the zenith to represent the sun orientation.

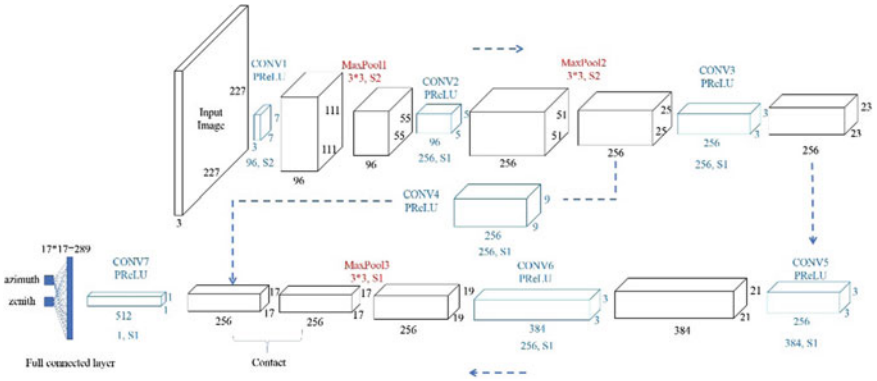

Fig. 1 SunOriNet: DCNN for sun orientation estimation. The CONV4 is used to connect an intermediate layer to high-level layer. CONV: convolution layer. MaxPool: max pooling layer. PReLU: parametric rectified linear units

2.2 SunOriNet

We propose a novel deep convolutional neural network for sun orientation estimation, named SunOriNet, as shown in Fig. 1. Our DCNN architecture has 7 convolutional layers and 3 max pooling layers. Sun orientation estimation should use both the low-level features and the high-level features. Thus, we use a contact layer to directly contact the intermediate feature maps to the high-level ones. Our network has two outputs, azimuth and zenith, which it predicts simultaneously.

2.3 The Nonlinear Activations

We use the Parametric Rectified Linear Units (PReLU) as the nonlinear activation functions [9], which is defined as:

$$g(x_i) = \begin{cases} x_i, x_i \geq 0 \\ a_i x_i, x_i < 0 \end{cases}, \tag{1}$$

where, a_i is a learnable parameter for each activation map.

2.4 The Loss Function

The loss functions used for traditional image classification tasks are always the softmax loss or cross entropy loss. Our task is to predict two real values of the

azimuth and the zenith. Thus, we define our loss function as Euclidean Distance (ED loss):

$$\frac{1}{2N}\sum_{\mathrm{i}=1}^{N}\left(||a_{pi}-a_{gi}||_2^2+||z_{pi}-z_{gi}||_2^2\right), \tag{2}$$

where, N is the number of the training images. a_{pi} and z_{pi} are the predicted azimuth and zenith. z_{pi} and z_{gi} are the ground truth azimuth and zenith.

2.5 The Dataset

We use a deep convolutional neural network with 11 layers to predict the sun orientation from a single image. The training data which fed into the our SunOriNet is quite important. We adopt the webcam dataset [10] which contains ground-truth sun orientations of 657,146 images. This dataset has the following advantages.
Large-scale: This dataset contains roughly 657, 146 images taken from 54 webcam sequences, totaling a combined 10,500 days (28 years) worth of images, which amounts to 34 GB worth of data, which are sufficient for our DCNN training.
Long time: the recording time of each scene is above half a year. From 4 am to 19 pm, they took photos every 10 min. The long-time records provide large-scale sun orientation information of a single recording camera position, which are good for DCNN training.

2.6 DCNN Training

We use the Webcam dataset to train our proposed SunOriNet. Firstly, the image data in the Webcam dataset should be pre-processing before fed into the DCNN.
Image Refinement: Long-time shooting produces many noises in the images, which can influent the feature extraction of the DCNN. The rain, cloud, camera logos and some insects are the main noise sources. We remove these images manually.
Image Scaling: The resolutions of the images in the Webcam dataset are not the same. We scale all the resolutions of the images into 227*227*3 as the input of our SunOriNet.

After the above 2 steps, 643,374 images are remained. We split the remained images to training set and validation/testing set using the ratio 3:1. 480,043 images from 43 webcams are used for training. 163,331 images from remained 11 webcams are used for validation/testing. We use the Caffe framework [11] to train and test our models. The learning policy is set to step. Stochastic gradient descent is used to train our model with a mini-batch size of 32 images, a momentum of 0.9, a gamma of 0.5, and a weight decay of 0.0005. The max number of iterations is 325000. The training time is about 5 days using GTX980-Ti GPU.

3 Experimental Results

In this section, we show the experimental results of our proposed method and the comparison with the state of the art methods.

We randomly select 1 scene. 3 images are randomly selected to show the predicted results. We show the compared results with the base line DCNN method [13]. The results are shown in Fig. 2.

These randomly chosen samples reveal that the predicted errors of our proposed SunOriNet are less than those of the SUN-CNN averagely. The ranges of errors of the predicted sun orientations of our methods are less than 30° and 10°, respectively.

We show more results of inserting 3D models into outdoor images. As shown in Fig. 3, the illumination effect of the inserted 3D models is similar as that in the original real scenes. The shadow orientation is determined by the estimated virtual sun orientation by our method.

We also compare our method with DCNN based methods [13]. As shown in Fig. 4, we randomly choose 1000 images not in the training set or the validation set. Our proposed SunOriNet outperforms the modern DCNN based method [13].

Ground Truth (radian)		-4.2667,1.5982		-4.0758,1.3841		-1.6457,1.462	
AlexNet	Predicted (radian)	-3.7561	1.0245	-3.1546	1.0259	-2.9942	1.7513
	Error (degree)	29.27	32.88	52.80	20.53	77.3	16.58
SunOri Net	Predicted (radian)	-3.8023	1.2352	-3.6645	1.2640	-2.3248	1.4578
	Error (degree)	26.62	20.8	23.57	6.88	38.92	0.2

Fig. 2 The predicted results using our SunOriNet and the DCNN: SUN-CNN with ED loss [13]. The ground truth and the predicted orientations are shown in radian. The predicted errors are shown in angle

Fig. 3 Inserting 3D models to outdoor images

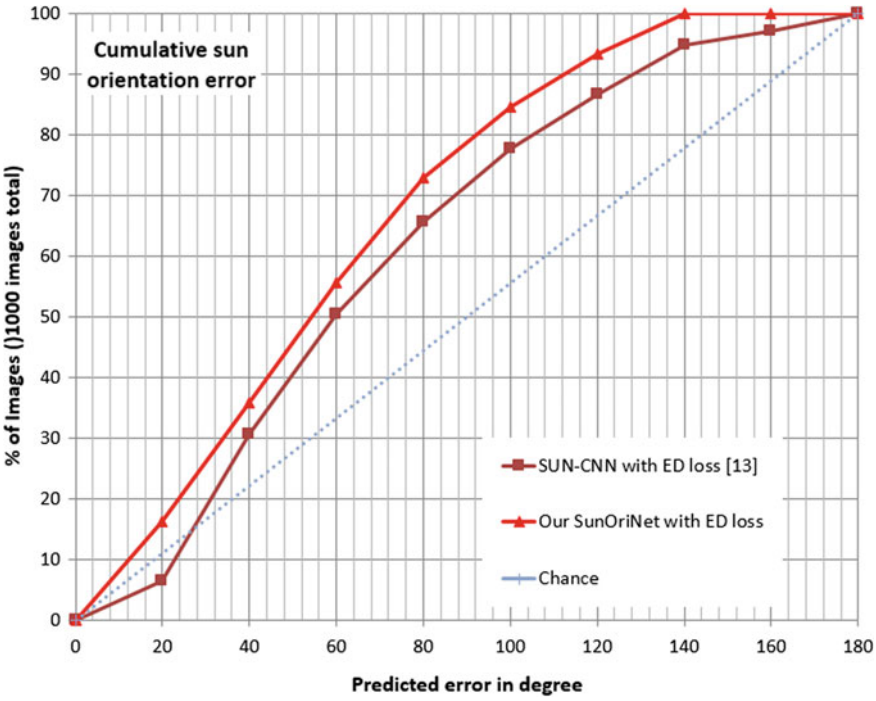

Fig. 4 Comparison with [13]. Cumulative sun orientation error (angle between predicted and ground truth directions) for different methods

4 Conclusions

We propose a novel DCNN SunOriNet, which provides an end to end way of sun orientation estimation from a single non-cloudy image. This can be used for create virtual-real artworks. Our SunOriNet learns both low-level and high-level features from a large-scale dataset with annotated ground truth sun orientations. The experiments reveal that our DCNN can well estimate sun orientation from a single outdoor image. Our method outperforms the modern deep convolutional neural networks.

Acknowledgements We thank all the reviewers and ACs. This work is partially supported by the National Natural Science Foundation of China (Grant Nos. 61772047, 61772513, 61402021), the Science and Technology Project of the State Archives Administrator (Grant No. 2015-B-10), the open funding project of State Key Laboratory of Virtual Reality Technology and Systems, Beihang University (Grant No. BUAA-VR-16KF-09), the Fundamental Research Funds for the Central Universities (Grant No. 3122014C017), the China Postdoctoral Science Foundation (Grant No. 2015M581841), and the Postdoctoral Science Foundation of Jiangsu Province (Grant No. 1501019A).

References

1. Basri, R., Jacobs, D., Kemelmacher, I.: Photometric stereo with general, unknown lighting. Int. J. Comput. Vis. **72**, 239–257 (2007)
2. Debevec, P.: Rendering synthetic objects into real scenes: bridging traditional and image-based graphics with global illumination and high dynamic range photography. Proceedings of the Annual Conference on Computer Graphics and Interactive Techniques, New York, pp. 189–198 (1998)
3. Frahm, J.M., Koeser, K., Grest, D., et al.: Markerless augmented reality with light source estimation for direct illumination. In: Proceedings of the European Conference on Visual Media Production, London, pp. 211–220 (2005)
4. Lalonde, J.F., Efros, A., Narasimhan, S.: Estimating natural illumination from a single outdoor image. In: Proceedings of the IEEE International Conference on Computer Vision, Kyoto, pp. 183–190 (2009)
5. Lalonde, J.-F., Efros, A.A., Narasimhan, S.G.: Estimating the natural illumination conditions from a single outdoor image. Int. J. Comput. Vis. (IJCV). **98**(2), 123–145 (June 2012)
6. Chen, X., Jin, X., Wang, K.: Lighting virtual objects in a single image via coarse scene understanding. Sci. China Inf. Sci. (SCIS) **57**(9), 1–14 (2014)
7. Liu, Y., Gevers, T., Li, X.: Estimation of sunlight direction using 3D object models. IEEE Trans. Image Process. **24**(3), 932–942 (March 2015)
8. Krizhevsky, A., Sutskever, I., Hinton, G.E.: Imagenet classification with deep convolutional neural networks. In: Advances in Neural Information Processing Systems (NIPS), pp. 1097–1105 (2012)
9. He, K., Zhang, X., Ren, S., Sun, J.: Delving deep into rectifiers: surpassing human-level performance on imagenet classification. In: ICCV (2015)
10. Lalonde, J.-F., Efros, A.A., Narasimhan, S.G.: Webcam clip art: appearance and illuminant transfer from time-lapse sequences. ACM Trans. Graph. (SIGGRAPH Asia 2009), **28**(5) (2009)
11. Jia, Y., Shelhamer, E., Donahue, J., Karayev, S., Long, J., Girshick, R., Guadarrama, S., Darrell, T.: Caffe: convolutional architecture for fast feature embedding (2014). arXiv:1408.5093
12. Zhang, J., Lalonde, J.F.: Learning high dynamic range from outdoor panoramas. In: IEEE International Conference on Computer Vision (ICCV), Venice, pp. 4529–4538 (2017)

13. Ma, W.-C., Wang, S., Brubaker, M.A., Fidler, S., Urtasun, R.: Find your way by observing the sun and other semantic cues. In: IEEE International Conference on Robotics and Automation (ICRA), Singapore, 29 May–3 June 2017
14. Hold-Geoffroy, Y., Sunkavalli, K., Hadap, S., Gambaretto, E., Lalonde, J.-F.: Deep outdoor illumination estimation. In: IEEE Conference on Computer Vision and Pattern Recognition (CVPR) (2017)
15. Lu, H., Li, Y., Mu, S., Wang, D., Kim, H., Serikawa, S.: Motor anomaly detection for unmanned aerial vehicles using reinforcement learning. IEEE Internet Things J. (2017). https://doi.org/10.1109/jiot.2017.2737479
16. Lu, H., Li, Y., Chen, M., Kim, H., Serikawa, S.: Brain intelligence: go beyond artificial intelligence. Mob. Netw. Appl. 1–8 (2017)
17. Lu, H., Li, B., Zhu, J.: Wound intensity correction and segmentation with convolutional neural networks. Concurr. Comput. Pract. Exp. (2017). https://doi.org/10.1002/cpe.3927
18. Lu, H., Li, Y., Uemura, T., Kim, H., Serikawa, S.: Low illumination underwater light field images reconstruction using deep convolutional neural networks. Futur. Gener. Comput. Syst. (2018). https://doi.org/10.1016/j.future.2018.01.001
19. Serikawa, S., Lu, H.: Underwater image dehazing using joint trilateral filter. Comput. Electr. Eng. **40**(1), 41–50 (2014)

A Novel Sliding Mode Control for Human Upper Extremity with Gravity Compensation

Ting Wang and Wen Qin

Abstract The paper studied the reaching movements of redundant human upper extremity muscles by a sliding mode control based on fuzzy adaptive scale adjustment. A two-link planar human musculoskeletal arm model is adopted on the basis of the Hill type with six redundant muscles. The study focused on the gravity compensation for the muscle input during the reaching movements process. Through the fuzzy adaptive system, the sliding mode controller may achieve adaptive approximation of switching scale so as to eliminate chattering. The numerical simulations are performed in order to verify the control. The results revealed that the human upper extremity can very well accomplish the reaching moments with proposed sliding mode controller.

Keywords Musculoskeletal model · Human upper extremity
Gravity compensation · Sliding mode control

1 Introduction

Once the electrical signals between the brain and muscles have interrupted, it may result spinal cord injuries (SCI) and cause paralysis on patients [1]. The patients may be trained and exercised by Functional Electrical Simulation (FES) for rehabilitation. The FES stimulates the peripheral nerves of disable limbs by impaired motor control [2]. From recent researches, the motor control may efficiently improved the recovery of upper extremity movements as the stimulation associated with the voluntary attempt [3].

In early research, the most common control method for FES is the feed forward control [4]. The obvious advantage of the feed forward control is that it is very simple to implement without requiring sensors. The drawback of the feed forward control

T. Wang (✉) · W. Qin
College of Electrical Engineering and Control Science,
Nanjing Tech University, Nanjing, China
e-mail: wangting0310@njtech.edu.cn

H. Lu (ed.), *Cognitive Internet of Things: Frameworks, Tools and Applications*, Studies in Computational Intelligence 810,
https://doi.org/10.1007/978-3-030-04946-1_7

is that it too much depends on accurate parameters of the model due to the absence of sensors. As researches go deep, more and more researchers focus on the feedback control utilizing sensors to detect arm properties and to modify actual actions to desired behaviors. The feedback control of human upper extremity involved shoulder function, elbow extension and so on [5–7].

Other advanced and intelligent control strategies for the human musculoskeletal arm model are investigated as follow. Blana et al. proposed the control combining the feed forward and feedback control [8]. Tahara et al. firstly studied the nonlinear Hill-typed human musculoskeletal arm model with 2 degrees of freedom (DOF) [9, 10]. Vatankhah et al. designed an adaptive optimal neuro-fuzzy controller and applied it to the reaching movements control [11]. Atawnih et al. also focused on the reaching movements control of redundant musculoskeletal human arm and proposed a controller based on the redundant arm torque controller [12]. Freeman et al. proposed the iterative learning control to apply FES to the upper extremity for rehabilitation [2]. Jagodnik and other researchers studied the PD controller based on the reinforcement learning structure and used it to accomplish the FES control of high-level upper-extremity [13]. Jagodnik et al. proposed a proportional-derivative (PD) controller. They verified their PD controller to a 3-dimensional bio- mechanical human arm model of a human arm with 5 DOF [9].

Many researchers studied the sliding mode control (SMC) and applied it to mimic human arm reaching movements. The SMC is simple to use and is suitable transient performance with quick response [1]. Corradini et al. proposed a discrete-time SMC for robotic manipulators [12]. Sharifi et al. acquiring the optimal performance of the SMC controller by an optimal policy and they used it to the planar human musculoskeletal arm movements [13]. An inherent problem of SMC is chattering, which may cause damages to the system. To shorten chattering, many researchers suggested many different methods. Ngo et al. added the fuzzy logic to SMC control accomplishing the trajectory of robots' manipulators [14]. Moussaoui et al. designed a fuzzy approximation-based SMC controller with adaptive scheme to solve under actuated systems with uncertain nonlinear perturbation [8, 15–18].

In order to avoid the chattering, a fuzzy adaptive scaling adjustment based SMC is proposed to accomplish the human arm reaching movements in this paper. The human musculoskeletal arm adopted a 2 joint Hill typed planar model with 6 muscles, which introduced in Sect. 2. The fuzzy adaptive scaling adjustment based SMC controller is explained in Sect. 3. Numerical simulation and discussion of results analyzed in Sect. 4. Future work and some conclusion have been given in the conclusion part.

2 Planar Human Arm Model

The planar human arm model is shown in Fig. 1, involving two links. The upper link is the upper extremity, and the lower part including the forearm and the hand. The two rotational joints are the elbow and the shoulder respectively. The gravitational effects are taking into account in the model.

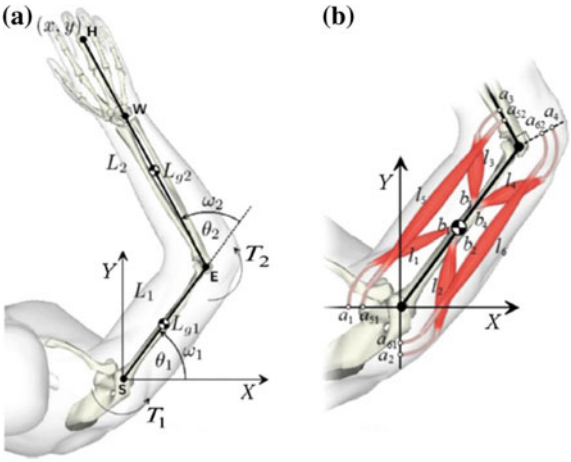

Fig. 1 The planar human musculoskeletal arm model

The forward kinematics of model is written as

$$X = \begin{bmatrix} x_1 \\ x_2 \end{bmatrix} = \begin{bmatrix} L_1 \cos\theta_1 + L_2 \cos(\theta_1 + \theta_2) \\ L_1 \sin\theta_1 + L_2 \sin(\theta_1 + \theta_2) \end{bmatrix}. \tag{1}$$

The lengths of two links represent by L_1 and L_2, and angles of two links represent by θ_1 and θ_2 as shown in Fig. 1. Through inverse kinematics, the following relation may obtain:

$$\begin{bmatrix} \theta_1 \\ \theta_2 \end{bmatrix} = \begin{bmatrix} tg^{-1}(\frac{x_2}{x_1}) + \frac{\pi}{2}\mathrm{sgn}(x_2)(1 + \mathrm{sgn}(x_1)) - \cos^{-1}(\frac{r^2 + L_1^2 - L_2^2}{2L_1 r}) \\ \pi - \cos^{-1}(\frac{r^2 + L_1^2 - L_2^2}{2L_1 r}) \end{bmatrix}. \tag{2}$$

Then, the relationship between the end-point's linear velocity and the angular velocity is written as

$$\dot{X} = J\dot{\theta} = \begin{bmatrix} -L_2 \sin(\theta_1 + \theta_2) - L_1 \sin\theta_1 & -L_2 \sin(\theta_1 + \theta_2) \\ -L_2 \cos(\theta_1 + \theta_2) - L_1 \cos\theta_1 & -L_2 \cos(\theta_1 + \theta_2) \end{bmatrix} \dot{\theta}, \tag{3}$$

where the angular velocity is indicated by $\dot{\theta}$ and the Jacobian matrix J is expressed in detail. Define six muscles' lengths as $q_i = f(a_{ij}, b_{ij})$, $i = 1, 2$, $j = 1 \ldots 6$ (i and j represent the subscript of joint and the subscript of muscles respectively), and the relationship between $\dot{q}_i$ and muscles lengths' changing rate is written as

$$\dot{q} = [\dot{q}_1, \dot{q}_2, \dot{q}_3, \dot{q}_4, \dot{q}_5, \dot{q}_6]^T = W\dot{\theta} = \begin{bmatrix} -a_1 & a_2 & 0 & 0 & -a_{51} & a_{61} \\ 0 & 0 & -a_3 & a_4 & -a_{52} & a_{62} \end{bmatrix} \dot{\theta}. \tag{4}$$

The muscle contractile velocities relating to joints angular velocities is defined by a Jacobian matrix W. Moments of muscles forces may be computed as $\tau = -W^T F$, according to the virtual work principle, where τ is the effective moment vector and F is muscles' tensile force vector. The dynamic motion equation may be expressed as

$$
\begin{aligned}
&M(\theta)\ddot{\theta} + C(\theta, \dot{\theta})\dot{\theta} + G(\theta) = \tau,\\
&M(\theta) = \begin{bmatrix} \frac{1}{3}m_1L_1^2 + \frac{1}{3}m_2L_2^2 + m_2L_1^2 + m_2L_1L_2\cos\theta_2 & \frac{1}{3}m_2L_2^2 + \frac{1}{2}m_2L_1L_2\cos\theta_2 \\ \frac{1}{3}m_2L_2^2 + \frac{1}{2}m_2L_1L_2\cos\theta_2 & \frac{1}{3}m_2L_2^2 \end{bmatrix},\\
&C(\theta, \dot{\theta}) = \begin{bmatrix} -m_2L_1L_2\dot{\theta}_2\sin\theta_2 & -\frac{1}{2}m_2L_1L_2(\dot{\theta}_1 + \dot{\theta}_2)\sin\theta_2 \\ \frac{1}{2}m_2L_1L_2\dot{\theta}_1\sin\theta_2 & 0 \end{bmatrix},\\
&G(\theta) = \begin{bmatrix} m_1g + \frac{L_1}{2}\sin\theta_1 + m_2gL_1\sin\theta_1 + m_2g\frac{L_2}{2}\sin(\theta_1 + \theta_2) \\ m_2g\frac{L_2}{2}\sin(\theta_1 + \theta_2) \end{bmatrix},
\end{aligned}
\tag{5}
$$

where g is the gravitation constant, and M, C, G are the mass inertia matrix, viscosity matrix and gravity matrix respectively.

With taking into account the damping effect of muscles' contractile element, the Hill force–velocity relationship for the nonlinear skeletal muscle model may be written in a simple hyperbolic equation as follow [12]:

$$(f_i + a)(\dot{l}_i + b) = b(f_{0i} + a). \tag{6}$$

The muscle's tensile force output represented by f. The muscle's contractile velocity represented $\dot{l}$. The maximum muscle isometric tensile force represented by f_0. a and b are the lengths represented the heat constant and the energy liberation constant. Taking into account of the muscle intrinsic damping, the dynamics equation of the muscle is modeled as [13]

$$
\begin{aligned}
&f_i(\bar{\alpha}_i, \dot{l}_i) = p_i\left\{\bar{\alpha}_i - (\bar{\alpha}_i c_i + c_{0i})\dot{l}_i\right\},\\
&p_i = \frac{0.9l_{0i}}{0.9l_{0i} + \left|\dot{l}_i\right|}, c = \begin{cases} \frac{0.25}{0.9l_{0i}}, \dot{l}_i \geq 0 \\ \frac{2.25}{0.9l_{0i}}, otherwise. \end{cases}
\end{aligned}
\tag{7}
$$

The control input of muscles is $\bar{\alpha}$, where $\bar{\alpha} = f_0\bar{\alpha}$. l_0 is muscle's free length and c is the intrinsic damping parameter, $c>0$, $0< p < l$. All the values of parameters in this section are illustrated in Tables 1 and 2.

Table 1 Physical parameters of the musculoskeletal arm [14]

Title	Value
Mass of the upper extremity	2.089 kg
Mass of the forearm and hand	1.192 kg
Length of the first link	0.298 m
Length of the second link	0.419 m
Inertia moment of the first link	0.0159 kg m^2
Inertia moment of the second link	0.0257 kg m^2
Center of the mass of the first link	0.152 m
Center of the mass of the first link	0.181 m
Joint viscosity	$\begin{bmatrix} 0.74 & 0.1 \\ 0.1 & 0.82 \end{bmatrix}$

Table 2 Muscles lengths [14]

a_1, a_2, a_{51}, a_{61}	a_3, a_4, a_{52}, a_{62}	b_1, a_2	b_3, a_4
0.055	0.045	0.08	0.12

3 Fuzzy Adaptive Scaling Adjustment Based SMC

Defining the tracking error as $\mathbf{e} = \boldsymbol{\theta}_d - \boldsymbol{\theta}$, and the error function is defined as follows:

$$\begin{aligned} &\mathbf{s} = \dot{\mathbf{e}} + \boldsymbol{\lambda}\mathbf{e}, \lambda = diag[\lambda_1, \ldots \lambda_i, \ldots \lambda_n], \lambda_i > 0, \\ &\dot{\boldsymbol{\theta}}_e = \dot{\boldsymbol{\theta}} - \mathbf{s} = \dot{\boldsymbol{\theta}}_d - \breve{\mathbf{e}}, \ddot{\boldsymbol{\theta}}_e = \ddot{\boldsymbol{\theta}} - \dot{\mathbf{s}} = \ddot{\boldsymbol{\theta}}_d - \boldsymbol{\lambda}\dot{\mathbf{e}}. \end{aligned} \tag{8}$$

The fuzzy system can achieve accurate approximation to arbitrary continuous function. Therefore, the scale of the control law can be adaptive approximated by the fuzzy system. The control law based on the fuzzy scale adjustment is written as:

$$\tau = M\ddot{\theta}_e + C\dot{\theta}_e + G - As - K, \quad K = [k_1, \cdots, k_n], \tag{9}$$

where k_i is the output of the i-th fuzzy system. The membership function used to represent fuzzy sets is designed as

$$\mu_A(x_i) = \exp\left[-\left(\frac{x_i - u}{\sigma}\right)^2\right]. \tag{10}$$

The output of the fuzzy system is

$$k_i = \frac{\sum_{m=1}^{M} \theta_{k_i}^m \mu_{A^m}(s_i)}{\sum_{m=1}^{M} \mu_{A^m}(s_i)} = \boldsymbol{\theta}_{k_i}^T \boldsymbol{\Psi}_{k_i}(s_i), \tag{11}$$

where

$$\boldsymbol{\theta}_{k_i} = \left[\theta_{k_1}, \cdots, \theta_{k_n}\right]^T, \boldsymbol{\Psi}_{k_i}(s_i) = \left[\psi_{k_i}^1(s_i), \cdots, \psi_{k_i}^M(s_i)\right]^T,$$
$$\psi^m(x) = \frac{\Pi_{i=1}^n \mu_{A_i^m}(x_i^*)}{\sum_{m=1}^{M} \Pi_{i=1}^n \mu_{A_i^m}(x_i^*)},$$

$\boldsymbol{M}$ is the number of the fuzzy rules. Substituting the control law based on the fuzzy scale adjustment into the dynamic equation yields

$$\mathbf{M}\dot{\mathbf{s}} = -(\mathbf{C} + \mathbf{A})\mathbf{s} + \Delta\mathbf{f} - \mathbf{k}. \tag{12}$$

Taking $k_i = \boldsymbol{\theta}_{k_{id}}^T \boldsymbol{\Psi}_{k_i}(s_i)$ as the approximation of the ideal Δf_i, according to the universal approximation theorem, there exist $\omega_i > 0$ and the relation $\left|\Delta f_i - \boldsymbol{\theta}_{k_{id}}^T \boldsymbol{\Psi}_{k_i}(s_i)\right| \leq \omega_i$. The adaptive law adopted as $\dot{\hat{\boldsymbol{\theta}}}_{k_i} = s_i \psi_{k_i}(s_i)$.

4 Numerical Simulations and Results

The initial angles and angle velocities are $\theta_{10} = \frac{\pi}{6}, \theta_{20} = \frac{\pi}{4}, \dot{\theta}_{10} = \dot{\theta}_{20} = 0$. The final angles and angle velocities are $\theta_{1d} = \frac{\pi}{3}, \theta_{2d} = \frac{5\pi}{12}$. Taking the fuzzy adaptive scaling adjustment based SMC, the results of simulation are demonstrated as following pictures. Angle error tracking of shoulder joint and elbow joint respectively displayed in Fig. 2(a). Effective torque input displayed in Fig. 2(b) and the adaptive adjustment scales of SMC displayed in Fig. 2(c). Trough the simulation results, it revealed that the novel SMC controller can accomplish the reaching movements of human arm with proposed model.

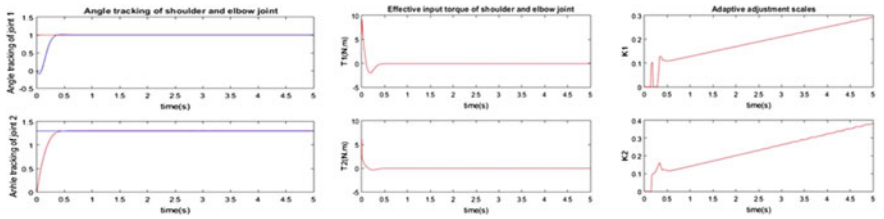

Fig. 2 Results of simulation

5 Conclusion

The reaching movements of human musculoskeletal arm model is studied and implemented by proposed fuzzy adaptive scaling adjustment based SMC controller. The model took a Hill-type two links model with six muscles with taking into account the gravitational effects. A novel SMC controller is designed based on the fuzzy adaptive scale adjustment. Since the slide surface can be adaptive via adjusting of the scales, it quickly moved to the state variables as the state variables moving to it. Via the fuzzy adaptive scale adjustment, it may efficiently avoid the chattering of the SMC. To verify the controller, the paper performed the numerical simulation of tracking of desired shoulder and elbow angles. Results showed the effectiveness and good performance of the proposed novel SMC controller. Future work will go on to focus on the reaching movements of the human musculoskeletal arm considering the fatigue factors of muscle.

Acknowledgements This work was supported by the Natural Science Foundation of the Jiangsu [grant numbers BK20171019].

References

1. Shahbazzadeh, Z.J., Ardakani, F.F, Vatankha, R.: Exponential sliding mode controller for a nonlinear musculoskeletal human arm model. International Conference on Modeling, pp. 1–5 (2017)
2. Freeman, C.T., Hughes, A.M., Burridge, J.H., Chappell, P.H., Lewin, P.L., Rogers, E.: Iterative learning control of FES applied to the upper extremity for rehabilitation. Control. Eng. Pract. **17**, 368–381 (2009)
3. Jagodnik, K., van den bogert, A.: A proportional derivatives FES controller for planer arm movement. The 12th Annual Conference of the International FES Society November 2007. Philadelphia, PA, USA (2007)
4. Peckham, P.H., Knutson, J.S.: Functional electrical stimulation for neuromuscular applications. Ann. Rev. Biomed. Eng. **7**, 327–360 (2005)
5. Lynch, C.L., Popovic, M.R.: Functional electrical stimulation: Closed-loop control of induced muscle contractions. IEEE Control. Syst., 40–50 (2008)
6. Jagodnik, K., Blana, D., Van, Kirsch, R.F.: An optimized proportional-derivative controller for the human upper extremity with gravity. J. Biomech., **483**, 692–3700 (2015)
7. Tahara, K., Hitoshi, K.: Reaching movements of a redundant musculoskeletal arm: Acquisition of an adequate internal force by iterative learning and its evaluation through a dynamic damping ellipsoid. Adv. Robot. **24**(5-6), 783–818 (2010)
8. Vatankhah, R., Mehrdad, B., Aria, A.: Adaptive optimal multi-critic based neuro-fuzzy control of MIMO human musculoskeletal arm model. Neurocomputing **173**, 1529–1537 (2016)
9. Atawnih, A., Dimitrios, P., Zoe, D.: Reaching for redundant arms with human-like motion and compliance properties. Robot. Auton. Syst. **62**(12), 1731–1741 (2014)
10. Jagodnik, K.M.: Reinforcement learning and feedback control for high-level upper-extremity neuroprostheses. Dissertation, Case Western Reserve University, Cleveland, OH, USA (2014)
11. Corradini, M.L., Giantomassi, A., Ippoliti, G., Orlando, G.: Robust control of robot arms via quasi sliding modes and neural networks. In: Advances and Applications in Sliding Mode Control systems, vol. 576, pp. 79–105. Springer Publishing (2015)

12. Sharifi, M., Hassan, S., Saeed, B.: Nonlinear optimal control of planar musculoskeletal arm model with minimum muscles stress criterion. J. Comput. Nonlinear Dyn. **12**(1), 011014 (2017)
13. Lochan, K., Suklabaidya, S., Roy, B. K.: Sliding mode and adaptive sliding mode control approaches of two link flexible manipulator. Conference on Advances in Robotics, p. 58. ACM (2015)
14. Moussaoui, S., Abdesselem B., Sundarapandian V.: Fuzzy adaptive sliding-mode control scheme for uncertain underactuated systems. Advances and Applications in Nonlinear Control Systems, pp. 351–367. Springer International Publishing (2016)
15. Lu, H., Serikawa, S.: Underwater image dehazing using joint trilateral filter. Comput. Electr. Eng. **40**(1), 41–50 (2014)
16. Lu, H., Li, Y., Su, M., Dong, W., Kim, H.: Motor anomaly detection for unmanned aerial vehicles using reinforcement learning. IEEE Internet Things J. https://doi.org/10.1109/jiot.2017.2737479 (2017)
17. Lu, H., Li, Y., Chen, M., Kim, H., Serikawa, S.: Brain intelligence: Go beyond artificial intelligence. Mob. Netw. Appl., 1–8 2017
18. Lu, H., Li, B., Zhu, J., Li, Y.: Wound intensity correction and segmentation with convolutional neural networks, concurrency and computation: practice and experience. https://doi.org/10.1002/cpe.3927 (2017)

Compressive Sensing-Based Optimal Design of an Emerging Optical Imager

Gang Liu, Desheng Wen, Zongxi Song, Zhixin Li, Weikang Zhang and Xin Wei

Abstract The emerging optical imager can greatly reduce system weight and size compared to conventional telescopes. The compressive sensing (CS) theory demonstrates that incomplete and noisy measurements may actually suffice for accurate reconstruction of compressible or sparse signals. In this paper, we propose an optimized design of the emerging optical imager based on compressive sensing theory. It simplifies data acquisition structure and reduces data transmission burden. moreover, the system robustness is improved.

Keywords Optical instrument · Interferometry · Compressive sensing Photonic integrated circuit

1 Introduction

Space telescopes are significant instruments located in outer space to observe distant planets, galaxies and other astronomical objects. However, conventional space telescopes can be bulky, heavy and power consuming for consisting of large optics, supporting structures and precise thermal controls. Launching large and heavy objects into space is also expensive. These factors restrict the development of space telescopes. Telescopes with large apertures which can reduce the volume, weight and power are demanding for urgently.

The emerging imaging technology is called compact passive coherent imaging technology with high resolution (CPCIT) that utilizes interference. In 2010, Fontaine et al. [2] outlined the possibility of accurate measurements of amplitude and phase. In 2013, the segmented planar imaging detector for EO reconnaissance (SPIDER)

G. Liu · D. Wen · Z. Song (✉) · Z. Li · W. Zhang · X. Wei
Xi'an Institute of Optics and Precision Mechanics, Chinese Academy of Sciences, Xi'an 710119, Shaanxi Province, China
e-mail: zxsong@opt.ac.cn

G. Liu · Z. Li · W. Zhang · X. Wei
University of Chinese Academy of Sciences, Beijing 100049, China

H. Lu (ed.), *Cognitive Internet of Things: Frameworks, Tools and Applications*, Studies in Computational Intelligence 810,
https://doi.org/10.1007/978-3-030-04946-1_8

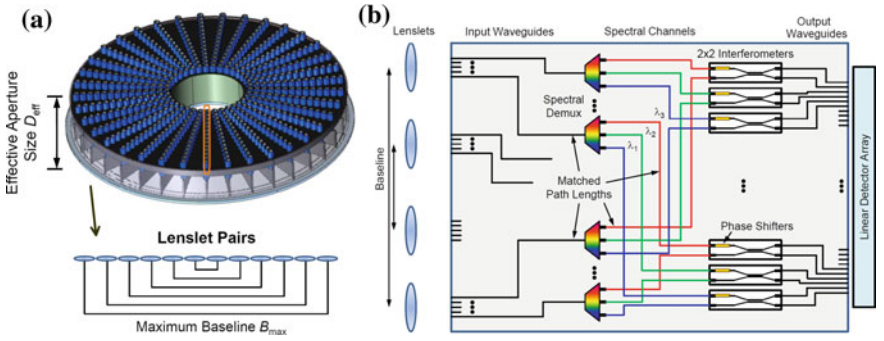

Fig. 1 **a** An example SPIDER imager concept. **b** Schematic view of a single PIC card from the SPIDER imager. The figures are taken form the literature [1]

[1, 3, 4] was developed applied this technology for the first time. Figure 1a shows an example SPIDER imager concept. SPIDER can be seen as a small-scale interferometric imager that uses a 2D lenslet array to simultaneously form many baselines. Photonic integrated circuits (PICs) are located behind the lenslet array to miniaturize the beam combination hardware. As shown in Fig. 1b, a PIC contains various components necessary for making the visibility measurements, such as spectral demultiplexers, delay lines, phase modulators, beam combiners, and detectors. SPIDER contains plenty of baselines and samples a large amount of visibility data. It is a heavy transmission burden that these data are transmitted from the imager in space back to the ground station. In addition, these data are easily corrupted by noise during transmission. In CPCIT theory, sampling data are spatial frequency components of object, which have sparse and compressible features. Compressive Sensing (CS) theory is suitable to process data with those features [5, 6].

This paper proposes an optimized CPCIT structure (OPSP) based on CS and SPIDER, which simplifies the data acquisition structure of the PIC backend. Compared to SPIDER, the amount of data required for reconstructing image is greatly reduced, and the system's robustness is improved. The remaining sections of the paper are structured as follows. Section 2 discusses the basic aspects of CPCIT. Section 3 reviews compressive sensing theory briefly. The optimized OPSP structure is discussed in Sect. 4. Simulation experiment of the proposed system is presented in Sect. 5. Finally a discussion and conclusions are given in Sect. 6.

2 Compact Passive Coherent Imaging Technology with High Resolution

In this section, we discuss the basic aspects of CPCIT. CPCIT and radio interferometry have similarities in basic principles [7, 8]. A radio interferometer is an array of spatially separated antennas that images the sky at higher resolution than possible with a single dish, thus synthesizing a larger aperture. Similarly, CPCIT consists

of mass of lenslets arranged in a radial-spoke pattern, each spoke is a 1D lenslet array composes of a set of lenslets. Each pair of lenslet measures phase and amplitude of a Fourier component of the intensity distribution across the sky. Through the measurements of these Fourier components, the sky is effectively imaged.

According to Van-Zernike Theorem [9], for an incoherent optical source with the intensity distribution $I_s(\boldsymbol{\sigma})$, the complex visibility of the observed source for each lenslet pair is given by:

$$y(\mathbf{u}) = \int_{\boldsymbol{R^2}} I_s(\boldsymbol{\sigma}) exp(i2\pi\boldsymbol{\sigma} \cdot \mathbf{u}) d\boldsymbol{\sigma}. \tag{1}$$

Here $\boldsymbol{\sigma} \in \mathbb{R}^2$ denotes a location lies in the optical source region. $\mathbf{u} = (u, v) \in \mathbb{R}^2$ are the corresponding Fourier coordinates defined by the baseline: $\mathbf{u} = \frac{\mathbf{b}}{\lambda}$. In this context, a visibility contains a Fourier component of the sky intensity distribution at the spatial frequency $\mathbf{u}$. The total number of points $\mathbf{u}$ probed by all lenslet pairs of the array provides incomplete coverage in the Fourier plane, which is the so-called u-v coverage.

In CPCIT, the visibility is measured in PIC. Incoming electric fields pass through a pair of lenslets can be expressed as:

$$E_S = A_S e^{-j(\omega t + \varphi_1)}, \tag{2a}$$

$$E_R = A_R e^{-j(\omega t + \varphi_2)}, \tag{2b}$$

where A_S, A_R are amplitudes, ω is angular frequency, φ_1, φ_2 are initial phases [10]. We consider a monochromatic signal for expressing concisely. The two incoming electric fields are then cross-correlated in optical hybrid [11, 12] and generate p_Q signal (quadrature phase signal) and p_I signal (in-phase signal) as follows:

$$p_Q = I_{S+jR} - I_{S-jR} = A_S A_R \sin(\varphi_1 - \varphi_2), \tag{3a}$$

$$p_I = I_{S+R} - I_{S-R} = A_S A_R \cos(\varphi_1 - \varphi_2). \tag{3b}$$

Then we can obtain the complex visibility of a lenslet pair.

Complex visibility cannot be measured for all Fourier coordinates since the array of lenslets is arranged discretely. The Fourier transform relation of Eq. 1 cannot be inverted directly to obtain an accurate estimation of $I_s(\boldsymbol{\sigma})$. The missing samples of complex visibility leave Eq. 1 as an ill-posed inverse problem, which has an infinite possible solution numbers.

3 Compressive Sensing

Compressive sensing [5, 13] is a sampling and compression theory based on the sparsity of an observed signal. CS relies on two key principles: sparsity and incoherence. Sparsity illustrates the fact the signal can be sparsely represented in a proper

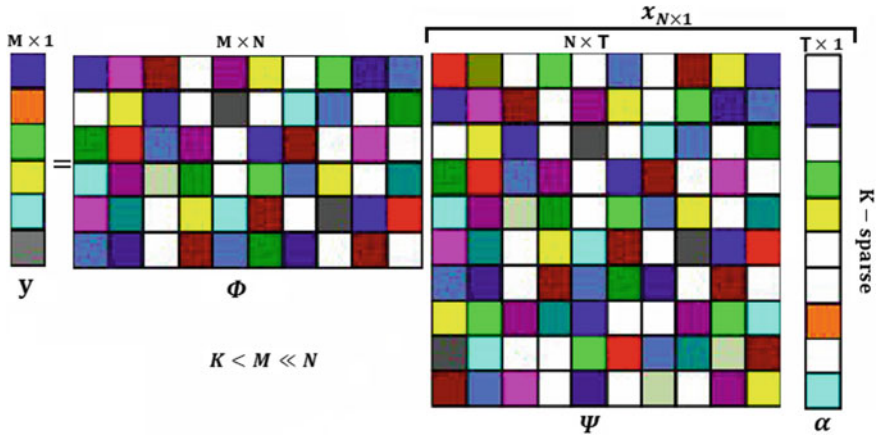

Fig. 2 Compressive sensing diagram

dictionary $\boldsymbol{\Psi}$. For instance, we consider a real signal identified by its Nyquist-Shannon sampling as $\boldsymbol{x} = \{x_i\}_{1\leq i\leq N} \in \mathbb{R}^N$. This signal may be not sparse in its time domain, but in some space, $\mathbf{x}$ can be decomposed as $\mathbf{x} = \boldsymbol{\Psi\alpha} = \sum_{\mathbf{i=1}}^{\mathbf{K}} \mathbf{(i)}_{\mathbf{i}}$.

Here the dictionary $\Psi = \{\psi_1, \psi_2, \ldots, \psi_T\} = \{\psi_{it}\}_{1\leq i\leq N, 1\leq t\leq T} \in \mathbb{R}^{N\times T}$ may be either orthogonal, with $T = N$, or redundant, with $T > N$. $\boldsymbol{\alpha} = \{\alpha_j\}_{1\leq j\leq T} \in \mathbb{R}^T$ is a sparse representation of $\mathbf{x}$ that it only contains a small number $K \ll N$ of non-zero or significant coefficients respectively in $\boldsymbol{\Psi}$. Incoherence expresses the duality between time and frequency that the sampling waveforms in $\boldsymbol{\Psi}$ must have an extremely different representation from the interested signal.

Suppose that the signal is probed by M real linear measurements $\boldsymbol{y} = \{y_r\}_{1\leq r\leq M} \in \mathbb{R}^M$ in some real basis $\boldsymbol{\Phi} = \{\Phi_{ri}\}_{1\leq r\leq M, 1\leq i\leq N} \in \mathbb{R}^{M\times N}$:

$$\boldsymbol{y} = \boldsymbol{\Phi\Psi\alpha} + \boldsymbol{n} = \boldsymbol{\Theta\alpha} + \boldsymbol{n}. \tag{4}$$

Here $\boldsymbol{\Theta} = \boldsymbol{\Phi\Psi} \in \mathbb{R}^{M\times T}$is called sensing basis, $\boldsymbol{n} = \{n_r\}_{1\leq r\leq M} \in \mathbb{R}^M$ represents independent and identically distributed noise. This number M of projections is typically assumed to be smaller than the dimension N of the signal vector, so that the inverse problem Eq. 4 is ill-posed. It is possible and practical to solve the problem with the signal sparsity assumption. Figure 2 gives the schematic diagram of CS.

CS theory demonstrates that when Θ satisfies restricted isometry property (RIP) condition [6, 14], the ill-posed problem can be solved through l_1-norm minimization problem:

$$\min \| \boldsymbol{\alpha} \|_{l_1} \quad \textit{subject to} \quad \| \boldsymbol{y} - \boldsymbol{\Theta\alpha} \|_{l_2} \leq \epsilon, \tag{5}$$

where the l_1-norm is defined by $\| \boldsymbol{\alpha} \|_{l_1} = \sum_i |\alpha_i|$.Various basises satisfy RIP condition, such as Gaussian random basis [15], Bernoulli basis [16], Toplit basis [17] etc.

Common reconstruct algorithms can be summarized into two categories. One is greedy pursuit algorithm and its improved algorithm, which are based on minimal l_0-norm, such as matching pursuit (MP), regularized orthogonal matching pursuit (ROMP) [18], orthogonal matching pursuit (OMP) [19] etc. The other includes convex optimization algorithms with a minimal l_1-norm, such as basis pursuit (BP) [20], iterative thresholding (IT) [21], fast iterative shrinkage-thresholding (FIST) [22] and gradient projection for sparse reconstruction (GPSR) [23].

4 OPSP Design

CS theory enables the design of new imaging devices and techniques. In this section, an optimized structure of sampling and transmission based on CS principle and SPIDER, i.e., OPSP is designed and described. In addition, its implementation algorithm and image reconstruction algorithm will also be discussed here. In CPCIT, the outputs signal p_I and p_Q for each lenslets pair are measured respectively. In other words, CPCIT requires $2N$ signal detectors for N lenslet pairs. In contrast, OPSP combines all the p_I in one output $\mathbf{P_I}$ and all the p_Q in one output $\mathbf{P_Q}$. In the meanwhile, a control gate is inserted into every waveguide, which can be used to control the on-off states of waveguides and form a pseudorandom binary pattern. As a result, OPSP requires only two signal detectors for N lenslets pairs, as shown in Fig. 3. OPSP has a concise structure and less measurement data compared to CPCIT.

Assume that $1D$ lenslet array contains $2N$ waveguides, which form to N baselines. The outputs signal $\mathbf{P_I} = [p_{I1}, p_{I2}, \ldots p_{IN}]^T \in \mathbb{R}^{N\times 1}$ and $\mathbf{P_Q} = [p_{Q1}, p_{Q2}, \ldots p_{QN}]^T$

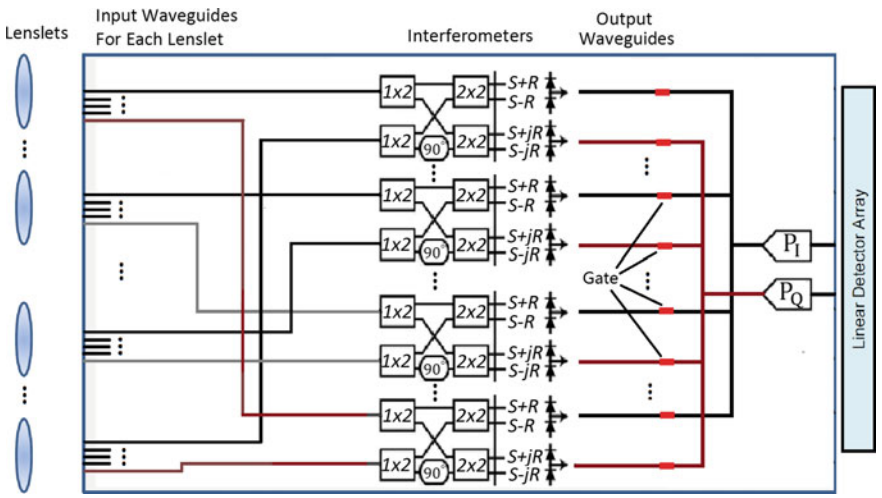

Fig. 3 Schematic view of OPSP. The output waveguide number is reduced to two

$\in \mathbb{R}^{N\times 1}$. Since the $\mathbf{P_I}$ and $\mathbf{P_Q}$ signal are measured and calculated separately, we take $\mathbf{P_Q}$ signal as an example for the following analysis. The M times different states of the control gates compose the measurement basis $\boldsymbol{\Phi} = [\Phi_1, \Phi_2, \ldots \Phi_N]^T \in \mathbb{R}^{M\times N}$. The measurement vector $\boldsymbol{y} \in \mathbb{R}^{M\times 1}$ is represented as:

$$\boldsymbol{y} = \boldsymbol{\Phi}\mathbf{P_Q} + \boldsymbol{n}. \tag{6}$$

Here $\boldsymbol{n}$ is the system noise. Then we can reconstruct $\mathbf{P_Q}$ from $\boldsymbol{y}$ through CS theory. OPSP reduces the measurement number from N to M, which greatly alleviates the transmission burden of data from the equipment to the base station. Furthermore, OPSP has better robustness property because l_1-norm has a strong denoising property for Gaussian noise. A variety of algorithms can be used to solve the problem described by Eq. 6, such as BP, MP etc. Besides, software packet l_1-magic [24] can be used conveniently to solve this problem. Here we use the greedy algorithms OMP, which is easy implementation and fast speed.

5 Experiment and Simulation

In this section, we evaluate the performance of OPSP through numerical simulation. The test image used in all simulations is M51, the famous Whirlpool Galaxy.[1] We use discrete model of size 255×255 as ground truth image. The test image and its Fourier transform diagram are shown in Fig. 4a and Fig. 4b, respectively. The reconstruction algorithm used is OMP, which is described in Sect. 4. The lenslet array arranged in a radial-spoke pattern with 137 $1D$ lenslet arrays in different orientation. Each 1D lenslet array is composed of 24 lenslets and 30 waveguides behind each lenslet. Thus there are 360 baselines in each 1D lenslet array. Regarding the CS algorithm, the input $N = N^{\frac{1}{2}} \times N^{\frac{1}{2}}$, sparse parameter $K = N/8$, and measurement parameter $M = 4K\log(N/K)$.

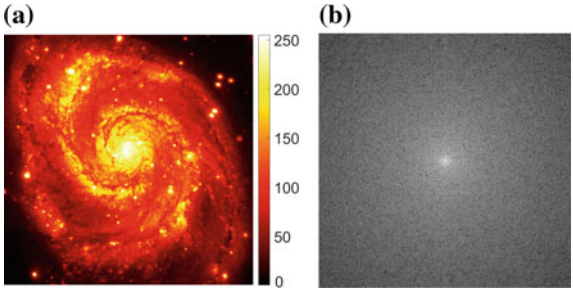

Fig. 4 **a** The original 255×255 test image, M51. **b** Fourier transform diagram of the test image

[1] Available at http://chandra.harvard.edu/.

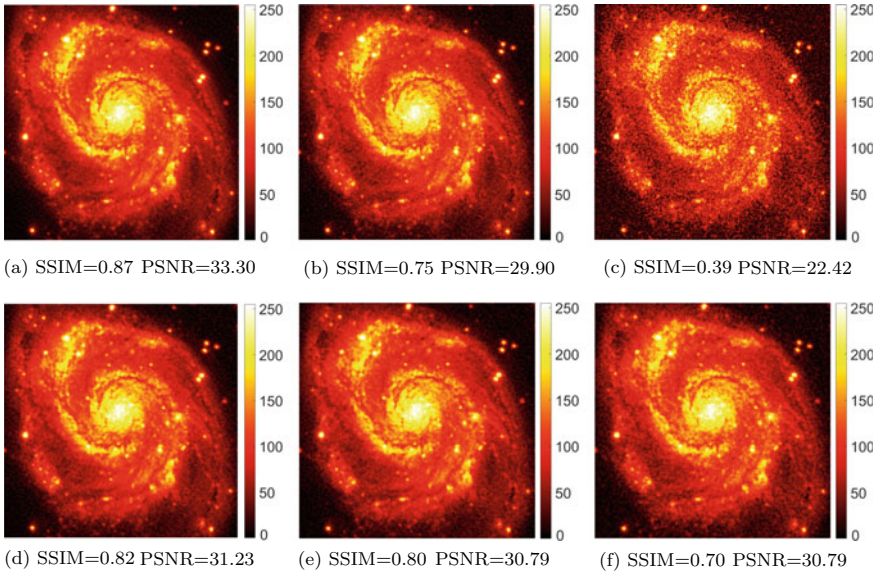

(a) SSIM=0.87 PSNR=33.30 (b) SSIM=0.75 PSNR=29.90 (c) SSIM=0.39 PSNR=22.42

(d) SSIM=0.82 PSNR=31.23 (e) SSIM=0.80 PSNR=30.79 (f) SSIM=0.70 PSNR=30.79

Fig. 5 Dirty maps of SPIDER and OPSP. **a** Dirty map of SPider without noise. **b** Dirty map of SPIDER with noise (ISNR = 20 dB). **c** Dirty map of spider with noise (ISNR = 10 dB). **d** Dirty map of OPSP without noise. **e** Dirty map of OPSP with noise (ISNR = 20 dB). **f** Dirty map of OPSP with noise (ISNR = 10 dB)

We use the structural similarity index (SSIM) and the peak signal to noise ratio (PSNR) [25] as reconstruction quality metric. The complex Gaussian noise which corrupted the visibilities are defined as an input SNR:

$$ISNR = 10 \log_{10} \frac{\delta_y^2}{\delta_n^2}, \tag{7}$$

where δ_y^2 and δ_n^2 stand for the sampled variances of the original signal $\mathbf{y}$ and of the noise $\mathbf{n}$.

We have experiments with noise at 0 dB, 10 dB, 20 dB, respectively. As shown in Fig. 5a, d, SPIDER and OPSP both have good reconstruction ability without noise. Although the performance of SPIDER is a bit better than OPSP, OPSP only needs less than half of the data sampled by SPIDER, which is significant for data transmission. In the situation of noise, OPSP has better performance than SPIDER. When the ISNR is 10dB, the image reconstructed by SPIDER is corrupted seriously. In contrast, the image reconstructed by OPSP is much less affected by the nose. The result suggests that OPSP has much better robustness than SPIDER, as shown in Fig. 5a–f.

6 Discussion and Conclusion

In this paper, we propose an optimized CPCIT structure based on Compressive Sensing and SPIDER, which simplifies the data acquisition structure of the PIC backend. Furthermore, the total transmission data have been greatly reduced and the robustness of the system is improved. Another attractive feature of the system is that it decreases the complexity and power consumption of the device through offloading data processing burden form data collection to data reconstruction. With the development and maturity of CPCIT technology in the future, the traditional telescopes will be innovated not only in the space telescope but also in other aspects.

Acknowledgements This work is supported by China Lunar Exploration Project (CLEP) and Youth Innovation Promotion Association, CAS.

References

1. Kendrick, R.L., Duncan, A., Ogden, C., Wilm, J., Stubbs, D.M., Thurman, S.T., Su, T., Scott, R.P., Yoo, S.: Flat-panel space-based space surveillance sensor. In: Proceedings of the Advanced Maui Optical and Space Surveillance Technologies Conference (2013)
2. Fontaine, N.K., Scott, R.P., Zhou, L., Soares, F.M., Heritage, J., Yoo, S.: Real-time full-field arbitrary optical waveform measurement. Nat. Photonics **4**(4), 248–254 (2010)
3. Duncan, A., Kendrick, R., Thurman, S., Wuchenich, D., Scott, R.P., Yoo, S., Su, T., Yu, R., Ogden, C., Proiett, R.: Spider: next generation chip scale imaging sensor. In: Advanced Maui Optical and Space Surveillance Technologies Conference (2015)
4. Scott, R.P., Su, T., Ogden, C., Thurman, S.T., Kendrick, R.L., Duncan, A., Yu, R., Yoo, S.: Demonstration of a photonic integrated circuit for multi-baseline interferometric imaging. In: 2014 IEEE Photonics Conference (IPC), pp. 1–2. IEEE (2014)
5. Candès, E.J., Wakin, M.B.: An introduction to compressive sampling. IEEE Signal Process. Mag. **25**(2), 21–30 (2008)
6. Candès, E.J., Romberg, J., Tao, T.: Robust uncertainty principles: Exact signal reconstruction from highly incomplete frequency information. IEEE Trans. Inf. Theory **52**(2), 489–509 (2006)
7. Pearson, T., Readhead, A.: Image formation by self-calibration in radio astronomy. Annu. Rev. Astron. Astrophys. **22**(1), 97–130 (1984)
8. Haniff, C.: An introduction to the theory of interferometry. New Astron. Rev. **51**(8), 565–575 (2007)
9. Goodman, J.W.: Statistical Optics. Wiley (2000)
10. Guyon, O.: Wide field interferometric imaging with single-mode fibers. Astron. Astrophys. **387**(1), 366–378 (2002)
11. Zimmermann, L., Voigt, K., Winzer, G., Petermann, K., Weinert, C.M.: c-band optical 90°-hybrids based on silicon-on-insulator 4×4 waveguide couplers. IEEE Photonics Technol. Lett. **21**(3), 143–145 (2009)
12. Hashimoto, T., Ogawa, I.: Optical hybrid integration using planar lightwave circuit platform. In: Proceedings of the SPIE, vol. 4652, pp. 58–67 (2002)
13. Baraniuk, R.G.: Compressive sensing [lecture notes]. IEEE Signal Process. Mag. **24**(4), 118–121 (2007)
14. Candès, E.J., et al.: Compressive sampling. In: Proceedings of the International Congress of Mathematicians, vol. 3, pp. 1433–1452, Madrid, Spain (2006)
15. Candes, E.J., Tao, T.: Decoding by linear programming. IEEE Trans. Inf. Theory **51**(12), 4203–4215 (2005)

16. Candes, E.J., Tao, T.: Near-optimal signal recovery from random projections: universal encoding strategies? IEEE Trans. Inf. Theory **52**(12), 5406–5425 (2006)
17. Candes, E.J., Romberg, J.K., Tao, T.: Stable signal recovery from incomplete and inaccurate measurements. Commun. Pure Appl. Math. **59**(8), 1207–1223 (2006)
18. Needell, D., Vershynin, R.: Uniform uncertainty principle and signal recovery via regularized orthogonal matching pursuit. Found. Comput. Math. **9**(3), 317–334 (2009)
19. Tropp, J.A., Gilbert, A.C.: Signal recovery from random measurements via orthogonal matching pursuit. IEEE Trans. Inf. Theory **53**(12), 4655–4666 (2007)
20. Chen, S.S., Donoho, D.L., Saunders, M.A.: Atomic decomposition by basis pursuit. SIAM Rev. **43**(1), 129–159 (2001)
21. Daubechies, I., Defrise, M., De Mol, C.: An iterative thresholding algorithm for linear inverse problems with a sparsity constraint. Commun. Pure Appl. Math. **57**(11), 1413–1457 (2004)
22. Beck, A., Teboulle, M.: A fast iterative shrinkage-thresholding algorithm for linear inverse problems. SIAM J. Imaging Sci. **2**(1), 183–202 (2009)
23. Figueiredo, M.A., Nowak, R.D., Wright, S.J.: Gradient projection for sparse reconstruction: application to compressed sensing and other inverse problems. IEEE J. Sel. Top. Signal Process. **1**(4), 586–597 (2007)
24. Candes, E., Romberg, J.: l1-magic: recovery of sparse signals via convex programming, vol. 4, p. 14 (2005). www.acm.caltech.edu/l1magic/downloads/l1magic.pdf
25. Wang, Z., Bovik, A.C., Sheikh, H.R., Simoncelli, E.P.: Image quality assessment: from error visibility to structural similarity. IEEE Trans. Image Process. **13**(4), 600–612 (2004)

A Method of Film Clips Retrieval Using Image Queries Based on User Interests

Ling Zou, Han Wang, Pei Chen and Bo Wei

Abstract The emergence of entertainment industry motivates the explosive growth of automatically film trailer. Manually finding desired clips from these large amounts of films is time-consuming and tedious, which makes finding the moments of user major or special preference becomes an urgent problem. Moreover, the user subjectivity over a film makes no fixed trailer meets all user interests. This paper addresses these problems by posing a query-related film clip extraction framework which optimizes selected frames to both semantically query-related and visually representative of the entire film. The experimental results show that our query-related film clip retrieval method is particularly useful for film editing, e.g. showing the abstraction of the entire film while playing focus on the parts that matches the user queries.

Keywords Film trailer · Multimedia retrieval · Deep learning

1 Introduction

With the development of media and entertainment industry development, thousands of TV videos and movies are produced every year. It is a time consuming and labor expensive work to process these videos manually. For film industry, it often takes several days to complete a movie trailer to arouse consumers' interests. Moreover, when different consumers' preferences are considered, the clips extracted from a film may need to vary according to various preferences. How to automatically extract personalized film clips becomes an urgent problem to be solved.

L. Zou (✉)
Digital Media School, Beijing Film Academy, Beijing, China
e-mail: zouling@bfa.edu.cn

H. Wang · P. Chen
School of Information and Technology, Beijing Forestry University, Beijing, China
e-mail: wanghan@bjfu.edu.cn

B. Wei
Hangzhou Dianzi University, Zhejiang, China

H. Lu (ed.), *Cognitive Internet of Things: Frameworks, Tools and Applications*, Studies in Computational Intelligence 810,
https://doi.org/10.1007/978-3-030-04946-1_9

Several attempts are made to automatically extract important information from the videos. Early methods concentrated on exploring low-level visual appearance and motion features for video clip extraction. By this means, one can obtain clips from a video based on the visual qualities while ignoring the parts that provide semantic information. However, the intrinsic content of a film is ignored and the extracting results are sameness for everyone. Different clips may arouse interests of different audience. How to obtain personalized film clips for varies people becomes an open problem in both film trailer and video retrieval field.

There are two main challenges that impede development of the research on customization film trailer. First, since there is no labeled information other than the user queries is available to leverage the film clips. How to obtain knowledge to process film clip extraction on the semantic level with regard to the user queries; Second, besides the query-dependent content, the query-independent content (e.g. such as quality, composition and the interestingness of the frame itself) should also be considered to provide users with more complete information about the video itself.

In an attempt to solve the first problem, traditional methods learn models for user preference via abundant of labeled data whose labeling process is time-consuming and laborious. Motivated by the gradually mature web image search engines, our methods try to learn supervised information from the Web images to liberate people from tedious and strenuous labeling work. An unsupervised query-related film clip extraction framework is proposed in this paper to provide personalized film trailer. Under this framework, the video frames and image-queries are projected onto a visual-semantic embedding space which captures the similarity between video frames and queries.

For the second problem, we further enforce a query-independent regularity on the rest of the videos to guarantee the representative and diversity of the whole clips. In this paper, we enforce the diversity on the video frames with the determinantal point process (DPP), a recently introduced probabilistic model for diverse subset selection.

Figure 1 shows an overview of our complete pipeline. Above all, this paper makes the following contributions:

1. An unsupervised film clips extraction framework is explored with regard to user preference on the film.
2. Under this framework, both query-dependent and query-independent term is proposed to make the extracted results focus on the clips matching the query while showing all the quality and diversity of the content itself.

2 Related Work

To the best our knowledge, we show the first-ever at automatically creating a movie trailer. Following, we briefly review some of the video highlights extraction methods which are most related to ours.

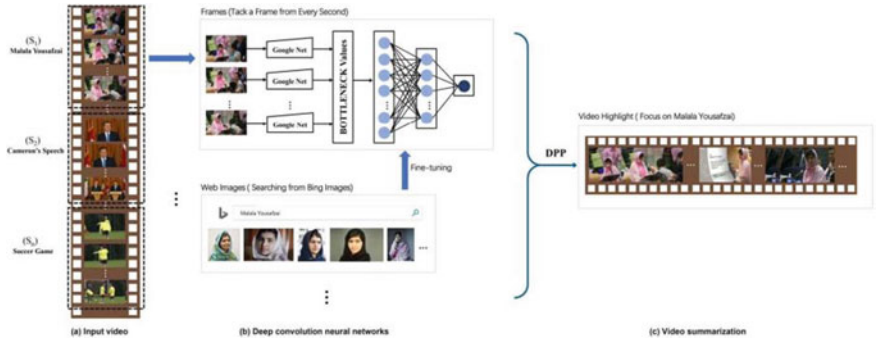

Fig. 1 Query-related film clip extraction framework. **a** The input video is divided into a set of alternative segments. **b** There two steps in this part. We first crawl abundant of web images to fine-tune the GoogleNet and learn a visual-semantic embedding space for transfer learning. Then a query-related convolution neural network architecture for highlight prediction is devised for scoring the video segments. **c** A determinantal point process is finally enforced on the extraction results to make the extraction results not only representative by showing a glimpse of the entire video but also playing more focus on the parts matching the query

The research field of query-related video highlights detection is gaining an increasing amount of attention recently [1–4]. The objective of the highlight extraction is to find a subset of frames that gives a user an abstraction of the video's content at a glance [5]. Early video summarization methods use low-level features [6–8], while recently more semantic and high-level information are introduced in the summarization frameworks. Most of these methods that predict frame belonging to a highlight are based on supervised learning. The prediction problem can be formulated as classification [1, 9], regression [10], or, as is now most common, as a ranking problem [11–14]. Mahasseni et al. [15] minimizing distance between training videos and their summaries to obtain high-level summarization in an unsupervised way. All above methods are generally focusing on two properties: representative of the selected frames and their diversity, ignoring the user preference over the videos. In this paper, the queries of users and the diversity of the frames are jointly considered in a unified framework.

Query-focused video highlights extraction problem is also been attracted more and more researchers' attention [16, 17]. Determinantal point process (DPP) [18], which is initially applied in document summarization area, is further employed to ensure the diversity property of the extraction performance [19, 20] recently. Its variation, sequential DPP [21] is used to maintain diversity for video summarization. Gong et al. first study query-focused video summarization through a Sequential and Hierachical Determinantal DPP (SH-DPP) [22], and extend their work to a new dataset in [23]. Our method apply DPP upon the query-related subsets, while maintaining the diversity of the extraction over the entire video.

Most related to our work is the method of [22], who represents an approach for query-focused video summarization considering both semantically relevance and

visually diversity. Their method, however, limits to a small, fixed set of queries. In this work, we formulated user query concept modeling as a transfer learning process from vast web images.

3 Technical Approach

3.1 Problem Formulation

Our overall goal is to generate a clip sequence for an input raw film sequence with the consideration of users' preference. Figure 1 provides an overview of our model and approach. Given an input film and a single image, our method should provide as output (1) visually diversity and (2) the corresponding clip sequences of any image related information contained within.

Given a query image Q proposed by a user, our goal is to pick a set of clips from the entire film $\mathcal{V}$ with a sense of the user preference delivered from the query image. We denote $S = \{s_1, \ldots, s_t\}$ as segments of a raw film $\mathcal{V}$ which is divided by temporal sequences, and use r_i to present the features extracted from the i-th segment. The extraction of query-related clips on film $\mathcal{V}$ can be solved by

$$v(Q, \mathcal{V}) \leftarrow argmax_{b \subseteq S} P(b|Q, \mathcal{V}), \tag{3.1.1}$$

in which b consists of a subset of video segments S and indicates which segment is selected.

3.2 Asymmetric Comparisons Using CNN Features

To obtain image-film embedding space for query images and raw films, we leverage the feature representation of a pre-training Inception-v3 network [24] on ImageNet [25]. Motivated by [26], we replace the softmax layer of Inception-v3 with two fully connected layers (Fig. 1) to make the pre-trained model achieving better performance after transferring to the film frames. The architecture of the top three layers are F1024-F1000-F25. We use the hidden layer with 1000 nodes as the clip features for each film frame. We refer to this model as query-inception model in the rest of the paper. Then, we use images given by users with consideration of the film to fine-tune the query-inception model in order to transfer semantic knowledge from the images to the query-related model.

Further, we use Fisher vectors to enhance our matching process. Using this technique, the similarity of two images is measured by the similarity of two FVs, one for each image. In some visual retrieval problems, however, one is not interested

in measuring how similar the query and database items are, but rather if the query image id contained in a database image, or vice versa.

We first sum up the similarity scores of frames that belong to a segment and then rank the whole video segments and selected top one segment.

Our model should learn to satisfy the rank constrain that given a query q, the relevance score of the segment s_j is higher than the relevance score of the irrelevant segment s_i, which can be expressed as

$$p(s_j|q_i) \succ (s_k|q_i) \tag{3.1.2}$$

4 Experiments

4.1 Datasets

We consider evaluating the query results on the real film, The Great Gatsby, which is a 2013 3D romantic drama film officially released by Bazmark Films and Village Roadshow Pictures. It is an adaptation of F. Scott Fitzgerald's 1925 novel of the same name. The story of the film is primarily about the characters. We use the pictures of two leading actors to query from the entire film expecting for returning semantically related clips. Since different story lines are expected to be divided by our method. For this film, we provide several pictures of different scene and wish corresponding scene clips may ideally returned through our framework.

It is worth noting that our method do not need any supervised information provided by human annotation.

4.2 Setting

To evaluate our extraction results, we first split the video into a set of ten-minute segments evenly sampled across raw film. And for each video segment, we randomly sample one frame per second. The final clip scores are computed as the sum of the all frames. For Inception-v3, we choose to use the output of pool5 layer for the feature description of each video frame. We use two fully connected layers to replace the softmax layer of Inception-v3.

Since the film trailer is a relatively subjective problem, in the spirit of Turing Test, we also asked a question about whether they feel that automatically machine extraction was used in retrieving the film clips. The participants of the survey cover a wide range of education backgrounds, including linguistics, physics, business, sports, computer science, and design.

4.3 Results

Since the film editing is a subjective task, we directly show some samples from our framework of the query results. From the results, we observe that our model is able to provide strong semantic accordance with the query images. The right most three column are the sample frames extracted from selected clips randomly and are arranged in similarity scores. The first column is two query images cut from the movie (Figs. 2 and 3).

To further illustrate the effectiveness of our method, we also give some Quantitative results. The experiments are performed on 10 news videos of British Broadcasting Corporation (BBC) dated from July 17th–22th, 2013. Table 1 summaries the precision and recall results of our approach compared to other methods (baseline method [1] (referred as Superframe in the following experiment), SVM based method as well as convolutional network (Inception-v3) [24]). As is expected, our method

Fig. 2 Example film clip extraction results on person from the film *The Great Gatsb*. The first column are two query images cut from the movie. The rest three columns are sample frames randomly selected from retrieved clips. We list top-3clips sorted by similarity score

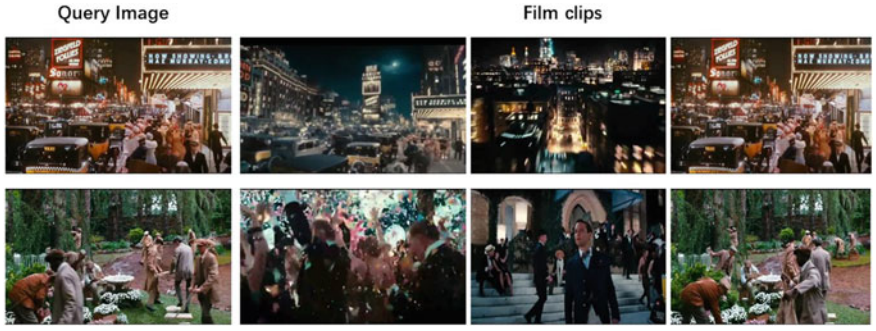

Fig. 3 Example film clip extraction results on scenes from the film *The Great Gatsby*. The first column are two query images cut from the movie. The rest three columns are sample frames randomly selected from retrieved clips. We list top-3clips sorted by similarity score

Table 1 Comparison of precision and recall (%) between our method and other methods on the BBC

Method	Superframe	SVM	Inception-v3	Ours
Precision	23.4	20.32	30.45	**32.16**
Recall	37.21	36.22	38.56	**57.67**

combined with query-focus and diversity outperforms the other methods. One interesting observation is that although we place more focus on the queries, our method can also perform well on predicting the rest of films than Superframe method. Our method outperforms neural network which demonstrate the transfer learning ability of our query-inception model of learning knowledge from the query image. SVM based method performs unsatisfactory partly because that it only settle the frame classification problem and do not concentrate on exploring the representative visual information through the whole film. Our method shows significant advantages on the BBC. This is because the content of BBC news is composed of small news one after another. There are no intrinsic connections between them. Our query-related method can quickly locate those moments that are semantically related to the query and find out the news that users are really interested in.

5 Conclusion

In this paper, we proposed an unsupervised film clips extraction framework in which the decision to select a film clip as highlight depends on both (1) the relevance between the segment and the user query and (2) the diversity situation of the segmentation regarding the whole film sequences. Based on these properties, we first project queries and video segments onto a visual-semantic embedding space to make them can be compared with our query-inception model. To preserving visual diversity of the extraction results as well, we further employ a probabilistic model, Determinantal Point Process, to make the extracted those segments representing a sense of entire film. Finally, we evaluate our method on twp real films. The results show that our method is doing a good job in querying semantically and visually similar film clips.

References

1. Gygli, M., Grabner, H., Riemenschneider, H., Gool, L.V.: Creating summaries from user videos. In: European Conference on Computer Vision, pp. 505–520 (2014)
2. Joshi, N., Kienzle, W., Toelle, M., Uyttendaele, M., Cohen, M.F.: Real-time hyperlapse creation via optimal frame selection. ACM Trans. Graph. **34**(4), 63 (2015)
3. Ghosh, J., Yong, J.L., Grauman, K.: Discovering Important People and Objects for Egocentric Video Summarization, vol. 157, no. 10, pp. 1346–1353 (2012)

4. Lu, Z., Grauman, K.: Story-driven summarization for egocentric video. In: IEEE Conference on Computer Vision and Pattern Recognition, pp. 2714–2721 (2013)
5. Truong, B.T., Venkatesh, S.: Video abstraction: a systematic review and classification. ACM Trans. Multimed. Comput. Commun. Appl. **3**(1), 3 (2007)
6. Dan, B.G., Curless, B., Salesin, D., Seitz, S.M.: Schematic Storyboarding for Video Visualization and Editing, pp. 862–871 (2006)
7. Bacco, R., Lambert, P., Lambert, P., Ionescu, B.E.: Video summarization from spatio-temporal features. In: ACM Trecvid Video Summarization Workshop, pp. 144–148 (2008)
8. Liu, T., Kender, J.R.: Optimization algorithms for the selection of key frame sequences of variable length. In: European Conference on Computer Vision, pp. 403–417 (2002)
9. Potapov, D., Douze, M., Harchaoui, Z., Schmid, C.: Category-specific video summarization. In: European Conference on Computer Vision, pp. 540–555 (2014)
10. Yong, J.L., Ghosh, J., Grauman, K.: Discovering important people and objects for egocentric video summarization. In: IEEE Conference on Computer Vision and Pattern Recognition, pp. 1346–1353 (2012)
11. Gygli, M., Song, Y., Cao, L.: Video2gif: automatic generation of animated gifs from video. In: Computer Vision and Pattern Recognition, pp. 1001–1009 (2016)
12. Lu, H., Li, Y., Chen, M., Kim, H., Serikawa, S.: Brain intelligence: go beyond artificial intelligence. Mob. Netw. Appl. **23**, 368–375 (2018)
13. Yao, T., Mei, T., Rui, Y.: Highlight detection with pairwise deep ranking for first-person video summarization. In: Computer Vision and Pattern Recognition, pp. 982–990 (2016)
14. Sun, M., Zeng, K.H., Lin, Y., Ali, F.: Semantic highlight retrieval and term prediction. IEEE Trans. Image Process. **26**(7), 3303–3316 (2017)
15. Mahasseni, B., Lam, M., Todorovic, S.: Unsupervised video summarization with adversarial LSTM networks. In: Conference on Computer Vision and Pattern Recognition (2017)
16. Li, Y., Lu, H., Li, J., Li, X., Li, Y., Serikawa, S.: Underwater image de-scattering and classification by deep neural network. Comput. Electr. Eng. **54**, 68–77 (2016)
17. Vasudevan, A.B., Gygli, M., Volokitin, A., Van Gool, L.: Query-Adaptive Video Summarization via Quality-Aware Relevance Estimation, pp. 582–590 (2017)
18. Kulesza, A., Taskar, B.: Determinantal point processes for machine learning. Found. Trends Mach. Learn. **5**(2–3), 17 (2012)
19. Zhang, K., Chao, W.L., Sha, F., Grauman, K.: Video summarization with long short-term memory. In: ECCV, pp. 766–782 (2016)
20. Azadi, S., Feng, J., Darrell, T.: Learning Detection with Diverse Proposals (2017)
21. Gong, B., Chao, W.L., Grauman, K., Sha, F.: Diverse sequential subset selection for supervised video summarization. In: International Conference on Neural Information Processing Systems, pp. 2069–2077 (2014)
22. Sharghi, A., Gong, B., Shah, M.: Query-focused extractive video summarization. In: European Conference on Computer Vision, pp. 3–19 (2016)
23. Sharghi, A., Laurel, J.S., Gong, B.: Query-Focused Video Summarization: Dataset, Evaluation, and a Memory Network Based Approach (2017)
24. Szegedy, C., Vanhoucke, V., Ioffe, S., Shlens, J., Wojna, Z.: Rethinking the Inception Architecture for Computer Vision, pp. 2818–2826 (2015)
25. Deng, J., Dong, W., Socher, R., Li, L.J., Li, K., Li, F.F.: Imagenet: a large-scale hierarchical image database. In: Computer Vision and Pattern Recognition, pp. 248–255 (2009)
26. Zhang, C.L., Luo, J.H., Wei, X.S., Wu, J.: In defense of fully connected layers in visual representation transfer. In: Pacific-Rim Conference on Multimedia (2017)

Multi-task Deep Learning for Fine-Grained Classification/Grading in Breast Cancer Histopathological Images

Xipeng Pan, Lingqiao Li, Huihua Yang, Zhenbing Liu, Yubei He, Zhongming Li, Yongxian Fan, Zhiwei Cao and Longhao Zhang

Abstract The fine-grained classification or grading of breast cancer pathological images is of great value in clinical application. However, the manual feature extraction methods not only require professional knowledge, but also the cost of feature extraction is high, especially the high quality features. In this paper, we devise an improved deep convolution neural network model to achieve accurate fine-grained classification or grading of breast cancer pathological images. Meanwhile, we use online data augmentation and transfer learning strategy to avoid model overfitting. According to the issue that small inter-class variance and large intra-class variance exist in breast cancer pathological images, multi-class recognition task and verification task of image pair are combined in the representation learning process; in addition, the prior knowledge (different subclasses with relatively large distance and small distance between the same subclass) are embedded in the process of feature extraction. At the same time, the prior information that pathological images with different magnification belong to the same subclass will be embedded in the feature extraction process, which will lead to less sensitive with image magnification. Experimental results on two different pathological image datasets show that the performance of our method is better than that of state-of-the-arts, with good robustness and generalization ability.

Keywords Multi-task deep learning · Histopathological image classification Fine-grained · Convolutional neural network · Breast cancer

Xipeng Pan, Lingqiao Li—Authors contributed equally.

X. Pan · L. Li · H. Yang (✉) · Z. Li · Z. Cao · L. Zhang
School of Automation, Beijing University of Posts and Telecommunications, Beijing, China
e-mail: yhh@bupt.edu.cn

L. Li · H. Yang · Z. Liu (✉) · Y. Fan
School of Computer Science and Information Security, Guilin University of Electronic Technology, Guilin, China
e-mail: zbliu@guet.edu.cn

Y. He
School of Computing and Information Systems, University of Melbourne, Melbourne, Australia

H. Lu (ed.), *Cognitive Internet of Things: Frameworks, Tools and Applications*, Studies in Computational Intelligence 810,
https://doi.org/10.1007/978-3-030-04946-1_10

1 Introduction

Cancer is one of the top killer diseases in modern society that threatens health and life of humans. Breast cancer (BC), with different subtypes and risk stratification, is the most common cancer among women. According to the International Cancer Research Center (IARC) data released in 2014, BC is the second cause of death in women, and its incidence is increasing year by year as well as a young trend [1]. Histopathological analysis is a time-consuming and laborious task, and the diagnosis results are easily influenced by many subjective factors. With the help of Computer-Aided Diagnosis (CAD) system, the automatic classification of pathological image can not only improve the efficiency of diagnosis, but also provide more accurate and objective diagnostic results for doctors. Noticeably, fine-grained classification or grading of pathological images [2–4] is much more significant than binary one [5–8]. It will help patients get accurate diagnosis, guide doctors to develop more scientific and reasonable treatment plan, reduce treatment insufficiency or over treatment. Meanwhile, early detection and intervention can improve the prognosis.

In this work, we propose a novel fine-grained classification/grading approach for large-scale complex pathological images. The major contributions lie in three-fold. First, we propose an improved deep convolution neural network model to achieve accurate and precise classification or grading of breast cancer pathological images. Second, multi-class recognition task and verification task of image pair are combined in the representation learning process; in addition, the prior knowledge (different subclasses with relative big distance and small distance between the same subclass) are embedded in the process of feature extraction, which will effectively overcome the intractable problem (small inter-class variance and large intra-class variance in pathological image). At the same time, the verification task is only related to the category of pathological image, and is independent of magnification, that is to say, a priori information (pathological images with different magnification belong to the same subclass) will be embedded in the feature extraction process, that will lead to less sensitive with image magnification.

The rest of the work is organized as follow. Recent methods or algorithms for the classification of BC pathology images will be reviewed in Sect. 2. Section 3 elaborates our methodological contributions in detail, while the experimental results and comparisons with the recently published methods are described in Sect. 4. Section 5 draws a conclusion to the paper.

2 Related Work

In this section, we review the relevant works which are divided into two major categories: (1) classical classification algorithms: classification algorithms based on human feature engineering and classical machine learning; (2) deep learning methods: the recent booming methods based on deep learning.

(1) **Classical Classification Algorithms**. Gupta et al. [9] proposed a framework over multiple magnifications for BC histopathological image classification. The authors employed joint color-texture features and classifiers to demonstrate that some of these features and classifiers were indeed effective. Dimitropoulos et al. [3] published a dataset with 300 annotated breast carcinoma images of grades 1, 2 and 3, and presented a manifold learning model for grading of invasive breast carcinoma. Spanhol et al. [8] introduced a BC histopathology images dataset named BreaKHis. Based on the dataset, six kinds of feature descriptors, including Local Binary Patterns (LBP), gray level co-occurrence matrix (GLCM), and four kinds of classifiers, such as support vector machines and random forests, are applied to classify the data. The accuracy rate is about 80–85%. It is worth noting that the above classification methods lack a unified standard of comparison, and there is no comparability between the accuracy metric. More importantly, these algorithms are based on manual feature extraction method, which not only need domain knowledge, but also consume a lot of time and energy to complete, in addition, the key issue is that extraction of high-quality discriminative features is still very difficult.

(2) **Deep Learning Methods**. Deep learning can automatically learn features from the data, which will avoid the complexity and some limitations of the traditional algorithms. Spanhol et al. [7] employed AlexNet to extract the deep feature and combined different feature fusion strategies for BC recognition. The performance of the proposed model is much better than the traditional ones. Wei et al. [10] proposed a novel method based on deep CNN (named as BiCNN) to address the two-class BC pathological image classification. This model considered class and sub-class labels of BC as prior knowledge, which could restrain the distance of features of different BC pathological images. Han et al. [2] employed GoogLeNet as the basis network and proposed a BC multi-classification method. The structured model has achieved remarkable performance on a large-scale dataset, which is a potential tool for BC multi-classification in clinical settings. Song et al. [11, 12] Combined ConvNet with Fisher Vector (FV) and designed a new adaptation layer to further boost the discriminative power and classification accuracy for histopathology image classification. Most of the existing classification methods of breast pathological images are basically two categories. However, fine-grained classification of pathological images is of more important significance.

3 Methodology

In this paper, we propose an improved fine-grained pathological image classification model based on Xception network [13]. We adopt two schemes to improve the classification performance of pathological images.

3.1 Deep Convolutional Neural Networks

(a) **Architecture Design**. In order to prevent overfitting and improve the training speed, we choose parts of network layers in the Xception network to extract the feature of pathological image. The new model architecture mainly composed of input layer, convolution layer, depthwise separable convolution, batchnormalization layer, maxpooling layer and activation function layer (ReLU), which is shown in Fig. 1.
Embedding the prior information in the feature extraction process is beneficial to train a fine-grained classification model for pathological images with strong discriminative ability. The multi-task network model is designed, as shown in Fig. 2. Specifically, the input consists of the paired pathological images, their corresponding labels, and the attribute value that whether the images belong to the same class. The Xception based network structure removes the top layer and connects with the output of the proposed model, which formulates the training model. Cross entropy loss is obtained by cross entropy function with Softmax probability distribution and one-hot form labels as inputs. Contrastive loss is obtained by contrast loss function with the distance of image pairs as input. The two loss values are combined through the weights as the final loss, which is used for the training of the proposed model, as shown in Sect. 3.3.

(b) **Implementation Details**. The implementation is based on keras [14]. The data set is randomly divided into three parts: 20% validation set, 20% test set and the other is training set, meanwhile, none of which overlap with others. The experimental results are the mean and variance of the 5 random data set experiments. In order to verify the effectiveness of transfer learning, two training strategies are adopted: random initialization training and transfer learning. Furthermore, the result of only softmax loss is comparison with that combination with softmax loss and contrastive loss to verify the effectiveness of multitask learning.

3.2 Data Augmentation and Transfer Learning

Data augmentation: The training data set is augmented by affine transformation and some data augmentation techniques (e.g., small rotations, zoom, mirror operation, horizontal flipping and vertical flipping) are also applied. In the training process, every batch size images are transformed online with the combination of above strategy, so as to achieve the purpose of data enhancement. It will save physical storage space and promote the training speed comparing with the traditional off-line data enhancement mode.

Transfer learning: In this paper, we will transfer the pre-trained model in ImageNet (including more than 1.2 million natural images and 1000 different categories) datasets to pathological image classification tasks. The specific operation is to freeze the parameters of the shallow layers, and to train the model parameters of the high level layers.

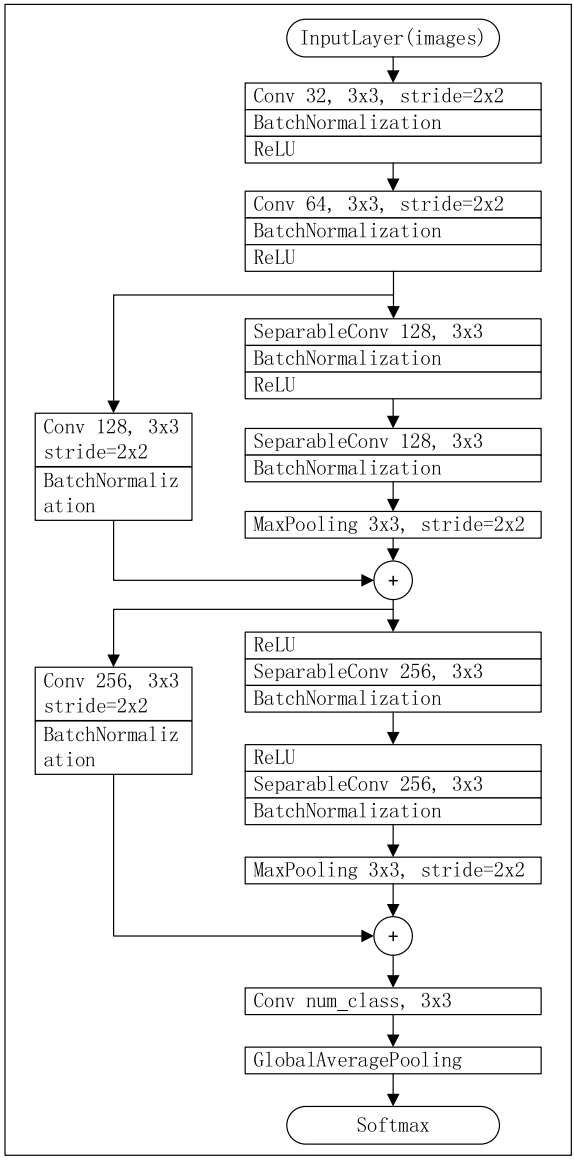

Fig. 1 Xception based network architecture

3.3 Multi-task Loss

First, the input image pairs are generated from the training dataset, and the basic unit includes (x_i, x_j, y_i, y_j, y_{ij}). Among them, x_i and x_j represent the input images; y_i and y_j are their corresponding labels. If x_i and x_j belong to the same class, the attribute value y_{ij} is 1, if x_i and x_j do not belong to the same class, y_{ij} is 0.

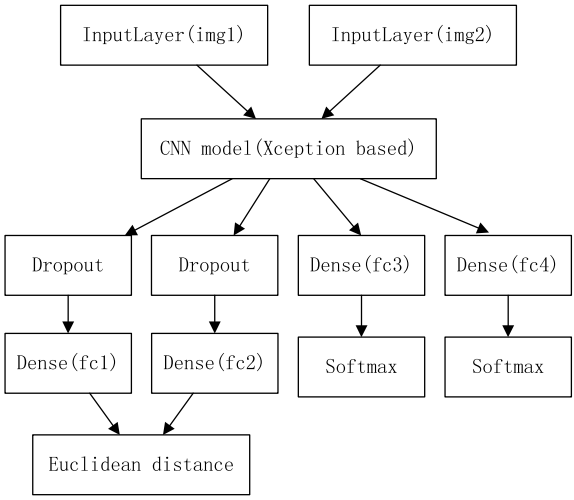

Fig. 2 A network model for multi-task fine-grained classification of pathological images

Second, Euclidean distance between f_i and f_j, which are the extracted features of network with the x_i and x_j as inputs, is calculated. Third, according to the softmax loss function and the formula of the contrastive loss, the loss values can be obtained respectively. The two loss values are combined through the weights as the final loss, which is used for the training of the proposed model. Finally, the Nadam optimization method is used for training.

The fine-grained classification features of pathological images are learned by two supervised signals (tasks). The first one is the multi-class recognition signal. In order to divide the pathological images into different categories (for example, 8 categories), a probability distribution of 8 categories is obtained through connecting the 8-way softmax layer after CNN. The network is trained by minimizing the cross-entropy loss, as shown in formula (1).

$$L_{softmax} = L(\mathbf{x}, y, \boldsymbol{\theta}) = -\frac{1}{N}\left[\sum_{i=1}^{N}\sum_{j=1}^{k} 1\{y_i = j\} \log \frac{e^{\theta_j^T x_i}}{\sum_{j=1}^{k} e^{\theta_j^T x_i}}\right] \tag{1}$$

where $1(y_i = j)$ is the indicative function, and the rule of value is: $1\{\text{expression is true}\} = 1$, and $1\{\text{expression is false}\} = 0$. N is the number of images, and k is the number of image categories. θ represents the parameters of the softmax classifier.

The second is the verification signal, which encourages that distance between the features of the same class images is as small as possible and distance between the features of the different types of images is as far as possible. The verification signal can effectively reduce the change of the extracted features of similar pathological image, and increase the difference of the extracted features of different pathological images, which will make the model to be more discriminative. Inspired by the liter-

ature [15–18], we adopt the following loss function to constrain the extraction of the feature, as shown in formula (2).

$$L_{contrastive} = L\left(f_i, f_j, y_{ij}, m\right) = y_{ij}\left(f_i - f_j\right)^2 + \left(1 - y_{ij}\right)\max\left(0, m - \left(f_i - f_j\right)^2\right) \tag{2}$$

where f_i, f_j, and y_{ij} have been described above, and m is a learning parameter, which usually set to 1. The total loss of the model is shown in formula (3). $L^1_{softmax}$ and $L^2_{softmax}$ are the softmax loss of the two inputs, respectively. $L_{contrastive}$ is the contrast loss. ω_1, ω_2 and ω_3 are the weights of three different losses. The weights are verified by experiments and set as $\omega_1 = \omega_2 = 0.35$ and $\omega_3 = 0.3$, respectively.

$$C = \omega_1 L^1_{softmax} + \omega_2 L^2_{softmax} + \omega_3 L_{contrastive} \tag{3}$$

4 Experiments and Results

4.1 Dataset Description

We evaluated our proposed models on two different kinds of dataset: (1) BreaKHis. (2) Grading of invasive breast carcinoma. **(1) BreaKHis**. The dataset consists of 7909 BC histopathology images acquired on 82 patients with different magnification (40×, 100×, 200×, and 400×) [8]. **(2) Grading of invasive breast carcinoma**. This dataset contains cases of breast carcinoma histological specimens received in General Hospital of Thessaloniki, Greece [3]. It consists of 300 annotated images with resolution 1280×960 corresponding to 21 different patients with invasive ductal carcinoma of the breast of grades 1–3 (grade 1: 107, grade 2: 102 and grade 3: 91 images).

4.2 Performance Metrics

There is only the image level information in grading of invasive breast carcinoma dataset, so we calculate the recognition rate from the image level. N_{all} represents the number of validation and test set of pathological images, N_r is the number of pathological images that are correctly classified. So, the image level recognition rate can be expressed as:

$$Recognition\ Rate = \frac{N_r}{N_{all}} \tag{4}$$

4.3 Experimental Results and Analysis

The study is implemented with python2.7 on a workstation with Intel(R) Xeon(R) E5-2650 v2 CPU, 32 GB memory and the model of GPU is GTX1080. Comparison experiments are conducted between our proposed methods and the recently published state-of-the-art models or approaches.

(1) BreaKHis Dataset

The comparison results between our proposed method and the recently state-of-the-arts are shown in Table 1. From Table 1, we can draw several conclusions: (1) the same method obtains the similar performance from the validation set and the test set, indicating that the model has good generalization ability. (2) In general, the performance of multi-task CNN is better than single task CNN, and fine-tuning multi-task CNN is superior to multi-task CNN training from scratch. (3) The results of our method are superior to that of literatures [3, 6–8, 11, 12], although results of these articles provided are binary classification. We all know that fine-grained classification (multi-classification) is more difficult than the binary classification.

The performance of our proposed method (fine-tuning multi-task CNN) is 3% better than that of CSDCNN+Raw [2] in all magnification factors. Most of the results of our proposed method (fine-tuning multi-task CNN) are better than that of CSDCNN+Aug, and the performance is slightly worse than that of CSDCNN+Aug when magnification is 400×. However, CSDCNN+Aug has expanded 14 times for the training datasets, and we simply enhanced the data online, which greatly reduced the data storage space. From Fig. 3, we can see that the training was stopped due to the absence of further improvement in validation loss and accuracy after less than 110 epochs. Actually, it begins to obtain a relatively good performance while the epoch is about 60.

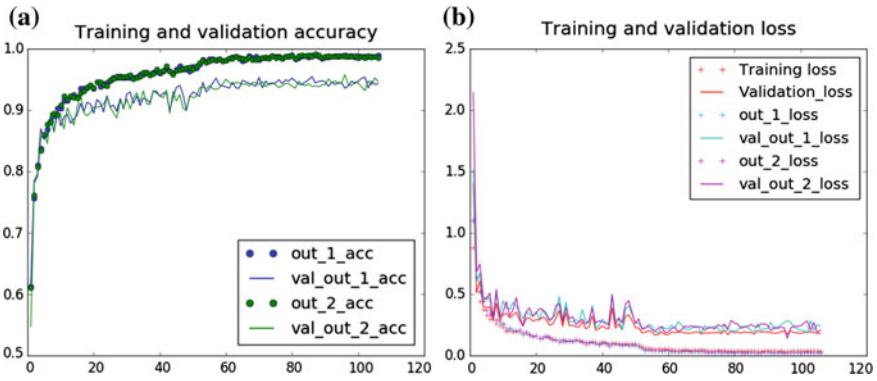

Fig. 3 Performance curves when MT FT Xception (multi-task fine tuning the Xception model training from ImageNet). **a** Training and validation accuracy against training steps. **b** Training and validation loss against training steps

Table 1 The comparison results of the fine-grained classification of BreaKHis images

Methods	Magnification factors				
	40×	100×	200×	400×	All
ST (valid)	92.42 ± 0.39	93.29 ± 0.81	92.29 ± 0.39	90.81 ± 1.42	92.25 ± 0.26
ST (test)	94.11 ± 0.52	91.77 ± 0.83	92.12 ± 0.51	90.25 ± 2.11	92.08 ± 0.28
MT (valid)	92.89 ± 1.18	91.65 ± 0.73	93.03 ± 0.6	91.42 ± 0.54	92.25 ± 0.3
MT (test)	94.69 ± 0.8	93.8 ± 0.63	92.66 ± 0.68	92.24 ± 1.11	93.36 ± 0.19
MT SCR Xception (valid)	86.69 ± 3.79	83.12 ± 4.61	84.32 ± 4.95	86.54 ± 2.04	85.08 ± 3.85
MT SCR Xception (test)	87.95 ± 2.79	83.67 ± 4.56	85.04 ± 3.63	85.22 ± 2.11	85.50 ± 3.17
MT FT Xception (valid)	**95.26 ± 0.49**	93.37 ± 1.08	93.09 ± 1.45	91.65 ± 1.66	93.36 ± 0.83
MT FT Xception (test)	94.8 ± 0.33	**94.03 ± 1.19**	**93.85 ± 0.24**	90.71 ± 0.71	**93.43 ± 0.47**
CSDCNN+Raw [2]	89.4 ± 5.4	90.8 ± 2.5	88.6 ± 4.7	87.6 ± 4.1	–
CSDCNN+Aug [2]	92.8 ± 2.1	93.9 ± 1.9	93.7 ± 2.2	**92.9 ± 1.8**	–
Dimitropoulos et al. [3]	91.8	92.1	91.4	90.2	91.38
Gupta et al. [6]	86.96	88.92	90.32	86.85	–
Spanhol et al., IJCNN16 [7]	89.6 ± 6.5	85.0 ± 4.8	82.8 ± 2.1	80.2 ± 3.4	–
Spanhol et al., TBE16 [8]	81.6 ± 3.0	79.9 ± 5.4	85.1 ± 3.1	82.3 ± 3.8	–
Song et al., ISBI17 [11]	87.0 ± 2.6	86.2 ± 3.7	85.2 ± 2.1	82.9 ± 3.7	–
Song et al., MICCAI17 [12]	87.7 ± 2.4	87.6 ± 3.9	86.5 ± 2.4	83.9 ± 3.6	–

Abbreviations: *ST* single task, *MT* multi-task, *SCR Xception* training from scratch, *FT Xception* fine tuning the Xception model training from ImageNet, *Raw* raw dataset, *Aug* augmented dataset

(2) Grading of Invasive Breast Carcinoma

The comparison results between our proposed method and the recently state-of-the-arts are shown in Table 2. From Table 2, we can draw almost the same conclusions as the experiments of BreaKHis dataset. In [3], experiments were implemented with different patch sizes and patching strategies which contained overlapping, non-overlapping and random patches. Patches of 8×8 size provide the best classification

Table 2 The comparison results of the grading of invasive breast carcinoma

Methods	Grading of invasive breast carcinoma			
	Grade1	Grade2	Grade3	All
ST (valid)	78.79 ± 2.14	98.41 ± 2.24	92.59 ± 2.62	89.62 ± 2.04
ST (test)	81.82 ± 11.13	96.83 ± 2.24	92.98 ± 2.48	90.32 ± 5.27
MT (valid)	87.88 ± 2.14	98.41 ± 2.24	87.04 ± 2.62	91.26 ± 0.77
MT (test)	84.85 ± 4.29	95.24 ± 3.89	92.98 ± 6.56	90.86 ± 2.01
MT SCR Xception (valid)	78.79 ± 2.14	**100.0 ± 0.0**	94.44 ± 4.54	90.71 ± 2.04
MT SCR Xception (test)	77.27 ± 9.82	96.83 ± 2.24	**98.25 ± 2.48**	90.32 ± 4.75
MT FT Xception (valid)	**89.39 ± 2.14**	98.41 ± 2.24	96.30 ± 5.24	94.54 ± 1.55
MT FT Xception (test)	86.36 ± 7.42	**100.0 ± 0.0**	92.98 ± 4.96	93.01 ± 1.52
Dimitropoulos et al., 8×8, overlapping [3]	–	–	–	**95.8**
Dimitropoulos et al., 16×16, overlapping [3]	–	–	–	91.5
Dimitropoulos et al., 32×32, random [3]	–	–	–	85.1
Dimitropoulos et al., 64×64, random [3]	–	–	–	82.3

rate (95.8% for overlapping). Other best classification rate of different patch sizes and patching strategies can be seen in Table 2. Results show that patches of 8×8 size contain sufficient dynamics and appearance information for the classification of histological images, while the strategy of overlapping patches (with 50% overlap between patches) results in 151,376 Grassmannian points in each histological image.

5 Conclusions

In this paper, we proposed a fine-grained classification/grading model for pathological images. Both qualitative and quantitative experimental results on BreaKHis and Grading of invasive breast carcinoma datasets show that our method obtains the promising performance and is superior to several state-of-the-art approaches.

Acknowledgements The authors would like to thank Spanhol et al. [8], and Dimitropoulos et al. [3] for publishing the datasets. We would like to express our gratitude to anonymous reviewers and editor for helpful comments. This research was supported in part by the National Natural Science Foundation of China (Grant Nos. 21365008, 61462018, 61762026 and 61562013), and Natural Science Foundation of Guangxi Province (No. 2017GXNSFDA198025 and 2017GXNSFAA198278).

References

1. Stewart, B., Wild, C.P.: World Cancer Report 2014. International Agency for Research on Cancer, World Health Organization (2014)
2. Han, Z., Wei, B., Zheng, Y., Yin, Y., Li, K. Li, S.: Breast cancer multi-classification from histopathological images with structured deep learning model. Sci. Rep. **7**(1) (2017). https://doi.org/10.1038/s41598-017-04075-z
3. Dimitropoulos, K., Barmpoutis, P., Zioga, C., Kamas, A., Patsiaoura, K., Grammalidis, N.: Grading of Invasive Breast Carcinoma through Grassmannian VLAD encoding. PLoS ONE **12**(9), e0185110 (2017)
4. Janowczyk, A., Madabhushi, A.: Deep learning for digital pathology image analysis: a comprehensive tutorial with selected use cases. J. Pathol. Inform. **7**, 29 (2016)
5. Gupta, V., Singh, A., Sharma, K., et al.: Automated classification for breast cancer histopathology images: is stain normalization important? In: Computer Assisted and Robotic Endoscopy and Clinical Image-Based Procedures (2017)
6. Gupta, V., Bhavsar, A.: Breast cancer histopathological image classification: is magnification important? In: IEEE Conference on Computer Vision and Pattern Recognition Workshops (CVPRW), pp. 769–776. Honolulu, HI (2017)
7. Spanhol, F.A., Oliveira, L.S., Petitjean, C., Heutte, L.: Breast cancer histopathological image classification using convolutional neural networks. In: 2016 International Joint Conference on Neural Networks, pp. 2560–2567, Vancouver, BC, Canada (2016)
8. Spanhol, F.A., Oliveira, L.S., Petitjean, C., et al.: A dataset for breast cancer histopathological image classification. IEEE Trans. Biomed. Eng. **63**(7), 1455–1462 (2016)
9. Gupta, V., Bhavsar, A.: An integrated multi-scale model for breast cancer histopathological image classification with joint colour-texture features. In: Computer Analysis of Images and Patterns: 17th International Conference, CAIP, Ystad, Sweden (2017)
10. Wei, B., Han, Z., He, X., Yin, Y.: Deep learning model based breast cancer bistro pathological image classification. In: 2017 IEEE 2nd International Conference on Cloud Computing and Big Data Analysis (ICCCBDA) (2017)
11. Song, Y., Zou, J., Chang, H., et al.: Adapting fisher vectors for histopathology image classification. In: International Symposium on Biomedical Imaging, pp. 600–603. IEEE Press (2017)
12. Song, Y., Chang, H., Huang, H., Cai, W.: Supervised Intra-embedding of fisher vectors for histopathology image classification. In: Descoteaux M., Maier-Hein L., Franz A., Jannin P., Collins D., Duchesne S. (eds.) Medical Image Computing and Computer-Assisted Intervention—MICCAI 2017. Lecture Notes in Computer Science, vol. 10435. Springer, Cham (2017)
13. Chollet, F.: Xception: Deep Learning with Depthwise Separable Convolutions (2016). arXiv:1610.02357
14. https://github.com/fchollet/keras
15. Sun, Y., Chen, Y., Wang, X., et al.: Deep learning face representation by joint identification-verification. In: International Conference on Neural Information Processing Systems, pp. 1988–1996. MIT Press (2014)
16. Lu, H., Li, Y., Chen, M.: Brain Intelligence: Go Beyond Artificial Intelligence (2017)
17. Lu, H., Li, B., Zhu, J.: Wound intensity correction and segmentation with convolutional neural networks. J. Concurr. Comput. Pract. Exp. (2016)
18. Lu, H., Li, Y., Uemura, T.: FDCNet: filtering deep convolutional network for marine organism classification. J. Multimed. Tools Appl. 1–14 (2017)

Medicine Discrimination of NIRS Based on Regularized Collaborative Representation Classification with Gabor Optimizer

Zhenbing Liu, Huanhuan Ji and Shujie Jiang

Abstract Counterfeit medicine still exists widely, which have affected our health and life. So the discrimination (classification) of medicine is becoming more and more important. Then near-infrared spectroscopy (NIRS) is a popular and effective technique used on the medicine classification with nondestructive characteristics. To solve the discrimination of medicines, the sparse signal representation model is established in the presence of spectrum crossover and overlapping. However, the sparsity of nonzero representation coefficients is low during solving the L_2-norm on representation model. To overcome this problem, in this paper a novel classification model—regularized collaborative representation classification with Gabor optimizer (RCRCG) is proposed. Gabor filter is adopted to control the L_2-norm for the more relevant factor vectors. Then Lasso regulation on local classification is proved to improve the accuracy on the medicine discrimination. The experiments using NIRS samples from the three datasets (active substance, Erythromycin Ethylsuccinate and Domperidone) show that the proposed method is more effective and robust than the existing ones, and it has speed-up about 1 times compared with the Sparse Representation based Classification (SRC) and Class L_1-optimizer classifier with the closeness rule (C_CL1C).

Keywords Medicines discrimination · Near-infrared spectroscopy (NIRS) Collaborative representation classification · Gabor filter · Sparsity representation

Z. Liu (✉)
Guangxi Key Lab of Trusted Software, Guilin University of Electronic Technology, Guilin, China
e-mail: zbliu@guet.edu.cn

H. Ji · S. Jiang
School of Electronic Engineering and Automation, Guilin University of Electronic Technology, Guilin, China

H. Lu (ed.), *Cognitive Internet of Things: Frameworks, Tools and Applications*, Studies in Computational Intelligence 810,
https://doi.org/10.1007/978-3-030-04946-1_11

1 Introduction

Near-infrared spectroscopy (NIRS) provides non-destructive measurement of many chemical varieties with high potential since its characteristics such as rapidity, simplicity and nondestructive measurements [1, 2]. Due to this advantage, this technique has been extensively used for quantitative analysis of complex samples in different fields, such as food analysis, environment, the interaction of water and ethanol and the discriminant on Chinese medicine [3–6]. The information in NIRS extracted from many overlapping peaks is used to discriminate the various samples [7]. In this paper we can extend pattern recognition method to solve the problem on the discrimination of medicines.

For the discrimination techniques, Soft Independent Modeling of Class Analogy (SIMCA) [8], Partial Least Squares Discriminant Analysis (PLS-DA) [9] and K nearest neighbor (KNN) [10] for classification were commonly based on mass spectra, high computational complexity and suffered from poor performance. Then, Storme [11] proposed the SVM classification model for counterfeit pharmaceuticals discrimination. Although Artificial Intelligence approaches have been widely spread by NIRS signal in many areas, some shortcomings were still existed. For dealing with the classification problem of medicines, the SRC [12] model was adopted as a sparse linear combination from all the training samples of NIRS, the test sample was classified by the minimum representation error evaluated from per class [13]. However, the SRC model was mainly for multi-label classification [14]. Therefore, Yang et al. [12] put forward some justifications for local classed based classification to obtain an excellent performance. Collaborative Representation Classifier based regularized optimize least square (CRC_RLS) was proposed [13] to reduce the time-consuming and to improve the classification performance. Then, Meng Yang proposed the SRC with Gabor occlusion dictionary in the literature [15]. Recently, Lu et al. [16] proposed Brain Intelligence: Go beyond Artificial Intelligence using Brain Intelligence learning model to generates new ideas about events without having experienced them by using artificial life with an imagine function. At present, the sparse signal representation methods are commonly focused on signal analysis, so establishing the classification model using NIRS data has potential significance for modeling in NIRS with many crossovers and overlaps [17].

In this paper, the RCRCG model is adopted due to its characteristics, which has the more relevant facture vector and low classification errors for classification on massive crossed and overlapping spectra. By using Gabor filter to handle "Sparsity" to obtain the more relevant factor vectors and adding some justifications for local classed, RCRCG classification model can obtain an effective performance and low time-consuming.

2 Related Work

As the binary classification problem, the training samples are defined as a matrix $A = [A_1, A_2, \ldots, A_i, \ldots, A_N] \in R^{N\times M}$, $i = 1, \ldots, N$ [14]. Let A_i be the matrix formed by the training samples of two classes, including labeled positively (genuine) $y_i = +1$ or negatively (counterfeit) $y_i = -1$. The testing sample $y \in \mathrm{IR}^{N\times M}$ from the same class will be represent by the linear. The SRC is written by solving of L_1-norm:

$$(L_1) \qquad \hat{\omega}^1 = \arg\min ||\omega||_1 \, st. \, A\omega = y. \tag{1}$$

Then L_2-norm is proposed by the regularized least square method to represent classification [13]. The model of CRC_RLS is defined follow:

$$\min \hat{r}(y) = ||y - A\delta_i\left(\hat{\omega}^2\right)||_2 + \lambda_1 ||\delta_i\left(\hat{\omega}^2\right)||_2 \tag{2}$$

where λ_1 is the regularization parameter. Form the regularized least square, the $\hat{\rho}$ can be easily obtained by L_2-norm solution as follow:

$$\hat{\rho} = \delta_i\left(\hat{\omega}^2\right) = \left(A^T A + \lambda_1 \cdot I\right)^{-1} A^T \tag{3}$$

where, $\hat{\rho}$ is the coefficient vector associated with one class and similar to the form by $\hat{\omega}^1$ in the SRC [13]. For the "sparsity" of L_2-norm, $||\hat{\rho}_i||_2$ can makes collaborative representation very fast, yet this sparsity is weaker than that by L_1-norm.

For the overdetermined and non-sparsity problem of L_2 optimization, this paper adopts Gabor filter to handle "sparsity" to the solution $\hat{\rho}$. However, Gabor filter generates highly redundant features and extremely time-consuming as a multi-scale and multi-orientation feature extraction technique [18]. So the mean of $\hat{\rho}$ is defined as a Gabor dictionary $\bar{\hat{\rho}}$ to perform the collaborative representation. The solution $\hat{\rho}$ can be reconstructed as $\tilde{\rho}$ by Eq. (4) as follow:

$$\tilde{\rho}_i = o\left(\psi_{\mu,\nu}\left(\hat{\rho}_i\right) - \psi_{\mu,\nu}\left(\bar{\hat{\rho}}_i\right)\right). \tag{4}$$

To distinguish the sparse signal representation methods for multi-label global optimizer, Yang et al. [12] proposed some justifications for local classed based classification to address the binary classification problem. The Lasso criterion is adopted for the square reconstruction residual and avoiding overfitting of NIRS. If the training samples of NIRS have enough size sets, the normalized Lasso distance is defined by:

$$\tilde{r}(y) = ||y - x_i \cdot \tilde{\rho}_i||_2 \Big/ ||\tilde{\rho}_i||_2 + \lambda_2 ||\bar{\tilde{\rho}}_i||_1 \Big/ ||\tilde{\rho}_i||_2 \tag{5}$$

where, $\bar{\bar{\rho}}_i = \delta_i\left(\bar{\bar{\omega}}^2\right) == \left[\alpha_{1yi}^2 \| \upsilon_{1yi} - \bar{\upsilon}_1 \|, \ldots, \alpha_{iyi}^2 \| \upsilon_{iyi} - \bar{\upsilon}_i \|, 0, \ldots, 0\right]^T$, $\left[\alpha_{1y_i}^2, \ldots, \alpha_{iy_i}^2, 0, \ldots, 0\right]^T$ is a coefficient vector for solving L_2-norm, and the parameter λ_2 in Lasso was chosen as 0.01 in the literature [12] and $A = \left[\upsilon_{1yi}, \upsilon_{2yi}, \ldots, \upsilon_{1yi}, \ldots, \upsilon_{Ny_i}\right]$ are support training samples and the mean of these support training samples is $\bar{\upsilon}_1 = \frac{1}{i}\sum_{j=1}^{i} \bar{\upsilon}_{iy_i}$, as the origin to center the data locally and then use $\upsilon_{1yi} - \upsilon_1, \ldots, \upsilon_{1yi} - \upsilon_i$ as axes to form the local coordinate system [12]. Combining two methods, the RCRCG is constructed to address the discrimination of medicine using NIRS in this paper.

3 Materials and Methods

3.1 Sample Preparation

To demonstrate the classification performance of the different classification methods in the classification of medicines, all the samples are divided randomly into two parts (Positive and Negative). Three NIRS data sets for the training set size have been selected as show in Table 1.

Data 1: The active substance on published pharmaceutical tablets dataset (http://www.models.kvl.dk/Tablets) is adopted for the discrimination of medicines form the different dosages [19]. We construct artificial sets on two parts in the experiment to discriminate the two different concentrations for pharmaceutical tablets in Table 1. The sample is labeled positively if the spectrum data are the genuine medicines (see Fig. 1a 5 mg dosages) or negatively if the spectrum data are counterfeit medicines (see Fig. 1a 10, 15 and 20 mg dosages). Finally, the spectrum dataset contains 72 genuine and 238 counterfeit medicines.

Table 1 Feature description of the training set from three different data sets

Pharmaceuticals (wavelength range)	Dim	Variety	Amount	The number of medicine samples	
				Negative samples	Positive samples
Data 1: Active Substance (7500–10,500 nm)	404	4	310	5 mg 5.6%w/w dosages (72)	10, 15 and 20 mg 8.0%w/w Dosages (238)
Data 2: Erythromycin Ethylsuccinate (4500–9000 nm)	1247	35	249	Other medicines Other manufactory (171)	Erythromycin Ethylsuccinate (78)
Data 3: Domperidone (4000–12,000 nm)	2000	266	1050	Other medicines Other product species (960)	Domperidone (80)

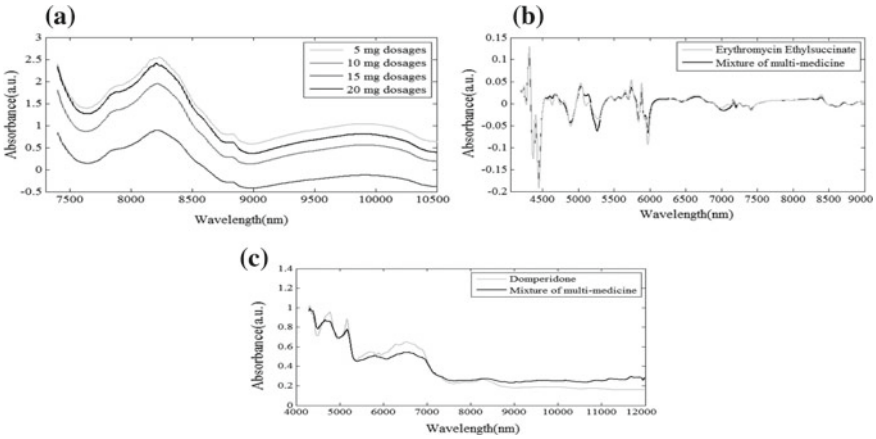

Fig. 1 **a** Spectra of Active Substance per tablet including 5 mg (5.6%w/w), and 10, 15 and 20 mg (8.0%w/w), **b** Spectra of the mixture of multi-medicine from other factories and Spectra of Erythromycin Ethylsuccinate form the Xi'an-Janssen pharmaceutical factors and **c** Spectra of the mixture of multi-medicine from other pharmaceuticals and Spectra of Domperidone

Data 2: As showed in Table 1, all the pharmaceutical samples of NIRS are produced by the Xi'an-Janssen pharmaceutical factors and other factories. The sample is labeled positively if the spectrum data is the genuine medicines or negatively if the spectrum data are counterfeit medicines (see Fig. 1b Erythromycin Ethylsuccinate, Mixture of multi-medicine). Finally, the spectrum dataset contains 78 genuine and 171 counterfeit medicines.

Data 3: All the pharmaceutical samples of NIRS are produced by National Institute for the Control of Pharmaceutical and Biological Products. The sample is labeled positively if the spectrum data is the genuine medicines or negatively if the spectrum data are counterfeit medicines (see Fig. 1c Domperidone, Mixture of multi-medicine). The spectrum dataset contains 80 genuine and 970 counterfeit medicines.

As can be seen the crossover and overlap severely for absorption spectra in Fig. 1, it is difficult to address the identification problem of medicines. In this task, the absorption spectra are performed data processing and modeling by using MATLAB 2014a software (The Mathworks, Natick, MA, USA). We experiment to determine the parameters best values by grid optimization and focus on the RBF kernel for the SVM model (2010, http://www.csie.ntu.edu.tw/~cjlin/libsvm/index.html). The SRC model is performed using a series of m-files written in MATLAB environment from the literature [12]. Meanwhile, The NC-CL1C model is from the literature [13]. In addition to, the MATLAB m-files of CRC_RLS modeling can be downloaded at http://www4.comp.polyu.edu.hk/~cslzhang/code.htm. The parameter λ_1 is adjusted as 1 in this experiment.

The F-measure is used as the performance evaluation criteria for all the models [18] especially for datasets with huge class imbalance. F-measure and the classification accuracy are used to assess the classification performance as follow:

$$F-measure = \frac{2 \times \text{Precision} \times \text{Recall}}{\text{Precision} + \text{Recall}}. \tag{6}$$

The higher the F-measure the "better" the quality of the evidences are provided by overlaps from the class imbalance sets in literature [18]. The SCI of a coefficient vector $x_i \in IR^{N \times M_i}$ is represented the "sparsity" from the relevant coefficient vector and it influences the classification performance of sparse signal representations as follow:

$$SCI(x) = \frac{k \cdot \max_i ||\delta_i(x)||_1 \big/ ||x||_1 - 1}{k - 1} \in [0, 1]. \tag{7}$$

For a solution $\hat{\rho}$ or $\tilde{\rho}$ found by solving L_1-norm and L_2-norm respectively, if $SCI(\hat{x}) \rightarrow 1$, the test samples are represented using only samples from a single object, and if $SCI(\hat{x}) \rightarrow 0$, the sparse coefficients are spread evenly over all classes [20]. For the binary classification problem in this paper, the value of SCI means that a solution of $\tilde{\rho}$ or $\hat{\rho}$ change sparser with declining the value of SCI.

3.2 Data Preprocessing

For reducing the noise, the smoothing way of Savitzky-Golay is used. The segment size of smoothing is 7 to eliminated the high frequency noises. After smoothing, the vector normalization and first derivative (SNV-1stD) are investigated to pre-process the NIRS data. Those methods can eliminate the offset and drift caused by the spectrum fluctuations. The spectra are pretreated by smoothing, vector normalization and first derivative (SNV-1stD). Then, the PLS-DA, ICA and PCA are applied to each sample spectrum to produce a feature vector for the initial absorption spectra. The experiments are repeated in 20 different random partitions of the NIRS data into training respectively from 200, 200 and 800 training samples and test sets as form as described in Table 1. It can be seen in Table 2 that the PCA provides a robust and correct results for classification with lower time-consuming and stronger stability of outputting dimensions compared with ICA, PLS-DA.

4 Results and Discussion

4.1 The RCRCG Classification Model with the Different Number of Training Samples

In this study, The RCRCG classification model is applied to investigate the NIRS data of medicines, and the spectrograph scanning the region 400–1200 nm. Several Artificial Intelligence approaches are applied to compare with the RCRCG. During

Table 2 The three data sets and independent test sets from three Feature Extractions methods that are repeated in 20 different random partitions of the original datasets as the scheme described in Sect. 3.1 (the performance is presented by their means and standard deviations Mean ± std)

	Compression Dim	Compression time-consuming	Avg. test error in % (Avg. test F-measure)			
			SVM	SRC	NC-CL1C	RCRCG
Data 1						
PCA	**50**	**0.0078**	**61.36 ± 0.20 (0.42)**	**21.05 ± 0.03 (0.44)**	**20.27 ± 0.03 (0.38)**	**13.86 ± 0.03 (0.78)**
ICA	40	0.1498	27.27 ± 0.00 (NaN)	27.27 ± 0.00 (NaN)	30.41 ± 0.02 (0.11)	**23.05 ± 0.03 (0.35)**
PLS-DA	2–3	1.2643	27.27 ± 0.00 (NaN)	27.27 ± 0.00 (NaN)	27.27 ± 0.00 (NaN)	**34.63 ± 0.04 (NaN)**
Data 2						
PCA	**50**	**0.0174**	**43.06 ± 0.01 (0.72)**	**5.10 ± 0.03 (0.95)**	**4.90 ± 0.04 (0.95)**	**4.29 ± 0.04 (0.96)**
ICA	120	1.2279	57.14 ± 0.00 (0.69)	56.12 ± 0.02 (0.72)	42.86 ± 0.00 (0.69)	**24.90 ± 0.09 (0.70)**
PLS-DA	2–3	0.3851	**13.37 ± 0.07 (0.87)**	36.02 ± 0.12(0.72)	39.08 ± 0.09 (0.70)	26.12 ± 0.08 (0.69)
Data 3						
PCA	**50**	**0.0210**	**8.80 ± 0.00 (NaN)**	**1.45 ± 0.01 (0.93)**	**1.45 ± 0.01 (0.93)**	**1.08 ± 0.02 (0.95)**
ICA	200	1.7139	8.80 ± 0.00 (NaN)	8.80 ± 0.00 (NaN)	25.60 ± 0.04 (NaN)	**27.40 ± 0.05 (0.27)**
PLS-DA	2–3	8.0748	8.80 ± 0.00 (NaN)	8.80 ± 0.00 (NaN)	36.22 ± 0.05 (0.64)	**21.58 ± 0.04 (0.78)**

the process of optimizing the parameters by these methods, the average values of test error rate and the F-measure are the key selection criteria for classification model. After obtaining the optimal parameters, the three training data sets are repeated in 20 different random partitions of the NIRS from the different number of training samples. The results are shown in Table 4.

Data 1: Each instance for those classification models is performed with increasing the number of training samples as shown in Table 3. The results of the RCRCG achieve the best performance with an F-measure and the average values of test error rate of: $12.05 \pm 0.02\%$ (0.75) for 120 training samples, $12.43 \pm 0.03\%$ (0.78) for 180 and $13.86 \pm 0.03\%$ (0.78) for 200. Moreover, the SRC and NC-CL1C have the lower error rate at than CRC_RLS, SVM, ELM and BP to illustrate the SRC and NC-CL1C availability. Consequently, the SVM, ELM and BP model are not achievement due to imbalanced data sets for classification.

Data 2: As same as the results of Data 1, the results of the RCRCG achieve the best performance with an F-measure and the average values of test error rate of: $1.21 \pm 0.03\%$ (0.98) for 150 training samples, $3.19 \pm 0.02\%$ (0.96) for 180 and $4.29 \pm 0.04\%$ (0.96) for 200. The F-measure of the RCRCG classifier is range from 0.96 to 0.98 to illustrate the less misclassification than the SRC and NC-CL1C. According to the Table 3, the RCRCG has better performance than the others to address the identification problem by NIRS.

Data 3: With increasing the number of training samples, the F-measure of the RCRCG is range from 0.93 to 0.95 and the error rate of the RCRCG achieves the best performance than others at $1.08 \pm 0.02\%$ (0.95) for 800 training samples and $5.40 \pm 0.03\%$ (0.93) for 1000 (Seen in Table 3). However, the error rate of the RCRCG is higher than the SRC and NC-CL1C when the training samples are about less than two-thirds. It can be seen that SRC and NC-CL1C have better robustness for the problem of small training set size.

To sum up, the RCRCG has the best classification performance for the discrimination of medicines using the samples of NIRS from the different dosages, factors and pharmaceutical species.

4.2 The RCRCG Classification Model with the Different Classification Models

To prove the RCRCG method availability, the three training data sets are repeated in 20 different random partitions of the original datasets respectively from 200, 200 and 800 training samples as shown in Table 4. The average values of test error rate, F-measure, training SCI and time-consuming are as shown in Table 4.

Data 1: The results of the RCRCG achieve the best performance in data sets 1. If $SCI(\hat{x}) \rightarrow 0$, it means the sparser for a solution $\hat{\rho}$ or $\tilde{\rho}$. It is evidence in Table 4 that the average values of SCI for SRC and NC-CL1C are less than CRC_RLS and

Table 3 The results from the different number of training samples (P means the number of position training samples and N means the number of negative training samples, and the performance are presented by their means and standard deviations Mean ± std)

The number of training samples	Avg. test error in % (Avg. test F-measure)						
	BP	ELM	SVM	CRC_RLS	SRC	NC-CL1C	RCRCG
Data 1							
120 (P: 30; N: 90)	22.00 ± 0.07 (NaN)	46.07 ± 0.07 (NaN)	47.63 ± 0.24 (0.42)	26.32 ± 0.00 (NaN)	16.13 ± 0.01 (0.62)	15.13 ± 0.02 (0.57)	**12.05 ± 0.02 (0.75)**
180 (P: 40; N: 140)	21.62 ± 0.05 (NaN)	46.27 ± 0.07 (NaN)	61.54 ± 0.16 (0.47)	30.77 ± 0.00 (NaN)	20.92 ± 0.02 (0.56)	19.12 ± 0.02 (0.49)	**12.43 ± 0.03 (0.78)**
200 (P: 50; N: 150)	25.75 ± 0.10 (NaN)	44.75 ± 0.07 (NaN)	61.36 ± 0.20 (0.42)	27.27 ± 0.00 (NaN)	21.05 ± 0.03 (0.44)	20.27 ± 0.03 (0.38)	**13.86 ± 0.03 (0.78)**
Data 2							
150 (P: 50; N: 100)	52.76 ± 0.15 (NaN)	42.61 ± 0.04 (0.36)	69.50 ± 0.00 (0.38)	13.54 ± 0.05 (0.68)	3.43 ± 0.02 (0.94)	3.43 ± 0.02 (0.94)	**1.21 ± 0.03 (0.98)**
180 (P: 50; N: 130)	35.57 ± 0.14 (NaN)	43.03 ± 0.06 (0.44)	60.29 ± 0.03 (0.57)	35.22 ± 0.06 (0.30)	4.78 ± 0.02 (0.94)	4.49 ± 0.02 (0.94)	**3.19 ± 0.02 (0.96)**
200 (P: 50; N: 150)	25.22 ± 0.06 (NaN)	48.27 ± 0.03 (0.50)	43.06 ± 0.01 (0.72)	53.27 ± 0.05 (0.23)	5.10 ± 0.03 (0.95)	4.90 ± 0.04 (0.95)	**4.29 ± 0.04 (0.96)**
Data 3							
600 (P: 50; N: 550)	18.04 ± 0.13 (NaN)	16.28 ± 0.05 (NaN)	4.89 ± 0.00 (NaN)	4.89 ± 0.00 (NaN)	0.64 ± 0.01 (0.93)	**0.62 ± 0.01 (0.95)**	0.76 ± 0.01 (0.93)
800 (P: 50; N: 750)	15.88 ± 0.23 (NaN)	19.66 ± 0.04 (NaN)	8.80 ± 0.00 (NaN)	8.80 ± 0.00 (NaN)	1.45 ± 0.01 (0.93)	1.45 ± 0.01 (0.93)	**1.08 ± 0.02 (0.95)**
1000 (P: 50; N: 950)	31.75 ± 0.04 (NaN)	45.10 ± 0.02 (NaN)	44.00 ± 0.00 (NaN)	44.00 ± 0.00 (0.93)	5.80 ± 0.03 (0.93)	5.80 ± 0.03 (0.93)	**5.40 ± 0.03 (0.93)**

Table 4 The three data sets and independent test sets from three classifiers that are applied to compare with the RCRCG method including the average values of test error rate, F-measure, training SCI and time-consuming (the performance is presented by their means and standard deviations Mean ± std)

	CRC_RLS	SRC	NC-CL1C	RCRCG
Data 1				
Avg. test error in %	27.27 ± 0.00	21.05 ± 0.27	20.27 ± 0.27	**13.86 ± 0.25**
Avg. F-measure	NaN	0.38 ± 0.12	0.43 ± 0.12	**0.77 ± 0.04**
Avg. training SCI	0.98 ± 0.06	**0.29 ± 0.01**	**0.29 ± 0.01**	0.97 ± 0.00
Avg. training time (s)	**0.0027 ± 0.00**	1.40 ± 0.07	1.43 ± 0.06	1.30 ± 0.05
Data 2				
Avg. test error in %	53.27 ± 0.05	4.96 ± 0.03	5.10 ± 0.03	**3.69 ± 0.03**
Avg. F-measure	NaN	0.95 ± 0.03	0.96 ± 0.03	**0.97 ± 0.03**
Avg. training SCI	0.40 ± 0.03	**0.21 ± 0.03**	**0.21 ± 0.03**	0.26 ± 0.01
Avg. training time (s)	**0.0032 ± 0.00**	0.92 ± 0.05	0.93 ± 0.05	0.63 ± 0.03
Data 3				
Avg. test error in %	8.80 ± 0.00	1.45 ± 0.01	1.45 ± 0.01	**1.08 ± 0.02**
Avg. F-measure	NaN	0.93 ± 0.04	0.93 ± 0.04	**0.95 ± 0.03**
Avg. training SCI	0.35 ± 0.07	**0.23 ± 0.00**	**0.23 ± 0.00**	0.34 ± 0.00
Avg. training time (s)	**0.1002 ± 0.01**	11.35 ± 0.60	11.47 ± 0.63	5.93 ± 0.37

RCRCG to illustrate that the solution $\hat{\rho}$ or $\tilde{\rho}$ is sparser. It can be clearly seen that the RCRCG has better performance and sparsity than the CRC_RLS in Table 4.

Data 2: The SCI of the SRC and NC-CL1C are higher than CRC_RLS and RCRCG at 0.21 ± 0.03 due to the best sparsity of L_1 optimization. The SCI of the RCRCG at 0.26 ± 0.01 is sparser than the CRC_RLS at 0.40 ± 0.03 to prove the Gabor filter availability. Seen Table 4, the CRC_RLS represents speed-up about 1 times compared with the SRC and NC-CL1C.

Data 3: As same as the results of Data 2 the RCRCG of test error rate, F-measure, training SCI and time-consuming have the best performance in Table 4.

In brief, the RCRCG is shorter on time-consuming and better performance than other machine learning methods. Meanwhile, it sparser than CRC_RLS.

5 Conclusions

The RCRCG is constructed to address the discrimination of medicine using NIRS in this paper. By using the Gabor filter to handle the sparsity, the RCRCG model can obtain the more relevant factor vectors of NIRS signal. In addition to, adding the Lasso parameter justifications by the training samples. Getting through those optimizers processing, the classification accuracy of the RCRCG model become

robust and correctly. From comparison with other Artificial Intelligence approaches, the results demonstrate that the RCRCG is the most effective one for the identification problem using NIRS data.

Acknowledgements This work was supported by the National Natural Science Foundation of China (Grant No. 61562013), Natural Science Foundation of Guangxi Province (CN) (2017GXNSFDA198025), and Guangxi Key Lab of Trusted Software (kx201730). We thank Xi'an-Janssen Pharmaceutical Factory for useful datasets of Near Infrared spectra samples. We would like to express our appreciation to all supporters above mentioned for their strongly financial support.

References

1. Lu, H.Y., Wang, S.S., Cai, R., et al.: Rapid discrimination and quantification of alkaloids in Corydalis Tuber by near-infrared spectroscopy. J. Pharm. Biomed. Anal. **59**, 44–49 (2012)
2. Li, X., Yong, H., Hui, F.: Non-destructive discrimination of Chinese bayberry varieties using Vis/NIRS spectroscopy. J. Food Eng. **81**(2), 357–363 (2007)
3. Qu, J.H., Liu, D., Cheng, J.H., et al.: Applications of near-infrared spectroscopy in food safety evaluation and control: a review of recent research advances. Crit. Rev. Food Sci. Nutr. **55**(13), 1939–1954 (2015)
4. Reilly, A.O., Coffey, R., Gowen, A., et al.: Evaluation of near-infrared chemical imaging for the prediction of surface water quality parameters. Int. J. Environ. Anal. Chem. **95**(5), 403–418 (2015)
5. Shao, X., Cui, X., Liu, Y., et al.: Understanding the molecular interaction in solutions by chemometric resolution of near-infrared spectra. Chem. Select. **2**(31), 10027–10032 (2017)
6. Xu, Z., Liu, Y., Li, X., et al.: Discriminant analysis of Chinese patent medicines based on near-infrared spectroscopy and principal component discriminant transformation. Spectrochim. Acta Part A Mol. Biomol. Spectrosc. **149**, 985–990 (2015)
7. Haughey, S.A., Graham, S.F., Cancouët, E., et al.: The application of Near-Infrared Reflectance Spectroscopy (NIRS) to detect melamine adulteration of soya bean meal. J. Food Chem. **136**, 1557–1561 (2013)
8. Sacré, P.Y., Deconinck, E., Beer, T.D., et al.: Comparison and combination of spectroscopic techniques for the detection of counterfeit medicines. J. Pharm. Biomed. Anal. **53**, 445–453 (2010)
9. Luo, W., Huan, S., Fu, H., et al.: Preliminary study on the application of near infrared spectroscopy and pattern recognition methods to classify different types of apple samples. J. Food Chem. **128**, 555–561 (2011)
10. Lyndgaard, L.B., Berg, F.V.D., Juan, A.D.: Quantification of paracetamol through tablet blister packages by Raman spectroscopy and multivariate curve resolution-alternating least squares. J. Chemom. Intell. Lab. Syst. **125**, 58–66 (2013)
11. Storme-Paris, I., Rebiere, H., Matoga, M., et al.: Challenging near infrared spectroscopy discriminating ability for counterfeit pharmaceuticals detection. J. Analytica chimica acta **658**, 163–174 (2010)
12. Yang, J., Zhang, L., Xu, Y., et al.: Beyond sparsity: The role of L1-optimizer in pattern classification. J. Pattern Recogn. **45**, 1104–1118 (2012)
13. Zhang, L., Yang, M.: Sparse representation or collaborative representation: which helps face recognition? In: IEEE International Conference on Computer Vision, pp. 471–478. IEEE (2012)
14. Wright, J., Yang, A.Y., Ganesh, A., et al.: Robust face recognition via sparse representation. IEEE Trans. Pattern Anal. Mach. Intell. **31**, 210–227 (2009)
15. Yang, M., Zhang, L., Shiu, S.C.K., et al.: Gabor feature based robust representation and classification for face recognition with Gabor occlusion dictionary. J. Pattern Recogn. **46**, 1865–1878 (2013)

16. Lu, H., Li, Y., Chen, M., et al.: Brain intelligence: go beyond artificial intelligence. Mob. Netw. Appl. **23**(2), 368–375 (2018)
17. Rakotomamonjy, A., Flamary, R., Yger, F.: Learning with Infinitely Many Features. Kluwer Academic Publishers (2013)
18. Zhang, W., Shan, S., Gao, W., et al.: Local gabor binary pattern histogram sequence (LGBPHS): a novel non-statistical model for face representation and recognition. In: International Conference on Computer Vision, vol. 1, pp. 786–791 (2005)
19. Dyrby, M., Engelsen, S.B., Nørgaard, L., et al.: Chemometric quantitation of the active substance (containing C≡N) in a pharmaceutical tablet using Near-Infrared (NIRS) transmittance and NIRS FT-Raman Spectra. J. Appl. Spectrosc. **56**, 579–585 (2002)
20. Zhang, Z., Jung, T.P., Makeig, S., et al.: Compressed sensing for energy-efficient wireless telemonitoring of noninvasive fetal ECG via block sparse Bayesian learning. IEEE Trans Biomed Eng. **60**, 300–309 (2013)

Multi-objective Bird Swarm Algorithm

Dongmei Wu and Hao Gao

Abstract Most real-world optimization problems involve multiple objectives and parameters. In this paper, bird swarm algorithm (BSA) is modified with non-dominated sorting approach and parallel coordinates. A developed algorithm, known as multi-objective BSA (MOBSA) is proposed. When the external archive for non-dominated solutions is full to overflowing, the solution with greatest density would be rejected. The approaches were tested and compared on benchmark problems. Based on these results, the MOBSA has access to better convergence and spread of Pareto front.

Keywords Bird swarm algorithm · MOBSA · Non-dominated sorting

1 Introduction

Many real-word optimization problems concern optimization of multiple conflicting goals concurrently. The fields of aeroengine design, constellation designation, cross-modal retrieval, unmanned aerial vehicles, and image processing are refers to multiple objectives [1–5]. Classical optimization methods suggest converting the multi-objective optimization problem to a single-objective optimization problem with adding weight vector for objectives, then finding one particular Pareto-optimal solution at a time. Based on the unique optimal solution, some objectives are improved, with deterioration of others. To deal with such trouble, it is hopeful to find compromise solutions at each simulation run. The popularization of multi-objective evolutionary algorithms (MOEAs) provides a possible approach for MOOPs, such as NSGA-II [6], MOPSO [7], PAES [8], etc. These MOEAs are population-based algorithms, which inherit all of the favorable properties from their single objective

D. Wu (✉) · H. Gao
Nanjing University of Posts and Telecommunications, Nanjing, China
e-mail: wudm@njupt.edu.cn

H. Gao
e-mail: tsgaohao@gmail.com

H. Lu (ed.), *Cognitive Internet of Things: Frameworks, Tools and Applications*, Studies in Computational Intelligence 810,
https://doi.org/10.1007/978-3-030-04946-1_12

relatives and allow them to explore the different parts of the Pareto front simultaneously.

The bird swarm algorithm (BSA) is a new bionic optimization algorithm (2015) [9]. This algorithm simulates the foraging behavior, defensive behavior and flight behavior of birds. The algorithm has the advantages of few parameters and easy to adjust. At present, the improvement work of this algorithm focused on single-objective optimization problem, so far, there are no literatures published to deal with the MOOPs. Therefore, in this study Pareto optimal solutions are introduced into BSA, so as to find multiple optimal solutions at a time.

2 Brief View of Bird Swarm Algorithm

From the foraging, defense and flight of the bird flock, five rules can be summarized [9]: (1) Each bird freely converts between defense and foraging behavior, which is a random act. (2) In the process of foraging, each bird can record and update its own optimal information and population optimal information about the food. This information is used to find new sources of food. At the same time, the whole population shares the social information. (3) During the defense, each bird tries to move toward the center, but this behavior is influenced by competition among populations. Birds with high alertness are more likely to approach the center than low-alert birds. (4) The flock flies to another place each time. The most alert bird becomes producer, while the lowest alert bird becomes scrounger. The bird with alertness between the two birds randomly becomes a producer or a scrounger. (5) Producers actively seek food, and scroungers follow the producers at random. The above five rules are described in mathematical terms as follows:

The size of the flock is M, the number of dimensions N, x_i^t is the position of each bird, where, t represents the current number of iterations, $i = 1, 2, \ldots, N$. Foraging behavior in rule (2) is formulated,

$$x_i^{t+1} = x_i^t + c_1 r_1 (p_i - x^t) + c_2 r_2 (g - x_i^t) \tag{1}$$

c_1 and c_2 are non-negative constants. r_1 and r_2 are the random numbers within [0, 1]. p_i, g are the historical optimal location of the ith bird and the historical optimal location of the whole flock respectively.

According to the rule (3), birds in the flock are trying to get close to the central area, but there is a competitive relationship between birds and birds. These behaviors can be expressed as follows,

$$x_{i,j}^{t+1} = x_{i,j}^t + A_1 r_3 (mean_j - x_{i,j}^t) + A_2 r_4 (p_{k,j} - x_{i,j}^t) \tag{2}$$

$$A_1 = a_1 \times e^{\left(-\frac{pFit_i}{sumFit+\varepsilon} \times N\right)} \tag{3}$$

$$A_2 = a_2 \times e^{\left(\frac{pFit_i - pFit_k}{|pFit_k - pFit_i| + \varepsilon} \times \frac{N \times pFit_k}{sumFit+\varepsilon}\right)} \tag{4}$$

Among them, a_1 and a_2 are the constants of (0, 2), $pFit_i$ represents the optimal value of the ith bird, $sumFit$ represents the sum of the optimal value of the whole flock. ε is the smallest real number of the computer. $mean_j$ is average value of positions in the jth dimension. r_3 is the random number between (0, 1), r_4 is the random number between $(-1, 1)$, $k \neq i$.

According to the rule (4), Every once in a while FQ, birds may fly to another place, some of the birds can become producers, others will become scroungers, behavior of producers and scroungers can be interpreted as,

$$x_{i,j}^{t+1} = x_{i,j}^{t} + r_5 x_{i,j}^{t} \tag{5}$$

$$x_{i,j}^{t+1} = x_{i,j}^{t} + FLr_6(x_{k,j}^{t} - x_{i,j}^{t}) \tag{6}$$

r_5 is a gaussian random number that satisfies the variance of 0 and the mean 1. r_6 is the random number between (0, 1), and FL stands for scroungers following producers.

3 Multi-objective Bird Swarm Algorithm

3.1 Multi-objective Optimization

Multi-objective optimization problem (MOOP) aims to find an acceptable set of solutions, in contrast with single objective problems where there is only one solution. Solutions in MOOPs intend to achieve a compromise between different criteria, enabling the existence of several optimal solutions. The general description for MOOP is,

$$Minf(X) = [f_1(X), f_2(X), \ldots, f_m(X)] \tag{7}$$

$$g_i(X) \leq 0\,, \quad i = 1, 2, \ldots, k \tag{8}$$

$$h_i(X) = 0, \quad i = 1, 2, \ldots, l \tag{9}$$

where, solution vector $\boldsymbol{X} = [x_1, x_2, \ldots, x_n]^T$, $f_i(\boldsymbol{X})$, $i = 1, 2, \ldots, m$ are functions of objectives. The solution to MOOP is to obtain as many Pareto-optimal solutions as possible.

3.2 Parallel Cell Coordinate System (PCCS)

Multi-objective optimization problem involves more than two objectives optimized in the meantime. Inspired by the concept of parallel coordinates, multi-dimensional Pareto front could be convert to two-dimensional plane grid, meanwhile the cartesian

coordinates of Pareto front are converted to the integral value coordinates using the Eq. (10),

$$L_{k,m} = ceil\left(K\frac{f_{k,m} - f_m^{\min}}{f_m^{\max} - f_m^{\min}}\right) \tag{10}$$

where, $k = 1,2,\ldots,K$, K is the number of Pareto solutions in the external archive. $f_m^{\min}$ and $f_m^{\max}$ are minimum and maximum of mth objective on Pareto front. $L_{k,m} \in [1, K]$ are integral labels of $f_{k,m}$ in Parallel coordinates. If $f_{k,m} = f_m^{\min}$, $L_{k,m} = 1$.

3.3 External Archive Update

The Pareto solutions in the external archive are evaluated using density of each solution in PCCS. First of all Pareto solutions are projected into PCCS, density of the ith solution is defined as Eq. (11).

$$D(i) = \sum_{\substack{j=1 \\ j\neq i}}^{K} \frac{1}{Dpc(i,j)^2} \tag{11}$$

$Dpc(i, j)$ represents parallel cell distance between two different Pareto solutions.

$$Dpc(i,j)\begin{cases} 0.5, & if\ \forall m, L_{i,m} = L_{j,m} \\ \sum_{m=1}^{M} \left|L_{i,m} - L_{j,m}\right|, & if\ \exists m, L_{i,m} \neq L_{j,m} \end{cases} \tag{12}$$

The external archive has a maximum size, which is set by the user to reflect the desired number of final solutions. Whether the new solution is a non-dominated solution is evaluated by the non-dominated sorting approach [12].

3.4 Formulation for MOO

p_i in Eq. (1) is non-dominated solution for ith so far, and g is one of non-dominated solution selected from the external archive, rule of which is that g resides low-density in PCCS. A_1 and A_2 in Eq. (2) are modified as,

$$A_1 = a_1 \times \left(-\sum_{m=1}^{M} \frac{pFit_{i,m}}{sumFit_m + \varepsilon} \times pop \times \frac{1}{M}\right) \tag{13}$$

$$A_2 = a_2 \times \sum_{m=1}^{M} \left(\frac{pFit_{i,m} - pFit_{k,m}}{|pFit_{k,m} - pFit_{i,m}| + \varepsilon} \times \frac{pop \times pFit_{k,m}}{sumFit_m + \varepsilon} \right) \times \frac{1}{M} \tag{14}$$

where, $pFit_{i,m}$ means best value of mth objective for ith bird. $sumFit_m$ is the sum of fitness for mth objective. pop is total number of birds. M is number of objectives. Other variables are the same with Eqs. (3) and (4).

The basic rule (4) of BSA, there is just one fitness function, it is easily to judge the smallest and the biggest values, however it has more than one objective to be evaluated in MOO, the optimal solution means set of non-dominated solutions. In the proposed MOBSA, the current position of birds is to be divided into two parts: non-dominated solutions and dominated solutions. It is supposed that the birds whose positions are non-dominated by other birds would be producers, in other words, birds with dominated positions would be scroungers. The structure of MOBSA is shown in Fig. 1.

4 Evaluation and Analyses

4.1 Performance Merits

Convergence performance of multi-objective optimization approaches are usually evaluated using number of non-dominated solutions, two set coverage, generational distance (GD, [10]), maximum Pareto front error (ME), and so on [6, 10, 11]. The convergence performance merit used is GD. The smaller the value of GD, the better the convergence toward the Pareto front. The second performance metrics used for the experiments are the two set coverage and spacing metric, which is commonly estimated by distribution function Δ.

$$GD = \frac{\left(\sum_{i=1}^{n'} d_i^p\right)^{1/p}}{n'} \tag{15}$$

where, n' is number of found non-dominated solutions, d_i is Euclidean distance from each Pareto solution obtained using algorithm to the true Pareto solutions, and the formula is Eq. (16). If the obtained solutions are located on the known Pareto optimal front, $d_i = 0$.

$$d_i = \min \sqrt{\sum_{k=1}^{M} (f_k^i - f_k^j)^2}, \quad j = 1, 2, \ldots, n \tag{16}$$

n is number of known non-dominated solutions, f_k^i is the kth objective value of ith individual.

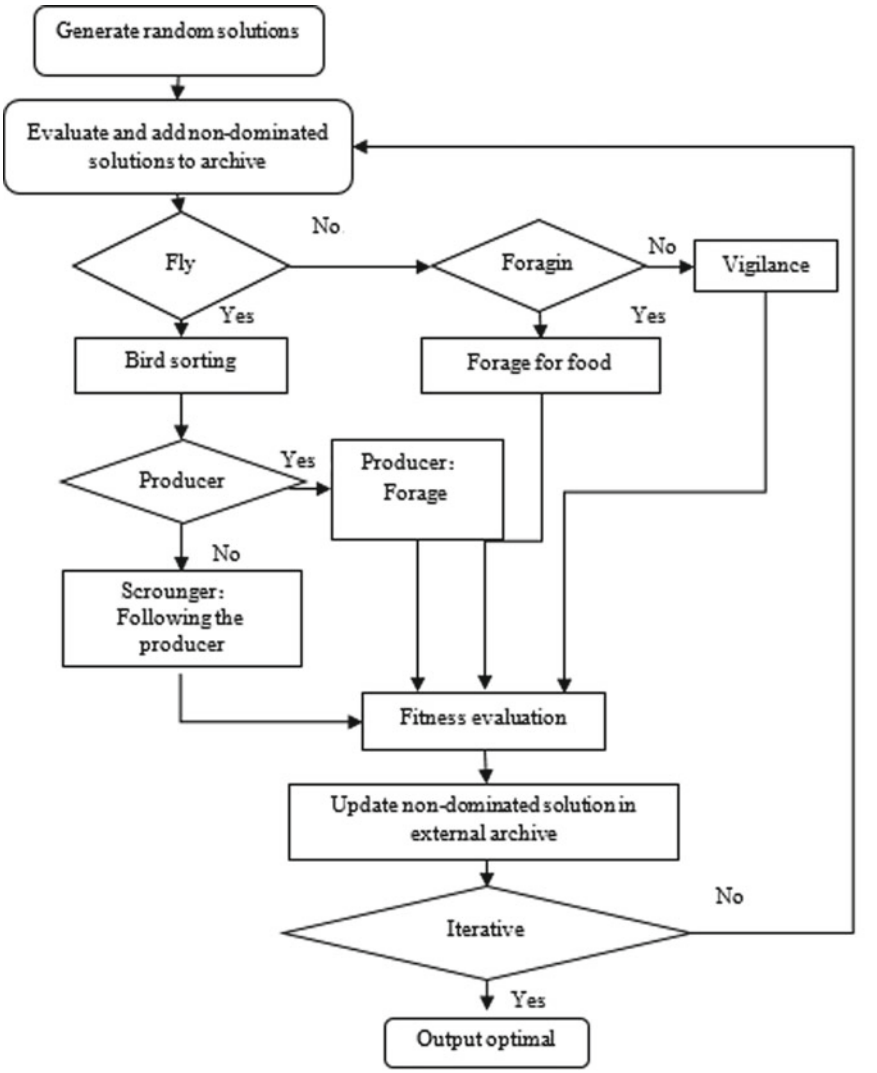

Fig. 1 Structure of MOBSA

$$\Delta = \frac{\sum_{m=1}^{M} d_m^e + \sum_{i=1}^{N-1} \left| d_i - \bar{d} \right|}{\sum_{m=1}^{M} d_m^e + (n-1)\,\bar{d}} \tag{17}$$

where, d_i is the Euclidean distance between consecutive solutions in the obtained set of Pareto-optimal solutions. d_m^e is Euclidean distance between extreme solution and

the boundary solutions of the found non-dominated set for mth objective component. $\bar{d}$ is the average of all d_i. If the achieved solutions are well uniformly distributed, that is $d_i = \bar{d}$, in addition those extreme solutions on obtained Pareto front and true Pareto front coincide, $\Delta = 0$, otherwise $\Delta > 0$. The smaller Δ, the better Pareto front spread out.

4.2 Test Functions

Four test problems without constraint were used for evaluating MOBSA, NSGA-II, and MOPSO. SCH function is the most common problem, proposed by Schaffer, 1985, and used by almost all MOEA. FON function [13] was also tested in this study. ZDT3 and ZDT6 (Zitzler et al.) were adopted as test functions. All problems have two objectives. Other details are described in Table 1. The population size for SCH function was set to 500, since the MOPSO and MOBSA do not work with a small amount of particles occasionally. The repository of external archive is 100. For MOBSA, population of bird is 50. $c_1 = c_2 = 1.5$, $a_1 = a_2 = 1$, $P \in [0.8, 1]$, $FL \in [0.5, 0.9]$, $FQ = 10$. The swarm for MOPSO also has 50 individuals. The solution space is divided into 49 hypercube. $\omega \in [0.5, 0.9]$, $r_1 = r_2 = \text{rand}$. As for NSGA-II, population is 100, and toursize is set to 2 [12–14].

4.3 Discussion of the Results

All of three algorithms were simulated 200 iterations on benchmark functions. The results are graphically shown in Figs. 2, 3, 4 and 5. Each algorithm was tested 20 times, with 100 iterations respectively. Tables 2, 3, 4 and 5 show the mean and variance of the convergence metrics (GD, Δ) obtained using three algorithms MOPSO, NSGA-II, and MOBSA. Average and standard deviation of GD in SCH, ZDT3, and ZDT6 using MOBSA are smaller than using other two algorithms. With regard to FON function, the average of GD based on MOBSA is a little bigger than that of MOPSO, however the standard deviation is the smallest in the three algorithms. To evaluate another merit of Δ, the average values for SCH, FON and ZDT6 using MOBSA are better than others. Whereas average Δ of ZDT3 get the best values based on MOPSO. Based on these statistical results, it could draw a conclusion that the MOBSA is superior to MOPSO and NSGA-II.

Table 1 Test problems

Problem	Function	n	Bounds	Optimal solution	Description of Pareto front
FON	$f_1(x) = 1 - \exp\left(-\sum_{i=1}^{n}\left(x_i - \frac{1}{\sqrt{n}}\right)^2\right)$ $f_2(x) = 1 - \exp\left(-\sum_{i=1}^{n}\left(x_i + \frac{1}{\sqrt{n}}\right)^2\right)$	3	$[-4, 4]$	$x_1 = x_2 = x_3$ $\in \left[-1/\sqrt{3}, 1/\sqrt{3}\right]$	Nonconvex
SCH	$f_1(x) = x^2$ $f_2(x) = (x-2)^2$	1	$[-10^3, 10^3]$	$x \in [0, 2]$	Convex
ZDT3	$f_1(x) = x_1, f_2(x) = g \cdot h$ $g = 1 + \frac{9}{n-1}\sum_{i=2}^{n} x_i$ $h = 1 - \sqrt{\frac{f_1(x)}{g}} - \frac{f_1(x)}{g}\sin(10\pi f_1)$	10	$[0, 1]$	$x_1 \in$ $[0, 0.0830015349] \cup [0.1822287280,$ $0.257762334] \cup [0.4093136748,$ $0.4538821041] \cup [0.6183967944,$ $0.6525117038] \cup [0.8233317983,$ $0.8518328654]$ $g(x) = 1$	Disconnected, convex
ZDT6	$f_1(x) = 1 - e^{-4x_1}\sin^6(6\pi x_1), f_2(x) = g \cdot h$ $g = 1 + 9\left[\left(\sum_{i=2}^{n} x_i / (n-1)\right)^{0.25}\right], h = 1 - \left(\frac{f_1(x)}{g}\right)^2$	10	$[0, 1]$	$x_1 \in [0.2807753191, 1]$ $g(x) = 1$	Nonuniform spaced, nonconvex

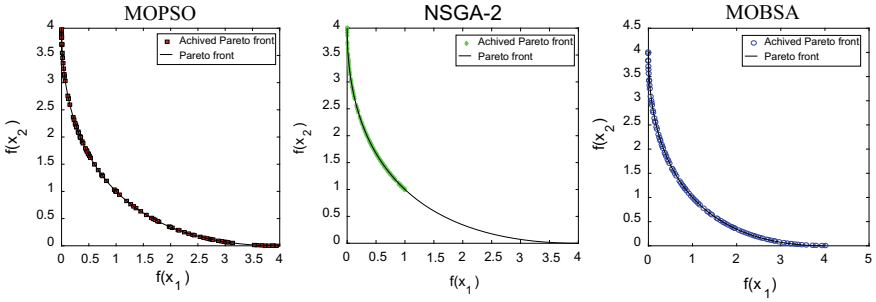

Fig. 2 SCH function using MOPSO, NSGA-II and MOBSA

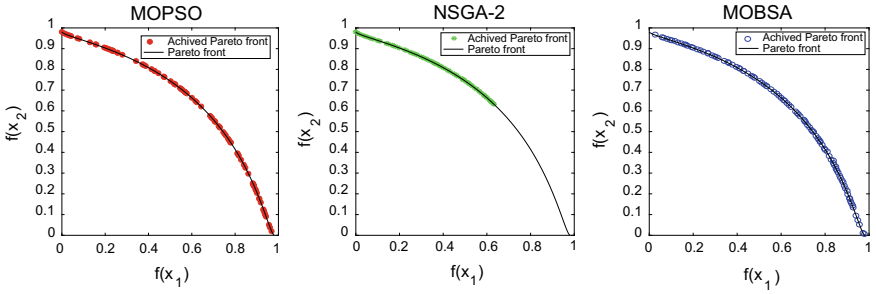

Fig. 3 FON function using MOPSO, NSGA-II and MOBSA

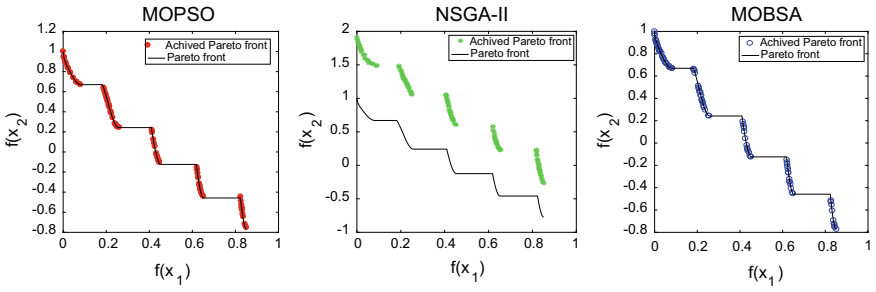

Fig. 4 ZDT3 function using MOPSO, NSGA-II and MOBSA

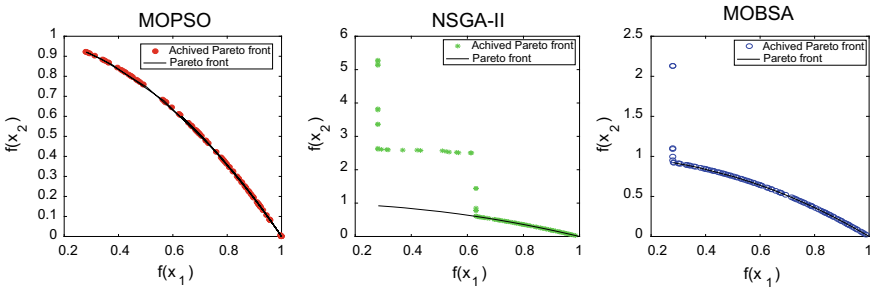

Fig. 5 ZDT6 function using MOPSO, NSGA-II and MOBSA

Table 2 Performance merits (GD, Δ) of SCH function

	GD				Δ			
	Max	Min	AVE	Sd.	Max	Min	AVE	Sd.
MOPSO	5.10E−03	4.40E−03	4.70E−03	2.21E−04	0.992	0.857	0.912	0.034
NSGA-II	0.025	4.40E−03	0.006	0.005	1.277	0.802	0.883	0.134
MOBSA	4.80E−03	4.50E−03	**4.65E−03**	**9.75E−05**	0.729	0.637	**0.679**	**0.025**

Table 3 Performance merits (GD, Δ) of FON function

	GD				Δ			
	Max	Min	AVE	Sd.	Max	Min	AVE	Sd.
MOPSO	6.98E−04	4.09E−04	**4.65E−04**	6.06E−05	0.928	0.851	0.882	0.019
NSGA-II	0.004	4.32e−04	0.001	9.1500E−04	1.047	0.797	0.887	0.090
MOBSA	5.32E−04	4.49e−04	4.98e−04	**2.29e−05**	0.704	0.617	**0.659**	**0.019**

Table 4 Performance merits (GD, Δ) of ZDT3 function

	GD				Δ			
	Max	Min	AVE	Sd.	Max	Min	AVE	Sd.
MOPSO	0.118	2.00E–04	0.047	0.037	1.004	0.845	**0.939**	0.042
NSGA-II	0.106	0.063	0.081	0.012	0.986	0.844	0.889	**0.036**
MOBSA	0.057	3.00E−04	**0.020**	**0.018**	1.240	0.843	1.055	0.131

Table 5 Performance merits (GD, Δ) of ZDT6 function

	GD				Δ			
	Max	Min	AVE	Sd.	Max	Min	AVE	Sd.
MOPSO	0.844	0.001	0.158	0.235	1.325	0.890	1.062	0.120
NSGA-II	0.6160	0.3167	0.486	0.0684	1.125	0.978	1.013	**0.031**
MOBSA	0.089	0.002	**0.042**	**0.026**	1.111	0.645	**0.954**	0.094

5 Conclusion

This paper extended the BSA based on non-dominated sorting strategy, to cope with multi-objective optimization problem without constraint. In terms of the proposed algorithm, named as MOBSA, parallel cell coordinate system was applied, and the external archive is updated using non-dominated sorting approach and density evaluation method. The proposed MOBSA was compared with MOPSO and NSGA-II, on different test functions. It was proved that the MOBSA could achieve better spread of solutions and convergence in most of test functions. The future work focuses on handling constraint MOO with MOBSA and its application on engineering problems.

References

1. Serikawa, S., Lu, H.: Underwater image dehazing using joint trilateral filter. Comput. Electr. Eng. **40**(1), 41–50 (2014)
2. Lu, H., Li, Y., Mu, S., Wang, D., Kim, H., Serikawa, S.: Motor anomaly detection for unmanned aerial vehicles using reinforcement learning. IEEE Internet Things J. (2017). https://doi.org/10.1109/jiot.2017.2737479
3. Lu, H., Li, Y., Chen, M., Kim, H., Serikawa, S.: Brain intelligence: go beyond artificial intelligence. Mob. Netw. Appl. 1–8 (2017)
4. Lu, H., Li, B., Zhu, J., Li, Y., Li, Y., Xu, X., He, L., Li, X., Li, J., Serikawa, S.: Wound intensity correction and segmentation with convolutional neural networks. Concurr. Comput.: Pract. Exp. (2017). https://doi.org/10.1002/cpe.3927
5. Xu, X., He, L., Lu, H., Gao, L., Ji, Y.: Deep adversarial metric learning for cross-modal retrieval. World Wide Web J. (2018). https://doi.org/10.1007/s11280-018-0541-x
6. Deb, K., Pratap, A., Agarwal, S., et al.: A fast and elitist multi-objective genetic algorithm: NSGA-II. IEEE Trans. Evol. Comput. **6**(2), 182–197 (2002)
7. Coello Coello, C.A., Lechuga, M.S.: MOPSO: a proposal for multiple objective particle swarm optimization. In: Proceedings of Congress Evolutionary Computation (CEC'2002), Honolulu, HI, vol. 1, pp. 1051–1056 (2002)
8. Knowles, J., Corne, D.: The Pareto archived evolution strategy: a new baseline algorithm for Pareto multi-objective optimisation. In: Proceedings of Congress on Evolutionary Computation (1999)
9. Meng, X.-B., et al.: A new bio-inspired optimisation algorithm: Bird Swarm Algorithm. J. Exp. Theoret. Artif. Intell. (2015)
10. Van Veldhuizen, D.A.V., Lamont, G.B.: Evolutionary Computation and Convergence to a Pareto Front, pp. 221–228. Stanford University California (1998)
11. Zhou, A., Jin, Y., Zhang, Q., et al.: Combining model-based and genetics-based offspring generation for multi-objective optimization using a convergence criterion. In: IEEE Congress on Evolutionary Computation, CEC 2006, pp. 892–899 (2006)
12. Schaffer, J.D.: Multiple objective optimization with vector evaluated genetic algorithms. In: Grefensttete, J.J. (ed.) Proceedings of the First International Conference on Genetic Algorithms, pp. 93–100. Lawrence Erlbaum, Hillsdale, NJ (1987)
13. Fonseca, C.M., Fleming, P.J.: Multi-objective genetic algorithms made easy: selection sharing and mating restriction. In: First International Conference on Genetic Algorithms in Engineering Systems: Innovations and Applications, pp. 45–52. Galesia. IET (1995)
14. Kalyanmoy, D.: Multi-objective genetic algorithms: problem difficulties and construction of test problems. Evol. Comput. **7**(3), 205–230 (2014)

Performance Modeling of Spark Computing Platform

Jie Ding, Yunyue Xie and Meihua Zhou

Abstract Big Data has been widely used in all aspects of society. For solving the problem of massive data storing and analyzing, many big data solutions have been proposed. Spark is the newer solution of the universal parallel framework which like Hadoop MapReduce. Compare the Hadoop, Spark's performance has been increased significantly. As a data analysis framework, researchers are particularly concerned about its performance. So in this paper, we use a stochastic process algebra (PEPA) to model the Spark architecture. This model will give the usability of the compositional approach in modeling and analysis Spark architecture. This research obtains an algorithm that generated the service flow of the PEPA model. In the end, we will state the benefit of this compositional method in modeling a large parallel system.

Keywords Big Data · Spark · Stochastic process algebra · Performance evaluation

1 Introduction

Spark is the second generation of big data solution. The first age of big data solution is Hadoop [1]. Hadoop uses HDFS (Hadoop Distributed File System) for distributed storage and uses MapReduce for distributed computing. Spark is an open-source project. It stores data in memory and calculates it on a memory basis, which enables it to provide near real-time processing performance for data from many different data sources. In fact, Spark and Hadoop are not at one level. Spark is just a computational model. It should be at the same level as MapReduce, so it is common for the spark to work with Hadoop's HDFS (Hadoop Distributed File System) [2] and YARN [3]. Spark as a nearly real-time data computing model, lots of areas can combine the Spark to achieve faster and more accurate results. Such as the image processing [4],

J. Ding · Y. Xie (✉) · M. Zhou
School of Information Engineering, Yangzhou University, Yangzhou 225000, China
e-mail: 18602511639@163.com

J. Ding
e-mail: jieding@yzu.edu.cn

H. Lu (ed.), *Cognitive Internet of Things: Frameworks, Tools and Applications*, Studies in Computational Intelligence 810,
https://doi.org/10.1007/978-3-030-04946-1_13

reinforcement learning [5], artificial intelligence [6], neural networks [7, 8], deep learning [9]. Its performance is very important for the users. Moreover, Spark handles lots of user's applications at the same time and involves a large number of concurrent and choice actions on its internal components. For users, the response speed is what they are concerned about, for Spark, how to configure and take advantages of resources is the most important. In this paper, we will investigate a compositional approach PEPA to analysis the Spark performance. Performance evaluation process algebra (PEPA) is a stochastic process algebra. It can describe a large scale parallel system and give the quantitative analysis. Response time and throughput are two important metrics in analyzing a system. So in the end, we will give the response time and throughput by simulation.

2 PEPA Formalism

This section will introduce a stochastic process algebra PEPA.

PEPA is a compositional approach that decomposes a system into subsystems that are smaller and more easily modeled [10–12] and it has been applied to many aspects [13, 14]. A system can be viewed as different components interact with each other. Both physical and logical resources can be considered as components. The component transfers from one state to another after performing an action. If the action is concurrency, there may be multiple components involved. PEPA transforms a complex system into a combination of a few small, simple components. In order to better introduce PEPA, a simple example will be given. A banking service system is seen as an interaction of Service component and Queue component. Service component handles the business and Queue component executes call number activity.

Prefix: $(\alpha, \gamma).P$. Prefix describes the basic relationship between components and actions. α represents the action type and the duration of this action executing satisfies the exponential distribution with rate γ. After executing this action, this component will behave as P.

Constant: $A \stackrel{\text{def}}{=} P$. This equation represents the behavior of constant is similar to the behavior of component P. In our example, after Service component handling the client's business, the Service component may transfer into a wait state. So we can obtain the PEPA formula as:

$$Service \stackrel{\text{def}}{=} (handle, r_1) \cdot Service_{wait}$$

Choice: $P + Q$. This component represents the system may either behave as P or Q. There is competition between P and Q. The activities of P and Q both are enabled. When a component wins the race, i.e. an activity has completed, other activities will be discarded. For example, Service Component may execute the print documents action or execute the signature action when handling different business.

$$Service \overset{\text{def}}{=} (print, r_2) \cdot Service_1 + (signature, T) \cdot Service_2$$

Symbol T represents the rate of the signature action depends on other components. Because the action of signature need to wait for customers to sign, not controlled by the Service component, so here the rate cannot be determined.

Parallel: $P||Q$. The component $P||Q$ represents two concurrent but completely independent components.

Cooperation: $P \underset{L}{\bowtie} Q$. This means that the P and Q components must cooperate with each other to complete the activity. The set L is called cooperation set which represents an action whose action type is L must be completed by the interaction of P and Q components. But, the P and Q components run independently of the actions is not in set L. In the banking system, the entire system is the service components and queue components to work together to complete. And corporate banking and private business are two parallel queues but may be handled in the same service component. So we can obtain the PEPA formula:

$$(Queue_{corporate}||Queue_{private}) \underset{handle}{\bowtie} Service$$

3 Modelling

Spark operating model has many ways which include local mode, standalone mode, YARN model, etc. SparkContext, DAGScheduler, etc., can be viewed components in PEPA, the interaction between components is the activity, the duration of activity is satisfied exponential distributed. Next, the standalone mode of the PEPA model will be given below. The Standalone model uses the built-in resource scheduling framework which takes the Master/Slave architecture. This is the same as the Hadoop framework. As the Fig. 1 shown, the Standalone mode has three type nodes. The Client node, the Master Node, and the Worker Node. Drive Program generates SparkContext which is in charge of splitting tasks and allocating tasks. It can run on both Master node and Client Node. And a PEPA model will be given to model Spark Architecture. It can analyze the model by tracing a sequence of actions occurring with certain probabilities. According to the PEPA model, we will give some measurements for interpreting the performance of Spark model. Spark is an open-source cluster computing system introduced by the Apache company which is fast and general-purpose. It provides a comprehensive, unified framework for managing the need for big data processing of various datasets and data source (bulk data or real-time streaming data) with different properties (text data, chart data, etc.). The main difference compared to Hadoop is computing speed. Spark puts the data processing in memory and interacts with local disks only as data is entered and output. So computing speed can even improve 100 times.

The sequence of Spark performs as the Fig. 2 depicts. In general, Spark includes three nodes: Client node, Master node, and Worker node. Jobs can be submitted on

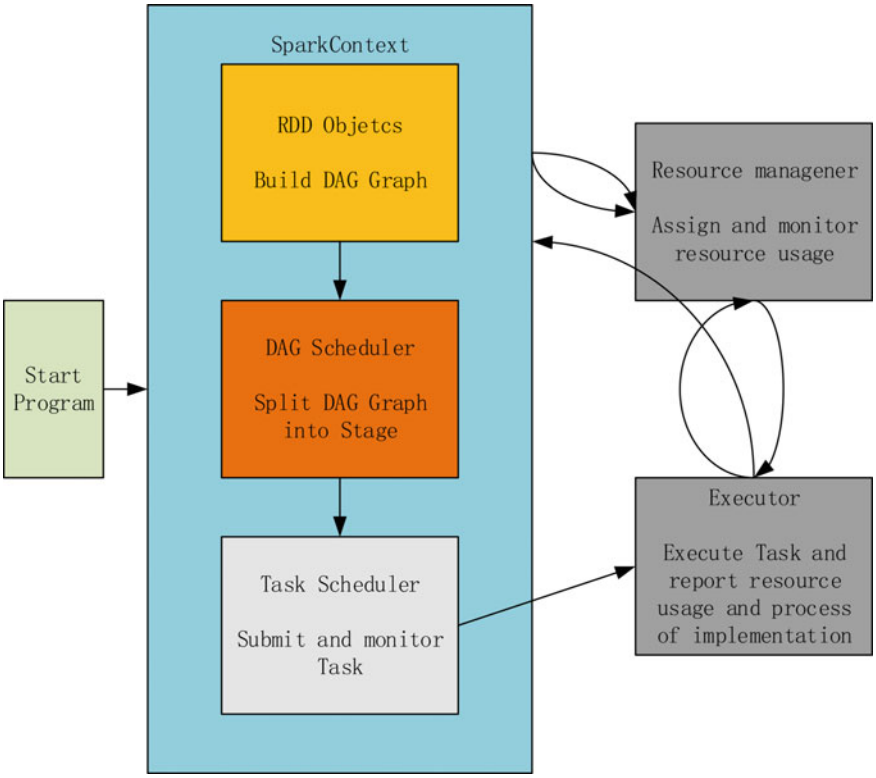

Fig. 1 Standalone architecture

any type node and SparkContext can be built in Client node or Worker node, so we do not consider specific nodes, only consider the specific order of execution. First, the task is submitted to Spark, SparkContext will be built. During the process of the building, a series of initial actions will be executed. The SparkEnv object will be created, it initializes a series of objects, including memory management module, communication management module, etc. After SparkEnv initialization, heartbeat mechanism, schedulerBackend, taskScheduler and DAGScheduler will be created. After the SparkContext is created, SparkContext will register and apply resources to the resource manager for Application. The resource manager is responsible for allocating and monitoring resource usage. At the same time, SparkContext will build the DAG graph, then DAGScheduler will split the DAG graph into stage (Taskset), TaskScheduler will deal with the stage which is responsible for submitting tasks to the executor. SparkContext communicate with executor by heartbeat.

SparkContext: Once jobs have been submitted, SparkContext performs the first action *init_spc*. This action will initialize a set of the system environment. Then it will execute the *reg_spc* action which registers this sparkContext on ClusterManager via the network. The following action is *reg_exc*. This action is initiated by

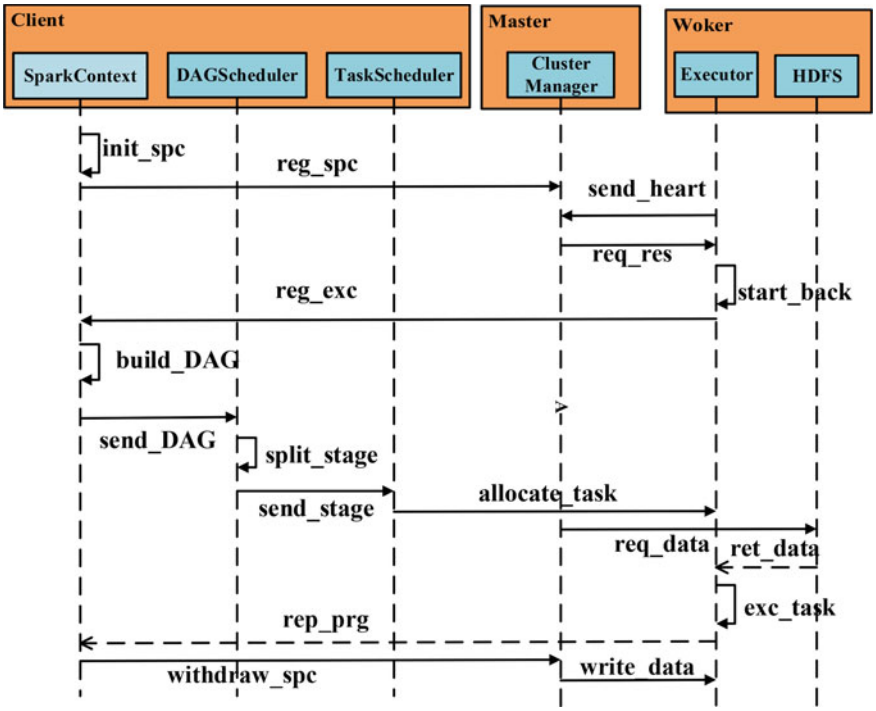

Fig. 2 The process of Spark operating

the Executor components. So SparkContext needs to wait for Executor to start StandaloneExecutorBackend registration. The subsequent action is *build_DAG*, SparkContex will build the DAG graph and submit the DAG graph to the DAG Scheduler (*send_DAG*), after other components completing the relevant actions, Executor will report the execution of the task. For sparkContext, this is a passive action. When all the tasks have completed, SparkContext will log out to master and free resources.

$$SparkContext_1 \stackrel{\text{def}}{=} (init\_spc, r_{init\_spc}) \cdot SparkContext_2$$

$$SparkContext_2 \stackrel{\text{def}}{=} (reg\_spc, r_{reg\_spc}).SparkContext_3$$

$$SparkContext_3 \stackrel{\text{def}}{=} (reg\_exc, \mathrm{T}).SparkContext_4$$

$$SparkContext_4 \stackrel{\text{def}}{=} (build\_DAG, r_{build\_DAG}).SparkContext_5$$

$$SparkContext_5 \overset{\text{def}}{=} (send\_DAG, r_{send\_DAG}).SparkContext_6$$

$$SparkContext_6 \overset{\text{def}}{=} (rep\_prg, \mathrm{T}).SparkContext_7$$

$$SparkContext_7 \overset{\text{def}}{=} (wtdraw\_spc, r_{wtdraw\_spc}).SparkContext_1$$

DAGScheduler: DAGScheduler component also on the Client Node which is in charge of split DAG graph. After receiving DAG graph from SparkContext (*send_DAG*), it will split DAG into stage (*split_stage*). The Stage is a set of task. Next, DAGScheduler will send task set to TaskScheduler (*send_stage*).

$$DAGScheduler_1 \overset{\text{def}}{=} (send\_DAG, \mathrm{T}) \cdot DAGScheduler_2$$

$$DAGScheduler_2 \overset{\text{def}}{=} (split\_stage, r_{split\_stage}) \cdot DAGScheduler_3$$

$$DAGScheduler_3 \overset{\text{def}}{=} (send\_stage, r_{send\_stage}) \cdot DAGScheduler_1$$

TaskScheduler: After TaskScheduler receiving the task set (*send_stage*), it will assign tasks to the appropriate worker node and then run by Executor node (*allocate_task*).

$$TaskScheduler_1 \overset{\text{def}}{=} (send\_stage, \mathrm{T}).TaskScheduler_2$$

$$TaskScheduler_2 \overset{\text{def}}{=} (allocate\_task, r_{allocate\_task}).TaskScheduler_1$$

ClusterManager: ClusterManager is a unified scheduling management center. Other components will register with it. First, SparkContext will register with it (*reg_spc*). Worker nodes will report his status to him through heartbeat (*send_heart*) and this is a shared action, ClusterManager will request resources from Worker Nodes (*req_res*). When TaskScheduler has completed the assignment of tasks. ClusterManager will request the data from HDFS (*req_data*). Once the SparkContext sends the task completion message to ClusterManager (*withdraw_spc*), the final result is written to HDFS (*write_data*).

$$ClusterManager_1 \overset{\text{def}}{=} (reg\_spc, \mathrm{T}).ClusterManager_2$$

$$ClusterManager_2 \overset{\text{def}}{=} (send\_heart, \mathrm{T}).ClusterManager_3$$

$$ClusterManager_3 \overset{\text{def}}{=} (req\_res, r_{req\_res}).ClusterManager_4$$

$$ClusterManager_4 \overset{\text{def}}{=} (req\_data, r_{req\_data}).ClusterManager_5$$

$$ClusterManager_5 \overset{\text{def}}{=} (wtdraw\_spc, \mathrm{T}).ClusterManager_1$$

Executor: Executors periodically send heartbeat to ClusterManager to report its status (*send_heart*). After receiving the request of the task, ClusterMananger decides which Worker nodes to allocate and request resources (*req_res*). Then Worker nodes start StandaloneExecutorBacked (*start_back*). Then StandaloneExecutorBacked will register with SparkContext. After TaskScheduler has assigned tasks, HDFS will return the data needed for calculation (*ret_data*). After all the data is ready, Executor starts executing the task (*exc_task*) and regularly report the execution status of the task to SparkContext (*rep_prg*). In the end, the final computing result will write to HDFS (*write_data*).

$$Executor_1 \overset{\text{def}}{=} (send\_heart, r_{send\_heart}).Executor_2$$

$$Executor_2 \overset{\text{def}}{=} (req\_res, \mathrm{T}).Executor_3$$

$$Executor_3 \overset{\text{def}}{=} (start\_back, r_{start\_back}).Executor_4$$

$$Executor_4 \overset{\text{def}}{=} (reg\_exc, r_{reg\_exc}).Executor_5$$

$$Executor_5 \overset{\text{def}}{=} (allocate\_task, \mathrm{T}).Executor_6$$

$$Executor_6 \overset{\text{def}}{=} (ret\_data, \mathrm{T}).Executor_7$$

$$Executor_7 \overset{\text{def}}{=} (exc\_task, r_{exc\_task}).Executor_8$$

$$Executor_8 \overset{\text{def}}{=} (rep\_prg, r_{rep\_prg}).Executor_9$$

$$Executor_9 \overset{\text{def}}{=} (write\_data, r_{write\_data}).Executor_1$$

HDFS: HDFS is responsible for reading and writing data, intermediate results are not written to HDFS. After receiving the data request (*req_data*), HDFS will return data to Executor (*ret_data*) and the final result will write to HDFS (*write_data*).

$$HDFS_1 \overset{\text{def}}{=} (req\_data, \mathrm{T}).HDFS_2$$

$$HDFS_2 \overset{\text{def}}{=} (ret\_data, r_{ret\_data}).HDFS_3$$

$$HDFS_3 \overset{\text{def}}{=} (write\_data, \mathrm{T}).HDFS_1$$

Through the above various components of the model, we can obtain the system equation. This system equation describes the interaction of the various components. We assume the shorthand for the same activity type for $C[M] := (C||...||C)$, so we can express the system formula as:

$$SparkContext[M] \underset{\{L_1\}}{\bowtie} DAGScheduler[N] \underset{\{L_2\}}{\bowtie} TaskScheduler[O] \underset{\{L_3\}}{\bowtie}$$

$$ClusterManager[P] \underset{\{L_4\}}{\bowtie} Executor[Q] \underset{\{L_5\}}{\bowtie} HDFS[1]$$

where

$L_1 = \{reg\_spc, send\_DAG, withdraw\_spc\}, L_2 = \{send\_stage\},$
$L_3 = \{allocate\_task\}, L_4 = \{send\_heart, rep\_prg, write\_data\}, L_5 = \{req\_data, ret\_data\}.$

4 Simulation and Results Analysis

This section will give the response time and throughput of the model, these two metrics can reflect the performance and processing capabilities of a system. Tables 1 and 2 illustrates the execution rate of each action and the initial number of each component.

4.1 Simulation of Response Time

Service Flow is defined as the sequence of actions execution in a response. We can get the service flow as below. After getting the service sequence, we can get the response time by Monte Carlo simulation.

$$init\_spc \rightarrow reg\_spc \rightarrow send\_heart \rightarrow req\_res \rightarrow start\_back \rightarrow reg\_exc \rightarrow reg\_exc$$

Table 1 Action rate parameters

Action	Description	Duration	Rate
init_spc	Initializing the component SparkContext	0.002	500
reg_spc	SparkContext registers with the ClusterManager	0.0016	610
build_DAG	SparkContext builds the DAG	0.0033	300
send_DAG	SparkContext sends the DAG to DAGScheduler	0.002	500
wtdraw_spc	SparkContext withdraw from the ClusterManager	0.001	1000
split_stage	DAGScheduler split the DAG into stage	0.0033	300
send_stage	DAGScheduler sends the stage to TaskScheduler	0.002	500
allocate_task	DAGScheduler allocates the task to the Executor	0.0033	300
req_res	Executor requests the resource from ClusterManager	0.002	500
req_data	ClusterManager requests the data from HDFS	0.002	500
send_heart	Executor sends the heartbeat to ClusterManager	0.005	200
start_back	Executor starts the ExecutorBackend instance	0.01	100
reg_exc	Executor registers with SparkContext	0.0025	400
exc_task	Executor executes the tasks	0.001	1000
rep_prg	Executor reports the task progress to SparkContext	0.002	500
write_data	Executor writes the result data to HDFS	0.0016	600
ret_data	HDFS returns the data to Executor	0.002	500

Table 2 Number of components

Component	Number
SparkContext	10
DAGScheduler	10
TaskScheduler	10
ClusterManager	1
Executor	100
HDFS	1

$$\rightarrow build\_DAG \rightarrow send\_DAG \rightarrow split\_stage \rightarrow send\_stage \rightarrow allocate\_task \rightarrow$$

$$req\_data \rightarrow ret\_data \rightarrow exc\_task \rightarrow rep\_prg \rightarrow withdraw\_spc \rightarrow write\_data$$

Next, we will illustrate the response time and throughput of the model. These two indicators can show the performance of a system. The response time refers to the time from the start of the first action to the end of the last action. throughput represents the number of actions performed by the components per unit of time.

Figure 3 shows the influence of the number of executor component to response time. As the number of executor components increases, the curve gradually moves downward, which means the response time is gradually decreasing. This is because the executor component handles tasks in parallel. With the increasing of the number of components, the processing capacity is greatly increased, the processing speed is increased, and the task response time is reduced.

As the Fig. 4 shown, it illustrates the relationship between the throughput of the Executor component executing the *exc_task* action and the number of users. Throughput refers to the number of actions completed in a unit of time. So as the number of users increases, the number of tasks increases, the throughput increases, but after a certain period, the entire system has reached a bottleneck, throughput tends to smooth, this represents the maximum number of tasks that the activity of *exc_task* can handle.

Figure 5 exhibits the effect of changes in the rate of the activity *split_stage* on the response time. We can see that as the rate increases, the response time gradually decreases, but when the rate increases to a certain extent, the response time no longer changes. That's because the component DAGScheduler's activity *split_stage* in charge of allocating tasks and as task assignments accelerating, the total response time will decrease. However, the response and processing capabilities of other components have not improved. Although the tasks have been allocated, they cannot be processed immediately, so the response time cannot be reduced.

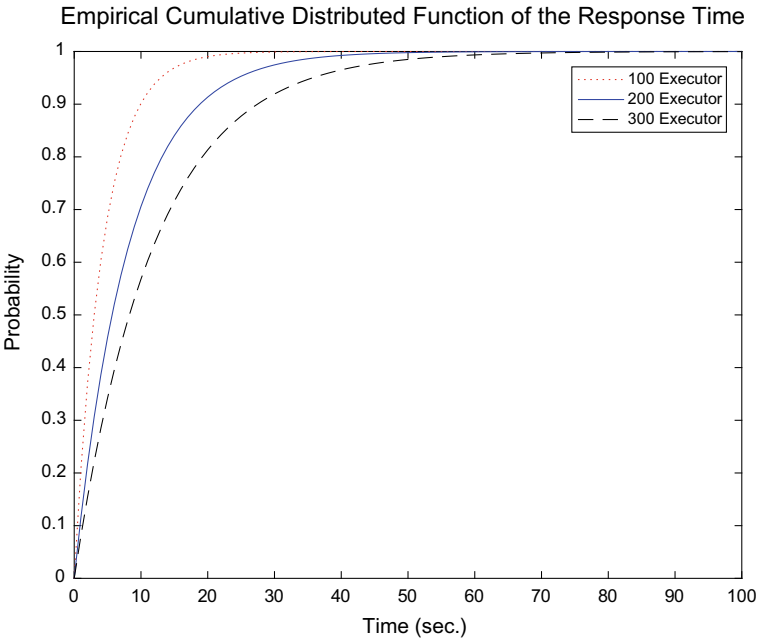

Fig. 3 Response time versus number of executors

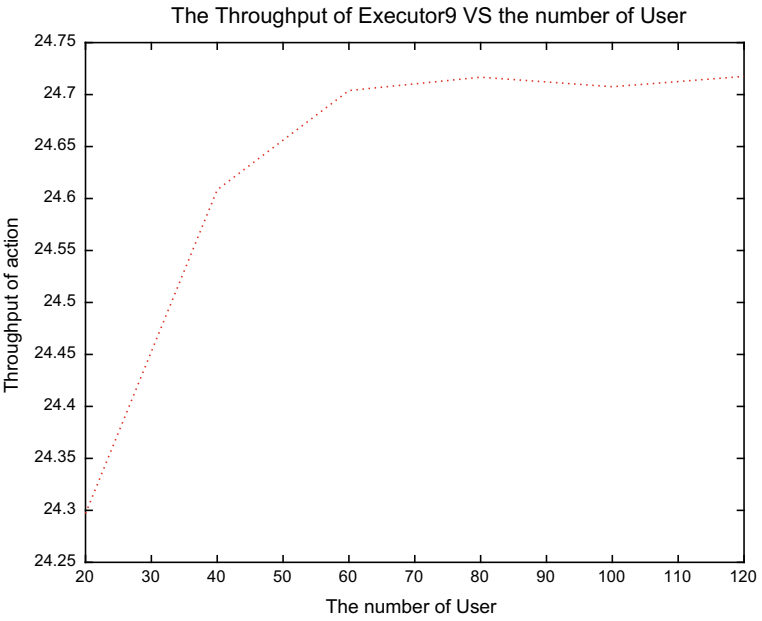

Fig. 4 Throughput of Exc_Task versus number of user

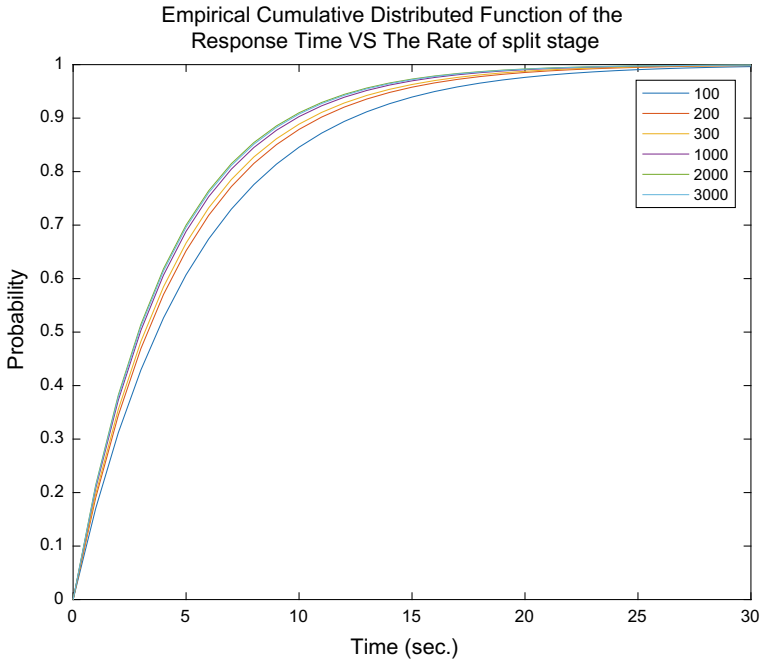

Fig. 5 Response time versus rate of the split_stage

5 Conclusion

This paper gives the model of the Big Data architecture Spark and analysis the performance based on the PEPA. We have considered this model separately from the two dimensions of response time and throughput. Moreover, this paper illustrates a compositional modeling approach, PEPA. PEPA can analyze the performance of a combined parallel system in the steady state due to its characteristics. But in PEPA, the end of a service flow must return to the initial state, and only one token exist during the execution of a service flow. So next, we will try to convert a PEPA model to Stochastic Petri Nets [15]. Stochastic Petri Nets is a mathematical representation of discrete parallel systems. It is suitable for describing asynchronous, concurrent computer system models. Stochastic Petri Nets not only have strict mathematics expression methods but also have intuitive graphical expressions. There are rich system description methods and system behavior analysis techniques. Next steps we will analyze the Stochastic Petri Nets model's result.

Acknowledgements The authors acknowledge the financial support by the National Natural Science Foundation of China under Grant 61472343.

References

1. What Is Apache Hadoop? May 2018. http://hadoop.apache.org/
2. Chandakanna, V.R.: REHDFS: a random read/write enhanced HDFS. J. Netw. Comput. Appl. **103**, 85–100 (2018)
3. Won, H., Nguyen, M.C., Gil, M.S., Moon, Y.S.: Advanced resource management with access control for multitenant hadoop. J. Commun. Netw. **17**(6), 592–601 (2015)
4. Serikawa, S., Huimin, L.: Underwater image dehazing using joint trilateral filter. Comput. Electr. Eng. **40**(1), 41–50 (2014)
5. Lu, H., Li, Y., Mu, S., Wang, D., Kim, H., Serikawa, S.: Motor anomaly detection for unmanned aerial vehicles using reinforcement learning. IEEE Internet Things J. (2017). https://doi.org/10.1109/JIOT.2017.2737479
6. Lu, H., Li, Y., Chen, M., Kim, H., Serikawa, S.: Brain intelligence: go beyond artificial intelligence. Mob. Netw. Appl. 1–8 (2017)
7. Lu, H., Bin, L., Zhu, J., Serikawa, S.: Wound intensity correction and segmentation with convolutional neural networks. Concurr. Comput.: Pract. Exp. (2017). https://doi.org/10.1002/cpe.3927
8. Lu, H., Li, Y., Uemura, T., Kim, H., Serikawa, S.: Low illumination underwater light field images reconstruction using deep convolutional neural networks. Future Gener. Comput. Syst. 142–148 (2018). https://doi.org/10.1016/j.future.2018.01.001
9. Xu, X., He, L., Lu, H., Gao, L., Ji, Y.: Deep adversarial metric learning for cross-modal retrieval. World Wide Web J. (2018). https://doi.org/10.1007/s11280-018-0541-x
10. Hillston, J.: A Compositional Approach to Performance Modelling. Cambridge University Press (1996)
11. Ding, J., Wang, R., Chen, X.: Performance modeling and evaluation of real-time traffic status query for intelligent traffic systems. In: Proceedings of 2016 22nd Asia-Pacific Conference on Communications (APCC) (2016)
12. Ding, J.: A comparison of fluid approximation and stochastic simulation for evaluating content adaptation systems. Wirel. Pers. Commun. **84**, 231–250 (2015)
13. Ding, J., Zhu, X., Wang, M.: Fluid analysis for a PEPA model. In: Proceedings of the 2015 Chinese Intelligent Systems Conference, vol. 2, pp. 181–190 (2015)
14. Hillston, J.: Fluid flow approximation of PEPA models. In: Second International Conference on the Quantitative Evaluation of Systems (2005)
15. Molloy, M.K.: Performance analysis using stochastic Petri Nets. IEEE Trans. Comput. **31**, 913–917 (1982)

An Improved Unsupervised Band Selection of Hyperspectral Images Based on Sparse Representation

Fei Li, Pingping Zhang and Huchuan Lu

Abstract Hyperspectral images have far more spectral bands than ordinary multispectral images. Rich band information provides more favorable conditions for the tremendous applications as well as many problems such as the curse of dimensionality. Band selection is an effective method to reduce the spectral dimension which is one of popular topics in hyperspectral remote sensing. Motivated by previous sparse representation method, we present a novel framework for band selection based on multi-dictionary sparse representation (MDSR). By obtaining the sparse solutions for each band vector and the corresponding dictionary, the contribution of each band to the raw image is derived. In terms of contribution, the appropriate band subset is selected. Five state-of-art band selection methods are compared with the MDSR on three widely used hyperspectral datasets. Experimental results show that MDSR achieves marginally better performance in hyperspectral image classification, and better performance in average correlation coefficient and computational time.

Keywords Band selection · Hyperspectral images · Sparse representation Classification

1 Introduction

Hyperspectral data has both spectrum and spatial information of observed material, and the number of spectral bands usually reaches hundreds or even thousands [1]. This powerful advantage enhances and expands the potential application of

F. Li (✉)
Engineering Training Center, Shenyang Aerospace University, Shenyang, China
e-mail: alinafeili@mail.dlut.edu.cn

F. Li · P. Zhang · H. Lu
School of Information and Communication Engineering,
Dalian University of Technology, Dalian, China
e-mail: jssxzhpp@mail.dlut.edu.cn

H. Lu
e-mail: lhchuan@dlut.edu.cn

H. Lu (ed.), *Cognitive Internet of Things: Frameworks, Tools and Applications*, Studies in Computational Intelligence 810,
https://doi.org/10.1007/978-3-030-04946-1_14

hyperspectral imaging (HSI). However, some challenging problems exist in the hyperspectral imagery processing owing to high spectral dimensionality, such as problem of storage and transmission, increment of computation, Hughes phenomenon (curse of dimensionality) [2–5]. Therefore, dimensionality reduction is a necessary method for efficient HIS applications to dispose of the above issues.

In general, there are two dimensionality reduction methods: feature extraction and band selection. The former usually generates a low-dimensional spectral data by using a transformation matrix based on a certain criteria. The latter is to identify the best subset of bands from all the original bands based on an adaptive selection criterion [6]. In this paper we focus on the band selection methods because they can preserve the spectral physical characteristics which are extremely significant in some applications.

Recently, the idea of sparse representation (SR) was introduced into band selection [7–12]. There are mainly two groups, some algorithms represent the original image by multiplication of the dictionary and sparse coefficient matrix which is derived by K-SVD or orthogonal matching pursuit (OMP) [7, 10]; And other SR based methods pre-clustered basis bands with similar spectral properties [9], or preselect bands using linear prediction (LP) algorithm and further refine them [8]. However, there are some issues existed in these BS methods. One is that the preprocessing will consume time, since it need to pre-select or cluster the original bands. Another is that all the dictionaries should be overcompleted, but the length of the band vector is far greater than the number of bands, so it is necessary to ensure that this is a part of the loss of image space information. Contrary to previous works, in this paper we propose a novel unsupervised band selection algorithm for hyperspectral image processing that utilizes the sparsity of the input sample vector. Our proposed algorithm is based on an effective sparse representation model in which the spatial image of a band is approximately represented by linear combinations of a few spatial image group (called atoms) from the entire hyperspectral image.

The rest of this paper is organized as follows. In Sect. 2, we introduce the proposed unsupervised band selection method. Then we present the experimental results on some well known hyperspectral images in Sect. 3. Finally, we draw conclusions in Sect. 4.

2 Band Selection Based on Sparse Representation

In this section, we first introduce sparse representation based image processing algorithm that represents the sample through a sparse linear combination of samples from a dictionary. We then presents the proposed multi-dictionary sparse representation method to solve the band selection problem.

2.1 Sparse Representation Model for Band Selection

The sparsity of signals has become a particularly powerful prior not only in the area of computer vision and pattern recognition but also in the field of hyperspectral image processing [13–16]. In methods of hyperspectral image classification, pixels are the performed objects which can be represented by a dictionary or basis with specific sparse constraints. A few coefficients derived from the representation can carry important information of the pixels, and can be treated as the feature of pixels. At last, a pixel can be signed a label by searching the minimum reconstruction error through the coefficients and dictionary elements.

The main purpose of band selection is to find an optimal or suboptimal band subset instead of the original hyperspectral image, which can be used in sequential applications. In another word, the subset of bands is the set that can approximately represent the original bands under some measures or the subset of bands is the collection of bands which mainly contribute to the whole hyperspectral image. We should find out the contribution of each band to the whole image, and then choose the band according to its contribution. Sparse representation is an effective method to rank the contribution. When a band image is approximated by a linear combination of a dictionary, which consists of other band images, the sparse coefficients or weights will represent the contribution of each dictionary atom to the target band image. If the weight is large, the band will make great contribution to the target band, while if the weight is small, the band will make little contribution to the target band. We calculate sparse representation for each band by corresponding dictionaries and get a series of weights. The contribution of each band to the whole image can be obtained by statistical weights.

In this work, the spatial image of each band becomes the performed object. Let $\boldsymbol{Y} \in R^{W \times H \times B}$ be the original hyperspectral image. The spatial image of every band is stretched into a real-value vector instead of a two-dimensional matrix, thus we get

$$\boldsymbol{Y} = [\boldsymbol{y}_1, \boldsymbol{y}_2, \ldots, \boldsymbol{y}_B], \tag{1}$$

where $\boldsymbol{y}_i \in R^L$ $(i = 1, 2, \ldots, B)$ is the image vector of the i-th band, B is the number of spectral bands, $L = W \times H$ is the number of pixels in the image, and W and H are the width and height of the band image, respectively. The purpose of band selection is to select a best subset from the original band set. The resulting number of bands in that subset is less than B. If there is a best subset which can be found from original band set, the subset can approximately represent the original band set. We can use the following equation to present the relation,

$$\boldsymbol{y}_i \approx \boldsymbol{D}_i \alpha_i, \boldsymbol{D}_i \subset \boldsymbol{Y}, \tag{2}$$

where $\boldsymbol{D}_i$ is the band subset which is exclusive of $\boldsymbol{y}_i$ and α_i is the linear combination coefficient for the i-th image vector on the subset $\boldsymbol{D}_i$. It should be noted that there is a trivial solution for the above equation. In the whole band set $\boldsymbol{Y}$, there is a column

vector, e.g., $\boldsymbol{y}_i$, therefore, one can use the whole band set $\boldsymbol{Y}$ as the basis, leading to the coefficient α_i is one, and others are zeros. As a result, the coefficient vector $\boldsymbol{\alpha}$ will be an identity vector which lead to same weights for all band vectors. In order to avoid the case, we assign each band vector to a band subset $\boldsymbol{D}_i$ (also called sub-dictionary). We will use the new sub-dictionaries $\boldsymbol{D}_i$ hereafter. In addition, if we describe all bands by the defined band subset, the above equation can be represented as

$$\boldsymbol{Y} \approx \boldsymbol{D}\boldsymbol{\alpha}, \tag{3}$$

where $\boldsymbol{D}$ is the set $\{\boldsymbol{D}_i\}(i = 1, 2, \ldots, B)$ and $\boldsymbol{\alpha}$ is the set of coefficient weight α_i.

According to the previous expressions, we can convert every represented band vector as

$$\boldsymbol{y}_i = \boldsymbol{D}_i\alpha_i + \boldsymbol{\beta}_i, \tag{4}$$

where $\boldsymbol{\beta}_i$ is the approximation error vector. By evaluating the value of α_i, we can determine the contribution of each band in $\boldsymbol{D}_i$ to the target image vector $\boldsymbol{y}_i$. With sparse constraints on $\boldsymbol{\alpha}$, which means that if $\boldsymbol{y}_i$ is independent with the j-th column of $\boldsymbol{D}$, the value of j-th element in $\boldsymbol{\alpha}$ is zero, we can select the most important bands based on the approximation error. If we calculate the sparse representation of all bands in $\boldsymbol{Y}$, a sparse coefficient matrix will be obtained. Each band vector's weight is the sum of the corresponding row in the coefficient matrix. The best α_i value can be found by the following optimization problem. We will elaborate it in detail.

2.2 Multi-dictionary Learning

To find the optimal linear combination coefficients, we propose a novel multi-dictionary learning method. Formally, the sparse coefficient α_i can be derived by solving the constrained optimization problem,

$$\begin{aligned} \hat{\boldsymbol{\alpha}} &= \arg\min\|\boldsymbol{\alpha}\|_0 \\ s.t \quad \boldsymbol{y}_i &= \boldsymbol{D}_i\alpha_i + \boldsymbol{\beta}_i \end{aligned} \tag{5}$$

where $||*||_0$ is the L_0 norm, which is the total number of non-zero elements in a vector. Because the approximation error is usually restricted to a controllable interval in empirical data, the constraint in previous equation can be relaxed to the inequality form,

$$\begin{aligned} \hat{\boldsymbol{\alpha}} &= \arg\min\|\boldsymbol{\alpha}\|_0 \\ s.t \quad \|\boldsymbol{D}_i\alpha_i - \boldsymbol{y}_i\|_2 &\leq \sigma \end{aligned} \tag{6}$$

where σ is the error tolerance. Thus, the above optimization problem can be further interpreted as minimizing the approximation error at a certain sparse level,

$$\begin{aligned} \hat{\alpha_i} &= \arg\min \|\boldsymbol{D}_i \alpha_i - \boldsymbol{y}_i\|_2 \\ &s.t \quad \|\boldsymbol{\alpha}\|_0 \leq K_0 \end{aligned} \tag{7}$$

where $||*||_2$ is the L_2 norm and K_0 is an upper bound of given sparsity degrees. Though this minimisation problem is still regarded as a NP-hard problem by computer scientists, and almost impossible to solve, α_i can be approximately derived by greedy pursuit algorithms, such as orthogonal matching pursuit (OMP) [17, 18] or subspace pursuit (SP) [19]. After each band image is represented by the corresponding dictionaries, we get a coefficient matrix $\boldsymbol{X} \in R^{B \times B}$. In $\boldsymbol{X}$, most of entries would be equal to zero, since the sparsity constraint K_0 is added to the Eq. (8). The greater the absolute value of coefficients is, the more important the corresponding basis of dictionary is in forming the original hyperspectral image. For each row of the coefficient matrix $\boldsymbol{X}$, we count the number of entries which are not zero. Then we get a histogram of the corresponding indices which are the band number. If h denotes the histogram, it is computed by

$$h = \sum_{i=1}^{B} g(\alpha_i)/B \tag{8}$$

where $g(x) = 1$ if $x \neq 0$, $g(x) = 0$ if $x = 0$. The bands with the first $\tilde{B}$ greater values of histogram series should be selected as the target bands. The following Algorithm 1 gives the overall computing workflow for our band selection method.

Algorithm 1 Multi-dictionary Sparse Representation Method.

Require:

Hyperspectral image $\boldsymbol{Y} \in R^{W \times H \times B}$, number of pixels N ($N \ll B$), sparsity level K_0, target band dimension $\tilde{B}$.

Ensure:

Reduced-band hyperspectral image $\tilde{\boldsymbol{Y}} \in R^{W \times H \times \tilde{B}}$;

1: Convert $\boldsymbol{Y}$ into $\boldsymbol{Y} = [\boldsymbol{y}_1, \boldsymbol{y}_2, \ldots, \boldsymbol{y}_B]$, $\boldsymbol{y}_i \in R^{WH}$;
2: Randomly select N pixels in $\boldsymbol{Y}$ to form a new sample set $\hat{\boldsymbol{Y}} = [\hat{\boldsymbol{y}}_1, \hat{\boldsymbol{y}}_2, \ldots, \hat{\boldsymbol{y}}_B]$, $\hat{\boldsymbol{y}}_i \in R^N$;
3: Construct a group of overcompleted dictionaries, i.e., $\boldsymbol{D}_i = [\hat{\boldsymbol{y}}_1, \hat{\boldsymbol{y}}_2, \ldots, \hat{\boldsymbol{y}}_{i-1}, 0, \hat{\boldsymbol{y}}_{i+1}, \ldots, \hat{\boldsymbol{y}}_B]$;
4: Apply OMP algorithm to Eq. (7) and find the coefficient matrix $\tilde{\boldsymbol{X}} \in R^{\tilde{B} \times N}$;
5: Count nonzero entries in every row of $\tilde{\boldsymbol{X}}$ by Eq. (8);
6: Sort the number of nonzero entries in descending order.
7: Select the bands with the first $\tilde{B}$ indices.
8: Build $\tilde{\boldsymbol{Y}}$ with selected bands.

3 Experiments

3.1 Evaluation Metrics and Compared Methods

In this paper, the proposed band selection method is mainly used for hyperspectral image classification. Therefore,following previous works [20, 21], K-nearest neighborhood (KNN) is used to classify the image after band selection and the overall classification accuracy (OCA) is the main evaluation metric used in the experimental analysis. In addition, to compare the performance of each method in eliminating the data redundancy, the correlation coefficient of selected bands and the time of computation are also calculated and compared.

We compare several classical band selection methods, i.e., linear prediction (LP) based band selection [22, 23], orthogonal subspace projection (OSP) based band selection [22], and cluster based band selection [24]. In addition, the comparison also includes the traditional dimensionality reduction methods, such as PCA based feature extraction.

3.2 Hyperspectral Datasets

Three real-world hyperspectral image datasets are used for experimental verifications, they are described as follows.

(1) *Salinas-A Scene dataset*: It is a subset of the Salinas Scene dataset, gathered by AVIRIS (Airborne Visible/Infrared Imaging Spectrometer) sensor in 1998, over Salinas Valley in California. There are 86×83 pixels with 224 bands including 20 bands of water abortion. The groundtruth of this dataset contains 6 classes.
(2) *Pavia University Scene dataset*: It was acquired by the ROSIS (Reflective Optics System Imaging Spectrometer) sensor over the Engineering School, Pavia University, northern Italy. The number of spectral bands is 103, and the number of pixels is 610×340. There are 9 classes in this dataset.
(3) *Indian Pines Scene dataset*: This dataset was also gathered by AVIRIS sensor in 1992, over the Indian Pines test site in north-western Indiana.

It consists of 145×145 pixels and 200 spectral reflectance bands excluding water absorbtion bands. The Indian Pines Scene dataset contains two-thirds agriculture, and one-third forest or other natural perennial vegetation. The ground truth available is designated into 16 classes and is not all mutually exclusive.

3.3 Sample Number Analysis

In the proposed band selection method, several dictionaries should be created during the optimization process, meanwhile these dictionaries must be overcompleted. Since

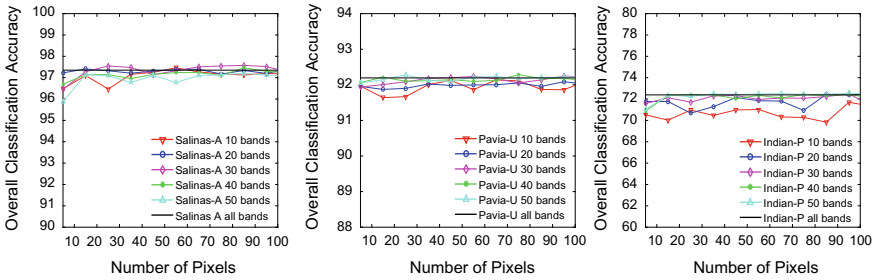

(a) Salinas-A Scene dataset (b) Pavia University Scene dataset (c) Indian Pines Scene dataset

Fig. 1 Illustration of the effect on the OCA with different numbers of sampling pixels

the number of pixels in hyperspectral images is greater than the number of bands, not all the pixels are involved in the optimization. In order to ensure the completeness of the dictionaries, we select a part of the pixels in the entire image as processing objects, omitting the rest before the optimization. To investigate the effect of different numbers of samples on the classification accuracy, we change the sample number from 5 to 100. Figure 1 illustrates the classification results. It can be seen that the classification accuracy almost remains unchanged with the increase of sample number, and only minor fluctuations (the value is not greater than 2%) appear at several specific locations. We can draw the conclusion that the number of sampling points has little effect on the result of band selection. In the following experiments, we empirically set the number of pixels to be 50 (N = 50) for classification evaluation, without further parameter tuning.

3.4 Selected Band Analysis

In Algorithm 1, the coefficient matrix $\tilde{\boldsymbol{X}}$ is the key support of band selection. To figure out which kind of bands our method has selected, Fig. 2 shows bar diagrams which illustrate the ratio of the count of non-zero entries to the count of all entries in one column of coefficient matrix $\tilde{\boldsymbol{X}}$. This ratio represents the contribution of one band in the hyperspectral image to the whole image, or the proportion of bands associated with this band in the image. We can see that the contribution of each band to the original hyperspectral image is very different and the weight distribution is not uniform over the bands. These experimental results further indicate that there are many redundancies in the hyperspectral bands and only a few bands are useful.

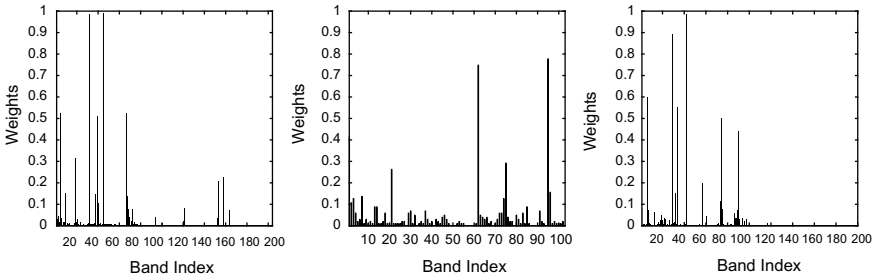

(a) Salinas-A Scene dataset (b) Pavia University Scene dataset (c) Indian Pines Scene dataset

Fig. 2 The histograms of coefficients on the three datasets. The distribution of the band contribution is nonuniform. Most weights of bands are very low

3.5 Sparse Level Analysis

In solving the coefficient matrix $\tilde{\boldsymbol{X}}$, the sparsity level K_0 should be set appropriately. Figure 3 shows the classification accuracy curves when the sparsity level K_0 changes from 1 to 50 on the three datasets. There are several fundamental observations in Fig. 4: (1) for the Salinas-A dataset, when K_0 is less than 3, the classification accuracy is relatively low. When K_0 is greater than 3, the classification performance first increases, then drops down slightly. The classification performance of the model with 10 bands fluctuates more drastically than other models. This indicates that the model with very few bands is sensitive to the sparse level K_0. The same trend can be observed in other two datasets. (2) for the Pavia-U dataset, the classification performance with different sparse levels and selected bands remains almost unchanged (no more than 2% fluctuation), even they vary locally. This result shows that our method is very robust in this dataset under different sparse levels. (3) for the Indian-P dataset, the models with more bands are better in the classification performance. The models

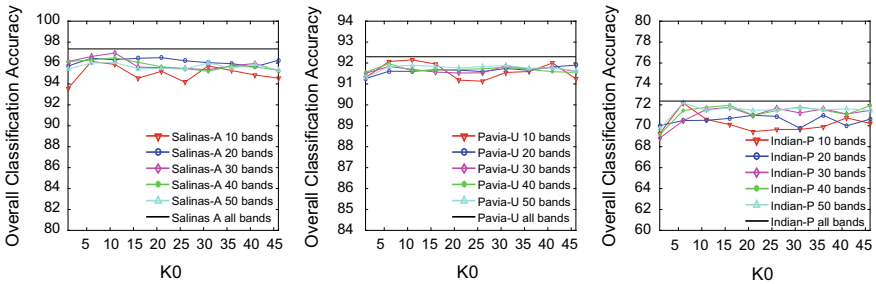

(a) Salinas-A Scene dataset (b) Pavia University Scene dataset (c) Indian Pines Scene dataset

Fig. 3 The overall classification accuracy with different sparsity levels

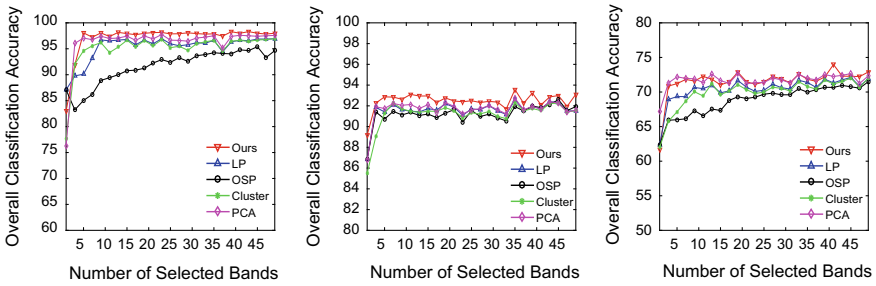

(a) Salinas-A Scene dataset (b) Pavia University Scene dataset (c) Indian Pines Scene dataset

Fig. 4 The classification results of different band selection methods on the three datasets

are more fluctuated on this dataset under different K_0. Based on above facts, we set $K_0 = 6$ in the following experiments.

3.6 Comparison with Other Methods

Overall Classification Performance For the classification performance evaluation, 20 samples are selected randomly in each classes. For our method, we set $K_0 = 6$. In order to reduce the randomness, we perform all the compared methods with 10 trials and use the averaged results. We report the results with different selected band number n, ranging from 1 to 50. The Fig. 4 shows the classification performance of the proposed method and compared algorithms on the three datasets. From the comparison results, we can see that our proposed method consistently outperforms other methods by a large margin, especially on the Salinas-A and Pavia-U datasets. More specifically, the OSP method achieves the lowest recognition rate. The LP and cluster based methods have similar classification results, which are inferior to our method. Even though the PCA method is superior to other methods, it is not better than our proposed method.

Band Correlation Analysis Generally, the lower the correlation among spectral bands is, the better the subset of selected bands is. Figure 5 illustrates the average correlation coefficient with the compared methods other than PCA. On the three data subsets, our method ranks first or second in this metric. This further confirms that our method is able to select the most informative and separative bands for the real-world applications.

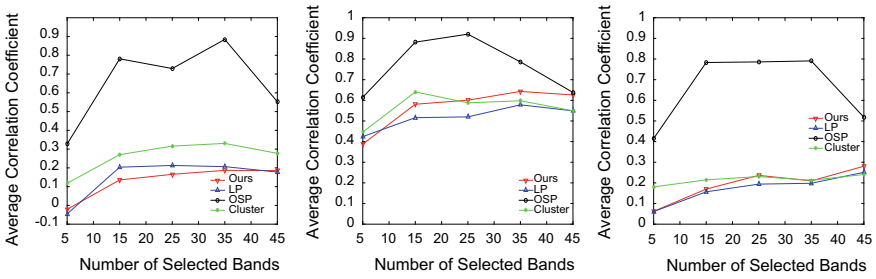

(a) Salinas-A Scene dataset (b) Pavia University Scene dataset (c) Indian Pines Scene dataset

Fig. 5 Comparison of average correlation coefficients with different band selection methods on three datasets

4 Conclusion

In this work, we propose a novel band selection method based on the multi-dictionary sparse representation. The proposed method is fully unsupervised and consists of three main components: (1) creating multi-dictionaries; (2) optimizing sparse coefficients; (3) computing and sorting weights of desire bands. Our proposed method not only reduces the dimension of spectral bands, but also preserves the original information of bands. Extensive experimental results show that the proposed method is very effective and outperforms other competitors. Of course, the method can be improved. For example, because of the large number of dictionaries, the amount of calculation increases. In the future, how to design an effective framework to reduce the number of dictionaries and the amount of calculation is the next work.

References

1. Chang, C.I.: Hyperspectral Imaging: Techniques for Spectral Detection and Classification. Plenum Publishing Co. (2003)
2. Hughes, G.P.: On the mean accuracy of statistical pattern recognizers. IEEE Trans. Inf. Theory **14**(1), 55–63 (1968)
3. RichardErnest: Adaptive Control Processes: A Guided Tour. The University Press (1961)
4. Bo, C., Lu, H., Wang, D.: Spectral-spatial k-nearest neighbor approach for hyperspectral image classification. Multimed. Tools Appl. **77**(9), 1–18 (2018)
5. Li, P., Wang, D., Wang, L., Lu, H.: Deep visual tracking: review and experimental comparison. Pattern Recogn. (2017)
6. Jia, X., Kuo, B.-C., Crawford, M.M.: Feature mining for hyperspectral image classification. Proc. IEEE **101**(3), 676–697 (2013)
7. Li, S., Qi, H.: Sparse representation based band selection for hyperspectral images. In: IEEE International Conference on Image Processing, pp. 2693–2696 (2011)
8. Du, Q., Bioucas-Dias, J.M., Plaza, A.: Hyperspectral band selection using a collaborative sparse model. In: Geoscience and Remote Sensing Symposium, pp. 3054–3057 (2012)

9. Chien, H.C., Lai, C.H., Liu, K.H.: Unsupervised band selection based on group-based sparse representation. In: Asian Conference on Computer Vision, pp. 389–401 (2016)
10. Sun, K., Geng, X., Ji, L.: A new sparsity-based band selection method for target detection of hyperspectral image. IEEE Geosci. Remote Sens. Lett. **12**(2), 329–333 (2015)
11. Sun, W., Jiang, M., Li, W., Liu, Y.: A symmetric sparse representation based band selection method for hyperspectral imagery classification. Remote Sens. **8**(3), 238 (2016)
12. Bo, C., Lu, H., Wang, D.: Hyperspectral image classification via JCR and SVM models with decision fusion. IEEE Geosci. Remote Sens. Lett. **13**(2), 177–181 (2016)
13. Wright, J., Ma, Y., Mairal, J., Sapiro, G., Huang, T.S., Yan, S.: Sparse representation for computer vision and pattern recognition. Proc. IEEE **98**(6), 1031–1044 (2010)
14. Chen, Y., Nasrabadi, N.M., Tran, T.D.: Hyperspectral image classification via kernel sparse representation. IEEE Trans. Geosci. Remote Sens. **51**(1), 217–231 (2013)
15. He, L., Ruan, W., Li, Y.: Sparse representation based hyperspectral imagery classification via expanded dictionary. In: Workshop on Hyperspectral Image and Signal Processing: Evolution in Remote Sensing, pp. 1–4 (2012)
16. Chen, Y., Nasrabadi, N.M., Tran, T.D.: Sparse representation for target detection in hyperspectral imagery. IEEE J. Sel. Top. Signal Process. **5**(3), 629–640 (2011)
17. Pati, Y.C., Rezaiifar, R., Krishnaprasad, P.S.: Orthogonal matching pursuit: recursive function approximation with applications to wavelet decomposition. In: Conference Record of The Twenty-Seventh Asilomar Conference on Signals, Systems and Computers, pp. 40–44 (1993)
18. Tropp, J.A., Gilbert, A.C.: Signal recovery from random measurements via orthogonal matching pursuit. IEEE Trans. Inf. Theory **53**(12), 4655–4666 (2007)
19. Dai, W., Milenkovic, O.: Subspace pursuit for compressive sensing signal reconstruction. IEEE Trans. Inf. Theory **55**(5), 2230–2249 (2009)
20. Chang, C.-I., Du, Q., Sun, T.-L., Althouse, M.L.: A joint band prioritization and band-decorrelation approach to band selection for hyperspectral image classification. IEEE Trans. Geosci. Remote Sens. **37**(6), 2631–2641 (1999)
21. Yuan, Y., Zhu, G., Wang, Q.: Hyperspectral band selection by multitask sparsity pursuit. IEEE Trans. Geosci. Remote Sens. **53**(2), 631–644 (2014)
22. Du, Q., Yang, H.: Similarity-based unsupervised band selection for hyperspectral image analysis. IEEE Trans. Geosci. Remote Sens. Lett. **5**(4), 564–568 (2008)
23. Yang, H., Du, Q., Chen, G.: Unsupervised hyperspectral band selection using graphics processing units. IEEE J. Sel. Top. Appl. Earth Observ. Remote Sens. **4**(3), 660–668 (2011)
24. Martınez-Usó, A., Pla, F., Sotoca, J.M., Garcıa-Sevilla, P.: Clustering-based multispectral band selection using mutual information. In: International Conference on Pattern Recognition (2006)

Feature-Based Tracking via SURF Detector and BRISK Descriptor

Sangeen Khan and Sehat Ullah

Abstract Marker-less tracking has become vital for a variety of vision-based tasks because it tracks some natural regions of the object rather than using fiducial markers. In marker-less feature-based tracking salient regions in the images are identified by the detector and information about these regions are extracted and stored by the descriptor for matching. Speeded-Up Robust Feature (SURF) is considered as the most robust detector and descriptor so far. SURF detects the feature points that are unique and repeatable. It uses integral images which provide a base for the low computational expense. However, descriptors generation and matching for SURF is a time-consuming task. Binary Robust Invariant Scalable Key-points (BRISK) is a scale and rotation invariant binary descriptor. It reduces the computational cost due to its binary nature. This paper presents a marker-less tracking system that tracks natural features of the object in real-time and is very economical in terms of computation. The proposed system is based on SURF detector, as it identifies highly repeatable interest points in the object and BRISK descriptor, due to its low computational cost and invariance to scale and rotation which is vital for every visual tracking system.

Keywords Features · Detection · Description · Matching · Tracking

1 Introduction

Vision-based tracking determines the position and orientation of the camera with respect to the real environment by using image processing methods [1]. It is classified into Marker-based and Marker-less tracking. In Marker-based tracking methods, fiducial markers are placed in the real scenes which are tracked by a video camera [2]. While Marker-less tracking approaches make use of some naturally occurring

S. Khan (✉) · S. Ullah
University of Malakand, Lower Dir, KPK, Pakistan
e-mail: sangeenkhan2050@gmail.com

S. Ullah
e-mail: sehatullah@uom.edu.pk

H. Lu (ed.), *Cognitive Internet of Things: Frameworks, Tools and Applications*, Studies in Computational Intelligence 810,
https://doi.org/10.1007/978-3-030-04946-1_15

regions of the object for tracking [3]. Marker-less feature-based tracking has become vital for many vision-based tasks because it does not need any kind of fiducials for tracking. In feature-based tracking, some local features are tracked in the image sequences acquired from the camera [4]. Features may be corners, points or blobs [5]. Feature-based tracking copes with image variations and large inter-frames displacements effectively [4]. For that reason, it has been used in a number of areas including Augmented Reality, Indoor monitoring, scientific simulations and object tracking [6–9]. In feature-based tracking, the first step is features detection in which interest points in the images are identified by the detector [10]. The second step is descriptors generation in which information about the interest points are collected and stored as a feature vector by the descriptor. The third step is descriptors matching in which the descriptor vectors are compared between the images to achieve the best correspondence [11]. Feature-based tracking is performing well for various vision-based tasks, especially in the situations where the use of fiducials is not applicable e.g. in large workspaces and huge buildings. Using CCTV footages a suspicious person can be easily located and tracked in a hundred story building or shopping mall, traffic Warden can easily identify and track a car violating traffic rules, Airplanes can easily recognize and track the runway by using tracking algorithms. SIFT (Scale Invariant Feature Transform) is an appealing detector and descriptor in computer vision and has been used for a variety of applications, i.e. object recognition, panorama stitching, image retrieval and visual navigation. The major disadvantage of SIFT is that its computational cost is very high, which makes it inappropriate for real-time tracking and object recognition [12]. SURF (Speeded-Up Robust Feature) is a competent feature detector and descriptor and has been used by a number of computer vision applications due to its robustness, especially for object tracking [9, 13]. SURF detector has enhanced the detection process of SIFT without scarifying excellence of the detected feature points [14]. It uses an approximation of the Hessian matrix due to its high accuracy. Blob-like structures are detected in the places where determinant of the matrix has a maximum value. The determinant of the Hessian matrix is also employed for the selection of scale. In the approximation of the Hessian matrix, integral images are used that reduce the computation time enormously [15]. However, the descriptors generation and matching of SURF is a time-consuming task which affects its efficiency for tracking systems, as they operate in real-time. SURF descriptors rely on histograms of gradients, i.e. the gradient of each pixel in the patch need to be computed. These computations consume much time [16]. Binary descriptors cope with the mentioned limitation of SURF through efficient and fast computation and comparison. Furthermore, they have very low memory requirements [12]. BRISK is a binary string and is obtained simply by comparing the brightness values of the images. Once the keypoints are selected, BRISK uses a sampling pattern in the keypoints neighborhood. The pairs of pixels are categorized as long distance pairs and short distance pairs. The short distance pairs are used for descriptors generation and long distance pairs are used for the determination of orientation [17]. BRISK achieves high-class description with much less computational requirements [18]. It offers both rotation and scale invariance [19]. Thus the aim of the paper is to integrate

SURF detector and BRISK descriptor in order to develop a computationally efficient real-time tracking system.

The remaining paper is organized as follow: In Sect. 2 various kinds of features detectors and descriptors are discussed in detail. Section 3 explains the proposed tracking system in detail. Section 4 shows the experimental results of the scheme and in Sect. 5 we have concluded the work.

2 Related Work

2.1 Feature Detectors

The first algorithm for image recognition was based on color histograms. In 1991, Swain and Ballard [20] presented an approach based on Color Histograms for the representation of multicolored objects. Color histograms are efficient object representations within the existence of occlusion and over viewpoint change, and they can make a distinction among a sizable amount of objects. However, without any information about the shape or the texture of the objects, similar objects having different colors may be indistinguishable because they rely on color histograms only. In 1988, Harris and Stephen [21] proposed an algorithm which was based on corners and edges. The algorithm detects robust features from the images. But as it is only based on corners detection so it has a lack of connectivity of features which shows that it does not have a high level of description. In 1997, Smith and Brady [22] introduced another detector named SUSAN. SUSAN uses no derivatives; as a result, no noise reductions or extra computations are required. They detect such features that are repeatable, invariant to rotation and translation changes. However, they have no invariance to different scales and other transformations. In 1999, Lowe [23] introduced SIFT. As compared to many of other feature point detectors SIFT detects more interest points because it accumulates interests points at different resolutions and scales. SIFT is a competent interest point detector and is flexible to various image deformations. However, it has a very high computational cost. In 2002, Matas et al. [24] presented MSER. It is a blob detector. The algorithm for MSER extracts those regions of the image which are co-variant. These are called MSER's. The algorithm performs well for small areas. It is affine invariant and has good repeatability. However, it shows poor performance in case of motion blur. In 2006, Bay et al. [11] presented the SURF algorithm. SURF has speeded SIFT's detection process with no scarifying the brilliance of the detected feature points. Blob-like structures are detected in the places where determinant of the matrix has a maximum value. The determinant of the Hessian matrix is also used for the selection of scale. The major limitation is that SURF is not steady to illumination changes. In 2006, Rosten and Drummond [25] also presented a speedy corner detector named as FAST which works on a circle around a point P called candidate point. P is considered as a corner if there exists a neighboring arc as a minimum of nine pixels which are

darker or brighter than using a threshold. FAST is drastically faster which makes it appropriate for real-time vision applications. The major limitation of FAST is that it is less effective while detecting corners in a much cluster image background. In 2008, Motilal Agrawal et al. [26] proposed CenSurE for real-time feature detection and matching, which is an approximation of the Laplacian of Gaussian filter and also makes use of integral images and box filters. Censure is fast in computation however it is anesthetized to the rotation. In 2010, Mair et al. [27] presented AGAST which improves the performance of FAST and changes the method by which the decision tree is generated. As compared to Fast, AGAST has higher performance from speedup prospective. The major limitation is its poor performance over scale change and increase in the viewpoint angle. In 2011, Ethan Rublee et al. [28] presented ORB. It is a binary detector and provides scale-invariant feature points. The detector is transformed to calculate the orientation of a feature point, which is then employed in the descriptors generation stage to offer robustness to the rotation. However, the performance in zoom transformation is not satisfactory. In 2011, Stefan Leutenegger et al. [18] presented a binary detector BRISK. The major limitation of AGAST and FAST is, no identification of scale-invariant feature points which is desired for many applications BRISK tackles the mentioned limitation of both these methods efficiently. However, it has poor performance in a blur.

2.2 Feature Descriptors

Recently various kinds of descriptors have been proposed, which have their own pros and cons. In 1999, Lowe [23] introduced a non-binary descriptor SIFT. It robustly extracts the distinct feature points. However, the computation of the SIFT descriptor is a complicated task and its operation is costly in terms of time. In 2005, Mikolajczyk and Schmid [29] proposed GLOH, which is the extension of the SIFT descriptor. It enhances the distinctiveness and robustness of the SIFT. GLOH performs best than SIFT, especially in illumination changes. However, it is more expensive in terms of computational cost than SIFT. In 2006, Bay et al. [11] introduced the SURF descriptor. SURF makes use of integral images which provide a base for fast computation. However, the high dimensionality of the SURF descriptor makes its hard for real-time applications. In 2010, Michael Calonder et al. [30] introduced a binary descriptor BRIEF. It has the lowest computation time and storage requirements however, it has a lack of rotation and scale invariance. In 2011, Ethan Rublee et al. [28] presented ORB which is another binary descriptor. ORB tackles the problem of rotation invariance of the BRIEF descriptor. The major limitation of ORB is having no scale invariance. In 2011, Stefan Leutenegger et al. [18] proposed BRISK which is an efficient alternative to BRIEF and ORB. BRISK provides a high-quality description with much less computational requirements. It also provides scale and rotation invariance. However, it cannot perform efficiently in a blur. In 2012, Alexandre Alahi et al. [31] introduced FREAK which is a binary descriptor and is motivated by the

human visual system. FREAK is robust to various image deformations. However, it has poor performance over viewpoint changes.

3 Proposed Tracking System

The proposed tracking approach is based on the integration of the SURF interest points detector and BRISK descriptor. The system identifies and tracks the objects in real-time. SURF detects the feature points that are distinct and repeatable. BRISK collects the information about the areas surrounding the feature points quite well and in much less time. Consequently, a computationally efficient and robust real-time tracking system is developed. The proposed system consists of the following steps: Image acquisition, Feature detection, Feature description, Feature matching, Outlier removal, Object tracking contribution.

3.1 Image Acquisition

Image acquisition is the first step of the proposed system. Before the initialization of the system, an image of the object is acquired and stored. This image is known as a reference image. In the later stages, the reference image is used for matching with the image sequences obtained from the camera. Once the system is initialized, the image sequences are acquired by using a video camera. These images are used as input in the detection process.

3.2 Features Detection

The second step is feature detection. In this step, the interest points are detected from the image sequences acquired from the real scene. These interest points are distinct, repeatable and invariant to various transformations. For the detection of feature points SURF detector is used. The SURF interest point detector uses an approximation of the Hessian matrix because of its higher accuracy. Blob-like structures are detected in the places where determinant of the matrix has a maximum value. The determinant of the Hessian matrix is also used for the selection of scale. In the approximation of the Hessian matrix, integral images are employed which reduce the computation time immensely. The computation time is reduced by using a set of 9×9 box filters as Gaussian approximations. They are denoted by D_{xx}, D_{yy}, and D_{xy}. For the computational efficiency, the weights applied to the rectangular regions are kept simple. For scale invariance, SURF constructs a pyramid scale space and changes the box filters scale to apply the scale space because of using box filters and integral image.

3.3 Feature Description

Once the interest points are detected, then the next step is to generate the descriptors i.e. to store the information about the surrounding areas of the detected feature points in a feature vector. For any descriptor, scale and rotation invariance are the basic qualities. For the generation of descriptors, BRISK is used, because it is scale and rotation invariant, having a good computational time due to its binary nature. The descriptors are computed simply by concatenating the results of the brightness comparisons, and a bit-string of length 512 is obtained, thus the descriptors pair matching is performed very fast. After the selection of keypoint, it uses a sampling pattern in the keypoints neighborhood. The pairs of pixels are classified into long distance pairs and short distance pairs. The pairs whose distance is short are used for the creation of descriptors and the pairs whose distance is long are used for the determination of orientation.

3.4 Feature Matching

The fourth step is the feature matching. Brute Force matching algorithm is used for the matching of descriptors. Descriptors are compared between the reference image and the real images obtained from the camera. The descriptors are matched simply by computing their Hamming distance. The Hamming distance is a number which represents the difference between the two binary strings. To calculate the Hamming distance the first two bits are compared if they are the same “0” is recorded and if they are different “1” is recorded. In this way, each bit is compared in succession and a “1” or “0” is recorded. Finally, all the recorded zeros and ones are added to obtain the Hamming distance. If the Hamming distance is greater, the strings are dissimilar and vice versa.

3.5 Outlier Removal

The fifth step is outlier removal. During the matching process some false matches might occur, thus Random Sample Consensus (RANSAC) homography is applied to remove such erroneous matches.

3.6 Object Tracking

Finally, the object is tracked successfully as long as it is in the view of the camera. When the object is lost, then re-detection of features takes place and the tracking process continues. Figure 1 shows the overall tracking process of the proposed approach.

In the proposed approach the floating point descriptor is replaced by a binary descriptor as a result, the overall run time of the tracking system is improved enormously. Binary descriptors are generated and matched for each image obtained from the camera; in much less time as compared to the floating point descriptors, as a result, it leads the tracking system further closer towards real time.

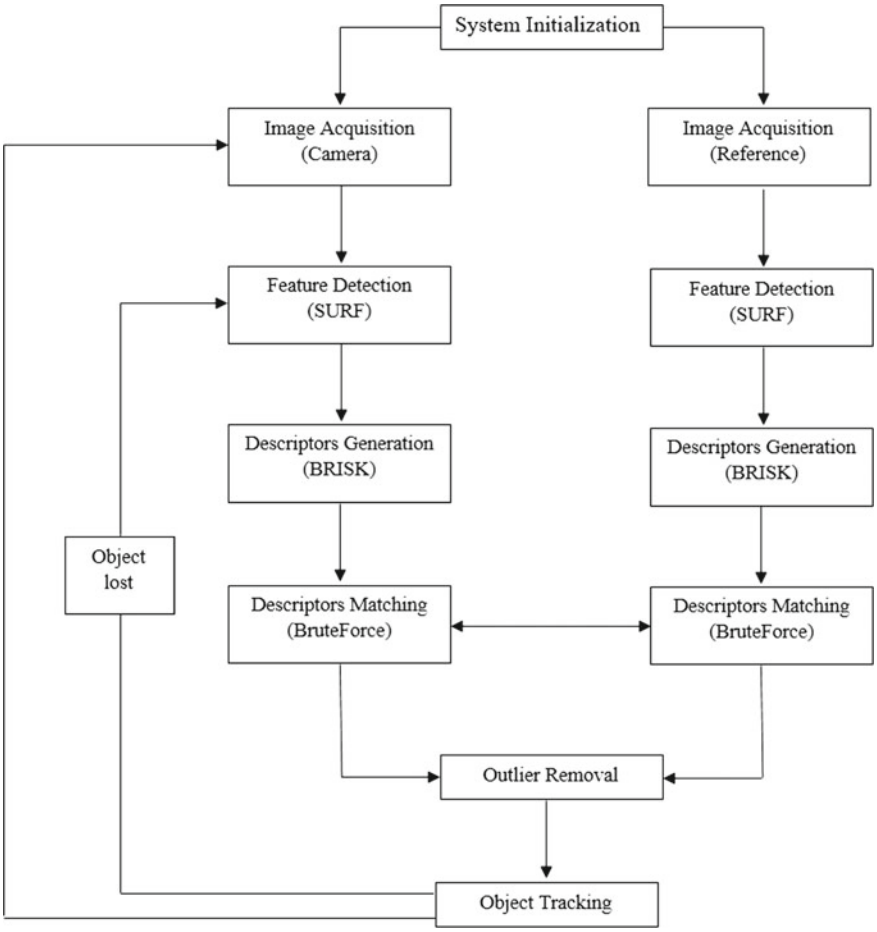

Fig. 1 Overall tracking process of the proposed approach

4 Experimental Results

For the purpose of evaluating the computational efficiency of the proposed approach, images were selected from the publically available Oxford datasets of images. For obtaining the detection and description timings; features were detected and descriptors were generated from the first image of the "Boat" sequence by using the existing methods and the proposed approach. Table 1 shows the detection and description timings for the existing algorithms and the proposed approach. For obtaining the matching timings; the descriptors were matched between the first and second image of the "Boat" sequence and the total matching time and the time per comparison was obtained. Table 2 presents the matching timings on the first and second image from the "Boat" sequence. The experiments were performed using Microsoft Visual Studio 2010 Ultimate, and computer vision library OpenCV 2.4.11 C++ environment on Intel(R) Core(TM) i7 laptop with 2.4 GHz CPU and 4 GB of RAM.

The results in Tables 1 and 2 show that the overall computation time of the proposed approach is lower than the existing SURF algorithm. For the performance evaluation of the proposed approach over the scale, rotation, viewpoint, blur and illumination changes; we employed the method and datasets of images used in [29]. The datasets contain images with a change in scale and rotation (Boat), viewpoint change (Graffiti), brightness change (Leuven) and blur (Trees). Comparisons were carried out on the basis of the first and fourth image in each dataset. Figure 2 illustrates the images from each dataset used for evaluation.

The evaluation criterion is based on *recall* and *1-Precision*. *recall* is the number of correct matches with respect to the number of corresponding matches. For an ideal descriptor the recall value is "1" for any precision value [32].

Table 1 Computation time for the first image of "Boat" sequence (850×680) in milliseconds

Algorithms	Keypoints	Detection time	Description time	Total time
SIFT	8849	2066.2	4738.9	6805.1
SURF	6737	717.4	3001.5	3718.9
BRISK	2420	253.4	40.3	293.7
Proposed approach	6027	732.7	121.9	854.6

Table 2 Matching time for the first and second image of "Boat" sequence in milliseconds

Algorithms	Keypoints Boat 1	Keypoints Boat 2	Matching time Boat 1–2	Time per comparison
SIFT	8849	8548	9444.4	1.07
SURF	6737	7200	4701.5	0.70
BRISK	2420	2427	573.5	0.23
Proposed approach	6027	6414	2844.3	0.47

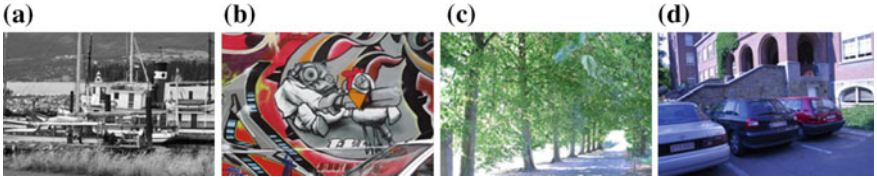

Fig. 2 Images from the Oxford datasets of images. **a** Boat, **b** graffiti, **c** tree, **d** leuven

$$recall = \frac{\#correct\ matches}{\#correspondences} \tag{1}$$

While *1-Precision* is the number of false matches with respect to the number of total correspondences.

$$1\text{-}Precision = \frac{\#false\ matches}{\#correct\ matches + \#false\ matches} \tag{2}$$

For the evaluation of performance; descriptors were generated and matched for each pair of images by using a certain threshold. The matches whose distance was lower than the given threshold were treated as correct matches. The remaining matches were considered as false matches. Tables 3, 4, 5 and 6 show the *recall* and *1-Precision* values for the first and fourth image of Boat, Graffiti, Tree and Leuven sequence respectively.

Table 3 *Recall* and *1-Precision* values for Boat 1–4

Algorithms	*Recall*	*1-Precision*
SURF	0.57	0.43
Proposed approach	0.68	0.32

Table 4 *Recall* and *1-Precision* values for Graffiti 1–4

Algorithms	*Recall*	*1-Precision*
SURF	0.22	0.78
Proposed approach	0.91	0.09

Table 5 *Recall* and *1-Precision* values for Tree 1–4

Algorithms	*Recall*	*1-Precision*
SURF	0.30	0.70
Proposed approach	0.22	0.78

Table 6 *Recall* and *1-Precision* values for Leuven 1–4

Algorithms	*Recall*	*1-Precision*
SURF	0.34	0.64
Proposed approach	0.19	0.81

5 Conclusion and Future Work

The proposed approach combines the SURF detector and BRISK descriptor in order to develop a natural features-based tracking system that reduces the computational time. The binary descriptor (BRISK) reduces the descriptors generation and matching time, as a result, the overall running time is improved enormously. Furthermore, the proposed system has a clear advantage over the existing SURF algorithm in scale and rotation (Boat 1–4) and viewpoint change (Graffiti 1–4). The system tracks the object in real time having the quality of scale and rotation invariance. In the future, we aim to examine the compatibility and performance of the proposed approach on smartphones and tablets.

References

1. Rabbi, I., Ullah, S.: A survey on augmented reality challenges and tracking. Acta Graphica **24**(1–2), 29–46 (2013)
2. Sridhar, S., Kamat, V.R.: A real-time markerless camera pose estimation system for augmented reality. UMCEE Report. University of Michigan, Ann Arbor (2011)
3. Kim, D., Moon, W., Kim, S.: A study on method of advanced marker array. IJSEIA **8**(6), 1–16 (2014)
4. Kusuma, G.P., Teck, F.W., Yiqun, L.: Hybrid feature and template-based tracking for augmented reality application. In: Asian Conference on Computer Vision, pp. 381–395 (2014)
5. Derntl, A.: Survey of feature detectors and descriptors in surgical domain. In: IEEE GSC, (2014)
6. Weng, E.N.G., et al.: Objects tracking from natural features in mobile augmented reality. Procedia-Soc. Behav. Sci. **97**, 753–760 (2013)
7. Demiroz, B.E., Ari, I., Eroglu, O., Salah, A.A., Akarun, L.: Feature-based tracking on a multi-omnidirectional camera dataset. In: International Symposium on Communications Control and Signal Processing, pp. 1–5 (2012)
8. Zhang, F., Lasluisa, S., Jin, T., Rodero, I., Bui, H., Parashar M.: In-situ feature-based objects tracking for large-scale Scientific simulations. In: High-Performance Computing, Networking, Storage and Analysis (SCC), pp. 736–740 (2012)
9. Monisha, R., Muthuselvam, M.: Feature based moving object detection and tracking. In: International Conference on Innovative Trends in Engineering and Technology (2017)
10. Shisode, S.P., Moholkar, K.P.: Real-time object identification, training and matching via SURF algorithm methods. Int. J. Adv. Res. Comput. Sci. Softw. Eng. **4**(6) (2014)
11. Bay, H., Ess, A., Tuytelaars, T., Gool, L.: Speeded-up robust features (SURF). Comput. Vis. Image Underst. **110**(3), 346–359 (2008)
12. Miksik, O., Mikolajczyk, K.: Evaluation of local detectors and descriptors for fast feature matching. In: International Conference on Pattern Recognition, Tsukuba Science City Japan, pp. 2681–2684, Nov 2012
13. Wang, W., Zhou, Y., Zhu, X., Xing, Y.: A real-time tracking method based on SURF. In: International Congress on Image and Signal Processing (CSIP), pp. 325–329. IEEE (2015)
14. El-Gayar, M.M., Soliman, H., Meky, N.: A comparative study of image low-level feature extraction algorithms. Egypt. Inf. J. **14**(2), 175–181 (2013)
15. Du, G., Su, F., Cai, A.: Face recognition using SURF features. In: Proceedings of SPIE, vol. 7496, pp. 749628–1, Oct 2009
16. Gil's Computer vision blog. https://gilscvblog.com. Accessed 31 Jan 2017

17. Kashif, M., Deserno, T.M., Haak, D., Jonas, S.: Feature description with SIFT, SURF, BRIEF, BRISK, or FREAK? A general question answered for bone age assessment. Comput. Biol. Med. **68**, 67–75 (2016)
18. Leutenegger, S., Chli, M., Siegwart, R.Y.: BRISK: binary robust invariant scalable keypoints. In: Proceedings of the IEEE International Conference on Computer Vision, pp. 2548–2555, Nov 2011
19. Heinly, J., Dunn, E., Frahm, J.M.: Comparative evaluation of binary features. In: Proceedings of the 12th European Conference on Computer Vision, pp. 759–773 (2012)
20. Swain, M.J., Ballard, D.H.: Color indexing. Int. J. Comput. Vis. **7**(1), 11–32 (1991)
21. Harris, C., Stephens, M.: A combined corner and edge detector. Alvery Vis. Conf. **15**(50), 10–5244 (1988)
22. Smith, S.M., Brady, J.M.: SUSAN—a new approach to low-level image processing. Int. J. Comput. Vis. **23**(1), 45–78 (1997)
23. Lowe, D.G.: Distinctive image features from scale-invariant keypoints. Int. J. Comput. Vis. **60**(2), 91–110 (2004)
24. Obdrzalek, S., Matas, J.: Object recognition using local affine frames on distinguished regions. BMVC **1**, 3 (2002)
25. Rosten E., Drummond, T.: Machine learning for high-speed corner detection. In: Computer Vision ECCV, pp. 430–443 (2006)
26. Agrawal, M., Konolige, K., Blas, M.R.: Censure: center surround extremas for real-time feature detection and matching. In: European Conference on Computer Vision, pp. 102–115. Springer (2008)
27. Mair, E., Hager, G.D., Burschka, D., Suppa, M., Hirzinger, G.: Adaptive and generic corner detection based on the accelerated segment test. In: European Conference on Computer Vision, pp. 183–196. Springer, Berlin Heidelberg (2010)
28. Rublee, E., Rabaud, V., Konolige, K., Bradski, G.: ORB: an efficient alternative to SIFT or SURF. In: 2011 IEEE International Conference on Computer Vision (ICCV), pp. 2564–2571. IEEE (2011)
29. Mikolajczyk, K., Schmid, C.: A performance evaluation of local descriptors. IEEE Trans. Pattern Anal. Mach. Intell. **27**(10), 1615–1630 (2005)
30. Calonder, M., Lepetit, V., Strecha, C., Fua, P.: BRIEF: binary robust independent elementary features. In: Computer Vision ECCV, pp. 778–792 (2010)
31. Alahi, A., Ortiz, R., Vandergheynst, P.: FREAK: fast retina keypoint. In: Computer Vision and Pattern Recognition (CVPR), pp. 510–517. IEEE (2012)
32. Hassaballah, M., Abdelmgeid, A.A., Alshazly, H.A.: Image features detection, description and matching. In: Image Feature Detectors and Descriptors Studies in Computational Intelligence, pp. 11–45. Springer (2016)

Nuclear Norm Regularized Structural Orthogonal Procrustes Regression for Face Hallucination with Pose

Dong Zhu, Guangwei Gao, Hao Gao and Huimin Lu

Abstract In real applications, the observed low-resolution (LR) face images usually have pose variations. Conventional learning based methods ignore these variations, thus the learned representations are not beneficial for the following reconstruction. In this paper, we propose a nuclear norm regularized structural orthogonal Procrustes regression (N2SOPR) method to learn pose-robust feature representations for efficient face hallucination. The orthogonal Procrustes regression (OPR) seeks an optimal transformation between two images to correct the pose from one to the other. Additionally, our N2SOPR uses the nuclear norm constraint on the error term to keep image's structural information. A low-rank constraint on the representation coefficients is imposed to adaptively select the training samples that belong to the same subspace as the inputs. Moreover, a locality constraint is also enforced to preserve the locality and the sparsity simultaneously. Experimental results on standard face hallucination databases indicate that our proposed method can produce more reasonable near frontal face images for recognition purpose.

Keywords Face hallucination · Regression analysis · Pose variations
Low-rank constraint

D. Zhu · H. Gao
School of Automation, Nanjing University of Posts and Telecommunication, Nanjing, China

G. Gao (✉)
Institute of Advanced Technology, Nanjing University of Posts
and Telecommunication, Nanjing, China
e-mail: csgwgao@njupt.edu.cn

G. Gao
Fujian Provincial Key Laboratory of Information Processing
and Intelligent Control, Minjiang University, Fuzhou, China

H. Lu
Department of Mechanical and Control Engineering, Kyushu Institute of Technology,
Kitakyushu, Japan

H. Lu (ed.), *Cognitive Internet of Things: Frameworks, Tools and Applications*, Studies in Computational Intelligence 810,
https://doi.org/10.1007/978-3-030-04946-1_16

1 Introduction

Face recognition (FR) is a classic problem in the computer vision and pattern recognition, it is widely used in many fields. In the past few decades, with the efforts of researchers, great progress has been made in the field of face recognition. However, in real applications, the observed face images usually have low-resolution. Face hallucination is a technology to acquire high-resolution (HR) face images from low-resolution (LR) observation, providing more facial features for the upcoming recognition process [1–4].

In the recent years, the patch-based methods have been hot topics in the field of face hallucination. Chang et al. [5] presented a Neighbor Embedding (NE) based face hallucination method. Many researchers state that the position information plays an important role in the reconstruction. Ma et al. [6] proposed a position-patch based super-resolution method. In the Least Square Representation (LSR), position information is used efficiently, but the solution of the method is unstable when the number of training samples is bigger than the dimension of patch. To obtain a much more stable and accurate solution, Jun et al. [7] applied sparsity prior to the LR patch representation, and proposed a sparse-representation (SR) based face hallucination method. To overcome the problem that SR method overemphasizes sparsity and ignores locality, Jiang et al. [8] incorporated a locality constraint into the least square inverse problem to maintain locality and sparsity simultaneously. Pang et al. [9] proposed kernel locality-constrained adaptive iterative neighbor embedding (KLAINE) method. The algorithm projects the LR face image blocks and the training sample blocks to a high-dimensional feature space by using a nuclear trajectory [10], so that the linear non-separable high-frequency detail features in the original space become linearly separated. In the process of neighbor iterations, the best neighbor K value of each iteration is adaptively determined by the mean of the Euclidean distance between the previously synthesized HR image block and the HR training sample block. Gao et al. [11] proposed locality-constrained iterative based matrix regression (LNIMR) face hallucination method. The algorithm is based on nuclear norm reconstruction and can accurately describe the error matrix. Using matrix regression to learn the weight coefficients is desired to preserve the original geometry structure. Recently, with the development of the sparse representation theory, many position-patch based methods [12–18] have been proposed to deal with the face hallucination problem.

These above methods have satisfactory hallucination results on the frontal view face images. However, when learning the LR patch representations, they ignore the pose variations, thus the learned representations are sensitive to these variations. To handle face hallucination with pose variations, we propose a nuclear norm regularized structural orthogonal Procrustes regression (N2SOPR) method in this paper. N2SOPR seeks an optimal transformation between two images so as to correct the pose from one to the other, and imposes the nuclear norm constraint on the error term so as to keep image's structural information. Also, N2SOPR clusters the input into the most accurate subspace from the training dictionary by low-rank representation.

Locality constraint is introduced to enable recovery of local manifold form local patches. Experimental results on the FERET database show the superiority of our method over some existing face hallucination methods.

The rest of the paper is organized as follows. Section 2 presents our proposed method. Section 3 evaluates the performance of our method on FERET face database. The conclusions are given in Sect. 4.

2 The Proposed N2SOPR

2.1 Problem Formulation

Let $x \in \Re^{d\times d}$ denotes each image block of LR test image X, $A_m \in \Re^{p\times q}$ ($m = 1, \ldots, N$) denote the blocks of well-aligned training face images (N is the number of samples). To handle the different pose between the test and training samples, we introduce an orthogonal matrix Q to correct the pose. We can get the following linear representation:

$$xQ = \sum_{i=1}^{N} \omega_i A_i + E \tag{1}$$

where E is the reconstruction error, ω_j is the jth element in the coefficient vector. Then, the nuclear norm constraint is performed on the error term so as to reveal the structure information. Also, a locality constraint is introduced via a similarity metric between the input and training samples to reveal the locality and sparsity simultaneously. Our model is formulated as follows:

$$\min \|xQ - A(\omega)\|_* + \eta \|d \otimes \omega\|_2^2 \;\; s.t.\; Q^{\mathrm{T}}Q = I \tag{2}$$

Here, $A(\omega) = \omega_1 A_1 + \omega_2 A_2 + \ldots + \omega_N A_N$ is a linear map from space $\Re^N$ to $\Re^{d\times d}$, $d = (d_1, \ldots, d_N)^T$ is distance vector, $\otimes$ denotes the element wise product, η is balancing parameter for controlling contribution from the locality constraint. To better use the training samples for reconstruction, we use a low-rank constraint to cluster the input into its most relevant subspace, in which the original input can be linearly represented by the similar training ones. Mathematically, our model can be obtained as follows:

$$\min \|xQ - A(\omega)\|_* + \lambda \|Hdiag(\omega)\|_* + \eta \|d \otimes \omega\|_2^2 \;\; s.t.\; Q^{\mathrm{T}}Q = I \tag{3}$$

where $H = [Vec(A_1), Vec(A_2), \ldots, Vec(A_N)]$ and $Vec(\cdot)$ denotes the vectorization operation of the matrix. λ is the regularization parameter to control the low-rank term.

2.2 Optimization via ADMM

We can transform the above problem to the following model:

$$\begin{aligned} &\min \|S\|_* + \lambda\|T\|_* + \eta\|d \otimes \omega\|_2^2 \\ &s.t.\ S = xQ - A(\omega),\ T = Hdiag(\omega),\ Q^{\mathrm{T}}Q = I \end{aligned} \tag{4}$$

The Lagrangian function [19] of the above equation becomes

$$\begin{aligned} L(Q, \omega, S, T) = &\min \|S\|_* + \lambda\|T\|_* + \eta\|d \otimes \omega\|_2^2 \\ &+ \frac{\mu}{2}\left(\left\|xQ - A(\omega) - S + \frac{1}{\mu}y_1\right\|_F^2 + \left\|Hdiag(\omega) - T + \frac{1}{\mu}y_2\right\|_F^2\right) \\ &- \frac{1}{2\mu}\left(\|y_1\|_2^2 + \|y_2\|_2^2\right) \end{aligned} \tag{5}$$

where μ is the penalty parameter, and y_1, y_2 are the Lagrange multipliers.

The followings are the process using Alternating Direction Method of Multipliers (ADMM) [20, 21] to solve the model (5):

Fix *ω, S, and T,* update *Q*

$$Q^{k+1} = \arg\min_{Q} \frac{\mu}{2}\left\|xQ - A\left(\omega^k\right) - S^k + \frac{1}{\mu}y_1^k\right\|_F^2 \tag{6}$$

where ω^k, S^k, y_1^k is respectively the kth updated value of ω, S, y_1.

Let $U\Sigma V^{\mathrm{T}}$ denote the SVD of $\left(A\left(\omega^k\right) + S^k - \frac{1}{\mu}y_1^k\right)^{\mathrm{T}}x$, then the solution is:

$$Q^{k+1} = VU^{\mathrm{T}} \tag{7}$$

Fix *Q*, *ω*, and *T*, update *S*

$$S^{k+1} = \arg\min_{S} \frac{1}{\mu}\|S\|_* + \frac{1}{2}\left\|S - \left(xQ^{k+1} - A\left(\omega^k\right) + \frac{1}{\mu}y_1^k\right)\right\|_F^2 \tag{8}$$

Fix *Q*, *ω*, and *S*, update *T*

$$T^{k+1} = \arg\min_{T} \frac{\lambda}{\mu}\|T\|_* + \frac{1}{2}\left\|T - \left(Hdiag\left(\omega^k\right) + \frac{1}{\mu}y_2^k\right)\right\|_F^2 \tag{9}$$

Model (8) and (9) can be solved using singular value thresholding (SVT) [22].

Fix Q, T, and S, update ω

$$\omega^{k+1} = \arg\min_{\omega} \ \eta\|d \otimes \omega\|_2^2 + \frac{\mu}{2}\left(\left\|xQ^{k+1} - A(\omega) - S^{k+1} + \frac{1}{\mu}y_1^k\right\|_F^2 + \left\|Hdiag(\omega) - T^{k+1} + \frac{1}{\mu}y_2^k\right\|_F^2\right) \tag{10}$$

The optimal solution of ω^{k+1} is:

$$\omega^{k+1} = (b + diag(b_1))\backslash b_2 \tag{11}$$

where

$$\begin{aligned} b &= \mu H^{\mathrm{T}}H + 2\eta diag(d) \otimes diag(d) \\ b_1 &= \mu(H \otimes H)^{\mathrm{T}}1, \\ b_2 &= \mu H^{\mathrm{T}}b_3 + \mu\left(T^{k+1} \otimes H\right)^{\mathrm{T}}1 - \left(y_2^k \otimes H\right)^{T}1, \\ b_3 &= Vec\left(xQ^{k+1} - S^{k+1} + \frac{1}{\mu}y_1^k\right) \end{aligned}$$

Updating Lagrange multipliers.

$$y_1^{k+1} = y_1^k + \mu\left(xQ^{k+1} - A\left(\omega^{k+1}\right) - S^{k+1}\right) \tag{12}$$

$$y_2^{k+1} = y_2^k + \mu\left(Hdiag\left(\omega^{k+1}\right) - T^{k+1}\right) \tag{13}$$

Check the convergence conditions:

$$\|xQ - A(\omega) - S\|_\infty \le \varepsilon \ and \ \|Hdiag(\omega) - T\|_\infty \le \varepsilon \tag{14}$$

where ε is error tolerance.

2.3 Face Hallucination via N2SOPR

Let A_H^m denote the HR training face images, while A_L^m ($m = 1, \ldots, N$) denote their LR counterparts. The face hallucination task aims to acquire the HR face image Y from its LR observation X.

Firstly, the LR input and each training faces are divided into overlapped patch matrices and denoted as $X(i, j)$, $A_L^m(i, j)$ and $A_H^m(i, j)$. For each patch matrix $X(i, j)$, it is represented as a linear combination over the LR training patch matrices $A_L^m(i, j)$ $(m = 1, \ldots, N)$ using N2SOPR. By replacing the LR training patch matrices with the corresponding HR counterparts and keeping the combination coefficients, the desired HR patch matrix can be synthesized. The target HR face image can be obtained by concatenating all the HR patch matrices and averaging values in the overlapping regions. The whole face hallucination algorithm is summarized in Algorithm 1.

Algorithm 1. Face hallucination via N2SOPR

Input: HR training images $A_H{}^1,\ldots,A_H{}^N$, corresponding LR training images $A_L{}^1,\ldots,A_L{}^N$, input LR images X.

1: **For** each input patch matrix in X:

a) Compute the distance between the LR input $X(i,j)$ and each of the LR training patch matrices $A_L{}^m(i,j)$ (m=1,…, N):

$$d_m(i,j) = \left\| X(i,j) - A_L^m(i,j) \right\|_2^2, m = 1,\mathsf{K}\ , N$$

b) Calculate the optimal weights $w^*(i,j)$ with regard to the LR input $X(i,j)$ using **N2SOPR**;

c) Construct the desired HR patch by $Y(i,j) = \sum_{m=1}^{N} A_H^m(i,j) w_m^*(i,j)$

2: **End for**

3: The target HR image Y can be obtained by integrating all the reconstructed HR patch matrices.

Output: The hallucinated HR face image Y.

3 Experimental Results and Discussions

3.1 Dataset Description

We use the FERET database [23] to evaluate the performance of the proposed method. The database includes the same person with various expressions, poses, illumination and ages. We select 180 frontal expressionless images as training samples (some examples are shown in Fig. 1), and another 20 face images with pose changes as the testing set (some examples are shown in Fig. 2). We crop the region of the faces and normalize the HR images to the size of 80 × 80. The LR face images are obtained by smoothing (an averaging filter of size 4 × 4) and down-sampling (the down-sampling factor is 4) the HR face images, therefore the size of LR face image is 20 × 20.

Fig. 1 HR training sample images

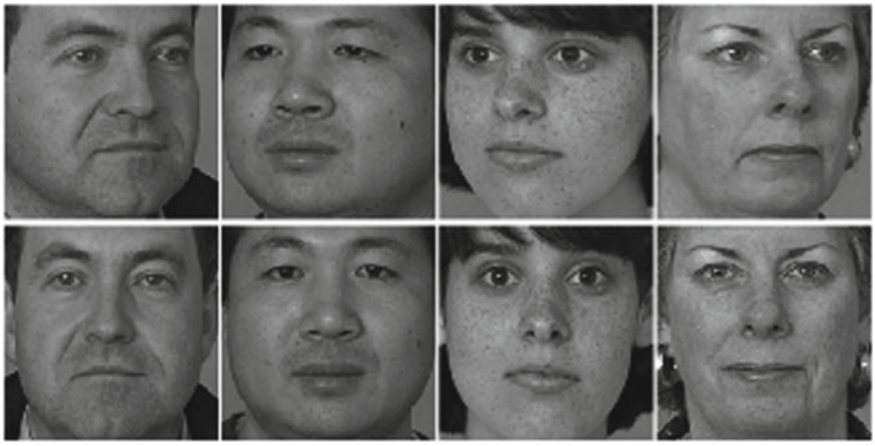

Fig. 2 Test face images with pose changes and the corresponding frontal face images

3.2 Comparison Results on FERET Database

In this section, we compare our N2SOPR method with other state-of-the-art methods, such as LSR method [6], SR method [7], LCR method [8], KLAINE method [9] and SRCNN method [24]. As for local patch-based methods, we suggest using the size 3×3 pixels for LR patch and the overlaps between its neighbor patches are 3×1 pixels, while the corresponding HR patch size is 12×12 pixels with an overlap of 12×4 pixels.

Table 1 The average PSNR and SSIM value of different methods

Reconstruction methods	PSNR (dB)	SSIM
LSR [6]	18.3648	0.3899
SR [7]	18.5988	0.4171
LCR [8]	19.4243	0.5045
KLAINE [9]	19.4254	0.5047
SRCNN [24]	19.4464	0.5156
N2SOPR	20.7319	0.6127

Figure 3 lists some representative hallucinated results generated by different methods. We can see that the images synthesized by LSR and SR methods are seriously distorted, especially in the contour of eyes. Compared with these three methods, the results of LCR method are improved. But the synthesized face images are still blurred. The face image synthesized by KLAINE method has richer face details, but there is still distortion. In addition to the distortion, we can also find that the pose variations are still existed in the synthesized images, which will reduce the performance of following recognition system. The face image synthesized by SRCNN method has richer face details, but there is still blurring. By introducing an orthogonal matrix low-rank constraint, our N2SOPR method can obtain more clear images, and the recovered faces are very close to the original HR face images. In order to further highlight the effectiveness of our method, we also give the quantitative comparisons in terms of PSNR and SSIM [25] in Table 1.

4 Conclusions

This paper proposes a nuclear norm regularized structural orthogonal Procrustes regression (N2SOPR) method for face hallucination with pose variations. N2SOPR adds an optimal transformation between two images to correct the pose from one to the other, and imposes nuclear norm constraint on the error term to keep image's structural information. In addition, the low-rank and locality constrained are taken into consideration on the representations, enforcing to adaptively select the training samples from the same subspace with input. Experiments on the FERET face database have demonstrated that our method could yield better hallucinated performance than some state-of-the-art methods.

Fig. 3 Hallucinated faces on the FERET database by different methods. From top to bottom: LR input face images, the hallucinated face images by LSR, SR, LCR, KLAINE, SRCNN, our N2SOPR method and original frontal HR face images

Acknowledgements This work was partially supported by the National Natural Science Foundation of China under Grant nos. 61502245, 61503195, 61772568, the Natural Science Foundation of Jiangsu Province under Grant no. BK20150849, Research Fund of SKL of Ocean Engineering in Shanghai Jiaotong University (1315;1510), Research Fund of SKL of Marine Geology in Tongji University (MGK1608), Open Fund Project of Fujian Provincial Key Laboratory of Information Processing and Intelligent Control (Minjiang University) (No. MJUKF201717). Guangwei Gao is the corresponding author.

References

1. Park, S.C., Min, K.P., Kang, M.G.: Super-resolution image reconstruction: a technical overview. IEEE Signal Process. Mag. **20**(3), 21–36 (2003)
2. Lu, H., Li, Y., Chen, M., Kim, H., Serikawa, S.: Brain intelligence: go beyond artificial intelligence. Mob. Netw. Appl. **23**, 368–375 (2018)
3. Li, Y., Lu, H., Li, K., Kim, H., Serikawa, S.: Non-uniform de-scattering and de-blurring of underwater images. Mob. Netw. Appl. **23**, 352–362 (2018)
4. Lu, H., Li, Y., Uemura, T., Kim, H., Serikawa, S.: Low illumination underwater light field images reconstruction using deep convolutional neural networks. Future Gener. Comput. Syst. **82**, 142–148 (2018)
5. Chang, H., Yeung, D.Y., Xiong, Y.: Super-resolution through neighbor embedding. Proceedings of the Computer Vision & Pattern Recognition, vol. 1, pp. 275–282, Jan 2004
6. Ma, X., Zhang, J., Qi, C.: Hallucinating face by position-patch. Pattern Recogn. **43**(6), 2224–2236 (2010)
7. Wright, J., Yang, A.Y., Ganesh, A., et al.: Robust face recognition via sparse representation. IEEE Trans. Pattern Anal. Mach. Intell. **31**(2), 210–227 (2009)
8. Jiang, J., Hu, R., Wang, Z., Han, Z.: Noise robust face hallucination via locality constrained representation. IEEE Trans. Multimed. **16**(5), 1268–1281 (2014)
9. Pang, H., Gao, G., Jing, X., et al.: Kernel locality-constrained adaptive iterative neighbor embedding for face hallucination. In: IEEE International Conference on Wireless Communications & Signal Processing, pp. 1–5 (2016)
10. Schölkopf, B., Smola, A., Müller, K.R.: Nonlinear component analysis as a kernel eigenvalue problem. Neural Comput. **10**(5), 1299–1319 (1998)
11. Gao, G., Pang, H., Wang, C., et al.: Locality-constrained iterative matrix regression for robust face hallucination. In: International Conference on Neural Information Processing, pp. 613–621 (2017)
12. Jung, C., Jiao, L., Liu, B., et al.: Position-Patch Based Face Hallucination Using Convex Optimization. IEEE Signal Process. Lett. **18**(6), 367–370 (2011)
13. Rohit, U., Abdu, R.V., George, S.N.: A robust face hallucination technique based on adaptive learning method. Multimed. Tools Appl. **76**, 1–21 (2017)
14. Lu, T., Pan, L., Wang, H., Zhang, Y., Wang, B., et al.: Face hallucination using deep collaborative representation for local and non-local patches. In: IEEE International Symposium on Circuits & Systems, pp. 1–4 (2017)
15. Shi, J., Qi, C.: Face hallucination based on PCA dictionary pairs. In: IEEE International Conference on Image Processing, pp. 933–937 (2014)
16. Li, Y., Cai, C., Qiu, G., Lam, K.M.: Face hallucination based on sparse local-pixel structure. Pattern Recogn. **47**(3), 1261–1270 (2014)
17. Wang, Z., Jiang, J., Xiong, Z., Hu, R., Shao, Z.: Face hallucination via weighted sparse representation. IEEE Int. Conf. Acoust. **32**(3), 2198–2201 (2013)
18. Jiang, J., Hu, R., Wang, Z., Xiong, Z.: Support-driven sparse coding for face hallucination. In: IEEE International Symposium on Circuits & Systems, pp. 2980–2983 (2013)

19. Lin, Z., Chen, M., Ma, Y.: The augmented lagrange multiplier method for exact recovery of corrupted low-rank matrices. Eprint Arxiv (2010)
20. Yin, W.: The alternating direction method of multipliers. In: Imaging Science a Workshop in Honor of Stanley Osher (2012)
21. Ghadimi, E., Teixeira, A., Shames, I., Johansson, M.: Optimal Parameter Selection for the Alternating Direction Method of Multipliers (ADMM): Quadratic Problems. IEEE Trans. Autom. Control **60**(3), 644–658 (2013)
22. Cai, J.F., Cand, E.J.S., Shen, Z.: A singular value thresholding algorithm for matrix completion. Siam J. Optim. **20**(4), 1956–1982 (2008)
23. Phillips, P.J., Wechsler, H., Huang, J., et al.: The FERET database and evaluation procedure for face-recognition algorithms. Image Vis. Comput. **16**(5), 295–306 (1998)
24. Dong, C., Loy, C.C., He, K., et al.: Image super-resolution using deep convolutional networks. IEEE Trans. Pattern Anal. Mach. Intell. **38**(2), 295–307 (2016)
25. Hore, A., Ziou, D.: Image quality metrics: PSNR vs. SSIM. In: International Conference on Pattern Recognition, pp. 2366–2369 (2010)

A New Dataset for Vehicle Logo Detection

Shuo Yang, Chunjuan Bo, Junxing Zhang, Meng Wang and Lijun Chen

Abstract This paper establishes a multilevel dataset for solving the vehicle logo detection task; we call it 'VLD-30'. Vehicle logo detection is applied to the Intelligent Transport System widely, such as vehicle monitoring. As for the object detection algorithm of deep-learning, a good dataset can improve the robustness of it. Our dataset has a very high reliability by including analysis on various factors. In order to confirm the dataset performance, we use the typical target detection algorithm, such as Faster-RCNN and YOLO. The experimental results show that our dataset achieves significant improvements for the small object detection, and vehicle logo detection is potential to be developed.

Keywords VLD-30 · Deep-learning · Vehicle logo detection

1 Introduction

In the research of intelligent transportation systems, vehicle monitoring is always a crucial problem. Solving the vehicle monitoring in a complex scene by selecting effective information rapidly is efficient in consideration of the complexity of vehicle information, the diversification problems, and the easiness of changing the license plate of cars [1, 2]. Vehicle logo has a distinct characteristic, such as special shape. The same brand of vehicle manufacturers has different auto styles, but the vehicle

S. Yang · J. Zhang (✉) · M. Wang · L. Chen
College of Electromechanical Engineering,
Dalian Minzu University, Dalian 116600, China
e-mail: zhangjunxing@dlnu.edu.cn

C. Bo
College of Information and Communication Engineering,
Dalian Minzu University, Dalian 116600, China

C. Bo
Key Laboratory of Intelligent Perception and Advanced Control of State Ethnic Affairs
Commission, Dalian Minzu University, Dalian 116600, China

H. Lu (ed.), *Cognitive Internet of Things: Frameworks, Tools and Applications*, Studies in Computational Intelligence 810,
https://doi.org/10.1007/978-3-030-04946-1_17

logo has the characteristics of uniqueness and stability. Vehicle logo detection can therefore assist in the monitoring and recognition of vehicles.

Recently, object detection algorithm of deep-learning has made a good performance in computer vision tasks. In view of large object detection datasets, such as VOC0712, the precision of the object detection algorithm based on deep learning is 80%, and this result is beyond that of the traditional object detection algorithm. However, detecting small objects is still a difficult problem in computer vision for object detection. The main cause of detecting difficultly is poor canonical data, the small size of the object and so on. So, in this paper, we propose a good dataset to solve the vehicle logo detection task.

Logo detection in still images [3, 4] has been gaining considerable attention in the last decade. The logos in still images are generally clear. However, in the real-time complex scene, the vehicle logo is often deformed and blurred due to the effects of illumination variations and the camera angle. Combination of the real images and literature [5, 6], this paper divides the influential factors into six parts.

- Illumination fluctuations: Most of vehicle logos have the characteristic of high reflectance luminous in bright light, but it will be mixed with many types of outside noise. In addition, the vehicle logo in low light is unfavorable for extracting features.
- Complex and varied shape: The vehicle logo object has complex and rich feature information, but it is harmful to extract the key information and complete the detection tasks.
- Scale changes: The size of vehicle logo comparatively changes because of the different shooting angles and distances. If the vehicle logo is small, then we will lose the feature information of the object.
- Location: The location of vehicle logo varies depending on various brand manufacturers. Most logos are installed on the radiator grille. Some logos are on the front hood of the car. Thus, we cannot use the relevance of the vehicle and logo to achieve the detection tasks.
- Background disturbance: Numerous foreground distractors exist given the proportion of the vehicle logo in the image area is small, such as in the radiator grille, traffic sign, and front bumper. These factors result in increased background false detection rate.
- Object resolution: The vehicle logo has considerable color and grain information. The pixel of the datasets is usually fairly small. Acquiring distinct object information for the vehicle logo detection is thus a difficult problem.

We establish the vehicle logo dataset that combines the influence factors to overcome the above-mentioned obstacles, and call the dataset is “VLD-30”. Meanwhile, we use the object detection algorithm for evaluating the VLD-30, including Faster-RCNN [7, 8] and YOLO [9, 10].

Fig. 1 The brands of vehicle

2 VLD-30

2.1 Dataset Construction

When training samples are sufficient, the method can obtain an optimal result for the object detection method of deep-learning. At present, we have not a public training data on vehicle logo detection. Meanwhile, most of methods are still data driver to improve the detection accuracy of vehicle logos. Having a high-quality dataset for the vehicle logo detection task is important. In this study, we propose a good dataset for the vehicle logo detection. The dataset is called VLD-30 (vehicle logo detection), because the dataset have thirty categories for the vehicle, as shown in Fig. 1.

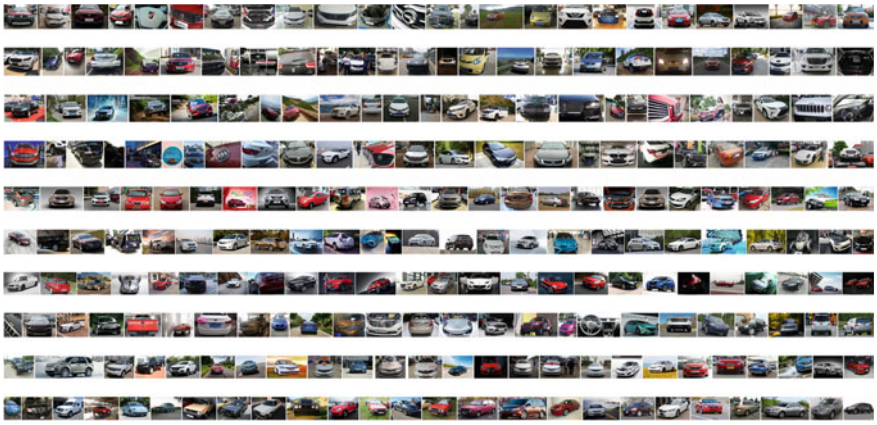

Fig. 2 The samples of our dataset

Table 1 The statistics of dataset size

	VLD-30
Target length size (in pixels)	10 ~ 200 (±5)
Target width size (in pixels)	10 ~ 100 (±5)
Maximum size	4608 × 3450
Minimum size	320 × 240

2.2 Dataset Statistics

By compiling web crawler to acquire the images and analyzing the data, we propose the vehicle logo detection dataset formally. The VLD-30 currently contains thirty categories of vehicle brands, and has 2010 images. In addition, each class containing 67 images. The single objects of image, its proportion in total images are 95%. In VLD-30, we divide the dataset into train and test groups. The test group has 600 images, and each class has 20 images. And all images of dataset are in JPG form. For solving the changes of multi-scale for logo in an image, the entire range of dataset scale is from 320 × 240 pixels to 4608 × 3450 pixels. With the dimensional change of image, we can overcome the deformation problem of vehicle logo.

Figure 2 show the VLD-30's samples. And Table 1 shows the statistics of target size and image size. From Table 1, we can see that our dataset has a biggish dimension span. In this way, we can improve the generalization ability of the training model.

3 Experiments

In our experiment, we use the typical algorithms of object detection for checking our dataset, including Faster-RCNN and YOLO. Faster-RCNN is a fast two-stage detector and has a good performance for the object detection. YOLO, it has three versions for object detection, it's a high-speed and practical one-stage detector of object detection. In this experiment, we use the more stable detection algorithm that YOLOv2. We determine whether our dataset has better assistant ability for algorithm of small object detection through the experimental method. The contrastive experiments evaluate the dataset of VLD-30 in the rationality of construction for the vehicle logo detection task.

In experiment, we have designed two strategies to verify the dataset. At first, the average overlap rate is used to estimate the detector model, we want to show that the algorithm determine the position accuracy of the object. Finally, we use the MAP (mean average precision) values for evaluating the performance of algorithm in the VLD-30 dataset.

3.1 Experiment for the Position Accuracy

The Faster-RCNN and YOLOv2 were tested under the GPU to accelerate the operation. The standard in this study is the average overlap rate and time consumed for each photo. Table 2 shows the results.

3.2 Comprehensive Performance Test

We use the 600 test image from VLD-30 to show our result. With P (precision) and R (recall) in the primary category, we can calculate the area of the P–R curve, and the area name is called AP (average precision). We use the AP as index of accuracy for the primary category. For multiple categories, we take the average value that is called MAP (mean average precision). Table 3 shows the experimental results.

Table 2 Result of accuracy experiment

Algorithm	Average overlap rate	Time/s
Faster-RCNN(VGG16)	0.81	1.6
YOLOv2 (DarkNet19)	0.76	0.02

Table 3 Result of detection experiment

Number	Name	Faster-RCNN	YOLOv2
0001	Beijing Automotive	0.852	0.863
0002	Ford	0.774	0.733
0003	SKODA	0.871	0.854
0004	Venucia	0.817	0.824
0005	HONDA	0.982	0.922
0006	NISSAN	0.969	0.952
0007	Cadillac	0.765	0.742
0008	SUZUKI	0.874	0.883
0009	GEELY	0.824	0.854
0010	Porsche	0.854	0.812
0011	JEEP	0.642	0.602
0012	BAOJUN	0.977	0.963
0013	ROEWE	0.865	0.878
0014	LINCOLN	0.834	0.786
0015	TOYOTA	0.977	0.988
0016	BUICK	0.873	0.857
0017	CHERY	0.923	0.904
0018	KIA	0.872	0.822
0019	HAVAL	0.781	0.653
0020	Audi	0.977	0.982
0021	LAND ROVER	0.879	0.859
0022	Volkswagen	0.917	0.908
0023	Trumpchi	0.924	0.915
0024	CHANGAN	0.803	0.786
0025	Morris Garages	0.832	0.820
0026	Renault S.A	0.92-	0.896
0027	LEXUS	0.867	0.869
0028	BMW	0.934	0.912
0029	MAZDA	0.899	0.883
0030	Mercedes-Benz	0.953	0.879
	MAP	0.875	0.853
	Time/s	1.5	0.02

4 Conclusion

In this work, we propose a dataset called VLD-30 for vehicle logo detection. Meanwhile, we used the object detection algorithm for evaluating the performance of VLD-30 dataset. The detection result proves the effectiveness of VLD-30 and the robustness of our framework. Of cause, some problems still need to be solved in the

future, including the rich variations in vehicle logo contents, and the application of vehicle logo detection.

Acknowledgements This work is supported by Key Research Guidance Plan Project of Liaoning Province (No. 2017104013), Natural Science Foundation of Liaoning Province (No. 201700133).

References

1. Huimin, L., Li, Y., Chen, M., Kim, H., Serikawa, S.: Brain intelligence: go beyond artificial intelligence. MONET **23**(2), 368–375 (2018)
2. Li, P., Wang, D., Wang, L., Lu, H.: Deep visual tracking: review and experimental comparison. Pattern Recogn. **76**, 323–338 (2018)
3. Mao, S., Ye, M., Li, X., Pang, F., Zhou, J.: Rapid vehicle logo region detection based on information theory. Comput. Electr. Eng. **39**(3), 863–872 (2013)
4. Bianco, S., Buzzelli, M., Mazzini, D., Schettini, R.: Logo recognition using CNN features. In: International Conference on Image Analysis and Processing, pp. 438–448 (2015)
5. Liao, Y., Lu, X., Zhang, C., Wang, Y., Tang, Z.: Mutual enhancement for detection of multiple logos in sports videos. In: IEEE International Conference on Computer Vision, pp. 4856–4865 (2017)
6. Du, S., Ibrahim, M., Shehata, M., et al.: Automatic license plate recognition (ALPR): a state-of-the-art review. IEEE Trans. Circuits Syst. Video Technol. **23**(2), 311–325 (2013)
7. Girshick, R.: Fast R-CNN. In: IEEE International Conference on Computer Vision, pp. 1440–1448 (2015)
8. Ren, S., He, K., Girshick, R., Sun, J.: Faster R-CNN: towards real-time object detection with region proposal networks. IEEE Trans. Pattern Anal. Mach. Intell. **39**(6), 1137–1149 (2017)
9. Redmon, J., Divvala, S., Girshick, R., Farhadi, A.: You only look once: unified, real-time object detection, pp. 779–788 (2016)
10. Redmon, J., Farhadi, A.: YOLO9000. Better, faster, stronger. In: IEEE Conference on Computer Vision and Pattern Recognition, pp. 6517–6525 (2017)

A Class of Chaos-Gaussian Measurement Matrix Based on Logistic Chaos for Compressed Sensing

Hongbo Bi, Xiaoxue Kong, Di Lu and Ning Li

Abstract Accurate compressed sensing recovery theoretically depends on a large number of random measurements. In this study, we demonstrated the correlation properties of non-piecewise and piecewise Logistic chaos system to follow Gaussian distribution. The correlation properties can generate a class of Chaos-Gaussian measurement matrix with the low complexity, hardware-friendly implementation and desirable sampling efficiency. Thus, the proposed algorithm constructs Chaos-Gaussian measurement matrix by the sequences. Experimental results show that Chaos-Gaussian measurement matrix can provide comparable performance against Gaussian and Bernoulli random measurement matrix.

Keywords Compressed sensing · Logistic chaos · Correlation properties Chaos-Gaussian measurement matrix

1 Introduction

Traditional techniques to sample and reconstruct a signal of interest are based on the principle of the Shannon–Nyquist's sampling theory: the sampling rate is dictated by the bandwidth presented in the signal. However, due to the high sampling rate, this paradigm increases the storage consumption and transmission bandwidth in some emerging applications exhibiting high frequency. Compressed sensing (CS) initiated

H. Bi (✉) · X. Kong · D. Lu · N. Li
School of Electrical and Information Engineering, Northeast Petroleum University, Daqing, China
e-mail: bhbdq@126.com

X. Kong
e-mail: kxxwds@163.com

D. Lu
e-mail: 18810463560@163.com

N. Li
e-mail: LNLNDY@126.com

H. Lu (ed.), *Cognitive Internet of Things: Frameworks, Tools and Applications*, Studies in Computational Intelligence 810,
https://doi.org/10.1007/978-3-030-04946-1_18

by Candès can recover the signal from far fewer samples than what is conventionally deemed requirement [1–3]. Recently, it has already widely been used in the information theory, wireless communication, earth sciences, optics, and biomedical engineering, etc.

CS theory mainly consists of three key technologies, namely, signal sparse representation, measurement matrix construction, and measurement matrix reconstruction algorithms. Exact sampling performance is highly determined by the structure of the measurement matrix. Therefore, the existing well-designed sensing matrices can be classified into two categories in terms of their inner elements: random sensing matrices and deterministic sensing matrices. A crucial advantage of random matrices, including the Bernoulli matrix and Gaussian matrix, is universal and efficient in signal recovery. Nonetheless, random matrices naturally have three major shortcomings: (1) low storage efficiency; and (2) high complexity; and (3) difficult to design in hardware. In order to overcome the drawbacks of random matrices, deterministic matrices have been proposed. Unfortunately, due to loss of randomness, deterministic matrices have poor performance in its applications [4].

Consequently, to combine the merits of both random constructions and deterministic ones, many researchers apply the pseudo-random properties of chaotic system to construct the CS measurement matrix. Yu et al. established the construction of a feasible measurement matrix based on the Logistic maps [5]. Similarly, Guo et al. proposed a measurement matrix algorithm based on Logistic Chaos-Bernoulli sequence according to the pseudo-random property of chaos sequence [6]. Meanwhile, Lin et al. presented a deterministic measurement matrix based on chaotic sequence [7]. Moreover, Parvaz et al. constructed a deterministic measurement matrix based on composite chaotic mapping including Tent, Sine and Logistic mapping [8]. Existed chaotic matrices exhibit an encouraging performance. However, most constructed algorithms are not universal and simple in Logistic chaos system.

In this study, we find potential correlation properties of the Logistic chaotic system, and exploited the correlation properties to propose a general algorithm. Primarily, the non-piecewise and piecewise Logistic chaotic system can generate the pseudo-random sequence, which is based on the deterministic equation. Thereafter, a class of spread spectrum sequences with good correlation properties is generated by symbol function mapping. The new sequences follow the Gaussian distribution. Thus, the CS measurement matrix can be constructed, and the algorithm is universally applicable to a class of Logistic chaotic system. The experimental results prove that the constructed Chaos-Gaussian measurement matrix is equal or better than the common random measurement matrices, such as Gaussian and Bernoulli random measurement matrices.

The rest of this paper is outlined as follows. Section 2 illustrates how to construct a class of Chaos-Gaussian measurement matrix. Section 3 tackles about the experiments that are conducted to simulate the performance of the Chaos-Gaussian measurement matrix. Finally, Sect. 4 concludes this paper.

2 Construction of a Class of Chaos-Gaussian Measurement Matrix

2.1 Logistic Chaotic System

The chaotic system can produce uncertain trajectories based on deterministic rules and has the characteristics of high sensitivity to initial conditions. Hence, it has excellent pseudo-random properties, and is widely used in the field of CS to further enhance the performance of recovery. The classical one-dimensional Logistic chaotic system is defined as follows:

$$x_{n+1} = 1 - ux_n^2 = f(x_n),\ x \in [-1, 1] \tag{1}$$

where the parameter $u \in [1.872, 2.0]$ is defined. In recent years, the Logistic chaotic system is improved with more superior non-linear characteristics. Zhang et al. proposed a new nonlinear piecewise logistic chaotic mapping [9]. The new chaotic system is defined as:

$$x_{n+1} = \begin{cases} 1 - 4 * u * (x_n + 0.5)^2 & -1 < x_n < 0 \\ 4 * u * (x_n - 0.5)^2 - 1 & 0 \le x_n < 1 \end{cases}, \tag{2}$$

where the parameter u is identical with logistic system. The piecewise logistic system is able to generate sequences with good traversal performance within the value range of parameters u and x, which is also an improvement for original logistic system

2.2 Correlation Function

$\{a_i | i = 1, 2, \ldots, N\}$ and $\{b_i | i = 1, 2, \ldots, N\}$ are defined as two binary sequences with period N and the corresponding sequences of elements of $\{+1, -1\}$.

The even cross-correlation function R_{ab} is defined as follows:

$$R_{ab}(\tau) = C_{ab}(\tau) + C_{ab}(\tau - N) \tag{3}$$

Meanwhile, the odd cross-correlation function R_{ab} is defined as follows:

$$R_{ab}(\tau) = C_{ab}(\tau) - C_{ab}(\tau - N) \tag{4}$$

2.3 Probability Distribution of Correlation Function

Take the non-piecewise logistic system as an example, set $\{x_n\}_0^{N-1}$ as the output chaotic sequence generated by Logistic mapping with the initial condition x_0 and parameter $u = 2.0$, i.e.,

$$x_{n+1} = 1 - 2x_n^2 = f(x_n),\ x \in [-1, 1] \tag{5}$$

Let the sequence $\{a_n\}_0^{N-1}$ denote the map of the spread spectrum sequence $\{x_n\}_0^{N-1}$ by the symbol function sgn(.) as follows:

$$a_n = \mathrm{sgn}(x_n)\ \ n = 0, 1, 2, \ldots, N-1 \tag{6}$$

In [7], the spread spectrum sequence is proved to be a Bernoulli sequence that satisfies the RIP. Assuming that the sequence length N is long, the sequences $\{a_n\}_0^{N-1}$ and $\{b_n\}_0^{N-1}$ are generated by Formulas (6). The two sequences are two binary sequences with length N. The correlation function distribution of the sequences $\{a_n\}_0^{N-1}$ and $\{b_n\}_0^{N-1}$ follows the Gaussian distribution with a mean of 0 and a variance of N in [10].

Proof of Gaussian distribution. Take an example of an even cross-correlation function. Let P(k) denote the probability that the even cross-correlation function is equal to k. Given the sensitive dependence of chaos on the initial conditions, $\{a_n\}$ and $\{b_n\}$ are independent Bernoulli sequences. Therefore, the even cross-correlation distribution of $\{a_n\}$ and $\{b_n\}$ follows the binomial distribution. Particularly, when N is large, the even cross-correlation distribution follows the Gaussian distribution. Given the perspective of set averaging, and that the amount of even cross-correlation changes can be a multiple of 4, P(k) must be corrected as follows:

$$P(k) \approx \frac{4}{\sqrt{2\pi N}} e^{-\frac{k^2}{2N}} |k| \le N,\ k \equiv N + e \mod 4 \tag{7}$$

According to the ergodicity of chaos, the conclusion also holds true for the time average, and the meaning of P(k) becomes the frequency of occurrence of the correlation value k. For even cross-correlation, parameter e = 0 or 2, depending on the sequences $\{a_n\}$ and $\{b_n\}$. Then, according to the relationship between P(k) and k, the theoretical result is shown in Fig. 1. By the same token, this theoretical proof also applies to odd cross-correlation, and correlation distributions of piecewise Logistic chaotic systems.

For the analysis of the simulation results, the even cross-correlation distribution of spread spectrum sequences with N = 4,096 is given, and the relationship between the number of occurrences and the correlation value is denoted in Fig. 1. The comparison

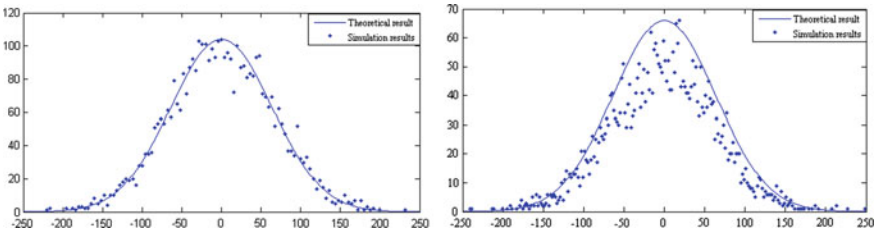

(a) Even cross-correlation distribution (b) Odd cross-correlation distribution

Fig. 1 Correlation distribution of two spread spectrum sequences with N = 4096 by the non-piecewise Logistic map

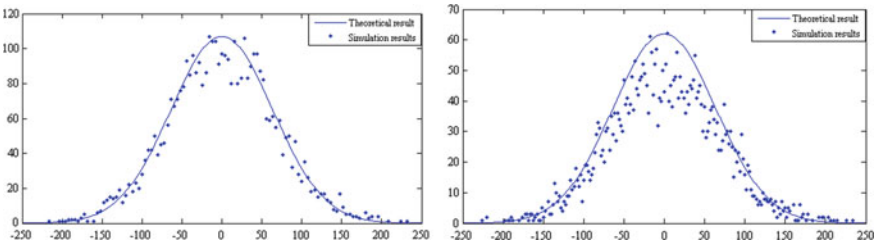

(a) Even cross-correlation distribution (b) Odd cross-correlation distribution

Fig. 2 Correlation distribution of two spread spectrum sequences with N = 4096 by the piecewise Logistic map

to the theoretical results of the Gaussian distribution proves that the even cross-correlation distribution follows the Gaussian distribution with a mean of 0 and a variance of N. Similarly, the correlation distributions in non-piecewise logistic system and piecewise logistic system are shown in Fig. 2.

2.4 Construction of Chaos-Gaussian Measurement Matrix

The Chaos-Gaussian measurement matrix is constructed is as follows:

Step 1: For the non-piecewise logistic chaotic system, the constructed measurement matrix is determined to be feasible and effective with parameter $u = 2.0$ and the initial values $x_0 = 0.23$ and $y_0 = 0.37$ after conducting several experimental comparisons. Similarly, parameter $u = 2.0$ and the initial values $x_0 = 0.13$ and $y_0 = 0.57$ are effective for the piecewise logistic chaotic system. Therefore, the chaotic sequences $\{x_n\}_0^{N-1}$ and $\{y_n\}_0^{N-1}$ are generated by the non-piecewise Logistic chaotic system (the piecewise logistic chaotic system) with the previously presented conditions, and the sequence length is $n = M \times N - 1$.

Step 2: We let the sequences $\{a_n\}_0^{N-1}$ and $\{b_n\}_0^{N-1}$ denote the symbol map of the chaotic sequences $\{x_n\}_0^{N-1}$ and $\{y_n\}_0^{N-1}$ using Formula (6).

Step 3: The correlation distribution of the sequences $\{a_n\}_0^{N-1}$ and $\{b_n\}_0^{N-1}$ from step 2 is obtained using Formula (3) [Formula (4)]. Subsequently, the correlation sequence is cut off to form the M × N-dimensional measurement matrix Φ.

3 Experimental Results

In this study, two-dimensional images are simulated to verify the feasibility and validity of the class of Chaos-Gaussian measurement matrix and compared with the Gaussian and Bernoulli random matrices. The images lena, cameraman, and peppers with the size of 256 × 256 are simulated under different compression ratios (M/N). We use wavelet transform to sparsely represent the image, construct the Chaos-Gaussian measurement matrix, and utilize the OMP algorithm to reconstruct the image.

Initially, for the sake of visual observation, we take the lena image as an example, and the reconstruction performance of different measurement matrices is discussed under the compression ratio M/N = 0.5. Figure 3 exhibits the experimental results.

Figure 3 depicts that the Chaos-Gaussian measurement matrix reconstruction effect is better than other measurement matrices. For the further explanation of the

(a) Chaos-Gaussian measurement matrix (“n-p”)

(b) Gaussian measurement matrix

(c) Chaos-Gaussian measurement matrix (“p”)

(d) Bernoulli measurement matrix

Fig. 3 Comparison of image reconstruction results of each measurement matrix (M/N = 0.5)

experimental results shown in Fig. 3, the peak signal-to-noise ratio (PSNR) with the compression ratio for lena images under different measurement matrices is shown in Fig. 4. Given that the other measurement matrices used for comparison are random matrices, the average of 20 experiments is selected as the experimental data. For the convenience of writing, "ec", and "oc" represent even cross-correlation and odd cross-correlation, respectively. And "n-p" represents non-piecewise logistic chaotic system. Similarly, "p" represents piecewise logistic chaotic system.

Figure 4 illustrates that the proposed Chaos-Gaussian measurement matrix for non-piecewise Logistic chaotic system has approximately 0.5–2.0 dB average improvement of the PSNR compared with the Gaussian and Bernoulli random measurement matrices. Particularly, in the compression ratio range of 0.3–0.4, this performance improvement of Chaos-Gaussian measurement matrix is evident. For the piecewise logistic chaotic system, the performance of the Chaos-Gaussian measurement matrix is similar to that of the Gaussian and Bernoulli matrix, which validates the proposed construction of a class of Chaos-Gaussian matrix.

In order to prove the universal applicability of the proposed algorithm, simulations are also carried out for more images. The results of the Chaos-Gaussian matrix with different images are listed in Tables 1 and 2. From the simulation data, results with different image are consistent with the trend of PSNR on the class of Logistic system.

The simulation results confirm that the Chaos-Gaussian measurement matrix is a deterministic measurement matrix, and that the reconstruction effect is better than or similar with that of the Bernoulli and Gaussian random measurement matrices.

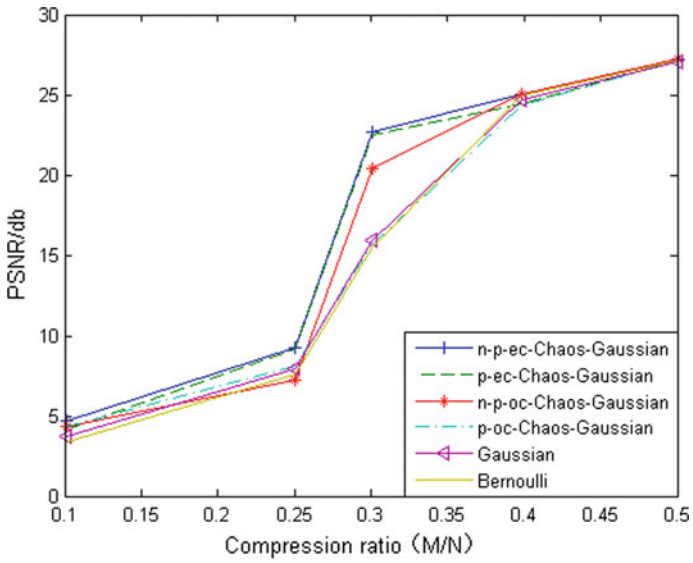

Fig. 4 Comparison of the PSNR of lena image for different measurement matrices with compression ratio

Table 1 The PSNR of different measurement matrices (For non-piecewise Logistic chaotic system)

	Compression ratio(M/N)	Gaussian	Bernoulli	n-p-ec-Chaos-Gaussian	n-p-oc-Chaos-Gaussian
Peppers	0.5	25.6653	25.8643	**26.0784**	26.0174
	0.4	23.0187	23.4355	**23.6801**	23.3856
	0.3	14.5764	14.8274	**20.4302**	18.347
	0.25	8.7057	8.5625	**9.5971**	7.5763
	0.1	3.8880	3.7824	**4.8314**	4.7994
Cameraman	0.5	20.2279	20.1883	**20.3348**	21.8414
	0.4	18.2727	18.4899	19.4462	**20.6856**
	0.3	12.4526	11.9557	14.3015	**18.0805**
	0.25	7.5633	7.341	**8.1046**	5.9022
	0.1	4.0419	3.6156	**5.0603**	4.3552

Table 2 The PSNR of different measurement matrices (For piecewise Logistic chaotic system)

	Compression ratio(M/N)	Gaussian	Bernoulli	n-p-ec-Chaos-Gaussian	n-p-oc-Chaos-Gaussian
Peppers	0.5	25.6653	**25.8643**	25.6828	25.4658
	0.4	23.0187	**23.4355**	23.2082	22.7656
	0.3	14.5764	14.8274	**19.7031**	17.3301
	0.25	8.7057	8.5625	**9.949**	7.1399
	0.1	3.8880	3.7824	**4.4624**	4.3263
Cameraman	0.5	20.2279	20.1883	21.5915	**21.6029**
	0.4	18.2727	18.4899	20.3956	**20.5831**
	0.3	12.4526	11.9557	**17.9985**	14.9089
	0.25	7.5633	7.341	**11.6107**	9.8868
	0.1	4.0419	3.6156	3.6647	**4.2251**

4 Conclusion

In this study, according to the chaotic pseudo-random characteristics of nonlinear dynamics systems, the non-piecewise and piecewise Logistic chaotic system are primarily fully mapped with a good pseudo-random chaotic sequence; then, symbolic function mapping is performed; and finally, the mapped sequence achieves a good correlation.

The correlation distribution follows the Gaussian distribution of with the mean value of 0 and the variance of N. Therefore, on the basis of this theory, a class of Chaos-Gaussian measurement matrix construction algorithm is proposed. The simulation results confirm that the Chaos-Gaussian measurement matrix is a deterministic measurement matrix, and that the reconstruction effect is better than or similar with that of the Bernoulli and Gaussian random measurement matrices. Particularly, the

PSNR of the reconstructed signal exhibits evident improvement in the case of a large compression ratio for Logistic chaotic system. The deterministic dynamic equation of the chaotic system effectively overcomes the shortcoming of hardware that is difficult to achieve due to randomness, thus the class of Chaos-Gaussian measurement matrix provides an effective solution for the compressed sensing.

Acknowledgements This work is supported by the NEPU Natural Science Foundation under Grant No. 2017PYZL-05, JYCX_CX06_2018 and JYCX_JG06_2018.

References

1. Candès, E.J., Tao, T.: Decoding by linear programming. IEEE Trans. Inf. Theory **51**(12), 4203–4215 (2005)
2. Wang, Q., et al.: Joint encryption and compression of 3D images based on tensor compressive sensing with non-autonomous 3D chaotic system. Multimed. Tools Appl. **77**(10), 1–20 (2017)
3. Alemazkoor, N., Meidani, H.: A near-optimal sampling strategy for sparse recovery of polynomial chaos expansions. J. Comput. Phys. **371,** 137–151 (2018)
4. Yu, H., Cao, G., Burk, L., Lee, Y., Lu, J., Santago, P., Zhou, O., Wang, G.: Compressive sampling based interior reconstruction for dynamic carbon nanotube micro-CT. J. X-ray Sci. Technol. **17**(4), 295–303 (2009)
5. Yu, L., et al.: Compressive sensing with chaotic sequence. IEEE Signal Process. Lett. **17**(8), 731–734 (2010)
6. Guo, J.B., Wang, R., Lab, S.K.: Construction of a circulant compressive measurement matrix based on chaotic sequence and RIPless theory. Acta Physica Sinica **63**(19), 198402–198402 (2014)
7. Bin, L., Yulou, P.: Composition algorithm for compressed sensing measurement matrix based on chaotic sequences. Comput. Eng. Appl. 49(23), 199–202 (2013) (in Chinese)
8. Parvaz, R., Zarebnia, M.: A combination chaotic system and application in color image encryption. Opt. Laser Technol. **101**, 30–41 (2018)
9. Zhang, X.F., Fan, J.L.: A new piecewise nonlinear chaotic map and its performance. Acta Physica Sinica **59**(4), 2298–2304 (2010)
10. Cong, L., Songgeng, S.: Correlation distribution of spreading sequences based on logistic maps. Chin. J. Electron. 140–141(1999) (in Chinese)

Salt and Pepper Noise Suppression for Medical Image by Using Non-local Homogenous Information

Hu Liang and Shengrong Zhao

Abstract In this paper, we propose a method to suppress salt and pepper noise for medical images based on the homogenous information obtained by non-symmetrical and anti-packing model (NAM). The NAM could divide the image into several homogenous blocks and it is sensitive to the additive extra energy. Thus the noise could be detected effectively due to the usage of bit-plane during the division. Then corrupted points are estimated by using a distance based weighted mean filter according to the homogenous information in its non-local region, which could keep local structure. Experimental results show that our method can obtain denoising results with high quality.

Keywords Medical image · Pepper and salt noise · Non-symmetry Anti-packing model

1 Introduction

With the development of computer networks and electronic management of medical records, medical images can be shared across the world. Thus, the data acquisition, transmission and exchange become frequent and common. However, the medical images are usually corrupted by salt and pepper noise, Gaussian noise, and Poisson noise in the process of image acquisition and transmission. Moreover, the digital watermarking has been widely used for medical images [1, 2], which could preserve the authenticity and integrity of the content of medical images. And in the watermarked images, salt and pepper noise is one of the common factors lowering and degenerating the image quality. The quality of medical images corrupted by the

H. Liang · S. Zhao (✉)
College of Information, Qilu University of Technology (Shandong Academy of Sciences), Jinan 250353, China
e-mail: zhaosr2006@126.com

H. Liang
e-mail: cvlianghu@gmail.com

H. Lu (ed.), *Cognitive Internet of Things: Frameworks, Tools and Applications*, Studies in Computational Intelligence 810,
https://doi.org/10.1007/978-3-030-04946-1_19

salt and pepper noise would be reduced significantly. Therefore, the salt and pepper noise in medical images should be suppressed, and a variety of algorithms for noise removing have been developed in the literature, such as [3–8].

Median filter [4] is the corner stone for salt-and-pepper noise removing due to its strong denoising ability and computational simplicity. Median filter use the local median value to instead of the noise point. However, some image details may be blurred by heavy noise [5]. At present, a series of methods have been proposed to improve and refine it over the years, such as, weighted median filtering [4, 6], central weighted median filtering [9], directional weighted median filtering [10], switching median filtering [11] and adaptive median filter [12], et al. One of the most important things in median filter is how to define the local region. Most commonly used method is to predefine a sliding window with a fixed size. By using this method, the local region usually contains inconsistent information and leaves consistent information out of the local region. The existing methods usually ignore the structure of the image inconsistency, including global structure inconsistency and local structure inconsistency. The information from different structure may provide very little help to recover corrupted points, even generating larger estimation error. Only using the information from the same structure, the closest estimation with less error would be found.

Inspired by idea that the salt and pepper noise could add impulse energy to the pixels randomly and the layout of the image is sensitive to the salt and pepper noise, we applied packing information to detect and remove this kind of noise. Firstly, the image is divided into blocks, where it owns the same structure by using NAM method. In this way, we can find the potential noise points automatically. Then a distance based method is used to estimate the corrupted points, which could keep consistency of local image structure. In the distance method, the corrupted points are computed by using the weighted average of the points which contains homogenous information. Experimental results on a series of images showed that the proposed method outperformed the comparisons in different noise density.

The rest of this paper is organized as follows. Section 2 describes the NAM in details. In Sect. 3, the new method based on NAM for removing salt and pepper noise is introduced. The implementation results and comparison are provided in Sect. 4. The conclusion is presented in Sect. 5.

2 Non-symmetry and Anti-packing Model

In this section, a brief review of NAM would be given, which is the basic of the denoising method proposed in this work. The quadtree [13] and the tetromino [14] are the widely used methods which can divide images into a number of specific, distinct regions, and these methods could divide images into symmetric blocks. Oppositely, the NAM method would divide images into asymmetric blocks.

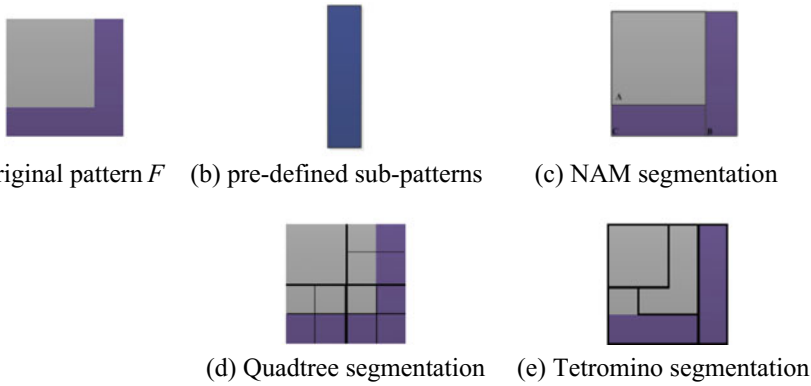

(a) original pattern F (b) pre-defined sub-patterns (c) NAM segmentation

(d) Quadtree segmentation (e) Tetromino segmentation

Fig. 1 A simple example of NAM quadtree and tetromino

Figure 1 shows a simple example to demonstrate the merit of NAM, Quadtree and Tetromino. Figure 1a presents a given packed pattern, Fig. 1b presents $N=1$ pre-defined sub-patterns, i.e., the rectangle sub-pattern. Figure 1c is the reconstructed pattern. In Fig. 1c, blocks A, B, C, are rectangle blocks and the total number of blocks obtained is $n=3$. For the rectangle block, the top-left point (x, y), length, L and width H are recorded, thus, $B=(a_1, a_2)$, where $a_1 =(x, y)$ and $a_2 =(L, H)$. Square is a special case of rectangle when $L=H$. Figure 1d and e are the segmentation results of Quadtree and Tetromino methods. Compared with NAM method, these two methods destroy the non-local consistency.

3 Salt and Pepper Noise Removing

Denote x is the original image and $x_{i,j}$ is the gray value of the image at location (i, j). According to characteristics of the salt and pepper noise, the following formulation can be used:

$$y_{i,j} = \begin{cases} 0, & p(0) = p_0/2 \\ 255, & p(255) = p_0/2 \\ x_{i,j}, & 1 - p_0 \end{cases} \tag{3}$$

where p_0 means noise probability density in location (i, j).

3.1 Noise Detection

The salt and pepper noise would destroy local coherence and original packing information as it adds impulse energy to the pixels randomly. By this, the relevance and the similarity in each one non-local region may be separated into several regions as the additive impulse energy stops the local similarity search. Thus, in our work, we detect the noisy points by using the NAM method based on the non-local consistency. In a medical image, pixels are supposed to change smoothly, and adjacent pixels tend to have similar values. For an image that is degraded by salt and pepper noise, the value of some pixels changed to 255 or 0 suddenly. Thus, the NAM method could detect the noise point.

In the following, taking the salt noise as an example, Fig. 2 briefly shows the noise detection process by using the NAM method. Figure 2a, e present two examples, and the pixel values of each example are 200 and 67, respectively. If the two examples are divided by the NAM method, only one block would be obtained for each example, as shown in Fig. 2c, g. Figure 2b and 2f present the images polluted by salt noise corresponding to (a) and (e) respectively. The division results are presented in Fig. 2d and 2h, respectively. The gray value of the salt noise is 255 as shown in Eq. 3, which is in the same bit-plane as Fig. 2a and in the different bit-plane from the points in Fig. 2e. Thus, in Fig. 2d, the noise point will be separated into the same block with the other points. And in Fig. 2h, the integrity of the homogeneous region is destroyed by the noise point.

As for the pepper noise, the gray value of which is 0. It belongs to the bit-plane [0, $2^{\circ} - 1$]. When the image is polluted by the pepper noise, the noise point (or points) will be isolated by a pre-defined pattern.

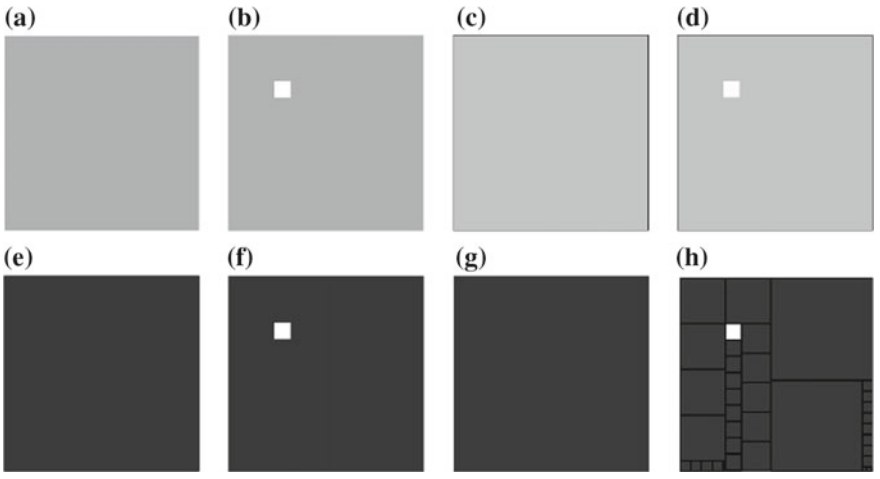

Fig. 2 A sample of NAM method sensitive to the noise point

In general, two kinds of points are supposed to be candidate noisy points: (1) in the segmented blocks, the point is of large difference with the neighborhood points and its gray value is 0 or 255; (2) The block just contains one kind of points and its gray value is 0 or 255.

Finally, a binary matrix S is used to record the location of the candidate noisy points, and

$$S_{i,j} = \begin{cases} 1, \ satisfy \\ 0, \ otherwise \end{cases} \tag{4}$$

where $S_{i,j}$ is the value of location (i, j) of binary matrix S. $S_{i,j} = 1$ means $y_{i,j}$ is possible salt and pepper noise point, and $S_{i,j=0}$ means $y_{i,j}$ is noiseless or recovered point.

3.2 Salt and Pepper Noise Suppression

Once the candidate noise points are recorded, next we have to restore these points. The corrupted points could be solved by using the points in its non-local block whose value is 0 in the matrix S or the points which have been filtered. In this way, the method can effectively and efficiently handle all the noise points and avoid the error caused by artificial threshold. Mathematically, for any block B, we use ξ to indicate whether the block contains noise points:

$$\xi = \sum_{p(u,v) \in B} S(u, v) \tag{5}$$

In Eq. 5, if $\xi = 0$, thus, no noise point is contained in the block. Otherwise, $\xi > 0$ indicates that the block B contains noise points. And the following three strategies are developed to estimate the corrupted points,

If $0 < \xi < N$ (N denotes the total number of pixels in block B) and the size of B is larger than 1, the noise-free points in the block are used to recover the noise point with the weight w. The weight depends on the distance between the noise point and the noise-free point, which means pixels far from the noise point have a smaller weight while others have a larger weight. Mathematically, it can be written as:

$$w_{p(k,l) \to p(m,n)} = \frac{1}{|k - m| + |l - n|}, where (k, l) \neq (m, n) \tag{6}$$

where, p(k, l) is a noise point, and $p(m, n)$ is a noise-free point.

If $\xi = N$ we only use its surrounding noise-free points in region R to recover this block in the following two cases: (1) the size of B is larger than 1, (2) the size of B is 1 * 1. Let $p(k, l)$ is the center of region R, and r is the radius. Enlarge r gradually until a point $p(m, n)$ is found. The point $p(m, n)$ is another unrecovered noise point or a point with sharp gradient changing. In the region R, find a bit-plain which contains

most noise-free and recovered points $BP = \max_k \{num_k = \text{count}(p(i,j)|p(i,j) \in R, k = 1, \ldots, 8)\}$. And the region composed by these points is denoted as follows:

$$P = \{p(i,j)|p(i,j) \in R, S(i,j) = 0, p(i,j) \in BP\} \tag{7}$$

In the found region, Eq. 6 is used to compute the weights of every point in set P. And the corrupted pixel could be estimated by:

$$\hat{x}_{k,l} = \frac{\sum_{k,l=1}^{r} S \otimes W \otimes \Omega}{\sum_{k,l=1}^{r} S \otimes W} \tag{8}$$

where W is the matrix of weights, $\otimes$ means the Hadamard product, S denotes indicator matrix, and Ω denotes the region used to recover the noise point. For the recovered points, the corresponding points in matrix S changed to 0.

4 Experimental Results

To evaluate the performance of the proposed method, a series of experiments are designed. In this section, we will compare the proposed method with some state-of-the-art methods, such as DBAIN [3], NAFSM [4], PSMF [7], and NFCA [8]. To show the performance of these methods, six medical images are used, which are shown in Fig. 3. We test the proposed method with the comparison methods with signal to noise ratio (SNR) level of 0.15, 0.2, 0.25, 0.3, 0.35, 0.4, and 0.45.

To evaluate the performance of the proposed method compared with the existing methods, peak signal-to-noise ratio (PSNR) and structural similarity (SSIM) and the

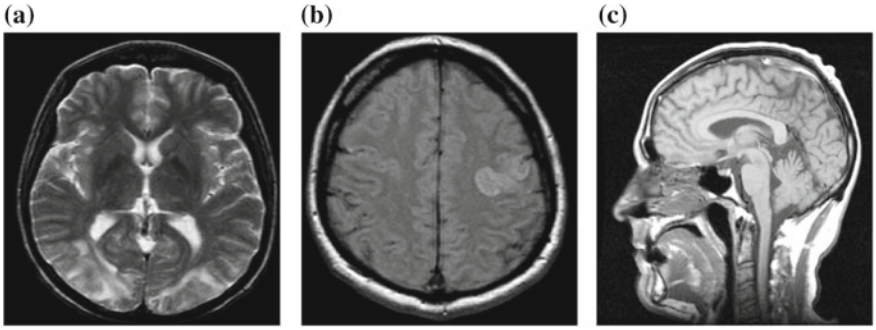

Fig. 3 The test medical images

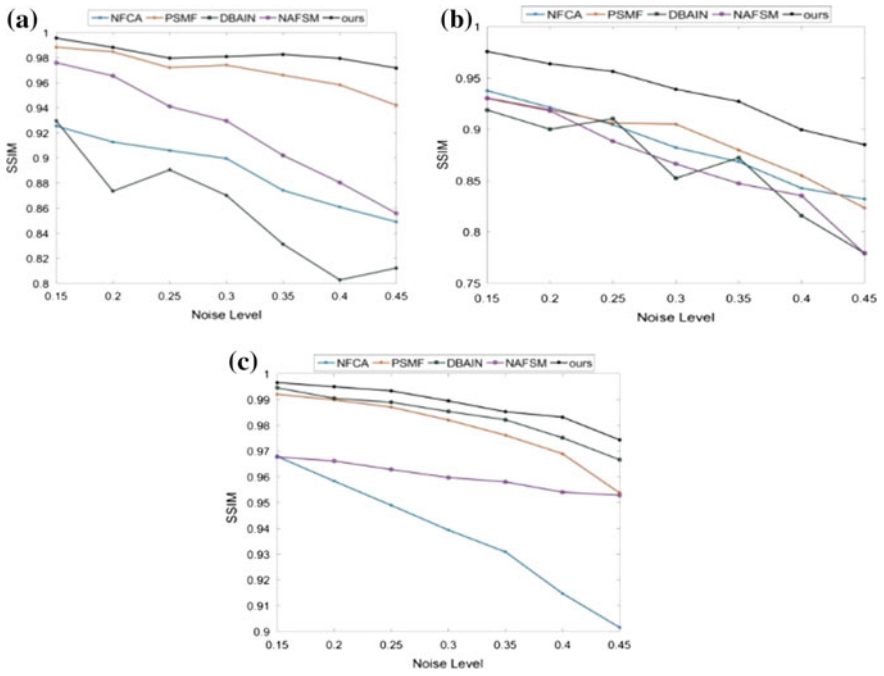

Fig. 4 SSIM for the test images presented in Fig. 4

error images between the reconstructed results and the original images are used to test the performance.

In Table 1, the PSNR values are compared with the existing methods under SNR = 0.15–0.45, respectively. According to its definition, the larger value of PSNR, the better the quality of the reconstructed image is. It is obvious that the performance of the proposed method is better than other algorithms. The corresponding SSIM values are shown in Fig. 4. Generally speaking, from low noise density (i.e. SNR = 0.15) to high noise density (SNR = 0.45), the SSIM and the PSNR values of all the methods are decreased.

In Figs. 5 and 6, the reconstructed images by using the NFCA and PSMF methods respectively still contain some salt and pepper noise. The artificial artifacts exist in the reconstructed images obtained by DBAIN method. The reconstructed images obtained by NAFSM and our proposed methods have removed noise obviously but still exist reconstruction errors.

Table 1 The PSNR results for the medical images presented in Fig. 3

SNR	Figure 3a					Figure 3b					Figure 3c				
	psmf	dbain	nafsm	NFCA	ours	psmf	dbain	nafsm	NFCA	ours	psmf	dbain	nafsm	NFCA	ours
0.15	28.94	20.95	25.37	18.77	**33.10**	20.7	19.82	20.48	23.54	**25.17**	28.10	29.71	22.36	26.87	**31.68**
0.20	27.70	18.28	23.56	18.41	**28.82**	20.06	18.91	19.91	22.51	**23.42**	27.03	27.33	22.00	26.10	**30.03**
0.25	25.05	18.96	21.97	18.57	**26.45**	19.36	19.42	18.81	22.27	**22.60**	25.97	26.68	21.55	25.11	**28.87**
0.30	25.41	18.19	20.98	18.44	**26.74**	19.26	17.15	18.10	**21.49**	21.13	24.53	25.49	21.27	24.72	**26.88**
0.35	24.2	14.72	19.86	18.07	**27.14**	18.2	17.88	17.62	**20.97**	20.33	23.3	24.62	21.03	24.18	**25.43**
0.40	23.28	16.2	18.69	17.90	**26.39**	17.3	16.21	17.16	**20.48**	18.95	22.16	23.21	20.71	23.91	**24.83**
0.45	21.79	16.50	18.02	17.8	**24.99**	16.40	15.4	15.88	**20.03**	18.30	20.39	21.94	20.41	**23.06**	23.00

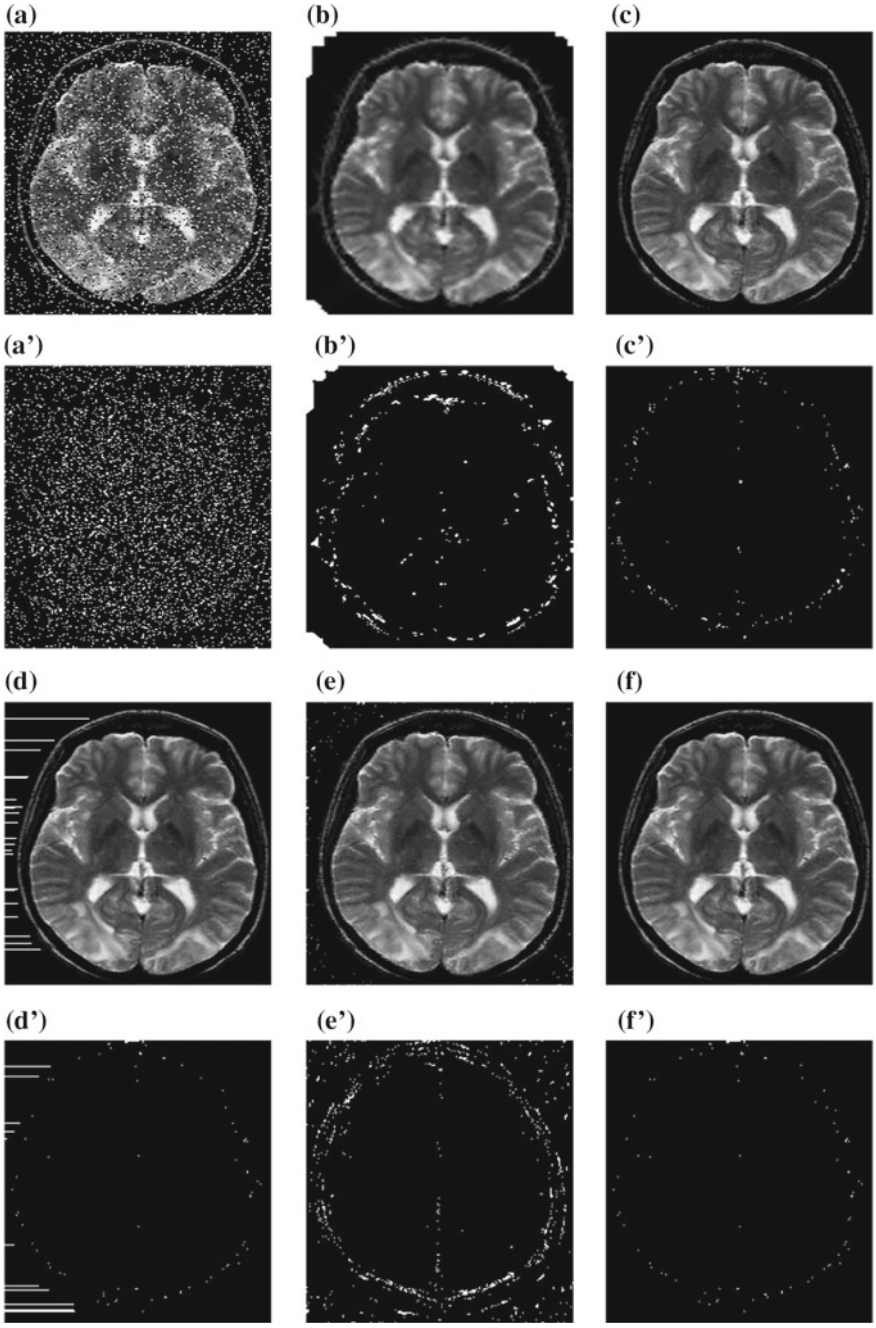

Fig. 5 The reconstructed image for Fig. 4a with SNR = 0.15. **a** Original noisy image; **b** NFCA method; **c** PSMF method; **d** DBAIN method; **e** NAFSM method; **f** ours. And $\mathbf{a}'$ to $\mathbf{f}'$ are corresponding error images

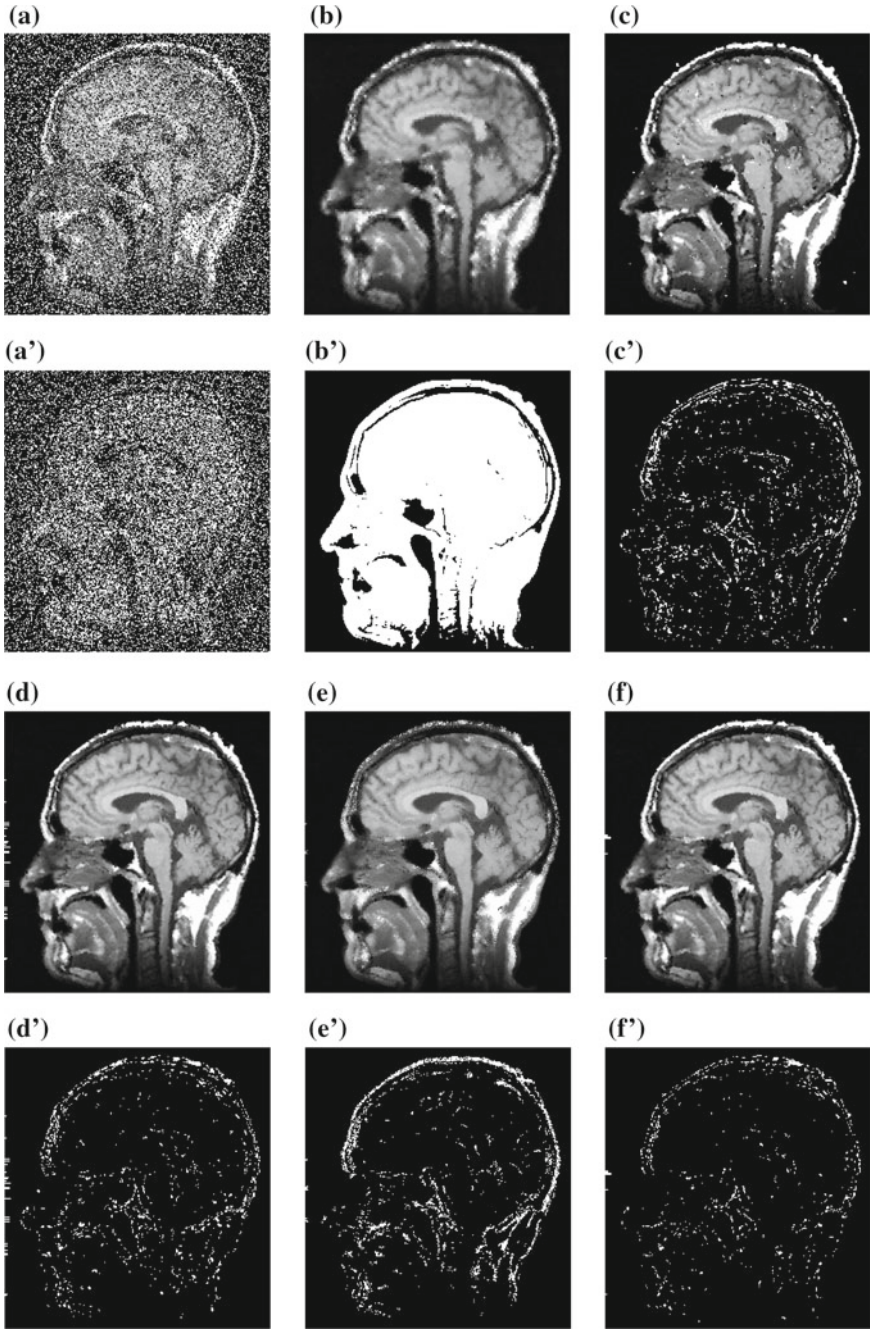

Fig. 6 The reconstructed image for Fig. 4c with SNR = 0.45. **a** original noisy image; **b** NFCA method; **c** PSMF method; **d** DBAIN method; **e** NAFSM method; **f** ours. And **a′** to **f′** are corresponding error images

5 Conclusion

In this paper, a novel salt and pepper noise removing method for medical images is proposed. The proposed method is a two-stage weighted mean filter method. In the first stage, the candidate noise points are detected and recorded. In the second stage, the corrupted points are recovered by a non-local region which contains points from the same structure. The experimental results on a series of medical images show that compared with several existing methods, the proposed method obtains better results.

Acknowledgements This work is supported by NSFC (No. 61802213) and Shandong Provincial Natural Science Found (No. ZR2017LF016, ZR2018LF004).

References

1. Serikawa, S., Lu, H.: Underwater image dehazing using joint trilateral filter. Comput. Electr. Eng. **40**(1), 41–50 (2014)
2. Lu, H., Li, Y., Mu, S., Wang, D., Kim, H., Serikawa, S.: Motor anomaly detection for unmanned aerial vehicles using reinforcement learning. IEEE Internet Things J. (2018). https://doi.org/10.1109/jiot.2017.2737479 (In Press)
3. Phophalia, A., Rajwade, A., Mitra, S.K.: Rough set based image denoising for brain MR images. Signal Process. **103**, 24–35 (2014)
4. Morillas, S., Gregori, V., Peris-Fajarnés, G., et al.: Local self-adaptive fuzzy filter for impulsive noise removal in color images. Signal Process. **88**(2), 390–398 (2008)
5. Chan, R.H., Ho, C.W., Nikolova, M.: Salt-and-pepper noise removal by median-type noise detectors and detail-preserving regularization. IEEE Trans. Image Process. **14**(10), 1479–1485 (2005)
6. Yli-Harja, O., Astola, J., Neuvo, Y.: Analysis of the properties of median and weighted median filters using threshold logic and stack filter representation. IEEE Trans. Signal Process. **39**, 395–410 (1991)
7. Liu, Y., Ma, Y., Liu, F., et al.: The research based on the genetic algorithm of wavelet image denoising threshold of medicine. J. Chem. Pharm. Res. **6**(6), 2458–2462 (2014)
8. Tourtounis, D., Mitianoudis, N., Sirakoulis, G.C.: Salt-n-pepper noise filtering using cellular automata. J. Cellu. Autom. **13**(1), 81–101 (2018)
9. Crnojević, V., Senk, V., Trpovski, Z.: Advanced impulse detection based on pixel-wise MAD. IEEE Signal Process. Lett. **11**(7), 589–592 (2004)
10. Dong, Y., Xu, S.: A new directional weighted median filter for removal of random-valued impulse noise. IEEE Signal Process. Lett. **14**(3), 193–196 (2007)
11. Wang, Z., Zhan, D.: Progressive switching median filter for the removal of impulse noise from highly corrupted images. IEEE Trans. Circuits Syst. II Analog Dig. Signal Process **46**(1), 78–80 (1999)
12. Hwang, H., Hadded, R.A.: Adaptive median filter: new algorithms and results. IEEE Trans. Image Process. **4**(4), 499–502 (1995)
13. Liang, H., Zhao, S.R., Chen, C.B., et al.: The NAMlet transform: a novel image sparse representation method based on non-symmetry and anti-packing model. Signal Process. **137**, 251–263 (2017)
14. Krommweh, J.: Tetrolet transform: a new adaptive haar wavelet algorithm for sparse image representation. J. Vis. Commun. Image Represent. **21**(4), 364–374 (2010)

Saliency Detection via Objectness Transferring

Quan Zhou, Yawen Fan, Weihua Ou and Huimin Lu

Abstract In this paper, we present a novel framework to incorporate top-down guidance to identify salient objects. The salient regions/objects are predicted by transferring objectness prior without the requirement of center-biased assumption. The proposed framework consists of the following two basic steps: In the top-down process, we create a location saliency map (LSM), which can be identified by a set of overlapping windows likely to cover salient objects. The corresponding binary segmentation masks of training windows are treated as high-level knowledge to be transferred to the test image windows, which may share visual similarity with training windows. In the bottom-up process, a multi-layer segmentation framework is employed, providing local shape information that is used to delineate accurate object boundaries. Through integrating top-down objectness priors and bottom-up image representation, our approach is able to produce an accurate pixel-wise saliency map. Extensive experiments show that our approach achieves the state-of-the-art results over MSRA 1000 dataset.

Keywords Salient object detection · Objectness priors · Location saliency map Multi-layer segmentation

Q. Zhou (✉) · Y. Fan
National Engineering Research Center of Communications and Networking, Nanjing University of Posts & Telecommunications, Nanjing, People's Republic of China
e-mail: quan.zhou@njupt.edu.cn

Q. Zhou
State Key Lab. for Novel Software Technology, Nanjing University, Nanjing, People's Republic of China

W. Ou
School of Big Data and Computer Science, Guizhou Normal University, Guiyang, People's Republic of China

H. Lu
Department of Mechanical and Control Engineering, Kyushu Institute of Technology, Kitakyushu, Japan

H. Lu (ed.), *Cognitive Internet of Things: Frameworks, Tools and Applications*, Studies in Computational Intelligence 810,
https://doi.org/10.1007/978-3-030-04946-1_20

1 Introduction

The human visual system (HVS) has an outstanding ability to quickly detect the most interesting regions in a given scene. In last few decades, the highly effective attention mechanisms of HVS have been extensively studied by researchers in the fields of physiology, psychology, neural systems, image processing, and computer vision [1–8]. The computational modeling of HVS enables various vision applications, e.g., object detection/recognition [9, 10], image matching [8, 11], image segmentation [12], and video tracking [13].

Visual saliency can be viewed from different perspectives. Top-down (supervised) and bottom-up (unsupervised) are two typical categories. The first category often describes the saliency by the visual knowledge constructed from the training process, and then uses such knowledge for saliency detection on the test images [14, 15]. Based on the biological evidence that the human visual attention is often attracted to the image center [16], the center-biased assumption is often employed as the location prior for estimating visual saliency in top-down models [15, 17]. While the salient regions are mostly located in the image center, the inverse might not necessarily be true [18, 19]. Not all image center regions tend to be more salient. The salient object might be located far away from image center, even on the image boundary. Furthermore, a center-biased assumption always supposes that there is only one salient object within each image, yet it often fails when nature image contains two or more salient objects [18]. Thus, to detect salient regions without center-biased constrains, some semantic knowledge (e.g., face and pedestrian) are integrated in a top-down process, which is mostly based on object detectors [14, 17, 20]. The integration, however, acts rather more general on object category level than at the saliency-map level.

In this paper, we propose a novel method to integrate bottom-up, lower-level features and top-down, higher-level priors for salient object detection. Our approach is fully automatic and requires no center-biased assumption. The key idea of our top-down process is inspired by Kuettel and Ferrari [22], where the binary segmentation masks are treated as prior information to be transferred from the supervised training image set to the testing image set. Then, the transferred segmentation masks are used to derive specific location prior of salient object in the test image. Figure 1 illustrates the overview of our method. The basic intuition is that the windows with similar visual appearance often share similar binary segmentation masks. Since these transferred windows exhibit less visual variability than the whole scenes and are often centered on the salient regions, they are much suitable for location transfer with better support regions. As a result, we utilize the method of [9] to extract candidate windows that are likely to contain salient objects, and then transfer training window segmentation masks that share visual similarity to windows in the test image. In spite of providing location prior using LSM, object shapes are always not well preserved, where the delineated object boundaries are often required for salient object detection. In order to automatically abstract accurate shape and boundary for salient object, we employ the multi-layer over-segmentation framework based on low-level image stimuli features.

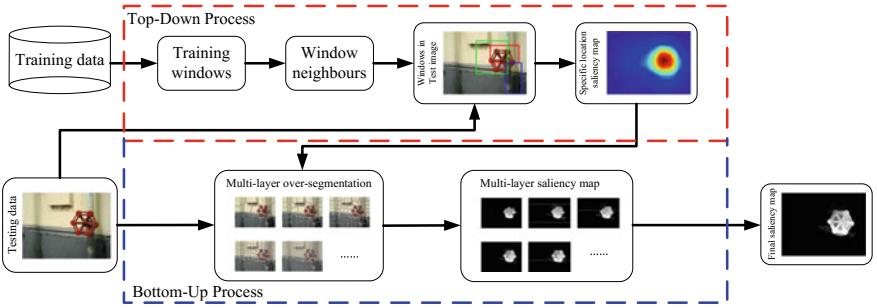

Fig. 1 Our approach consists of two components: (1) Top-down process. Given the training data consists of images with annotated binary segmentation masks, we first employ the technique of [9] to detect windows likely to contain salient objects on all training images and testing images. Then the binary segmentation masks of training windows are transferred to each detective windows in testing image with the most similar appearance (window neighbours). The transferred segmentation masks are used to derive the location saliency map (LSM); (2) Bottom-up process. Using the over-segmentation technique of [21], an input testing image is first partitioned to multi-layer segmentation in a coarse to fine manner. Given the prior information of LSM, a saliency map is produced for each layer of segmentation. These saliency maps are finally integrated to a pixel-accurate saliency map (Best viewed in color)

The representation of multi-layer segmentation provides a large amount of region candidates within different sizes and scales, which are complement each other to get more reliable predictions for object shapes. The contributions of our approach are two-fold: (1) In the top-down process, it proposes a specific location prior for salient object detection. Through window mask transferring, our method is able to provide more accurate location prior to detect salient regions, which results in more accurate and reliable saliency maps than the models using center-biased assumptions, such as [16, 17]; (2) Compared with most competitive models [2, 14, 17, 19, 23–29], our method achieves the state-of-the-art results over MSRA 1000 dataset.

2 Our Approach

In this section, we elaborate on the details of our method. We first introduce how to obtain the location saliency map (LSM) by transferring window masks, and then elaborate on the details of using multi-layer over-segmentations to refine delineate salient object shape and boundaries.

2.1 Location Saliency Map (LSM)

Finding Similar Windows. In order to utilize the prior knowledge of annotated binary segmentation mask in the training set, we first detect windows likely to contain

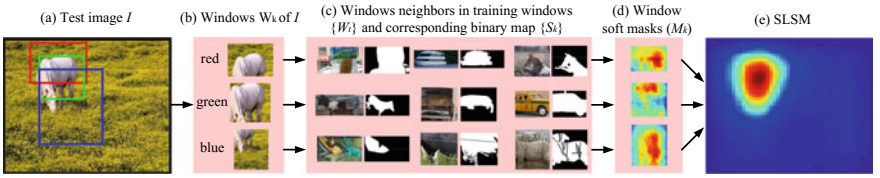

Fig. 2 An example of the full pipeline for producing LSM. Given a test image I in (**a**), three top windows (denoted as red, green and blue rectangles) are highlighted out of $\mathcal{N}$ windows, as shown in (**b**). The window neighbors are displayed in (**c**). It is shown that green window is tightly centered on an object and gets very good neighbors, while for red and blue windows, the neighbors are good matches for transferring segmentation mask, even though these windows do not cover the "horse" perfectly. This results in an accurate transfer mask for each window of I, as illustrated in (**d**). On the rightmost column of (**e**), we integrate the soft mask M_k from all windows into a soft mask for the whole scene, which is used to derive the LSM. Note blue color denotes low saliency, while red color represents high saliency (Best viewed in color)

an object using the "objectness" technique of [9]. It tends to return more windows covering an object with a well-defined boundary, rather than amorphous background elements. In our experiments, sampling only $\mathcal{N}$ windows per image (e.g., $\mathcal{N} = 100$) seems enough to cover most salient objects. Putting all the training windows together, we obtain the training window set $\{W_t\}$. This leads to retrieving much better neighborhood windows with similar appearance, whose segmentation masks are more suitable to transfer for test image. Given a new test image I as illustrated in Fig. 2a, the $\mathcal{N}$ number of "objectness" windows are also extracted using [9] as well as for the training images. Figure 2b shows top three "objectness" windows in the test image I, and it is observed that many detective windows are centered on the salient object "horse". For one specific test window $W_k, k = \{1, 2, \ldots, \mathcal{N}\}$, we compute GIST feature [30] inside W_k to describe its appearance, and compare GIST descriptors with the ℓ^2-norm distance to all training windows $\{W_t\}$ to find window neighbors. Thus, the set $\{S_k^j\}$, $j = \{1, 2, \ldots, \mathcal{M}\}$ containing the segmentation masks of the top $\mathcal{M}$ training windows most similar to W_k is used for transferring. Figure 2c illustrates that the nearest neighbor windows accurately depict similar animals in similar poses, resulting in well-matched binary segmentation masks.

Segmentation Transfer. Let $S_T(x, y)$ be the LSM, which defines the probability of pixel at location (x, y) to be salient. We construct $S_T(x, y)$ for each pixel from the segmentation masks transferred from all windows containing it.

(1) Soft masks for windows. For the kth test window W_k, we have a set of binary segmentation masks $\{S_k^j\}$ of neighbor windows from the training set. Here we compute a soft segmentation mask M_k for each W_k as the pixel-wise mean of the masks in $\{S_k^j\}$. To this end, all masks in $\{S_k^j\}$ are resized to the resolution of W_k. Let $\{S_k^{j'}\}$ be the resized masks, then the soft mask M_k for window W_k is defined as:

$$M_k = \frac{1}{\mathcal{M}} \sum_{j'=1}^{\mathcal{M}} S_k^{j'} \tag{1}$$

In this aligned space, a pixel value in M_k corresponds to the probability for it to be a salient object in $\{S_k^{j'}\}$. Figure 2d shows the corresponding M_k for the detected windows. Note the resolution of each soft window mask M_k is the same as the one of detected window in Fig. 2b.

(2) Soft mask for the test image. After obtaining soft masks M_k, we integrate M_k for all windows into a single soft segmentation mask $M(x, y)$ for the test image I. For each window W_k, we place its soft mask M_k at the image location (x, y) defined by W_k. The soft mask $M(x, y)$ of the test image is the pixel-wise mean of all $\mathcal{N}$ placed masks $M_k(x, y)$:

$$M(x, y) = \frac{1}{\mathcal{N}} \sum_{k=1}^{\mathcal{N}} M_k(x, y) \tag{2}$$

A pixel value in $M(x, y)$ is the probability for it to be salient, according to all transferred segmentations (as illustrated in Fig. 2d). Therefore, we define the LSM $S_T(x, y)$ as

$$S_T(x, y) = M(x, y) \tag{3}$$

Due to the integration of all soft segmentation masks $M_k(x, y)$ from the individual windows, our approach achieves even more robust results. The key step of our approach is that we extract many windows (e.g., 100 per image) overlapping salient object. One effect is that a certain window might not have good neighbors in the training set, leading to transferring an inaccurate or even completely incorrect mask $M_k(x, y)$. However, other overlapping windows will probably have good neighbors, diminishing the effect of the inaccurate $M_k(x, y)$ in the integration step. Another effect may happen when the transferred windows may not cover a salient object, (e.g., detecting a patch on the backgrounds, as the blue window shown in Fig. 1). This does not pose a problem to our approach, as the training images are decomposed in the same type of windows [9]. Therefore, a background window will probably also has similar appearance neighbors on backgrounds in the training images, resulting in correctly transferring a background binary segmentation mask. As a result, our approach is fully symmetric over salient and background windows. Figure 3 exhibits some LSMs of nature images over MSRA 1000 dataset.

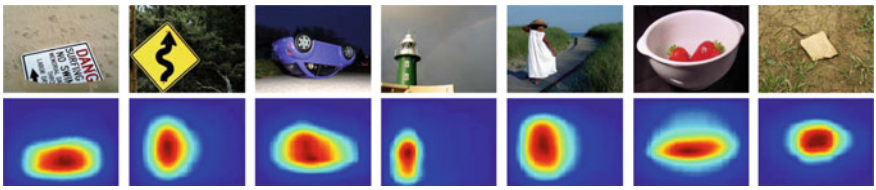

Fig. 3 Illustration of LSM on MSRA 1000 dataset. The blue color denotes low saliency, while red color represents high saliency (Best viewed in color)

2.2 *Saliency Refinement*

As shown in Fig. 3, LSM is able to estimate the rough location of salient object, yet it achieves poor results on object shape and delineated boundaries. To solve this problem, we employ the image representation of superpixels as units for saliency refinement. A superpixel is a group of neighboring pixels that are similar in visual appearance (e.g., color and texture) and is often obtained by clustering pixels based on low-level visual similarity. Superpixels are beneficial by encoding shape information, as they naturally reflect a low-level image structure such as object boundary [31, 32].

Multi-layer Segmentation. In order to make full use of superpixels with different sizes and scales, we employ the multi-layer segmentation framework. Traditionally, an image is typically represented by a two-dimensional array of RGB pixels. With no prior knowledge of how to group these pixels, we can compute only local cues, such as pixel colors, intensities or responses to convolution with bank of filters [33, 34]. Alternatively, we use the SLIC algorithm [21] to implement over-segmentation, since it performs more efficiently. In practice, we partition test image I into J layers of segmentations. There are two parameters to be tuned for this segmentation algorithm, namely (rgnSize, regularizer), which denote the number of segments used for over-segmentation and the trade-off appearance for spatial regularity, respectively. As shown in Fig. 4, the advantages of using this technique are that it can often group the homogeneous regions with similar appearance and preserve the true boundary of objects.

Multi-layer Saliency Integration. Denote $S_j(x, y)$ be the saliency map for the jth segmentation layer of a test image, so that $S_j(x, y)$ also gives the probability of pixel at location (x, y) to be salient. With the guidance of LSM, we construct $S_j(x, y)$ for each pixel from the segmentation results via the partitioned superpixels containing it.

Fig. 4 Image representation by multi-layer segmentation. From left to right are the original images and their over-segmentation results in a coarse to fine manner. Different segments are separated by white boundaries

(1) Saliency Refinement by the supervision of LSM. Let $r_{ij}(x, y)$ be the ith superpixel in jth layer of segmentation after performing [21]. According to the LSM, we utilize the mean probability score of all contained pixels to measure how $r_{ij}(x, y)$ is distinct with respect to the entire image, then the saliency $S_{ij}(x, y)$ of $r_{ij}(x, y)$ is defined as:

$$S_{ij}(x, y) = \frac{1}{|r_{ij}(x, y)|} \sum_{(x,y)\in r_{ij}(x,y)} S_T(x, y) \tag{4}$$

where $|r_{ij}(x, y)|$ denotes the total number of pixels contained in $r_{ij}(x, y)$. Collecting all superpixels in jth segmentation layer, the $S_o^j(x, y)$ is constructed as follows:

$$S_j(x, y) = \bigcup_i S_{ij}(x, y) \tag{5}$$

where $S_j(x, y)$ is normalized among all pixels to a fixed range [0, 1].

(2) Saliency Combination for testing image. We now incorporate the $S_j(x, y)$ for all segmentation layers into a single saliency map for the test image I. Then the final saliency map $S(x, y)$ is defined as:

$$S(x, y) = \frac{1}{J} \sum_{j=1}^{J} S_j(x, y) \tag{6}$$

where $S(x, y)$ is also normalized to a fixed range [0, 1].

3 Experimental Results

To validate our proposed method, we carried out several experiments on MSRA 1000 dataset using the Precision-Recall curve and F-measure [24, 25]. The MSRA 1000 dataset [24] is the most widely used and as baseline benchmark for evaluating salient object detection models. It contains 1000 images with resolution of approximate 400×300 or 300×400 pixels, which only have one salient object per image and provides accurate object-contour-based ground truth.

Baselines. To show the advantages of our method, we selected 12 state-of-the-art models as baselines for comparison, which are spectral residual saliency (SR [26]), spatiotemporal cues (LC [29]), visual attention measure (IT [2]), graph-based saliency (GB [27]), frequency-tuned saliency (FT [24]), salient region detection (AC [23]), context-aware saliency (CA [14]), global-contrast saliency (HC and RC [25]), saliency filter (SF [28]), low rank matrix recovery (LR [17]), and geodesic saliency (SP [19]). In practice, we implemented all the 12 state-of-the-art models using a Dual Core 2.6 GHz machine with 4 GB memory over two datasets to generate saliency maps.

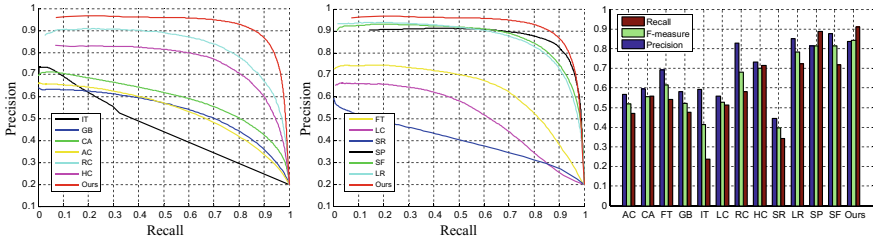

Fig. 5 Quantitative comparison for all algorithms with naive thresholding of saliency maps using 1000 publicly available benchmark images. Left and middle: PRC of our method compared with CA [14], AC [23], IT [2], LC [29], SR [26], GB [27], SF [28], LR [17], FT [24], SP [19], HC and RC [25]. Right: Average precision, recall and F-measure with adaptive-thresholding segmentation. Our method shows high precision, recall, and F_β values on the MSRA 1000 dataset (Best viewed in color)

Implemented Details. In order to make our approach work well, we employ the full PASCAL VOC 2006 [35] as our training dataset, since it includes more than 5000 images with accurate annotated object-contour-based ground truth. The parameter settings are: $\mathcal{N} = 100$ for sampling windows per image, $\mathcal{M} = 100$ for window neighbors for one sampling window, $J = 5$ for segmentation layers in a coarse to fine manner, (rgnSize, regularizer) are initialized as $\{25, 10\}$, and rgnSize is updated as $\{25, 50, 100, 200, 400\}$ with fixed regularizer.

Overall Results. The average PRC and F-measure on MSRA 1000 dataset are illustrated in Fig. 5. It clearly shows that our method outperforms other approaches. It is interesting to note that the minimum recall value of our methods starts from 0.08, and the corresponding precision is higher than those of the other methods, probably because the saliency maps computed by our methods contain more pixels with the saliency value 255. The improvement of recall over other methods is more significant, which means our method are likely to detect more salient regions, while keeping a high accuracy. Figure 5 also reports the comparison results in terms of F-measure. Our method achieves the state-of-the-art results and higher F-measure value (ours = 0.84) than other competitive models (SF = 0.82, LR = 0.78, RC = 0.69, and HC = 0.70), which clearly shows the validity of our approach in the case of more than one salient object within each image. Visual comparison with different methods on MSRA 1000 dataset are shown in Fig. 6. Compared with other models, our method is very effective in eliminating the cluttered backgrounds, and uniformly highlighted salient regions with well-defined object shapes, no matter whether salient objects locate in image center, or far away from image center, even on the image boundary.

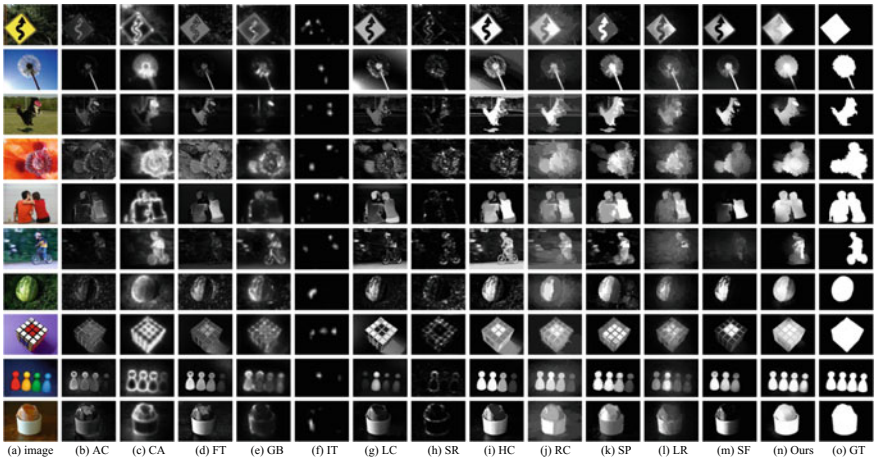

Fig. 6 Visual comparison of previous approaches with our method. See the legend of Fig. 5 for the references to all methods

4 Conclusion and Future Work

In this paper, we propose a novel framework for salient object detection using location information as top-down prior by transferring segmentation masks from windows in the training images that are visually similar to windows in the test image. Compared with existing competitive models, the extensive experiments show that our approach achieves the state-of-the-art results over MSRA 1000 dataset. In the future, there are two areas that we would like to improve upon. The first one is incorporating bottom-up contrast measures to further improve the performance. We are also interested in extending our model to predict region saliency in spatio-temporal domain (e.g., video sequence).

Acknowledgements This work was partly supported by the National Natural Science Foundation of China (Grant No. 61876093, 61881240048, 61571240, 61501247, 61501259, 61671253, 61762021), Natural Science Foundation of Jiangsu Province (Grant No. BK20181393, BK20150849, BK20160908), Huawei Innovation Research Program (HIRP2018), and Natural Science Foundation of Guizhou Province (Grant No. [2017]1130).

References

1. Borji, A., Tavakoli, H.R., Sihite, D.N., Itti, L.: Analysis of scores, datasets, and models in visual saliency prediction. In: CVPR, pp. 921–928 (2013)
2. Itti, L., Koch, C., Niebur, E.: A model of saliency-based visual attention for rapid scene analysis. TPAMI **20**(11), 1254–1259 (1998)
3. Jiang, H., Wang, J., Yuan, Z., Wu, Y., Zheng, N., Li, S.: Salient object detection: a discriminative regional feature integration approach. In: CVPR, pp. 2083–2090 (2013)

4. Li, X., Lu, H., Zhang, L., Ruan, X., Yang, M.H.: Saliency detection via dense and sparse reconstruction. In: ICCV (2013)
5. Marchesotti, L., Cifarelli, C., Csurka, G.: A framework for visual saliency detection with applications to image thumbnailing. In: ICCV, pp. 2232–2239 (2009)
6. Yan, Q., Xu, L., Shi, J., Jia, J.: Hierarchical saliency detection. In: CVPR, pp. 1155–1162 (2013)
7. Yang, C., Zhang, L., Lu, H., Ruan, X., Yang, M.H.: Saliency detection via graph-based manifold ranking. In: CVPR, pp. 3166–3173 (2013)
8. Zhao, R., Ouyang, W., Wang, X.: Person re-identification by salience matching. In: ICCV, pp. 73–80 (2013)
9. Alexe, B., Deselaers, T., Ferrari, V.: What is an object? In: CVPR. pp. 73–80 (2010)
10. Gao, D., Han, S., Vasconcelos, N.: Discriminant saliency, the detection of suspicious coincidences, and applications to visual recognition. TPAMI **31**(6), 989–1005 (2009)
11. Toshev, A., Shi, J., Daniilidis, K.: Image matching via saliency region correspondences. In: CVPR, pp. 1–8 (2007)
12. Jung, C., Kim, C.: A unified spectral-domain approach for saliency detection and its application to automatic object segmentation. TIP **21**(3), 1272–1283 (2012)
13. Mahadevan, V., Vasconcelos, N.: Saliency-based discriminant tracking. In: CVPR, pp. 1007–1013 (2009)
14. Goferman, S., Zelnik-Manor, L., Tal, A.: Context-aware saliency detection. In: CVPR, pp. 2376–2383 (2010)
15. Liu, T., Yuan, Z., Sun, J., Wang, J., Zheng, N., Tang, X., Shum, H.: Learning to detect a salient object. TPAMI **33**(2), 353–367 (2011)
16. Tatler, B.: The central fixation bias in scene viewing: selecting an optimal viewing position independently of motor biases and image feature distributions. J. Vision **7**(14), 1–17 (2007)
17. Shen, X., Wu, Y.: A unified approach to salient object detection via low rank matrix recovery. In: CVPR, pp. 853–860 (2012)
18. Borji, A., Sihite, D.N., Itti, L.: Salient object detection: A benchmark. In: ECCV, pp. 414–429 (2012)
19. Wei, Y., Wen, F., Zhu, W., Sun, J.: Geodesic saliency using background priors. In: ECCV (2012)
20. Judd, T., Ehinger, K., Durand, F., Torralba, A.: Learning to predict where humans look. In: ICCV, pp. 2106–2113 (2009)
21. Achanta, R., Shaji, A., Smith, K., Lucchi, A., Fua, P., Süsstrunk, S.: SLIC superpixels. EPEL, Tech. Rep 149300 (2010)
22. Kuettel, D., Ferrari, V.: Figure-ground segmentation by transferring window masks. In: CVPR, pp. 558–565 (2012)
23. Achanta, R., Estrada, F., Wils, P., Susstrunk, S.: Salient region detection and segmentation. Comput. Vision Syst. 66–75 (2008)
24. Achanta, R., Hemami, S., Estrada, F., Susstrunk, S.: Frequency-tuned salient region detection. In: CVPR, pp. 1597–1604 (2009)
25. Cheng, M., Zhang, G., Mitra, N., Huang, X., Hu, S.: Global contrast based salient region detection. In: CVPR, pp. 409–416 (2011)
26. Hou, X., Zhang, L.: Saliency detection: a spectral residual approach. In: CVPR, pp. 1–8 (2007)
27. Harel, J., Koch, C., Perona, P.: Graph-based visual saliency. In: NIPS, pp. 545–552 (2006)
28. Perazzi, F., Krahenbuhl, P., Pritch, Y., Hornung, A.: Saliency filters: Contrast based filtering for salient region detection. In: CVPR, pp. 733–740 (2012)
29. Zhai, Y., Shah, M.: Visual attention detection in video sequences using spatiotemporal cues. In: ACMMM, pp. 815–824 (2006)
30. Oliva, A., Torralba, A.: Modeling the shape of the scene: a holistic representation of the spatial envelope. IJCV **42**(3), 145–175 (2001)
31. Wang, J., Lu, H., Li, X., Tong, N., Liu, W.: Saliency detection via background and foreground seed selection. Neurocomputing **152**, 359–368 (2015)
32. Zhou, Q.: Object-based attention: saliency detection using contrast via background prototypes. EL **50**(14), 997–999 (2014)

33. Comaniciu, D., Meer, P.: Mean shift: a robust approach toward feature space analysis. TPAMI **24**(5), 603–619 (2002)
34. Shi, J., Malik, J.: Normalized cuts and image segmentation. TPAMI **22**(8), 888–905 (2000)
35. Everingham, M., Zisserman, A., Williams, C.K.I., Van Gool, L.: The PASCAL visual object classes challenge 2006 (VOC2006) results. http://www.pascal-network.org/challenges/VOC/voc2006/results.pdf

A Target Detection-Based Milestone Event Time Identification Method

Zonglei Lu and Tingting Ji

Abstract The flight and departure time nodes for the port and departure flights yield important information about the cooperative decision system of an airport. However, at present, because it would affect normal flight management, airports cannot obtain these data by technical means. By installing a camera on the airport apron and employing a regional convolutional neural network model to identify the targets in the video, such as the aircraft, staff, and working vehicle, the times of the milestone events were determined according to the identified changes in the target shape and target motion state. Furthermore, prior knowledge on the plane gliding curve and ground support operations was obtained by implementing the least squares method to fit the plane gliding curve, and subsequently used to compensate for the occlusion-induced recognition error and enhance the robustness of the algorithm. It was experimentally verified that the proposed target detection-based milestone event time recognition method is able to identify the flight times during the over-station, plane entry, and the milestone launch event.

Keywords Target detection · Regional convolutional neural network
Least squares method · Prior knowledge

Z. Lu (✉) · T. Ji
College of Computer Science and Technology, Civil Aviation University of China, Tianjin, China
e-mail: zllv@cauc.edu.cn

T. Ji
e-mail: ttji@cauc.edu.cn

Z. Lu · T. Ji
Information Technology Research Base of Civil Aviation Administration of China, Civil Aviation University of China, Tianjin, China

H. Lu (ed.), *Cognitive Internet of Things: Frameworks, Tools and Applications*, Studies in Computational Intelligence 810,
https://doi.org/10.1007/978-3-030-04946-1_21

1 Introduction

In recent years, many people have begun to pay more attention to flight delays and their causes, such as bad weather, improper management of airlines, and air traffic control. The statistics on civil aviation flight normality issued by the Civil Aviation Bureau offers insight into the flight regularity of commercial flights to accurately, promptly, and comprehensively reflect the actual flight conditions, and to provide a reference that various departments can use to make important decisions related to the construction of development planning and related policies and regulations. Aircraft entry time and launch time are important parameters that are used to determine flight regularity. Although the airport cooperative decision-making system requires that all airports realize data sharing, there are still various types of data in the system that cannot be obtained, such as aircraft entry time and launch time. Because, at present, airports cannot obtain these types of data via technical means, deep learning and computer vision theories, in addition to comprehensive prior knowledge of the times of the airport milestone events, were utilized in this study to enable automatic data acquirement via the airport camera.

Deep learning is a branch of machine learning that has become a popular research topic in recent years as major breakthroughs have been achieved [1–5]. A new visual reference mark purposed for implementation in automatic identification applications has been introduced [6]. In 2006, Hinton and Salakhutdinov published an article [7] in Science on the idea of learning in neural networks. Carbonneau et al. [8] provided a comprehensive overview of the problems that can be solved with deep learning.

The application of computer vision technology in airport operation management has the potential to increase the efficiency of all airport service operations. Thus, domestic and international airports have recently begun working toward the development of an "intelligent airport," as all airports currently regularly implement some form of artificial intelligence (AI), which has been shown to be highly effective at promoting the travel experiences of passengers, enhancing security measures, improving the level of service, and improving the efficiency of innovation management. In particular, computer vision technology is implemented in various domestic airports to reduce the repetitive service work of airport staff and increase efficiency and the level of airport safety. To date, many innovative airports have already attempted water trials in all aspects, hoping to realize the intelligent operation of airports through AI technology. For example, Yinchuan airport and Xianyang airport in China have begun implementing such functional applications as dynamic control of the terminal building, witness verification of the security inspection port, identification of the members of the VIP room, intelligent navigation display, intelligent scheduling, and brush face boarding.

In the early 1960s, Hubel and Wiesel proposed the concept of receptive fields [9] through the study of the cat visual cortex, and provided deeper insight into the mechanism of layered processing of information in the visual cortex pathway. By the middle of the 1980s, Fukushima and Miyake [10] performed a study on pattern recognition based on the concept of receptive fields; this has been regarded as the first realization

of convolutional neural networks (CNNs). Subsequently, a study [11] focusing on the ability of deep CNNs to self-learn features was performed to demonstrate that deep CNNs can be effectively used for image annotation. Moreover, they focused on three aspects of the deep convolution feature, i.e., single-label tagging, multi-label tagging, and multi-feature fusion tagging, to develop a deep convolutional feature-learning method based on migration learning. The image restoration method and image enhancement method based on the deep CNN proposed in [12] were able to significantly reduce image blurring and uneven illumination in the image. Romanuke [13] carried out a study on the proper distribution of the pool layer in CNNs, and consequently formulated the best allocation rules for the maximum pool merging layer. Additionally, Havaei et al. [14] proposed an image segmentation method based on the concept of a deep neural network (DNS).

In this study, an efficient information collection system that can effectively supplement the missing data in the collaborative decision-making system of the airport was developed by using a regional CNN. Generally, when the ground support operations of an airport are not sufficient, full and timely command and dispatch must be implemented, the impact of emergencies must be effectively controlled, and the efficiency of the emergency response must be optimized. The ground support operations of an airport entail recording each task throughout the entire process via a video monitoring system, issuing a timely warning to the operations that do not conform to the operation standard, and building a protective wall to ensure safe operation.

2 Related Works

A CNN has a feature extractor that is composed of a volume layer and subsampling level, and neurons in the convolutional layer are only connected to neurons in an adjacent layer. The coiling layer usually contains a number of feature planes (featureMap), each of which comprises a number of neurons arranged in a rectangle; the neurons of a single feature plane share the same weights, and these weights are the convolution kernels, which are generally initialized in the form of a random decimal matrix. As the network is trained, a more reasonable weight is applied to each convolution kernel. Direct advantages of implementing shared weights (convolution kernel) are as follows: fewer connections between the layers of the network, and reduced risk of overfitting.

Subsampling is also referred to as pooling, and it typically has two forms: mean subsampling (mean pooling) and maximum subsampling (max pooling). Subsampling can be regarded as a special convolution process. Convolution and subsampling considerably simplify the complexity of the model and reduce the number of model parameters. The regional CNN (i.e., regions with CNN features, R-CNN) was proposed in 2014. The R-CNN requires that the candidate region be classified; next, each candidate region is input into the CNN to extract the features; these features are then input into a linear support vector machine (SVM). The line is classified. In this study, in order to increase positioning accuracy, a linear regression model

was also incorporated into an regional CNN, which modifies the candidate region coordinates. The CNN model was able to yield an average mean correct rate that is approximately 20% higher than that obtained via a conventional algorithm trained on the object detection data set of Pascal VOC, which uses a CNN to form the basis of the model structure as based on the object detection data. The area-CNN is a CNN that is based on target detection. The input to the R-CNN is an image, and the output is the type and position of the target in the image. Additionally, the R-CNN training process is carried out as follows:

1. Use Selective Search (SS) to find 2,000 candidate regions in each image. The scale and aspect ratio for each candidate region are adjusted to match the specifications of the image input into the CNN.
2. Implement Alexnet or VGGnet to initialize the CNN, which entails dividing the last 1,000 classifiers into 21 classifiers (i.e., 20 classifiers and the background), random weight initialization, and fine-tuning of the entire network. During training, the intersection-over-union (IOU) overlap in the selected region with grand-true box (GT box) is greater than the threshold value and represent the positive sample, whereas the remaining region comprises the negative sample.
3. Use the updated network described in Step 2 to extract and classify features via SVMs. The GT box is positive, and, in other candidate regions, the IOU containing the GT box is less than 0.3, and the other is rounding off.
4. Employ regression to precisely adjust the candidate box position. For each class, a linear regression model is trained to determine whether the box is appropriate.

After an image is input into the R-CNN, the detection process begins by first locating several object candidate frames, and then employing the CNN to extract the feature vectors of each candidate frame. The SVM algorithm subsequently classifies the objects in each candidate frame.

Curve fitting is a very important image analysis tool, with the most commonly implemented curve-fitting method being the least squares method, which has various fundamental limitations. Although many scholars have worked to overcome these limitations, the least squares method has been extended to develop a new piecewise linear fitting algorithm purposed to replace polynomial curve fitting; the aim of this new piecewise linear fitting algorithm is to establish a simplified mathematical model that affords a better fit to the point sequence.

3 Target Detection-Based Time Identification Method for Milestone Events

As previously mentioned, this study was purposed to develop a target detection-based time identification method that timestamps milestone events that occur at airports. Thus, an improved R-CNN was developed to calculate the running speed of aircraft. The robustness of the algorithm is enhanced by an aircraft entry slip curve fitting tool that takes into account the presence of obstacles that would affect aircraft entry time.

The original video is input into the R-CNN as a sequence of grayscale images, and the parameters of the candidate box in each frame are retained in the output layer. If the screen resolution is represented as height (H) × width (W), the monitoring area is divided into M equidistant regions in the vertical and horizontal directions, and the actual distance of the corresponding scene is respectively represented in the vertical and horizontal directions as W_1, W_2, …, W_M and H_1, H_2, … H_M. In each M area, the distance between the vertical and horizontal planes is $\frac{W_m}{H}$ and $\frac{H_m}{W}$, respectively. Additionally, the network compares the plane frame with the previous 30 frames; more specifically, the time interval between (x_1, y_1) to (x_2, y_2) is one second, which corresponds to the actual horizontal and vertical moving distances of $S_x = (x_2 - x_1)\ \frac{W_m}{H}$ and $S_y = (y_2 - y_1)\ \frac{H_m}{W}$, respectively. The actual movement distance of an aircraft is $S = \sqrt{Sx^2 + Sy^2}$; then, the average velocity of the aircraft is calculated as $v = \frac{S}{t}$, and the CNN outputs the aircraft speed in every M region. For landings, the aircraft is considered to be in position when the detected speed of the aircraft initially reaches zero. Likewise, the aircraft is considered to be initiating takeoff when the speed of the aircraft exceeds zero.

Because the algorithm described above is only effective under the condition of good visibility, the proposed method includes plane-gliding curve fitting, which fits a series of scattered points, to detect the position of the aircraft. Additionally, a best mean-square approximation method for discrete functions was developed to establish a mathematical model as based on the interpolation of given discrete data points and find out a series of tiny straight lines. Under the condition that the interval between interpolation points was appropriately selected, these data points are subsequently formed into smooth curves. An airplane entry curve is then constructed according to the center coordinates of the detected candidate frames to overcome the problem of inaccurate aircraft detection under low visibility. Least squares fitting of the aircraft entry slip curve is used to record the centerpoint coordinates of the aircraft candidate box at predetermined intervals (x_i, y_i), and a function $y=f(x)$ is set to measure the discrete point column (x_i, y_i), $i = 1, 2, \ldots, m$. The problem of constructing the entry slip curve of a plane is transformed into the relatively easily solved second-order mathematical problem $\boldsymbol{p(x) = a + bx + cx^2}$. Note that most of the points in the point column (x_i, y_i) can fall on or near the curve. Considering the calculus theory $Q(a, b, c) = \sum_{i=1}^{m} [p(x_i) - y_i]^2 = \sum_{i=1}^{m} (a + bx_i + cx_i^2 - y_i)^2$, in order to minimize the value $Q(a, b, c)$, we must satisfy the following fitting conditions:

$$\begin{cases} \frac{\partial Q(a,b,c)}{\partial a} = 2 * \sum_{i=1}^{m} (a + bx_i + cx_i^2 - y_i) = 0 \\ \frac{\partial Q(a,b,c)}{\partial b} = 2 * \sum_{i=1}^{m} (a + bx_i + cx_i^2 - y_i)x_i = 0 \\ \frac{\partial Q(a,b,c)}{\partial c} = 2 * \sum_{i=1}^{m} (a + bx_i + cx_i^2 - y_i)x_i^2 = 0 \end{cases}$$

Then, a, b, and c can be obtained as follows to enable airplane entry curve construction:

$$\begin{pmatrix} m & \sum_{i=1}^{m} x_i & \sum_{i=1}^{m} x_i^2 \\ \sum_{i=1}^{m} x_i & \sum_{i=1}^{m} x_i^2 & \sum_{i=1}^{m} x_i^3 \\ \sum_{i=1}^{m} x_i^2 & \sum_{i=1}^{m} x_i^3 & \sum_{i=1}^{m} x_i^4 \end{pmatrix} \begin{pmatrix} a \\ b \\ c \end{pmatrix} = \begin{pmatrix} \sum_{i=1}^{m} y_i \\ \sum_{i=1}^{m} x_i y_i \\ \sum_{i=1}^{m} x_i^2 y_i \end{pmatrix}$$

$$\begin{pmatrix} a \\ b \\ c \end{pmatrix} = \left(\begin{pmatrix} m & \sum_{i=1}^{m} x_i & \sum_{i=1}^{m} x_i^2 \\ \sum_{i=1}^{m} x_i & \sum_{i=1}^{m} x_i^2 & \sum_{i=1}^{m} x_i^3 \\ \sum_{i=1}^{m} x_i^2 & \sum_{i=1}^{m} x_i^3 & \sum_{i=1}^{m} x_i^4 \end{pmatrix}^{\mathrm{T}} * \begin{pmatrix} m & \sum_{i=1}^{m} x_i & \sum_{i=1}^{m} x_i^2 \\ \sum_{i=1}^{m} x_i & \sum_{i=1}^{m} x_i^2 & \sum_{i=1}^{m} x_i^3 \\ \sum_{i=1}^{m} x_i^2 & \sum_{i=1}^{m} x_i^3 & \sum_{i=1}^{m} x_i^4 \end{pmatrix} \right)^{-1} * \begin{pmatrix} m & \sum_{i=1}^{m} x_i & \sum_{i=1}^{m} x_i^2 \\ \sum_{i=1}^{m} x_i & \sum_{i=1}^{m} x_i^2 & \sum_{i=1}^{m} x_i^3 \\ \sum_{i=1}^{m} x_i^2 & \sum_{i=1}^{m} x_i^3 & \sum_{i=1}^{m} x_i^4 \end{pmatrix}^{\mathrm{T}} * \begin{pmatrix} \sum_{i=1}^{m} y_i \\ \sum_{i=1}^{m} x_i y_i \\ \sum_{i=1}^{m} x_i^2 y_i \end{pmatrix}$$

The average speed during aircraft entry is thus obtained after statistical measurements are performed. Then, the aircraft position during gliding can be predicted according to the aircraft candidate frame position, which is determined as based on the gliding curve and average speed of the aircraft. For example, consider that the position of the aircraft (x_1, y_1) cannot be obtained because aircraft visibility is currently obstructed by obstacles. Under this condition, the current aircraft position (x_2, y_2) can be obtained as based on Δt and the previous aircraft position (x_1, y_1) by solving $\begin{cases} p(x) = a + bx + cx^2 \\ \Delta t * \overline{v} = \sqrt{(y_2 - y_1)^2 + (x_2 - x_1)^2} \end{cases}$.

The speed of corridor bridges is used to handle obstacles that obstruct the predetermined entry position of an aircraft. Airport ground support operations require that the corridor bridge begin regulating aircraft operations within one minute after aircraft entry. When the final position of the aircraft is not detected, and upon the first instance of the detected speed of the corridor bridge exceeding zero, the aircraft is considered to be in position. Then, when the aircraft is in position, the aircraft is considered to be launched when the detected corridor bridge speed is greater than zero. The network model is shown in Fig. 1.

4 Experiments

In order to verify the performance of the proposed algorithm, it is applied to operations at an airport in China. Statistics on the multiple entry data of a single aircraft were used to fit the aircraft glide curve, and a least squares method was used for third-order fitting of the statistical data.

The aircraft entry process stops along the curve and stops near the stop line. The plane entry slip curve and average gliding speed were obtained for the experiment. Consequently, the proposed algorithm was able to accurately determine the aircraft entry time and flight time not only under the condition of good visibility, but also during rain and snow, and under the condition of random occlusion by obstacles during aircraft gliding. Several experimental screenshots are presented in Fig. 2. From Fig. 2, we can see that the experimental conditions are different; in particular, the size and position of the obstacles consistently differ. However, the network model illustrated in Fig. 1 was able to recognize these differences and generate the positional results presented in Fig. 2a–c in consideration of the taxiing speed of the aircraft. In contrast, Fig. 2d–f shows how the original area neural network is unable to identify the position of the aircraft because it is unable to precisely identify the obstacles, which thus obstructs the view of more than 90% of the aircraft. Furthermore, because the improved network model shown in Fig. 1 considers the plane gliding curve, aircraft average gliding speed, gliding time, and the state of bridge movement, the position of the aircraft and the state of the aircraft during entry can be obtained.

For further validation, a comparison between the actual location of an aircraft during entry in an airport and the entry position identified by the network model shown in Fig. 1 was performed; the results are illustrated in Fig. 3. The black line and blue circles in Fig. 3 represent the actual path of the aircraft and the estimated positions of the aircraft (Fig. 1), respectively, during the gliding process. As can be seen in Fig. 3, the estimated path of the identified aircraft is largely consistent with the actual gliding path. The pixel difference in the experimental video between the actual aircraft position and the estimated position was also determined; the average and maximum error of each frame were 78 and 872 pixels, respectively.

In the experiment, the pixel size of the aircraft was 800×600, and the screen size was 1308×853. The experimental design obstacles were determined to occupy

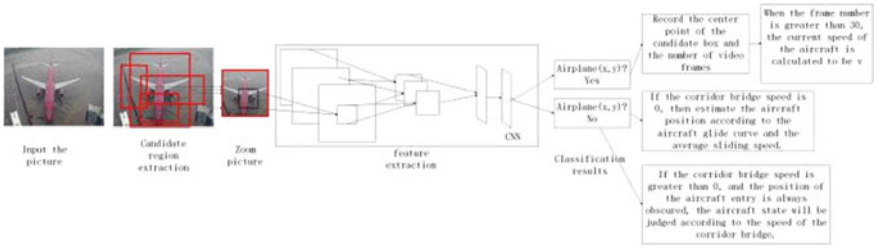

Fig. 1 Network structure

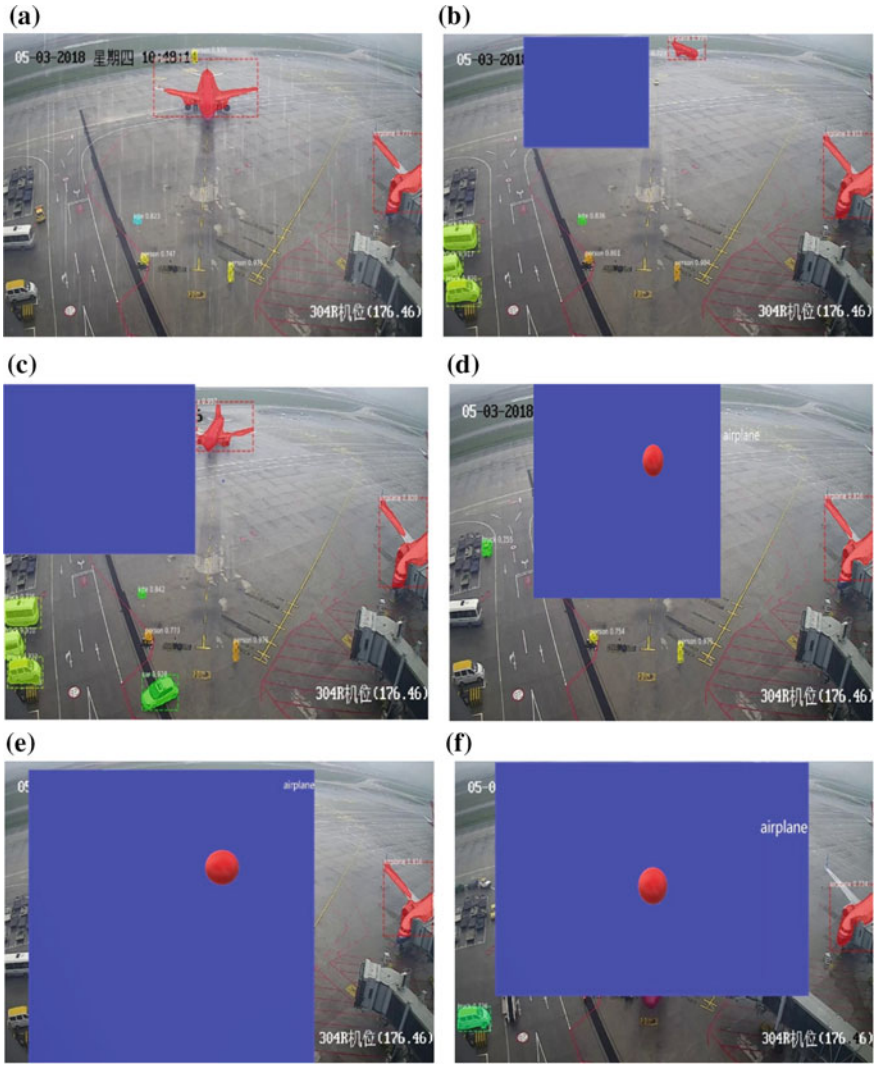

Fig. 2 Experimental screenshots

a screen area of 12%; this was determined as based on a 10×10-pixel window initiated at the top left corner of the screen that began with rightward movement. The experimental results and related parameters of the original R-CNN and proposed improved R-CNN (Fig. 1) are detailed in Tables 1 and 2. Note that the correct recognition of frames refers to the number of frames recognized throughout the entire flight. Tables 1 and 2 enumerate the recognition accuracy results of the original R-CNN and improved R-CNN with respect to the aircraft position when obstacles of varying size are present, and present the recognition accuracy for aircraft entry and exit.

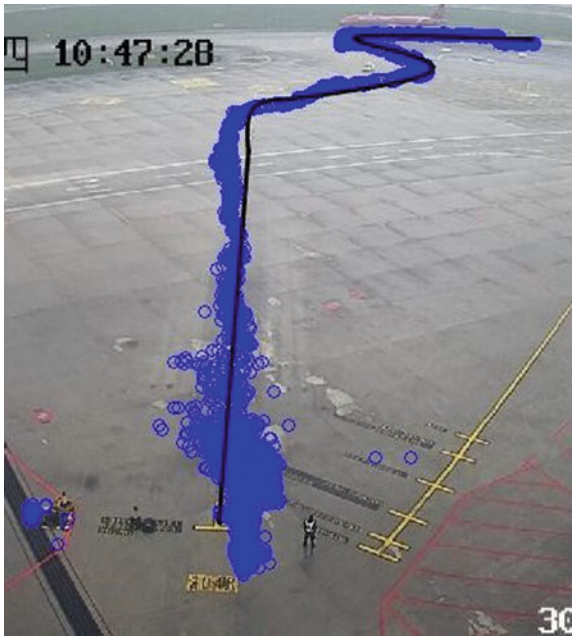

Fig. 3 Comparison of the actual and estimated results of aircraft location

Table 1 Comparison of original and improved R-CNN results for aircraft entry

Obstacle size	Occluding ratio (%)	Accuracy of original R-CNN recognition (%)	Accuracy of proposed R-CNN entry recognition (%)
156 × 102	12	71	100
260 × 170	20	43	99
600 × 800	40	14	95
785 × 512	60	7	91
1050 × 680	80	2	87

Tables 1 and 2 demonstrate that, as the occupying size of the obstacles increase from 12 to 100%, the differences between the original regional CNN and improved R-CNN become increasingly significant. Furthermore, Figs. 4 and 5 show that, as the obstacle size increases, the ability of the original area neural network to recognize aircraft entry and flight location rapidly deteriorates, whereas that of the improved R-CNN exhibits a slow decline.

Even if the obstacle completely obstructed the aircraft, the proposed algorithm demonstrated that is able to reasonably estimate the position of the aircraft as based on the gliding speed and gliding curve of the aircraft, and to determine the entry time as based on the flight time and prior knowledge of the times of milestone events

Table 2 Comparison of original and improved R-CNN results for aircraft exit

Obstacle size	Occluding ratio (%)	Identification accuracy of original R-CNN (%)	Accuracy of proposed R-CNN location recognition (%)
156 × 102	12	67	80
260 × 170	20	26	78
523 × 340	40	6	76
785 × 512	60	0	75
1050 × 680	80	0	69

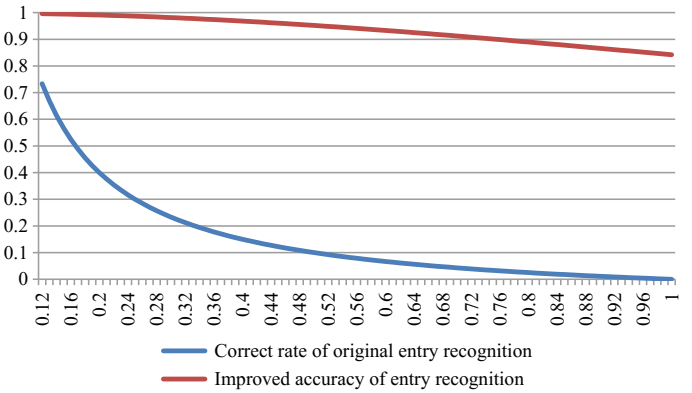

Fig. 4 Entry recognition statistics

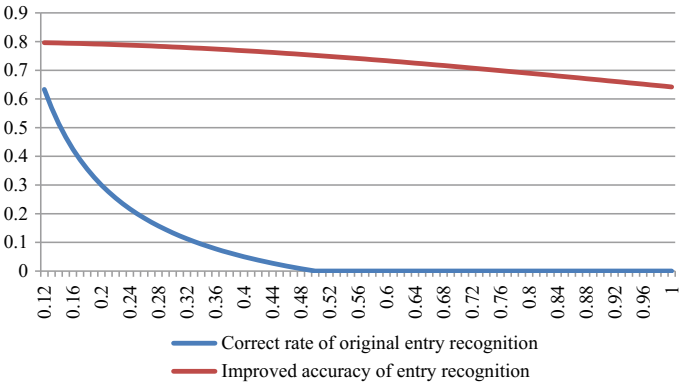

Fig. 5 out of place recognition statistics

at the airport. In summary, the experimental results show that the proposed target detection-based milestone event time identification method can identify aircraft entry time and aircraft launch time with reasonable accuracy.

5 Summary and Potential Application

The existing target detection-based video recognition algorithm can only identify specific targets, and cannot accurately determine the time of occurrence of specific milestone events. Thus, in this study, we focused on improving the existing regional CNN to increase the accuracy of network output aircraft entry path and aircraft launch time estimation. In order to enhance the robustness of the algorithm, a least squares method was used to fit the aircraft entry curve. Consequently, by considering prior knowledge of the gliding curve, the average velocity of an aircraft during entry, and the support of the airport ground operations, the proposed algorithm is able to identify the aircraft under the condition of low visibility. Moreover, the feasibility of target detection-based time milestone event identification was verified through application of the proposed algorithm to aircraft at different airports, and under varying degrees of visibility. Future work will focus on including the a priori knowledge on a larger number of airport milestones, increasing the accuracy of the aircraft entry time and bridge aircraft launch time predictions, and considering other factors that may affect aircraft identification, such as the lower gear and the opening of cargo cabins, in order to improve the recognition accuracy of the algorithm.

References

1. Hongtao, L., Qinchuan, Z.: Applications of deep convolutional neural network in computer vision. J. Data Acquis. Process. **31**(01), 1–17 (2016)
2. Lu, H., Li, Y., Uemura, T., Kim, H., Serikawa, S.: Low illumination underwater light field images reconstruction using deep convolutional neural networks. Future Gener. Comput. Syst. **82**, 142–148 (2018)
3. Zhang, Y., Gravina, R., Lu, H., Villari, M., Fortino, G.: PEA: parallel electrocardiogram-based authentication for smart healthcare systems. J. Netw. Comput. Appl. **117**, 10–16 (2018)
4. Lu, H., Li, Y., Mu, S., Wang, D., Kim, H., Serikawa, S.: Motor anomaly detection for unmanned aerial vehicles using reinforcement learning. IEEE Internet Things J. **5**(4), 2315–2322 (2018)
5. Lu, H., Li, Y., Chen, M., Kim, H., Serikawa, S.: Brain intelligence: go beyond artificial intelligence. Mob. Netw. Appl. **23**, 368–375 (2018)
6. Cruz-Hernández, H., de la Fraga, L.G.: A fiducial tag invariant to rotation, translation, and perspective transformations. Pattern Recogn. 81 (2018)
7. Hinton, G.E., Salkhutdinov, R.R.: Reducing the dimensionality of the data with neural networks. Science 313(5786), 504–507 (2006)
8. Carbonneau, M.A., Cheplygina, V., Granger, E., Gagnon, G.: Multiple instance learning: a survey of problem characteristics and applications. Pattern Recogn. 77 (2018)
9. Hubel, D.H., Wiesel, T.N.: Receptive fields, binocular interaction and functional architecture in the cat's visual cortex. J. Physiol. **160**(1), 106–154 (1962)

10. Fukushimak, K., Miyake, S.: Neocognitron: anewalgorithm for pattern recognition tolerant of deformations and shifts in position. Pattern Recogn. **15**(6), 455–469 (1982)
11. Guanghui, S.: Research on image labeling method based on migration learning and deep convolution features. Zhejiang University (2017)
12. Guohao, L.: Research on image restoration, enhancement and registration method for railway operation environment detection. Beijing Jiaotong University (2017)
13. Romanuke, V.V.: Appropriate number of standard 2×2 max pooling layers and their allocation in convolutional neural networks for diverse and heterogeneous datasets. Inf. Technol. Manage. Sci. 20(1) (2017)
14. Havaei, M., Davy, A., Warde-Farley, D., Biard, A., Courville, A., Bengio, Y., Pal, C., Jodoin, P.M., Larochelle, H.: Brain tumor segmentation with deep neural networks. Med. Image Anal. 35 (2017)

A Deep Architecture for Chinese Semantic Matching with Pairwise Comparisons and Attention-Pooling

Huiyuan Lai, Yizheng Tao, Chunliu Wang, Lunfan Xu, Dingyong Tang and Gongliang Li

Abstract Semantic sentence matching is a fundamental technology in natural language processing. In the previous work, neural networks with attention mechanism have been successfully extended to semantic matching. However, existing deep models often simply use some operations such as summation and max-pooling to represent the whole sentence to a single distributed representation. We present a deep architecture to match two Chinese sentences, which only relies on alignment instead of recurrent neural network after attention mechanism used to get interaction information between sentence-pairs, it becomes more lightweight and simple. In order to capture original features enough, we employ a pooling operation named attention-pooling to convergence information from the whole sentence. We also explore several excellent performance English models on Chinese data. The experimental results show that our method can achieve better results than other models on Chinese dataset.

Keywords Chinese · Semantic matching · Attention mechanism
Attention-pooling

H. Lai · Y. Tao (✉) · C. Wang · L. Xu · D. Tang · G. Li
Institute of Computer Application, China Academy
of Engineering Physics, Mianyang, China
e-mail: taolilan@126.com

H. Lai
e-mail: lawecs@126.com

C. Wang
e-mail: spring_willow@163.com

L. Xu
e-mail: xulunfan1994@outlook.com

D. Tang
e-mail: tdy2000@126.com

G. Li
e-mail: ligongliang1982@126.com

H. Lu (ed.), *Cognitive Internet of Things: Frameworks, Tools and Applications*, Studies in Computational Intelligence 810,
https://doi.org/10.1007/978-3-030-04946-1_22

1 Introduction

Semantic matching is a fundamental technology to many natural language processing tasks, such as question answering [1], information retrieval [2], and automatic summarization [3]. Semantic matching task is to find out if two pieces of sentences mean the same thing.

Natural language texts have complicated structures, both sequential and hierarchical, that are essential for understanding them. Many approaches have been proposed for semantic matching that uses lexical matching, linguistic analysis, and some semantic feature engineering, but these methods are often unsatisfactory. Recently, deep neural network based models have been applied in this area and achieved some important progress, such as DSSM [4] and DRCN [5]. And there are many large amounts of annotated English datasets such as Quora [6], SNLI [7], and MultiNLI [8] have contributed significantly to related work as well.

However, Because the grammatical structure and semantic context of Chinese sentences are more complicated and varied than English, the difficulty of calculating Chinese sentences similarity is increased. On the other hand, there is a lack of large-scale dataset released for Chinese short text semantic matching task in the past. The previous top-performing models which use rather complicated network architectures have achieved the state-of-the-art results on English, we can see that the matching degree between two sentences requires sentence representations from contextualized local perspectives in these models.

In this paper, we applied several excellent English models to the Chinese dataset for experiments, meanwhile we propose a simpler deep neural network architecture for semantic matching, we adopted pairwise comparisons which enables capturing interactive information for performance improvements, in addition, instead of the conventional summation operation, the attention-pooling mechanism is employed to convergence information from the whole sentence. The proposed architecture is shown in Fig. 1. We evaluate our model on Chinese dataset released by Ant Financial [9], by comparing and verifying with several other models, we hope to inspire the follow-up work in Chinese semantic matching.

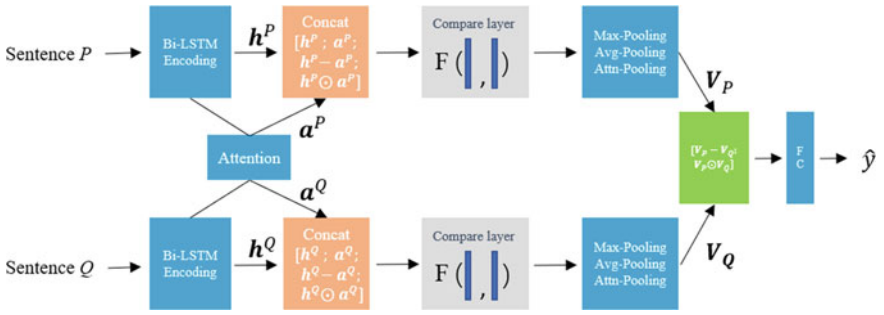

Fig. 1 Overview of our approach for Chinese semantic matching

2 Our Approach

Figure 1 gives an overview of our sentence matching architecture which is mainly composed of the following three components: (1) Input Encoding layer, (2) interaction layer and (3) composition and prediction layer. In our notation, we have two input sentences as $P = \{p_1, p_2, \ldots, p_m\}$ and $Q = \{q_1, q_2, \ldots, q_n\}$. First of all, we employ bi-directional long short-term memory (Bi-LSTM) to encode the two sentences (Sect. 2.1). We compute both the Q-aware representation for P and P-aware representation for Q, then using compare layer to fuse the contextual information and get the new representation (Sect. 2.2). Finally, we use three pooling mechanisms to represent the whole sentence to a single distributed representation and predict the result (Sect. 2.3).

2.1 Input Encoding Layer

Embedding. Firstly, the jieba [10] is used for word segmentation for the two sentences, then we map each word to a high-dimensional vector space. We use pre-trained word vectors to obtain the fixed word embedding of each word, the word vector that is trained on the relevant corpus in advance using Word2Vec [11]. The word embedding is fixed when training model. Now we have the representation $\boldsymbol{P} \in \mathbb{R}^{m \times d}$ and $\boldsymbol{Q} \in \mathbb{R}^{n \times d}$, where d means the dimension of both representations.

Encoding. In the encoding layer, the representation $\boldsymbol{P}$ and the representation $\boldsymbol{Q}$ is passed to a Highway Network Layer [12], so there are two representation $\hat{\boldsymbol{P}} \in \mathbb{R}^{m \times d}$ and $\hat{\boldsymbol{Q}} \in \mathbb{R}^{n \times d}$, then we employ Bi-LSTM to encode the two sentences to learn the representation of word and its context as follows:

$$\boldsymbol{h}_t^P = BiLSTM(\boldsymbol{h}_{t-1}^P, \hat{\boldsymbol{P}}_t) \tag{1}$$

$$\boldsymbol{h}_t^Q = BiLSTM(\boldsymbol{h}_{t-1}^Q, \hat{\boldsymbol{Q}}_t) \tag{2}$$

where $\hat{\boldsymbol{P}}_t \in \mathbb{R}^d$, $\hat{\boldsymbol{Q}}_t \in \mathbb{R}^d$ is the word representation of the t-th word of the two sentences, respectively. $\boldsymbol{h}_t^Q \in \mathbb{R}^d$ and $\boldsymbol{h}_t^P \in \mathbb{R}^d$ represent the encoding vector of the t-th word after the encoding. A Bi-LSTM runs a forward and backward LSTM on a sequence starting from the left and the right end, respectively. It can fully learn the information of the sentence, we also examined other recurrent memory blocks such as GRUs (Gated Recurrent Units) [13], but we found they are inferior to LSTM on our semantic matching task.

2.2 Interaction Layer

On the basis of sentence representations, we can model the interactions between a pair of sentences. The soft alignment attention is used to associate the relevant subcomponents between the two sentences. Firstly, we compute the attention weights between two sentences. The attention weights are denoted as $\boldsymbol{S} \in \mathbb{R}^{m \times n}$, where the similarity between the i-th word in the sentence P and the j-th word in the sentence Q is computed as:

$$\boldsymbol{S}_{ij} = \boldsymbol{h}_i^Q \cdot \boldsymbol{h}_j^P \tag{3}$$

where $\boldsymbol{h}_i^P$ and $\boldsymbol{h}_i^Q$ is the representation of the two sentences, which is already encoding the word itself and its context by Bi-LSTM with Eqs. (1–2), now we can compute the relevant semantics as follow:

$$\boldsymbol{a}_i^P = \sum_{j=1}^{n} \frac{\exp(\boldsymbol{S}_{ij})}{\sum_{k=1}^{n} \exp(\boldsymbol{S}_{ik})} \boldsymbol{h}_j^Q, \forall \mathrm{i} \in [1, .., \mathrm{m}] \tag{4}$$

$$\boldsymbol{a}_i^Q = \sum_{j=1}^{m} \frac{\exp(\boldsymbol{S}_{ij})}{\sum_{k=1}^{m} \exp(\boldsymbol{S}_{ik})} \boldsymbol{h}_j^P, \forall \mathrm{i} \in [1, .., \mathrm{n}] \tag{5}$$

where $\boldsymbol{a}_i^P \in \mathbb{R}^{m \times d}$ is a weighted summation of $\boldsymbol{h}^P$, it signifies sentence P words are most relevant to each word in sentence Q, the same is performed for the sentence Q with Eq. (5).

Next, the contextual representation and the attention vectors are combined together. After concatenating all the vectors, in the previous work, such as reading comprehension model of BiDAF [14] and semantic matching model of ESIM [15], they all applied another Bi-LSTM to fuse the contextual information and get the new representation for each word in the sentence, their framework is effective and have achieved good results on English dataset. To make our model lightweight and effective, inspired by Parikh et al. [16], we follow them to employ compare layer to align the semantic in two sentences, and we found that it can outperform to use Bi-LSTM and getting better efficiency. We compare the aligned phrases $\boldsymbol{G}^Q$ and $\boldsymbol{G}^P$ using a function F, separately, which in this work is a feed-forward network:

$$\boldsymbol{V}_i^P = \mathrm{F}\left(\boldsymbol{G}_i^P\right), \forall \mathrm{i} \in [1, .., \mathrm{m}] \tag{6}$$

$$\boldsymbol{V}_i^Q = \mathrm{F}\left(\boldsymbol{G}_i^Q\right), \forall \mathrm{i} \in [1, .., \mathrm{n}] \tag{7}$$

where F is a feed-forward neural network with ReLU activations [17], $\boldsymbol{V}^P \in \mathbb{R}^{m \times l}$ and $\boldsymbol{V}^Q \in \mathbb{R}^{n \times l}$ are comparison vectors, respectively, where l is the dimension of the feed-forward neural network output.

2.3 Composition and Predict Layer

We now have two sets of comparison vectors, in this layer, we adopt three pooling mechanisms to extract feature, it aims to convergence a sentence to a distributed representation, then feeds them to the final classifier to determine the overall semantic matching result. We first employ average pooling and max pooling to reduce the dimensions of the feature maps [18].

Attention-Pooling. Besides average pooling and max pooling. We also use attention-pooling [19] to aggregate over each comparison vectors in this paper. Firstly, the weight of each word representation in comparison vectors is calculated by a fully connected layer, then a softmax function is used. Finally, we get the weighted summation of $\boldsymbol{V}_{att}^{P}$, it can be shown as follow:

$$\boldsymbol{S}_i^P = \boldsymbol{W}_2 Act(\boldsymbol{W}_1 \boldsymbol{V}_i^P)$$

$$\boldsymbol{\alpha}_i^P = \exp(\boldsymbol{S}_i^P) / \sum_j^m \boldsymbol{S}_j^P \tag{8}$$

$$\boldsymbol{V}_{att}^P = \sum_{i=1}^m \boldsymbol{\alpha}_i^P \boldsymbol{V}_i^P$$

where m is the sentence length, $\boldsymbol{W}_1$ and $\boldsymbol{W}_2$ is the trainable weight parameter, Act is the activation function. The same is performed for $\boldsymbol{V}_{att}^{Q}$ as Eq. (8). We concatenate all these vectors to form the final fixed length vector $\boldsymbol{V}_P$ and $\boldsymbol{V}_Q$, then we compute the difference and the element-wise product between $\boldsymbol{V}_P$ and $\boldsymbol{V}_Q$ and concatenate them as follow:

$$\boldsymbol{V} = [\boldsymbol{V}_P - \boldsymbol{V}_Q; \boldsymbol{V}_P \odot \boldsymbol{V}_Q]. \tag{9}$$

We then put $\boldsymbol{V}$ into a final multilayer perceptron (MLP) classifier. The MLP has a hidden layer with ReLU activations [17] and sigmoid output layer in our experiments. The entire model (all two components described above) is trained end-to-end. For training, we use binary cross-entropy loss.

3 Experiments

In this section, we present the evaluation of our approach. Firstly, we perform quantitative evaluation comparing our model with other competitive English models on Chinese Dataset. We then conduct some qualitative analyses to understand how out model achieve the high-level understanding.

Table 1 Data samples from AETC

Question-pair	label
a. “花呗如何还款” -- “花呗怎么还款” (trans: "How to pay back in Ant Credit Pay" VS "How to repay in Ant Credit Pay")	1
b. “花呗如何还款” -- “我怎么还我的花被呢” (trans: "How to pay back in Ant Credit Pay" VS "What are my repayment methods in Ant Credit Pay")	1
c. “花呗分期后逾期了如何还款” -- “花呗分期后逾期了哪里还款” (trans: "How do I repay overdue payments after an installment plan is applied in Ant Credit Pay" VS "Where do I repay overdue payments after an installment plan is applied in Ant Credit Pay")	0
...	...

3.1 Dataset

The experiment data is derived from Ant Financial Artificial Competition (ATEC)-Financial Intelligence NLP Service [9], which contains 100,000 pairs of annotation data, including synonymous pairs and non-synonymous pairs, participants are required to determine, by using algorithms, whether the provided two Chinese sentences express the same semantics. This contest topic is evaluated based on the accuracy and F1-score. The data samples are shown in Table 1:

(1) True Positive (TP) indicates a synonym decision which is correct, and the TP value indicates the number of correct synonym decisions; (2) similarly, the False Positive (FP) value indicates the number of erroneous synonym decisions; (3) accordingly, the True Negative (TN) value indicates the number of correct non-synonym decisions; (4) and the False Negative (FN) value indicates the number of erroneous non-synonym decisions. We can calculate the precision rate, recall rate, accuracy, and F1-score as follows:

(1) precision rate = TP/(TP + FP);
(2) recall rate = TP/(TP + FN);
(3) accuracy = (TP + TN)/(TP + FP + TN + FN);
(4) F1-score = 2 * precision rate * recall rate/(precision rate + recall rate).

In this paper, we follow this method to evaluate all our experiments., it means that the accuracy and F1-score are final evaluation criteria.

3.2 Implementation Details

For each Chinese sentence, the jieba [10] is used for word segmentation, then map to the 300-D pre-trained word vector space and keep it fixed during training, while the out-of-vocabulary word is randomly initialized with uniform distribution. The

Table 2 **a** The performance of our model and other competing approaches. **b** The performance of our model's ablations on development set

(a) Results on ATEC-NLP dataset

Model	#Para	Acc (dev)	F1 (dev)	F1 (test)
(1) DSSM [4]	1.7 M	80.9	56.2	63.4
(2) 1D CNN [22]	2.5 M	81.7	56.7	63.8
(3) Decomposable attention [16]	786 K	82.6	57.6	64.5
(4) ESIM [15]	8.8 M	82.1	58.1	65.0
(5) Our approach	2.1 M	83.8	59.2	**65.8**

(b) Ablation on the dev set

	F1 (dev)
(1) No Bi-LSTM	56.8
(2) No compare layer	56.4
(3) Replace compare with Bi-LSTM	58.1
(4) No attention-pooling	58.7
(5) No diff and mul	58.6

parameters in the Bi-LSTM network are randomly initialized to obey normal distribution N (0, 0.1), while the number of nodes in the forward and reverse hidden layers is set to 150, the dropout [20] rate of 0.2 is used for all multilayer perceptron. To train our model, we employ the Adam algorithm [21] with the initial learning rate as 0.001 and the mini-batch size as 128. The exponential moving average is applied to all trainable variables with a decay rate of 0.999.

3.3 Results on Our Model

Table 2a shows the results of different models. We compare our result with all other English models, these models have achieved the state-of-the-art performance on English dataset in the past. Note that all models do not use any feature engineering, including character features and syntactical features. DSSM [4] adopts two-layer LSTM and attention mechanisms to capture sentence-level semantics, 1D CNN [22] use 6 kernel sizes of 1D convolution obtain different grams of words. Decomposable Attention [16] does not use LSTM to encoding, instead of only relies on alignment and is fully computationally decomposable with respect to the input text. Enhanced Sequential Inference Model [15] employ long short-term memory-network (LSTMN) with deep attention fusion that links the current word to previous word stored in memory. We show our model has better performance than all other models on Chinese dataset.

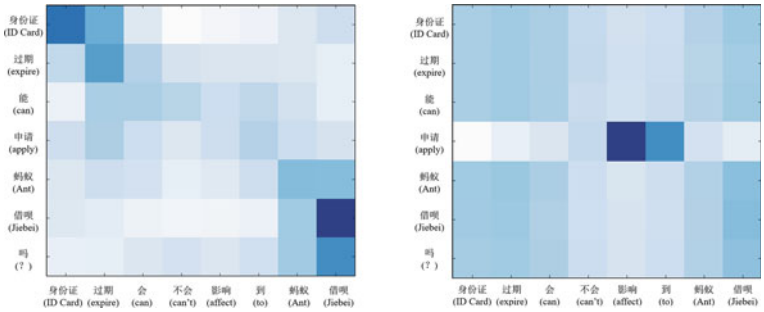

(a) Encoding layer **(b)** Compare layer

Fig. 2 Visualization of attentive weights

3.4 Analysis and Discussion

Ablation Study. We conduct an ablation study on our model to examine the effectiveness of each component. The result is shown in Table 2(b). In experiment 1, wo show how Bi-LSTM encoding layer contribute in enriching the feature space in interaction tensor, if we remove this layer completely, then we'll obtain a 56.8% for F1 score in development set. The result demonstrates the encoding layer have the powerful capability of encoding word and its context. To evaluate the compare layer, in experiment 2, we remove compare layer, thus directly pooling operation after interaction, and the performance degraded to 56.4%, if we replace compare with Bi-LSTM in experiment 3, the result shows that the compare layer is more effective, and it more efficient than Bi-LSTM after interaction layer. The results of 4 show that difference and the element-wise product operations could help sharpen semantic information between two vectors and capture semantic relationships. The results of experiment 5 demonstrate that the attention pooling operation has more powerful capability extracting feature to learn textual semantics.

Visualization. We visualize representation from the encoding layer and the compare layer in Fig. 2. We pick a sentence pair whose sentence P is " 身份证过期能申请蚂蚁借呗吗(Can I apply for Ant credit loan if my ID card expires)." and the sentence Q is " 身份证过期会不会影响到蚂蚁借呗(My ID card has expired, will it affect the Ant credit loan)." Because most of words in both sentences, we can see that " 身份证(ID card)", " 过期(expire)" and " 借呗(Ant Credit loan)" are more important words than others in classifying the label, as the layers get deeper in the next picture, we can see that the relevance between "申请(apply)" and " 影响(affect)" is the maintained as a clue of classification, we know the semantics of these two words are different, our model determines the label as a non-synonymous.

4 Related Work

The early exploration of sentence matching mainly relies on language analysis and feature engineering methods, the effect of this method is very limited. As many large-scale annotated datasets released, deep learning, deep adversarial metric learning and reinforcement learning [22, 23] have achieved rapid development in the natural language processing [24] and image processing [25–27]. In the English text similarity tasks field. The first type of these approaches is sentence-encoding-based methods [28, 29], Recently, External resources are also used for sentence matching. Chen et al. [15] used syntactic parse trees or WordNet to measure the semantic relationship among the words. These operations and architectural developments using deeper layers have led more progress in performance.

In the Chinese field, because there is a lack of large-scale data set released for Chinese short text Semantic matching task, the progress is slower than English. Ant Financial is holding a competition of Artificial Competition (ATEC) [9], it released a dataset which contains 100,000 pairs of annotation data, including synonymous pairs and non-synonymous pairs. In this paper, while exploring the excellent performance model of English on Chinese data, we present a model which uses Bi-LSTM with Pairwise Comparisons and Attention-Pooling to enhance representation power for semantic matching.

5 Conclusions

In this paper, we introduce a neural network model for Chinese sentence semantic matching. The results on ATEC Chinese dataset outperformed the previous models, including those employing more complicated network architectures. Based on this, we compare and analyze different models and show that combining global sentence-level representations and pairwise comparisons can get better improvement. We additionally show the incorporating attention-pooling operation contributes to our best result, it further improves the performance.

Acknowledgements We are especially grateful to Ant Financial for allowing us to use the dataset from Ant Financial Artificial Competition for experiments.

References

1. Berger, A., Caruana, R., Cohn, D., Freitag, D., Mittal, V.: Bridging the lexical chasm: statistical approaches to answer-finding. In: Proceedings of the 23rd Annual International ACM SIGIR Conference on Research and Development in Information Retrieval, 192–199 (2000)
2. Lu, Z., Li, H.: A deep architecture for matching short texts. Adv. Neural Inf. Process. Syst. (NIPS), 1367–1375 (2013)

3. Aliguliyev, R.M.: A new sentence similarity measure and sentence based extractive technique for automatic text summarization. Expert Syst. Appl. (2009)
4. Huang, P.-S., He, X., Gao, J., Deng, L., Acero, A., Heck, L.: Learning deep structured semantic models for web search using click through data. In: Proceedings of the 22nd ACM International Conference on Information & Knowledge Management (CIKM), pp. 2333–2338 (2013)
5. Palangi, H., Deng, L., Shen, Y., Gao, J., He, X., Chen, J., Song, X., Ward, R.K.: Deep sentence embedding using the long short term memory network: analysis and application to information retrieval. CoRR abs arXiv:1502.06922 (2015)
6. Csernai, K.: Quora question pair dataset (2017)
7. Bowman, S.R., Angeli, G., Potts, C., Manning, C.D.: A large annotated corpus for learning natural language inference. In: Proceedings of the 2015 Conference on Empirical Methods in Natural Language Processing (EMNLP). Association for Computational Linguistics (2015)
8. Williams, A., Nangia, N., Bowman, S.R.: A broad-coverage challenge corpus for sentence understanding through inference. arXiv:1704.05426 (2017)
9. Ant Financial. Ant Financial Artificial Competition. https://dc.cloud.alipay.com/index#/-topic/data?id=3
10. Junyi, S.: jieba. https://github.com/fxsjy/jieba
11. Mikolov, T., et al.: Efficient estimation of word representations in vector space. https://arxiv.org/abs/1301.3781
12. Srivastava, R.K., Greff, K., Schmidhuber, J.: Highway networks. arXiv:1505.00387 (2015)
13. Cho, K., van Merrienboer, B., Bahdanau, D., Bengio, Y.: On the properties of neural machine translation: encoder-decoder approaches. In: Wu, D., Carpuat, M., Carreras, X., Vecchi, E.M. (eds) Proceedings of SSST@EMNLP 2014 (2014)
14. Seo, M.J., Kembhavi, A., Farhadi, A., Hajishirzi, H.: Bidirectional attention flow for machine comprehension. arXiv:1611.01603 (2016)
15. Chen, Q., Zhu, X.: Enhanced LSTM for natural language inference. In: Proceedings of the 55th Annual Meeting of the Association for Computational Linguistics, pp. 1657–1668
16. Parikh, A.P., Täckström, O., Das, D., Uszkoreit, J.: A decomposable attention model for natural language inference. https://arxiv.org/pdf/1606.01933
17. Glorot, X., Bordes, A., Bengio, Y.: Deep sparse rectifier neural networks. In: Proceedings of AISTATS (2011)
18. Lu, H., Li, Y., Chen, M., Kim, H., Serikawa, S.: Brain intelligence: go beyond artificial intelligence. Mob. Netw. Appl. 1–8 (2017)
19. Natural Language Computing Group, Microsoft Research Asia. R-NET: Machine Reading Comprehension With Self-matching Networks. https://www.microsoft.com/en-us/research/publication/mrc/
20. Srivastava, N., Hinton, G.E., Krizhevsky, A., Sutskever, I., Salakhutdinov, R.: Dropout: a simple way to prevent neural networks from overfitting. JMLR (2014)
21. Kingma, D.P., Adam, J.B.: A method for stochastic optimization. https://arxiv.org/abs/1412.6980
22. Xu, X., He, L., Lu, H., Gao, L., Ji, Y.: Deep adversarial metric learning for cross-modal retrieval. World Wide Web J. https://doi.org/10.1007/s11280-018-0541-x (2018)
23. Lu, H., Li, Y., Mu, S., Wang, D., Kim, H., Serikawa, S.: Motor anomaly detection for unmanned aerial vehicles using reinforcement learning. IEEE Internet Things J. https://doi.org/10.1109/jiot.2017.2737479 (2017)
24. Deshpande, A.: Diving into natural language processing. https://dzone.com/articles/-natural-language-processing-adit-deshpande-cs-unde
25. Serikawa, S., Huimin, L.: Underwater image dehazing using joint trilateral filter. Comput. Electr. Eng. **40**(1), 41–50 (2014)
26. Lu, H., Li, Y., Uemura, T.: Low illumination underwater light field images reconstruction using deep convolutional neural networks. Future Gener. Comput. Syst. https://doi.org/10.1016/j.future.2018.01.001 (2018)
27. Lu, H., et al.: Low illumination underwater light field images reconstruction using deep convolutional neural networks. Future Gener. Comput. Syst. https://doi.org/10.1016/j.future.2018.01.001 (2018)

28. Choi, J., Yoo, K.M., Lee, S.: Learning to compose task-specific tree structures. AAAI (2017)
29. Nie, Y., Bansal, M.: Shortcut-stacked sentence encoders for multi-domain inference. arXiv: 1708.02312 (2017)

Robust Multi-user Detection Based on Hybrid Grey Wolf Optimization

Yuanfa Ji, Zhuo Fan, Xiyan Sun, Shouhua Wang, Suqing Yan, Sunyong Wu, Qiang Fu and Kamarul Hawari Ghazali

Abstract The search for an effective nature-inspired optimization technique has certainly continued for decades. In this paper, a novel hybrid Grey wolf optimization and differential evolution algorithm robust multi-user detection algorithm is proposed to overcome the problem of high bit error rate (BER) in multi-user detection under impulse noise environment. The simulation results show that the iteration times of the multi-user detector based on the proposed algorithm is less than that of genetic algorithm, differential evolution algorithm and Grey wolf optimization algorithm, and has the lower BER.

Keywords Grey wolf optimization algorithm · Differential evolution algorithm Hybrid optimization · Multi-user detection · Impulse noise

1 Introduction

Multiple access interference (MAI) and near-far interference effect are the main factors affecting the capacity and performance of Code Division Multiple Access (CDMA) systems [1, 2]. As the result, the multi-user detection (MUD) has been used to eliminate the adverse effects of them on the system. Previous, several ideal Gauss white noise channel environment models have been proposed. However, the major drawback of these models is that the actual wireless transmission channel is not obey the Gauss distribution, but has certain impulse noise characteristics because of the complex interference from outside.

Y. Ji · Z. Fan · X. Sun (✉) · S. Wang · S. Yan · S. Wu · Q. Fu
Guangxi Key Laboratory of Precision Navigation Technology and Application, Guilin University of Electronic Technology, Guilin 541004, China
e-mail: sunxiyan1@163.com

K. H. Ghazali
University Malaysia Pahang, Gambang, Malaysia

H. Lu (ed.), *Cognitive Internet of Things: Frameworks, Tools and Applications*, Studies in Computational Intelligence 810,
https://doi.org/10.1007/978-3-030-04946-1_23

Grey wolf optimization algorithm is a novel intelligent optimization algorithm proposed by Mirjalili in 2014 [3–5]. The algorithm has simple structure and fast convergence speed, it has been applied to many engineering problems, such as power system dispatching [6, 7], 3D route planning [8], motor optimal control and so on [9]. On other hand, differential evolution algorithm which a typically evolutionary algorithm, has strong local convergence and robustness.

The rest of the paper is organized as follows. Section 2 briefly introduces some preliminaries. Main idea of the improved Grey wolf algorithm and its implementation are presented in Sect. 3 in detail. Section 4 describes the comparative results to evaluate the proposed method. Finally, concluding remarks are summarized in Sect. 5.

2 Preliminaries

2.1 Robust Multi-user Detection Model

Assume that a synchronous CDMA communication system with N users, the signal received by the receiver at some point can be expressed as:

$$r(t) = \sum_{k=1}^{N} \sum_{i=-M}^{M} A_k b_k[i] s_k(t - iT) + n(t) \tag{1}$$

where T is the pseudo code transmission period of the user. A_k is the amplitude of the kth signal arriving at the base station. $b_k[i] \in \{1, -1\}$ represents the data information transmitted by the kth user. $n(t)$ is the channel noise. $s_k(t)$ is the normalized feature waveform assigned to the kth user. Impulse noise can be established by α stable distribution model. The characteristic function of α stable distribution is:

$$\begin{cases} \exp\{jut - \gamma|t|^{\alpha}[1 + j\beta \mathrm{sgn}(t) \tan(\frac{\alpha\pi}{2})]\}, \alpha \neq 1 \\ \exp\{jut - \gamma|t|^{\alpha}[1 + j\beta \mathrm{sgn}(t) \frac{2}{\pi} \log|t|]\}, \alpha = 1 \end{cases} \tag{2}$$

where $\alpha \in (0, 2]$ is characteristic factor, which represents the tail-flick level of the probability density function of stable distribution. $\beta \in [-1, 1]$ is symmetric parameter, $\gamma > 0$ is dispersion coefficient which indicates the degree to a random variable deviates from its mean value. $-\infty < u < \infty$ is position coefficient.

Based on Huber theory, robust multi-user detectors can be represented by the sum of the non-fast increasing functions of residuals ρ.

$$\hat{b} = \arg\min_{b} \sum_{j=1}^{N} \rho\left(r_j - \sum_{k=1}^{K} s_{jk} A_k b_k\right) \tag{3}$$

The penalty function $\rho(\cdot)$ based on the Huber M estimator can be expressed as

$$\rho(x_j) = \begin{cases} \frac{x_{j2}}{2z_{j2}}, |x_j| <= \varepsilon_j z_{j2} \\ \varepsilon_j \left| x_{j2} \right| - \frac{\varepsilon_{j2} z_{j2}}{2}, |x_j| > \varepsilon_j z_{j2} \end{cases} \tag{4}$$

Set $\varepsilon_j = \frac{3}{2z_j}$, $r_j = \sqrt{2} z_j$, the value of z_j is correlated with value of γ. γ is the deviation of noise.

2.2 *Differential Evolution Algorithm Based on Evolutionary Direction*

JADE algorithm. JADE algorithm is a differential evolutionary algorithm based on "DE/current to p-best" mutation strategy and parameter adaptive adjustment. Assuming that A represents the set of inferior solutions, P represents the set of population elements in the current iteration, then "DE/current to p-best" variation direction vector can be represented by Eq. (5) [10].

$$V_{i,g} = x_{i,g} + F_i(x^p_{best,g} - x_{i,g}) + F_i(x_{r1,g} - \tilde{x}_{r2,g}) \tag{5}$$

where $x^p_{best,g}$ represents an individual arbitrarily selected from the population whose fitness is in top $100p\%$ from the beginning of the algorithm to that of the current iteration, $p \in (0, 1]$. xi, g and $x_{r1,g}$ represents the individual from parent population in current iteration and the individual randomly selected from the set P respectively. $\tilde{x}_{r2,g}$ belongs to an individual arbitrarily selected from the set $A \bigcup P$. The crossover probability and variation factor of JADE algorithm is independently generated by the following Eq. [10].

$$CR_i = randn_i(u_{CR}, 0.1) \tag{6}$$

$$F_i = randc_i(u_F, 0.1) \tag{7}$$

where $randn(\cdot)$ represents normal distribution, $randc_i$ represents Cauchy distribution, u_{CR} and u_F are initialized to 0.5, and the two parameters are updated based on Eqs. (8)–(9) [10].

$$u_{CR} = (1 - c) \cdot u_{CR} + c \cdot mean_A(SCR) \tag{8}$$

$$u_F = (1 - c) \cdot u_F + c \cdot mean_L(S_F) \tag{9}$$

where c is a constant between 0 and 1, usually make the value c satisfy the condition $1/c \in [5, 20]$. S_{CR} and S_F represents the set of crossover probabilities and variation factors that indicates the successful execution of mutation operation during the

iterative process of the algorithm respectively. $mean_A$ represent the arithmetic mean value, $mean_L$ represent the Lehmer mean value

$$mean_L(S_F) = \frac{\sum_{F \in SF} F^2}{\sum_{F \in SF} F} \tag{10}$$

3 Robust Multi-user Detection Method Based on Hybrid Grey Wolf Optimization

3.1 Typical Optimizing Process of Grey Wolf Optimization

The hunting process of the Grey wolf optimization algorithm mainly includes searching, tracking and hunting. The mathematical model of the behavior of the wolves attacking prey is as follows [3]:

$$D = |C \cdot Xp(t) - X(t)| \tag{11}$$

$$X(t+1) = Xp(t) - A \cdot D \tag{12}$$

where D represents the distance between an Grey wolf individual and the prey. Equations (11) and (12) represents the position updating formula of the Grey wolf. While $|A| > 1$, the Grey wolf algorithm will expand the search range to find a better solution. While $|A| < 1$, the Grey wolf algorithm will narrow the search area to achieve the process of encircling prey. t represents the number of iterations of the algorithm,A and C is coefficient vector, Xp represents the position of prey, X is the position vector of the Grey wolf. The vector A and C can be obtained by Eqs. (13) and (14), where r_1 and r_2 represents a random number in the range of [0, 1].

$$A = 2a \cdot r_1 - a \tag{13}$$

$$C = 2 \cdot r_2 \tag{14}$$

The coefficient a is called the convergence factor which is expressed by Eq. (15), where max represents the maximum number of iterations. The value of coefficient a is decreases linearly from 2 to 0 with the number of iterations increases.

$$a = 2 - 2(\frac{t}{\max}) \tag{15}$$

When the Grey wolf group determines the position of the prey, the α wolf leads the β wolf and the δ wolf to encircle the prey (the target position). The distance information between the ω wolf and the three wolves is represented by expressions (16)–(18) [3].

$$D_\alpha = |C_1 \cdot X_\alpha - X| \tag{16}$$

$$D_\beta = \left|C_2 \cdot X_\beta - X\right| \tag{17}$$

$$D_\delta = |C_3 \cdot X_\delta - X| \tag{18}$$

where X_α, X_β, X_δ, X represents the current location of α wolf, β wolf, δ wolf and ω wolf respectively. The location information of the Grey wolf population is updated by Eqs. (19)–(22) [3]

$$X_1 = X_\alpha - A_1 \cdot D_\alpha \tag{19}$$

$$X_2 = X_\beta - A_2 \cdot D_\beta \tag{20}$$

$$X_3 = X_\delta - A_3 \cdot D_\delta \tag{21}$$

$$X(t+1) = \frac{X_1 + X_2 + X_3}{3} \tag{22}$$

The Grey wolf optimization algorithm mainly evaluates the location of prey (target) by the location information of the α wolf, the β wolf and the δ wolf, and the candidate solution is distributed in the random circle of the three positions.

3.2 Improved Grey Wolf Optimization Algorithm

The typical Grey wolf optimization algorithm updates the location of wolf population merely by the arithmetic average position information of α wolf, β wolf and δ wolf. In this way, it cannot fully preserve the previous search direction information per iteration. In addition, in order to ensure the diversity of the initial population of the algorithm, the idea of adversarial learning is considered [11, 12].

$$\tilde{X}_i^k = \gamma * (l + u) - X_i^k \tag{23}$$

The range of values X_i^k is $[l, u]$, $k = \alpha, \beta, \delta$, γ is a random number that is uniformly distributed between 0 and 1. The initial set of samples of the Grey wolf optimization algorithm based on the combination of the $\tilde{X}_i^k$ and X_i^k.

For multi-user detection, the actual transmitted bit information is usually a combination of 1 and -1. Therefore, aiming at the problem of multi-user detection, and combining search direction information of the algorithm, replaces the algorithm position update Eq. (22) with Eqs. (24)–(26). The location update principle of the improved Grey wolf optimization algorithm is shown in Fig. 1.

$$\bar{X}(t+1) = X_{srch} + a_1 * (X_1 - \bar{X}_i^k) + a_2 * (X_2 - \bar{X}_i^k) + a_3 * (X_3 - \bar{X}_i^k) \tag{24}$$

$$X'(t+1) = \frac{1}{1 + \exp(-\bar{X}(t+1))} \tag{25}$$

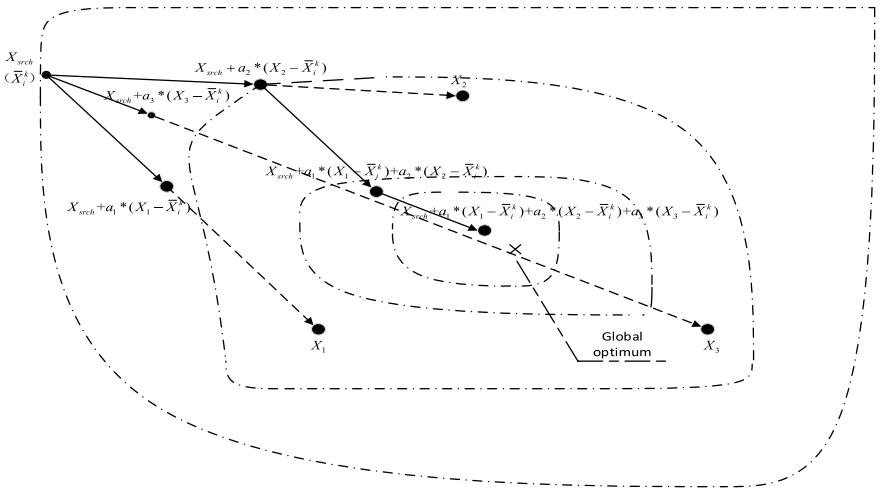

Fig. 1 The location update principle of the improved Grey wolf optimization algorithm. The dot dashed curves display the contours of the optimization problem. The dashed curves display the direction vector X_{srch} represents the location of ω wolf. X_1, X_2, X_3 represents the location of α wolf, β wolf, δ wolf respectively

$$X(t+1) = \begin{cases} -1, & rand > X'(t+1) \\ 1, & otherwise \end{cases} \tag{26}$$

where X_{srch} is a random integer with a range of $[-6, 6]$, the estimated location should also be limited to this range. $\bar{X}_i^k$ represents the initial population individual, the expression (25) is called sigmoid function. The sigmoid function converts the estimated position $\bar{X}(t+1)$ to a number between 0 and 1, and finally converted into the form of estimated data information bits by the adjudicative formula (26). a_1, a_2, a_3 represents the fitness value of α wolf, β wolf and δ wolf respectively. $rand$ represents a random number between 0 and 1.

The main idea of the improved Grey wolf optimization algorithm is that the position updating of the Grey wolf group takes the position of the three wolves as the reference information. Using the relative direction vector of the three wolf's position to get the next optimization direction, and through the weighted operation of the different direction vectors, the improved algorithm further highlight the different leadership and command roles of the α wolf, the β wolf and the δ wolf in the algorithm optimization process. The improved Grey wolf optimization algorithm based on evolutionary direction will ensure the correctness and robustness of the algorithm's optimization direction.

3.3 Implementation Process of Robust Multi-user Detector Based on Hybrid Wolf Optimization

The fitness function of multi-user detection can be expressed as

$$f_{fitness} = 1/\left(\sum_{j=1}^{N} \rho(r_j - \sum_{k=1}^{K} s_{jk} A_k b_k\right) + K) \tag{27}$$

where K = 0.01. The larger the fitness function is, the better the individual adaptability is. The implementation steps of the HGWO algorithm are as follows:

Step 1 Initialize the relevant algorithm parameters including the mean parameters of crossover probability and variation factor, population size, maximum iteration number and so on.

Step 2 Initializing parent population using adversarial learning method, and determine the α wolf, the β wolf and the δ wolf in the population.

Step 3 The parent population is updated with the improved position updating equation mentioned in Sect. 3.2, and the population individuals are sorted according to the fitness value from large to small.

Step 4 According to JADE algorithm, using parent population to produce offspring individuals and take crossover and mutation operation.

Step 5 Compare the fitness of the updated population with that of the three Grey wolf individuals at initialization.

Step 6 Terminates the loop if the algorithm iteration ends, and output optimal location information. Otherwise, return to step 4.

The pseudo code diagram of hybrid Grey wolf optimization algorithm is shown in Fig. 2.

4 Simulation Results and Analysis

4.1 Experimental Setting

Assuming that there is an impulse noise in the transmission channel of the CDMA communication system, the maximum normalized coefficient of spread spectrum sequence codes is 9/31. Modeling impulse noise by α stable distribution model, and let the feature index equals 1.5. The performance of the novel robust multi-user detection algorithm HGWO is compared with that of Genetic Algorithm (GA), Differential Evolutionary algorithm (DE) and Grey Wolf Optimization algorithm (GWO). The initialization parameters of genetic algorithm and differential evolution algorithm are set according to reference [13], the Grey wolf optimization algorithm and the HGWO algorithm are set up with reference to the preceding chapters of this paper.

Algorithm 1 Hybrid grey wolf optimization

Initialize: u_{CR},u_F=0.5; c,p=0.1; A_{mat}=$\emptyset$; $GV1$=$\emptyset$; $GV1_{temp}$=$\emptyset$; GV=$\emptyset$; Setting the population size of the algorithm:npop; Maximum number of iterations:MaxIt; Parent population obtained by the formula(24); Determine α wolf, β wolf and δ wolf in the parent population.
for $g = 1$; $g <= MaxIt$; $g++$ **do**
  S_F, S_{CR}=$\emptyset$
  Combine the method in section 3.1 and section 3.2 to update the location of the parent population, and ranking the parent population according to the fitness function.
  for $i = 1$; $i <= npop$; $i++$ **do**
    Setting CR_i and F_i according to formula(7) to formula(8).
    Randomly select individual $x^p_{best,g}$ from the parent population whose fitness is in top 100p%; Randomly select individual $x_{r1,g}$ from parent population P, and $x_{r1,g} \neq x_{i,g}$; Randomly select individual $\tilde{x}_{r2,g}$ from $A_{mat} \cup$ P, and $\tilde{x}_{r2,g} \neq x_{r1,g} \neq x_{i,g}$
    if GV $\neq \emptyset$ **then**
      Randomly select individual $x_{r3,g}$ from GV.
      $V_{i,g} = x_{i,g} + F_i * (x^p_{best,g} - x_{i,g}) + F_i * (x_{r1,g} - \tilde{x}_{r2,g}) + F_i * (x_{r3,g})$
    else
      $V_{i,g} = x_{i,g} + F_i * (x^p_{best,g} - x_{i,g}) + F_i * (x_{r1,g} - \tilde{x}_{r2,g})$
    end if
    Generating random integers j_{rand} within a range (1,D). D represents the dimension of the parent population
    for $j = 1$; $j <= D$; $j++$ **do**
      if j=j_{rand} or $rand < CR_i$ **then**
        $u_{j,i,g} = V_{j,i,g}$
      else
        $u_{j,i,g} = x_{j,i,g}$
      end if
    end for
    $u_{i,g}$ represents an individual obtained after the cross mutation operation.
    if $f_{fitness}(x_{i,g}) >= f_{fitness}(u_{i,g})$ **then**
      $x_{i,g+1} = x_{i,g}$
    else
      $(u_{i,g} - x_{i,g}) \rightarrow GV1$
      $x_{i,g+1} = u_{i,g}, x_{i,g} \rightarrow A_{mat}, CR_i \rightarrow S_{CR}, F_i \rightarrow S_F$
    end if
  end for
  Confirm that the number of the set A_{mat} elements is not exceed npop. If excess, remove one individual randomly from A_{mat}; Renew u_{CR} and u_F according to formula(9) to formula(10).
  x_g represent the individual whose fitness is better than any one of the three wolves
  if $f_{fitness}(x_g) > f_{fitness}(\alpha)$ **then**
    $(x_g - \alpha) \rightarrow GV_{temp}$
    $\alpha = x_g$
  else if $f_{fitness}(x_g) > f_{fitness}(\beta)$ **then**
    $(x_g - \beta) \rightarrow GV_{temp}$
    $\beta = x_g$
  else
    $(x_g - \delta) \rightarrow GV_{temp}$
    $\delta = x_g$
  end if
  $GV = GV1 \cup GV_{temp}$
end for

Fig. 2 Pseudo code diagram of hybrid Grey wolf optimization algorithm

4.2 Experimental Results

Effect of initialization parameter settings on system BER when used hybrid wolf optimization algorithm. Assuming that the signal power of all users is equal, the number of users is 10, the length of data signal transmission is 10,000 bit, the generalized Signal-to-Noise Ratio (SNR) is 5 dB, and the number of iterations is 5.

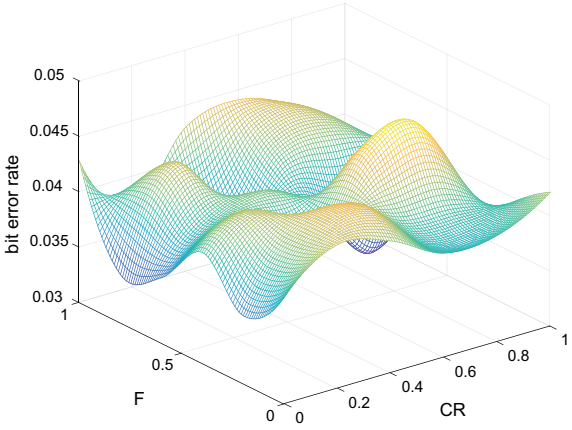

Fig. 3 Relationship between coefficient CR, F and BER

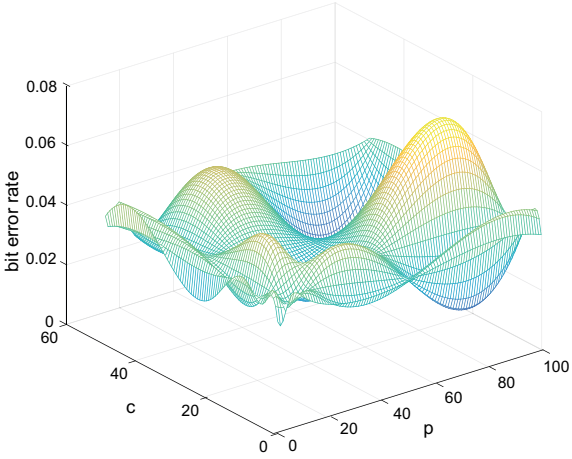

Fig. 4 Relationship between coefficient c, p and BER

The relationship between initialization parameter setting and BER using the HGWO optimization algorithm for multi-user detection is shown in Figs. 3 and 4.

Iterative speed performance test of algorithm. The iterative speed of different algorithms was measured under impulse noise channel, assuming equal signal power of all users, the number of users is 10, the length of data is 10,000 bit, and the generalized SNR is 5 dB, Fig. 5 shows the relationship between the number of iterations of the algorithm and the accuracy of the estimated data bit information.

Anti-noise performance test of algorithm under impulse noise environment. The noise insensitivity of different algorithms was assessed under impulse noise channel, assuming equal signal power of all users, the number of users is 10, and the length of data is 10,000 bit. The relationship between the generalized SNR and the accuracy of transmission data bit estimation is shown in Fig. 6.

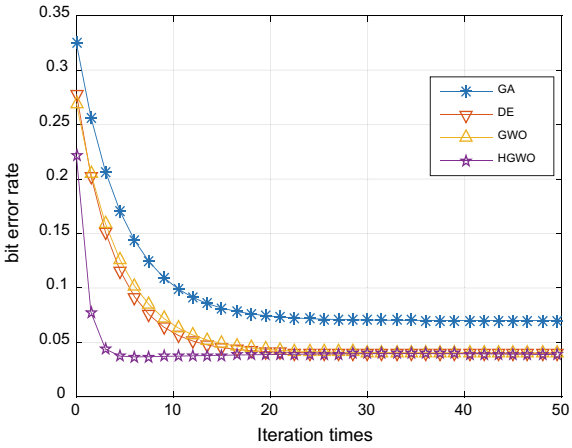

Fig. 5 Relationship between BER and iteration times

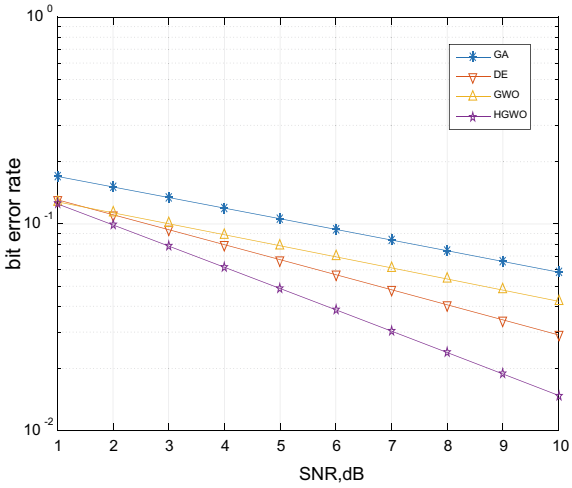

Fig. 6 Relationship between BER and generalized SNR

Anti near-far effect performance test of algorithm under impulse noise environment. The anti near-far effect performance of different algorithms was measured under impulse noise channel. Assuming that the number of users is 10, the generalized SNR of user 1 is fixed at 5 dB, all other users have the same and varying SNR. Figure 7 shows the relationship between the accuracy of data bit information estimation of user 1 and the Near-Far Ratio (NFR).

Communication capacity test of algorithm under impulse noise environment. When there is no near-far effect between users and the generalized SNR is 5 dB, the relationship between the number of users of the communication system and the accuracy rate of the data bit information estimation is shown in Fig. 8. It can be

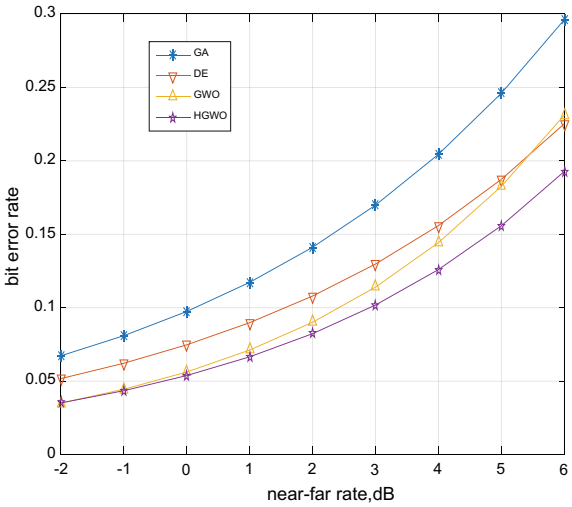

Fig. 7 Relationship between BER and NFR

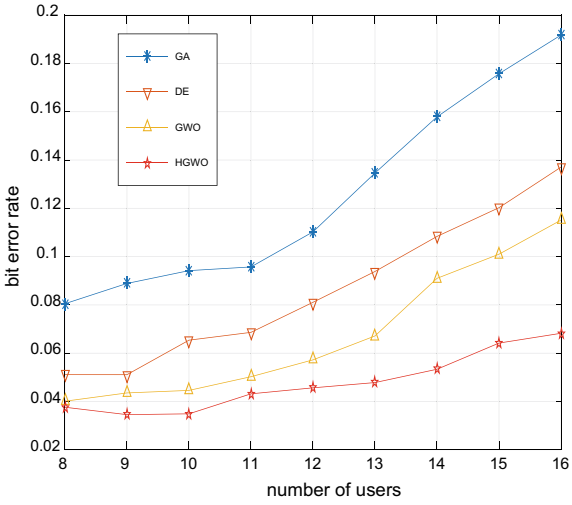

Fig. 8 Relationship between BER and number of users

seen from Fig. 8 that the communication capacity of multi-user detector based on the HGWO algorithm will be greatly increased.

4.3 Summary of Experimental Results

From the simulation above, the proposed algorithm has obvious advantages compared with the genetic algorithm, Grey wolf optimization algorithm and differential evolution algorithm in the convergence speed, noise resistance performance and com-

munication capacity. In addition, it is clear that the multi-user detection algorithm under impulse noise environment is more strict than Gauss noise environment in the requirement of algorithm optimization ability in that there are some large deviation "outliers" which are random distributed in the received signal when the impulse noise exists. This makes the BER increase if only use the traditional hard decision method in the detection process. Therefore, the detector (feature function) must be redesigned to reduce the influence of outliers.

5 Conclusions

This paper proposed combining the Grey wolf optimization algorithm with JADE algorithm by using the evolutionary direction information of the algorithm to solve the problem of multi-user detection under impulse noise environment. In this way, it can satisfy the high requirement of the optimization ability of the algorithm when using intelligent algorithm for multi-user detection under complex environment.

Acknowledgements This work was supported by the National Natural Science Foundation of China (61561016, 11603041), Innovation Project of GUET Graduate Education (2018YJCX19), Guangxi Information Science Experiment Center funded project, Department of Science and Technology of Guangxi Zhuang Autonomous Region (AC16380014, AA17202048, AA17202033).

References

1. Moshavi, S.: Multi-user detection for DS-CDMA communications. IEEE Commun. Mag. **34**(10), 124–136 (2002)
2. Zhou, H., Woo, W.L., Sharif, B.S.: Subspace-based blind adaptive multi-user detection using Kalman filter. IEE Proc. Commun. **152**(3), 302–310 (2005)
3. Mirjalili, S., Mirjalili, S.M., Lewis, A.: Grey wolf optimizer. Adv. Eng. Softw. **69**(3), 46–61 (2014)
4. Lu, H., Li, Y., Uemura, T., Kim, H., Serikawa, S.: Low illumination underwater light field images reconstruction using deep convolutional neural networks. Future Gener. Comput. Syst. **82**, 142–148 (2018)
5. Lu, H., Li, Y., Chen, M., Kim, H., Serikawa, S.: Brain intelligence: go beyond artificial intelligence. Mob. Netw. Appl. **23**, 368–375 (2018)
6. Jayakumar, N., Subramanian, S., Ganesan, S., et al.: Grey wolf optimization for combined heat and power dispatch with co-generation systems. Int. J. Electr. Power Energy Syst. **74**, 252–264 (2016)
7. Pradhan, M., Roy, P.K., Pal, T.: Grey wolf optimization applied to economic load dispatch problems. Int. J. Electr. Power Energy Syst. **83**, 325–334 (2016)
8. Radmanesh, M., Kumar, M.: Grey wolf optimization based sense and avoid algorithm for UAV path planning in uncertain environment using a Bayesian framework. In: International Conference on Unmanned Aircraft Systems, pp. 68–76. IEEE (2016)
9. Das, K.R., Das, D., Das, J.: Optimal tuning of PID controller using GWO algorithm for speed control in DC motor. In: International Conference on Soft Computing Techniques and Implementations, pp. 108–112. IEEE (2016)
10. Zhang, J., Sanderson, A.C.: JADE: adaptive differential evolution with optional external archive. IEEE Trans. Evol. Comput. **13**(5), 945–958 (2009)
11. Rahnamayan, S., Tizhoosh, H.R., Salama, M.M.A.: Opposition-based differential evolution. IEEE Trans. Evol. Comput. **12**(1), 64–79 (2008)

12. Huang, L., et al.: Adversarial machine learning. In: ACM Workshop on Security and Artificial Intelligence, pp. 43–58. ACM (2011)
13. Yen, K., Hanzo, L.: Genetic algorithm assisted multi-user detection in asynchronous CDMA communications. In: IEEE International Conference on Communications, vol. 3, pp. 826–830. IEEE (2001)

Correlation Filter Tracking Algorithm Based on Multiple Features and Average Peak Correlation Energy

Xiyan Sun, Kaidi Zhang, Yuanfa Ji, Shouhua Wang, Suqing Yan and Sunyong Wu

Abstract The traditional target tracking algorithm adopts artificial features. However, the artificial features are not strong enough to illustrate the appearance of the target. So it is difficult to apply to complex scenes; moreover, the traditional target tracking algorithm does not judge the confidence of the response. This paper proposes the Multiple Features and Average Peak Correlation Energy (MFAPCE) tracking algorithm, MFAPCE tracking algorithm combines deep features with color features and uses average peak correlation energy to measure confidence. Finally, according to the confidence to determine whether to update the model. Compared with the traditional tracking algorithm, MFAPCE algorithm can improve the tracking performance according to experiment.

Keywords Correlation filter · Target tracking · Deep features
Average peak correlation energy

1 Introduction

The main task of visual tracking is to estimate the trajectory of target, In recent years, the target tracking algorithm has made great progress [1–3]. Henriques et al. [4] proposed to improve tracking performance by using cyclic structure and kernel function. The periodic cyclic structures are obtained by intensive sampling. Wang et al. [5] proposed to use the average peak correlation energy to detect the confidence of the target response. Recently, more tracking algorithms adopt deep features, such as [6, 7]. Our algorithm exploits semantic information of last layers to handle large appearance changes, alleviate drifting by using features of early layers for precise localization. Color histogram information is used as color features, context patches is used to optimize background information [8], and average peak correlation energy

X. Sun · K. Zhang · Y. Ji (✉) · S. Wang · S. Yan · S. Wu
Guangxi Key Laboratory of Precision Navigation Technology and Application,
Guilin University of Electronic Technology, Guilin 541004, China
e-mail: jiyuanfa@163.com

H. Lu (ed.), *Cognitive Internet of Things: Frameworks, Tools and Applications*, Studies in Computational Intelligence 810,
https://doi.org/10.1007/978-3-030-04946-1_24

[5] is used to measure confidence of response. MFAPCE algorithm is tested on the OTB100 dataset and compared with other tracking algorithms, result show that MFAPCE algorithm has better performance.

2 Proposed Approach

2.1 Context Aware Correlation Filter Tracking

We add target context information to tracking framework during learning phase. Take deer sequence in OTB100 dataset as example: as show in Fig. 1, we sample k patches $a_i \in \mathbb{R}^n$ around target $a_0 \in \mathbb{R}^n$, the corresponding circulant matrices is $A_i \in \mathbb{R}^{n\times n}$ and $A_0 \in \mathbb{R}^{n\times n}$. These context patches are added to ridge regression equation as a regularizer [8], parameter λ_2 is used to prevent over-fitting.

The implementation of MFAPCE algorithm is similar to the KCF method.

$$\min_{w} \|A_0 w - y\|_2^2 + \lambda_1 \|w\|_2^2 + \lambda_2 \sum_{i=1}^{k} \|A_i w\|_2^2 \tag{1}$$

The objective function f can be obtained by stacking the context patches with target patch into a new data matrix, yielding: y is a vectored image of a 2D Gauss:

$$f(w, B) = \|Bw - \bar{y}\|_2^2 + \lambda_1 \|w\|_2^2 \tag{2}$$

$$B = \begin{bmatrix} A_0 \\ \sqrt{\lambda_2 A_1} \\ \vdots \\ \sqrt{\lambda_2 A_k} \end{bmatrix} \text{ and } \bar{y} = \begin{bmatrix} y \\ 0 \\ \vdots \\ 0 \end{bmatrix} \tag{3}$$

f can be solved by setting the gradient to zero, yielding:

$$w = (B^T B + \lambda_1 I)^{-1} B^T \bar{y} \tag{4}$$

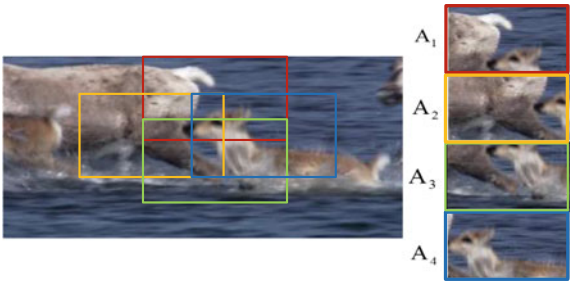

Fig. 1 Context patches around the target. The context patches of the MFAPCE algorithm are shown on the figure above, and the context patches are located at the top side (A_1), down side (A_3), left side (A_2) and right side (A_4) of the target

The circulant matrices are made diagonal by the discrete Fourier transform:

$$X = F diag(\hat{x}) F^H \tag{5}$$

$\hat{x}$ is the discrete Fourier transform of vector x, $\hat{x} = \mathcal{F}(x)$. F is a constant matrix independent of x, and is the unique matrix that computes the DFT of any input vector, for instance, $F(z) = \sqrt{n} F z$.

The closed form solution for Eq. 4 in Fourier domain is obtained by the upper equation.

$$\hat{w} = \frac{\hat{a}_0^* \odot \hat{y}}{\hat{a}_0^* \odot \hat{a}_0 + \lambda_1 + \lambda_2 \sum_{i=1}^{k} \hat{a}_i^* \odot \hat{a}_i} \tag{6}$$

The detection equation is:

$$f(X, w) = Xw \Leftrightarrow \hat{f} = \hat{x} \odot \hat{w} \tag{7}$$

The solution in the dual domain is given by [9]:

$$\hat{\alpha} = \begin{bmatrix} \mathrm{diag}(\mathrm{d}_{00}) & \cdots & \mathrm{diag}(\mathrm{d}_{0k}) \\ \vdots & \ddots & \vdots \\ \mathrm{diag}(\mathrm{d}_{k0}) & \cdots & \mathrm{diag}(\mathrm{d}_{kk}) \end{bmatrix}^{-1} \begin{bmatrix} \hat{\mathrm{y}} \\ \vdots \\ 0 \end{bmatrix} \tag{8}$$

where the vector $\mathrm{d}_{jl} (j, l \in \{1, \ldots, k\})$ are given by:

$$\begin{cases} \mathrm{d}_{00} = \hat{\mathrm{a}}_0 \odot \hat{\mathrm{a}}_0^* + \lambda_1 \\ \mathrm{d}_{jj} = \lambda_2 (\hat{\mathrm{a}}_j \odot \hat{\mathrm{a}}_j^*) + \lambda_1, j \neq 0 \\ \mathrm{d}_{jl} = \sqrt{\lambda_2} (\hat{\mathrm{a}}_j \odot \hat{\mathrm{a}}_l^*), j \neq l \end{cases} \tag{9}$$

Since B contains context patches, detection equation can be rewritten as:

$$\hat{\mathrm{r}}_d = \hat{\mathrm{z}} \odot \hat{\mathrm{a}}_0^* \odot \hat{\alpha}_0 + \sqrt{\lambda_2} \sum_{i=1}^{k} \hat{\mathrm{z}} \odot \hat{\mathrm{a}}_i^* \odot \hat{\alpha}_i \tag{10}$$

2.2 *Multiple Features Description of Target Appearance*

MFAPCE uses color histogram and deep features to illustrate target appearance.

Deep features. In this paper, the trained VGG-NET-19 [10] on ImageNet is used for deep features extraction. The feature maps of *conv*3−4, *conv*4−4 and *conv*5−4 are collected to illustrate the appearance of the target. However, as the depth of the

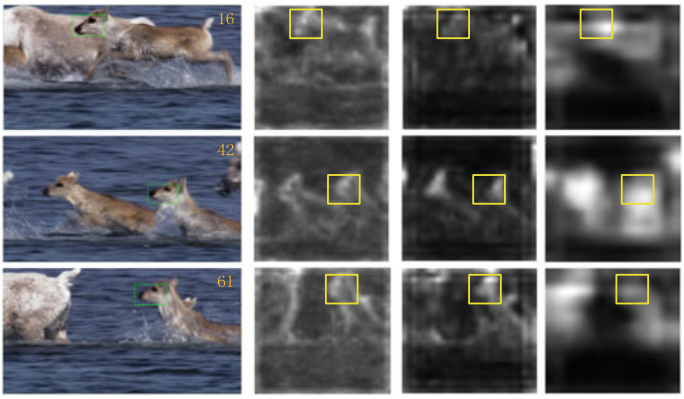

Fig. 2 Visualization of convolutional features. Three frames from the deer sequence. The first row is the 16th frame and convolutional features, the second row is the 42nd frame of deer sequence and convolutional features, the third row is the 61st frame and convolutional features

convolutional neural network increases, the spatial resolution will gradually decrease due to the pooling operation, and such low spatial resolution is insufficient to locate targets accurately. The feature maps of different resolutions are adjusted to a fixed size by bilinear interpolation, assuming x is an upsampled feature map, f is a low resolution feature map, and weight w dependents on the feature maps around position i and k neighboring feature vectors respectively, the feature vector for the ith location is:

$$\mathrm{x_i} = \sum_k w_{ik} \mathrm{f}_k \tag{11}$$

We visualize feature maps by using bilinear interpolation as show on Fig. 2:

The first row in Fig. 2 is the third, fourth, and fifth convolutional feature maps at the 16th frame. The second and third row are also the same. By row comparison, it is found that early convolutional features can encode more fine-grained details, but with the increase of depth, there is also a high brightness at target position. By column comparison, it is found that the extracted appearance features can still distinguish target when object has fast motion and background clutter.

The operation of image preprocessing is required before the extraction of deep features. The process is as follows: Assuming that the image to be extracted is *imag*. And the three channels of *imag* are *imag_R*, *imag_G*, *imag_B*. And then we get the mean values of three channels: *imag_R_ave*, *imag_G_ave* and *imag_B_ave*. The preprocessed image *imag_pre* is expressed as follows:

$$\begin{cases} imag\_pre\_R = imag\_R - imag\_R\_ave \\ imag\_pre\_G = imag\_G - imag\_G\_ave \\ imag\_pre\_B = imag\_B - imag\_B\_ave \end{cases} \tag{12}$$

Convolutional features of *imag_pre* can be obtained after forward propagation through convolutional neural network. Assume that the extracted deep features are df_layer_n, n is number of layer. However, the boundary effect still exists in this algorithm, it is necessary to define a two dimensional hanning window to mitigate the boundary effect. Details as follows:

First, the one dimensional hanning window is defined in the x, y direction.

$$\begin{cases} hannwin\_x(N) = 0.5\left[1 - \cos\left(\dfrac{2\pi n}{N+1}\right)\right], 1 \le n \le N \\ hannwin\_y(M) = 0.5\left[1 - \cos\left(\dfrac{2\pi m}{M+1}\right)\right], 1 \le m \le M \end{cases} \tag{13}$$

The N and M are the length and width of the idealized output y respectively, and the two-dimensional hanning window *hannwin* is expressed as:

$$hannwin = hannwin\_x * hannwin\_y' \tag{14}$$

Finally, the deep features used to illustrate the appearance of the target are:

$$f_n = df\_layer_n * hannwin \tag{15}$$

Color histogram features. Assuming that the real target region is o, the rectangular region marked in the image is O, and the rectangular region around the target is S. The probability model of the target region is α_{H_0} [11].

$$\alpha_{\mathrm{H}_0} = \begin{cases} \frac{H_O^I(b_{\mathrm{X}})}{H_O^I(b_{\mathrm{X}}) + H_S^I(b_{\mathrm{X}})} & \text{if } I(\mathrm{x}) \in I(O \cup S) \\ 0.5 & otherwise \end{cases} \tag{16}$$

As shown on Fig. 3, taking the 50th frame for an example, the left image is a sample image,and the right image is obtained from the above model. As shown on the figure, there is a higher brightness at the target location.

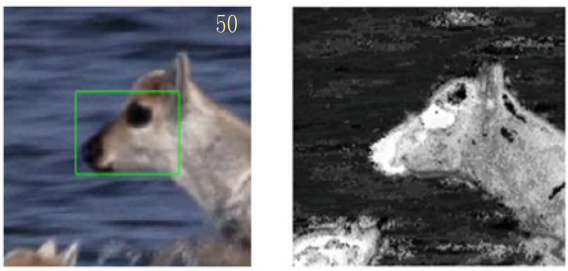

Fig. 3 Color histogram features. The image on the left is the original image, and on the right is the image of color histogram features

2.3 Confidence Estimation Based on APCE

Average peak correlation energy. The disturbing degree of response is judged by the average peak correlation energy (*APCE*). The average peak correlation energy is expressed as follows:

$$APCE = \frac{|R_{max} - R_{min}|^2}{mean\left(\sum_{w,h}(R_{w,h} - R_{min})^2\right)} \tag{17}$$

where R_{max}, R_{min} and $R_{w,h}$ denote the maximum, minimum and the wth row hth column elements of response.

The estimation of response confidence. Most tracking algorithms do not consider whether the tracking results are reliable, and when the target is affected by occlusion or background clutters, the tracking algorithm will learn the information beyond the target and eventually lead to drift or even failure of tracking. As shown on Fig. 4, at frame 26, when the target has motion blur and the background clutters, the response disturbance violently and the multiple peaks influence detection. When object is not disturbed by motion blur and background clutters at frame 66, the response has a definite peak and less disturbance.

Therefore, the disturbing degree of response can reflect the confidence of the tracking results, when the detected target matches the correct target well, the response has only one sharp peak and the disturbance is not obvious. On the contrary, the response fluctuates violently. As shown on Fig. 4, when the response disturbing is little, the target correctly detects, *APCE* will be at a higher value.

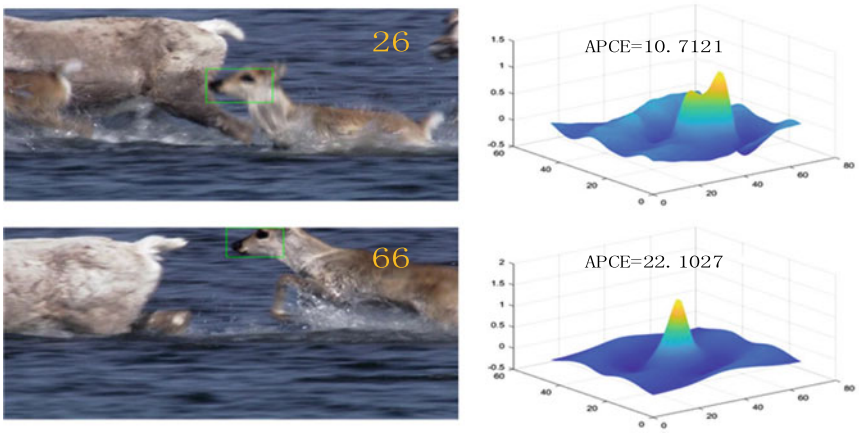

Fig. 4 APCE and response. The first row is 26th frame of the deer sequence and APCE of response. The second row is 66th frame of the deer sequence, and the APCE of response

When the response disturbing is greatly, the target is disturbed by background clutters and motion blur, *APCE* will be at a lower value.

It can be seen from above that the average peak correlation energy reflects the disturbing degree of the response and confidence of response.

3 Experiment

The experimental environment of this paper is configured as follows: Win10 operating system, i5-7500 (3.60 GHz) processor, 8 GB RAM, Matlab R2017a. The benchmark dataset is OTB100, which contains common problems in visual tracking such as illumination variation, scale variation, occlusion, motion blur and so on. $conv3-4$, $conv4-4$ and $conv5-4$ are selected to illustrate appearance of the target, three repsonse of these layers are weighted by 0.25, 0.5 and 1 respectively. λ_1 is 0.00001 and λ_2 is 0.5. All parameters are fixed in the course of the experiment. We evaluate the proposed algorithm with comparisons to 7 tracking algorithms. The 7 algorithms in this experiment is: STAPLE_CA algorithm, STAPLE algorithm, KCF algorithm, STRUCK algorithm, TLD algorithm, CSK algorithm and MIL algorithm.

3.1 Quantitative Analysis

The algorithm is evaluated through precision plot and success plot. The precision plot is defined as the percentage of the frame within the given distance between the estimated position and the actual position. The success plot refers to the overlap rate of the bounding box, given the target bounding box r_t detected by the detection algorithm and the target bounding box r_a of the actual labeling, the overlap rate is defined as: $S = \frac{|r_t \cap r_a|}{|r_t \cup r_a|}$, where $\cup$ and $\cap$ represent the union and intersection of the two regions respectively, $|\cdot|$ represents the number of pixels.

Figure 5 shows precision plot and success plot, OUR is algorithm of this paper. OUR algorithm is superior to other algorithms. OUR algorithm has improved precision by 0.2% compared with SPTALE_CA, and the success has increased by 1.6%. Compared with STAPLE, the precision of OUR algorithm is increased by 2.4% and success is increased by 3.5%. Compared with the KCF algorithm, the precision of OUR algorithm is increased by 15.3%, success is increased by 33.2%.

Figures 6 and 7 are the precision plots and success plots for background clutter (a), deformation (b), illumination variation (c) and in-plane rotation (d). It can be seen from the Figs. 6 and 7 that because OUR algorithm uses deep features that can better illustrate the appearance, more robust color features for object motion and the average peak correlation energy to judge the confidence of the response, the precision plot and success plot are better than other tracking algorithms.

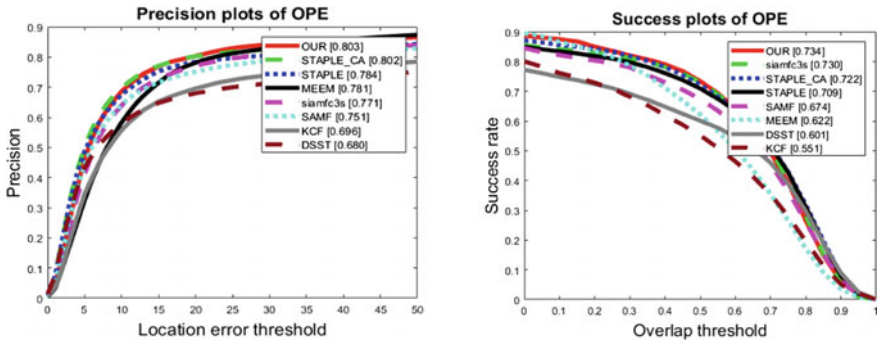

(a) Precision plots **(b)** Success plots

Fig. 5 Precision plot for OUR algorithm: The legend of distance precision contains threshold scores at 20 pixels. Our proposed algorithm performs favorably against the state-of-the-art trackers. Success plot for OUR algorithm: The legend of overlap success contains area under-the-curve score for each tracker. Our proposed algorithm performs favorably against the state-of-the-art trackers

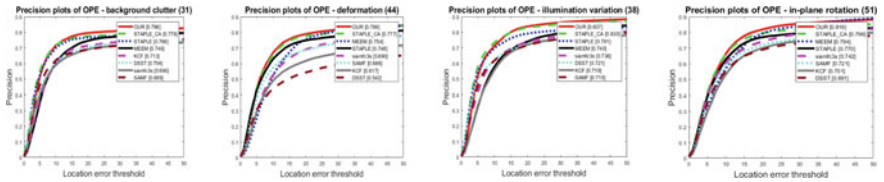

(a) background clutter **(b)** deformation **(c)** illumination variation **(d)** in-plane rotation

Fig. 6 Precision plots for BC, DEF, IV, and IPR subsets

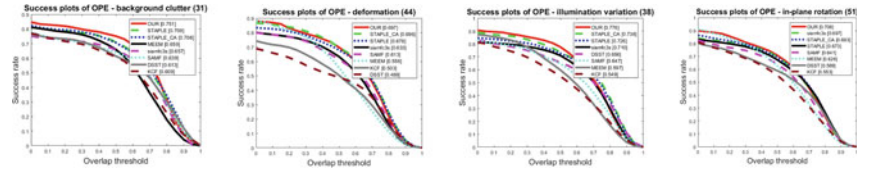

(a) background clutter **(b)** deformation **(c)** illumination variation **(d)** in -plane ro tation

Fig. 7 Success plots for BC, DEF, IV, and IPR subsets. Our proposed algorithm performs favorably against the state-of-the-art trackers

3.2 Qualitative Analysis

Taking the soccer and football video sequences in Fig. 8 as examples, the contrast algorithm is STAPLE_CA algorithm. In OTB100 datasets, soccer video sequences have properties such as illumination variation, occlusion, motion blur, fast motion etc. Football video sequences have properties such as occlusion, background disturbance etc. Following is comparison of the tracking results for different video sequences.

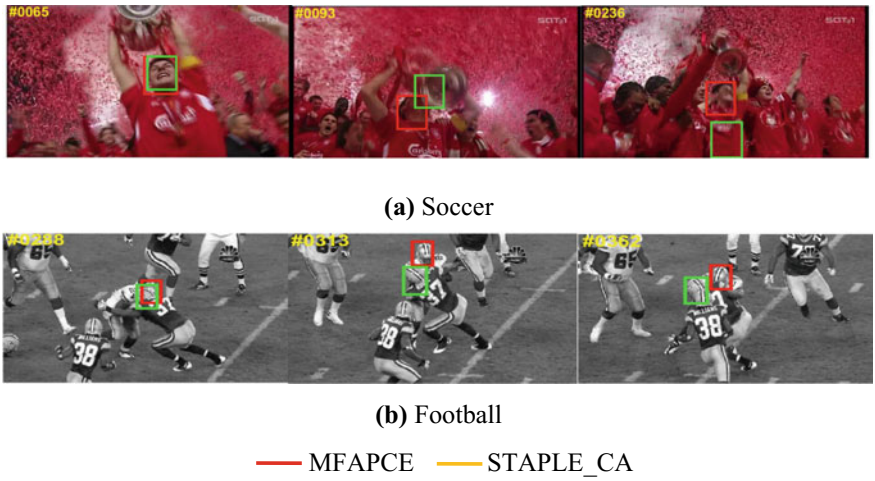

Fig. 8 Comparison of tracking results between MFAPCE and STAPLE_CA. The above pictures are tracking results about different tracking algorithm

Soccer video sequence: at 65th frame, both methods can track the target, but by the 93rd frame, STAPLE_CA gradually gets out of the target. By the 236th frame, STAPLE_CA has completely left the target. However, OUR algorithm uses the average peak correlation energy to judge the confidence of the response. OUR algorithm has better tracking performance.

Football video sequence: First, at 288th frame, it can be seen that both methods can track the target, and STAPLE_CA has begun to gradually get out of the target. After the 313th frame, STAPLE_CA has completely far away from target. OUR algorithmcan can still track when target is disturbed by background information.

4 Conclusion

The traditional tracking algorithm employs artificial features that are not strong enough to illustrate the target's appearance. And there is no confidence judgment on the target response. MFAPCE algorithm uses deep features and color features to illustrate the appearance of the target. And the average peak correlation energy is used to detect the confidence of the response and to determine whether to update the model; and the algorithm uses context information to constrain the background information. Experiment shows that the proposed algorithm outperforms the traditional algorithm in precision plots and success plots.

Acknowledgements This work was supported by the National Natural Science Foundation of China (61561016, 11603041), Guangxi Information Science Experiment Center funded project, Department of Science and Technology of Guangxi Zhuang Autonomous Region (AC16380014, AA17202048, AA17202033).

References

1. Wang, N., Yeung, D.Y.: Learning a deep compact image representation for visual tracking. In: International Conference on Neural Information Processing Systems, pp. 809–817. Curran Associates Inc (2013)
2. Gao, J., Ling, H., Hu, W., et al.: Transfer learning based visual tracking with Gaussian processes regression. In: Computer Vision—ECCV 2014, pp. 188–203. Springer International Publishing (2014)
3. Valmadre, J., Bertinetto, L., Henriques, J., et al.: End-to-End representation learning for correlation filter based tracking. 5000–5008 (2017)
4. Henriques J.F., Caseiro R, et al.: Exploiting the circulant structure of tracking-by-detection with kernels. In: Computer Vision—ECCV 2012, pp. 702–715. Springer, Berlin, Heidelberg (2012)
5. Wang, M., Liu, Y., Huang, Z.: Large margin object tracking with circulant feature maps 4800–4808 (2017)
6. Qi, Y., Zhang, S., Qin, L., et al.: Hedged deep tracking. In: IEEE Conference on Computer Vision and Pattern Recognition, pp. 4303–4311 (2016)
7. Ma, C., Huang, J.B., Yang, X., et al.: Hierarchical convolutional features for visual tracking. In: IEEE Conference on IEEE International Conference on Computer Vision, pp. 3074–3308 (2016)
8. Mueller, M., Smith, N., Ghanem, B.: Context-aware correlation filter tracking. In: IEEE Conference on Computer Vision and Pattern Recognition, pp. 1387–1395. IEEE Computer Society (2017)
9. Henriques, J.F., Caseiro, R., Martins, P., et al.: High-speed tracking with kernelized correlation filters. IEEE Trans. Pattern Anal. Mach. Intell. **37**(3), 583–596 (2015)
10. Simonyan, K., Zisserman, A.: Very deep convolutional networks for large-scale image recognition. Comput. Sci. (2014)
11. Possegger, H., Mauthner, T., Bischof, H.: In defense of color-based model-free tracking. In: IEEE Conference on Computer Vision and Pattern Recognition, pp. 2113–2120 (2015)

Analysis of Urban Bicycles' Trip Behavior and Efficiency Optimization

Haoyu Wen, Sheng Zhou, Zie Wang, Feier Qiu and Han Yu

Abstract Bicycle sharing systems are becoming more and more prevalent in urban environments. They provide a low environmental friendly transportation alternative city. The management of these systems brings many optimization problems. The most important of these problems is the individual maintenance of bicycle rebalancing and shared facilities, and the use of systems by creating requirements in asymmetrical patterns. In order to solve the problem of unbalanced use of bicycles, based on real data sets, a series of data mining is developed around these issues. By analyzing the characteristics of each site, the site is modeled from the perspective of individuals and clusters, through different models. The evaluation indicators to detect the accuracy of the results provide an effective method for predicting shared bicycles.

Keywords Shared bicycles · Data mining · Clustering · Forecasting

1 Introduction

With the economic development, human activities have caused more and more serious pollution and damage to the natural environment in recent years. Therefore, sustainable development has become the consensus of the international community [1]. In this case, the bicycle sharing system (BSS) was developed as a substitute for short-distance vehicles due to its low pollution, low energy consumption, and high flexibility. As of the end of 2016, more than 1,100 cities actively operated the automated bicycle sharing system, which deployed 2,000,000 public bicycles worldwide. With the bicycle sharing system, users can easily use a smart card to rent a bicycle at a nearby station, use it on short trips, and return at another station [2].

According to reports, this bicycle was rented more than 6,000 times and it rode more than 20,000 km within three years. Similarly, the most tireless bicycles in 2016

H. Wen (✉) · S. Zhou · Z. Wang · F. Qiu · H. Yu
School of Information and Safety Engineering, Zhongnan University of Economics and Law, Wuhan, China
e-mail: haoyuwen@zuel.edu.cn

H. Lu (ed.), *Cognitive Internet of Things: Frameworks, Tools and Applications*, Studies in Computational Intelligence 810,
https://doi.org/10.1007/978-3-030-04946-1_25

have been rented 5,616 times, an average of more than 15 times a day. In 2012, the maintenance cost of the Hangzhou bicycle sharing system was close to 6 million yuan. The contemporary bicycle share plan refers to the provision of bicycles to achieve short-term leases from one station to another [3]. Intuitively, operators can guide users to use undesired bikes to balance the use of bicycles based on the number of uses per bicycle. However, it is unrealistic for leading users to rent specific bikes. Therefore, by introducing active site attributes, we turned the issue of selecting bicycles into recommended lending and returning stations. In order to satisfy the user's needs to the maximum extent, a regulation system is needed to maintain the pre-optimal number of bicycles at each station [4].

Science and technology change lives, and no one can resist this tide [5]. The reason why the sharing of bicycles can set off a wave in the short time that is comparable to that of the Internet dating cars in the past is enough to prove that its emergence is a trend.Of course, no new thing can be perfect, and the shared bicycle that is rapidly booming is no exception. Due to the increasing importance of bicycle sharing programs and the operational difficulties in managing them, people are very concerned about various issues related to bicycle sharing [6].

2 Related Works

At present, researchers have done a lot of research to describe the nature of bicycle sharing systems, business models, how they spread in time and space, and why they are adopted. Currently, most clustering methods can identify the movement patterns in bicycle use and divide these sites into clusters based on usage. For example, in [7], two clustering techniques use activity statistics, which are derived from the evolution of station occupancy or the number of bicycles available on the day [8]. However, most of these studies are focused on the study of vehicle scheduling problems through clustering and forecasting, and are unable to implement the regional distribution of the site and the content of the vehicle itself. And These papers also have inspired us.

Site-level bike sharing demand forecasts are more challenging and have attracted considerable interest from researchers. Independent variables, such as demographic factors and built environment factors, are extracted based on a 400 m buffer around each site [9]. Faghih-Imani et al. [10] built a similar linear hybrid model based on the two-day dataset of the Montreal BIXI bicycle sharing system to predict the hourly bicycle sharing needs at the station [10]. Yang et al. [8] proposed a probabilistic movement model that takes into account previous checkout records and journey duration to estimate the future registration number for each site [8]. However, for bicycle inspections or demand forecasts, they apply a random forest tree algorithm for each individual site, without using spatial or temporal correlations between sites [11].

The research in this article is based on site-level bike sharing needs. The main issues discussed include site activity, vehicle scheduling, and vehicle maintenance.We use K-means clustering and XBGOOST algorithm to predict all the features extracted from the data preprocessing stage. The results are evaluated using REMS and MAE. The prediction results are ideal.

3 Framework

The leasing company collects user data through the public bicycle service system. After obtaining the shared bicycle data, we separately list the important information in the data and analyze them separately. For the purpose of forecasting, the first thing to discuss here is whether or not borrowing a car and returning a car need to be discussed. After analyzing the data, we find that the borrowing mode of the vehicle is basically the same. Both have similar characteristics and can use a common model.

The experimental process is shown in the Fig. 1.

4 Data Analysis

4.1 Data Set

The data set for this article is from a shared bicycle rental company. The attributes of the data set are shown in Table 1.

By dividing the data set, we use the data from May to July 2015 as the training set and the data from August as the test set. In the experiment process, this article takes the characteristics of time, site, car, returning car, and analysis process as input, and uses site, time, car and return amount as forecast results.

Feature Explain For example, for the borrowing information of vehicles, we randomly selected some sites, and then compared these sites by car and returning the

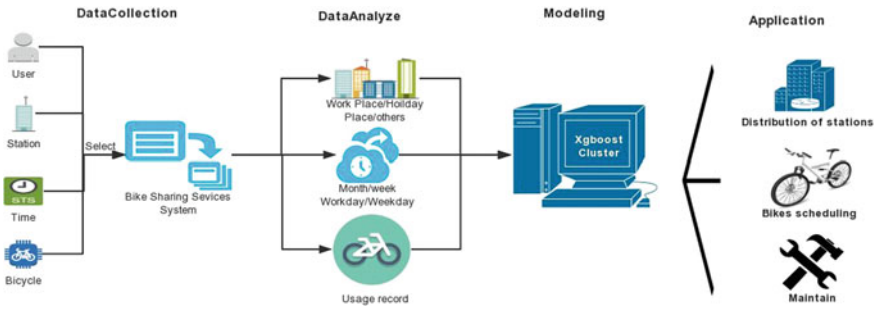

Fig. 1 The experimental process of the proposed framework

Table 1 1 Dataset properties

LEASEDATE	*CARDSN*	*RTLOCATIVEID*
LEASETIME	*RTSHEDID*	*VIPCARDSN*
USETIME	*RTDATE*	*OPTYPE*
SHEDID	*RTTIME*	*OPNAME*
LOCATIVEID	*OVERTIME*	

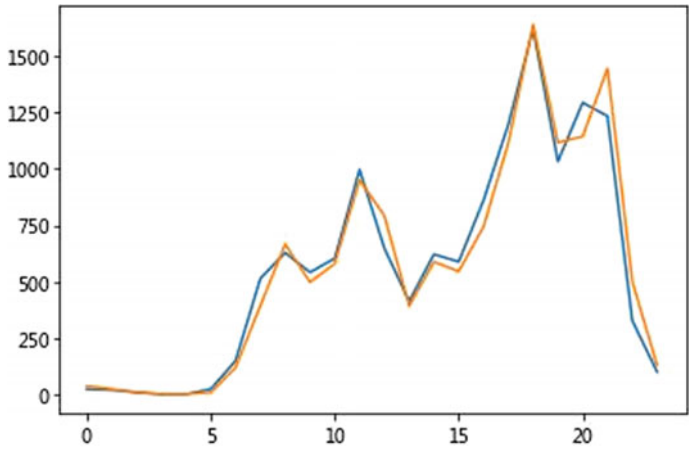

Fig. 2 LEASE/RETURN information

car information. The effect is shown in Fig. 2. The blue broken line in the figure indicates the condition of returning the car, and the orange curve indicates the amount of borrowed cars. The curves for borrowing and returning cars are very similar, and the curves are basically consistent. It can be inferred that the situation of borrowing at each site is similar in general and there is no significant difference.

5 Modeling

5.1 Problem Definition

Definition 1 (*Trip*) Travel $Tr = (So, Sd, o, d)$ is a bicycle usage record, where So represents the starting station, represented by *RTSHEDID*; Sd represents the destination station, represented by *LEASESHEDID*; o and d are the bicycle Check-out and Check-in time [12].

Definition 2 (*Time Interval*) The bicycle use time period $Time = \{Tv, Tw, Tr\}$, Tv and Tw are WorkDay and WeekDay, respectively, and Tr is the peak daily use of the bicycle.

Definition 3 (*Check-out/in*) Check out/Check in refers to the number of bicycles that are loaned out and retired by a *Time*.

Definition 4 (*Usage Counter*) Usage Counter refers to the number of uses per bicycle.

Definition 5 (*Problem definition*) Check in/Check out prediction problem. Given a set of historical trips $TH = \{Tr1, Tr2, Tr3, \ldots, TrH\}$, we want to predict the Check in/Check out of each site within a certain time.

Modeling from a single site: Each site's information is discussed through monthly, weekly, daily, and work day and off-site considerations from a site, and the peak period of site usage is compared to the average period. The discovery of these factors can have a greater impact on the site's Check in/Check out.

Modeling from a site cluster/aggregation perspective: Sites are divided into three levels with different levels of activity. Below the average daily number of borrowed/returned quarters is the low active site; above average daily Three-quarters of the number of borrowed/returned cars are active sites; others are general sites.

5.2 Algorithms

This article uses the *XGBoost* algorithm to solve the shared bicycle prediction problem. *XGBoost* implements a generic Tree Boosting algorithm. One representative of this algorithm is the Gradient Boosting Decision Tree (*GBDT*), which was born in February 2014 and focuses on gradient learning algorithms. The library has received extensive attention due to its excellent learning effect and efficient training speed. It combines many of the previous work on the gradient lifting algorithm, and has done a lot of optimization in the project implementation, and is one of the most successful machine learning algorithms.

The objective function of xgboost is as follows:

$$\Omega\left(f_t\right) = \gamma \mathrm{T} + \frac{1}{2}\lambda \sum_{j=1}^{\mathrm{T}} w_j^2 \tag{1}$$

The regular term controls the complexity of the model, including the number of leaf nodes T and the L2 modulus square of the leaf score.

$$o_{bj} = \sum_{i=1}^{n} \left(y_i, \hat{y}_i\right) + \sum_{k=1}^{K} \Omega\left(f_k\right) \tag{2}$$

Formula derivation details describe references [13]. We now mainly look at the formula used when splitting the tree nodes in xgboost:

$$Gain = \frac{G_L^2}{H_L + \lambda} + \frac{G_R^2}{H_R + \lambda} + \frac{(G_L + G_R)^2}{H_L + H_R + \lambda} - \Upsilon \tag{3}$$

This formula formally agrees with the ID3 algorithm (using entropy to calculate the gain) and the CART algorithm [14] (which uses the gini index to calculate the gain). The gamma in the above equation is the threshold, which is the coefficient of the number of leaf nodes T in the regular term, so *XGBOOST* is equivalent to the objective function at the same time. Doing pre-pruning. In addition, there is a coefficient lambda in the above formula, which is the coefficient of L2 norm square of the leaf score in the regular term. Smoothing the leaf score also plays a role in preventing overfitting. This is a feature not found in the conventional *GBDT*. Moreover, regularization is used in *XGBOOST*. The standard *GBM* implementation does not have regularization steps like *XGBOOST*. Regularization is also helpful in reducing overfitting. It has a high degree of flexibility, allowing users to define custom optimization goals and evaluation criteria. *XGBOOST* has built-in rules for handling missing values.

5.3 Evaluation Indicators

The metrics used were RMSE [15] (Root-Mean-Square Error) and MAE (Mean Absolute Error). Root mean square error is also called the standard error. It is the square root of the square of the observed deviation from the true value and the ratio of the observed times n. The average absolute error is the average of the absolute error. The average absolute error can better reflect the actual situation of the prediction error. This article uses two kinds of evaluation indicators to display and compare the evaluation results, so as to make the prediction results more rigorous.

This article uses the *XGBOOST* algorithm to make predictions, taking $\{Time, Station, RT, LEASE, F1, \ldots, Fn\}$ as input, where *Time* represents time, *Station* represents site, *RT* and *LEASE* are borrowed and returned respectively, $F1$ through *Fn* represent Analyze the available features. The output is $\{Time, Station, RT, LEASE\}$, the number of cars borrowed and returned at each site at a certain time.

6 Experiments

6.1 Site Distribution

At this stage, public bicycle stations have obvious problems of irrational distribution. This will result in no-visit access to sites in small-use areas and waste of resources. In some regions, the use of bicycles is large and the number of stations is small. This

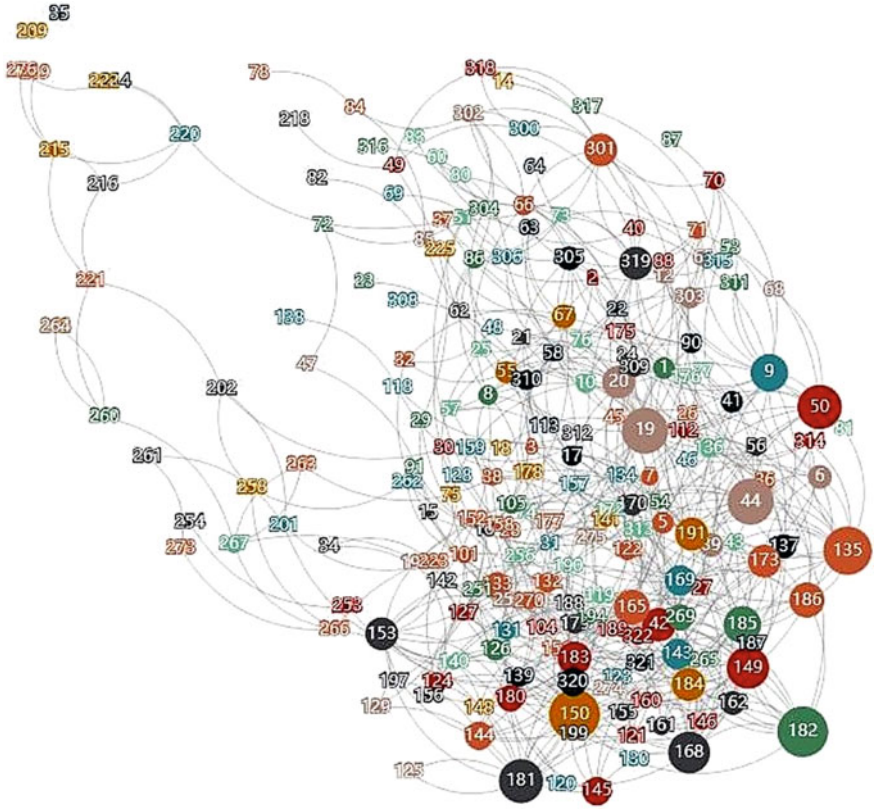

Fig. 3 May 4th, 8:00–8:30 am

has led to the use of vehicles in the region concentrated on a small number of sites, and the pressure on these stations is excessive.

For example, the sites in Fig. 3 with the numbers 182, 168, and 135 in the lower right corner have large site usage, but there are few available sites. Consider creating new sites in the nearby areas to reduce the pressure on individual sites. There are also many types of these two types of sites, such as 222, 318 sites with less bicycle use, 181, 301 sites with a large amount of use, etc. Reasonably reduce the number of sites in areas with low site usage, and in high-use areas Newly built sites relieve pressure on individual sites and can effectively achieve a rational and efficient allocation of public bicycle sites.

6.2 Vehicle Scheduling

Method Comparison In the course of the experiment, some features of data analysis are proposed, and the time-related Check in/Check out and site-related Check in/Check out are input into the *XGBOOST* prediction respectively, and the RMSE/MAE score is used to compare the results with all input features. The results were compared. By comparing the deviations of different feature prediction results, we can observe the influence of the corresponding features on the prediction results.

Then compare the K-means clustering with the prediction results of the *XGBOOST* algorithm to find out which method is more suitable for the prediction problem of shared bicycles.

Results Comparison In the experiment, some features were extracted, and the daily and weekly time characteristics and all time characteristics were input respectively. The site's loan repayment amount and site liveness were input respectively, and the results were tested by RMSE and MAE. The comparison results are shown in Table 2.

Analysis of Results In the experiment, through the comparison of the results in the previous section, it can be seen that the different features have different influences on the prediction results, and the characteristics of the time dimension have greater influence than the site dimension. However, when all the sets of valid features are used as input, the effect is not good. This is because other features discussed in the data analysis are also included in the experiment.

This article uses the above experimental results to predict the amount of vehicles to be retired at each site, implement effective vehicle scheduling, and distribute public bicycles to each site. This relieves pressure on the peak usage of the site while balancing the use of bicycles and avoiding the status quo where no car is available or nowhere to be returned.

6.3 Vehicle Maintenance

In order to realize the long-term development of public bicycles, there is another problem that needs to be solved is the maintenance of bicycle equipment. As we all

Table 2 Analysis of results

Feature	RMSE	MAE
Every day	9.3282	6.0824
Working days/days off	10.1171	6.5500
Time features	10.0124	6.8103
Site repayments	9.9555	6.3723
Site activity	9.9641	6.3999
Site features	9.9595	6.3751
All features	10.4201	6.7787

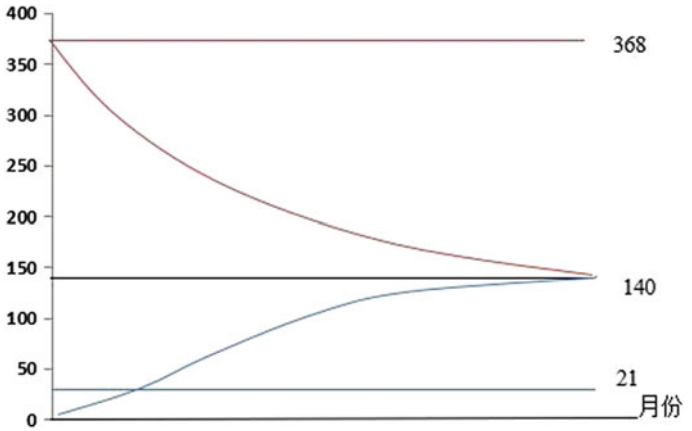

Fig. 4 The result of the vehicle maintenance

know, the cost of each bicycle is very high, and the situation of damage or abandonment of bicycles often occurs, or when some bicycles are used too frequently, if they cannot be repaired or scrapped in time, this requires a Effective solution.

Frequent bicycles use more than 2–3 times per day, while low-utility bicycles are left untouched for months, which leads to a polarization situation. For this kind of situation, we propose a corresponding countermeasure, which divides the two boundaries from the ones that are used too frequently and are too sparse. Considering that there are relatively few vehicles with extremely frequent use in data sets, the number of uses for the previous 30th percentile (116) is a limit, and vehicles with less than 116 uses are less frequently used; The number of uses of the quintile (198 times) is another limit.

In Fig. 4, the red line represents a vehicle that is used too frequently, and the blue line (a straight line) represents a vehicle that is used less frequently. Now, the difference in the number of visits between the two is relatively large, and it is in an extremely uneven state. After applying our analysis and solution methods, the curves of the two curves are shown in the graph. The number of visits to vehicles that are under-use will gradually increase, while the number of visits to vehicles that are frequently used will gradually decrease. Finally, the two will gradually approach each other. Mean, reaching a relatively balanced state.

7 Discussion

7.1 Open Issues

Of course, the use of public bicycles is becoming more and more widespread and the problems faced will also be more and more. For instance, the repatriation of site-style public bicycles needs to be completed at a fixed site, and they need to be

rented via magnetic cards. This limits the use of public bicycles and cannot really allow citizens to borrow cars at any time and anywhere. Moreover, the current social citizenship is not enough to achieve a normal loan for each bike. For lost vehicles, it cannot be recovered in many cases. This requires a new public bicycle service system that can solve the current dilemma of public bicycles while the input cost is within a controllable range.

Although current flexible and parked bicycles (such as OfO and Mobike) are very popular, the current page has a huge problem, that is, too many vehicles affect the traffic, but it hinders people's normal travel. So we need a convenient, low-cost, lightweight and convenient travel tool. A new type of shared device may soon find its way into our eyes—folding shared bicycles that are light and fast, take up less space, and avoid parking problems.

8 Conclusion

This paper discusses the convenience and problems faced by urban bicycles from different perspectives of users, bicycles, and businesses by studying the behaviors of sharing bicycles in cities. Based on the actual data of the public bicycle company for 15 years, this paper conducts a series of data mining. Through data visualization and comparative analysis methods, it points out the current problems faced by public bicycles, gives appropriate recommendations, and promotes the sharing of bicycle equipment. The positive development of sharing equipment can better serve our society.

References

1. Demaio, P.: Bike-sharing: history, impacts, models of provision, and future. J. Public Transp. **12**(4) (2009)
2. Hu, J., Yang, Z., Shu, Y., Cheng, P., Chen, J.: Data-driven utilization-aware trip advisor for bike-sharing systems. In: 2017 IEEE International Conference on Data Mining (ICDM), vol. 00, pp. 167–176 (2018). https://doi.org/10.1109/ICDM.2017.26
3. Fishman, E., Washington, S., Haworth, N.: Bike share: a synthesis of the literature. Urban Transp. China **33**(2), 148–165 (2013)
4. Chemla, D., Meunier, F., Calvo, R.W.: Bike sharing systems: solving the static rebalancing problem. Discret. Optim. **10**(2), 120–146 (2013)
5. Lu, H., Li, Y., Chen, M., Kim, H., Serikawa, S.: Brain intelligence: go beyond artificial intelligence. MONET **23**, 368–375 (2018)
6. O'Mahony, E., Shmoys, D.B.: Data analysis and optimization for (citi)bike sharing. In: Twenty-Ninth AAAI Conference on Artificial Intelligence, pp. 687–694 (2015)
7. Froehlich, J., Neumann, J., Oliver, N.: Sensing and predicting the pulse of the city through shared bicycling. In: IJCAI 2009, Proceedings of the International Joint Conference on Artificial Intelligence, Pasadena, CA, pp. 1420–1426 (2009)
8. Yang, Z., Hu, J., Shu, Y., Cheng, P., Chen, J., Moscibroda, T.: Mobility Modeling and Prediction in Bike-Sharing Systems, pp. 165–178 (2016)

9. Rixey, R.A.: Station-level forecasting of bikesharing ridership. Transp. Res. Rec. J. Transp. Res. Board **2387**(-1), 46–55 (2013)
10. Faghih-Imani, A., Eluru, N., El-Geneidy, A.M., Rabbat, M., Haq, U.: How land-use and urban form impact bicycle flows: evidence from the bicycle-sharing system (bixi) in montreal. J. Transp. Geogr. **41**, 306–314 (2014)
11. Lin, L., He, Z., Peeta, S.: Predicting station-level hourly demands in a large-scale bike-sharing network: A graph convolutional neural network approach. Transp. Res. Part C: Emerg. Technol.**97**, 258–276 (2018)
12. Li, Y., Zheng, Y., Zhang, H., Chen, L.: Traffic prediction in a bike-sharing system. In: Sigspatial International Conference on Advances in Geographic Information Systems, pp. 1–10 (2015)
13. Chen, T., Guestrin, C.: Xgboost: A Scalable Tree Boosting System. arXiv:1603.02754
14. Prasad, A.M., Iverson, L.R., Liaw, A.: Newer classification and regression tree techniques: bagging and random forests for ecological prediction. Ecosystems **9**(2), 181–199 (2006)
15. Chai, T., Draxler, R.R.: Root mean square error (rmse) or mean absolute error (mae)?-arguments against avoiding rmse in the literature. Geosci. Model. Dev. Discuss. **7**(3), 1247–1250 (2014)

Pedestrian Detection in Unmanned Aerial Vehicle Scene

Qianqian Guo, Yihao Li and Dong Wang

Abstract With the increasing adoption of unmanned aerial vehicles (UAVs), pedestrian detection with use of such vehicles has been attracting attention. Object detection algorithms based on deep learning have considerably progressed in recent years, but applying existing research results directly to the UAV perspective is difficult. Therefore, in this study, we present a new dataset called UAVs-Pedestrian, which contains various scenes and angles, for improving test results. To validate our dataset, we use the classical detection algorithms SSD, YOLO, and Faster-RCNN. Findings indicate that our dataset is challenging and conducive to the study of pedestrian detection using UAVs.

Keywords Pedestrian detection · UAVs-Pedestrian dataset · Deep learning

1 Introduction

At present, the market and market scale of civil small unmanned aerial vehicles (UAVs) are developing and growing rapidly. With the continuous progress of technology, UAVs play a substantial role no longer only in the military but also in the civilian field.

Drones are widely used in many areas, including film and television, surveillance, delivery, and accident assistance. Consequently, pedestrian detection using UAVs is becoming important and necessary. For example, prompt target detection can accelerate a rescue mission. Given the height and angle of existing pedestrian detection equipment, present datasets cannot be a good representation of pedestrian detection with UAVs. Compared with the perspective of ground cameras, an aerial perspective has significant advantage and flexibility. Excessive blocking among targets can be effectively avoided with aerial cameras' shooting angles and ranges. However, from

Q. Guo · Y. Li · D. Wang (✉)
School of Information and Communication Engineering,
Dalian University of Technology, Dalian 116024, China
e-mail: wdice@dlut.edu.cn

H. Lu (ed.), *Cognitive Internet of Things: Frameworks, Tools and Applications*, Studies in Computational Intelligence 810,
https://doi.org/10.1007/978-3-030-04946-1_26

the perspective of aerial photography, the interference caused by obstacle shielding and object deformation is an urgent problem. To solve this issue, we propose a new dataset, which is called UAVs-Pedestrian and obtained by drones from different angles and heights and under varying scenarios.

Visual target detection refers to detecting, extracting, and identifying the content in a video image sequence and then estimating the position and size of the target object. The detector outputs the target number, orientation, and shape information in the video stream content to the client and subsequently needs to determine whether the target is within the image and the size of the target object is not limited. The detector should be robust for any given class of objects.

Object detection algorithms based on deep learning have substantially progressed in recent years. Existing target detection algorithms are mainly divided into two categories, namely, (1) two-stage approaches, including those in [1–4], and (2) one-stage approaches, including those in [5, 6]. A two-stage approach consists of two parts. The first step generates a set of candidate object proposals, and the second step uses a convolution network to determine the accurate object regions and corresponding class tags. Two-stage detection methods have exhibited good accuracy on the PASCAL VOC [7] and MS COCO [8] datasets.

The one-stage approaches are attracting more attention than are the two-stage ones mostly due to the former's computation efficiency. A one-stage approach involves a single network predicting bounding boxes and class probabilities directly from a full image in one evaluation. Such an approach detects objects similarly as does RPN [3] and SSD and uses multiple feature maps at different resolutions to cover objects at various scales. YOLO computes a global feature map and utilizes a fully connected layer to generate predictions in a fixed set of regions. Meanwhile, YOLOv2 [6] adds batch normalization on all convolution layers and adopts convolution layers with anchor boxes instead of fully connected layers to predict bounding boxes to improve accuracy. YOLOv3 [9] uses deeper networks to extract features and generate predictions on the basis of different feature maps. The main advantage of YOLOv3 is high efficiency in detecting objects and computations, whereby the detection speed can meet real-time performance.

2 UAVs-Pedestrian Dataset

Although much research has been conducted on pedestrian detection, applying existing results directly to the UAV perspective is difficult. Many false and missed detections in pedestrian scenes can occur, especially in areas directly below the UAV. Figure 1 presents the proposed dataset UAVs-Pedestrian, which contains 1160 images captured by UAVs. In this section, we present details of the dataset.

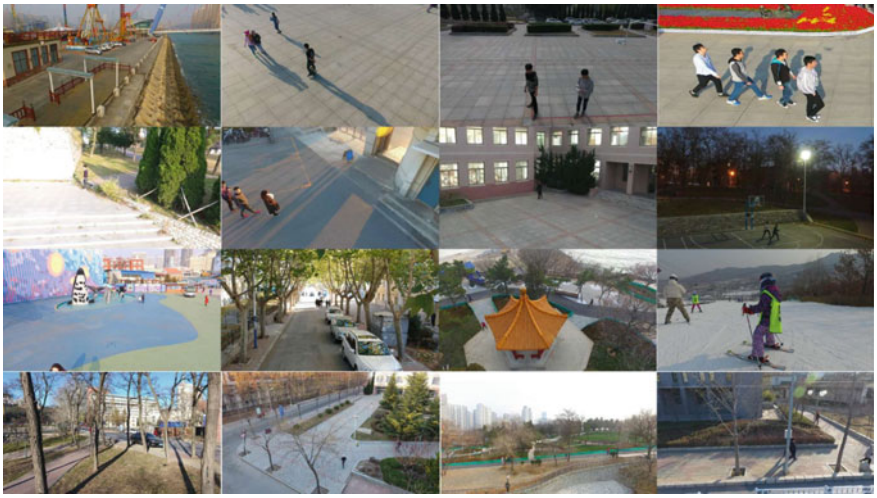

Fig. 1 Sampled images from proposed dataset

2.1 Dataset Construction

Pedestrian detection in UAV scene, which is more complicated than that in ordinary scene, has the following difficulties.

- Illumination Fluctuations: Time and weather affect lighting in photo capture. Bright light introduces many types of outside noise, and low light is unfavorable for extracting features. Hence, the effect of light should be considered.
- Occlusion: In sophisticated scenarios, a pedestrian can be obscured by objects such as trees, thereby potentially affecting test results.
- Deformation: Drones' perspective can make a difference in a person's shape that renders recognition difficult.
- Motion Blur: Moving target areas can result in blurred images.
- Background Clutter: The background can have similar in color and texture to the target.
- Small Objects: Available target features are limited due to the small target size caused by the high altitude of aerial photography.
- Geographical Coverage Area: Geographical environment complexity is high in aerial video images. Complexity is high, when the target motion to the more complex areas, will be building geographical factors such as barriers, but because of the limitation of aerial high goal is small, so all goals are more likely to keep out.

2.2 *Details of the Dataset*

Drones were flown 3–10 m high to ensure access to pedestrians of different sizes. Our images were collected under different scenes, such as streets, buildings, playgrounds, and playgrounds; angles; and weather conditions, such as cloudy and sunny. The proposed dataset contains 1,160 images. With consideration of the factors mentioned in Sect. 2.1, our dataset images were captured from UAVs flying at different altitudes, angles, and scenes. All images of the dataset are in JPG and PNG formats. The image length–width ratio is in the range of 1.3–2.07, and the entire range of the dataset scale is from 720×405 to 1920×1080 pixels. Figure 1 illustrates several examples from our dataset.

In Fig. 1, the first, second, third, and fourth rows comprise images captured from different heights, under varying light conditions, in different scenes, and under different occlusions, respectively.

3 Experiments

In our experiments, we used algorithms typically adopted for object detection, including Faster-RCNN (VGG16), SSD, and YOLOv3 (Darknet53). Faster-RCNN is a two-stage detector that has good performance in object detection. SSD detects an object with different aspect ratios and at varying scales by obtaining features from different stages of the network. Therefore, SSD can detect small targets well. YOLOv3 uses deeper networks to extract features and generate predictions on the basis of different feature maps. The main advantage of YOLOv3 is high computational efficiency. In addition, it can perform real-time detection, and its modified version is effective for object detection. The contrastive experiments performed in this work evaluated UAVs-Pedestrian in the rationality of construction for the pedestrian detection task. We divided the dataset into two parts, whereby 825 images were grouped to form the training set and 325 images were placed in the test set. We trained 80,000 times on a GTX1080. Although the procedure does not require such a large number of iterations, we decided to have as many testing times to observe the change in the error curve during early training and select the appropriate learning rate from the change trend. This step could achieve enhanced results.

We used map as an evaluation metric, as is commonly selected in object detection tasks [10–12]. In our case, with only one class (“Pedestrian”), we utilized average precision and obtained the result on the test set of UAVs-Pedestrian. Table 1 presents the experimental results on the test data of UAVs-Pedestrian, and Fig. 2 shows the sample detections of existing pedestrian detection algorithms.

In Fig. 2, the first, second, and third rows display the image detection results of YOLOv3, Faster-RCNN, and SSD, respectively. The results show that our dataset is effective and robust.

Table 1 Experimental results

Algorithm	SSD	Faster-RCNN	YOLOv3
AP	0.647	0.782	0.827

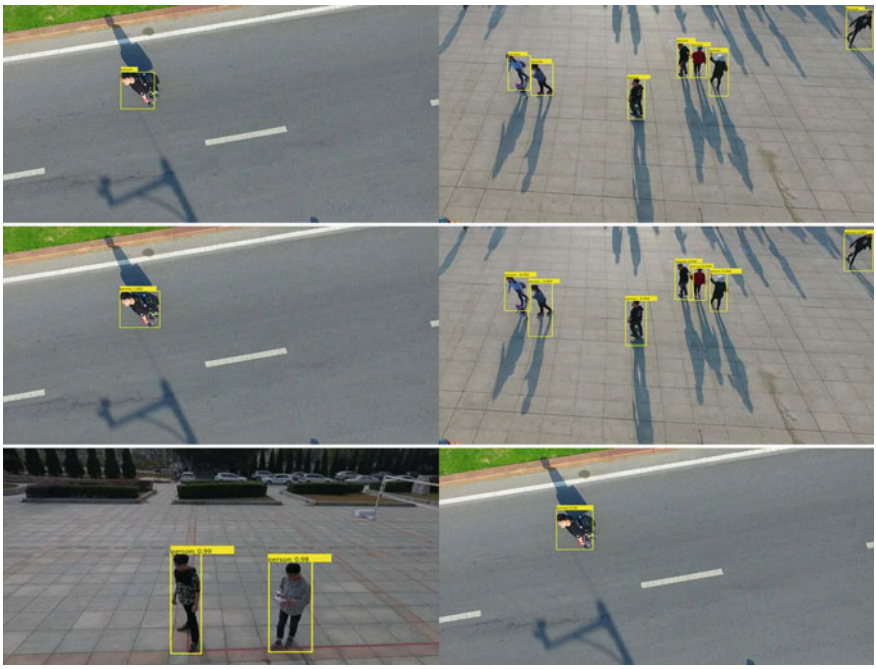

Fig. 2 Pedestrian test results

4 Conclusion

In this work, we present UAVs-Pedestrian, a new dataset for concurrent human action detection, and evaluated it using classical detection algorithms. Results show that our dataset is sufficiently challenging and robust for UAV pedestrian detection. For future work, for the UAV scenario, we will expand the image samples from multiple directions and estimate the scene depth of field, build different models for different depths of field, and improve the accuracy of the model algorithm.

Acknowledgements This work was supported by the Fundamental Research Funds for the Central Universities (No. DUT18JC30) and Undergraduate Innovation and Entrepreneurship Training Program (No. 201810141020101107 5).

References

1. Cai, Z., Fan, Q., Feris, R.S., Vasconcelos, N.: A unified multi-scale deep convolutional neural network for fast object detection. In: European Conference on Computer Vision, pp. 354–370 (2016)
2. Girshick, R.: Fast R-CNN. IEEE Int. Conf. Comput. Vis. 1440–1448 (2015)
3. Ren, S., He, K., Girshick, R., Sun, J.: Faster R-CNN: towards real-time object detection with region proposal networks. IEEE Trans. Pattern Anal. Mach. Intell. **39**(6), 1137 (2017)
4. Liu, W., Anguelov, D., Erhan, D., Szegedy, C., Reed, S.E., Fu, C., Berg, A.C.: SSD: single shot multibox detector. Eur. Conf. Comput. Vis. 21–37 (2016)
5. Redmon, J., Divvala, S., Girshick, R., Farhadi, A.: You only look once: unified, real-time object detection. IEEE Conf. Comput. Vis. Pattern Recognit. 779–788 (2016)
6. Redmon, J., Farhadi, A.: YOLO9000: better, faster, stronger. IEEE Conf. Comput. Vis. Pattern Recognit. 6517–6525 (2017)
7. Everingham, M., Gool, L.J.V., Williams, C.K.I., Winn, J.M., Zisserman, A.: The pascal visual object classes (VOC) challenge. Int. J. Comput. Vis. **88**(2), 303–338 (2010)
8. Lin, T., Maire, M., Belongie, S.J., Hays, J., Perona, P., Ramanan, D., Dollar, P., Zitnick, C.L.: Microsoft COCO: common objects in context. Eur. Conf. Comput. Vis. 740–755, (2014)
9. Redmon, J., FarhadiRedmon, A.: YOLOv3: an incremental improvement. IEEE Conf. Comput. Vis. Pattern Recognit. (2018)
10. Wang, L.: Places205-VGGNet models for scene recognition. IEEE Conf. Comput. Vis. Pattern Recognit. 1135–1155 (2015)
11. Liu, W., Anguelov, D., Erhan, D., Szegedy, C., Reed, S., Fu, C.Y., Berg, A.C.: SSD: single shot multibox detector. Eur. Conf. Comput. Vis. 21–37 (2016)
12. Huang, J., Rathod, V., Sun, C., Zhu, M., Balan, A.K., Fathi, A., Fischer, I., Wojna, Z., Song, Y., Guadarrama, S., Murphy, K.: Speed/Accuracy Trade-offs for Modern Convolutional Object Detectors (2016). arXiv:1611.10012

Two-Sided Sparse Learning with Augmented Lagrangian Method

Xiaohua Xu, Baichuan Fan, Ping He, Yali Liang, Yuan Lou, Zhijun Zhang and Xincheng Chang

Abstract In this paper, we propose a novel sparse learning model, named Two-Sided Sparse Learning with Augmented Lagrangian Method, and apply it to the classification problem. Existing dictionary learning method only emphasizes the sparsity of cases, but neglect the sparsity of features. In the context of classification, it is crucial to take into account the correlation among features and find the most representative features in a class. By representing training data as sparse linear combination of rows and columns in dictionary, this model can be more suitable for classification problem. Experimental results demonstrate that our model achieves superior performance than the state-of-the-art classification methods on real-world datasets.

Keywords Classification · Sparse learning · Dictionary learning
Sparse representation

1 Introduction

Sparse learning is a promising model and has been successfully applied in a variety of problems, including medical diagnosis [1–3]. The purpose of sparse learning model is to represent an input instance by an over-complete dictionary and the sparse representation of it under this dictionary.

The performance of sparse learning mostly depends on the dictionary. Some methods use the entire training set as dictionary and represent a sample by a sparse linear combination of this dictionary [4–6]. However, these methods emphasize the column-wise sparsity of a dictionary, i.e., the constraint on the number of selected training samples, but neglect the row-wise sparsity of features, i.e., the constraint on the number of selected features. In context of classification, we can find the most representative features in different class by applying row-wise sparsity, thus it's significant to include both column-wise and row-wise sparse representation of dictionary.

X. Xu · B. Fan · P. He (✉) · Y. Liang · Y. Lou · Z. Zhang · X. Chang
Department of Computer Science, Yangzhou University, Yangzhou, China
e-mail: angeletx@gmail.com; arterx@gmail.com

H. Lu (ed.), *Cognitive Internet of Things: Frameworks, Tools and Applications*, Studies in Computational Intelligence 810,
https://doi.org/10.1007/978-3-030-04946-1_27

In this paper, we propose a novel Two-Sided Sparse Learning (TSSL) model for classification. Compared with existing model, our proposed model represents an instance with both a column-wise and row-wise sparse representation of dictionary. Then, we use alternating direction method of multipliers (ADMM) [7] algorithm to solve the non-differentiable optimization problem. We evaluate the performance of proposed model on the task of classification of gene expression data for tumor and brain disease diagnosis. Experimental results demonstrate the superiority of our model compared with the state-of-the-art classification algorithms.

The rest of this paper is organized as follows: Sect. 2 gives a brief introduction of sparse learning. Section 3 proposes the Two-Sided Sparse Learning model and the optimization of it. In Sect. 4, we evaluate the performance of proposed model in comparison with other state-of-the-art classification methods on real-world gene expression data. Section 5 concludes the whole paper.

2 Sparse Learning Model

We use $\Phi \in \mathbb{R}^{m \times n} (m \ll n)$ to denote the training data matrix consisting of n input samples whose classes is known in advance. Given an arbitrary sample $\boldsymbol{y} \in \mathbb{R}^m$, sparse learning model aims to find the sparse representation $\boldsymbol{x}$ of $\boldsymbol{y}$ under Φ:

$$\boldsymbol{y} = \Phi \boldsymbol{x} \tag{1}$$

where $\boldsymbol{x} \in \mathbb{R}^n$ and the number of nonzero elements in $\boldsymbol{x}$ should not more than a specific threshold k.

For computational convenience, the optimization problem can be written as:

$$\min_{\boldsymbol{x}} \|\boldsymbol{x}\|_1, \text{ s.t. } \boldsymbol{y} = \Phi \boldsymbol{x} \tag{2}$$

where the constraint on $\boldsymbol{x}$ can be achieved by using a L_1 norm.

3 Two-Sided Sparse Learning

In this paper, instead of only considering the column-wise sparsity, but taking into account the row-wise sparsity of features, we propose the Two-Sided Sparse Learning model. In the context of classification, the two-sided sparsity can reduce the reconstruction error and find several most representative features.

The proposed model is as following:

$$\boldsymbol{y} = \mathbf{D} \Phi \boldsymbol{x} \tag{3}$$

where $\boldsymbol{y} \in \mathbb{R}^m$ an arbitrary sample vector with m features is, $\Phi \in \mathbb{R}^{m \times n} (m \ll n)$ is the dictionary consisting of n training samples, $\mathbf{D} \in \mathbb{R}^{m \times m}$ ensures the sparsity of features, $\boldsymbol{x} \in \mathbb{R}^n$ is the sparse representation of $\boldsymbol{y}$.

To solve Eq. (3), we stack multiple samples to be classified as $\mathbf{Y}$. Then, optimization problem can be formed as:

$$\min \frac{1}{2} \|\mathbf{Y} - \mathbf{D}\Phi\mathbf{X}\|_F^2 + \lambda_1 \|\mathbf{X}\|_1 + \lambda_2 \Omega(\mathbf{D}) \tag{4}$$

where parameters $\lambda_1, \lambda_2 > 0$ and $\Omega(\mathbf{D})$ is a penalty term. We consider two common-used forms of penalty term: L_1 norm and F norm.

We use ADMM algorithm to solve the Eq. (4). Since the optimization problem is non-convex, we alternatively solve one variable by fixing the other at each iteration. The basic idea of the algorithm is as follows:

(1) When fixing $\mathbf{D}$, according to ADMM, Eq. (4) could be written as:

$$\min \frac{1}{2} \|\mathbf{Y} - \mathbf{D}\Phi\mathbf{X}\|_F^2 + \lambda_1 \|\mathbf{Z}\|_1 \text{ s.t. } \mathbf{X} - \mathbf{Z} = \mathbf{0} \tag{5}$$

Therefore, the augmented Lagrange function is:

$$L_{\rho_1}(\mathbf{X}, \mathbf{Z}, \mathbf{U}) = \frac{1}{2} \|\mathbf{Y} - \mathbf{D}\Phi\mathbf{X}\|_F^2 + \lambda_1 \|\mathbf{Z}\|_1 + \text{tr}(\mathbf{U}^T(\mathbf{X} - \mathbf{Z})) + \frac{\rho_1}{2} \|\mathbf{X} - \mathbf{Z}\|_F^2 \tag{6}$$

where $\mathbf{U}$ is the dual matrix regarding to the original matrix $\mathbf{X}$ in augmented Lagrange multiplier method, $\rho_1 > 0$ is a penalty parameter of augmented term. Therefore, we can obtain the update rules of factors:

$$\mathbf{X}^{k+1} = ((\mathbf{D}\Phi)^T(\mathbf{D}\Phi) + \rho_1 \mathbf{I})^{-1}(\rho_1(\mathbf{Z}^k - \mathbf{V}^k) + (\mathbf{D}\Phi)^T\mathbf{Y}) \tag{7}$$

$$\mathbf{Z}^{k+1} = S_{\lambda_1/\rho_1}(\mathbf{X}^{k+1} + \mathbf{V}^k) \tag{8}$$

$$\mathbf{V}^{k+1} = \mathbf{V}^k + \mathbf{X}^{k+1} - \mathbf{Z}^{k+1} \tag{9}$$

where we set scaled dual variable $\mathbf{V} = (1/\rho_1)\mathbf{U}$ to simplify the form and the soft-threshold operator S is defined as:

$$S_K(a) = \begin{cases} a - K, & a > K \\ 0, & |a| < K \\ a + K, & a < -K \end{cases} \tag{10}$$

(2) Then, when fixing $\mathbf{X}$, according to ADMM, Eq. (4) could be written as:

$$\min \frac{1}{2} \|\mathbf{Y} - \mathbf{D}\Phi\mathbf{X}\|_F^2 + \lambda_2 \Omega(\mathbf{Z}) \text{ s.t. } \mathbf{D} - \mathbf{Z} = \mathbf{0} \tag{11}$$

Therefore, the augmented Lagrange function is:

$$L_{\rho_2}(\mathbf{D}, \mathbf{Z}, \mathbf{U}) = \frac{1}{2}\|\mathbf{Y} - \mathbf{D}\Phi\mathbf{X}\|_F^2 + \lambda_2\Omega(\mathbf{Z}) + \mathrm{tr}(\mathbf{U}^T(\mathbf{D} - \mathbf{Z})) + \frac{\rho_2}{2}\|\mathbf{D} - \mathbf{Z}\|_F^2 \quad (12)$$

where the matrix $\mathbf{U}$ is the dual matrix regarding to the original matrix $\mathbf{D}$ in augmented Lagrange multiplier method and $\rho_2 > 0$ is the penalty parameter of augmented term. Therefore, we can obtain the update rules of factors:

$$\mathbf{D}^{k+1} = (\rho_2(\mathbf{Z}^k - \mathbf{V}^k) + \mathbf{Y}(\Phi\mathbf{X})^T)((\Phi\mathbf{X})(\Phi\mathbf{X})^T + \rho_2\mathbf{I})^{-1} \quad (13)$$

$$\mathbf{Z}^{k+1} = \begin{cases} S_{\lambda_2/\rho_2}(\mathbf{D}^{k+1} + \mathbf{V}^k), \ \Omega(\mathbf{Z}) = \|\mathbf{Z}\|_1 \\ (\mathbf{D}^{k+1} + \mathbf{V}^k)/(2\lambda_2/\rho_2 + 1), \ \Omega(\mathbf{Z}) = \|\mathbf{Z}\|_F^2 \end{cases} \quad (14)$$

$$\mathbf{V}^{k+1} = \mathbf{V}^k + \mathbf{D}^{k+1} - \mathbf{Z}^{k+1} \quad (15)$$

where we set scaled dual variable $\mathbf{V} = (1/\rho_1)\mathbf{U}$ to simplify the form.

(3) Repeat step (1) (2) until stop criteria satisfied.

After getting the solution $\mathbf{D}$ and $\boldsymbol{x}$, we can assign a test sample $\boldsymbol{y}$ to a class with the minimal residual.

$$i = \arg\min_i \|\boldsymbol{y} - \mathbf{D}\Phi\delta_i(\boldsymbol{x})\| \quad (16)$$

where feature function $\delta_i(\boldsymbol{x})$ keeps the i-th elements of $\boldsymbol{x}$ fixed and sets the others elements as 0, for example, given a vector $\boldsymbol{b} = [111]$, then $\delta_2(\boldsymbol{b}) = [010]$. Finally, the class with the smallest residual is the class of $\boldsymbol{y}$.

4 Experiments

In this section, we evaluate the performance of the proposed TSSL model on the task of classification of gene expression data on two real world datasets: SRBCT and Brain. SRBCT dataset contains gene expression level of 2308 genes from 83 patients suffers with 4 subtype tumors and Brain contains gene expression level of 5920 gens from 90 patients with 5 kinds of brain diseases. The performance is evaluated by the classification accuracy and we compare our proposed algorithm with the other three classic methods: SVM, C4.5 and KNN.

Due to the limitation of gene expression data, for example, the small size of samples and the relatively large number of genes, we firstly use SVD to reduce the dimension of datasets to 4, 8, 16, 32 and 64 for classification respectively.

Considering the essence of 2 forms of penalty term is the same and the results are extremely close, we only report the highest classification accuracy among them (Tables 1 and 2).

Table 1 The classification accuracy on SRBCT

Method	Dimension				
	4	8	16	32	64
TSSL	0.7229	0.9036	**0.9759**	**0.9880**	**0.9880**
SVM	**0.8795**	**0.9759**	0.9639	0.9639	0.9518
C4.5	0.7470	0.8193	0.8193	0.8072	0.7831
KNN	0.7590	0.8916	0.8554	0.8554	0.8675

Table 2 The classification accuracy on Brain

Method	Dimension				
	4	8	16	32	64
TSSL	0.7778	**0.8222**	**0.8778**	**0.8667**	**0.8889**
SVM	**0.8111**	0.7889	0.8111	0.8000	0.8111
C4.5	0.7333	0.7111	0.6667	0.6889	0.6667
KNN	0.7556	0.7333	0.7667	0.7222	0.7444

It is obvious that the performance of our proposed model is better and achieves higher classification accuracy when dimension is not reduced too low. The results demonstrate that our proposed model is capable of classifying gene expression data well. In addition, compared to the other classic methods, the classification accuracy of it is more stable and remains high when dimension is not too low. In addition, results show that the performance of our method gets better with the increase of dimension, which indicates that we could get the best results once find the most appropriate dimension for different datasets.

5 Conclusion

In this paper, we propose a Two-Sided Sparse Learning model for classification and use ADMM to solve the optimization problem. In addition, we incorporate two forms of penalty term and the results of them are extremely close. Promising results demonstrate that our model outperform the state-of-the-art classification methods on real world gene expression datasets.

Acknowledgements This research was supported in part by the Chinese National Natural Science Foundation under Grant nos. 61402395, 61472343 and 61502412, Natural Science Foundation of Jiangsu Province under contracts BK20140492, BK20151314 and BK20150459, Jiangsu overseas research and training program for university prominent young and middle-aged teachers and presidents, Jiangsu government scholarship funding.

References

1. Monika, R., Dhanalakshmi, S., Sreejith, S.: Coefficient random permutation based compressed sensing for medical image compression. Advances in Electronics, Communication and Computing. Springer, Singapore (2018)
2. Gibson, R.M., Amira, A., Ramzan, N., et al.: Matching pursuit-based compressive sensing in a wearable biomedical accelerometer fall diagnosis device. Biomed. Signal Process. Control. (2017)
3. Peller, J., Thompson, K.J., Siddiqui, I., et al.: Hyperspectral imaging based on compressive sensing to determine cancer margins in human pancreatic tissue ex vivo. Optical Biopsy XV: Toward real-time spectroscopic imaging and diagnosis. Int. Soc. Opt. Photonics (2017)
4. Wright, J., Yang, M., Ganesh, A., Sastry, S., Ma, Y.: Robust face recognition via sparse representation. TPAMI **31**(2), 210–227 (2009)
5. Aharon, M., Elad, M., Bruckstein, A.: K-SVD: design of dictionaries for sparse representation. Proceedings of SPARS **5**, 9–12 (2005)
6. Aharon, M., Elad, M., Bruckstein, A.M.: The K-SVD: an algorithm for designing of overcomplete dictionaries for sparse representations. IEEE Trans. Image Process. **54**, 4311–4322 (2006)
7. Boyd, S., Parikh, N., Chu, E., et al.: Distributed optimization and statistical learning via the alternating direction method of multipliers. Foundations and Trends® in Machine Learning (2011)

Medical Diagnosis Based on Nonlinear Manifold Discriminative Projection

Ping He, Xincheng Chang, Xiaohua Xu, Zhijun Zhang, Tianyu Jing, Yuan Lou and Lei Zhang

Abstract In recent years, medical diagnosis based on machine learning has become popular in the interdiscipline research of computer science and medical science. It is closely related with classification, which is one of the important problems in machine learning. However, the traditional classification algorithms can hardly appropriately solve high-dimensional medical datasets. Manifold learning as nonlinear dimensionality reduction algorithm can efficiently process high dimensional medical datasets. In this paper, we propose an algorithm based on Nonlinear Manifold Discriminative Projection (NMDP). Our algorithm incorporates the label information of medical data into the unsupervised LLE method, so that the transformed manifold becomes more discriminative. Then we apply the discriminant mapping to the unlabeled test data for classification. Experimental results show that our method exhibits promising classification performance on different medical data sets.

Keywords Medical diagnosis · Machine learning · Classification
Discriminant projection · Unlabeled test data

1 Introduction

In the field of medical diagnosis, doctors have subjective impact on diagnosis of traditional diseases, resulting in lower diagnostic efficiency. Recently, researchers show that the diagnostic accuracy of medical diagnosis technology based on machine learning can make the efficiency higher [1, 2]. In the past research, practitioners in the field of intelligent diagnosis have adopted many classical classification algorithms, such as the support vector machine (SVM) [3], k-nearest neighbor (KNN) [4] and so on. However, classical classification algorithms do not effectively process high-dimensional medical data. For this reason, researchers try to simplify the original data by employing dimension reduction techniques before classification. It effectively

P. He · X. Chang · X. Xu (✉) · Z. Zhang · T. Jing · Y. Lou · L. Zhang
Department of Computer Science, Yangzhou University, Yangzhou, China
e-mail: arterx@gmail.com

H. Lu (ed.), *Cognitive Internet of Things: Frameworks, Tools and Applications*, Studies in Computational Intelligence 810,
https://doi.org/10.1007/978-3-030-04946-1_28

improves the classification accuracy of medical diagnosis. The dimension reduction algorithms based on manifold learning can find low-dimensional manifold structure in high-dimensional medical data, so as to obtain low-dimensional medical data.

Many approaches have been developed under manifold assumption, including Locally Linear Embedding (LLE) [5]. The main idea of LLE is to maintain the local linear structure of neighbors when data is mapped into the low-dimensional subspaces. However, as an unsupervised algorithm, LLE does not make good use of discrimination information of medical data. In order to effectively use the supervised information, Supervised LLE (SLLE) [6] integrates the category information of the sample points into the distance calculation of the neighbors. However, above algorithms lack an effective extension to the unlabeled data.

In this paper, we propose a Nonlinear Manifold Discriminative Projection method (NMDP). NMDP adapts the local linear weight matrix accordingly to class information, which maintains the similarity of the homogeneous data and extends the difference of heterogeneous data. Then, in order to improve the generalization ability of the algorithm, NMDP is extended to the unlabeled data and applies the trained linear SVM classifier to the transformed test data.

In Sect. 2, we briefly introduce the local linear embedding algorithm. In Sect. 3, we describe NMDP in details. Finally, the experimental results are shown in Sect. 4.

2 Locally Linear Embedding

Local Linear Embedding (LLE) constructs the weight matrix by the idea of linear representation, so that each point can be linearized representation by its k nearest neighborhood as much as possible, and the potential low-dimensional embedded data is obtained by keeping the weight information between data points. We define $X = \{x_1, x_2, \ldots, x_N\}$ as a medical dataset, $\mathrm{x_i} \in \mathbb{R}^{\mathrm{D}}$ is sampled from a high-dimensional nonlinear manifold. By minimizing the error of this linear representation, the following model can be established,

$$\min \varepsilon(\Omega) = \sum_{i=1}^{N} ||x_i - \sum_{j=1}^{k} \omega_{ij} x_{ij}||^2 \tag{1}$$

In Eq. (1), Ω is the reconstruction weight matrix, whose element ω_{ij} records the linear reconstruction weight of x_i.

Due to the assumption of LLE, the locally geometrical structure of manifold remains unchanged after dimension reduction. We minimize the loss function to obtain the low-dimensional embedding Y.

$$\min \Phi(Y) = \sum_{i=1}^{N} ||y_i - \sum_{j=1}^{k} \omega_{ij} y_{ij}||^2 \tag{2}$$

where y_i and y_{ij} correspond to the embedding of x_i and x_{ij} in low-dimensional space respectively.

3 Nonlinear Manifold Discriminative Projection

Inspired by traditional LLE algorithm, we propose a novel medical diagnosis method based on Nonlinear Manifold Discriminative Projection (NMDP). NMDP incorporates label information into the weight matrix.

3.1 Local Weight Matrix Adaptation

First, we divide the medical dataset into training data $X_S = [x_1, x_2, \ldots, x_M]$ with label l_S and test data $X_T = [x_{M+1}, x_{M+2}, \ldots, x_N]$ without label information. The embedded representation of X_S is denoted as $Y_S = [y_1, y_2, \ldots, y_M]$. Next, we find k-nearest neighbors by K-NN in its original high-dimensional space and estimate the local linear reconstruction weight matrix Ω.

$$\min \varepsilon(\Omega) = \sum_{i=1}^{M} ||x_i - \sum_{j=1}^{k} \omega_{ij} x_{ij}||^2 \tag{3}$$

In order to increase the proportion of the local reconstruction weight matrix of the intra-class data points and reduce the proportion of the local reconstruction weight matrix of the inter-class points, we adjust the linear weight by combining the label information.

$$\widehat{\omega}_{ij} \leftarrow \begin{cases} \omega_{ij} + |\omega_{ij}| \times \delta & \text{if } l_i \neq l_j \\ \omega_{ij} - |\omega_{ij}| \times \delta & \text{otherwise} \end{cases} \tag{4}$$

where $\delta \in [0, 1]$ adjusts the weight ratio of data.

3.2 Nonlinear Discriminative Projection

Based on the adjusted local reconstruction weight matrix, we embed the training data into a low-dimensional discriminant space. NMDP preserves the local linear structure in high-dimensional space by minimizing the following reconstruction error.

$$\min \Phi(Y_S) = \sum_{i=1}^{M} ||y_i - \sum_{j=1}^{k} \widehat{\omega}_{ij} y_{ij}||^2 = tr\left(Y_s Q Y_s^T\right) \tag{5}$$

where $Q = \left(I - \widehat{\Omega}\right)\left(I - \widehat{\Omega}\right)^T$. To ensure the uniqueness of solution, Y_S satisfies the orthogonality constraint. Therefore, the optimal solution of Y_S is composed of the d eigenvectors corresponding to the largest eigenvalues of Q, i.e. $Y_S = [v_1, v_2, \ldots, v_d]$, where v_i satisfies $Qv_i = \theta_i v_i$, θ_i is the eigenvalue of Q, $\forall i = 1, \ldots, d$.

3.3 Classification of Unlabeled Test Data

Assume $x \in X_T$ represents an unlabeled test data. We define $\omega_{X_S}(x)$ as the relationship between X_S and x on the original manifold, which can be optimized as follows.

$$\omega_{X_S}(x) = \arg\min ||x - \sum_{j=1}^{k} \omega_{ij} x_S^j||^2 \tag{6}$$

where x_S^j represents the jth nearest training data points of the test data.

We also define $Y_S^T \Theta y$ as the relationship between Y_S and y on the target manifold. $\Theta = diag(\theta_1, \theta_2, \ldots, \theta_d)$ is the diagonal matrix composed of the d largest eigenvalues. Therefore, the optimal mapping of test data on the target manifold is

$$\begin{aligned} y^* &= \arg\min ||\omega_{X_S}(x) - Y_S^T \Theta y||^2 \\ &= \Theta^{-1}\left(Y_S Y_S^T\right)^{\dagger} Y_S \omega_{X_S}(x) \end{aligned} \tag{7}$$

For the embedded data in low-dimensional space, NMDP algorithm directly uses linear SVM [7] for classification.

4 Experiments

In order to study the performance of the NMDP algorithm, we compare the classification accuracy of LLE, SLLE and NMDP on different medical data sets. These data sets are from the UCI data set. In our experiments, we search for the optimal parameter δ by grid search, and use cross-validation to compute the average classification performance. We use the Dick de Ridde's method [8] to select the dimension d of the low-dimensional embedded space and use *libsvm* to implement the construction of the classifier. All the experiments in this paper are implemented

Table 1 Comparison of classification accuracy among different algorithms

Date sets	LLE (%)	SLLE (%)	NMDP (%)
Eye	82.03	84.80	88.48
Diabetes	75.00	75.52	78.15
Heart	75.96	76.29	81.40
Mammographic mass	70.20	71.08	80.04
VLBW infant	86.00	87.31	94.35
Breast cancer	92.08	95.55	97.25

in Matlab 2016a. Table 1 reports the comparison of classification accuracy among different algorithms. Due to the integration of supervised information, supervised algorithms have higher classification performance than unsupervised algorithm and NMDP performs consistently better than the other algorithms.

5 Conclusions

In this paper, we present a novel nonlinear manifold projection algorithm for medical diagnosis. Our algorithm adapts the reconstruction weight matrix by using the label information of the training data, thereby enhancing the similarity of isomorphic data and expanding the difference of heterogeneous data. The comparison with other algorithms demonstrates the superiority of our proposed method on medical data sets.

Acknowledgements This research was supported in part by the Chinese National Natural Science Foundation with Grant nos. 61402395, 61472343 and 61379066, Natural Science Foundation of Jiangsu Province under contracts BK20140492 and BK20151314, Jiangsu government scholarship funding, Jiangsu overseas research and training program for university prominent young and middle-aged teachers and presidents.

References

1. De Bruijne, M.: Machine learning approaches in medical image analysis: from detection to diagnosis. Med. Image Anal. **33**, 94–97 (2016)
2. Trambaiolli, L.R., et al.: Improving Alzheimer's disease diagnosis with machine learning techniques. Clin. EEG Neurosci. **42**(3), 160 (2011)
3. Zhang, S., Li, X., Zong, M., Zhu, X., Cheng, D.: Learning k, for knn classification. ACM Trans. Intell. Syst. Technol. **8**(3), 43 (2017)
4. Platt, J.: A fast algorithm for training support vector machines. J. Inf. Technol. **2**(5), 1–28 (1998)
5. Roweis, S.T., Saul, L.K.: Nonlinear dimensionality reduction by locally linear embedding. Science **290**(5500), 2323–2326 (2000)

6. Ridder, D.D., Kouropteva, O., et al.: Supervised locally linear embedding. In: Joint International Conference on Artificial Neural Networks and Neural Information Processing, pp. 333–341. Springer (2003)
7. Ukil, A.: Support vector machine. Comput. Sci. **1**(4), 1–28 (2002)
8. Ridder, D.D., Duin, R.P.W.: Locally linear embedding for classification. IEEE Trans. Pattern Anal. Mach. Intell. (2002)

Improved Image Enhancement Method Based on Retinex Algorithm

Tingting Zhang, Weiduo Zhu, Yujie Li, Yun Li and Bin Li

Abstract In order to improve the visibility of foggy images, this paper uses two models to iteratively refine the image. In the first model, the image is first enhanced by histogram equalization and then enhanced by the Retinex algorithm. In the second model, the image is firstly enhanced with the Retinex algorithm, and then the gamma correction is used to adjust the brightness. From a theoretical analysis and practical experiments, this method improves the sharpness of the image while enhancing the image detail information and restoring the image color.

Keywords Foggy image · Iterative refinement · Histogram equalization · Retinex Gamma correction

1 Introduction

The development of modern industrialization and the popularity of family cars will have an impact on the environment to a certain extent. Exhaust emissions of factories and vehicles cause hazy days. Not only will hazy days do harm to human health, but also cause traffic accidents. It is more difficult for monitoring and imagining the road conditions because the images are blurred. Therefore, the defogging algorithm has been proposed and continuously developed.

Image dehazing is not a new research field, so many researches have been done on it. After induction, it can be divided into two types. The first one is based on the physical model [1–5], and the second is based on the image enhancement [6–10]. Narasimhan et al. [1] proposed geometric constraints by simulating the color effects of atmospheric scattering and a series of experiments. Thereby, the foggy image is subjected to dehazing treatment to restore the "sunny" scene. In the image enhancement method, histogram equalization [6] has received much attention due to its high efficiency and intuitive image enhancement. The Retinex algorithm [7] has

T. Zhang (✉) · W. Zhu · Y. Li · Y. Li · B. Li
School of Information Engineering, Yangzhou University, Yangzhou, China
e-mail: 2729196243@qq.com

H. Lu (ed.), *Cognitive Internet of Things: Frameworks, Tools and Applications*, Studies in Computational Intelligence 810,
https://doi.org/10.1007/978-3-030-04946-1_29

advantages in contrast and detail information processing, and color constancy is also improved. Gamma correction is an efficient tool typically used to adjust the contrast and brightness of digital images [11].

This article aims to improve the accuracy of image enhancement, so two models were chosen for iterative refinement. First, the histogram model is used to equalize the image to obtain the preprocessed image. Secondly, the Retinex algorithm model is used to enhance the image of the preprocessed image to complete the image defogging process. For low-contrast images, the Retinex algorithm and gamma correction method are used to enhance and adjust the image. In the later stage, the UIQM [12] evaluation method was used to evaluate the method proposed in this paper from underwater image color metric (UICM), underwater image sharpness measurement (UISM) and underwater image contrast measurement (UIConM).

2 The Related Work

2.1 Histogram Equalization Algorithm

When the image pixels are evenly distributed, the image contrast is high. Histogram equalization utilizes this image characteristic to map the original image so that the image pixels are evenly distributed, thereby achieving the purpose of improving image contrast.

The function expression [13] for the histogram equalization of the image is:

$$s_{k=T(r_k)=(L-1)\sum_{j=0}^{k} Pr(r_j)=\frac{L-1}{MN}\sum_{j=0}^{k} n_j, k=0, 1, 2, ..., L-1} \tag{1}$$

where MN is the total pixel of the image, n_k is the number of pixels with grayscale r_k, and L is the number of possible gray levels in the image.

$$p_r(r_k) = \frac{n_k}{MN} \tag{2}$$

Equation (2) is the probability that the gray level r_k appears in a digital image.

The histogram transformation technique makes the histogram of the target image meet the requirements by selecting the transformation function T(r). However, the histogram equalization algorithm often causes gray level merging after image enhancement, and there are problems such as local over-enhancement and loss of detail information.

2.2 Retinex Algorithm

Color constancy image enhancement technology is an enhancement method based on image visual effects, and the Retinex algorithm [7] proposed by Land et al. is the most influential color constant vision calculation theory.

The Retinex algorithm considers the perceptual image to be composed of the product of luminance information and reflection information. The formula is as follows:

$$\mathrm{I}(x, y) = L(x, y) \cdot R(x, y) \tag{3}$$

In Eq. (3), $I(x, y)$ represents the image observed by the human eye; $L(x, y)$ represents the luminance component of the image, which determines the dynamic range of an image; $R(x, y)$ represents the image the reflection component, which carries the details of the image.

In practical applications, we are more concerned with how to remove the luminance component and get the reflection image we ultimately need. The single-scale Retinex algorithm uses the center/surround method [8] to estimate the luminance component $L(x, y)$. The mathematical expression is as follows:

$$L(x, y) = I(x, y) * F(x, y) \tag{4}$$

In the above formula, * denotes a convolution operation, and $F(x, y)$ is the Center surround function. The mathematical expression of $F(x, y)$ is:

$$F(x, y) = \kappa \cdot exp\left[\frac{-\left(x^2 + y^2\right)}{\sigma^2}\right] \tag{5}$$

In the above formula, σ is the Gaussian surround scale, κ is between 80 to 100. k is a normalized molecule, satisfying $\iint F(x, y)dxdy = 1$; The smaller the scale σ is, the larger the dynamic range compression is, and the local details of the image are more obvious. The larger the scale σ, the better the overall effect of the image, the better the color recovery but the details are easily lost.

It can be seen from Eqs. (3) and (4) that the reflected light component of the image is expressed as:

$$R(x, y) = \log I(x, y) - \log[I(x, y) * F(x, y)] \tag{6}$$

At this time, $R(x, y)$ is a component of the logarithmic domain. The image we need is in the real number field, so we have to convert $R(x, y)$ as follows:

$$\mathrm{r(x, y)} = \exp(R(x, y)) \tag{7}$$

2.3 Gamma Correction

Gamma correction is also a widely used and cost-effective contrast enhancement method [14]. Its basic form can be formulated as:

$$\mathrm{T}(\ell) = \ell_{max}\left(\frac{\ell}{\ell_{max}}\right)^{\gamma} \tag{8}$$

where ℓ_{max} is the maximum intensity of the input, the intensity ℓ of each pixel in the input image is transformed as $\mathrm{T}(\ell)$ after performing. As expected, the gamma curves illustrated with $\gamma > 1$ have exactly the opposite effect as those generated with $\gamma < 1$.

3 Improved Method

In this paper, two models are used to iteratively refine the foggy image, which is divided into two steps. The first step is to improve the image contrast; the second step is to enhance the image detail and restore the image color.

3.1 First Model

The first model consists of Histogram equalization algorithm and Retinex algorithm. Firstly, using histogram equalization to obtain a preprocessed image $I(x, y)$ with a gray level of S_k. The transformation function is shown in Eq. (1). Secondly, the image is further enhanced with the Retinex algorithm to improve the accuracy.

The overall calculation formulas are shown in Eqs. (6) and (7), where I(x, y) is the image with gray level S_k after histogram equalization, r(x, y) is the output image.

3.2 Second Model

When dealing with low-contrast images, histogram equalization algorithm is over-enhanced. So, first use the Retinex algorithm to enhance the image, the formulas are shown in Eqs. (6) and (7). Next, adjust the image brightness by using Gamma correction. The output image can be obtained by:

$$\mathrm{r}'(\mathrm{x}, \mathrm{y}) = r(x, y)^{\gamma} \tag{9}$$

where $r(x, y)$ is the image enhanced with the Retinex algorithm, $r'(x, y)$ is the Gamma corrected map.

As described above, using histogram equalization can increase image contrast and widen the dynamic range of the image. Then, the Retinex algorithm is used for the local over-enhancement in the pre-processed image and the missing details of the partial picture block. While dealing with low-contrast images, the combination of Retinex algorithm and Gamma correction generates natural and realistic results.

4 Experimental Result

In order to test the universality of the method, we selected pictures taken in three different situations for testing. Figure 1a is an aerial area map, the overall brightness of the picture is low, and the fog of the building part reduces the visibility of the picture. Figure 2a is a map of the street fog area. The pedestrians are clearer, but the buildings behind the characters are basically covered by the fog, and the image appears blurred. Figure 3a [12] is an underwater image of a school of fish. The image is somewhat blurred due to particles and suspended matter in sea water. It can be seen that the original picture is blurred where the water is very muddy and the edges of the fish are blurred, making it difficult to distinguish between water and fish.

It can be seen from Figs. 1, 2 and 3 that the method proposed in this paper not only makes the image clearer, but also enhances the color of the processed image more vividly. The detailed information remains intact and conforms to the visual characteristics of the human eye.

To further prove that this method can be used for underwater image enhancement, we have selected 3 underwater images. Figure 4a is an image of the underwater machine. It can be seen from the figure that the upper part of the machine is fuzzy and the right side of the image is illegible. Figures 5a and 6a show two images with

(a) original image (b) Method of this paper

Fig. 1 Aerial fog image

(a) original image (b) Method of this paper

Fig. 2 Street fog image

(a) original image (b) Method of this paper

Fig. 3 Cluster of fish image

(a) original image (b) Method of this paper

Fig. 4 Underwater machine image

low-contrast ratio, Fig. 5a is darker than Fig. 6a. The area where the cup is located is brighter than the surrounding area, and the pattern of the cup lid is not clear.

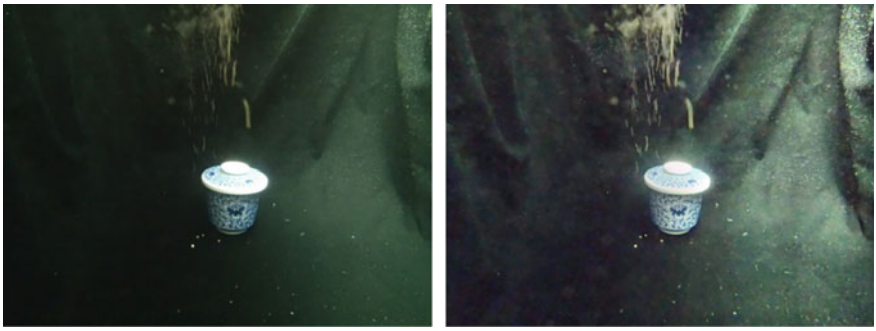

(a) original image (b) Method of this paper

Fig. 5 Underwater cup image

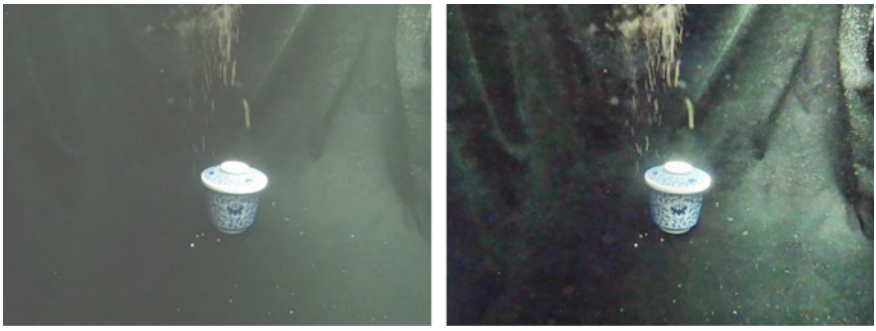

(a) original image (b) Method of this paper

Fig. 6 Underwater cup image

5 Image Quality Evaluation Online

In this paper, the UIQM image evaluation method is used to evaluate the image enhancement results from three aspects. The UIQM image evaluation method consists of underwater image color metric (UICM), underwater image sharpness measurement (UISM) and underwater image contrast measurement (UIConM).

Through the UIQM method, the original image is improved by the image proposed by the method improved in this paper. From the data point of view, the clarity of Fig. 1, the contrast of Fig. 2 and the contrast of Fig. 3 are greatly improved. Besides, the color of Fig. 4 is well restored. From the picture point of view, the smog in the upper part of Fig. 1 is deeper, the upper part of the enhanced image is very clear, and the image details are very good. The contrast improvement in Figs. 2 and 3 is better, making the whole picture clearer. The enhanced image of Fig. 4 has more observable details, and the whole image is more clarified. From the Figs. 5 and 6, the pattern on the cup lid has been repaired. Moreover, the left side of the Fig. 5 has been enhanced, and its textual is more obvious (Table 1).

Table 1 Measurement of different properties of six images

	UICM	UISM	UIConM
Figure 1a	1.2604	0.8114	0.4322
Figure 1b	**4.8564**	**3.3836**	**1.0920**
Figure 2a	1.9498	1.9862	0.5176
Figure 2b	**4.9477**	**3.0319**	**0.8737**
Figure 3a	0.2677	0.2866	0.2087
Figure 3b	**7.4591**	**2.6855**	**0.8861**
Figure 4a	3.2369	1.7085	0.3663
Figure 4b	**5.4276**	**1.9411**	**0.9260**
Figure 5a	1.1839	2.1845	0.7142
Figure 5b	**1.9141**	**2.2421**	**1.0392**
Figure 6a	0.8767	0.9964	0.3624
Figure 6b	**1.9427**	**2.0159**	**0.9827**

6 Conclusion

In this paper, an improved image defog measure was presented. This method uses two models to iteratively refine the image, enhance image detail and restore image color. According to the UIQM image evaluation index, this improved method not only enhances foggy images, but also underwater images. This method can effectively remove the fog area in the foggy image. Therefore, the contrast of the picture will be enhanced and the color of the picture will be restored. Besides, the image details get richer. To sum up, the method proposed can be widely applied to picture enhancement and its performance is practically and theoretically good.

References

1. Narasimhan, S.G., Nayar, S.K.: Vision and the atmosphere. IJCV **48**(3), 233–254 (2002)
2. Lu, H., Li, Y., Uemura, T., Kim, H., Serikawa, S.: Low illumination underwater light field images reconstruction using deep convolutional neural networks. Futur. Gener. Comput. Syst. **82**, 142–148 (2018)
3. Li, Y., Lu, H., Li, K., Kim, H., Serikawa, S.: Non-uniform de-scattering and de-blurring of underwater images. Mob. Netw. Appl. **23**, 352–362 (2018)
4. Li, Y., Lu, H., Li, J., Li, X., Li, Y., Serikawa, S.: Underwater image de-scattering and classification by deep neural network. Comput. Electr. Eng. **54**, 68–77 (2016)
5. Lu, H., Li, Y., Zhang, L., Serikawa, S.: Contrast enhancement for images in turbid water. J. Opt. Soc. Am. A **32**(5), 886–893 (2015)
6. Acharya, T., Ray, A.K.: Image Processing—Principles and Applications. Wiley, New York (2005)
7. Fan, T., Li, C., Ma, X., Chen, Z., Zhang, X., Chen, L.: An improved single image defogging method based on retinex. In: 2017 2nd International Conference on Image, Vision and Computing (ICIVC), Chengdu, pp. 410–413 (2017)

8. Jobson, D.J., Rahman, Z.U.: Properties and performance of a center/surround retinex. IEEE Trans. Image Process. **6**(3), 451–454 (1997)
9. Sheet, D., Garud, H., Suveer, A., Mahadevappa, M., Chatterjee, J.: Brightness preserving dynamic fuzzy histogram equalization. IEEE Trans. Consum. Electron. **56**(4), 2475–2480 (2010)
10. Arici, T., Dikbas, S., Altunbasak, Y.: A histogram modification framework and its application for image contrast enhancement. IEEE Trans. Image Process. **18**(9), 1921–1935 (2009)
11. Huang, S.C., Cheng, F.C., Chiu, Y.S.: Efficient contrast enhancement with adaptive gamma correction. IEEE Trans. Image Process. **22**(3), 1032–1041 (2013)
12. Panetta, K., Gao, C., Agaian, S.: Human-visual-system-inspired underwater image quality measures. IEEE J. Oceanic Eng. **41**(3), 541–551 (2016)
13. Gonzalez, R.C., Woods, R.E.: Digital Image Processing, pp. 72–77. 3rd. edn. Publishing House of Electronics Industry (2017)
14. Cao, G., Zhao, Y., Ni, R., Li, X.: Contrast enhancement-based forensics in digital images. IEEE Trans. Info. Forensics Secur. **9**(3), 515–525 (2014)

Fast Dynamic Routing Based on Weighted Kernel Density Estimation

Suofei Zhang, Quan Zhou and Xiaofu Wu

Abstract Capsules as well as dynamic routing between them are most recently proposed structures for deep neural networks. A capsule groups data into vectors or matrices as poses rather than conventional scalars to represent specific properties of target instance. Besides of pose, a capsule should be attached with a probability (often denoted as activation) for its presence. The dynamic routing helps capsules achieve more generalization capacity with many fewer model parameters. However, the bottleneck that prevents widespread applications of capsule is the expense of computation during routing. To address this problem, we generalize existing routing methods within the framework of weighted kernel density estimation, and propose a fast routing methods. Our method prompts the time efficiency of routing by nearly 40% with negligible performance degradation. By stacking a hybrid of convolutional layers and capsule layers, we construct a network architecture to handle inputs at a resolution of 64×64 pixels. The proposed models achieve a parallel performance with other leading methods in multiple benchmarks.

Keywords Capsule · Dynamic-routing · Clustering · Deep-learning

1 Introduction

During the last decade, deep learning algorithms, especially Convolutional Neural Networks (CNNs) have achieved remarkable progress on numerous practical vision tasks [7, 10, 11, 17]. However, the stack of convolutional filters and non-linearity units still implies difficulty of understanding the internal organization of neural net-

S. Zhang (✉) · Q. Zhou · X. Wu
Nanjing University of Posts and Telecommunications, Nanjing 210003, China
e-mail: zhangsuofei@njupt.edu.cn

Q. Zhou
e-mail: quan.zhou@njupt.edu.cn

X. Wu
e-mail: xfuwu@njupt.edu.cn

H. Lu (ed.), *Cognitive Internet of Things: Frameworks, Tools and Applications*, Studies in Computational Intelligence 810,
https://doi.org/10.1007/978-3-030-04946-1_30

works. It brings a reputation of "black box" to current neural networks [1, 12, 15]. Conversely, human vision systems always show much higher interpretability during the procedure of recognition. We can explicitly tell the specific cues such as shape, color, texture or intermediate semantic concepts, and build the part-whole relationship as proofs to our final decisions. The capsule structure introduces an analogous way to construct neural networks with higher interpretability. It uses grouped scalars as pose to represent specific properties of current part. Based on the multi-dimensional representation, it finds clusters within a "routing-by-agreement" framework as an interpretable representation during forward inference of network.

Dynamic routing has been proven as an effective approach with higher generalization capacity and fewer parameters [5]. However, it relies on intensive computation of clustering during inference. The expense of computation prevents capsules from widespread applications in practical vision tasks. To address this problem, we model dynamic routing from the perspective of nonparametric clustering and Kernel Density Estimation (KDE), proposing a target function to explain the procedure of routing. The main contributions of this paper are twofold: (1) We equip a simplified routing methods based on expectation maximization (EM) optimization strategies. Comparisons in different benchmarks empirically prove that our fast method significantly prompts the efficiency of routing with negligible performance degradation. (2) We propose a hybrid network structure consisting of both convolutional layers and capsules. The network can efficiently handle images with a resolution of 64×64 pixels. Experiments in multiple benchmarks show that our models achieve a parallel performance with other leading methods. We believe our research of simplified routing methods prompts the potentiality of capsule networks to be extensively applied in practical vision tasks.

1.1 Dynamic Routing Between Capsules

Capsule structure is originally proposed in [4]. Differing from a convolutional neural unit, each layer here is divided into small groups of neurons called *capsules*. For instance, an 128D vector of data is grouped into 8 capsules with 16D data as poses. Normally, an 1D activation is combined with the pose to represent the magnitude of current capsule. Based on such multi-dimensional representation, a dynamic routing mechanism over capsules [14] is designed between layers.

Dynamic routing is a reminiscent of the unsupervised clustering, which is purely based on the divergence between samples. Hence, different clustering methods were considered here as nonparametric routing framework [5]. Finally, the activations of capsules can be exploited for solving typical machine learning problems directly. Meanwhile, the pose of capsule can also be mapped to some specific properties as regularization. The capsule structure comes with attractive features such as higher interpretability and generalization capacity. However, the high complexity of clustering method also leads to low efficiency for both training and inference. This drawback prevents the structure from applications on large scale vision tasks such as ImageNet [13].

2 Dynamic Routing Based on Weighted KDE

KDE is a well known clustering technique for describing underlying empirical distribution over given samples. Despite the relationship between dynamic routing and clustering, there still exists two major problems preventing using KDE for dynamic routing directly. First, conventional KDE only considers the case of density estimation for one cluster, rather than routing between samples and multiple clusters. Second, there is no mechanism for including activation in the framework of KDE. To address these problems, we extend the density estimation from one cluster to mixture of clusters as

$$\hat{f}(\boldsymbol{v}, \boldsymbol{r}) \triangleq \frac{1}{n_l z_k} \sum_{j=1}^{n_{l+1}} \sum_{i=1}^{n_l} r_{ij} a_i^u k(d(\boldsymbol{v}_j - \boldsymbol{u}_i)), \tag{1}$$

where n_l and n_{l+1} are number of capsules at layer l and $l+1$, respectively. $\{\boldsymbol{v}_j | j = 1, \ldots, n_{l+1}\}$ are poses of capsule at layer $l+1$, i.e. the resulting clusters, while $\{\boldsymbol{u}_i | i = 1, \ldots, n_l\}$ are candidate samples at layer l. r_{ij} is parameter indicating the contribution from $\boldsymbol{u}_i$ to $\boldsymbol{v}_j$. Note that we actually use the transformed votes $\boldsymbol{u}_{i|j}$ instead of $\boldsymbol{u}_i$ for clustering. However, since the clustering only takes place in the scope of $\boldsymbol{v}_j$ and its corresponding votes $\{\boldsymbol{u}_{i|j} | i | j = 1, \ldots, n_l\}$, such change of notation will not break the following derivation. We will still use $\boldsymbol{u}_i$ for simplicity. $k(x)$ is a bounded function called *profile* function with support in univariate space $\mathbb{R}$. z_k is the normalization constant only related to specific $k(\cdot)$. The distance metric $d(\boldsymbol{v} - \boldsymbol{u}_i)$ refers to common distance definitions, e.g., ℓ_2 norm: $d(\boldsymbol{v} - \boldsymbol{u}_i) = ||\boldsymbol{v} - \boldsymbol{u}_i||^2$, or Mahalanobis distance: $(\boldsymbol{v} - \boldsymbol{u}_i)^T \Sigma^{-1} (\boldsymbol{v} - \boldsymbol{u}_i)$. Activation a_i^u of input capsule is introduced here as prior knowledge from below layer. It is a straightforward way to let samples with higher activations give more impact to final position of cluster. We introduce r_{ij} here to measures how much $\boldsymbol{u}_i$ contributes to the position of $\boldsymbol{v}_j$, namely routing weight between 2 capsules.

Since in the case of dynamic routing, clustering jointly takes place between samples and multiple clusters now. For the diversity of clusters, we want one sample can contribute to clusters in different proportions. Furthermore, the total contribution from each sample to final mixture of capsules should be equivalent. Therefore, we propose to model the procedure of dynamic routing as solving the following optimization question.

$$\boldsymbol{v}, \boldsymbol{r} = \arg\max_{\boldsymbol{v}, \boldsymbol{r}} \hat{f}(\boldsymbol{v}, \boldsymbol{r}) \qquad s.t. \quad \forall i, j : r_{ij} > 0, \sum_{j=1}^{n_{l+1}} r_{ij} = 1. \tag{2}$$

We will propose an EM based strategies to solve Eq. 2 in the following parts, and discuss the relationship between the proposed method and other existing routing methods.

2.1 Routing Based on Expectation Maximization

Equation 2 can be optimized within an EM framework [2]. Due to the symmetry of kernel function, $k(d(\boldsymbol{v}_j - \boldsymbol{u}_i))$ can be explained as the likelihood of sample $\boldsymbol{u}_i$ given the assumption of variable $\boldsymbol{v}_j$. From this point of view, Eq. 1 can be treated as an approximation of the log-likelihood function given samples from the mixture model which consists of $\boldsymbol{v}_j$ as components and r_{ij} as hidden weights. The EM algorithm can be exploited here to maximize $\hat{f}(\boldsymbol{v}, \boldsymbol{r})$ by alternately optimizing $\boldsymbol{v}_j$ and updating r_{ij} as its expectation. In analog to the standard EM algorithm, we explicitly introduce the mixture coefficient π_j to calculate the expectation of r_{ij}, getting Algorithm 1 as another strategy to solve Eq. 2.

Algorithm 1 Dynamic routing based on EM algorithm.

Require: poses $\boldsymbol{u}_i$, activations a_i^u
Initialize $\forall i, j$: $r_{ij} = 1/n_{l+1}$
for r iterations **do**
1. $\forall i, j$: $r'_{ij} \leftarrow \frac{r_{ij}}{\sum_j r_{ij}}$
2. $\forall j$: $\boldsymbol{v}_j \leftarrow \frac{\sum_i r'_{ij} a_i^u \boldsymbol{u}_i}{\sum_i r'_{ij} a_i^u}$
3. $\forall j$: $\pi_j \leftarrow \frac{\sum_i r'_{ij}}{\sum_j \sum_i r'_{ij}}$
4. $\forall i, j$: $r_{ij} \leftarrow \pi_j k(d(\boldsymbol{v}_j - \boldsymbol{u}_i))$
end for
return capsules with poses $\boldsymbol{v}_j$

Algorithm 1 basically follows the standard EM algorithm to maximize $\hat{f}(\boldsymbol{v}, \boldsymbol{r})$. Comparing with another well-known application scenario of EM algorithm, the Gaussian Mixture Model (GMM), our proposed mixture model based on KDE can be treated as a simplified version of standard GMM. The simplification mainly comes from that KDE is based on nonparametric kernel function, rather than the normal distribution configured by expectation $\boldsymbol{\mu}$ and variance $\boldsymbol{\Sigma}$. Hence the calculation of $k(d(\boldsymbol{v}_j - \boldsymbol{u}_i))$ requires much less computation than Gaussian function $N(\boldsymbol{\mu}, \boldsymbol{\Sigma})$. Also, the update of model in step 2 of Algorithm 1 only requires calculation about $\boldsymbol{v}$ without the variance $\boldsymbol{\Sigma}$ as in GMM.

Activation of capsule. For generic machine learning tasks, the activation of capsule is required as final result to reflect the magnitude of current capsule. It also appears in the routing procedure at above layer as prior knowledge. For the resulting capsule at layer $l + 1$, we propose a unified form of activation a_j^v for both routing methods as

$$a_j^v \triangleq softmax(\sum_{i=1}^{n_l} r'_{ij} a_i^u (k(\sum_{d=1}^{D} d(u_{id} - \beta_{jd} v_{jd}) + \beta_{j0})), \tag{3}$$

where r'_{ij} is the normalized version of r_{ij} as the result of step 1 in Algorithm 1. Here the distance metric is calculated at each dimension d separately. If we ignore the linear coefficients $\boldsymbol{\beta}_j \in \mathbb{R}^{D+1}$, one can see from Eq. 1 that activation is the absolute value of resulting density at $\boldsymbol{v}_j$ after routing. It is consistent with the original purpose of combining activation to capsule. Parameters $\boldsymbol{\beta} \in \mathbb{R}^{D+1}$ at each dimension are learned by standard back propagation to provide a linear combination rather than the rigid connection between pose and activation. Finally, a softmax function is exploited here as the guarantee of a probability distribution over activations.

3 Network Architecture

Dynamic routing has already been proven as an effective mechanism for classification tasks on datasets with small images such as MNIST [8] and smallNORB [9]. Our main concern here is about the efficiency and generality of dynamic routing. According to the observation of our implementation, they are the main bottleneck preventing dynamic routing from widespread utilization in practical vision tasks. Hence, we designed a relatively big network architecture for 64×64 image as in Fig. 1.

The proposed network is a hybrid architecture of convolutional layers and capsules with dynamic routing. For all convolutional layers, we adopt a stride of 1 for sliding kernels, and a padding of features to keep the feature map size. The network starts from convolutional layers for initialization of poses and activations of capsules. Then the primary dynamic routing takes place to represent 16 capsules with 8 capsules at every 2×2 field with a stride of 2. The feature maps are downsampled here with doubled number of capsules at every position.

For the rest part of the network, we stacked a homogeneous structure sequentially as shown in Fig. 1. The proposed structure consists of a capsule layer and a residual block. The residual block is analog to the structure in ResNet [3]. It takes poses

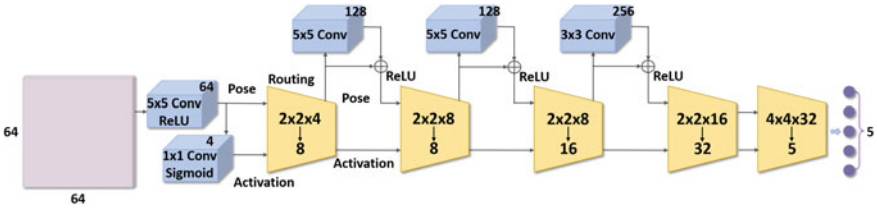

Fig. 1 The proposed network architecture for a 64×64 image. It contains 5 capsule layers where dynamic routing occurs. Except the last one, the dynamic routing at each capsule layer takes place within a 2×2 field with a stride of 2. At each block for dynamic routing, the number of input capsules is listed as width $\times$ height $\times$ number of capsules at each position. The number of output capsules is listed under the arrow. The side lengths of feature maps after each capsule layer are 32, 16, 8 and 4, respectively. The final dynamic routing takes all capsules within a 4×4 feature maps into account, resulting in 5 capsules as output. Here we take the smallNORB dataset for instance

from below layer as input. The poses are summed with their residual maps to ReLU functions as output. We exploit such structure to integrate convolutional layer and capsules as a generic building block for deeper and larger networks. The feature map will only be downsampled at capsule layer, along with the increase of capsules at each position. The residual structure ensures an identical or better version of pose to adapt the propagation of corresponding activation in the following dynamic routing.

We compose the pose of all capsules with 4×4 matrix as [5]. It requires many fewer parameters for transformation matrices during routing. This structure of pose leads to a network as in Fig. 1 with 1.2M parameters, in which nearly 90K parameters come from dynamic routing procedure. Differing from the stack of "ConvCaps" in [5], our network shares parameters for routing at different positions without overlap between neighboring receptive fields. So although our proposed network has more parameters than network in [5], it consumes less time for both training and inference.

4 Experiments

4.1 Implementation Details

We compared three routing methods and a CNN baseline in different benchmarks. Here the Fast Routing based on EM (FREM), and EM routing from [5] are implemented within the proposed network architecture for consideration.

In practical implementation, we use softmax function instead of standard normalization for the calculation of r'_{ij} in step 1 of above algorithms. This modification can relax the kernel bandwidth restriction in KDE with only trivial increase of computation. With these modifications, we adopt the Epanechnikov kernel and ℓ_1 norm: $d(\boldsymbol{v} - \boldsymbol{u}_i) = |\boldsymbol{v} - \boldsymbol{u}_i|$ as the default configuration for all experiments.

4.2 Evaluation on SmallNORB

We started our experiments from comparison of different routing methods on smallNORB dataset, which contains 5 categories of targets with an amount of 24,300 96×96 images. During training we randomly cropped 64×64 patches and augment data with random brightness and contrast. During test we directly cropped a 64×64 patch from the center of image. The image is centralized with unit deviation as input to the network. We implemented all the algorithms with TensorFlow 1.2.0 on a hardware with Intel Xeon E5-2680 CPU at 2.4GHz and NVIDIA Tesla P40 GPU. We train the network for 50 epochs with mini-batches of size 50.

We report the results of different methods in Table 1. All the models are trained with 2 routing iterations for clustering. The best result is achieved by exploiting FREM within our proposed network architecture. The test error 2.2% is in-par with

Table 1 Performance evaluation on smallNORB

Method	Inference time (s)	Training time (s)	Test error rate (%)
Baseline CNN	0.043 ± 0.003	0.064 ± 0.001	11.3
EM routing	0.252 ± 0.003	0.744 ± 0.003	2.3
FREM	0.158 ± 0.003	0.471 ± 0.002	2.2

Table 2 Results of proposed methods on different datasets

Method	MNIST (%)	Fashion-MNIST (%)	CIFAR10 (%)
Baseline CNN	0.65	7.6	19.2
EM routing	0.32	5.8	11.6
FREM	0.38	6.2	14.3

state-of-the-art performance gained by another routing method [5]. Note that our method achieves the results at a higher resolution with much higher efficiency.

From the perspective of efficiency, one can see that although routing methods consume more time for both training and inference than baseline CNN, they significantly reduce the test error by 80% with similar network architecture. Moreover, the FREM method reduces the time consumption by nearly 40% from EM routing. FREM slightly outperforms EM routing with our architecture.

4.3 Other Datasets

We also tested the proposed methods on MNIST, Fashion-MNIST [16] and CIFAR10 [6]. To adapt the size of images in these datasets, we removed the second capsule layer as well as the residual block from the network in Fig. 1. With four capsule layers the network can process an input image with 32×32 pixels. We resize all images to this resolution in the experiments.

We listed all results on different datasets for comparison in Table 2. For MNIST, all methods approximately achieve the same accuracy, since the results are nearly saturated. For Fashion-MNIST, our methods outperform another implementation of routing-by-agreement method with 8M parameters [16]. For CIFAR10, we modified the first 5×5 convolutional layer of network as 256 output channels with 3 color channels as input. The reported results are achieved by an ensemble of 5 models with the same hyper parameters as in the experiments on smallNORB. We omit the comparison of time consumptions of methods here since it is basically consistent to Table 1. In the case of lower resolution, there is a trivial gap between our methods and the EM routing. However, our efficient methods for routing still show high potentiality to prompt the performance of baseline CNN.

5 Conclusion

In this paper, we propose an efficient routing methods by generalizing existing routing methods within the framework of weighted KDE. Rather than constructing network with capsule structures independently for higher performance, we propose to exploit capsules and dynamic routing as effective complements with convolutional units. Experimental results show that such hybrid structure is promising to provide efficient solutions with much higher capacity for large scale vision tasks. In our future work, we plan to further prompt the performance of capsule networks on practical image datasets with higher resolution, e.g., STL-10.

Acknowledgements This work was supported by the Chinese National Natural Science Foundation (Grant No. 61701252, 61881240048), Natural Science Foundation in Universities on Jiangsu Province (16KJB510032) and HIRP Open 2018 Project of Huawei.

References

1. Alain, G., Bengio, Y.: Understanding Intermediate Layers using Linear Classifier Probes. arXiv:1610.01644 (2016)
2. Dempster, A.P., Laird, N.M., Rubin, D.B.: Maximum likelihood from incomplete data via the em algorithm. J. R. Stat. Soc. Series B (methodological), 1–38 (1977)
3. He, K., Zhang, X., Ren, S., Sun, J.: Deep residual learning for image recognition. In: Proceedings of the IEEE Conference on Computer Vision and Pattern Recognition, pp. 770–778 (2016)
4. Hinton, G.E., Krizhevsky, A., Wang, S.D.: Transforming auto-encoders. In: International Conference on Artificial Neural Networks, pp. 44–51. Springer (2011)
5. Hinton, G.E., Sabour, S., Frosst, N.: Matrix capsules with em routing. In: ICLR 2018 Conference. p. accepted (2018)
6. Krizhevsky, A., Hinton, G.: Learning Multiple Layers of Features from Tiny Images (2009)
7. LeCun, Y., Bengio, Y., Hinton, G.: Deep learning. Nature **521**(7553), 436 (2015)
8. LeCun, Y., Bottou, L., Bengio, Y., Haffner, P.: Gradient-based learning applied to document recognition. Proc. IEEE **86**(11), 2278–2324 (1998)
9. LeCun, Y., Huang, F.J., Bottou, L.: Learning methods for generic object recognition with invariance to pose and lighting. In: Proceedings of the 2004 IEEE Computer Society Conference on Computer Vision and Pattern Recognition, 2004. CVPR 2004, vol. 2, pp. II–104. IEEE (2004)
10. Lu, H., Li, B., Zhu, J., Li, Y., Li, Y., Xu, X., He, L., Li, X., Li, J., Serikawa, S.: Wound intensity correction and segmentation with convolutional neural networks. Concurr. Comput. Pract. Exp. **29**(6) (2016)
11. Lu, H., Li, Y., Chen, M., Kim, H., Serikawa, S.: Brain intelligence: go beyond artificial intelligence. Mob. Netw. Appl. **23**(2), 368–375 (2018)
12. Lu, H., Li, Y., Mu, S., Wang, D., Kim, H., Serikawa, S.: Motor anomaly detection for unmanned aerial vehicles using reinforcement learning. IEEE Internet Things J. **PP**(99), 1–1 (2017)
13. Russakovsky, O., Deng, J., Su, H., Krause, J., Satheesh, S., Ma, S., Huang, Z., Karpathy, A., Khosla, A., Bernstein, M., Berg, A.C., Fei-Fei, L.: Image net large scale visual recognition challenge. Int. J. Comput. Vis. (IJCV) **115**(3), 211–252 (2015). https://doi.org/10.1007/s11263-015-0816-y
14. Sabour, S., Frosst, N., Hinton, G.E.: Dynamic routing between capsules. In: Advances in Neural Information Processing Systems, pp. 3859–3869 (2017)

15. Serikawa, S., Lu, H.: Underwater Image Dehazing using Joint Trilateral Filter. Pergamon Press Inc. (2014)
16. Xiao, H., Rasul, K., Vollgraf, R.: Fashion-mnist: A Novel Image Dataset for Benchmarking Machine Learning Algorithms (2017)
17. Xu, X., He, L., Lu, H., Gao, L., Ji, Y.: Deep adversarial metric learning for cross-modal retrieval. In: World Wide Web-Internet & Web Information Systems, pp. 1–16 (2018)

A Novel Active Contour Model Using Oriented Smoothness and Infinite Laplacian for Medical Image Segmentation

Chunhong Cao, Chengyao Zhou, Jie Yu, Kai Hu and Fen Xiao

Abstract Active contour model (ACM) has been widely used in image segmentation. The original ACM has poor weak edge preservation ability and it is difficult to converge to the concave, especially long and thin indentation convergence. In order to address these defects, a series of models such as gradient vector flow (GVF) and general gradient vector flow (GGVF) were proposed. A new edge-preserving ACM using oriented smoothness, infinite Laplacian is proposed in this paper to further address these issues. Oriented smoothness and infinite Laplacian are adopted as the smoothness term in the energy function to promote the model's weak edge preservation and concave convergence ability. Furthermore, we employ a component-based normalization to accelerate the concave convergence rate. The experimental results show that the proposed method achieves better performance than the other comparative methods.

Keywords Active contour model · Medical image segmentation
Oriented smoothness · Infinite Laplacian

1 Introduction

Medical image segmentation is of great significance in clinical diagnosis, pathological analysis, treatment and has received much attention due to its practical applications in modern medical diagnosis [1].

It is noted that medical image segmentation methods have many problems, including blurring or weak edge, strong edge near the missing edge et al. [2]. Therefore, many methods were proposed to address these issues like thresholding based segmentation [3] and region-based method [4] as well as many advanced approaches such as neural network method [1] and active contour model (ACM) method [5].

C. Cao (✉) · C. Zhou · J. Yu · K. Hu · F. Xiao
Key Laboratory of Intelligent Computing and Information Processing
of Ministry of Education, Xiangtan University, Xiangtan 411105, China
e-mail: caoch@xtu.end.cn

H. Lu (ed.), *Cognitive Internet of Things: Frameworks, Tools and Applications*, Studies in Computational Intelligence 810,
https://doi.org/10.1007/978-3-030-04946-1_31

In recent years, convolutional neural network (CNN) plays an important role in medical segmentation which can be used to discover hierarchical relationships within data without laborious hand-crafting of features. CNN is widespread used [6–8] since Krizhevsky won the 2012 Imagenet Large Scale Visual Recognition Challenge. However, it may need a large amount of labelled training data and a large quantity of expertise to ensure proper convergence; also its generality and interpretability are limited. While ACM has mature theoretical support which contributes to low computation complexity. Moreover, because of its sub-pixel precision and easy to fuse various image information, ACM has been widely used in medical image segmentation [2, 5].

ACM can be roughly divided into two categories: parametric active contour model and geometric active contour model. Based on the advantages mentioned above and the low time complexity, this paper mainly studies the former. In 1987, Kass et al. [9] proposed the parametric active contour model method, namely snake model. This model uses the parametric form to represent the curve, and builds an energy function based on the curve as an independent variable. By achieving the minimum energy function as the target, the interaction between the internal force field and the external force field controls the evolution and deformation of the curve, and the final closed curve with the minimum energy is the required target contour. The evolution curve of parametric active contour model not only contains the priori information that is initialized around the object of interest, but also matches the local features of the image well.

However, there are still defects in the snake model, such as poor weak edge preservation, lack of concave convergence ability, small capture range and poor initialization insensitivity etc. As a result, many researches based on snake model were proposed [10–13]. For example, the gradient vector flow (GVF) model proposed by Xu and Prince [10] made a significant breakthrough in the construction of external force field. Then Xu et al. [14] proposed the general gradient vector flow (GGVF) model. In the iterative equation of external force field of GVF, the diffusion term and data term were added with two weight coefficients that were self-adaptive and adjusted according to local features of the image, which further improved the concave convergence ability, certain weak edge preservation ability and noise robustness. Ning et al. [11] proposed the GVF in the normal direction (NGVF) model by replacing the Laplacian operator in the GVF iteration process with the normal line directional diffusion operator. Subsequently, Liu and Wang et al. [15], on the basis of NGVF, retained the part diffusing along the tangent direction, added a weight coefficient changing according to the local features of the image before the part diffusing along the normal direction, and proposed the normally biased GVF external force (NBGVF) model. Qin et al. [12] proposed the component-based normalization (CN-GGVF) model based on the new observation of some features of the concave convergence ability of GVF model and GGVF model, which accelerated the concave convergence speed of GGVF model. Wu et al. [13] proposed an adaptive diffusion flow (ADF) model above infinity Laplacian function and the hypersurface function to improve weak edge preserving and concave convergence ability. Zhu et al. [5] put forward the NGGVF model in combination with the normalization of minimum

surface and component-based normalization, which has improved weak edge preservation ability. Generally, all the methods mentioned above are focused on improving the performance of long and thin indentation (LTI) convergence or weak boundary protection and evaluating performance of the segmentation accuracy on medical images.

In order to address the issues mentioned above, especially LTI and weak boundary protection, we propose a new ACM model to improve the accuracy of medical image segmentation. The specific contributions are summarized as follows:

(1) As the Laplacian diffusion from GVF and GGVF is isotropous, which means the external force will indiscriminately across all edges whether it's in the region of interest or not, the oriented smoothness from the optical flow and infinite Laplacian are incorporated to substitute smoothness energy term in the original GVF for taking image structure information into account to improve both weak edge preserving and concave convergence ability.
(2) By using component normalization instead of vector normalization, the ability of LTI convergence is enhanced and the concave convergence speed is accelerated.

2 Brief Review of the GVF Snake Model

In snake model, a continuous closed curve is defined as $c(s) = [x(s), y(s)]$, $s \in [0, 1]$. The evolution of this curve in the image is accomplished by minimizing the following energy function:

$$E(c(s)) = \int_0^1 (\alpha |c'(s)|^2 + \beta |c''(s)|^2) ds + \int_0^1 E_{ext}(c(s)) ds \tag{1}$$

where α and β are the weight coefficients controlling the elasticity and rigidity of the active contour curve respectively. The first and second integrals of (1) represent the internal and external energy of the curve respectively. In order to minimize the energy function $E(c(s))$, the deformation curve must satisfy the following Euler–Lagrange equation:

$$\alpha c''(s) - \beta c''''(s) - \nabla E_{ext}(c(s)) = 0 \tag{2}$$

Equation (2) is equivalent to the force balance equation:

$$F_{int}(c(s)) + F_{ext}(c(s)) = 0 \tag{3}$$

where $F_{int} = \alpha c''(s) - \beta c''''(s)$ represents the internal force, which ensures the smoothness and continuity of snake curves. $F_{ext} = -\nabla E_{ext}(c(s))$ represents the external force, which is the artificial limitation of the model evolution obtained through

calculation based on the image information of the region where the real contour exists, and is the key to make the curve move to the region of interest.

However, the snake model has several obvious defects. First, it has a small capture range and the initial curve must be close enough to the interested target edge. Second, the concave convergence ability is very poor [10]. Third, it is easy to penetrate weak boundary.

To solve the problem of snake model, Xu and Prince [10] proposed GVF model, where GVF field is used as the external force field to evolve the curve. The vector field can be written as $V(x, y) = [u(x, y), v(x, y)]$, and the corresponding energy function is as follows:

$$E = \iint \underbrace{[\mu(u_x^2 + u_y^2 + v_x^2 + v_y^2)}_{\text{smoothness energy}} + \underbrace{|\nabla f|^2|V - \nabla f|^2]}_{\text{edge energy}} dxdy \tag{4}$$

According to the variational principle, $V(x, y)$ of vector field should satisfy the following Euler–Lagrange equation:

$$\mu \underbrace{\nabla^2 V(x, y, t)}_{\text{diffusion term}} - \underbrace{|\nabla f|^2[V(x, y, t) - \nabla f]}_{\text{data attraction term}} = 0 \tag{5}$$

where f is the edge graph of the original image, ∇^2 is the Laplacian operator and μ is a positive weight coefficient controlling smooth energy and edge energy, which is positively correlated with image noise. Compared with snake model, GVF model improves concave convergence capability and has a larger capture range.

3 The Proposed Algorithm

The detailed description in terms of oriented smoothness, infinite Laplacian, component normalization and the proposed ACM are discussed in this section.

3.1 Oriented Smoothness

According to Nagel [16], the energy formula of oriented smoothness is expressed as follows:

$$E_{OS} = \iint \left\{ \left(\nabla g^T V + g_t\right)^2 + \eta^2 \text{trace}\left((\nabla V)^T W (\nabla V)\right) \right\} dxdy \tag{6}$$

Let $I(x, y)$ represent the image, and the vector $[g_x(x, y), g_y(x, y)]$ represent the gradient vector of the image $I(x, y)$. $\nabla g = \begin{pmatrix} u_x v_x \\ u_y v_y \end{pmatrix}$, $W = \frac{w+Id\gamma}{\text{trace}(w+Id\gamma)}$, where Id represents the identity matrix, $w = \left\{ \begin{pmatrix} g_y \\ -g_x \end{pmatrix} \begin{pmatrix} g_y \\ -gx \end{pmatrix}^T \right\}$. Then, the formula (6) can be written as the following form:

$$E_{OS} = \iint \left\{ \left(\nabla g^T V + g_t\right)^2 + \eta^2 \left(OC + \gamma \frac{u_x^2 + u_y^2 + v_x^2 + v_y^2}{||\nabla g||^2 + 2\gamma} \right) \right\} dxdy \tag{7}$$

where

$$\text{OC} := \frac{\left[\begin{pmatrix} u_x \\ u_y \end{pmatrix}^T \begin{pmatrix} g_y \\ -g_x \end{pmatrix} \right]^2}{||\nabla g||^2 + 2\gamma} + \frac{\left[\begin{pmatrix} v_x \\ v_y \end{pmatrix}^T \begin{pmatrix} g_y \\ -g_x \end{pmatrix} \right]^2}{||\nabla g||^2 + 2\gamma}$$

The first item in the (7) represents the data item, indicating the gray value conservation constraint; the second term represents the smooth term, indicating the oriented smoothness (OS) constraint. It is known from OC that after ignoring the denominator, remaining numerator part means the square of the optical flow vector projected perpendicular to the gray gradient direction, that is, the edge direction, and the remaining part in (7) except OC is Horn-Schunck (HS) smoothing constraint. When the force field spreads in a direction parallel to the edge, there exists a function of protecting the weak boundary.

3.2 Infinite Laplacian

Wang et al. [13] proposed an absolute minimal Lipschitz extension function, considering the L^p function:

$$E_p(u, v) = \frac{1}{p} \int |\nabla V|^p dx \tag{8}$$

Let $p \to \infty$, we get the infinite Laplacian function:

$$E_\infty(u, v) = \frac{1}{p} \int_\Omega |\nabla V|_{L^\infty(\Omega)} d\Omega \tag{9}$$

$\Omega \in R^2$ presents a bounded, open and connected domain with sufficiently smooth boundary. The minimization of (8) is an absolutely minimizing Lipschitz interpolant. Thus, the Euler–Lagrange equation for (9) can be written as:

$$\frac{1}{|\nabla V|^2}\Delta_\infty V = 0 \tag{10}$$

where $\Delta_\infty V = \sum_{i=1,j=1}^{2} V_{x_i} V_{x_j} V_{x_i x_j} = 0$ in Ω and Δ_∞ denote infinite Laplacian operator. Obviously, (10) is equivalent to the second derivative on the gray gradient which has good convergence efficiency according to NGVF [11].

3.3 Component-Based Normalization

According to the research of Qin et al. [12], the traditional vector normalization-based GVF and GGVF models have problems such as annihilation and noise interference when the concave convergence is performed, which limit the concave convergence ability, especially the LTI. Therefore, we employed component normalization in our algorithm to replace vector normalization, which improves the concave convergence ability of the GGVF model. Component normalization is defined as:

$$u_{cn}(x, y) = \begin{cases} 1, & u(x, y) > 0 \\ 0, & u(x, y) = 0 \\ -1, & u(x, y) < 0 \end{cases}, v_{cn}(x, y) = \begin{cases} 1, & v(x, y) > 0 \\ 0, & v(x, y) = 0 \\ -1, & v(x, y) < 0 \end{cases}$$

3.4 The Proposed Active Contour Model

In the second term of (7), it is easy to see that when (g_x, g_y) approaches $(0, 0)$, the energy formula will degenerate into the HS optical flow energy formula. The image domain is divided into edge regions and homogeneous regions [17]. When (g_x, g_y) approaches $(0, 0)$, the gray level in the image is almost unchanged, that is, in a homogeneous region where it is desirable to quickly move the curve close to the target of interest. Consequently, we do following steps: (1) Replace the constraints of HS with the infinite Laplacian, and omit the denominator in the OS constraint; (2) Add a coefficient that will be adaptively adjusted according to the image itself; (3) Use Gaussian kernel function to smooth external forces to reduce the effects of noise; (4) Use component normalization. The model has a diffusion force field that can be adaptively adjusted in parallel and perpendicular to the edge direction. In theory, it has good concave and weak boundary protection performance. As a result, the energy function is defined as:

$$E(u,v) = \iint g \cdot \left(-(1-m) \cdot \mathrm{H}_{L^\infty(\Omega)} + m \cdot \left(\left[\begin{pmatrix} j_x \\ j_y \end{pmatrix}^T \begin{pmatrix} g_y \\ -g_x \end{pmatrix} \right]^2 + \left[\begin{pmatrix} l_x \\ l_y \end{pmatrix}^T \begin{pmatrix} g_y \\ -g_x \end{pmatrix} \right]^2 \right) \right) dxdy + \iint h \cdot \left(|V - \nabla f|^2 \right) dxdy \tag{11}$$

$$m = \begin{cases} 1, & (|f| > \theta) \\ -\frac{f^3}{8\theta^3} + \frac{5f}{8\theta} + \frac{1}{2}, & (0 < |f| < \theta) \\ 0, & (|f| = 0) \end{cases} \tag{12}$$

where $\mathrm{H}_{L^\infty(\Omega)}$ is infinite Laplacian, $\mathrm{H}(j,l) := G_\sigma \otimes V(u,v)$ means the external force field smoothed by G_σ, which is Gaussian convolution kernel with standard deviation σ, $\otimes$ is a convolution operation, $g = e^{-|\nabla f|/K}$ and $h = 1 - e^{-|\nabla f|/K}$, (12) is the adaptive adjustment factor, f is the image gradient, and θ is the artificial set value, which is set to 0.1 in this paper.

The Euler–Lagrange equation corresponding to (11) is:

$$g \cdot \left((1-m) \cdot \frac{1}{|\nabla V|^2} \Delta_\infty V + m \cdot \left(g_y^2 H_{xx} + g_x^2 H_{yy} - 2 g_x g_y H_{xy} \right) \right) - h \cdot [V - \nabla f] = 0 \tag{13}$$

4 Experiment Results and Analysis

In this section, we will evaluate the performance of proposed model's LTI convergence and weak boundary protection. And then, we test the proposed model on the medical images which are typical weak boundary images to further testify the performance of LTI convergence and weak boundary protection. The comparison methods are GVF [10], GGVF [14], CN-GGVF [12], NGVF [11], NBGVF [15] and NGGVF [5]. The medical image we test is based on MedPix [18] and MICCAI 2009 [19]. Two parameters of snake deformed from (1) are set to $\alpha = 0.5$, $\beta = 0.5$, the time step τ is set to 1. The selection strategy of K from (11) is the same as μ from (4).

4.1 Long and Thin Indentation Convergence

The image used in this experiment is 6 pixels wide and 70 pixels long concave. The external force iteration of all methods is fixed at 100. The selection criterion for the snake iteration is to select the minimum iteration if the target converges successfully, otherwise the iteration in which the curve is no longer moving is selected. For the number of snake iteration, the proposed model is set as 28, CN-GGVF is 42, and all other methods are 60. As shown in Fig. 1, only CN-GGVF and proposed model successfully converge. However, the proposed model has less snake iteration.

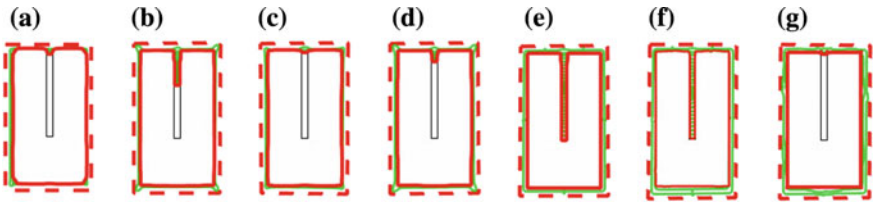

Fig. 1 Convergence results of GVF, GGVF, NGVF, NBGVF, CN-GGVF, NGGVF and proposed model towards LTI image. **a** GVF ($\mu = 0.2$), **b** GGVF ($K = 0.05$), **c** NGVF ($\mu = 0.4$), **d** NBGVF ($\mu = 0.2$, $K = 0.04$), **e** CN-GGVF ($K = 0.05$), **f** NGGVF ($K = 0.3$), **g** proposed ($K = 0.05$, $\sigma = 0.2$)

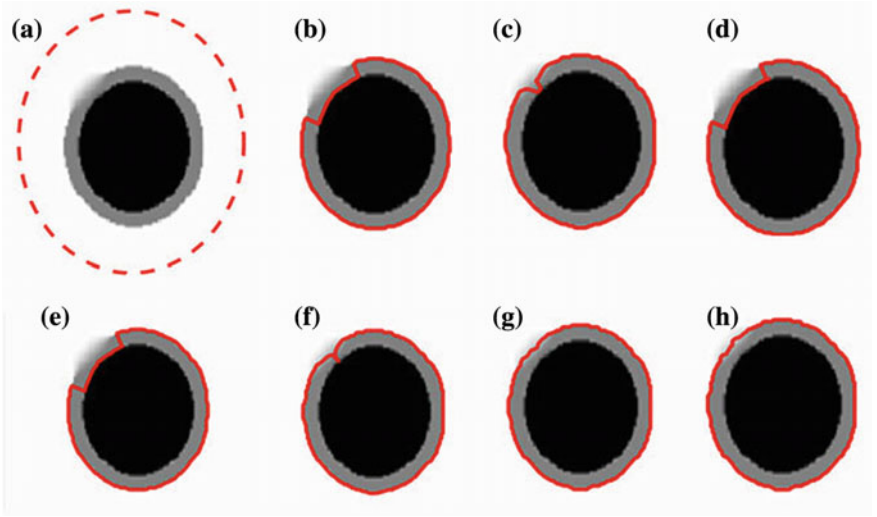

Fig. 2 Weak-edge preservation performance of each model. **a** Initial curve, **b** GVF ($\mu = 0.03$), **c** GGVF ($K = 0.03$), **d** NGVF ($\mu = 0.1$), **e** NBGVF ($\mu = 0.06$, $K = 0.1$), **f** CN-GGVF ($K = 0.03$), **g** NGGVF ($K = 0.01$), **h** proposed ($K = 0.03$, $\sigma = 0.5$)

4.2 Weak Edge Protection

This experiment is the weak boundary protection performance test on a weak-edge simulation image. It can be seen from Fig. 2 that only NGGVF and the proposed model successfully converge. In order to further compare the weak edge protection performance, the experiment will be carried out on the heart image in combination with the initial curve sensitivity. The first line in Fig. 3 is the convergence of the proposed model under three different initial curves, and the second line is the convergence of the NGGVF model under three different initial curves. It can be seen that the proposed model can successfully converge under three different initial curves, while NGGVF model only converges successfully in the last image.

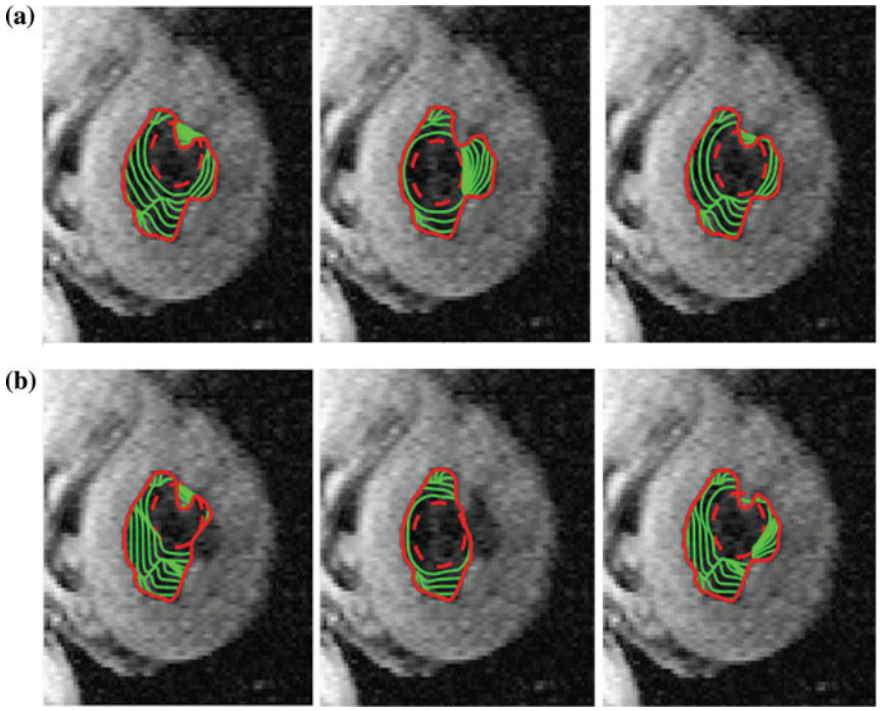

Fig. 3 Further weak-edge preservation experiment corresponding to three different initial curves. **a** Proposed ($K = 0.1$, $\sigma = 1$), **b** NGGVF ($K = 0.7$)

4.3 Medical Image Segmentation

In this experiment, a cortex image is used and the final segmentation results of each model are shown in Fig. 4 and the corresponding visual graphical result are shown in Fig. 5. F1 is a comprehensive evaluation of Precision and Recall [20]. It can be seen that the most important metric F1 is optimal.

5 Conclusion

In this paper we propose a novel active contour model for medical image segmentation that combined oriented smoothness, infinite Laplacian and component normalization. Comparing with GVF, GGVF, NGVF, NBGVF, CN-GGVF, NGGVF, the model not only maintains the advantages of GVF model, but also has better performance in convergence on LTI and weak boundary protection.

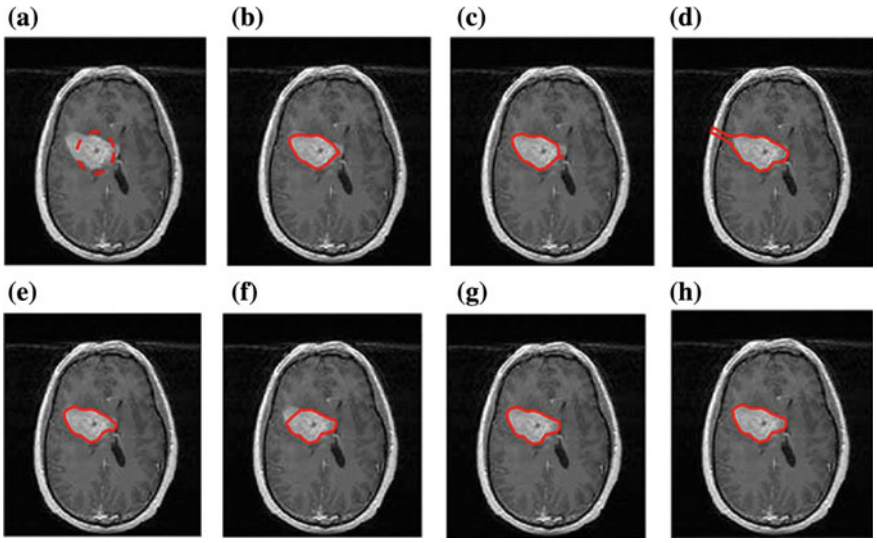

Fig. 4 Segmentation results of each model on cortex images. **a** Initial curve, **b** GVF, **c** GGVF, **d** NGVF, **e** NBGVF, **f** CN-GGVF, **g** proposed, **h** NGGVF

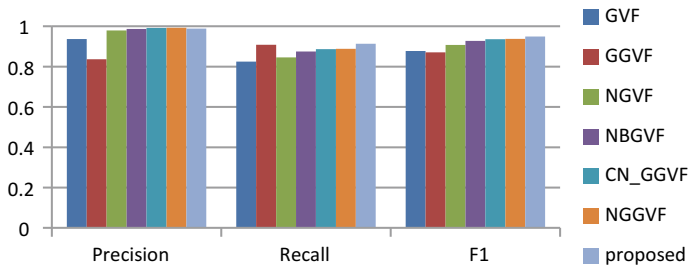

Fig. 5 Comparison of the precision, recall, and F1 results for the different methods on cortex

Acknowledgements This work was supported by the NSFC under Grants 61401386, 61802328.

References

1. Lu, H., Li, B., Zhu, J., Li, Y., Li, Y., Xu, X., Serikawa, S.: Wound intensity correction and segmentation with convolutional neural networks. Concurr. Comput. Pract. Exp. **29**(6), e3927 (2017)
2. He, L., Peng, Z., Everding, B., Wang, X., Han, C.Y., Weiss, K.L., Wee, W.G.: A comparative study of deformable contour methods on medical image segmentation. Image Vis. Comput. **26**(2), 141–163 (2008)
3. Mustaqeem, A., Javed, A., Fatima, T.: An efficient brain tumor detection algorithm using watershed & thresholding based segmentation. Int. J. Image Graph. Signal Process. **4**(10), 34 (2012)

4. Asari, K.V.: A fast and accurate segmentation technique for the extraction of gastrointestinal lumen from endoscopic images. Med. Eng. Phys. **22**(2), 89–96 (2000)
5. Zhu, S., Gao, R.: A novel generalized gradient vector flow snake model using minimal surface and component-normalized method for medical image segmentation. Biomed. Signal Process. Control **26**, 1–10 (2016)
6. Lu, H., Li, Y., Chen, M., Kim, H., Serikawa, S.: Brain intelligence: go beyond artificial intelligence. Mob. Netw. Appl. **23**(2), 368–375 (2018)
7. Lu, H., Li, Y., Uemura, T., Kim, H., Serikawa, S.: Low illumination underwater light field images reconstruction using deep convolutional neural networks. Futur. Gener. Comput. Syst. **82**, 142–148 (2018)
8. Lu, H., Li, Y., Mu, S., Wang, D., Kim, H., Serikawa, S.: Motor anomaly detection for unmanned aerial vehicles using reinforcement learning. IEEE Internet Things J. **5**(4), 2315–2322 (2018)
9. Kass, M., Witkin, A., Terzopoulos, D.: Snakes: active contour models. Int. J. Comput. Vis. **1**(4), 321–331 (1988)
10. Xu, C., Prince, J.L.: Snakes, shapes, and gradient vector flow. IEEE Trans. Image Process. **7**(3), 359–369 (1998)
11. Jifeng, N., Chengke, W., Shigang, L., Shuqin, Y.: NGVF: an improved external force field for active contour model. Pattern Recognit. Lett. **28**(1), 58–63 (2007)
12. Qin, L., Zhu, C., Zhao, Y., Bai, H., Tian, H.: Generalized gradient vector flow for snakes: new observations, analysis, and improvement. IEEE Trans. Circuits Syst. Video Technol. **23**(5), 883–897 (2013)
13. Wu, Y., Wang, Y., Jia, Y.: Adaptive diffusion flow active contours for image segmentation. Comput. Vis. Image Underst. **117**(10), 1421–1435 (2013)
14. Xu, C., Prince, J.L.: Generalized gradient vector flow external forces for active contours 1. Signal Process. **71**(2), 131–139 (1998)
15. Wang, Y., Liu, L., Zhang, H., Cao, Z., Lu, S.: Image segmentation using active contours with normally biased GVF external force. IEEE Signal Process. Lett. **17**(10), 875–878 (2010)
16. Nagel, H.H., Enkelmann, W.: An investigation of smoothness constraints for the estimation of displacement vector fields from image sequences. IEEE Trans. Pattern Anal. Mach. Intell. PAMI **8**(5), 565–593 (1986)
17. Li, C., Liu, J., Fox, M.D.: Segmentation of external force field for automatic initialization and splitting of snakes. Pattern Recognit. **38**(11), 1947–1960 (2005)
18. MedPix, Free Online Medical Image Database. http://rad.usuhs.mil/medpix
19. Radau, P., Lu, Y., Connelly, K., Paul, G., Dick, A., Wright, G.: Evaluation framework for algorithms segmenting short axis cardiac MRI. Midas J. 1–9 (2009). http://hdl.handle.net/10380/3070
20. Lui, D., Scharfenberger, C., Fergani, K., Wong, A., Clausi, D.A.: Enhanced decoupled active contour using structural and textural variation energy functionals. IEEE Trans. Image Process. **23**(2), 855–869 (2014)

Experimental Study on Learning of Neural Network Using Particle Swarm Optimization in Predictive Fuzzy for Pneumatic Servo System

Shenglin Mu, Satoru Shibata, Tomonori Yamamoto, Seigo Goto, Shota Nakashima and Kanya Tanaka

Abstract Based on the scheme of predictive fuzzy control combined with neural network (NN) for pneumatic servo system, the learning of NN using Particle Swarm Optimization (PSO) is studied according to experimental investigation in this research. A group of positioning experiments using existent pneumatic servo system were designed to confirm the effectiveness and efficiency of the NN's learning employing PSO in the imaginary plant construction for the pneumatic system in predictive fuzzy control. The analysis in the study was implemented comparing the results of traditional back-propagation (BP) type NN and the PSO type NN.

Keywords Pneumatic servo system · Position control · Predictive fuzzy control Neural network · Particle swarm optimization

1 Introduction

Along with the improvement of PCs' computing ability, intelligent algorithms such as Neural Network (NN), Fuzzy Logic (FL), and Particle Swarm Optimization (PSO), etc., have been introducing to various applications. Especially, to the control applica-

S. Mu (✉) · S. Shibata · T. Yamamoto · S. Goto
Graduate School of Science and Engineering, Ehime University, 3 Bunkyo-cho, Matsuyama, Ehime 7908577, Japan
e-mail: mu.shenglin.du@ehime-u.ac.jp

S. Nakashima
Graduate School of Sciences and Technology for Innovation, Yamaguchi University, 2-16-1 Tokiwa-dai, Ube, Yamaguchi 7558611, Japan

K. Tanaka
School of Science and Technology, Meiji University, 1-1-1 Higashi-Mita, Tama-ku, Kawasaki, Kanagawa 2148571, Japan

H. Lu (ed.), *Cognitive Internet of Things: Frameworks, Tools and Applications*, Studies in Computational Intelligence 810,
https://doi.org/10.1007/978-3-030-04946-1_32

tions the intelligent algorithms are expected to bring excellent characteristics [1–3]. Employing intelligent algorithms, some control schemes were developed for the control of pneumatic systems in literatures. Shibata et al. [4] proposed a fuzzy based control method with a neural network for obtaining appropriate fuzzy rules to a vertical type pneumatic servo system [4]. An advanced position tracking control method using NN, sliding mode and backstepping techniques was designed by Ba et al. [5]. In the proposed method, Lyapunov functions were employed to guarantee convergences. A harmony search algorithm, which is combined with the optimal hybrid scheme of dynamic neural network and PID control, for the position control of the PWM-driven pneumatic actuator was proposed by Mazare et al. [6]. Based on the dynamic NN and PID driven pneumatic actuator, the harmony search algorithm was used to unravel the optimal problem in the method.

In this research, based on the predictive fuzzy control algorithm proposed in [7], the swarm intelligent algorithm of PSO is introduced for the learning. Comparing with the traditional back-propagation (BP) type NN, the proposed learning method using Particle Swarm Optimization (PSO) requires no differential information of the plant. Meanwhile, the estimation is simple and efficient. The effectiveness and the efficiency of the proposed learning method for the predictive fuzzy control for pneumatic servo system is investigated. In this manuscript, the contents are written as follows. In Sect. 2, the proposed method of predictive fuzzy control combined with NN is introduced. The learning methods of BP type NN, Constriction Factor Approach (CFA) type PSO combined NN, and Inertia Weight Approach (IWA) type PSO combined NN are introduced in Sect. 3. To confirm the learning effectiveness of the algorithms, the experimental study of learning process in predictive fuzzy control is given in Sect. 4. The conclusions of the research are given in Sect. 5.

2 Predictive Fuzzy Control for Pneumatic Servo System

The predictive fuzzy control combined with NN was proposed in [7] can be depicted by the block diagram shown in Fig. 1. In the diagram, $r(k)$ is the desired value, $y(k)$ is the plant output, e_i is the errors between the desired value and output of imaginary plant, Δe_i is the variation of error signal, $u(k)$ means the control input. In the proposed method, predictive fuzzy control is applied to calculate the predicted positions by the imaginary plant generated from candidates changes of control input $\Delta^* u_n$.

Figure 2 shows the detailed calculation process in the proposed method. The predicted output $\hat{y}_n$ will be generated according to the changes of control input. Based on the difference between desired values $r(k)$ and the predicted output, and the variation of the difference, the evaluated values of α_n and β_n within the range of [0, 1]. According to degree calculation and control input estimation, the control input can be updated.

As introduced above, predictive fuzzy control is applied to estimate predicted position of plant according to the imaginary model. In the fuzzy logic design, the control rule is defined as follows.

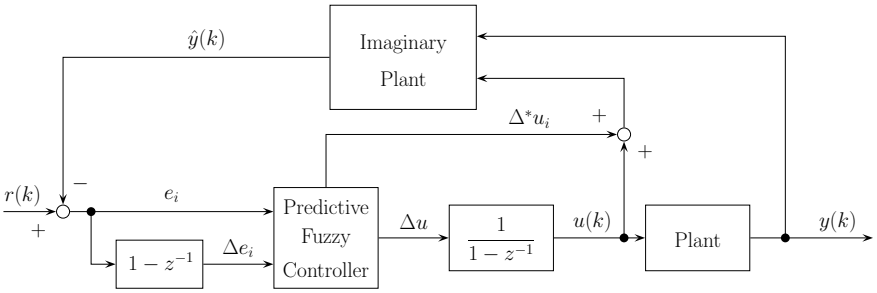

Fig. 1 Block diagram of control system using predictive fuzzy control

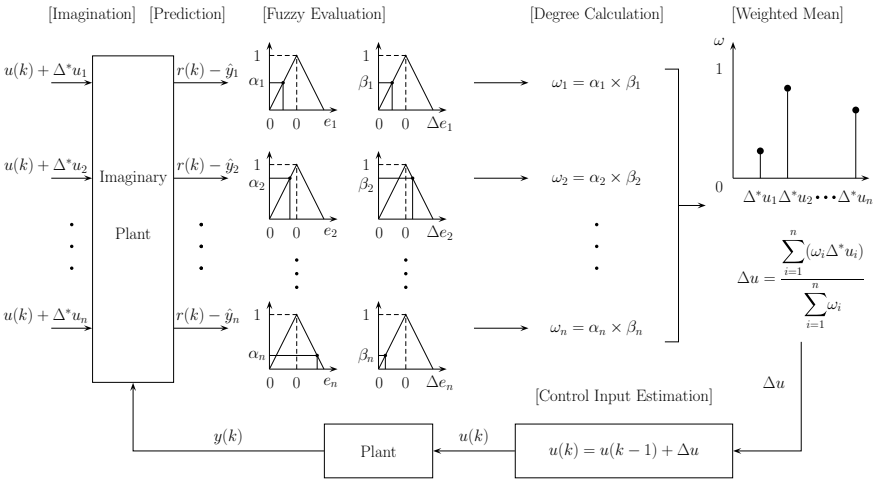

Fig. 2 Calculation in the control system using predictive fuzzy control

$$R_i : \text{if } (\Delta^* u \text{ is } C_i \rightarrow x \text{ is } A_i \text{ and } y \text{ is } B_i) \text{ then } \Delta u \text{ is } C_i \quad (i = 1, 2, \ldots, n) \tag{1}$$

where R_i is the ith control rule. $\Delta^* u$ is the control signal, and C_i is the ith possible values for $\Delta^* u$ in the possible set of $C = \{C_1, C_2, \ldots, C_n\}$. x, y are the variables for evaluating predicted value, when C_i was decided as $\Delta^* u$. A and B are the fuzzy sets with the elements of α_n and β_n respectively for fuzziness evaluation.

To estimate the fuzzy output, firstly, changes of control input $\Delta^* u_i$ (it means the control pattern of $i = 1, 2, \ldots, n$) which is each control command are added to current control input $u(k)$. Secondly, the virtual manipulating values $u(k) + \Delta^* u_i$, $(i = 1 \ldots n)$ are input to the imaginary plant, and the output $\hat{y}_i$, $(i = 1 \ldots n)$ are predicted. From the results, errors $e_i(k)$ between the desired values $r(k)$ and the predicted outputs $\hat{y}_i$, and changes of errors $\Delta e_i(k)$ between previous errors and current errors are calculated. The belonging degrees ω_i corresponded to each errors and changes of errors can be calculated as Eq. 2 shows.

$$\omega_i = \mu(e_i(k)) \times \mu(\Delta e_i(k)) = \alpha_i \times \beta_i \tag{2}$$

The desirable changes of control input Δu as the inference result is obtained by calculating the weighted average between the candidates of changes of control input $\Delta^* u_i$ and the fuzzy degree as shown in Eq. 3.

$$\Delta u = \frac{\sum_{i=1}^{n} (\omega_i \cdot \Delta^* u_i)}{\sum_{i=1}^{n} \omega_i} \tag{3}$$

The control input can be represented by adding obtained changes of control input Δu to previous control input $u(k-1)$ as follows.

$$u(k) = u(k-1) + \Delta u \tag{4}$$

The synthesized control input $u(k)$ is input to the real plant.

3 Neural Networks Combined with Intelligent Algorithms

3.1 BP Type NN in the Predictive Fuzzy

As introduced in [7], NN is used to construct imaginary plant of the pneumatic servo system. The structure of NN is designed as shown in Fig. 3. On the input layer, there are 7 units including threshold. The control outputs $\{y(k-1), y(k-2), y(k-3)\}$ and control inputs $\{u(k-1), u(k-2), u(k-3)\}$, are introduced as the input singnals. On the hidden layer, there are 13 units including threshold. On the output layer, there is one unit for the imaginary plant output $\hat{y}(k)$. For activation, sigmoid function shown in Eq. 5 is used for nonlinearity compensation

$$f_s(x) = \frac{X_g(1 - e^{-4x/X_g})}{2(1 + e^{-4x/X_g})} \tag{5}$$

where x is the weighted sum of units output in units of NN. X_g is the variable for adjustment. In the NN scheme, W^1_{qp} is the weight between input layer and hidden layer, W^2_q is the weight between hidden layer and output layer, where $p = (1, 2, \ldots 7)$, and $q = (1, 2, \ldots 13)$. The output of NN can be calculated by Eq. 6

$$\hat{y}(k) = f_s(\sum_{q}^{12} W^2_q(k) f_s(\sum_{p=1}^{6} W^1_{pq}(k) I_p(k))) \tag{6}$$

where $I_p(k)$ is the signal from input layer.

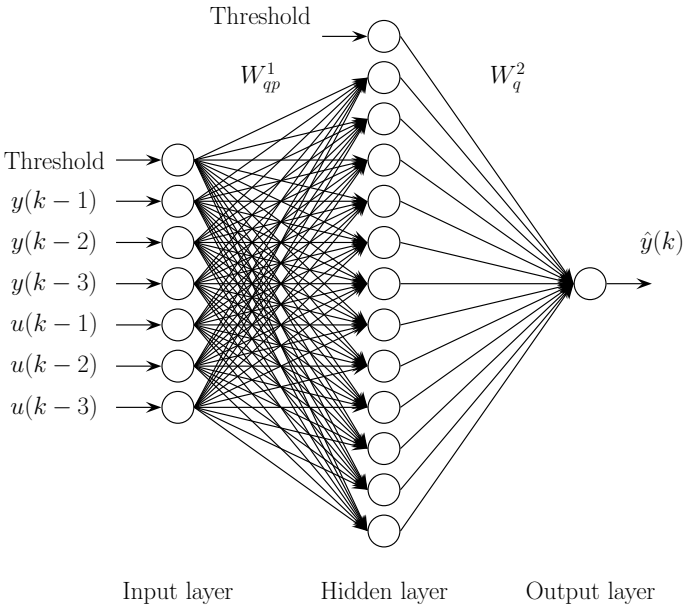

Fig. 3 Topologic structure of neural network

The learning of NN is implemented by BP algorithm. Pneumatic control input signals and outputs are employed as teaching signal for input and output characteristics. The errors $E(k)$ between teaching signals and plant signals are evaluated by the following equation.

$$E(k) = \frac{1}{2}(r(k) - \hat{y}(k))^2 \tag{7}$$

The variation of weights in output layer $W_q^2(k)$ can be expressed as

$$\Delta W_q^2(k) = -\eta \frac{\partial E(k)}{\partial W_q^2(k)} \tag{8}$$

where η ($\eta > 0$) is the learning rate which is usually adjusted by trial and error in the NN's learning. The limitations of the traditional BP method are the complexity in computing and differential information requirements.

3.2 PSO Type NN in the Predictive Fuzzy

Therefore, PSO, a global optimization algorithm is introduced to the NN's learning for the predictive fuzzy control. PSO is simple in estimation and easy to implement,

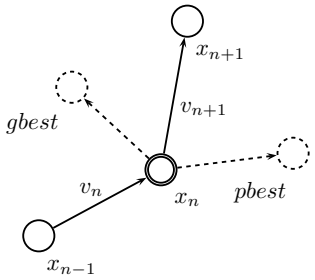

Fig. 4 Example of particle movement in PSO

it is quite attractive in the field of optimization in recent years [8, 9]. Figure 4 shows an example of particle movement of PSO. x_n means the position in the nth step, x_{n-1} and x_{n+1} mean the position of the $(n-1)$ step and the $(n+1)$ step, respectively. $gbest$ is the best position of the whole swarm, and $pbest$ is the best position of the particle. v_n, which expresses the position variance, is the velocity of the particle at the nth step. It is related to the best positions as the dash lines show in the figure. In NN learning, we define the value of weights as the position information contained by N particles. The weights of NN are designed to be updated by IWA and CFA type PSO algorithms.

The IWA type PSO is expressed as Eqs. 9 and 10 show.

$$X_{n+1} = X_n + V_n \tag{9}$$

$$V_{n+1} = \tau \cdot V_n + c_1 r_1 \cdot (pbest_n - X_n) + c_2 r_2 \cdot (gbest_n - X_n) \tag{10}$$

In Eq. 10, c_1 and c_2 are two positive constants, r_1 and r_2 are two random numbers within [0, 1]. In Eq. 9, the weight factor which balances the global and local search, is calculated as follows.

$$\tau = \tau_{max} - \frac{\tau_{max} - \tau_{min}}{episode_{max}} \cdot episode \tag{11}$$

where $episode$ means the number of current iteration, $episode_{max}$ presents the max iteration number in the searching. τ_{max} and τ_{min} are the weight factor's maximum and minimum value, respectively.

The CFA type PSO is expressed as Eqs. 9 and 12 show.

$$V_{n+1} = k \times [V_n + c_1 \times r_1 \times (pbest_n - X_n) + c_2 \times r_2 \times (gbest_n - X_n)] \tag{12}$$

In Eq. 12, the same with the IWA type PSO, c_1 and c_2 are two positive constants, r_1 and r_2 are two random numbers within [0, 1]. In Eq. 12, the constriction factor which balances the global and local search, is calculated as follows.

$$k = \frac{2}{|2 - \varphi - \sqrt{\varphi^2 - 4\varphi}|}, \varphi = c_1 + c_2, \varphi \geq 4 \tag{13}$$

By employing the algorithms introduced above, the weights in NN scheme can be updated effectively. To confirm the effectiveness and efficiency of the algorithms in NN's learning, experimental study was implemented.

4 Experimental Study

In the experimental study for the positioning control of pneumatic servo system, the NNs were applied to obtain the imaginary model of the pneumatic servo system. The learning employs the manipulating value $u(k)$ in the servo system as teaching signal of input. The output of the servo system $y(k)$ was applied as teaching signal of output. The output of NN $\hat{y}(k)$ will be applied as estimated value for prediction. The experiment was designed to evaluate the learning accuracy and convergences of the algorithms in NN. In the proposed scheme, existent PID control data was employed as teaching data in positioning control. The data was generated in the positioning control using PID on an existent horizontal type pneumatic servo system. The range of the cylinder in the pneumatic servo system was from −50 [mm] to +50 [mm]. The period of the fetched data was from 0 to 10 s.

In the learning of BP type NN, the learning rate was set as $\eta = 1.0$. In the learning of PSO the particle number was set as 10. All the particles are initialized by random numbers from −3.5 to 3.5. The particles are designed to be evaluated by the following function with the error signal $e(k) = y(k) - \hat{y}(k)$ as shown in Eq. 14.

$$fitness = \frac{1}{1 + e(k)^2} \tag{14}$$

In the IWA type PSO, the positive constants c_1 and c_2 were set as $c_1 = c_2 = 2.0$. The weight factor of τ_{max} and τ_{min} were set as 0.9 and 0.4, respectively. In the CFA type PSO, the positive constants c_1 and c_2 are set as different values, where $c_1 = c_2 = 2.5$. By employing the fitness in evaluation, the weights will be updated according to the error. The whole swarm of PSO will converge to the optimal with smaller error.

As shown in Fig. 5, the positioning response of the NNs converged to the teaching data from PID control. Comparing with the outputs of BP and CFA type NNs, there are some obvious overshoot in the output of IWA type NN. The plot of error shown in Fig. 6 confirmed the oscilation at the rising phase in the response of IWA type NN. The maximum value of error was around 4.5 [mm]. Relatively, the variations of error by BP and CFA type NNs were stable. In the learning process, the convergences of the algorithms revealed the possible reason of the phenomenon in responses. Figures 7 and 8 show the variation of weights between input and hidden layers and weights between hidden and output layers, respectively. It is easy to tell that the convergences

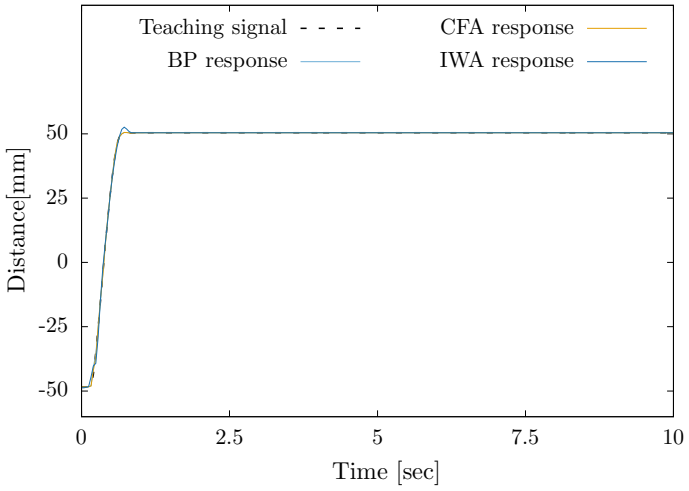

Fig. 5 Response of different algorithms

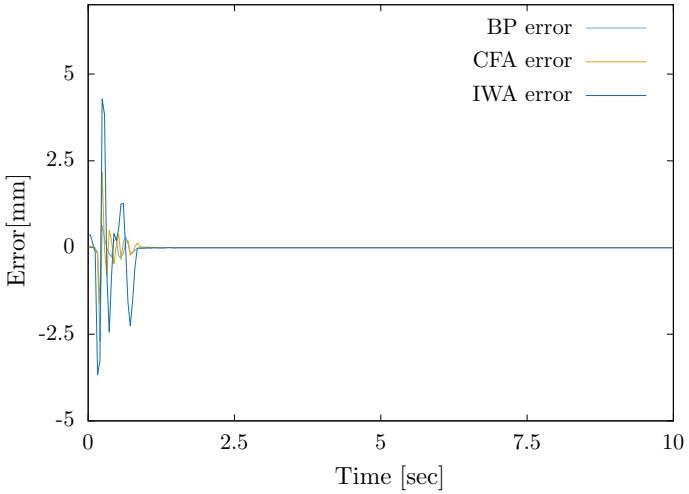

Fig. 6 Error variation in responses

of weights in BP and CFA type NNs were quicker and smoother than in IWA type NN. It is considered that the exploring movement of particles in IWA type NN was not good enough in the learning. Meanwhile, the convergence of CFA appeared at about the 2000th iteration, faster than BP and IWA type NN. With the quick convergence and high accuracy positioning, the CFA type NN is expected to play more important role to make the learning to real-time level. However, it has to be clear that optimal parameter setting of all the algorithms is still expected.

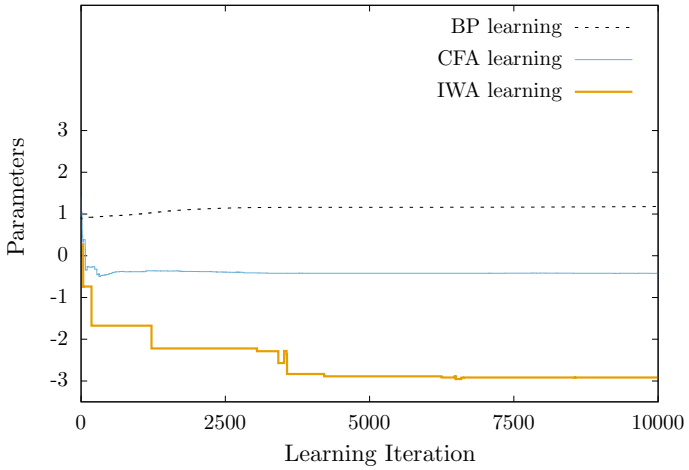

Fig. 7 Variation of weights on the input-hidden layer

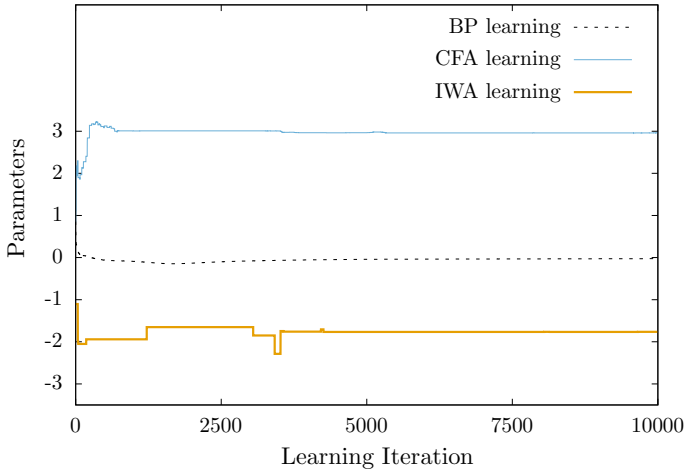

Fig. 8 Variation of weights on the hidden-output layer

5 Conclusions

In this research, based on the intelligent control method using predictive fuzzy control combined with neural networks, the PSO type learning algorithms were investigated for the positioning control of pneumatic servo system. The learning experiments for positioning control was implemented using BP type NN, CFA type NN and IWA type NN, respectively. According to the learning results, comparing with the convetional

BP type NN, the PSO type NN algorithms are with effectiveness and efficiency in the learning. Advanced parameter optimizations in the algorithms for high accuracy and real-time control are expected to be implemented in the future work.

References

1. Mu, S., Tanaka, K., Nakashima, S., Djoewahir, A.: Real-Time PID controller using neural network combined with PSO for ultrasonic motor. ICIC Express Lett. **8**(11), 2993–2999 (2014)
2. Kumar, V., Nakra, B.C., Mittal, A.P.: A review on classical and fuzzy PID controllers. Int. J. Intell. Control Syst. **16**(3), 170–181 (2011)
3. Li, J., Tanaka, K.: Intelligent control for pneumatic servo system. JSME Int. J. Ser. C **46**(2), 699–704 (2003)
4. Shibata, S., Jindai, M., Yamamoto, T., Shimizu, A.: Neuro-Fuzzy control for pneumatic servo systems. JSME Int. J. Ser. C **45**(2), 449–455 (2002)
5. Ba, D., Dinh, Q., Ahn, K.: An integrated intelligent nonlinear control method for a pneumatic artificial muscle. IEEE/ASME Trans. Mechatron. **21**(4), 1835–1845 (2016)
6. Mazare, M., Taghizadeh, M., Kazemi, M. G.: Optimal hybrid scheme of dynamic neural network and PID controller based on harmony search algorithm to control a PWM-driven pneumatic actuator position. J. Vib. Control 1–17 (2017). https://doi.org/10.1177/1077546317707102
7. Goto, S., Shibata, S., Yamamoto, T., Mu, S.: Position Control for Pneumatic Servo System, pp. 470–475. Kitakyushu, Japan (2017)
8. Kennedy, J., Eberhart, R.: Particle Swarm Optimization, Proceedings of IEEE International Conference of Neural Networks, Perth, Australia, pp. 1942–1948 (1995)
9. Djoewahir, A., Tanaka, K., Nakashima, S.: Adaptive PSO-based self-tuning PID controller for ultrasonic motor. Int. J. Innov. Comput. Inf. Control **9**(10), 3903–3914 (2013)

Discrete Hashing Based on Point-Wise Supervision and Inner Product

Xingyu Liu, Lihua Tian and Chen Li

Abstract Recent years has witnessed an increase popularity of supervised hashing in vision problems like image retrieval. Compared with unsupervised hashing, supervised hashing accuracy can be boosted by leveraging semantic information. However, the existing supervised methods either lack of adequate performance or often incur a low quality optimization process by dropping the discrete constraints. In this work, we propose a novel supervised hashing framework called discrete hashing based on point-wise supervision and inner product (PSIPDH) which using point-wise supervised information make hash code effectively correspond to the semantic information, on the basis of which the coded inner product is manipulated to introduce the punishment of Hamming distance. By introducing two kinds of supervisory information, a discrete solution can be applied that code generation and hash function learning processes are seen as separate steps and discrete hashing code can be directly learned from semantic labels bit by bit. Experiment results on data sets with semantic labels can demonstrate the superiority of PSIPDH to the state-of-the-art hashing methods.

1 Introduction

In recent years, hashing methods have been widely applied to approximate nearest neighbor search that it have attracted considerable attention in computer vision, machine learning, information retrieval and related areas [1, 6, 8–11, 14, 16, 17, 19]. Hashing methods construct a set of hash functions that map the original high-dimensional data into a compact binary space preserving the similarity among

X. Liu · L. Tian · C. Li (✉)
School of Software Engineering, Xian Jiaotong University, Xi'an, China
e-mail: lynnlc@126.com

X. Liu
e-mail: liuxingyu@stu.xjtu.edu.cn

L. Tian
e-mail: lhtian@mail.xjtu.edu.cn

H. Lu (ed.), *Cognitive Internet of Things: Frameworks, Tools and Applications*, Studies in Computational Intelligence 810,
https://doi.org/10.1007/978-3-030-04946-1_33

neighbours. Hence the high-dimensional data can be represented by a set of compact binary codes witch are extremely efficient for data storage, and the resulting binary codes enable fast similarity search on the basis of the Hamming distance obtained by XOR between codes.

Over the past decades,supervised hashing has attracted increasing attention. Because of the benefit of leveraging semantic (label) information for hashing function learning, the learned compact binary codes (typically ≤ 200) can effectively and highly efficiently index and organize massive data. It has demonstrated great accuracy in many real applications.

In general, hashing-code learning problem is essentially a discrete optimization problem which is hard to solve. To simplify the optimization involved in a binary code learning procedure, most existing supervised hashing methods, such as KSH [7], try to solve a relaxed continuous optimization problem by dropping the discrete constraints, but such an approximate solution breaks the constraint resulting in the solution will be far away from the real optimal solution [13] and often makes the resulting hash functions less effective possibly due to the accumulated quantization error. This has been confirmed by experiments [4, 15].

In early research work on directly learning the binary codes, point-wise supervised information can be formulated as a simple classification applying to take advantage of the label information [5, 15]. That is, the learned binary codes are expected to be optimal for the jointly learned classifier. However In hash-based image retrieval, We search for the approximate nearest neighbour by comparing the Hamming distance. Which means we usually want smaller Hamming distances for similar data and larger Hamming distances for dissimilar data when performing retrieve. Obviously, simply using a simple classifier can not achieve such an effect. The Hamming distance of pairwise codes should be valued during training.

In this work, we propose a novel supervised hashing framework called discrete hashing based on point-wise supervision and inner product (PSIPDH). This supervised hashing framework use both point-wise supervision and the correspondence between pairwise inner product and the Hamming distance.Then it can lead to high semantic consistency and implicit yet more effective optimization of Hamming distances which is more in line with the requirements of image retrieval based on hashing. In addition, the joint learning of point-wise supervision and inner product can makes the NP-hard problem effectively discrete solved by the code's separability. By means of discrete cyclic coordinate descent, at each step PSIPDH solves the associated binary optimization and obtains an analytical solution, which thus makes the whole optimization very efficient. Moreover We use a novel supervised hashing framework of which the learning goal is to generate the optimal binary hash codes for retrieve, hash function is then learned using a tractable and scalable solver based on the learned bits in step two. Experiment results on two popular large-scale image databases, illustrate that PSIPDH can outperform the state-of-the-art methods in real applications, such as image retrieval.

2 Notation and Problem Definition

I denotes the identity matrix. A_{i*} and A_{*j} denote the ith row and the jth column of A, respectively. A^{-1} denotes the inverse of A, and A^T denotes the transpose of A. $\|\cdot\|$ denotes the Frobenius norm of a vector or matrix. $sign(\cdot)$ is the element-wise sign function which returns 1 if the element is a positive number and return -1 otherwise.

Suppose we have n points $\{x_i \in R^d\}_{i=1}^n$ can be divided into c categories, where x_i is the feature vector of point i. We can denote the feature vectors of the n points in a compact matrix form $X \in R^{d*n}$, where $X_{*j} = x_i$. Besides the feature vectors, the training set of supervised hashing also contains a the ground truth label matrix $Y \in \{0, 1\}^{c\times n}$ and a semantic similarity matrix $S \in \{-1, 0, 1\}^{n\times n}$. $Y = \{y_i\}_{i=1}^n$, where $y_k i = 1$ if x_i belongs to class k and 0 otherwise, $k = 1 \ldots c$. Supervised information in S is given in terms of pairwise labels: 1 labels specify similar (or neighbour) pairs, and -1 labels designate dissimilar (or non-neighbour) pairs. Without loss of generality, we use 0 labels designate the pairs that the semantically similar or not between them is unknown.

The learning goal of supervised hashing framework in first step is to generate the optimal binary hash codes matrix $B \in \{-1, 1\}^{r\times n}$, where $B_{*j} = b_i$ denotes the q-bit code for training point i. Then learn hash functions based on learned B in step two.

3 Discrete Hashing Based on Point-Wise Supervision and Inner Product

This section presents the details of our proposed method called PSIPDH. Just like TSH [5, 15], the hashing learning problem can be decomposed into two steps: a binary code inference step and a hash function learning step based on the learned codes. So directly learning the binary codes without relaxations would be preferable if (and only if) a tractable and scalable solver is available.

In order to solve the cumulative quantization error problem of supervised hash learning process with relaxation scheme destroying the constraints, we use the discrete solution approach directly learning the binary codes without relaxations. We use hashing framework to generate the optimal binary hash codes for retrieve, hash function is then learned using a tractable and scalable solver based on the learned bits in step two.

3.1 Hashing Framework to Generate Binary Hash Codes

Over the past decades, point-wise relations with label information can be formulated as a simple classification term to guide the hash code learning. Here we introduces a set of hyperplanes $W \in \{0, 1\}^{d\times c}$ applying point-wise supervised information

$Y \in \{0, 1\}^{c\times n}$ to classify similar codes, and we iteratively solves this set of hyperplanes and binary coding to learn the binary code witch is optimal for the Hyperplanes classifier, so that the encoding of similar images can be better aggregated:

$$\begin{aligned} \min_{W,B} &\|W^T B - Y\|^2 + \lambda \|W\|^2 \\ s.t. &B \in \{1, -1\}^{r\times n} \end{aligned} \tag{1}$$

In order to meet the needs of hash-based retrieval, we hope that the Hamming distances of the codes correlate with the labels in S, that is, similar data pairs with $S_{ij} = 1$ will have the minimal Hamming distance 0, while dissimilar pairs with $S_{ij} = -1$ will have take the maximal Hamming distance,i.e. the number of hash bits r. Inspired by KSH [7], the Hamming distance and the code inner product is in one-to-one correspondence:

$$\begin{aligned} b_i \circ b_j &= |\{k|b_{ik} = b_{jk}, 1 \le k \le r\}| - |\{k|b_{ik} \ne b_{jk}, 1 \le k \le r\}| \\ &= r - 2D_h(x_i, x_j), \end{aligned} \tag{2}$$

where the $b_i = [b_{i1}, ..., b_{ir}] \in \{1, -1\}^{1\times r}$ is r-bit hash code of sample xi, the symbol $\circ$ stands for the code inner product, the $D_h(\cdot)$ stands for the Hamming distance.

Utilizing the algebraic equivalence between a Hamming distance and code inner product,We introduce the punishment of Hamming distance to the objective function in Problem (1) obtain the final formulation:

$$\begin{aligned} \min_{W,B} &\|B^T B - rS\|^2 + \|W^T B - Y\|^2 + \lambda \|W\|^2 \\ s.t. &B \in \{1, -1\}^{r\times n} \end{aligned} \tag{3}$$

In addition Problem (3) is a discrete optimization problem which is hard to solve. Most existing methods optimize it by dropping the discrete constraint [5, 7] which result in the problem that relaxation scheme destroyed the constraints caused by the cumulative quantization error. The joint learning of point-wise supervision and inner product in (3) introduced can make the problem of discrete solutions effectively solved.

3.1.1 W-Step

For problem (3), by fixing B, we rewrite function (3) as:

$$\min_{W} \|W^T B - Y\|^2 + \lambda \|W\|^2 \tag{4}$$

it is easy to solve W by the regularized least squares problem, which has a closed-form solution:

$$W = (BB^T + \lambda I)^{-1} BY^T \tag{5}$$

3.1.2 B-Step

It is challenging to solve for B due to the discrete constraints. With all variables but B fixed, Ignoring the irrelevant variables of W in (3), we require to solve the following problem:

$$\begin{aligned} &\min_{B} \|B^T B - rS\|^2 + \|W^T B - Y\|^2 \\ &\quad s.t. B \in \{1, -1\}^{r \times n} \end{aligned} \tag{6}$$

The above problem is NP hard. Here an important observation is that for problem (6) we can achieve a closed-form solution for one row of B by fixing all the other rows. It means that we can iteratively learn one bit b_k^T at a time. So we can transform the above problem to r binary quadratic programming (BQP) problems. Let b_k^T be the kth row of B that is one bit for all n samples, $\widetilde{B}$ be the matrix of B excluding b_k. Let q^T be the kth row of Q, $\widetilde{Q}$ the matrix of Q excluding q. Let w^T the kth row of W, $\widetilde{W}$ the matrix of W excluding w. Then applying discrete cyclic coordinate descent (DCC) method, problem can further simplified:

$$\begin{aligned} &\min_{B \in \{1,-1\}^{r \times n}} \|\sum_{k=1}^{r} b_k b_k^T - rS\|^2 + \|W^T B - Y\|^2 \\ &= \|b_k b_k^T - R_{k-1}\|^2 + Tr(B^T W W^T B) + Tr(B^T Q) \\ &= -2 b_k^T R_{k-1} b_k + 2 w^T \widetilde{W}^T \widetilde{B} b_k - 2 q^T b_k \\ &= -b_k^T R_{k-1} b_k + g b_k \end{aligned} \tag{7}$$

where $R_{k-1} = rS - \sum_{t=1}^{k-1} b_t b_t^T (R_0 = rS)$, $Q = WY$ and $Tr(\cdot)$ is the trace norm. $g = w^T \widetilde{W}^T \widetilde{B} - q^T$.

This binary quadratic programming problem can be solved by general integer programming solvers, such as Gurobi.,[1] but it could be time-consuming. Meanwhile, we empirically find that an approximate solution can already yield quite satisfactory results. Thus, we solve a approximate objective of (7) and obtain the following approximate solution:

$$b_k^T = sign(g R_{k-1}^{-1}) \tag{8}$$

Form (8), it is off no challenge for us to find that based on the pre-learned $r - 1$ bits $\widetilde{B}$ each bit b_k can be easily computed. This is expected since one can iteratively update each bit till the procedure converges with a set of better codes B. In our experiments, the whole r bits for X can be obtained through iteratively learning for $t \times r$ times by (8),where usually $t = 2 \sim 5$.

[1] http://www.gurobi.com/.

3.2 Hashing Function for Data Points

In this section, hash function can be training as a r binary classifiers based on the feature matrix X and the learned code matrix B with each bit corresponding to one classifier.

In order to capture the non-linear manifold structure hidden in the data ,we adopt a simple yet powerful non-linear form embedding learning algorithms for $F(x)$. Here we use

$$H(x) = sign(F(x)) \tag{9}$$

$$F(x) = P^T \phi(x) \tag{10}$$

where $\phi(x) = [exp(-\|x - a_1\|^2/\sigma), ..., exp(-\|x - a_m\|^2/\sigma)]^T$ is a m-dimensional column vector obtained by the RBF kernel mapping, where $\{a_j\}_{j=1}^m$ are m anchor points selected randomly from training samples and σ is the kernel width. The matrix $P \in R^{m \times r}$ projects the RBF kernel space data $\phi(x)$ onto the low dimensional space.

Only a simple multi-class linear classifier is demonstrated here:

$$\begin{aligned} &\min_F \sum_{i=1}^{n} \|b_i - F(x_i)\|^2 \\ &= \min_P \sum_{i=1}^{n} \|b_i - P^T \phi(x_i)\|^2 \end{aligned} \tag{11}$$

The projection matrix P can be easily computed by regression

$$P = (\phi(X)\phi(X)^T)^{-1}\phi(X)B^T \tag{12}$$

It's worth noting that besides using linear classifiers, more powerful nonlinear classifiers can also be used to train hash function, such as SVM with RBF kernel [5], deep convolutional network [18] and boosted decision trees [4] and so on. In general, the more powerful classifiers we use, the better accuracy we can achieve and also the more training time will be consumed [4, 5].

4 Experiments

In this section, we conducted extensive large-scale image retrieval experiments on two image benchmarks: CIFAR-10 [2] and MNIST [3]. We evaluate the proposed PSIPDH, and compare it against several state-of-the-art supervised hashing methods including supervised discrete hashing (SDH) [15], fast supervised hashing with decision trees for high-dimensional data (FastH) [4], supervised hashing with kernels (KSH) [7]. We use the public codes and suggested parameters of these meth-

ods from the corresponding authors. For PSIPDH, we empirically set to 1 and the maximum iteration number t is set to 3. For KSH, SDH and PSIPDH we use randomly sampled 1000 anchor point and we feed the same Gaussian RBF kernel $\phi(x, y) = exp(-\|x - y\|^2/2\sigma^2)$ The kernel parameter σ is tuned to an appropriate value on each data set. Note that we treat a query a false case if no point is returned when calculating precisions.

4.1 MNIST

The MNIST database of handwritten digits has a training set of 60,000 examples, and a test set of 10,000 examples. The digits have been size-normalized and centered in a fixed-size image. We represent each image in this data set by a GIST feature vector [12] of dimension 512 witch is extracted from the original color image of size 32 $times$ 32. All 60,000 examples used as data set, then uniformly randomly sample 1000 images constituting 1K labelled subsets for supervised training. The pairwise label matrices S are easy to acquired because the exact labels are available. 2K images are uniformly randomly sampled from MNIST test set to test all hashing methods. The comparative results are reported in Fig. 1.

As shown in Fig. 1, PSIPDH with only 32 binary bits and a limited amount of supervised information (labels) significantly outperforms other state-of-the-art supervised hashing methods and gets a pretty good precision and recall. The prominent superiority of PSIPDH corroborates that the Proposed supervised hashing framework and discrete optimization techniques are successful that both point-wise supervision and code inner product are maximally utilized.

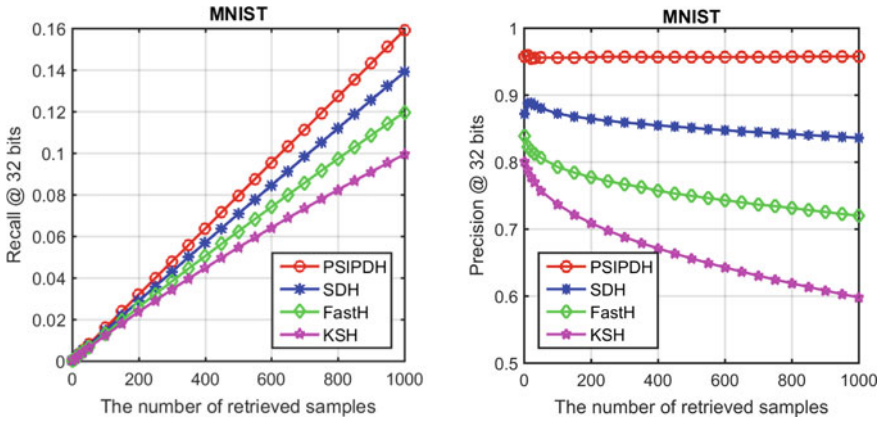

(a) Recall. (b) Precision.

Fig. 1 Retrieval performance of different supervised hashing methods on MNIST. Recall and Top-K precision with 32-bit codes w.r.t. different numbers of top returned images

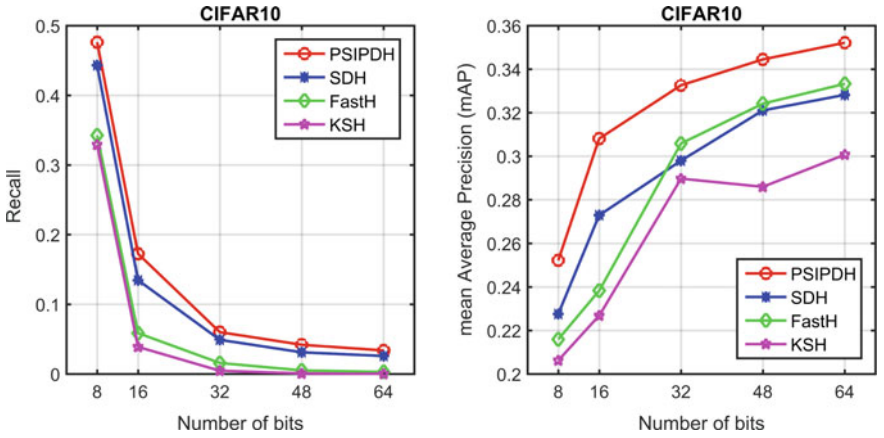

(a) Recall. (b) MAP.

Fig. 2 Supervised hashing methods use 2K label examples. compared methods in recall and MAP of Hamming distance 2 with code length from 8 to 64

4.2 CIFAR-10

CIFAR-10 consists of 60K images which are manually labelled as 10 object classes with 6K samples for each class. We represent each image in this data set by a GIST feature vector of dimension 512. We evenly sampled partitioned this data set from ten classes into two parts: 59K images for data set and 1K images for test set,then uniformly randomly sample 2000 images constituting 2K labelled subsets for supervised training. In terms of true semantic neighbours, We carry out hash lookup within a Hamming radius 2 and report the search the recall and MAP with 8bits, 16bits, 32bits, 48bits, 64bits code. Our method has all ready achieve a good results in data set MNIST. In the more challenging data set CIFAR10, PSIPDH still significantly outperform others by a large margin. All of the evaluation results are shown in Fig. 2. The recall and MAP of PSIPDH shown in Fig. 2 with all code length are also superior to other methods.

5 Conclusions

In this paper, we proposed a novel model called PSIPDH for supervised hashing. Adapting to the law of large-scale data retrieval,this model use both point-wise supervision and inner product. On the basis of the simple classification formulated by point-wise supervised information witch can guide the learning of binary code, the penalty of Hamming distance introduced by inner product can train hash code more suitable for hashing based large-scale retrieval. code generation and hash

function learning processes are seen as separate steps and discrete hashing code can be learned directly from semantic labels.

References

1. Gong, Y., Lazebnik, S.: Iterative quantization: a procrustean approach to learning binary codes. In: CVPR 2011, pp. 817–824, June (2011)
2. Krizhevsky, A.: Learning multiple layers of features from tiny images (2009)
3. Lcun, Y., Bottou, L., Bengio, Y., Haffner, P.: Gradient-based learning applied to document recognition. Proc. IEEE **86**(11), 2278–2324 (1998)
4. Lin, G., Shen, C., Shi, Q., Van Den Hengel, A., Suter, D.: Fast supervised hashing with decision trees for high-dimensional data. Comput. Vis. Pattern Recognit., 1971–1978 (2014)
5. Lin, G., Shen, C., Suter, D., Van Den Hengel, A.: A general two-step approach to learning-based hashing. In: IEEE International Conference on Computer Vision, pp. 2552–2559 (2014)
6. Liu, W., Wang, J., Chang, S.F.: Hashing with graphs. In: ICML (2011)
7. Liu, W., Wang, J., Ji, R., Jiang, Y.G., Chang, S. F.: Supervised hashing with kernels. In 2012 IEEE Conference on Computer Vision and Pattern Recognition, pp. 2074–2081, June (2012)
8. Lu, H., Li, B., Zhu, J., Li, Y., Li, Y., Li, J., Li, X., Xu, X., He, L., Serikawa, S.: Wound intensity correction and segmentation with convolutional neural networks. **29**(6) (2016)
9. Lu, H., Li, Y., Chen, M., Kim, H., Serikawa, S.: Brain intelligence: go beyond artificial intelligence. ArXiv e-prints, June (2017)
10. Lu, H., Li, Y., Mu, S., Wang, D., Kim, H., Serikawa, S.: Motor anomaly detection for unmanned aerial vehicles using reinforcement learning. IEEE Internet Things J. **PP**(99), 1–1 (2017)
11. Lu, H., Li, Y., Uemura, T., Kim, H., Serikawa, S.: Low illumination underwater light field images reconstruction using deep convolutional neural networks. Futur. Gener. Comput. Syst. **82**, 142–148 (2018)
12. Oliva, A.: Modeling the shape of the scene: a holistic representation of the spatial envelope. Int. J. Comput. Vis. **42**(3), 145–175 (2001)
13. Rao, S.S.: Engineering Optimization: Theory and Practice, 4th edn. Wiley (2009)
14. Serikawa, S., Lu, H.: Underwater image dehazing using joint trilateral filter. Comput. Electr. Eng. **40**(1), 41–50 (2014)
15. Shen, F., Shen, C., Liu, W., Shen, H. T.: Supervised discrete hashing. In: 2015 IEEE Conference on Computer Vision and Pattern Recognition (CVPR), pp. 37–45, June (2015)
16. Wang, J., Kumar, S., Chang, S.F.: Semi-supervised hashing for large-scale search. IEEE Trans. Pattern Anal. Mach. Intell. **34**(12), 2393–2406 (2012)
17. Weiss, Y., Torralba, A., Fergus, R.: Spectral hashing. In: International Conference on Neural Information Processing Systems, pp. 1753–1760 (2008)
18. Xia, R., Pan, Y., Lai, H., Liu, C., Yan, S.: Supervised hashing for image retrieval via image representation learning. In: AAAI Conference on Artificial Intelligence (2014)
19. Zhu, X., Huang, Z., Cheng, H., Cui, J., Shen, H.T.: Sparse hashing for fast multimedia search. ACM Trans. Inf. Syst. (TOIS)

Trustworthy Traceability of Quality and Safety for Pig Supply Chain Based on Blockchain

Yan Yuan, Xinliang Liu, Kunming Hong, Shaoyi Song and Wanlin Gao

Abstract Pork safety incidents happened frequently in China even if the traditional traceability system was established, which declines the consumers' confidence rapidly. Thus, this paper aims to explore a trustworthy traceability of quality and safety for the pig supply chain. We then proposed a framework for traceability of pig supply chain based on blockchain. In our research, we found that HACCP is suitable for screening key information in every link of pig supply chain, and GS1 can achieve the series connection of information on the pig supply chain, which reduces the isolated information and increases the transparency of the supply chain. However, information provided by traditional traceability system failed to guarantee the authenticity and credibility because of its hidden troubles such as monopoly, corruption, counterfeit, hacker attack and so on. To tackle this problem, we verified the validity and credibility of pig traceability information by deploying the smart contract on a consortium blockchain and analyzing its operating mechanism from the perspective of consumers.

Y. Yuan · X. Liu (✉) · K. Hong · S. Song
National Engineering Laboratory for Agri-Product Quality Traceability, Beijing 100048, People's Republic of China
e-mail: liuxinl@btbu.edu.cn

Y. Yuan
e-mail: 15652601498@163.com

Y. Yuan · X. Liu · K. Hong · S. Song
College of Computer and Information Engineering, Beijing Technology and Business University, Beijing 100048, People's Republic of China

W. Gao
College of Information and Electrical Engineering, China Agricultural University, Beijing 100083, People's Republic of China
e-mail: cau_szmtyjs@163.com

W. Gao
Chinese Ministry of Agriculture and its Key Laboratory of Agricultural Informatization Standardization, Beijing 100083, People's Republic of China

H. Lu (ed.), *Cognitive Internet of Things: Frameworks, Tools and Applications*, Studies in Computational Intelligence 810,
https://doi.org/10.1007/978-3-030-04946-1_34

Keywords Pig supply chain · Trustworthy traceability · Blockchain
Smart contract · Transparency · IoT

1 Introduction

With the rapid development of the economy and living standards in China, people are paying more and more attention to food quality and safety. Furthermore, pork has traditionally been the major source of meat for Chinese residents as yet, which holds the largest share in the consumption of livestock and poultry meat. According to the "China Statistical Yearbook-2017" [1], in 2016, the annual output of pork in China's livestock product was 52.991 million tons, accounting for 62.1% of the total meat production (85.378 million). The average per capita pork consumption in China was 19.6 kg, accounting for 75.1% of the total meat consumption (26.1 kg). However, the occurrence of the incidents includes "diseased pig", "zombie meat", " glued meat", "poisonous pork", "clenbuterol", induced confidence crisis in the quality and safety of pork. The real cause of the incidents is the information asymmetry, which intensified with the extension of the industry chain of food [2]. In this case which lack of trust, the effectiveness of the existing traceability information depends on the trust of the central system or a third-party organization. Moreover, the centralized system is the sole assessment to achieve information transparency in a sense in the supply chain [3]. However, because the centralized system is vulnerable to hacking, fraud, and corruption, it leads to system errors or data errors. Therefore, the issue lies in the reliability of the information shared by members in the supply chain and the credibility and authenticity of the information provided by the traceability system cannot be guaranteed. Fortunately, the proposal [4] and rise [5] of the blockchain indicates the direction for the above issues.

The article specifically explores the application of the combination of blockchain, HACCP and GS1 systems in the pig supply chain. Meanwhile, designing and deploying smart contracts are able to ensure that the data generated in the supply chain is credible and traceable. In this way, the reliable quality and safety of the pork can be achieved and the number of security incidents can be reduced.

The paper is structured as follows. Firstly, we review the literature of the traceability study of the pig supply chain and the application of blockchain technology. Secondly, a traceability framework diagram of the pig supply chain is presented, and the methods of the acquisition and connection of key information are identified. Thirdly, we propose the traceability framework of the pig supply chain based on blockchain and design the smart contract code for the pig supply chain. The fourth section discusses the operating mechanism of the pig supply chain based on consortium blockchain. Finally, we make a brief conclusion and propose the further study directions.

2 Literature Review

In China, an early prototype of a traceability system was designed and established for tracing the quality of pork [6]. Hai et al. [7] analyzed a number of factors that affects the quality of pork products (including vaccines, feeds, additives, and veterinary drugs), as well as the key control points in pig rearing, slaughter, and retailing. A practical application platform was developed. Meanwhile, a system of Meat Traceability Critical Control Point analysis (MTCCP) in the specific case of the Polish pork chain was proposed [8].

With the rapid growth of the Internet of Things (IoT), the continuous development technologies such as automatic identification [9], sensor, mobile communication, and Intelligent Decision-making [10] provided technical supports for traceability system construction [11]. Identification methods of farm animals had also changed from body signs to electronic ear tags, DNA fingerprinting, and retinal scans, which in a combination of the use of product identification including barcodes, 2D barcodes and RFID/Electronic Product Code (EPC) [12]. However, inability to link the food records which are accurate, error and delay, is the essence of a disease outbreak of food [13].

With the increasing attention and development of blockchain technology, the application of blockchain extended from the issuance transaction of electronic virtual currency to the financial field [14]. Currently, the rapid and synchronous development of blockchain 1.0, blockchain 2.0, and blockchain 3.0 has involved various industries in order to enhance consumers' trust, information transparency, and food safety [15]. Among quite a few activities that are likely to be transformed by blockchain, supply chain thus deserves special attention [16].

In January 2017, Microsoft launched the "Manifest Project" in cooperation with Mojix, using a blockchain platform to facilitate factories, distribution centers, and retailers in using RFID devices to track goods [17]. Lu and Xu [18] reconstructed the current traceability system by replacing the central database with a block chain that provides transparent and tamper-proof tracking data. Tian [19] established an agricultural food supply chain traceability system based on RFID and blockchain technology to enhance food safety quality in China's agri-food market. After that, Tian [20] established a real-time food tracking system based on HACCP, blockchain and the IoT, which provided the open, transparent, neutral, reliable, and secure information of platform for supply chain members. Leng et al. [21] proposed a public blockchain of agricultural supply chain system based on the architecture of the double chain, which could assess the openness and security of transaction information and the privacy of enterprise information.

3 Pig Supply Chain and the Acquisition and Connection of Key Information

3.1 Pig Supply Chain

Pig belongs to the animal husbandry agricultural product and pig supply chain belongs to the kind of farm-to-table [22]. The system of the pig supply chain including pig breeding, slaughter and processing, storage, transportation, and sale. The system which is shown in Fig. 1 is established for the purpose of providing pork for consumers effectively.

The traceability system that records key information at all stages of the pig supply chain can trace the product forward and reverse so as to perform supply chain management well [11]. The system offers a degree of information transparency and authenticity. However, there are several problems in the current traceability chain: (1) Not only the quality and safety system of China's agricultural products is still incomplete when compared with developed countries [23], but also the traceability information is neither continuous nor critical or core, of which lacks information that consumers really care about. (2) The credibility of information provided by each member of the supply chain cannot be guaranteed, and the hidden troubles such as monopoly, corruption, counterfeit and hacker attack exist. (3) The lack of convenient and quick methods for consumers to obtain reliable traceability information of products that they are interested in, which leads to the tracing of accountability after security incidents.

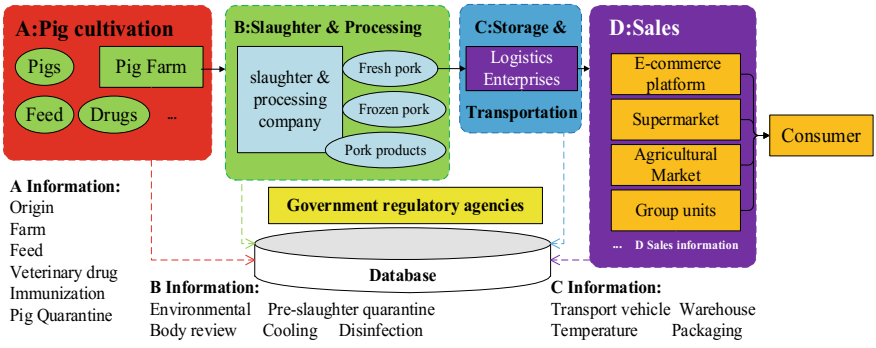

Fig. 1 Traceability framework diagram of the pig supply chain

3.2 HACCP

Aiming at solving the above problems (1), HACCP is found more suitable for screening key information in the field of food safety by comparing commonly used diagnostic and control models [24] (Table 1). Accordingly, this paper applies HACCP to find the weak links in pig supply chain.

The HACCP system (Hazard Analysis and Critical Control Point) was originally applied in the United States [25]. The system assesses, identifies and records key information in the pig supply chain, and exposes high-risk information from a monitoring perspective. Therefore, quality issues can be reduced or eliminated to some extent. Table 2 screens key control points [26] out according to the combination of HACCP and various links in Fig. 1.

Table 1 Common quality diagnosis and control models

Models	Principle	Application area
FTA (Fault Tree Analysis)	Gradually classifies the cause of an accident as an inverted tree until it finds the direct cause of the event, and a causal logic diagram will be formed in this way	Qualitative and quantitative analysis can both be used via the model, which is one of the main analytical methods in safety system engineering
Petri nets	The token moves towards the event-driven state in the directed graph which contains the library and the transition nodes in order to reflect the dynamic operation of the system	Processes model analysis for discrete event systems
FMECA (Failure Mode Effects and Criticality Analysis)	Classifies and analyzes the probability and severity of all possible failure to determine their harmfulness	Systems that can be accurately divided into phases and levels, and given basis of faulty judgments and constraints
HACCP (Hazard Analysis Critical Control Point)	Screens out critical control points through hazard analysis and setting critical limits; establishes monitoring and corrective actions and record files	Recognized as a preventive system for controlling food safety hazards
SPC (Statistical Process Control)	Uses statistical techniques like control charts to analyze the process and feedback information, and takes measures to maintain process stability in order to achieve quality control	Quality control and management processes

Table 2 HACCP hazard analysis on the pig supply chain

Critical control point	Potential hazards	Is the hazard significant?	Judgments based	Precaution	Is it a critical control point?
A Feed/veterinary drugs/immunity use	Biohazards	Yes	Epidemic infection	Control water resources and growth environment	Yes
	Chemical hazards	Yes	Do feed additives, veterinary drugs, and immune needles safe	Standardize procurement and management; make records well	
	Physical hazards	Yes	Metal residue	Metal troubleshoots	
A Live pig inspection and quarantine	Biohazards	Yes	Epidemic infection	Inspect by regulatory agencies; harmless treatment of diseased pigs	Yes
	Chemical hazards	Yes	Hormone, Carrageenan, Clenbuterol, etc. exceeded	Regulate the management of feeding behavior, veterinary drug using, and prevention and control of epidemic	
B Live pig acceptance/pre-slaughter inspection/waiting for slaughter	Biohazards	Yes	Pigs with microorganisms or pathogens	Animal inspection passed	Yes
	Chemical hazards	Yes	Feed and veterinary drug residues and the pigments of stamp	Inspection of lean meat and other residues. Guarantee the use of food coloring	
B Cool down	Biohazards	Yes	Excessive temperature, long storage time, and excessive microorganisms	Control temperature and storage time to ensure low temperature	Yes
B Segmentation	Biohazards	Yes	Workers' hands and equipment may cause microbial contamination	Low-temperature workspace control and process residence time control, regular disinfection and cleaning	Yes
C, D Packaging, storage, and sales	Biohazards	Yes	Not only packaging materials and equipment, but also excessive temperatures will cause the growth of microbial and pathogenic	Low-temperature and environmental hygiene control, QS inspection of packaging materials	Yes
	Physical hazards	Yes	Metal residue	The treatment of reducing bacterial for packaging materials and equipment. Correct use of metal detectors	

It is necessary to apply HACCP into all links in the supply chain, which can achieve more efficient analysis and scientific control of pork than before. Nonetheless, these information points can be isolated at different links. Therefore, the following section proposes the use of GS1 to achieve the series connection of information in the supply chain.

3.3 GS1

GS1 (Global standard 1) is built on coding technology and functions as data collection, data exchange, and electronic product code (EPC) identification [27]. Generally speaking, the purpose is to achieve the automatic collection [28] of information on feed, slaughter, and distribution in the pig supply chain, which includes information acquisition technologies like optics [29], electromagnetic sensors [30], GPS (Global Positioning System), laser scanners, etc. Besides, the carriers include ear tags of two-dimensional code or electronic ear tags, electronic tags (RFID radio frequency identification) and barcode [31, 32]. More specifically, the coding technology applies the GS1 coding system to encode the information of each link in pig supply chain [33]. For example, firstly, EPC coding for every live pig in the breeding section can satisfy the regulation of "livestock & poultry identification and farming archives management" and "One Animal One Yard", which makes every pig have an ID [34]. Secondly, GTIN (Global Trade Item Number) can be used to encode pig carcasses in the links of slaughter, processing, and sales, and SSCC (Serial Shipping Container Code Barcode) can be used to encode logistics information in the link of transport. Finally, consumers can obtain the key information of pork through the two-dimensional code which contains traceability code and query address.

Based on HACCP and GS1, the key information of pork in the supply chain can be effectively recorded and transmitted in series and the transparency of the product information can be achieved to some extent. However, the problem (2) has not yet been resolved. Therefore, this paper attempts to solve the credibility problem in the quality and safety of the pork based on blockchain.

4 Pig Supply Chain Based on Blockchain

4.1 The Concept of Blockchain

Blockchain is literally understood as the series connection of blocky areas in which data information is stored. It is a sequence of blocks connected by a "hash chain" with a time scale and completely stored in every full node, which makes the information of the blockchain cannot be tampered with. Blockchain integrates distributed data storage, P2P networks, consensus mechanisms, and encryption algorithms into a

technical system and has features including decentralization, collective maintenance, open source anti-counterfeiting, and time-series data [35]. A blockchain can be a public blockchain that allows anyone to use it, or can be a private chain, privately creating a closed, known group of participants such as a company's internal chain, and then centrally managed. Also it perhaps a consortium blockchain, establishing interoperability between industries and being maintained collectively [36].

4.2 Traceability Framework Base on Blockchain

The combination of the HACCP system and the GS1 system enables the key information in the pig supply chain to be efficiently collected, stored, transferred, shared, and checked, which ensures food quality and safety [37]. However, since the information of the supply chain is mastered by the internal members, monopoly enterprises can manipulate regulatory agencies and then modify or falsify data to present untrue information [38]. In this case, whether the information shared by members in the supply chain can be trusted? Likewise, traditional distributed systems (centralized control) also risk hacking, fraud, and corruption. Thus, the credibility and authenticity of the information provided by the system cannot be guaranteed.

As the key technology of the new distributed system, blockchain has been applied to solve the problems of information trust and transparency in other traceability areas [39]. In spite of that, very few researches applied blockchain technology to the traceability in the agricultural supply chain, not to mention the supply chain of pigs. For this reason, we propose a traceability framework (see Fig. 2) for the pig supply chain based on blockchain which combines HACCP and IoT. This framework can provide a safe, transparent, and credible environment for the pork market which accounts for the majority of meat consumption, and reduce food safety incidents.

4.3 Smart Contract Design and Application

Smart contracts are event-driven contracts of code that can be automatically executed on the chain. The difference between a smart contract and a traditional application is that the smart contract cannot be modified directly on the original contract as soon as it is deployed, even if there are bugs or business logic changes in the contract require being modified.

We use the "truffle migrate" command of the truffle framework to deploy and migrate the contract, and then call the "setPigData" and "setEnterpriseData" functions to store the data and trigger the contract event (Fig. 3). After this, network nodes recognize the triggered transaction and two events are found in the transaction pool (namely txpool). Subsequently, one of the authorization nodes generates a new block with signature verification and be marked as the most recent signature node (as shown in Fig. 4), who requires delaying or waiting for its next round until the

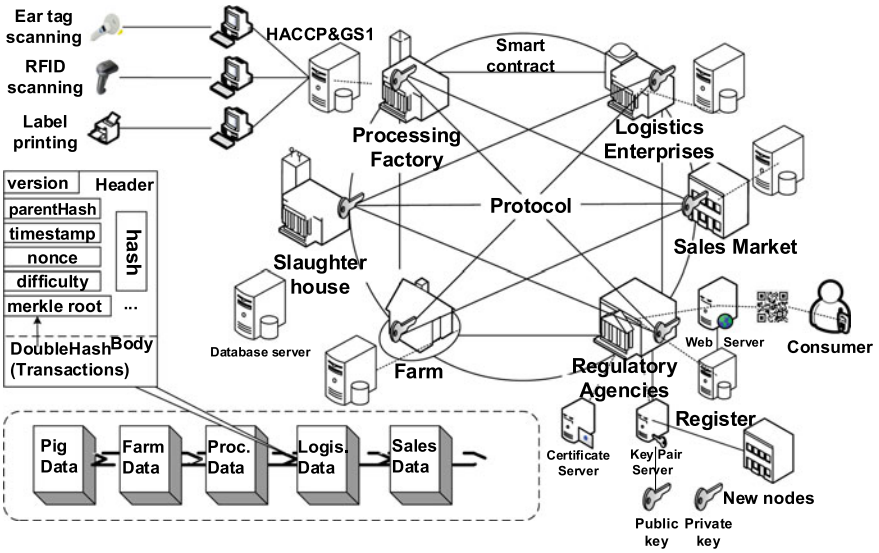

Fig. 2 Traceability framework of pig supply chain based on blockchain

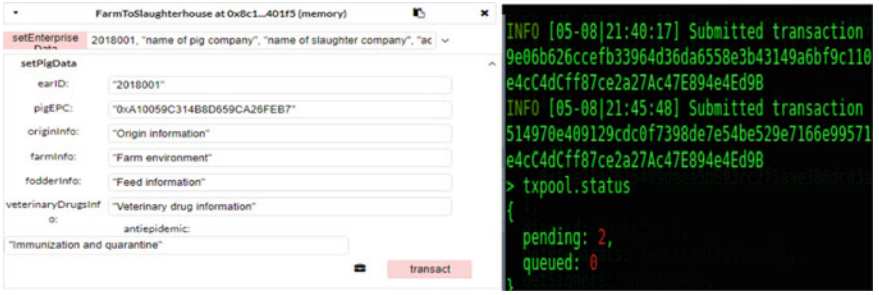

Fig. 3 Contract events are triggered by accessing data methods

other authorization nodes generate a certain amount of certified blocks. On the contrary, the non-authorized node does not possess the authority to generate the certified blocks. Finally, we query the stored information from the consortium blockchain by calling the "getPigData" and "getEnterpriseData" functions (Fig. 5).

4.4 Operating Mechanism

In the entire supply chain, there are many companies involved in each link as nodes. New nodes that intend to participate in the process must first be permitted by the regulatory agencies and then be permitted through voting by most of the nodes in the

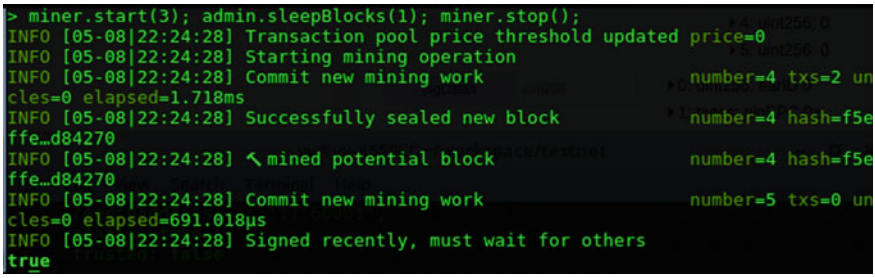

Fig. 4 An authentication node generates a new block with its signature

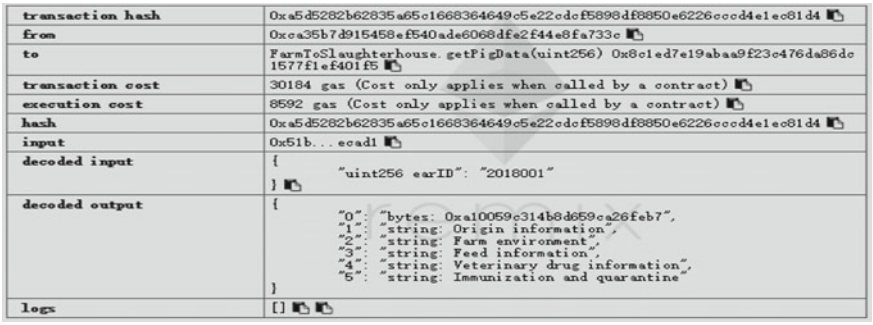

Fig. 5 The feedback for querying pig information

blockchain. These procedures generate a series of enterprise information files and new members are certified as legitimately authorized nodes. In addition, new members will be given a public and private key pair [40], which ensures the authentication and information security in the course of the transaction.

It is better for the participants to pass the certification of the various regulatory agencies on the key information of their products, and own their digital signature or electronic seal (similar to CA certification) with a timestamp. Otherwise, they will have the primary responsibility in case of an occurrence of security.

Following this principle, when the transaction occurs, every party must obey the digital contract to complete the transaction, what is more important, "stamped product" with key information will be published and broadcast peer to peer along with the transaction, according to which each node will be able to update the latest data through data dissemination protocols and verification mechanisms.

Under these conditions, key information identified through HACCP and collected by the GS1 encoding system can effectively concentrate the amount of data into the blockchain and enhance its scalability.

5 Conclusion and Future Research

Overall, this paper proposes a framework for traceability of pig supply chain based on the blockchain, as well as the combination of HACCP and GS1. Especially, the major contributions of this paper is that we verify the validity and credibility of pig traceability information by deploying the smart contract designed in the form of consortium blockchain, and this scheme increases information transparency so that consumers' confidence in food's information can be increased and the accountability after food safety accident can be easier.

The next step of the research should explore the rationality of the consensus mechanism and the design of smart contracts and Dapp (Decentralized Application). In addition, the government and regulators can use reasonable incentives and a small amount of cost to ensure that all members of the supply chain spontaneously maintain the consortium blockchain, and the mechanism is profit-oriented. In this way, information will prove to be transparent and trustworthy instead of fake. All in all, the aim is to ensure the quality and safety of the food and provide guidance for the further research.

Acknowledgements The research presented in this paper is supported by State Key Program for Research and Development of China (2016YFD0401205) and Beijing Science and Technology Program (Z161100001616004).

References

1. National Bureau of Statistics of the People's Republic of China: China Statistical Yearbook. Beijing: China Statistics Press (2017). http://www.stats.gov.cn/tjsj/ndsj/2017/indexch.htm
2. Liu, Z.J.: Study on Operating Mechanism of Pork Traceability System in China Based on Food Safety: Taking Beijing City as an Example. China Agricultural University, Beijing (2015)
3. Steiner, J., Baker, J., Wood, G., Meiklejohn, S.: Blockchain: The Solution for Transparent in Product Supply Chains. A white paper was written by Project Provenance Ltd. (2016)
4. Nakamoto, S.: Bitcoin: A Peer-to-Peer Electronic Cash System. Consulted (2008)
5. Yli-Huumo, J., Ko, D., Choi, S., Park, S., Smolander, K.: Where is current research on blockchain technology?—a systematic review. PLoS ONE **11**(10), e0163477 (2016). https://doi.org/10.1371/journal.pone.0163477
6. Xie, J., Lu, C., Li, B., et al.: Implementation of pork traceability system based on .NET framework. Trans. Chin. Soc. Agric. Eng. **22**(6), 218–220 (2006)
7. Hai, X.B., Qing-Yao, L., Liang, Y., et al.: A practical web-based tracking and traceability information system for the pork products supply chain. In: International Conference on Computers and Computing Technologies in Agriculture, pp. 725–733 (2007)
8. Zadernowski, M.R., Verbeke, W., Verhé, R., Babuchowski, A.: Toward meat traceability critical control point analysis in the Polish pork chain. J. Int. Food Agribus. Mark. **12**(4), 5–23 (2008). https://doi.org/10.1300/J047v12n04_02
9. Serikawa, S., Lu, H.: Underwater image dehazing using joint trilateral filter. Comput. Electr. Eng. **40**(1), 41–50 (2014)
10. Lu, H., Li, B., Zhu, J., Li, Y., Li, Y., Xu, X., et al.: Wound intensity correction and segmentation with convolutional neural networks. Concurr. & Comput. Pract. Exp. **29**(6) (2016)

11. Yang, X., Qian, J., Sun, C., et al.: Key technologies for establishment agricultural products and food quality safety traceability systems. Trans. Chin. Soc. Agric. Mach. **45**(11), 212–222 (2014)
12. Bai, H., Zhou, G.H., Hu, Y., Sun, A., Xu, X.-L., Liu, X., Lu, C.: Traceability technologies for farm animals and their products in China. Food Control **79**, 35–43 (2017). https://doi.org/10.1016/j.foodcont.2017.02.040
13. Badia-Melis, R., Mishra, P., Ruiz-García, L.: Food traceability: new trends and recent advances. A review. Food Control **57**, 393–401 (2015)
14. Swan, M.: Blockchain: Blueprint for a New Economy. O'Reilly Media, Inc. (2015)
15. Jeppsson, A., Olsson, O.: Blockchains as a solution for traceability and transparency. MSE thesis, Department of Design Sciences, Lund University, Lund, Sweden (2017)
16. Kshetri, N.: 1 Blockchain's roles in meeting key supply chain management objectives. Int. J. Inf. Manage. **39**, 80–89 (2018)
17. del Castillo, M.: Microsoft Unveils Project Manifest, A Plan for Blockchain Product Tracking (2017)
18. Lu, Q., Xu, X.: Adaptable blockchain-based systems: a case study for product traceability. IEEE Softw. **34**(6), 21–27 (2017)
19. Tian, F.: An agri-food supply chain traceability system for China based on RFID & blockchain technology. In: International Conference on Service Systems and Service Management, pp. 1–6. IEEE (2016)
20. Tian, F.: A supply chain traceability system for food safety based on HACCP, blockchain & Internet of things. In: International Conference on Service Systems and Service Management, pp. 1–6. IEEE (2017)
21. Leng, K., Bi, Y., Jing, L., et al.: Research on agricultural supply chain system with double chain architecture based on blockchain technology. Futur. Gener. Comput. Syst. (2018)
22. Yang, T.H., Chu, B.J.: Study on control system of food safety from farm to table. Food Sci. **26**(3), 264–268 (2005)
23. Ye, Y.: Research on Technology for Optimizing Agricultural Product Quality Traceability System. South Agricultural University, Guangzhou (2016)
24. Fu, Z., Xing, S.H.: Development trend of food quality safety traceability technology. Trans. Chin. Soc. Agric. Mach. **44**(7), 144–153 (2013)
25. Poumeyrol, G., Rosset, P., Noel, V., Morelli, E.: HACCP methodology implementation of meat pâté hazard analysis in pork butchery. Food Control **21**(11), 1500–1506. ISSN 0956-7135. https://doi.org/10.1016/j.foodcont.2010.03.017
26. Liu, S.C., Zhao, C.J., Yang, X.T., et al.: Microbiological hazard analysis and critical control points in the processing of chilled pork. Food Sci. (2013)
27. Cao, W., Zheng, L., Zhu, H., et al.: General framework for animal food safety traceability using GS1 and RFID. In: Computer and Computing Technologies in Agriculture III, Third IFIP TC 12 International Conference, CCTA 2009, Beijing, China, October 14–17, 2009, Revised Selected Papers, pp. 297–304. DBLP (2009)
28. Lu, H., Li, Y., Chen, M., Kim, H., Serikawa, S.: Brain intelligence: go beyond artificial intelligence. Mob. Netw. Appl. **23**(2), 368–375 (2018)
29. Lu, H., Li, Y., Uemura, T., Kim, H., Serikawa, S.: Low illumination underwater light field images reconstruction using deep convolutional neural networks. Futur. Gener. Comput. Syst. **82** (2018)
30. Lu, H., Li, Y., Mu, S., Wang, D., Kim, H., Serikawa, S.: Motor anomaly detection for unmanned aerial vehicles using reinforcement learning. IEEE Internet Things J. **PP(99)**, 1 (2017)
31. Ge, W., Zhao, C.: State-of-the-art and developing strategies of agricultural internet of things. Trans. Chin. Soc. Agric. Mach. **45**(7), 222–230+277 (2014)
32. Chen, X.D., Yuan, X.Y., Guo, P.Y., et al.: Progress and prospect in agricultural internet of things. J. Agric. Sci. Technol. (2015)
33. Yan, B., Shi, P., Huang, G.: Development of traceability system of aquatic foods supply chain based on RFID and EPC internet of things. Trans. Chin. Soc. Agric. Eng. **29**(15), 172–183 (2013)

34. Jiang, L.H., Yan, S.Q., Xie, J., et al.: Design of traceability system for the safety production entire processes of pork. Sci. Technol. Food Ind. (2008)
35. Yuan, Y., Wang, F.Y.: Blockchain: the state of the art and future trends. Acta Automatica Sinica (2016)
36. Underwood, S.: Blockchain beyond bitcoin. ACM (2016)
37. Feng, T.: A quality and safety control system for China's dairy supply chain based on HACCP & GS1. In: International Conference on Service Systems and Service Management, pp. 1–6. IEEE (2016)
38. Tian, F.: An information system for food safety monitoring in supply chains based on HACCP, blockchain and Internet of things. Doctoral thesis, WU Vienna University of Economics and Business (2018)
39. Foroglou, G., Tsilidou, A.L. Further applications of the blockchain. In: Student Conference on Managerial Science and Technology (2015)
40. Barcelo, J.: USER Privacy in the Public Bitcoin Blockchain (2014)

Distortion Correction Method of Zoom Lens Based on Vanishing Point Geometric Constraint

Zhenmin Zhu, Quanxin Liu, Xinyun Wang and Shuang Pei

Abstract In order to solve the problem that the nonlinear distortion of the zoom lens varies with the focal length changes, a fast correction method for zoom lens based on the minimum fitting error of vanishing points is proposed. Firstly, based on the radial distortion model, the equation between the vanishing point and the radial distortion coefficient is established according to the geometric constraint of the vanishing point. And then, according to the principle of the deviation error minimization, use the least squares to fit the equation of straight line of the corrected points. Finally, the variation of distortion parameters with focal length is analyzed, the distortion parameter table between distortion parameter and focal length and the empirical formula of fitting are established. The results of images correction show that the proposed method can effectively correct the nonlinear distortion of zoom lens.

Keywords Distortion correction · Zoom lens · Minimum fitting error
Vanishing points · Radial distortion model

1 Introduction

In recent years, with the rapid development of artificial intelligence, more and more researchers are engaged in it [1, 2]. And machine vision plays an important role in artificial intelligence, the zoom lens has been widely used in aerial photography,

Z. Zhu (✉) · Q. Liu · X. Wang · S. Pei
School of Electrical and Automation Engineering, East China Jiaotong University, Nanchang 330013, China
e-mail: zhuzhenmin1984@163.com

Q. Liu
e-mail: 596402685@qq.com

X. Wang
e-mail: 591727794@qq.com

S. Pei
e-mail: 1808522061@qq.com

H. Lu (ed.), *Cognitive Internet of Things: Frameworks, Tools and Applications*, Studies in Computational Intelligence 810,
https://doi.org/10.1007/978-3-030-04946-1_35

tracking and measurement [3, 4]. Due to the camera optical imaging system has some factors such as design, manufacture, adjustment and environmental control, these factors can cause nonlinear distortion in the image imaging process, and the distortion will have a great impact on the geometric position accuracy of the imaging. In order to improve the accuracy of quantitative analysis such as target detection and location, pattern matching [5, 6], and the accuracy of real-time stitching using its image [7], the distortion must be corrected. Neural networks have achieved significant applications in image processing related fields [8, 9], the true reproduction of images is of paramount importance for related applications in the visual field [10]. For zoom lenses, different focal lengths cause a change in the center of the distortion, and different focal lengths correspond to different nonlinear distortions [11]. Using the general camera calibration method (including Tsai [12] two-step method based on radial constraint, Zhang's calibration method based on the plane target [13] and the camera calibration method based on the rational functional lens distortion model [14]) is difficult to achieve camera online real-time correction.

In order to achieve fast and accurate correction of zoom lens distortion, the geometric constraint characteristics of the corner point lines in planar checkerboard images are presented in this paper, the distortion coefficient and the distortion center coordinate of the lens under different focal distances are solved by using the first-order single-parameter division model and the minimum fitting error constraint, the distortion parameter is fitted by curve fitting and LS-SVR. Finally, the empirical formula or distortion parameter lookup table of distortion parameter with focal length is obtained. In the experiments, the distortion parameters corresponding to the focal distance value are obtained by the above-mentioned empirical formula or lookup table method, and the nonlinear distortion of the scene image is corrected, there has been a noticeable improvement in the speed and automation of calibration.

2 Solving Distortion Parameters

2.1 Vanishing Point Geometry Constraint

The parallel lines in the 3D scene that are projected onto the image plane are not parallel, but intersect at one point, which is called the vanishing point. However, due to the influence of distortion and other factors, parallel lines in the same direction do not cross at a point [15].

As shown in Fig. 1, l_1, l_2, l_3 are the projections of spatial parallel lines on the image plane, the intersection points are v_1, v_2, v_3, respectively. Assuming that the actual vanishing point coordinates of this direction are $v(x_v, y_v)$, $A(x_A, y_A)$, $B(x_B, y_B)$ are any two points on the straight line l_2. Connect A and v two points, the straight l_{Av} can be expressed as:

$$y = \frac{y_v - y_A}{x_v - x_A}x + y_A - \frac{y_v - y_A}{x_v - x_A}x_A \tag{1}$$

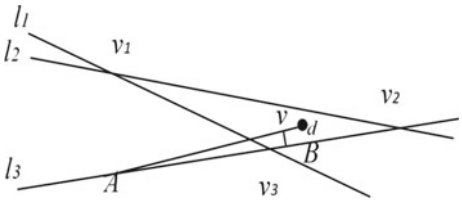

Fig. 1 The relationship between parallel line and vanishing point under radial distortion

The distance between the point B and the line l_{Av} is:

$$\begin{cases} d = \frac{|(x_B - x_A)(y_v - y_A) - (y_B - y_A)(x_v - x_A)|}{S_{Av}} \equiv 0 \\ S_{Av} = \sqrt{(x_v - x_A)^2 + (y_v - y_A)^2} \end{cases} \tag{2}$$

In the formula, S_{Av} is the length of the line segment Av. In the ideal case without distortion, the three points of A, B and v should be on a straight line, and the distance to d should be 0. Therefore, if $(x_{A'}, y_{A'})$ and $(x_{B'}, y_{B'})$ are the coordinates of the distortion point A′ and B′ on the original image, $r_{A'}$ and $r_{B'}$ are the distortion radius of the distortion point A′, B′ to the distortion center $e(e_{u0}, e_{v0})$. For $j = 1, 2, \ldots,$ m line, on each line $i = 1, 2, \ldots,$ n pairs of points, the corresponding vanishing point coordinates is $v(x_v, y_v)$.

In this paper, we use the division model (DM) introduced from Fitzgibbon to represent the lens distortion [16]. The expression is as follows:

$$\begin{cases} x_u - e_{u0} = \frac{(x_d - e_{u0})}{1 + k_1 r_d^2 + k_2 r_d^4 + \cdots} \\ y_u - e_{v0} = \frac{(y_d - e_{v0})}{1 + k_1 r_d^2 + k_2 r_d^4 + \cdots} \end{cases} \tag{3}$$

Using the first order radial distortion model, the distance from point B′ to straight line $l_{A'v}$ can be obtained by substituting formula (2) with formula (3) as shown in formula (4):

$$\begin{cases} F_{ij} = \left| \frac{\left[\left(\frac{x_{B'} - e_{u0}}{1 + k_1 (r_{B'})^2} - \frac{x_{A'} - e_{u0}}{1 + k_1 (r_{A'})^2} \right) \left(y_v - \frac{y_{A'} - e_{v0}}{1 + k_1 (r_{A'})^2} - e_{v0} \right) - \left(\frac{y_{B'} - e_{v0}}{1 + k_1 (r_{B'})^2} - \frac{y_{A'} - e_{v0}}{1 + k_1 (r_{A'})^2} \right) \left(x_v - \frac{x_{A'} - e_{u0}}{1 + k_1 (r_{A'})^2} - e_{u0} \right) \right]}{\sqrt{\left(x_v - \left(\frac{x_{A'} - e_{u0}}{1 + k_1 (r_{A'})^2} + e_{u0} \right) \right)^2 + \left(y_v - \left(\frac{y_{A'} - e_{v0}}{1 + k_1 (r_{A'})^2} + e_{v0} \right) \right)^2}} \right| \\ r_{A'} = \sqrt{(x_{A'} - e_{u0})^2 + (y_{A'} - e_{v0})^2}, r_{B'} = \sqrt{(x_{B'} - e_{u0})^2 + (y_{B'} - e_{v0})^2} \end{cases} \tag{4}$$

Therefore, the target function can be obtained

$$F = \sum_{j=1}^{m} \sum_{i=1}^{n} F_{ij} \tag{5}$$

Equation (5) is a nonlinear model of about the parameter (x_v, y_v, k_1), which is iterated and optimized using the Levenberg-Marquardt algorithm. The initial value of the parameter (x_v, y_v) can be obtained by randomly selecting the intersection of two lines, the initial value of the parameter k_1 can be set to 0. After optimization, the coordinates of the vanishing point (x_v, y_v) and the radial distortion coefficient k_1 can be obtained.

2.2 *Optimization of Distortion Center and Radial Distortion Coefficient*

Evaluation Criteria: To determine whether the correction accuracy can be further improved, the average deviation of all the corrected points to the fitted line (fitting by least squares method) is used as the quality evaluation criterion. If we consider $j = 1, 2, \ldots, m$ straight lines (the fitted line is represented as $y = a_j x + b_j$), and on each line has $i = 1, 2, \ldots, n$ corrected points, then the evaluation criterion M is:

$$M = \frac{1}{mn} \sum_{j=1}^{m} \sum_{i=1}^{n} \frac{\left| a_j x_i - y_i + b_j \right|}{\sqrt{a_j^2 + 1}} \tag{6}$$

First, assuming the distortion center is located in the center of the image, the radial distortion coefficient k_1 and the vanishing point coordinate are calculated using Eq. (5). In order to improve the accuracy of distortion correction, in the second iteration, it is assumed that the currently calculated k_1 value is a true value, and a suitable grid window is selected around the distortion center as a candidate for the distortion center, and iteratively optimized according to Eq. (6), the candidate value when M is the minimum value is the new distortion center. Next, based on the current distortion center, use Eq. (5) to optimize the estimate k_1. Repeat the above process until the M reaches minimum or the distortion coefficient changes very little.

3 Distortion Correction Process of Zoom Lens

After using the vanishing point to iteratively optimize the camera distortion center and the first-order radial distortion coefficient of a fixed focal length, we can use the above lens distortion model parameter estimation algorithm to solve the distortion parameters corresponding to each focal length, and perform the distortion parameter curve fitting or establish distortion parameter lookup table [17]. The distortion parameters corresponding to the focal length are solved by the parameter estimation algorithm of the lens distortion model. In the on-line correction, the actual working focal length is obtained according to the internal sensor of the camera, and the distortion parameter corresponding to the arbitrary focal length is obtained by calculate

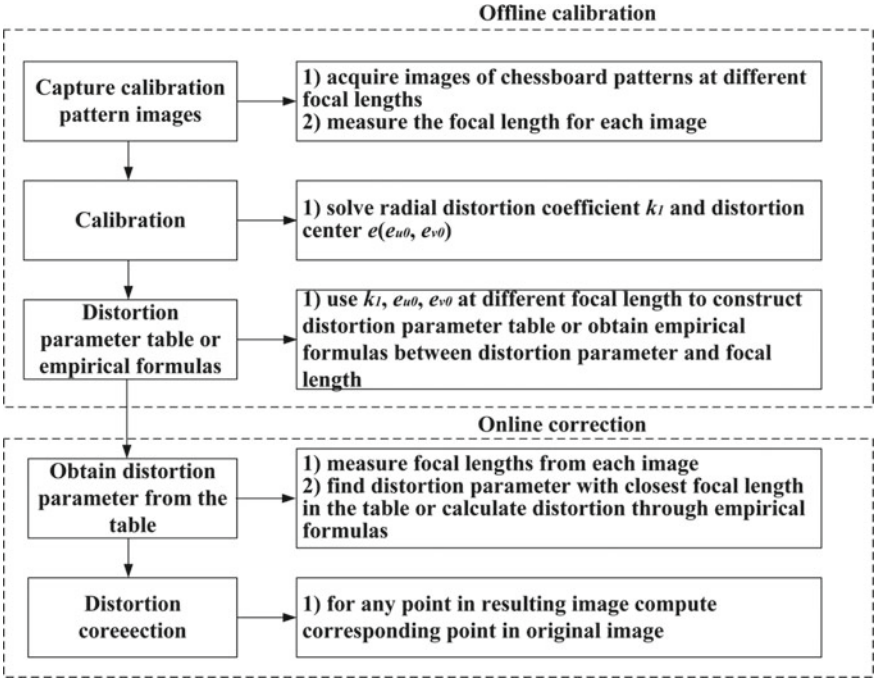

Fig. 2 Flow chart of nonlinear distortion correction algorithm for zoom lens

the above-mentioned distortion parameter curve fitting formula or look-up table. The coordinates of the corresponding points in the image are corrected to complete the distortion correction of the image. The correction algorithm flow is shown in Fig. 2.

4 The Calibration and Correction of Zoom Lens

In order to achieve rapid correction of the nonlinear distortion of the zoom camera lens, it is necessary to perform offline calibration of the camera in the laboratory to obtain lens distortion parameter values at different focal lengths [18]. The experiment selects the POINT GREY camera with FUJINON 12.5–50 mm lens, and uses a chessboard pattern containing 13×9 black and white squares as the plane template to calibrate, and size of each checkerboard is 20 mm × 20 mm.

In the experiment, one template image under different focal length (f = 12.5, 14, 15.9, 17.9, 20.2, 22.3, 25.2, 27.5, 32.6, 41.2 mm) was taken respectively, and then use the distortion model parameter estimation algorithm in Sect. 3 to solve the distortion parameters corresponding to each focal length. And the distortion coefficient k_1, the distortion center (e_{u0}, e_{v0}) under the different focal length were obtained, the trends between them are shown in Fig. 3a, b.

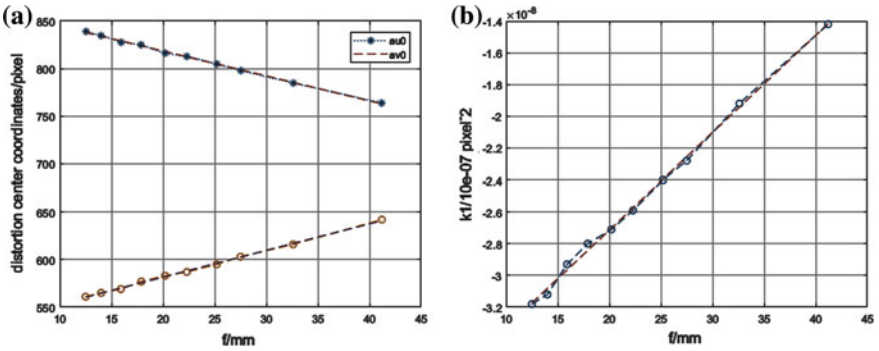

Fig. 3 Relationship between lens distortion parameters and focal length. **a** The relation between the distortion coefficient k_1 and the focal length f; **b** relationship between distortion center coordinates (e_{u0}, e_{v0}) and focal length f

By Fig. 3a, b, it can be found that the relationship between distortion center (e_{u0}, e_{v0}), distortion coefficient k_1 and focal length f satisfies the first order function. The relationship between pixel coordinates (e_{u0}, e_{v0}), distortion coefficient k_1 and focal length f in the center of distortion can be expressed approximately in Eq. (7):

$$e_{u0} = a_1 f + b_1, e_{v0} = a_2 f + b_2, k_1 = a_3 f + b_3 \tag{7}$$

where, a1 = −2.6149, b1 = 870.7596, a2 = 2.8049, b2 = 525.4844, a3 = 6.1239e-10, b3 = −3.939e-08.

In this paper, the images taken under three focal lengths (14.8, 45.4, 50 mm) are used for distortion correction. The three focal lengths are substituted into the formula to obtain their corresponding distortion centers and distortion coefficients are (832, 567, −3.03e-08), (752, 653, −1.16e-08), (740, 666, −8.77e-09), respectively. In addition, the least squares support vector regression (LS-SVR) is a machine learning method based on the support vector regression (SVR) [19], it has a significant effect on the classification and regression problem. The LS-SVR method can be used to establish the distortion reference lookup table. The distortion centers and the distortion coefficients corresponding to the three focal lengths are (832, 567, −3.03e-08), (754, 656, −1.16e-08), (744, 672, −8.79e-09), respectively.

Figure 4 shows the results of correcting the distortion parameters corresponding to different focal lengths by fitting the empirical formula and LS-SVR to establish the parameter table method.

In order to quantitatively analyze the correction accuracy of these algorithms, the harris corner extraction algorithm is used to extract the pixel coordinate positions of the checkerboard corners before and after correction, and the Zhang's calibration method is used to correct the image as ideal undistorted image. (x_{iu}, y_{iu}) represents the ideal undistorted corner coordinates of the ith checkpoint, (x_{id}, y_{id}) represents the corner coordinates in the distorted image of the ith checkpoint, and calculates

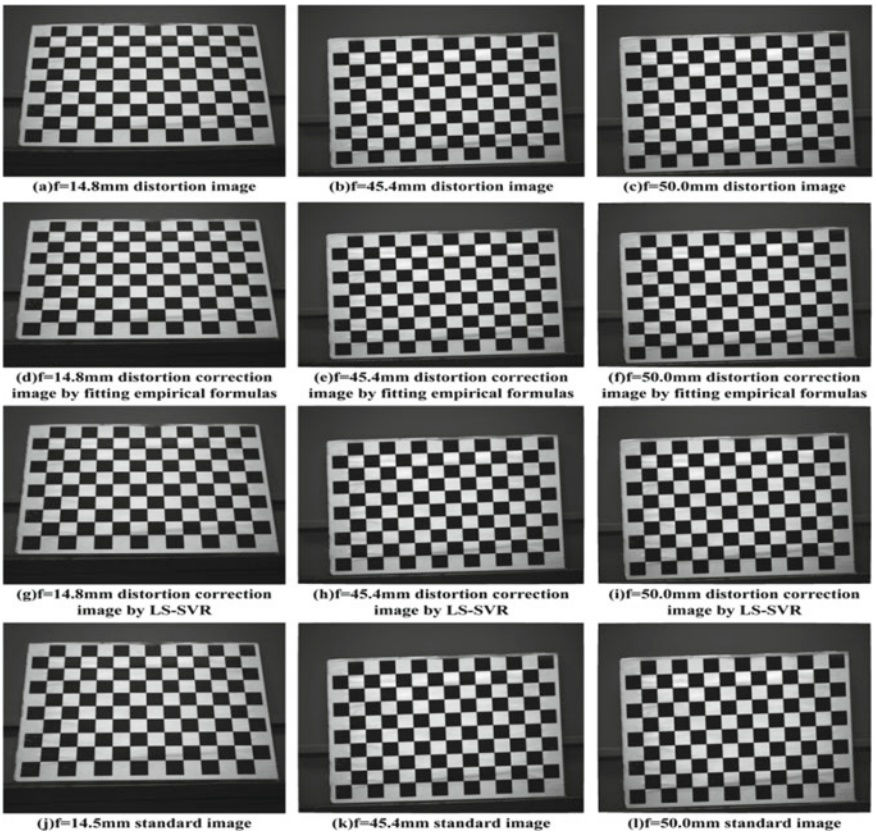

Fig. 4 Correction results of distorted images with different focal lengths

the row and column residuals of the distorted image and the corrected image under three different focal lengths, the formula is as follows:

$$d_{x_i} = x_{iu} - x_{id},\ d_{y_i} = y_{iu} - y_{id} \tag{8}$$

The d_{xi} in the formula is the column residuals of the ith checkpoint, and d_{yi} is the row residuals of the ith checkpoint.

The root mean square error (RMSE) [20] is used to measure the accuracy of the calibration. The formula is as follows:

$$f_{RMSE} = \sqrt{\frac{1}{n}\sum_{i=1}^{n}\left[(x_{id} - x_{iu})^2 + (y_{id} - y_{iu})^2\right]} \tag{9}$$

The row and column residuals before and after correction are shown in Fig. 5.

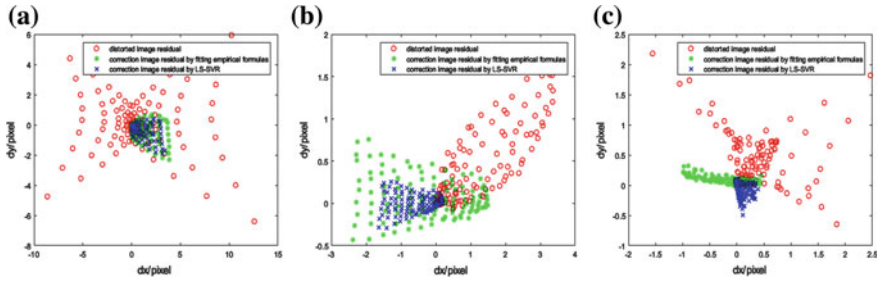

Fig. 5 Row and column residuals before and after image correction. **a** Row and column residuals of check points before and after f = 14.8 mm image correction; **b** row and column residuals of check points before and after f = 45.4 mm image correction; **c** row and column residuals of check points before and after f = 50.0 mm image correction

Table 1 Root mean square error of corner residuals before and after correction

	RMSE/pixel			Average RMSE/pixel
	f = 14.8 mm	f = 45.4 mm	f = 50.0 mm	
Distorted image	4.2804	1.7273	0.9379	2.3152
Correction image by fitting empirical formulas	1.7792	1.2198	0.4843	1.1611
Correction image by LS-SVR	1.4778	0.7960	0.2223	0.8320

The RMSE of all the checkpoints in the images at three focal lengths are calculated as shown in Table 1.

From Fig. 5, it can be seen that after correction by this method, the residual error of the row and column of each checkpoints is obviously reduced, from Table 1, it can be seen that the pixel difference between the corrected image and the Zhang's calibration method is very small, and the average correction of the parameter table method is established by LS-SVR, the mean square deviation is slightly smaller than the curve fitting method. The RMSE of LS-SVR method and curve fitting method are 1.1611 and 0.8320 pixel, respectively. This shows the accuracy of the vanishing point geometry constraint correction method and the correctness of the fitting equation of the zoom lens distortion parameter curve.

5 Conclusion

The zoom camera has been widely used in industrial environment because of its ability to change the focal length with the distance and proximity of the target without losing the tracking object. In this paper, a fast correction method based on the model of divisional distortion and the principle of parallel line vanishing point is proposed.

The first order radial division distortion model is used to correct lens distortion, and the equality relationship between vanishing point and radial distortion coefficient is established according to the geometric constraint condition of vanishing point formed by image of checkerboard lattice, and Levenberg-Marquardt is adopted. The first order radial distortion coefficient of the camera is estimated by the Levenberg-Marquardt algorithm, then the corrected point line is fitted by the least square method, and the coordinates of the distortion coefficient and the distortion center are re-optimized according to the principle of minimizing the deviation error between the point and the fitting line. Finally, the variation of distortion parameters with focal length is analyzed, the distortion parameter table between distortion parameter and focal length and the empirical formula of fitting are established. The calibration experiments of template images taken at any three focal lengths show that the root mean square error (RMS) of the corrected images is reduced. The mean RMS errors of the parameter table method and the curve fitting method are 1.1611 and 0.8320 pixel, respectively. It lays a good foundation for the engineering application of the nonlinear distortion correction of the subsequent zoom camera.

Acknowledgements This research is supported by the Program of Jiangxi Outstanding Youth Talent Assistance (Grant No. 20162BCB23047), and Science and Technology Pillar Program of Jiangxi Province (Grant No. 20151BBE50116).

References

1. Lu, H., Li, Y., Chen, M., Kim, H., Serikawa, S.: Brain intelligence: go beyond artificial intelligence. Mob. Netw. Appl. **23**(2), 368–375 (2018)
2. Lu, H., Li, Y., Mu S., Wang, D., Kim, H., Serikawa, S.: Motor anomaly detection for unmanned aerial vehicles using reinforcement learning. IEEE Internet Things J., 1–8 (2017)
3. Wang, Z., Mills, J., Xiao, W., Huang, R., Zheng, S., Li, Z.: A flexible, generic photogrammetric approach to zoom lens calibration. Remote. Sens. **9**(3), 1–15 (2017)
4. Wu, B., Hu, H., Zhu, Q., Zhang, Y.: A flexible method for zoom lens calibration and modeling using a planar checkerboard. Photogramm. Eng. Remote. Sens. **79**(6), 555–571 (2013)
5. Fang, W., Zheng, L.: Distortion correction modeling method for zoom lens cameras with bundle adjustment. J. Opt. Soc. Korea **20**(1), 140–149 (2016)
6. Zhou, Q., Liu, J.: Rapid nonlinear distortion correction of aerial optical zoom lens system. Acta Optica Sinica **35**(4), 0411001 (2015)
7. Yao, N., Lin, Z., Ren, C., Yang, K.: A distortion model suitable for nonliner distortion correction of digital video camera. Laser Optoelectron. Prog. **51**(2), 022204 (2014)
8. Lu, H., Li, B., Zhu, J., Li, Y., Li, Y., Xu, X., He, L., Li, X., Li, J., Serikawa, S.: Wound intensity correction and segmentation with convolutional neural networks. Concurr. Comput. Pract. Exp. **29**(6), 1–10 (2016)
9. Lu, H., Li, Y., Uemura, T., Kim, H., Serikawa, S.: Low illumination underwater light field images reconstruction using deep convolutional neural networks. Futur. Gener. Comput. Syst., 1–19 (2018)
10. Serikawa, S., Lu, H.: Underwater image dehazing using joint trilateral filter. Comput. Electr. Eng. **40**(1), 41–50 (2014)
11. Shin, H., Oh, J., Sohn, K.: Automatic radial distortion correction in zoom lens video camera. J. Electron. Imaging **19**(4), 2843–2850 (2010)

12. Tsai, R.Y.: A versatile camera calibration technique for high-accuracy 3D machine vision metrology using off-the-shelf TV cameras and lenses. IEEE J. Robot. Autom. **3**(4), 323–344 (2003)
13. Zhang, Z.: A flexible new technique for camera calibration. IEEE Comput. Soc. **22**(11), 1330–1334 (2000)
14. Huang, J., Wang, Z., Xue, Q., Gao, J.: Calibration of camera with rational function lens distortion model. Chin. J. Lasers **41**(5), 0508001 (2014)
15. Liu, D., Liu, X., Wang, M.: Automatic approach of lens radial distortion correction based on vanishing points. J. Image Graph. **19**(3), 407–413 (2014)
16. Fitzgibbon, A.W.: Simultaneous linear estimation of multiple view geometry and lens distortion. In: Proceedings of the 2001 IEEE Computer Society Conference on Computer Vision and Pattern Recognition, 2001. CVPR 2001, vol. 1, pp. I-125–I-132. IEEE (2001)
17. Zhou, Q., Liu, J.: Rapid nonlinear distortion correction of aerial optical zoom lens system. Acta Optica Sinica **35**(4), 0411001 (2015)
18. Zheng, S., Wang, Z., Huang, R.: Zoom lens calibration with zoom- and focus-related intrinsic parameters applied to bundle adjustment. ISPRS J. Photogramm Remote. Sens. **102**, 62–72 (2015)
19. Zhu, Z., Liu, Q., Song, R., Chen, S.: The sparse least square support vector regression for estimating illumination chromaticity. Color Res Appl. **43**(4), 517–526 (2018)
20. Chen, T., Ma, Z., Wu, X., Wu, D.: Robust correction method for camera lens distortion. Control. Decis. **28**(3), 461–465 (2013)

Computer Vision Method Applied for Detecting Diseases in Grape Leaf System

Ang Wu, Juanhua Zhu and Yujing He

Abstract Grape diseases detection is an important issue in sustainable agriculture. Recognition method of grape leaf diseases is put forward based on computer vision. A computer vision detection system is constructed to acquire the grape leaf disease images. The grape leaf disease regions are segmented by Otsu method, and the morphological algorithms are used to improve the lesion shape. Prewitt operator is selected to extract the complete edge of lesion region. Grape leaf diseases recognition model based on back–propagation (BP) neural network can efficiently inspect and recognize five grape leaf diseases: leaf spot, Sphaceloma ampelinum de Bary, anthracnose, round spot, and downy mildew. The results indicate that the proposed grape leaf diseases detection system can be used to inspect grape diseases with high classification accuracy.

Keywords Grape diseases · Computer vision · Feature extraction
BP neural network

1 Introduction

Plant diseases are the leading cause of crop losses all over the world. Plant diseases detection is the key of sustainable agriculture and has become one of the most important issues in agriculture [1, 2]. How to detect and identify plant diseases quickly and accurately is an important research direction. Plant leaf disease images can be identified by image analysis and processing and pattern recognition technology based on the diseases external features of color, texture, and shape. The plant leaf disease diagnosis based on computer vision technology is an effective and rapid method [3, 4].

In recent years, numerous domestic and foreign scholars have studied the techniques of plant disease segmentation, feature extraction, and disease diagnosis and

A. Wu · J. Zhu (✉) · Y. He
College of Mechanical and Electrical Engineering,
Henan Agricultural University, Zhengzhou, China
e-mail: zhujh88@sina.com

H. Lu (ed.), *Cognitive Internet of Things: Frameworks, Tools and Applications*, Studies in Computational Intelligence 810,
https://doi.org/10.1007/978-3-030-04946-1_36

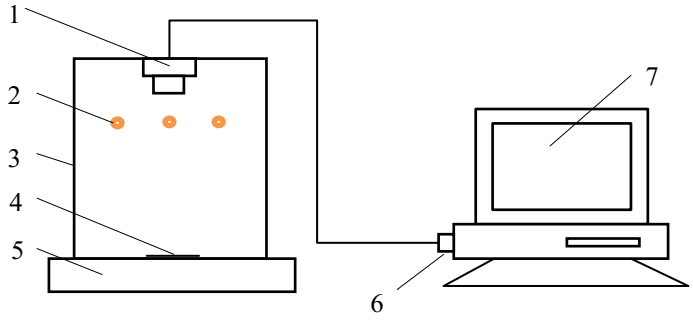

Fig. 1 Computer vision detection system. 1. CCD Camera, 2. annular light source, 3. lighting box, 4. leaf, 5. pedestal, 6. image acquisition card, 7. computer

achieved many results. Pydipati et al. [1] realized the identification of citrus disease using color texture features and discriminant analysis and achieved the classification accuracies of over 95%. Jordan [5] studied the classification of cotton diseases, which was not a real-time system. Sasaki et al. [6] studied the automatic diagnosis of cucumber anthracnose based genetic algorithm and established identification parameter that uses spectral reflectance and filtered images. Huang [7] extracted the phalaenopsis seedling diseases based on the detection of color and texture feature, and classified soft rot, leaf spot and black rot by neural networks. Sanyal and Patel [8] detected two diseases of rice blast and brown spot in rice plants using pattern recognition method and the recognition rate was 89.26%. Satti et al. [9] proposed an automatic leaf recognition system for plant identification using ANN classifier and machine vision technology, which provides good diagnostic accuracy with 93.3%.

Here, we are interested in grape leaf disease recognition based on computer vision, and it aims to provide important theoretical basis for the study of disease prevention automatic spray robot.

2 Computer Vision Detection System

The computer vision inspection system is shown in Fig. 1. It includes a lighting system, a CCD camera, an image acquisition card, and a computer. The lighting system consists of an annular LED light source, which can not only conducive to collecting grape leaves image information but also can be effectively reduced the noise produced in the process of collecting images. The image capture area is located at the bottom of the box. Clear sample images can be got by selecting white background. Industrial CCD camera is installed just above the bottom of the collecting areas. The collected images are converted to digital information by image acquisition card, which is stored in the computer.

3 Grape Disease Image Processing

The initial grape leaf images collected are easily affected by external environment, which cause certain image quality degradation, so they should be denoised and enhanced. Here, the sample images are pretreated in order to eliminate noise and segment accurately the areas of grape leaf diseases. First the color grape leaf images are transformed into the gray images by gray-scale transformation; then the Wiener filtering method based on wavelet transform (WT) is applied to denoise the images; the following is that grape leaf disease regions are segmented by Otsu method, which are expanded to fill in small holes and connect disjoint edges using standard morphological operations; finally, the complete edge is extracted based on Prewitt edge detection operator.

3.1 Wiener Filter Denoising

Noise should be removed prior to image segmentation [10]. WT has been widely used due to its time-frequency localization property, multi-resolution, decorrelation, and flexibility [11]. WT also exhibits convenience, simple computation, and effective denoising effect in denoising agricultural images. However, the result of wavelet denoising in multi-signal space is an approximate optimal solution. Wiener filter is optimal for any signal in terms of mean square error. Thus, the Wiener filtering algorithm for image denoising based on WT was adopted in the present study.

WT has excellent localization properties in time and frequency domains. For 2D discrete signal $f(x, y)$ such as a still image, the basic idea of WT is to decompose $f(x, y)$. Let h and g be the low-pass and high-pass filters of wavelet function, respectively, and the decomposition formula of dimensional WT is expressed as

$$\begin{aligned} f_i(m,n) &= \sum_{k_1,k_2\in z} h(k_1-2m)h(k_2-2n)f_{j-1}(k_1,k_2) \\ W_j^1 f(m,n) &= \sum_{k_1,k_2\in z} g(k_1-2m)h(k_2-2n)f_{j-1}(k_1,k_2) \\ W_j^2 f(m,n) &= \sum_{k_1,k_2\in z} h(k_1-2m)g(k_2-2n)f_{j-1}(k_1,k_2) \\ W_j^3 f(m,n) &= \sum_{k_1,k_2\in z} g(k_1-2m)g(k_2-2n)f_{j-1}(k_1,k_2) \end{aligned} \tag{1}$$

where $\mathrm{f}_j(m,n)(j>0)$ shows the low-frequency information of the original image at different scales in the horizontal and vertical directions; $W_j^1 f(m,n)$ represents the high- and low-frequency information in the horizontal and vertical directions, respectively; $W_j^2 f(m,n)$ represents the high- and low-frequency information in the vertical and horizontal directions, respectively; and $W_j^3 f(m,n)$ represents the detailed infor-

mation along the diagonal direction. Four–channel wavelets, namely, low-frequency, horizontal high-frequency, vertical high-frequency, and diagonal high–frequency wavelets, were generated using wavelet decomposition. Each channel corresponded to the information of the original image at different scales and directions.

Image denoising based on Wiener filter and WT comprises the following steps:

1. The noised image "F" is decomposed by the first WT to get low-frequency approximation image "F1" and three high-frequency detailed images: horizontal image "hd1", vertical image "vd1" and diagonal image "dd1".
2. The image "F1" is processed by Wiener filtering to get the image "F1w"; three high frequency images are processed separately by Wiener filtering and compounded to the image "G1w".
3. Low frequency image "F1w" and high frequency image "G1w" are transformed by inverse WT to get the image "F1w+G1w"; low frequency image "F1" and high frequency image "G1w" are transformed by inverse WT to get the image "F1+G1w".
4. The above conversion results are obtained by the first WT, and the second, third and fourth transform are similar to the situation.
5. According to the image signal-to-noise and visual effects, the best denoised images are ultimately determined.

The filtering results of image "F1" based on db2 wavelet function and 4 layer wavelet decomposition are shown in Fig. 2. Figure 2a is the color image of grape leaf spot; Fig. 2b is the lesion region color image taken from Fig. 2a; Fig. 2c is the grayscale image "F1" transformed from Fig. 2b; Fig. 2d is the first WT image of "F1"; Fig. 2e–p are the synthesized images of different methods obtained by the first, and the second and third WT; Fig. 2q is the low frequency image by the fourth WT; Fig. 2r is the filtering result of image "F1" directly performed by Wiener filter. As can be seen from the Fig. 2: Fig. 2j–l have good visual effect; the image decomposed by the first WT appears dark and has more noise; when the image is decomposed three or four times, high-frequency component is filtered excessively, which blurs the image.

3.2 Image Segmentation and Edge Detection

Image segmentation methods mainly include methods based on threshold segmentation [12], region segmentation [13], and edge segmentation [14]. Otsu method is one method of automatically determining threshold, which has the characteristics of simpleness, conveniency, and high efficiency. The optimal threshold segmentation criteria of Otsu method is the minimum infra-class variance and the maximum inter-class variance. Figure 2k is the image filtered, which is segmented and transformed into binary image by Otsu method. The segmentation result is shown in Fig. 3a.

The lesions and healthy sites of grape leaf are basically segmented by Otsu method. However there are still some small noise, small holes in lesion sites and error segmen-

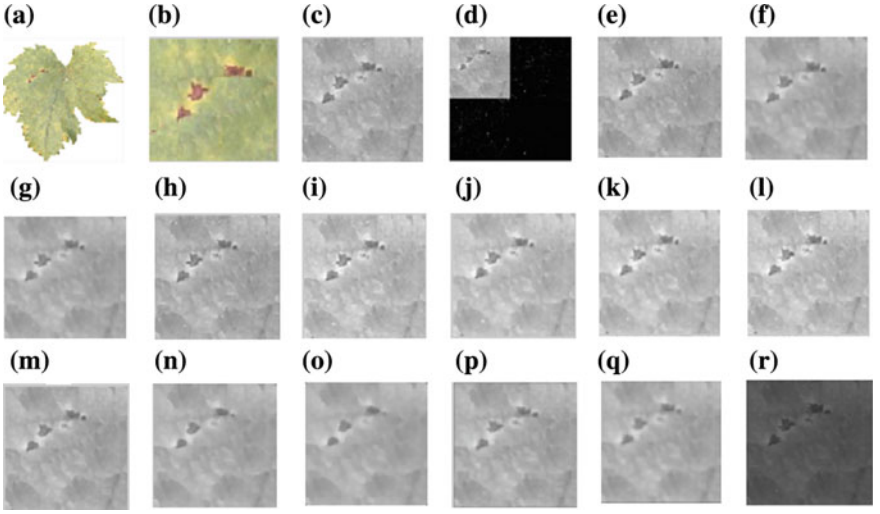

Fig. 2 The denoised results of grape diseases image based on Wiener filter and WT. **a** the color image of grape leaf spot; **b** the lesion region color image taken from (**a**); **c** the grayscale image; **d** one layer WT image; **e** F1; **f** F1w; **g** F1w+G1w; **h** F1+G1w; **i** F2; **j** F2w; **k** F2w+G2w; **l** F2+G2w; **m** F3; **n** F3w; **o** F3w+G3w; **p** F3+G3w; **q** F4; **r** Fw

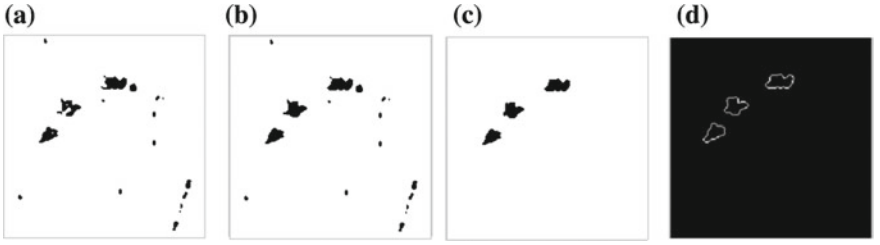

Fig. 3 Image segmentation and edge detection. **a** The binary image based on Otsu segmentation method; **b** closing operation; **c** opening operation; **d** edge detection based on Prewitt operator

tation in the image. The opening and closing operation of morphological operation can be used in de-noising, filling holes and edge connectors. In this paper, the closing operation based on circular structural element is used to fill voids and connect discontinuous boundary, and the opening operation based on linear structural elements is used to remove noise. In Fig. 3b, c, diseased spots are well extracted by the calculation.

Prewitt operator is first-order differential operator used for edge detection in an image. Edges are calculated by using gray-scale difference between corresponding pixel intensities of an image. It detects two types of edges: Horizontal edges and Vertical edges. The edge information decomposed by WT is mainly located in the horizontal and vertical high-frequency section. Using Prewitt operator to detect the edge is better. Figure 3d shows the boundary extraction result.

3.3 *Image Characteristic Extraction*

The purpose of grape diseases image segmentation is to extract disease characteristics and classify the image. The shape characteristics are very important in many pattern recognition problems, which describe the geometric properties of target region but regardless of the gray values of target region.

Here, the main shape characteristic parameters of grape diseases includes circumference, area, circularity, rectangularity, and shape complexity, which can be used as the characteristics vector for classification. This is a better extraction method for separation lesion region from leaf image. The calculations of grape diseases characteristic parameters can be referred to other related documents.

4 Grape Diseases Classifier Design

This paper adopts BP neural network as the classifier model. BP neural network is the most representative and used neural network at present. It has structure learning algorithm, unique approximation ability and simple structure. It has been successfully applied to the field of signal processing, pattern recognition, machine control, and expert systems. Agriculture disease recognition is an active subject based on BP neural network, and lots of achievements have been obtained [15]. Standard BP neural network model is shown in Fig. 4. It is constituted of input layer, hidden layer and output layer. The input layer serves as inputs for the hidden layer. The hidden layer uses the weighted sum transfer function to calculate the outputs that the output layer can use. Here, sigmoid function is chosen as the node function.

The process of BP network algorithm consists of reverse propagation and forward propagation. In the forward propagation process, the signal is transmitted layer by layer: from input layer to hidden layer and calculated in the hidden layer, then

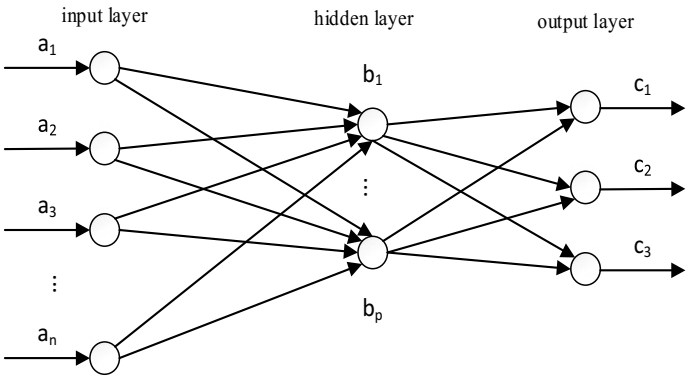

Fig. 4 BP neural network model

transmitted to the output layer, in which the states of neurons can only influence the neurons on next layer. If the desired output cannot be gotten on the output layer, it will turn to back propagation, and the error signal will turn back along the original connection. According to the predicted error the weights of neurons are modified in each layer to decrease the error signal until it reaches the required precision.

The grape diseases classifying steps using BP neural network are as follows:

(1) Enter the training sample. The eigenvalues of input samples are normalized to the range [0, 1];
(2) Network initialization.

Five nodes at input layer correspond respectively to five eigenvectors (perimeter, area, rectangularity, circularity and complex shape). Five nodes at output layer correspond respectively to five kinds of grape leaf diseases (brown spot, Sphaceloma ampelinum de Bary, anthracnose, round spot and grape downy mildew). The number of hidden layer nodes has relations with the neurons number of input layer and output layer. Because there is not a good analytical formula to calculate it, it is difficult to get the right node number. Generally we determine the number based on design experience and experiment. Here, we use the following empirical formula to calculate

$$\mathrm{n}_1 = \sqrt{n+m} + a \tag{2}$$

where n1 is the number of hidden layer neurons; n is the number of the output layer neurons; m is the number of the input layer neurons; a is a constant range between 1 and 10. By repeated training tests, we determine nine neurons at hidden layer. Then, the maximum number of model training is set to 2000, the inertia coefficients to 0.8, the overall maximum permissible error to 0.001, and the learning efficiency to 0.01. [y_1, y_2, y_3, y_4, y_5] is the desired output matrix, and its vectors corresponds respectively to five kinds of grape leaf diseases. The desired output matrix is given by

$$\begin{bmatrix} y_1 \\ y_2 \\ y_3 \\ y_4 \\ y_5 \end{bmatrix} = \begin{bmatrix} 0.99\ 0.01\ 0.01\ 0.01\ 0.01 \\ 0.01\ 0.99\ 0.01\ 0.01\ 0.01 \\ 0.01\ 0.01\ 0.99\ 0.01\ 0.01 \\ 0.01\ 0.01\ 0.01\ 0.99\ 0.01 \\ 0.01\ 0.01\ 0.01\ 0.01\ 0.99 \end{bmatrix};$$

(3) In the process of training BP neural network, the weights and threshold values are adjusted until the final results are available. Then the trained classifier is used to identify the test samples.

Table 1 The recognition rate of different diseases based on BP neural network

Disease category	Brown spot	Sphaceloma ampelinum de Bary	Anthracnose	Round spot	Downy mildew
Training samples	40	40	40	40	40
Test samples	20	20	20	20	20
Correct identification	19	20	18	16	18
Correct rate (%)	95	100	90	80	90
Average correct rate (%)	91				

5 Experimental Results and Analysis

A total of 60 samples are prepared for each type of grape leaf disease images (brown spot, Sphaceloma ampelinum de Bary, anthracnose, round spot and downy mildew). In order to ensure the reliability of the training results, for each type, 40 samples are taken randomly as training set and the rest 20 samples are used as the test sample set. Table 1 shows the recognition rate of different diseases based on BP neural network.

It can be seen from the test results in Table 1 that this method has higher recognition rate and is suitable for diseases detection. However there is different levels of error in detecting the disease leaves. The error occurs for several reasons:

1. Compared with round spot, the features of brown spot, Sphaceloma ampelinum de Bary, anthracnose and downy mildew are more obvious. Accordingly these diseases have higher recognition rate, but the accurate recognition rate of round spot disease is only 80%.
2. The lesion images collected are affected by angles, lighting and distance, which decreases the comparability of characteristic parameters such as the lesion area and perimeter. The visual system image acquisition is completed in a closed chamber using LED annular illumination. The white board is used as the image acquisition background. These factors can well suppress certain extent interference, but cannot eliminate absolutely the random noise.
3. The differences between the morphological characteristics of different kind of lesions are rather small, so they cannot be well distinguished by the few features. How to extract more effective features becomes the next focus of study.
4. Many factors such as the sensitivity unevenness of sensitive element in photoelectric conversion process, quantization noise in the digitization process, transmission errors, human factors etc. cause image deterioration and interfere with the disease identification.

6 Conclusion

The automatic detection method of grape leaf diseases is proposed based on Wavelet-Wiener filtering and BP neural network. A machine vision detection system is constructed to acquire the grape leaf disease images. The Wiener filtering method based on WT is applied to denoise the disease images. The grape leaf disease regions are segmented by Otsu method, and the morphological algorithms are used to improve the lesion shape. Prewitt operator is selected to extract the complete edge of lesion region. Five effective characteristic parameters, such as perimeter, area, circularity, rectangularity and shape complexity, describing grape leaf diseases are extracted. Grape leaf diseases recognition model based on BP neural network can efficiently inspect and recognize five grape leaf diseases–brown spot, Sphaceloma ampelinum de Bary, anthracnose, round spot and downy mildew. The results indicate that the proposed grape leaf diseases detection system based on Wavelet-Wiener filtering and BP neural network can be used to inspect grape diseases with high classification accuracy.

Acknowledgements This research is supported by National Natural Science Foundation of China (No. U1304305); Scientific Research Tackling Key Subject of Henan Province (No. 142102310550, No. 162102110122, No. 172102210300, No. 182102110116); Natural Science Foundation of Henan Province (No. 142300410419); Science and Technology Research Project of Zhengzhou (No. 121PPTGG465–2).

References

1. Pydipati, R., Burks, T.F., Lee, W.S.: Identification of citrus disease using color texture features and discriminant analysis. Comput. Electron. Agric. 52, 49–59 (2006)
2. Martinelli, F., Scalenghe, R., Davino, S., Panno, S.: Advanced methods of plant disease detection. A review. Agron. Sustain. Dev. **35**(1), 1–25 (2015)
3. Dhingra, G., Kumar, V., Joshi, H.D.: Study of digital image processing techniques for leaf disease detection and classification. Multimed. Tools Appl. **77**(15), 19951–20000 (2017)
4. Zhu, J., Wu, A., Li, P.: Corn leaf diseases diagnostic techniques based on image recognition. Commun. Comput. Inf. Sci. **288**, 334–341 (2012)
5. Jordan, J.B.: Vision guided insect handling system, modeling and simulation. Proc. Annu. Pitts **21**(5), 1995–2001 (1990)
6. Sasaki, Y., Okamoto, T., Imou, K.: Automatic diagnosis of plant diseases. J. Jpn. Soc. Agric. Mach. **61**(2), 119–126 (1999)
7. Huang, K.Y.: Application of artificial neural network for detecting Phalaenopsis seedling diseases using color and texture features. Comput. Electron. Agric. **57**(1), 3–11 (2007)
8. Sanyal, P., Patel, S.: Pattern recognition method to detect two diseases in rice plants. Appl. Eng. Agric. **6**(6), 319–325 (2008)
9. Satti, V., Satya, A., Sharma, S.: An automatic leaf recognition system for plant identification using machine vision technology. Int. J. Eng. Sci. Technol. **5**(2), 874–879 (2013)
10. Wu, A., Zhu, J., Tao, Z., Mao, C.: Automatic inspection and classification for thin-film transistor liquid crystal display surface defects based on particle swarm optimization and one-class support vector machine. Adv. Mech. Eng. **8**(11), 1–11 (2016)
11. Zhu, J., Wu, A., Liu, X.: Printed circuit board defect visual detection based on wavelet denoising. IOP Conf. Ser. Mater. Sci. Eng. **392**, 062055 (2018)

12. Cui, D., Zhang, O., Li, M.Z., Zhao, Y., Hartman, G.L.: Detection of soybean rust using a multispectral image sensor. Sens. Instrum. Food Qual. Saf. **3**(1), 49–56 (2009)
13. Han, D., Huang, X., Fu, H.: Measurement of plant leaf area based on image segmentation of color channel similarity. Trans. Chin. Soc. Agric. Eng. **28**(6), 179–182 (2012)
14. Mao, L., Xue, Y., Kong, D., Liu, G., Huang, K., Lu, Q., Wang, K.: Litchi image segmentation algorithm based on sparse field level set. Trans. Chin. Soc. Agric. Eng. **27**(4), 345–349 (2011)
15. Jia, W.K., Zhao, D., Liu, X., Tang, S., Ruan, C., Ji, W.: Apple recognition based on K-means and GA-RBF-LMS neural network applicated in harvesting robot. Trans. Chin. Soc. Agric. Eng. **31**(18), 175–183 (2015)

Pedestrian Attribute Recognition with Occlusion in Low Resolution Surveillance Scenarios

Yuan Zhang, Qiong Wang and Zhenmin Tang

Abstract In surveillance scenarios, the pedestrian images are often facing poor resolution problems or the images are often suffered the occlusion problems. These problems make pedestrian attribute recognition more difficult. In order to solve this problem, we propose an improved pedestrian attribute recognition method based on hand-crafted feature. In this method, we use Patch Match algorithm as pedestrian image preprocessing to enhance the pedestrian images. Experiments show that this method proposed performs excellent when the pedestrian images suffer occlusion problem and the method is robust to low resolution problem.

Keywords Pedestrian attribute recognition · Image enhancing · Patch match

1 Introduction

Artificial intelligence (AI) is a hot topic in the computer field. Many excellent results in AI field have been achieved. An anomaly detection system has been developed by Lu et al. [1] to help the drones operate properly at abnormal temperatures. Lu et al. [2] try to develop a new model called BI (Brain Intelligence) which can generate new ideas about things without the need of experiences. Similarly, artificial intelligence is also applied in the field of pedestrian attribute recognition. The current pedestrian attribute recognition methods mainly focus on two kinds of scenarios: natural scenarios and surveillance scenarios. Most researchers pay more attention to the attribute recognition of natural scenes and have achieved great success in object recognition, face recognition and so on. For example, attribute recognition in natural

Y. Zhang · Q. Wang (✉) · Z. Tang
Nanjing University of Science and Technology, Nanjing, China
e-mail: wangq@njust.edu.cn

Y. Zhang
e-mail: yuanzh@njust.edu.cn

Z. Tang
e-mail: tzm.cs@njust.edu.cn

H. Lu (ed.), *Cognitive Internet of Things: Frameworks, Tools and Applications*, Studies in Computational Intelligence 810,
https://doi.org/10.1007/978-3-030-04946-1_37

Fig. 1 Low resolution and occlusion issues, left is the low resolution image, right is the original image for every group

scenarios was first proposed by Ferrari and Zisserman [3]. Siddiquie et al. [4] explicitly model the correlation between different query attributes and generate a search list. Kumar et al. explored comparing facial attributes and modeling them with a binary classifier for facial verification. Zhang et al. [5] proposed a posture-aligned neural network to identify human attributes (such as age, gender, and expression) on images under unconstrained scenarios. In general, these methods [3–5] focus on high quality images. However, in surveillance scenarios, the image is blurred, the resolution is low, the difference between attributes is large, and the illumination varies greatly. Some examples of low resolution pedestrian images and occlusion pedestrian images are shown in Fig. 1. Therefore, monitoring the attribute recognition in these scenarios is more challenging. Of course, there are some good image enhancing methods that can solve image quality problems in harsh environments. For example, Serikawa et al. [6] proposed a new image enhancing method to enhance underwater images by image dehazing. Lu et al. [7] utilize an intensity inhomogeneity correction method and a spectral properties-based color correction method to improve the image quality.

In this paper, we discuss the influence of pedestrian images with poor resolution or occlusion problem for attribute recognition. According to the influence, we propose a method to deal with this problem. Our method includes an attribute classifier based on hand-crafted feature and an image enhancing approach based on Patch Match algorithm.

2 Related Work

Person is the main research object in surveillance scenarios. It is meaningful to recognize the basic attributes of pedestrian. In order to provide convenience for query and retrieval tasks in the traditional surveillance system, it is necessary to manually detect the basic attributes of the pedestrian, and then input the attribute label for the pedestrians that are interested in. However, this kind of work cannot satisfy the need for labeling the pedestrian attributes under a large number of surveillance data. It is an efficient method to label the pedestrian attributes automatically in surveillance by means of computer vision technology.

There are some groundbreaking work on attribute recognition in surveillance scenarios. Layne et al. [8] first used the support vector model (SVM) to recognize attributes (such as "sex", "backpack") to help pedestrians re-identification. In order to solve the problem of attribute recognition in mixed scenes, Zhu et al. [9] introduced the pedestrian database (APiS) and used enhanced algorithms to recognize attributes. Deng et al. [10] constructed the largest pedestrian attribution database (PETA), using SVM and Markov random field to recognize attributes.

As an important basic attribute of pedestrian, gender has always been a research hotspot. Sun et al. [11] used genetic algorithms to select part of feature points of human faces as a classification feature of gender, and used artificial neural network as a classifier to recognize. Shakhnarovich et al. [12] extracted image features of face integration and combined the Adaboost method to achieve the goal of gender classification. Luo et al. [13] used the Local Binary Pattern (LBP) feature to solve the problem of multi-angle face gender recognition. Jain et al. [14] used the Independent Component Analysis (ICA) technique to extract face features and trained the SVM classifier to recognize gender attribute and achieved great results. The work of Yaser and Davis [15] is more representative. In their work, the human face is first detected, then the facial organs are positioned. Then the hair is detected by a colorimetric statistical model, and then the color of the hair is targeted. The description of features such as interior and exterior outlines, and the position of the split ends will eventually enable gender recognition. Kozlowski and Cutting [16] recognized gender by analyzing the gait of the human body in the early stage and obtained a recognition accuracy of 63%. Moghaddam et al. [17] used support vector machines (SVM) to predict the gender of pedestrians.

Appearance attributes are mainly manifested in the understanding of pedestrian clothing, and are also an important content of pedestrian attribute recognition. Through the understanding of the clothing appearance, it is possible to provide

semantic attributes including the color, style of the clothing, whether or not to wear glasses, and whether to carry the package. In recent years, many researchers recognize the basic appearance of the pedestrian images effectively through the understanding of the pedestrian clothing, combing with contextual information of the environment. The early recognition of pedestrian clothing was merely a description of clothing. For example, one classic work of H. Chen et al. was to outline the clothing and realize the repainting of clothing with sketch effects [18]. A more challenging issue in the study of clothing recognition is how to segment the clothing area from the image. In order to solve this problem, Gallagher and Chen et al. proposed an algorithm for learning the clothing model from a set of images [19]. Through the analysis of the common information between pixels and human beings near the face, the images were loaded from multiple people. The model of the clothes is learned, and the clothes area in each image is segmented using a graph division method. Many literature descriptions of apparel attributes focus on classifications of types of clothing, brands, etc., and use attribute semantic words to describe them, users can search through semantic keywords. The system proposed by Bourdev et al. [20] learns the binary attributes of nine aspects of clothing (such as whether it is male, whether a T-shirt is worn, whether it is long-haired, etc.). Chen et al. proposed a more detailed attribute description [21]. In their work, they proposed a system that comprehensively describes the appearance attributes of clothes. It contains a total of 26 attributes, of which 23 are of the second-class attribute description and 3 are multi-category. The method not only considers the high-level attribute description information of the clothing, such as the category of the clothing: jackets, suits, windbreakers, etc., but also describes some detailed attributes such as whether there is a collar, a collar shape, a stripe, a spot, a pattern, and so on. Most analytical studies on clothing are limited to the recognition of clothing attributes, and there is very little that relates the relationship between clothing attributes and character attributes. In real life, many basic attributes of a character can be understood through clothing information. For example, clothing style can be used to distinguish its race, its career can be identified through its uniform, and its gender can be discriminated by wearing style. Therefore, we can make full use of the semantic features of the clothing to achieve the description of the characters.

In addition to these traditional methods, there are also many deep learning methods, especially the Convolutional Neural Network (CNN) [22], which has been proven to perform well on large-scale classification problems and achieve comparable performance to humans. Krizvhesky et al. achieve great success in the ILSVRC-2012 classification task [23]. In recent years, attributes have received increasing attention, and CNN's success has inspired researchers to use it for pedestrian attribute recognition.

3 Method

In this work, we propose an improved attribute classification method based on hand-crafted feature and an image enhancing approach based on Patch Match algorithm.

3.1 Image Enhancing for Pedestrian Images with Occlusion

Inspired by the research done by Fabbri et al. [24], we try to study the influence of resolution and occlusion for our attribute classification. Fabbri et al. has confirmed that improving the image resolution and remove the occlusion can improve the accuracy of attribute classification in deep learning. We try to apply this idea into our traditional method.

In surveillance, pedestrian may be occluded by another pedestrian and the occluded part may contain important information. We overlap the original images to produce the occluded pedestrian images and we call the images occPETA. In the occPETA dataset, the upper part, lower part or left part of pedestrian images may be occluded randomly.

Patch Match algorithm [25] is used to solve the problem. As shown in paper [25], this algorithm includes three steps: (a) Initialization; (b) Propagation; (c) Search. We show the algorithm in Fig. 2.

For Initialization, every pixel in A is given a random patch offset. For Propagation, check the neighboring patches of every pixel in A, if the patch offset of neighboring patches provides better matching, we set the neighbor's patch offset as its patch

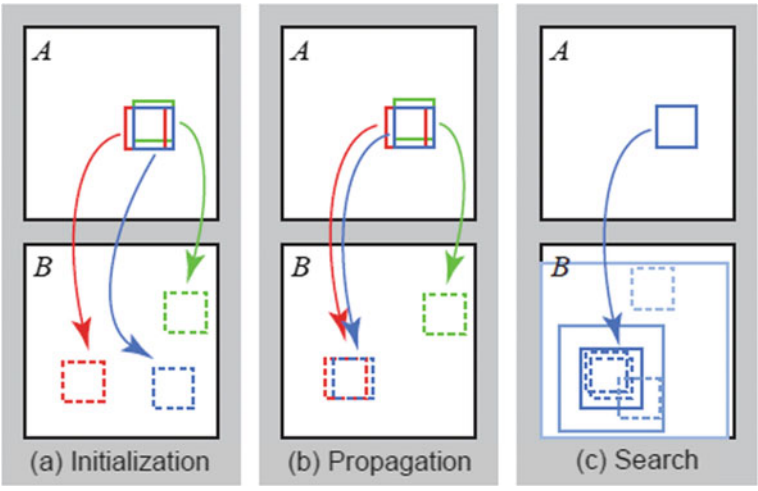

Fig. 2 Patch match algorithm [25]

offset. For Search, the current patch offset will be replaced by better patch offset by searching the around patch offset within a concentric radius. The range of concentric radius if from the size of the image to 1 and the concentric radius is halved each time. Finally, repeat step (b) and step (c) until the suitable patch offset is found for every pixel. In this algorithm, the matching degree is an important part. We compute the distance between two patch offsets as the similarity that is the matching degree. For example, there are two patches: patch A and patch B. The patch A has the same shape as patch B. The distance formula is shown in formula (1).

$$\text{distance} = \frac{\sum(patchA_{ij} - patchB_{ij})^2}{pixels} \tag{1}$$

In formula (1), $patchA_{ij}$ represents the pixels in patch A and $patchB_{ij}$ represents the pixels in patch B. Pixels is the number of the pixels in the patch, we use formula (2) to represent it.

$$\text{pixels} = \text{patchA} \cdot \text{shape}[0] * \text{patchB} \cdot \text{shape}[1] \tag{2}$$

3.2 Attribute Classification Based on Hand-Crafted Feature

Inspired by [8], we first extract the hand-crafted feature. For each pedestrian image, we first crop it into ten equal sized horizontal strips and the first three strips are the head-shoulder part, the third strip to the seventh strip is the upper-body part, the last five strips are the lower-body part. We extract features of different part for different attribute as the final feature vector. Of course, for special attribute, we can use special combination of strips. The hand-crafted features we extract include two parts: color feature and texture feature. For color feature, we choose three color space: RGB, YCbCr and HSV. Because channel Y in color space YCbCr and channel V in color space HSV are both luminance channel, we just choose channel Y in the next experiment. For texture feature, we extract one LBP feature. Eight Gabor filter features and thirteen Schmid filter features are extracted in the luminance channel. The parameter choices of Gabor filter are in Table 1 and the parameter choices of Schmid filter are shown in Table 2. In general, we totally extract 30 kinds of features. For each feature, we use a 16-bin histogram to represent. For different attribute, the final feature vector has different dimension.

We finally train an attribute classification by means of Support Vector Machines (SVM) with Intersection kernels. We train a classifier separately for each attribute.

For imbalanced attribute training, some attributes, such as sunglasses, V-necks, often have limited positive training examples. In order to avoid the deviations of attribute classification due to imbalanced data, we must preprocess the training data first. The paper [8] deals with this problem by subsampling the majority data at the regular interval ε for each attribute detector, setting ε as formula (3):

Table 1 The parameter choices of Gabor filter

Γ	θ	λ	Σ
0.3	0	4	2
0.3	0	8	2
0.4	0	4	1
0.4	0	8	1
0.3	π/2	4	2
0.3	π/2	8	2
0.4	π/2	4	1
0.3	π/2	8	1

Table 2 The parameter choices of Schmid filter

τ	2	4	4	6	6	6	8	8	8	10	10	10	10
σ	1	1	2	1	2	3	1	2	3	1	2	3	4

Table 3 The comparison results for subsampling

Methods	Random under sampling	Easy ensemble	Balance cascade
Trousers	0.7195	0.6007	0.57
longHair	0.6508	0.4494	0.4767
Shorts	0.765	0.635	0.66
Jeans	0.7881	0.6944	0.6841
SunGlasses	0.6719	0.5651	0.5554

$$\varepsilon = \begin{cases} 2 if T_p < T_n \\ 2\| \frac{T_p}{T_n} \| otherwise \end{cases} \tag{3}$$

where the T_p represents the length of positive training data for each attribute and the T_n represents the length of negative training data for each attribute.

In our work, we try three data subsampling methods: Random under sampling, Easy Ensemble and Balance Cascade.

For random under sampling, we try 10 times random under sampling to make balance between positive training data and negative training data, and then record the average accuracy as the accuracy for one attribute. For oth three subsampling methods, we use 5-fold cross validation for training. We choose five attributes for test. The comparison results are shown in Table 3.

As shown in Table 3, the random under sampling performs better than the other methods.

4 Experiments

We conduct our experiments on the PETA dataset [10]. The PETA dataset contains 8705 pedestrians for a total of 19,000 images and the dataset covers more than 60 attributes. More detail about PETA database is shown in Table 4. By comparing the ten subsets of the PETA dataset, we find that the VIPeR dataset has a relatively large sample size, fixed resolution and contains different perspectives and illumination changes. We choose VIPeR as the final dataset.

4.1 Experiments on Attribute Classification

We choose eight attributes to test the performance of our attribute classification. For each attribute, we under sample the training data 10 times and we take the average of the ten results as the final classification result. The method proposed in [8] is used to compare with our method, and the comparison is shown in Table 5. As we can see from the table, our method performs better.

Table 4 The composition of PETA dataset

Database	Images	Camera angle	View point	Illumination	Resolution	Scene
3DPes	1012	High	Varying	Varying	From 31 × 100 to 236 × 178	Outdoor
CAVIAR4REID	1220	Ground	Varying	Low	From 17 × 39 to 72 × 141	Outdoor
CUHK	4563	High	Varying	Varying	80 × 160	Outdoor
GRID	1275	Varying	Frontal and back	Low	From 29 × 67 to 169 × 365	Indoor
i-LIDS	477	Medium	Back	High	From 32 × 76 to 115 × 294	Indoor
MIT	888	Ground	Back	High	64 × 128	Outdoor
PRID	1134	High	Profile	Low	64 × 128	Outdoor
SARC3D	200	Medium	Varying	Varying	From 54 × 187 to 150 × 307	Outdoor
TownCentre	6967	Medium	Varying	Medium	From 44 × 109 to 148 × 332	Outdoor
VIPeR	1264	Ground	Varying	Varying	48 × 128	Outdoor
Total = PETA	19000	Varying	Varying	Varying	Varying	Varying

Table 5 The comparison results

Methods	Paper [8]	Ours
Shorts	0.74	0.754
Jeans	0.73	0.7846
Vnecks	0.53	0.60
SunGlasses	0.60	0.6128
Longhair	0.55	0.6565
Carrying	0.50	0.6432
Backpacks	0.52	0.7186
Logo	0.58	0.6089

Table 6 The comparison result between LowPETA and PETA

Datasets	LowPETA	PETA
Shorts	0.766	0.754
Jeans	0.7776	0.7846
Vnecks	0.62	0.60
SunGlasses	0.6039	0.6128
Longhair	0.6370	0.6565
Carrying	0.6355	0.6432
Backpacks	0.7036	0.7186
Logo	0.5967	0.6089

Experiments also show that our attribute classification method is robust to low resolution pedestrian images. To confirm this, we first preprocess the images to reduce the resolution. The original images (PETA) is downsampled $4\times$ and then upsampled to the original size, we call the images LowPETA. We show the comparison results in Table 6.

4.2 Experiments on Attribute Classification with Occlusion

We use Patch Match algorithm to reconstruct images from occluded pedestrian images, we finally use 5 iterations in our experiment and we call the reconstruct images dataset reconoccPETA for occluded images. Some reconstruct examples for occluded images are shown in Fig. 3.

We extract feature vectors from the reconstruct images and train attribute classification, the comparison results are shown in Table 7. From the comparison, we can see the classification performance is improved while we use patch match algorithm to reconstruct the occluded images.

Fig. 3 Examples of reconstruct images for occluded images (left is original images, middle is occluded images and right is reconstruct images for each image pair)

Table 7 The comparison result between occPETA and PETA

Methods	occPETA	reconoccPETA
Shorts	0.6900	0.7165
Jeans	0.7023	0.7471
Vnecks	0.5267	0.5717
SunGlasses	0.6051	0.6084
longhair	0.5503	0.6273
Carrying	0.6169	0.6441
Backpack	0.6689	0.7123
Logo	0.5728	0.5924

5 Conclusion

In this paper, we have proposed a pedestrian attribute classification method based on hand-crafted feature. We also considered the influence of occlusion and low resolution for attribute classification. On the basic of this method, we use Patch Match algorithm to restore the occluded images for attribute classification. Experiments has shown that our method performs better in occlusion problem and is robust in low resolution problem.

Acknowledgements This research was funded by National Science and Technology Major Project (Grant number 2015ZX01041101), Jiangsu International Science and Technology Cooperation Project (Grant number BZ2017064). This research was also funded by China Scholarship Council and Jiangsu Collaborative Innovation Center of Social Safety Science and Technology.

References

1. Lu, H., Li, Y., Mu, S., et al.: Motor Anomaly detection for unmanned aerial vehicles using reinforcement learning. IEEE Internet Things J. (2018)
2. Lu, H., Li, Y., Chen, M., et al.: Brain intelligence: go beyond artificial intelligence. Mob. Netw. Appl. (2017)

3. Ferrari, V., Zisserman, A.: Learning visual attributes. In: Proceedings of NIPS (2008)
4. Siddiquie, B., Feris, R.S., Davis, L.S.: Image ranking and retrieval based on multi-attribute queries. In: Proceedings of CVPR (2011)
5. Zhang, N., Paluri, M., Ranzato, M., Darrell, T., Bourdev, L.: Panda: pose aligned networks for deep attribute modeling. In: Proceedings of CVPR (2014)
6. Serikawa, S., Lu, H.: Underwater image dehazing using joint trilateral filter. Comput. Electr. Eng. **40**(1), 41–50 (2014)
7. Lu, H., Li, B., Zhu, J., et al.: Wound intensity correction and segmentation with Convolutional neural networks. Concurr. Comput. Pract. Exp. (2017)
8. Layne, R., Hospedales, T.M., Gong, S., Mary, Q.: Person re-identification by attributes. In: Proceedings of BMVC (2012)
9. Zhu, J., Liao, S., Lei, Z., Yi, D., Li, S.Z.: Pedestrian attribute classification in surveillance: database and evaluation. In: Proceedings of ICCV Workshops (2013)
10. Deng, Y., Luo, P., Loy, C.C., Tang, X.: Pedestrian attribute recognition at far distance. In: Proceedings of ACM Multimedia (2014)
11. Sun, Z., Yuan, X., Bebis, G., et al.: Neural-network-based gender classification using genetic search for eigen-feature selection. In: Proceedings of the 2002 International Joint Conference on Neural Networks, pp. 2433–2438 (2002)
12. Shakhnarovich, G., Viola, P.A., Moghaddam, B.: A unified learning framework for real time face detection & classification. In: International Conference on Automatic Face and Gesture Recognition, pp. 14–21 (2002)
13. Lian, H.C., Lu, B.L., Takikawa, E., et al.: Gender recognition using a min-max modular support vector machine. In: Advances in Natural Computation, pp. 438–441. Springer, Berlin, Heidelberg (2005)
14. Jain, A., Huang, J., Fang, S.: Gender identification using frontal facial images. In: IEEE International Conference on Multimedia and Expo, 2005, ICME 2005, p. 4. IEEE (2005)
15. Yacoob, Y., Davis, L.S.: Detection and analysis of hair. IEEE Trans. Pattern Anal. Mach. Intell. **28**(7), 1164–1169 (2006)
16. Kozlowski, L.T., Cutting, J.E.: Recognizing the sex of a walker from a dynamic point-light display. Atten. Percept. Psychophys. **21**(6), 575–580 (1977)
17. Moghaddam, B., Yang, M.H.: Learning gender with support faces. IEEE TPAMI **24** (2002)
18. Chen, H., Xu, Z.J., Liu, Z.Q., et al.: Composite templates for cloth modeling and sketching. In: CVPR, New York, NY, USA, pp. 943–950 (2006)
19. Gallagher, A.C., Chen, T.: Clothing cosegmentation for recognizing people. In: Computer Vision and Pattern Recognition, Anchorage, Alaska, USA, pp. 1–8 (2008)
20. Bourdev, L., Maji, S., Malik, J.: Describing people: poselet-based attribute classification. In: 2011 IEEE International Conference on Computer Vision (ICCV), IEEE, pp. 1543–1550 (2011)
21. Chen, H., Gallagher, A., Girod, B.: Describing clothing by semantic attributes. In: Computer Vision ECCV 2012, pp. 609–623. Springer, Berlin, Heidelberg (2012)
22. Dean, J., Corrado, G., Monga, R., Chen, K., Devin, M., Mao, M., Senior, A., Tucker, P., Yang, K., et al.: Large scale distributed deep networks. In: Advances in Neural Information Processing Systems, pp. 1223–1231 (2012)
23. Krizhevsky, A., Sutskever, I., Hinton, G.E.: Image net classification with deep convolutional neural networks. In: NIPS (2012)
24. Fabbri, M., Calderara, S., Cucchiara, R.: Generative adversarial models for people attribute recognition in surveillance. In: 2017 14th IEEE International Conference on Advanced Video and Signal Based Surveillance (AVSS), pp. 1–6
25. Barnes, C., Shechtman, E., Finkelstein, A., Goldman, D.: PatchMatch: a randomized correspondence algorithm for structural image editing. TOG, **28**(3), 24:1–24:11 (2009)

Adaptive Block Compressive Sensing for Noisy Images

Hui-huang Zhao, Paul L. Rosin, Yu-Kun Lai, Jing-hua Zheng and Yao-nan Wang

Abstract This paper develops a novel adaptive gradient-based block compressive sensing (AGbBCS_SP) methodology for noisy image compression and reconstruction. The AGbBCS_SP approach splits an image into blocks by maximizing their sparsity, and reconstructs images by solving a convex optimization problem. The main contribution is to provide an adaptive method for block shape selection, improving noisy image reconstruction performance. Experimental results with different image sets indicate that our AGbBCS_SP method is able to achieve better performance, in terms of peak signal to noise ratio (PSNR) and computational cost, than several classical algorithms.

Keywords Block Compressive Sensing (CS) · Adaptive · Convex Optimization Sparsity

1 Introduction

Compressive Sensing (CS) is a sampling paradigm that provides signal compression at a significantly lower rate than the Nyquist rate [8]. It has been successfully applied in a wide variety of applications in recent years, including image process-

H.-h. Zhao (✉) · J.-h. Zheng
Hunan Provincial Key Laboratory of Intelligent Information Processing and Application, Hunan, China
e-mail: happyday.huihuang@gmail.com

H.-h. Zhao · J.-h. Zheng
College of Computer Science and Technology, Hengyang Normal University, Hengyang, China

P. L. Rosin · Y.-K. Lai
School of Computer Science and Informatics, Cardiff University, Cardiff, UK

Y.-n. Wang
College of Electrical and Information Engineering, Hunan University, Changsha, China
e-mail: yaonan@hnu.cn

H. Lu (ed.), *Cognitive Internet of Things: Frameworks, Tools and Applications*, Studies in Computational Intelligence 810,
https://doi.org/10.1007/978-3-030-04946-1_38

ing [5, 15, 18], Internet of things [17, 23], video [16, 26], and solder joint image compression [28].

In this paper, we develop a novel CS algorithm named AGbBCS_SP for image compression and reconstruction, which is particularly beneficial for noisy images. The main contributions of this paper are summarized as follows:

- We propose a multi-shape block splitting strategy for block Compressive Sensing. Besides splitting the image into square blocks, we also split it into rectangular blocks with different shapes.
- Our adaptive Compressive Sensing scheme makes a practical assumption that only a small, randomly chosen image part requires to be known. Our method automatically selects the appropriate block shape which maximizes the sparsity of the signal in the known region.
- We propose an adaptive approach to selecting a suitable control factor, by comparing the sparsity of the reconstruction results.

2 Related Work

Compressive Sensing Algorithms: In recent years, many methods have been proposed which can be roughly divided into several categories: (1) Convex Optimization Algorithms. These techniques solve a convex problem which is used to approximate the target signal, including Greedy Basis Pursuit (GBP) [12]. (2) Greedy Iterative Algorithms. These methods include Orthogonal Matching Pursuit (OMP) [24], Compressive Sampling MP (CoSaMP) [20] and Subspace Pursuit (SP) [6]. (3) Iterative Thresholding Algorithms. Such as Hard thresholding [2]. (4) Combinatorial / Sublinear Algorithms. such as Heavy Hitters on Steroids (HHS) [22]. (5) Non Convex Minimization Algorithms. This techniques recover compressive sensing signals from far less measurements by replacing the l_1-norm by the l_p-norm where $p \leq 1$ [4]. (6) Bregman Iterative Algorithms. When applied to CS problems, the iterative approach using Bregman distance regularization achieves reconstruction in four to six iterations [21].

Block Based Compressive Sensing (BCS): In the methods above, a column or row of an image is normally viewed as a vector. But in many applications the nonzero elements of sparse vectors tend to cluster in blocks [9]. In order to improve the performance, [11] proposed and studied block compressive sensing for natural images and this method involves Wiener filtering and projection onto the convex set and hard thresholding in the transform domain. Mun and Fowler [19] proposed a BCS_SPL method with a variant of projected Landweber (PL) iteration and smoothing. Fowler et al. [10] developed BCS_SPL methods based on a smoothed projected Landweber reconstruction algorithm. BCS_SPL has obvious defects since the Wiener filter and iterative projected Landweber discard partial information in the image. Unde and Deepthi [25] proposed a block compressed sensing method based on iterative

re-weighted l_1 norm minimization. Zhao et al. [27] developed a block compressed sensing method for solder joint images based on CoSaMP.

3 Compressive Sensing Methodology

Given an image, the first step of CS is the construction of a k-sparse representation, where k is the number of the non-zero entries of the sparse signal.And most natural signals can be made sparse by applying orthogonal transforms, such as Wavelet Transform, Fast Fourier Transform and Discrete Cosine Transform (DCT) [3].

For a noisy image, Compressive Sensing can be represented as:

$$y = \Phi \Psi s + w, \tag{1}$$

where w is an N-dimensional noise signal (or measurement error), Ψ is an $N \times N$ orthogonal basis matrix and Φ is an $M \times N$ random measurement matrix ($M < N$). As expected, signal x Eq. (1) may be estimated from measurement y by solving the convex minimization problem [20] as follows.

$$\underset{x}{argmin} \, \|\Phi x - y\|_2^2 + \lambda \|x\|_1. \tag{2}$$

Generally Eq. (2) is a constrained minimization problem of a convex function. One of the simplest methods for solving a convex minimization problem is the gradient-based algorithm which generates a sequence x_k via

$$x_0 \in \mathbb{R}^N, x_k = x_{k-1} - t_k \nabla g(x_{k-1}), \tag{3}$$

where $g(x)$ is a convex function, and $t_k > 0$ is a suitable step size. For a signal in Eq. (1), let us think about an objective function $F(x) = g(x) + f(x)$, where $g(x)$ is convex, and $f(x) = \lambda \|x\|_1$. In our method, it is more natural to study the closely related problem Eq. (2)

At point x_{k-1}, the function $F(x)$ can be approximated by a quadratic function

$$Q_L(x, x_{k-1}) = g(x_{k-1}) + < (x - x_{k-1}), \nabla g(x_{k-1}) > + \frac{1}{2t_k} \| x - x_{k-1} \|_2^2, \tag{4}$$

This problem can be solved by the gradient-based method, in which t_k is replaced by a constant $1/L$ which is related to the Lipschitz constant [1].

4 The Adaptive Block Compressive Sensing with Sparsity

4.1 Multi-shape Block Split Strategy

Given an $N_1 \times N_2$ image, it is split into small blocks of size $n_1 \times n_2$. Let f_i represent the vectorized signal of the i-th block through raster scanning, i=1, 2, ..., K, and $K = \frac{N_1 N_2}{n_1 n_2}$. One is able to get an m-dimensional sampled vector y_B through the following linear transformation,

$$y_B = \Phi_B f_i, \tag{5}$$

where Φ_B is an $m \times n_1 n_2$ measurement matrix, $m \ll n_1 n_2$. The block CS method is memory efficient as we just need to store an $m \times n_1 n_2$ Gaussian random matrix Φ_B, rather than a full $M \times N_1 N_2$ one. Small data requires less memory storage and allows faster processing, while large data produces more accurate reconstruction.

In existing methods, the blocks in the Block Compressive Sensing are fixed as squares. However, there are many different block aspect ratios with the same number of pixels. Unlike common methods, we split the image into different shapes. Given an $N \times N$ image (assuming N is a power of 2 for simplicity), the shape of block is $w \times h$, so

$$\begin{cases} w = 2^a, \\ h = 2^b, \\ a = 0, 1, 2, 3, \ \ldots \ \log_2 N. \\ b = \log_2 N - a, \end{cases} \tag{6}$$

For example, 9 aspect ratios are defined to split a 256×256 image with the following block-shapes: 1×256, 2×128, 4×64, 8×32, 16×16, 32×8, 64×4, 128×2 and 256×1. As we will discuss later in Sect. 5.1, some block shapes (especially those closer to squares) are more likely to provide effective reconstruction. Also, using closer-to-square blocks also means that these blocks can be fit in smaller square regions, e.g. 8×32, 16×16, 32×8 blocks can be fit in 32×32 squares, whereas 1×256 blocks cannot. As we will discuss in Sect. 4.2, this makes adaptive selection more effective. Detailed discussions will be presented in experimental results.

4.2 Adaptive Block Shape Selection

In most cases, the information of the entire signal (image) is unknown. It is hard to select one block shape from several shapes if the image content is unknown. So we make a practical assumption that only a small part of the image is known and propose a new approach based on sparsity for block shape selection. We highlight the block shape selection step in our approach.

Algorithm 1: Block Shape Selection with Sparsity

Input : An input image s, a percentage p;
Output: The selected block size $w \times h$
:

Procedure:
Step 1:Split s into T blocks with size of $P \times Q$,$K_1 = T \times p$
K_1 regions (each of size $P \times Q$) are selected, and those regions collectively form $\hat{s}$.
Step 2: K_2 block shapes are considered: $w_1 \times h_1, w_2 \times h_2, ..., w_{K_2} \times h_{K_2}$.
$\hat{s}$ is split into K_3 blocks altogether with $w_k \times h_k$ through Eq. (6)
For the k-th block size $\hat{s}$=$\{\tilde{s}^{(k)}(1), \tilde{s}^{(k)}(2), \ldots, \tilde{s}^{(k)}(K_3)\}$.
for $k = 1$ *to* K_2 **do**
  $\hat{s}^{(k)} = \emptyset$.
  for $j = 1$ *to* K_3 **do**
    Add a new signal $\tilde{s}^{(k)}(j)$ to $\hat{s}^{(k)}$.
  end
end
for $k = 1$ *to* K_2 **do**
  Get $\hat{x}^k$ through Eq. (2) with $\hat{s}^{(k)}$
  $S_{p_k} = l_\varepsilon^0\left(\hat{x}^k \leq \varepsilon\right)$ through Eq. (7),
end
$S_{p_d} = \max\{S_{p_1}, S_{p_2}, ..., S_{p_k}\}$
The d-th block shape is chosen, and the block size is $w_d \times h_d$.
Output w_d and h_d.

First, we randomly select a small percentage of image pixels that make up known regions. These regions are then split into smaller block shapes considering the various aspect ratios specified in Eq. (6). We reconstruct them, calculate their sparsity, and then select the block shape which maximizes sparsity.

For an image, firstly, it is split into T non-overlapping regions with size $P \times Q$, where $K_1 = T \times p$ are known regions, and p is the proportion. So K_1 regions (size $P \times Q$) are selected. There are K_2 block sizes in Eq. (6) $w_k \times h_k$, $(k = 1, 2, ..., K_2)$ that fit within $P \times Q$ regions. Then for K_1 regions (size $P \times Q$), they are split into K_3 blocks with size of $w_k \times h_k$. Given that $\hat{x}$ is defined as the reconstructed result in Eq. (2), the summed sparsity of its blocks is defined as

$$S_p = l_\varepsilon^0\left(\hat{x}_{i,j} \leq \varepsilon\right), \tag{7}$$

where $\hat{x}_{i,j}$ is the element at location (i, j) in $\hat{x}$ the reconstructed result and $l_\varepsilon^0(\cdot)$ is a function defined in [13]. Thus, we propose the adaptive block shape selection with sparsity algorithm whose details are shown in Algorithm 1. For example, given a 256×256 image, we set $p = 0.25$. We consider splitting the image into $T = 64$ regions of size $P \times Q = 32 \times 32$, and $K_1 = 64 \times 0.25 = 16$ blocks are randomly selected, so that $K_3 = 16 \times 4 = 64$. With 32×32 regions, we consider $K_2 = 3$ block sizes 8×32, 16×16 and 32×8 which fit within the region.

Algorithm 2: Adaptive Gradient-based Block Compressive Sensing

Input : An image I of size $N \times N$; a sparse signal transform matrix $\Psi \in \mathbb{R}^{N\times N}$; a measurement matrix $\Phi \in R^{M\times N}$; M is the sample number; Lipschitz constant $L = 0.5$; the number of iterations $J = M/4$.

Output: The reconstructed image s.

:

Procedure

Step 1: I is split into T regions, and p is a percentage, $K_1 = T \times p$ regions are selected. One block shape $W \times H$ is chosen by Algorithm 1, I is split into K_4 blocks with $W \times H$ block size.

Step 2: Set the block counter k=1, $\lambda = 1$, and the iteration counter j=1, $S_{p_{max}} = 0$.

while $\lambda \leq 100$ **do**

  while $k \leq K_2$ **do**

    Transform each block into a data vector; $y_0 = x_0 = 0 \in R^N$, $t_1 = 1$;

    while $j \leq J$ **do**

      $z_j^k = PL(y_j^k)$, solved through [28].

      $t_{j+1}^k = \frac{1+\sqrt{1+4t_j^{k2}}}{2}$

      x_j^k=argmin$\{F(x^k) : x^k = z_j^k, x_{j-1}^k\}$

      $y_{j+1}^k = x_j^k + \frac{t_j^k}{t_{j+1}^k}(z_j^k - x_j^k) + \frac{t_j^k - 1}{t_{j+1}^k}(x_j^k - x_{j-1}^k)$

    end

    Collect all the $\hat{x}_J^k$ to form $\hat{x}$.

  end

  $S_p = l_\varepsilon^0\left(\hat{x} \leq \varepsilon\right)$ through Eq. (7),

  If $S_p > S_{p_{max}}$

    $S_{p_{max}} = S_p$

    $\hat{\hat{x}} = \hat{x}$

  Endif

end

$s' = \Psi^{-1}\hat{\hat{x}}$.

For each one-dimensional data vector in s', transform it into a $W \times H$ block.

Collect all the blocks to form the reconstructed image s.

4.3 Adaptive Block Compressive Sensing with Sparsity Algorithm

During the minimization of Eq. (2), λ can be used to improve the result with different sampling rate. Usually $\lambda = M/4$, but in our proposed method, we set $\lambda \in [1, 100]$, and we adaptively choose λ such that the largest sparsity is achieved. Thus, we propose our AGbBCS_SP algorithm whose details are shown in Algorithm 2, where the basic sparse optimization is based on [28].

5 Experiments and Discussion

In order to evaluate the quality of the reconstructed results, many researchers used the Peak Signal to Noise Rate (PSNR) to measure the result quality in image processing. In our study, the PSNR is also used to compare the experimental results. The experiments were implemented on a Intel Core i5 with 2.70 GHz CPU. The test images include some standard ones (such as *woman*), INRIA Holidays dataset (812 images) [14] to which $salt\&pepper$ noise is added with $\delta = 0.05$ by default. Since some methods require the image size to be a power of 2, we have cropped all the images to 256×256.

5.1 Experiments with Different Block Aspect Ratios

Given a 256×256 image, the block-shapes 1×256, 2×128, 4×64, 8×32, 16×16, 32×8, 64×4, 128×2 and 256×1, are considered. We used the INRIA Holidays dataset, containing 812 images and the noise is set $\delta = 0.05$. With sample number $M = 128$ and $\lambda = M/4$, we run different block shapes. Then we select the best shape, and the number of times that each block shape is best is shown in Fig. 1a, b for the two datasets, respectively.

We can find that a square block cannot always get the best results, and 8×32, 16×16, and 32×8 can achieve the top three results. So in our AGbBCS_SP method, three block shapes are chosen. As described above, we consider splitting a 256×256 image into 64 regions, each of size 32×32, and $64 \times 0.25 = 16$ blocks are randomly selected to calculate sparsity in the three block shapes. Then we choose the block shape which can get maximum sparsity for the given image.

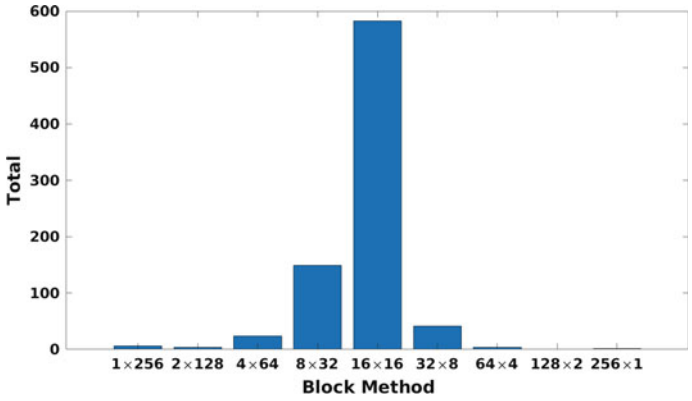

Fig. 1 The number of images that each block shape is best in the INRIA Holidays datasets

5.2 The Comparison of Reconstruction Results

Now let us compare the proposed AGbBCS_SP with the popular methods SP [6], OMP [24], BOMP [9], CoSaMP [7], BCoSaMP [27] and BCS_SPL [10]. In BOMP, BCoSaMP and BCS_SPL, the block size is set to a square block (size 16×16). The test image *woman* is used (size 256×256) with added noise $\delta = 0.03$, as shown in Fig. 2a. The reconstruction results based on popular methods with sample number $M = 200$ are shown in Fig. 2b–g and the reconstruction result based on our AGbBCS_SP with the same sample number, is shown in Fig. 2h.

We can see that our method can achieve a better result than SP, OMP, BOMP, CoSaMP, BCoSaMP and BCS_SPL. With more noise added and $M = 128$ in test image *woman*, the PSNR comparisons are shown in Fig. 3a. One can see from Fig. 3b that when $\delta > 0.025$, our method achieves a better PSNR result than BCS_SPL. With increasing samples in the noisy image (see Fig. 2a) the PSNR comparisons are shown in Fig. 3b that. And compared to SP, OMP, BOMP, CoSaMP and BCoSaMP, our method can achieve best result.

In the next experiment, we used the INRIA Holidays datasets with added noise $\delta = 0.05$. The comparison results are shown through the experiments with different sample numbers (from 0.1 to 0.9). The results are shown in Fig. 4a, b.

From Fig. 4, one can see that the proposed approach can always obtain better results in terms of PSNR as compared to SP, OMP, BOMP, CoSaMP, and BCoSaMP. Increasing the number of samples can improve the reconstruction results. When the sampling rate $u = M/N > 0.3$, the proposed algorithm can achieve better results than BCS_SPL too. With an increasing number of samples, BCS_SPL gets worse reconstruction results.

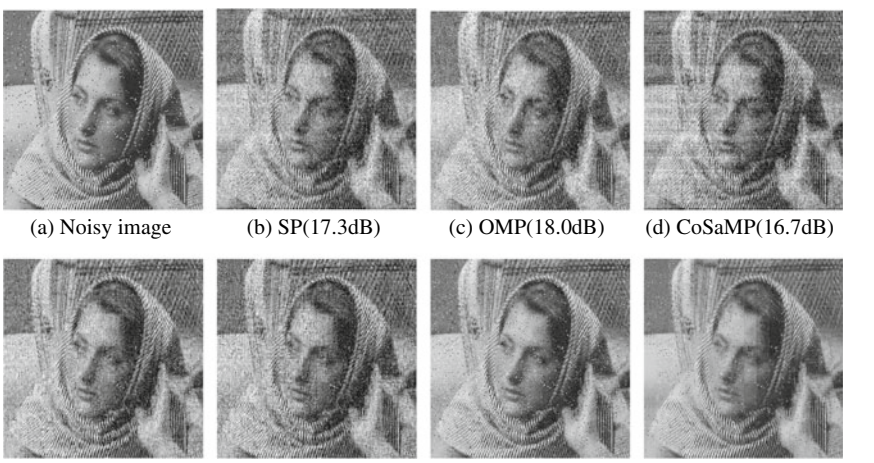

(a) Noisy image (b) SP(17.3dB) (c) OMP(18.0dB) (d) CoSaMP(16.7dB)

(e) BOMP(18.1dB) (f) BCoSaMP(17.0dB) (g) BCS_SPL(20.3dB) (h) AGb-BCS_SP(21.2dB)

Fig. 2 Reconstruction results based on different methods

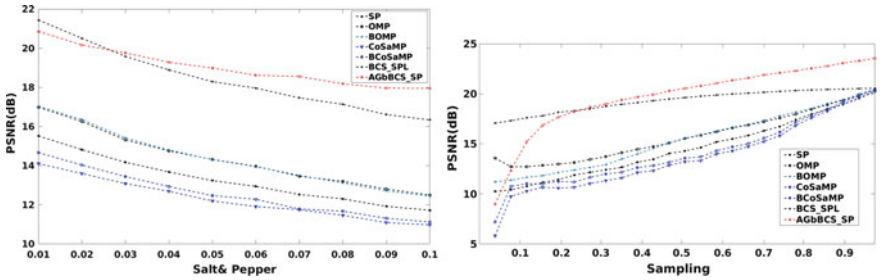

(a) Different noise level (b) Different sampling

Fig. 3 PSNR comparison based on different noise level added

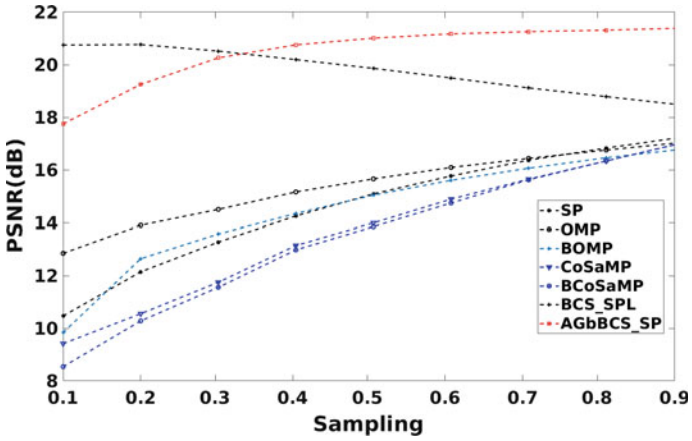

Fig. 4 Quantitative comparison based on different methods for INRIA datasets

6 Conclusions

This paper proposes an adaptive gradient-based block compressive sensing (AGb-BCS_SP) approach on the basis of the sparsity of the image. Experiments reveal that, in block compressive sensing, the square block shape cannot always produce the best results. Our algorithm can adaptively achieve better results by using the sparsity of pixels to adaptively select block shape. The proposed algorithm can achieve the best results in average PSNR than classical algorithms, SP, OMP, BOMP, CoSaMP, BCS_SPL and BCoSaMP with different datasets.

Acknowledgements This work was supported by National Natural Science Foundation of China (61733004, 61503128, 61602402), the Science and Technology Plan Project of Hunan Province (2016TP102), Scientific Research Fund of Hunan Provincial Education Department (16C0226), and Hunan Provincial Natural Science Foundation (2017JJ4001). We would like to thank NVIDIA for the GPU donation.

References

1. Beck, A., Teboulle, M.: A fast iterative shrinkage-thresholding algorithm for linear inverse problems. Siam J. Imaging Sci. **2**(1), 183–202 (2009)
2. Blumensath, T., Davies, M.E.: Iterative hard thresholding for compressed sensing. Appl. Comput. Harmon. Anal. **27**(3), 265–274 (2009)
3. Cai, T.T., Wang, L.: Orthogonal matching pursuit for sparse signal recovery with noise. IEEE Trans. Inf. Theory **57**(7), 4680–4688 (2011)
4. Chartrand, R.: Exact reconstruction of sparse signals via nonconvex minimization. Signal Process. Lett. IEEE **14**(10), 707–710 (2007)
5. Cui, H., Zhang, S., Gan, X., Shen, M., Wang, X., Tian, X.: Information recovery via block compressed sensing in wireless sensor networks. In: 2016 IEEE International Conference on Communications (ICC), pp. 1–6 (2016)
6. Dai, W., Milenkovic, O.: Subspace pursuit for compressive sensing signal reconstruction. IEEE Trans. Inf. Theory **55**(5), 2230–2249 (2009)
7. Davenport, M.A., Needell, D., Wakin, M.B.: Signal space cosamp for sparse recovery with redundant dictionaries. IEEE Trans. Inf. Theory **59**(10), 6820–6829 (2013)
8. Donoho, D.L.: Compressed sensing. IEEE Trans. Inf. Theory **52**(4), 1289–1306 (2006)
9. Eldar, Y.C., Kuppinger, P., BÃűcskei, H.: Block-sparse signals: uncertainty relations and efficient recovery. IEEE Trans. Signal Process. **58**(6), 3042–3054 (2010)
10. Fowler, J.E., Mun, S., Tramel, E.W.: Multiscale block compressed sensing with smoothed projected landweber reconstruction. In: Signal Processing Conference, 2011 European, pp. 564–568 (2015)
11. Gan, L.: Block compressed sensing of natural images. In: 2007 15th International Conference on Digital Signal Processing, pp. 403–406. IEEE (2007)
12. Huggins, P.S., Zucker, S.W.: Greedy basis pursuit. IEEE Trans. Signal Process. **55**(7), 3760–3772 (2007)
13. Hurley, N., Rickard, S.: Comparing measures of sparsity. IEEE Trans. Inf. Theory **55**(10), 4723–4741 (2009)
14. Jegou, H., Douze, M., Schmid, C.: Hamming embedding and weak geometric consistency for large scale image search. In: Computer Vision-ECCV 2008, pp. 304–317 (2008)
15. Lu, H., Li, B., Zhu, J., Li, Y., Li, Y., Xu, X., He, L., Li, X., Li, J., Serikawa, S.: Wound intensity correction and segmentation with convolutional neural networks. Concurr. Comput.: Pract. Exp. **29**(6), e3927 (2017)
16. Lu, H., Li, Y., Mu, S., Wang, D., Kim, H., Serikawa, S.: Motor anomaly detection for unmanned aerial vehicles using reinforcement learning. IEEE Internet Things J. (2017)
17. Lu, H., Li, Y., Chen, M., Kim, H., Serikawa, S.: Brain intelligence: go beyond artificial intelligence. Mob. Netw. Appl. **23**(2), 368–375 (2018)
18. Lu, H., Li, Y., Uemura, T., Kim, H., Serikawa, S.: Low illumination underwater light field images reconstruction using deep convolutional neural networks. Futur. Gener. Comput. Syst. (2018)
19. Mun, S., Fowler, J.E.: Block compressed sensing of images using directional transforms. In: 2009 16th IEEE International Conference on Image Processing (ICIP), pp. 3021–3024. IEEE (2009)
20. Needell, D., Tropp, J.A.: Cosamp: Iterative signal recovery from incomplete and inaccurate samples. Appl. Comput. Harmon. Anal. **26**(3), 301–321 (2009)
21. Osher, S., Mao, Y., Dong, B., Yin, W.: Fast linearized bregman iteration for compressive sensing and sparse denoising. arXiv preprint arXiv:1104.0262 (2011)
22. Qaisar, S., Bilal, R.M., Iqbal, W., Naureen, M., Lee, S.: Compressive sensing: from theory to applications, a survey. J. Commun. Netw. **15**(5), 443–456 (2013)
23. Serikawa, S., Lu, H.: Underwater image dehazing using joint trilateral filter. Comput. Electr. Eng. **40**(1), 41–50 (2014)
24. Tropp, J.A., Gilbert, A.C.: Signal recovery from random measurements via orthogonal matching pursuit. IEEE Trans. Inf. Theory **53**(12), 4655–4666 (2007)

25. Unde, A.S., Deepthi, P.: Block compressive sensing: individual and joint reconstruction of correlated images. J. Vis. Commun. Image Represent. **44**, 187–197 (2017)
26. Zhao, C., Ma, S., Zhang, J., Xiong, R., Gao, W.: Video compressive sensing reconstruction via reweighted residual sparsity. IEEE Trans. Circuits Syst. Video Technol. **27**(6), 1182–1195 (2017)
27. Zhao, H., Wang, Y., Qiao, Z., Fu, B.: Solder joint imagery compressing and recovery based on compressive sensing. Solder. Surf. Mt. Technol. **26**(3), 129–138 (2014)
28. Zhao, H., Zhao, H., Chen, J., Chen, J., Xu, S., Xu, S., Wang, Y., Wang, Y., Qiao, Z., Qiao, Z.: Compressive sensing for noisy solder joint imagery based on convex optimization. Solder. Surf. Mt. Technol. **28**(2), 114–122 (2016)

A No-Ambiguity Acquisition Algorithm Based on Correlation Shift for BOC (N, N)

Xiyan Sun, Fang Hao, Yuanfa Ji, Suqing Yan, Qinwen Miao and Qiang Fu

Abstract In the course of GPS modernization, Binary Offset Carrier (BOC) modulation technology is adopted to realize rational utilization of frequency, to avoid mutual interference between navigation signal frequency bands. Due to the multiple peaks of the auto-correlation function (ACF) of BOC modulated signal, an acquisition algorithm is proposed in this paper. This new method analyzed sub-correlation function of ACF, then, in the process of local design, it is designed one sub-signal and half-chip-shift sub-signal. It can achieve the homologous sub-correlation function of ACF by respectively correlating two local signals and received signal. The complexity of the algorithm as well as its detection probability based on the constant false alarm rate is analyzed. Simulations show that the proposed method can effectively solve the problem of ambiguous acquisition.

Keywords BOC · Sub-correlation · Unambiguity · Correlation-shift
Side-peak cancellation

1 Introduction

Nowadays, the application of satellite navigation has been deepened to all walks of life, and higher requirements are placed on the positioning accuracy and reliability of navigation systems. Therefore, a new modulation method is proposed—Binary Offset Carrier (BOC) modulation technique. Compared with the traditional BPSK (Binary Phase Shift Keying) modulation technology, BOC modulation technique on the one hand makes the spectrum of the signal move away from the center frequency band, avoiding the overlap with the traditional signal spectrum, and making full use of the limited frequency band resources. On the other hand, the BOC modulation technology decreases the auto-correlation peak width of BOC signal, which

X. Sun · F. Hao · Y. Ji (✉) · S. Yan · Q. Miao · Q. Fu
Guangxi Key Laboratory of Precision Navigation Technology and Application,
Guilin University of Electronic Technology, Guilin 541004, China
e-mail: jiyuanfa@163.com

H. Lu (ed.), *Cognitive Internet of Things: Frameworks, Tools and Applications*, Studies in Computational Intelligence 810,
https://doi.org/10.1007/978-3-030-04946-1_39

improves the positioning accuracy and anti-multipath performance. However, due to the introduction of subcarriers by BOC modulation, the auto-correlation function has multiple secondary peaks, which can easily, result in the problem of acquisition ambiguity during the receiver synchronization process.

In order to solve the problem of acquisition ambiguity, many solutions have been proposed. In recent years, the time-domain processing scheme [1–6] has received a great deal of attention. From the earliest proposed ASPeCT (Auto-correlation Side-Peak Cancellation Technique) algorithm [1, 2], the side-peak of autocorrelation function was effectively suppressed, but it is only suitable for sine modulation not for cosine modulated BOC signals. GRASS (General Removing Ambiguity via Side-peak Suppressing) [3, 4] algorithm has the ability to eliminate side-peaks by building a local auxiliary signal. In the literature [3], the method is suitable for high-order BOC signals. And the literature [4] constructs two local signals, but the pulse signal width selection is not flexible enough. In addition, the reconstruction algorithm about time domain signals is also a hot research direction. The core idea is [5–7]: splitting the correlation function with side-peaks, and then performing an algorithm operation, and recombined them to form a new correlation function with no side-peak correlation function.

This paper starts from the perspective of the sub-correlation functions of BOC autocorrelation function. Based on the shape characteristics of the sub-correlation functions, the local signal is designed. Two sub-correlation functions are obtained by correlating locally generated sub-signals with the received signals. A simple combination was used to obtain the correlation function with no side-peaks. Simulations show that this method effectively eliminates the side-peaks of autocorrelation and maintains the narrow-band correlation peaks. The feasibility of the algorithm is verified by the acquisition simulation diagram, detection probability and computational complexity.

2 Algorithm Analysis

2.1 BOC Modulation Signal Model

The BOC signal is divided into sine-BOC (sBOC) and cosine-BOC (cBOC) signals. The BOC baseband signal can be expressed as:

$$S_{sBOC}(t) = c(t)\text{sign}[\sin(2\pi f_{sc}t)] \tag{1}$$

$$S_{cBOC}(t) = c(t)\text{sign}[\cos(2\pi f_{sc}t)] \tag{2}$$

where $c(t)$ is the spread spectrum code, sign is the sign function, and f_{sc} is the frequency of the sub-carriers. For a BOC (m, n) modulation signal, where m represents the subcarrier frequency f_{sc} with a rate of m * 1.023 MHz, n denotes the

rate n * 1.023 MHz spreading code frequency f_c. The modulation order is defined as $N = 2m/n$.

Define rectangular pulse signal $p_i(t)$ as

$$p_i(t) = \begin{cases} 1 \; iT_c/N \le t \le (i+1)T_c/N \\ 0 \; others \end{cases} \tag{3}$$

In the formula, $i = 0, 1, 2, 3 \ldots N - 1$, $T_c = 1/f_c$ represents the length of a spread spectrum code, so the baseband signal for sBOC (m, n) can be expressed as:

$$S_{BOC}(t) = \sum_{i=-\infty}^{+\infty} \sum_{j=0}^{N-1} [c(t)(-1)^j] P_j(t - iT_C) \tag{4}$$

2.2 BOC Signal Sub-correlation Function

Assuming that the spread spectrum code sequence has an ideal auto-correlation property, the autocorrelation function of the BOC direct-spread spectrum signal can be expressed as:

$$\begin{aligned} R(\tau) &= E[s_{BOC}(t) s_{BOC}(t+\tau)] \\ &= \frac{1}{T_C} \int_0^{T_C} s_{BOC}(t) s_{BOC}(t+\tau) dt \\ &= \sum_{i=0}^{N-1} R_{BOC,i}(\tau) \end{aligned} \tag{5}$$

in the formula:

$$R_{BOC,i}(\tau) = \frac{1}{T_C} \int_0^{T_C} \sum_{j=0}^{N-1} (-1)^j P_j(t)(-1)^i P_i(t+\tau) dt \tag{6}$$

The formula (4) BOC signal can be written as:

$$s_{BOC}(t) = \sum_{i=0}^{N-1} s_{BOC,i}(t) \tag{7}$$

where:

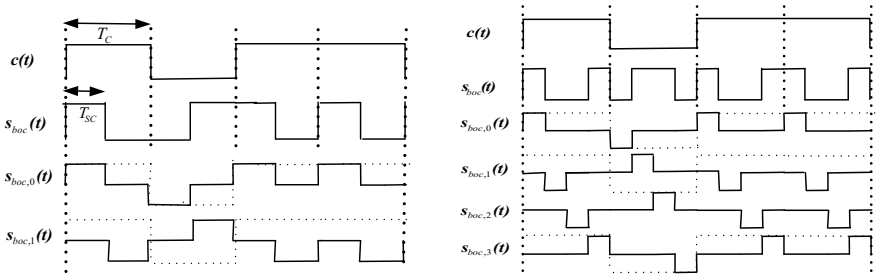

(a) sBOC (1, 1) sub-signal waveform (b) cBOC(1,1) sub-signal waveform

Fig. 1 BOC (1, 1) modulation signal and its decompositions

$$s_{BOC,i}(t) = \sum_{j=-\infty}^{+\infty} c(t)(-1)^i P_i(t - jT_C) \tag{8}$$

From it can be seen that the BOC (m, n) signal can be separated into N sub-signals $s_{BOC,i}(t), i = 0, 1, 2, 3 \ldots N - 1$. The i-th rectangular pulse in each spread chip of each sub-signal $s_{BOC,i}(t)$ remains unchanged, and the rest becomes 0 value. Therefore, the sBOC (1, 1) signal can be separated into two sub-signals. The cBOC (1, 1) signal can be separated into four sub-signals. All sub-signals are shown in Fig. 1.

According to Fig. 1, those separated sub-signals correlated with the received signals, and the result is $R_{BOC,i}(\tau)$, so the Eq. (6) can be further expressed as:

$$R_{BOC,i}(\tau) = \frac{1}{T_C} \int_0^{T_C} s_{BOC}(t) s_{BOC,i}(t + \tau) dt \tag{9}$$

In Eq. (9), $i = 0, 1, 2, 3 \ldots N - 1$. Therefore, each sub-signal correlates with the received BOC signals here can be called a sub-correlation function. All sub-correlation functions are added to obtain the autocorrelation function of the BOC (m, n) signal.

Figure 2 shows BOC (1, 1) auto-correlation function and sub-correlation function. For sBOC (1, 1) signal, each sub-correlation function is formed by the superposition of two triangular pulses; for cBOC (1, 1) signal, each a sub-correlation function is formed by the superposition of 4 triangular pulses. In addition, it can be found that for sBOC (1, 1) signal, sub-correlation function $R_{BOC,1}(\tau)$ can be obtained by sub-correlation function $R_{BOC,0}(\tau)$ if taking the opposite number and shifting left by 0.5 chips. For cBOC (1, 1) signal, the sub-correlation function $R_{BOC,2}(\tau)$ can be generated by $R_{BOC,0}(\tau)$ when takes the opposite number and shifts left by 0.5 chips. $R_{BOC,3}(\tau)$ can be obtained $R_{BOC,1}(\tau)$ using the same way. All sub-correlation functions are added to get the autocorrelation function of BOC (1, 1) signal. The autocorrelation function has side-peaks. It is possible to occur error acquisition in

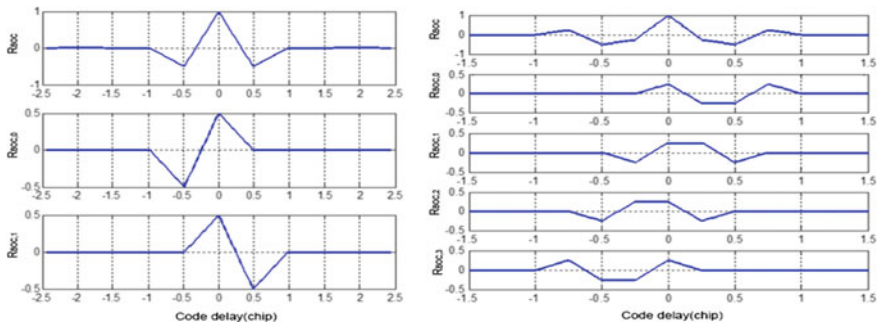

(a) sBOC(1,1) (b) cBOC(1,1)

Fig. 2 Auto-correlation and sub-correlation functions of BOC (1, 1)

acquisition process. So the key issue to be solved is how to eliminate the secondary peak for BOC (1, 1).

2.3 Correlation Shift Side-Peak Cancellation Technique (CSSPeCT)

For sBOC (1, 1) we multiply sub-correlation function $R_{BOC,1}(\tau)$ and sub-correlation function $R_{BOC,0}(\tau)$. For the cBOC (1, 1) signal, the sub-correlation function $R_{BOC,2}(\tau)$ can be obtained by sub-correlation function $R_{BOC,0}(\tau)$ if taking the opposite number and shifting to the left by 0.5 chips. $R_{BOC,3}(\tau)$ can be obtained by sub-correlation function $R_{BOC,1}(\tau)$ taking the opposite number and shifting left by 0.5 chips. Divide the sub-correlation functions into two groups: $\{R_{BOC,0}(\tau), R_{BOC,1}(\tau)\}$, $\{R_{BOC,2}(\tau), R_{BOC,3}(\tau)\}$. Add two groups of sub- correlation functions to each other:

$$R_{C1} = R_{BOC,0}(\tau) + R_{BOC,1}(\tau) \tag{10}$$

$$R_{C2} = R_{BOC,2}(\tau) + R_{BOC,3}(\tau) \tag{11}$$

R_{C1} and R_{C2} are the combined functions of the two sets of sub-correlation functions, and the combined function graphs are shown in Fig. 3.

From Fig. 3, it can be seen that the combined graphs R_{C1} and R_{C2} of the sub-functions are symmetric about the origin. The combined graphs R_{C1} and R_{C2} has equal correlation peaks at the symmetry code phases ± 0.25 and ± 0.5. This will serve as an important point to eliminate ambiguity.

After processing as in Eq. (12) and accumulating the results, it can get:

$$R_{G1} = |R_{C1}| + |R_{C2}| - |R_{C1} - R_{C2}| \tag{12}$$

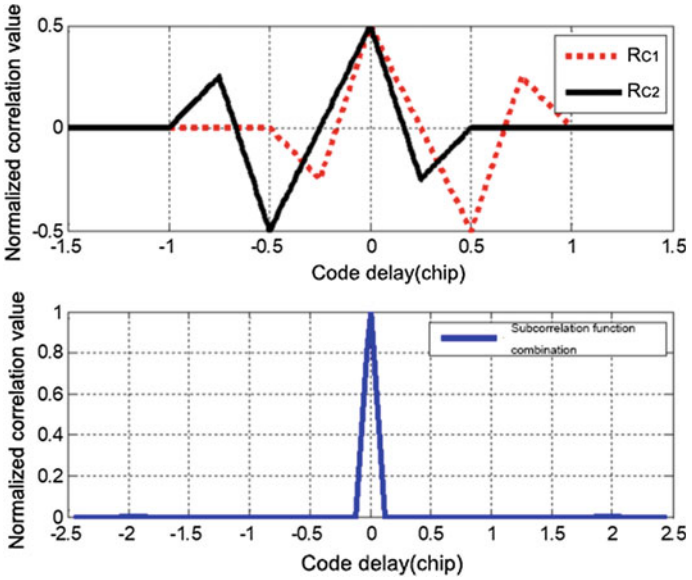

Fig. 3 Correlation function generated by optimization algorithm

Therefore, when designing the local code waveform, the receiver needs to generate two local sub-signals $s_{BOC,0}(t)$ and $s_{BOC,1}(t)$. By shifting 0.5 chips after IFFT, the sub-correlation function that composes all autocorrelation functions can be obtained. Then the combination of sub-correlation functions can be used to obtain the correlation function without side-peaks. Figure 4 below is a block diagram of the optimized acquisition algorithm for BOC (n, n).

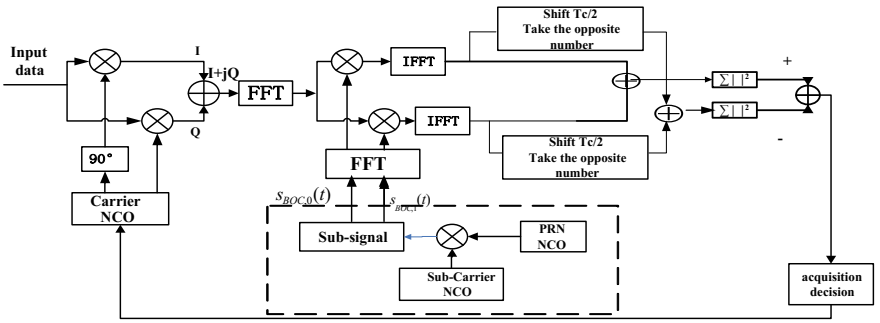

Fig. 4 Schematic diagram of correlation-shift side-peak cancellation technique acquisition optimization algorithm

3 Performance Analysis

Based on the Matlab platform, set the input signal intermediate frequency to 4.092 MHz, sampling rate is 40.92 MHz, the code phase offset is set to the 601th sampling point, the Doppler is 2500 Hz, the signal-to-noise ratio is −20 dB, compare the CSSPeCT, ASPeCT, and BPSK-LIKE acquisition methods to compare the performance of different algorithms.

3.1 2D Contrast Simulation of Acquisition Results

Figure 5 shows a two-dimensional acquisition comparison of several methods. For the acquisition of the BOC (1, 1) signal, it can be found that the optimized CSSPeCT algorithm is superior to the ASPeCTand BPSK-LIKE methods. In the main peak span, CSSPeCT main peak span of 20 sampling points (half chip width) is the same as the ASPeCT method and is better than the BPSK-LIKE method (80 sampling points, i.e. 2 chip widths); The peak-optimized CSSPeCT method is the same as the ASPeCT method and is 10% higher than the BPSK-LIKE method. In addition, compared to the ASPeCT method, the CSSPeCT method completely eliminates the influence of the secondary peak and the ASPeCT method still has two smaller secondary peaks.

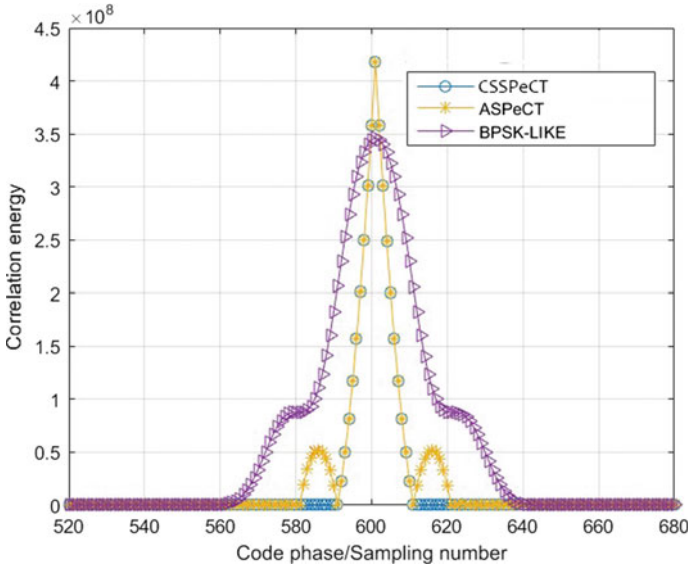

Fig. 5 Two-dimensional collation map of four acquisition methods

3.2 Detection Probability Comparison Simulation

The detection probability is the best way to measure the merits of an acquisition method.

Non-coherent detection statistics for traditional acquisition schemes can be expressed as:

$$T = \sum_{j=1}^{M} (I_j^2 + Q_j^2) \tag{13}$$

In (13)

$$\begin{cases} I_j = \sqrt{T_s C/N_0}\, \mathrm{sin}\, c(\pi \Delta f_D T_s) R(\Delta\tau) \cos(\Delta\varphi) + N_{i,j} \\ Q_j = \sqrt{T_s C/N_0}\, \mathrm{sin}\, c(\pi \Delta f_D T_s) R(\Delta\tau) \sin(\Delta\varphi) + N_{q,j} \end{cases} \tag{14}$$

In the above Equation, M is the non-coherent integration accumulative times; T_s is the coherent integration time, C/N_0 is the carrier-to-noise ratio; Δf_D, $\Delta\tau$ and $\Delta\varphi$ are the Doppler frequency error, code phase error and carrier phase error, respectively. $R(\Delta\tau)$ represents the correlation function of local chip and Receive BOC signal; $N_{i,j}$ and $N_{q,j}$ are Gaussian white noise with a mean value of 0 and a unilateral power spectrum of N_0.

When the target signal does not exist, it can also be said that the received signal is phase-aligned with the local signal code out of one chip. The detection statistic T_0 at this time obeys the χ^2 distribution with a degree of freedom of 2M, assume that the probability density function PDF at this time is p_{T0}, and the false alarm probability can be expressed as

$$P_{fa} = P[T_0 > V] = \int_{V}^{+\infty} P_{T0}(x)dx \tag{15}$$

Therefore, according to Eq. (15), the threshold value V can be found after giving the false alarm probability.

When the received signal and the locally generated chip are aligned, Eq. (13) is taken into Eq. (14). The detection statistic at this time is:

$$T = \sum_{j=1}^{M} \left[\begin{array}{l} (\sqrt{T_s C/N_0}\, \mathrm{sin}\, c(\pi \Delta f_D T_s) R(\Delta\tau) \cos(\Delta\varphi) + N_{i,j})^2 + \\ (\sqrt{T_s C/N_0}\, \mathrm{sin}\, c(\pi \Delta f_D T_s) R(\Delta\tau) \sin(\Delta\varphi) + N_{q,j})^2 \end{array} \right] \tag{16}$$

At this time, T obeys the non-centered χ^2 distribution with a degree of freedom of $2M$. Non-central parameters are:

$$\zeta^2 = MT_sC/N_0 \sin c^2(\pi \Delta f_D T_s) R^2(\Delta\tau) \tag{17}$$

Assuming a probability density of $P_T(x)$ at this time, the detection probability P_d is:

$$P_d = \int_V^{+\infty} P_T(x)dx \tag{18}$$

where V is the detection threshold, which can be calculated based on the given false alarm rate P_{fa}. From Eqs. (16) and (17), it can be seen that the statistical detection amount can only be maximized when the code phase error $\Delta\tau$ is close to zero.

The detection statistic for the CSSPeCT is:

$$T_1 = \sum_{j=1}^{M} \begin{bmatrix} (\left|I'_{1,j}\right| + \left|I'_{2,j}\right| - \left|I'_{1,j} - I'_{2,j}\right|)^2 + \\ (\left|Q'_{1,j}\right| + \left|Q'_{2,j}\right| - \left|Q'_{1,j} - Q'_{2,j}\right|)^2 \end{bmatrix} \tag{19}$$

In the equations, $I'_{1,j}$ and $Q'_{1,j}$ are the in-phase and quadrature branch outputs after coherent integration of the sub-signal combination with the received BOC signal, and $I'_{2,j}$, $Q'_{2,j}$ are the in-phase and quadrature branch outputs after coherent integration of the another sub-signal combination with the received BOC signal, which can be expressed as:

$$\begin{cases} I'_{1,j} = \sqrt{T_sC/N_0} \sin c(\pi \Delta f_D T_s)\left(R_{BOC,0}(\Delta\tau) + R_{BOC,1}(\Delta\tau)\right)\cos(\Delta\varphi) + N_{0,i,j} + N_{1,i,j} \\ Q'_{1,j} = \sqrt{T_sC/N_0} \sin c(\pi \Delta f_D T_s)\left(R_{BOC,0}(\Delta\tau) + R_{BOC,1}(\Delta\tau)\right)\sin(\Delta\varphi) + N_{0,q,j} + N_{1,i,j} \\ I'_{2,j} = \sqrt{T_sC/N_0} \sin c(\pi \Delta f_D T_s)\left(R_{BOC,2}(\Delta\tau) + R_{BOC,3}(\Delta\tau)\right)\cos(\Delta\varphi) + N_{2,i,j} + N_{3,i,j} \\ Q'_{2,j} = \sqrt{T_sC/N_0} \sin c(\pi \Delta f_D T_s)\left(R_{BOC,2}(\Delta\tau) + R_{BOC,3}(\Delta\tau)\right)\sin(\Delta\varphi) + N_{2,q,j} + N_{3,i,j} \end{cases} \tag{20}$$

Among them, $R_{BOC,0}(\Delta\tau)$, $R_{BOC,1}(\Delta\tau)$, $R_{BOC,2}(\Delta\tau)$ and $R_{BOC,3}(\Delta\tau)$ are sub-correlation functions. It can be shown that $I'_{1,j}(Q'_{1,j})$ and $I'_{2,j}(Q'_{2,j})$ are independent of each other, so the statistics can be simplified to:

$$T_1 = \sum_{j=1}^{M} \left[2(I'^2_{1,j} + Q'^2_{1,j}) + 2(I'^2_{2,j} + Q'^2_{2,j})\right] \tag{21}$$

Since both $\sum_{j=1}^{M}(I^2_{1,j} + Q^2_{1,j})$ and $\sum_{j=1}^{M}(I^2_{2,j} + Q^2_{2,j})$ obey the non-central χ^2 distribution with a degree of freedom of $2M$, the non-central parameters are:

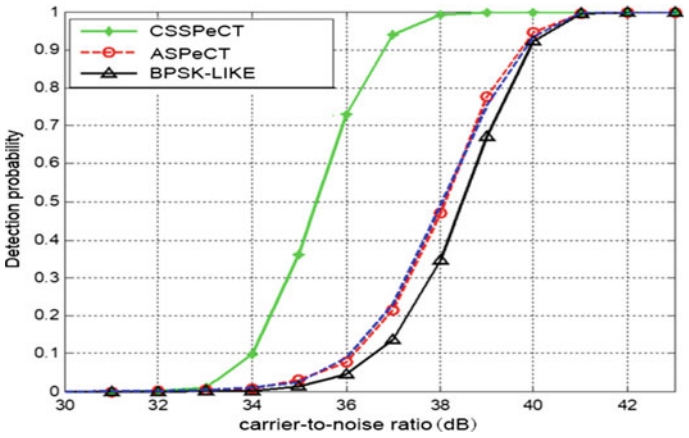

Fig. 6 Detection probability of four methods

$$\begin{cases} \zeta_1^2 = 2MT_sC/N_0 \sin c^2(\pi \Delta f_D T_s)\left(R_{BOC,0}(\Delta\tau) + R_{BOC,1}(\Delta\tau)\right)^2 \\ \zeta_2^2 = 2MT_sC/N_0 \sin c^2(\pi \Delta f_D T_s)\left(R_{BOC,2}(\Delta\tau) + R_{BOC,3}(\Delta\tau)\right)^2 \end{cases} \tag{22}$$

Since the digital characteristics of the detection statistics and the decision threshold expression are difficult to give, the performance comparison can only be given through simulation. The MonteCarlo method was used to simulate the detection probability comparison of BOC (1, 1) under different acquisition methods. The probability of false alarm is set $P_{fa} = 10^{-6}$, the cumulative number of times is M = 10, and the statistics of 20,000 times are as follows.

It can be seen from Fig. 6, for the BOC (1, 1) signal, the detection probability of the optimized correlation shift method CSSPeCT is significantly better than the ASPeCT, and BPSK-LIKE methods and the CSSPeCT can achieve an acquisition probability of more than 0.9 at 37 dBHz. ASPeCT and BPSK-LIKE need to reach 40 dBHz to achieve the same effect. Therefore, the optimized correlation shift method CSSPeCT is 3 dBHz better than ASPeCT in terms of sensitivity.

3.3 Algorithm Computation Analysis

Take 2.4 section matlab setting parameters as an example, adopt FFT parallel code phase search method, the search step length is 500 Hz, search frequency range: ±10 kHz; to complete a 16368 point FFT requires complex addition:

$$N \log_2 N = 16368 \log_2 16368 = 229152 \tag{23}$$

Table 1 Comparison calculation between the three algorithms

Number	Algorithm name	Multiplication/times	Additions/times
BPSK-like	$10N\log_2 N + 6N$	$17.5N\log_2 N + N-1$	BPSK-like
ASPeCT	$10N\log_2 N + 5N$	$17.5N\log_2 N + N-1$	ASPeCT
CSSPeCT	$6N\log_2 N + 4N$	$10.5N\log_2 N + 3N-3$	CSSPeCT

The number of complex multiplications that need to be completed is

$$\frac{N}{2}\log_2 N = \frac{16368}{2}\log_2 16368 = 114576 \tag{24}$$

Since complex multiplication can be accomplished by real number multiplication [8]. A complex multiplication can be divided into four real number multiplications and three real number additions, and a complex addition can be divided into two real number additions.

For the CSSPeCT algorithm, four real number multiplications, three real number additions, and three FFT operations are needed; The ASPeCT method requires 5 real number multiplications and 1 real number addition, and then 5 FFT operations. The BPSK-Like method requires 5 FFT operations, 6 real number multiplications and 1 real number additions to obtain the detection value. Therefore, the calculations of the different acquisition methods are compared as shown in Table 1. As can be seen from the table, the computational complexity of the proposed algorithm and the optimized algorithm is about 60% of the ASPeCT method and the BPSK-Like method.

4 Conclusions

This paper proposes a correlation shifting BOC unambiguous acquisition method. By analyzing the performance of the acquisition two-dimensional maps, detection probability and computational complexity, it shows that the proposed shift correlation function method has less computation and better acquisition performance than the two traditional acquisition methods of ASPeCT and BPSK-LIKE, which is of great significance for receiving the B1C signal in the three generation of the Beidou navigation system.

Acknowledgements This work was supported by the National Natural Science Foundation of China (61561016, 11603041), Guangxi Information Science Experiment Center funded project, Department of Science and Technology of Guangxi Zhuang Autonomous Region (AC16380014, AA17202048, AA17202033).

References

1. Julien, O., Macaiubian, C., Cannon, M., et al.: ASPeCT: Unambiguous sine–BOC (n, n) acquisition/tracking technique for navigation applications. IEEE Trans. Aerosp. Electron. Syst. **43**(1), 150–162 (2007)
2. Julien O., et al.: A new unambiguous BOC (n, n) signal tracking technique. In: Proceedings of the European Navigation Conference GNSS (2004)
3. Yan, T., Wei, J.L., Tang, Z.P., et al.: Unambiguous acquisition/tracking technique for high order sine-phased binary offset carrier modulated signal. Wirel. Pers. Commun. **84**(4), 2835–2857 (2015)
4. Qi, J.M., Chen, J.P., Li, Z.B., et al.: Unambiguous BOC modulated signals synchronization technique. IEEE Commun. Lett. **16**(7), 986–989 (2012)
5. Ji, Y.F., Liu, Y., Zhen, W.M., et al.: An unambiguous acquisition algorithm based on unit correlation for BOC (n, n) signal. IEICE Trans. Commun. **100**(8), 1507–1513 (2017)
6. Zhang, H.L., Ba, X.H., Chen, J., et al.: The unambiguous acquisition technology for BOC (m, n) signals. Aeronaut. Acta **38**(4), 217–226 (2017)
7. Cao, X.L., Guo, C.J.: A new unambiguity acquisition algorithm for BOC (n, n) signal. Glob. Position. Syst. **41**(6), 1–5 (2016)
8. Qian, B., Tian, M.H., Pan, C.S.: BOC modulated signal acquisition processor design based on FPGA. Command. Fire Control. **08**(8), 129–132 (2011)
9. Burian, A., Lohan, E.S., Renfors, M.: Low-complexity unambiguous acquisition methods for BOC-modulated CDMA signals. Int. J. Satell. Commun. Netw. **26**(6), 503–522 (2008)
10. Fishman, P., Betz, J.W.: Predicting performance of direct acquisition for the M-code signal. In: Proceedings of ION NMT, pp. 574–582 (2000)
11. Benedetto, F., Giunta, G., Lohan, E.S., et al.: A fast unambiguous acquisition algorithm for BOC-modulated signals. IEEE Trans. Veh. Technol. **62**(3), 1350–1355 (2013)
12. Underwater image dehazing using joint trilateral filter. Comput. Electr. Eng. **40**(1), 41–50 (2014)
13. Motor anomaly detection for unmanned aerial vehicles using reinforcement learning. IEEE Internet Things J. (2017). https://doi.org/10.1109/jiot.2017.2737479
14. Brain intelligence: go beyond artificial intelligence. Mob. Netw. Appl., 1–8 (2017)
15. Wound intensity correction and segmentation with convolutional neural networks. Concurr. Comput. Pract. Exp. (2017). https://doi.org/10.1002/cpe.3927
16. Low illumination underwater light field images reconstruction using deep convolutional neural networks. Futur. Gener. Comput. Syst. (2018). https://doi.org/10.1016/j.future.2018.01.001
17. Deep adversarial metric learning for cross-modal retrieval. World Wide Web J. (2018). https://doi.org/10.1007/s11280-018-0541-x

An Unambiguous Acquisition Algorithm for BOC (n, n) Signal Based on Sub-correlation Combination

Xiyan Sun, Qing Zhou, Yuanfa Ji, Qiang Fu, Qinwen Miao and Sunyong Wu

Abstract To overcome the acquisition problems caused by the multiple peaks of the auto-correlation function of Binary Offset Carrier (BOC) modulated signal, a technology to eliminate secondary peaks based on sub-combination correlation is proposed in this paper. According to the characteristics of the sub-function of the BOC autocorrelation, this new method recombined the sub-correlation function obtain the ability to eliminate the edge. MonteCarlo simulations show that the proposed method can improve 3 dBHz sensitivity in detection probability compared with ASPeCT when the number of non-coherent is 10 for BOCs (1, 1). In addition, it can be applied to BOCc (1, 1) and achieved the same the detection probability compared with the traditional BSPK-LIKE method by appropriately increasing the number of non-coherent.

Keywords BOC · Multiple peaks · Sub-correlation · Correlation-combination Unambiguous correlation function

1 Introduction

With the continuous promotion of the satellite systems application, higher requirements are placed on the user's positioning accuracy and reliability. Many signals employ binary offset carrier modulation (BOC) modulation technology. BOC removes the modulated signal energy from the center spectrum by multiplying the subcarrier enabling spectrum sharing within a limited navigation spectrum. However, the auto-correlation function of the BOC modulation signal has multiple secondary peaks. Therefore, erroneous acquisition is easy to occur in the process of receiver synchronization.

X. Sun · Q. Zhou · Y. Ji (✉) · Q. Fu · Q. Miao · S. Wu
Guangxi Key Laboratory of Precision Navigation Technology and Application, Guilin University of Electronic Technology, Guilin 541004, China
e-mail: jiyuanfa@163.com

H. Lu (ed.), *Cognitive Internet of Things: Frameworks, Tools and Applications*, Studies in Computational Intelligence 810,
https://doi.org/10.1007/978-3-030-04946-1_40

Many factors are of great significance for the elimination of wingers, such as deblurring and denoising [1–5]. There are many solutions to solve the problem of capturing ambiguity: (1) BPSK-LIKE [6–8]: This method uses a band-pass filter to filter the BOC signal to obtain the main lobes of two similar BPSK signal spectra, which can completely eliminate the ambiguity but it will lose 3 dB of energy. (2) GRASS [9]: It is to design a local auxiliary signal and use the piecewise linear function of trapezoidal signal correlation function to construct the unambiguous correlation function. But it just be used for the sinusoidal modulated BOC signal. (3) SCPC [10]: This method uses local generated in-phase and quadrature subcarrier signals to correlate with received signals respectively, and then adds the two correlation results. It needs more correlators than BPSK but achieves the same tracking performance as BPSK_LIKE. Methods (2) (3) can be categorized as related reconstruction, which is a hot research direction nowadays. Its core idea is [11–15]: The correlation functions with side-peaks are split and recombined to form a new correlation function without side-peaks.

Firstly, this paper proposes the shape code according to the definition of BOC signal, then using the shape code to deduce the mathematical expression of all BOC correlation function. Secondly, we divided BOC (1, 1) signal into different sub-signals and get the expression by shape code, and then get sub-correlation functions by correlating the sub-signals with received BOC signal. Finally, we recombined sub-correlations functions to obtain the correlation function with no side-peaks, which solves the problem of capturing fuzziness. Simulations show this method is suitable for BOC (n, n) signals. The detection probability and the calculation amount of the algorithm verify the feasibility of the algorithm.

2 Related Works

2.1 BOC Modulation Model

For BOC (m, n) modulated signals, where m represents the subcarrier rate is m * 1.023 MHz and n represents the spreading code rate is n * 1.023 MHz. The BOC signal is divided into a Sine-BOC (BOCs) signal and a cosine-BOC (BOCc) signal. The BOC baseband signal can be modeled as:

$$S_{BOC}(t) = c(t)sc(t), \tag{1}$$

where $c(t)$ is a pseudo-random code and $sc(t)$ is a sub-carrier of the modulation signal. The mathematical expression of the pseudo-random code is as follows:

$$c(t) = \sum_{i=-\infty}^{\infty} C_i P_{T_C}(t - iT_C), \tag{2}$$

$\{C_i\}$ is the symbol of the i-th chip, $C_i \in (-1, 1)$, T_C is the chip width of one spreading PRN; $P_{T_C}(t)$ is a rectangular pulse with the duration being T_C and the amplitude being 1. The square wave sub-carrier divides the pseudo-random code spreading symbol into N parts, and each length is $T_{SC} = T_C/N$, so the square wave sub-carrier can be expressed as:

$$P_{T_C}(t) = sc(t) = \sum_{j=0}^{N-1} d_j P_{T_{SC}}(t - jT_{SC}), \tag{3}$$

T_{SC} is a sub-carrier half-period width; $P_{T_{SC}}(t)$ is a rectangular pulse signal with a time period of T_{SC} and an amplitude of 1; N is the number of sub-carrier chips corresponding to a pseudo code chip time $T_C, d_j \in \{1, -1\}$ $(j = 0, 1, 2, \cdots, N-1)$. The value d_j of the BOCs and BOCc may not be the same, but the mathematical expression for a uniform BOC baseband signal can be expressed:

$$S_{BOC}(t) = \sum_{i=-\infty}^{\infty} \sum_{j=0}^{N-1} C_i d_j P_{T_{SC}}(t - iT_C - jT_{SC}). \tag{4}$$

2.2 BOC Shape Code

For Eq. (3), $d_j \in \{1, -1\}$ $(j = 0, 1, 2, \cdots, N-1)$ named shape code represents the j-th sub-carrier amplitude of the sub-carrier; In a pseudo code chip time T_C, all sub-carrier chip shape codes can be constituted of $d = [d_0\ d_1 \cdots d_{N-1}\ ]_N$, which is denoted as a shape code vector in the text. Sine-BOC signals and Cosine-BOC signals can be represented by different shape code vectors, as shown in Fig. 1.

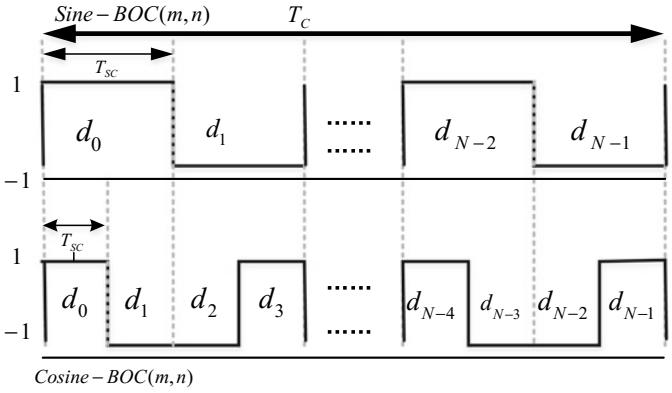

Fig. 1 Shape code of sub-carrier of the BOC

For BOCs (m, n), the sinusoidal modulated sub-carrier shape code vector is $d = [1\ \ -1\ \ 1 \ldots -1]_N$ when $N = 2m/n$. For example, the shape code vector of the BOCs (1, 1) signal; Similarly for BOCc (m, n), when $N_1 = 4m/n$, shape code vector is $d = [1\ \ -1\ \ -1 \ldots 1]_{N_1}$. For example, the shape code vector for BOCc (1, 1) is $d = [1\ \ -1\ \ -1\ \ 1]_4$.

According to the concept of the shape code vector, the sub-carrier modulation signals of any two channels of the spread-spectrum signal are shown as Eq. (5):

$$\begin{cases} s_1(t) = \sum_{j=0}^{N-1} d_j P_{T_{SC}}(t - jT_{SC}) \\ s_2(t) = \sum_{i=0}^{N-1} d_i' P_{T_{SC}}(t - iT_{SC}) \end{cases}. \tag{5}$$

The shape code vectors d and d' are not same, so the cross-correlation function of the BOC modulation signal can be obtained as:

$$\begin{aligned} R_{CCF}(\tau) &= E[s_1(t)s_2(t+\tau)] \\ &= \frac{1}{N}\sum_{i=0}^{N-1}\sum_{j=0}^{N-1} d_j d_i' \int_{-\infty}^{+\infty} P_{T_{SC}}(t - jT_{SC}) P_{T_{SC}}(t + \tau - iT_{SC}) dt. \end{aligned} \tag{6}$$

According to the characteristics of the square wave auto-correlation function:

$$\int_{-\infty}^{+\infty} P_{T_{SC}}(t) P_{T_{SC}}(t+\tau) dt = \Lambda_{T_{SC}}(\tau), \tag{7}$$

$\Lambda_{T_{SC}}(\tau)$ is an isosceles triangle function waveform entered at zero, with a base width of $2T_{SC}$ and amplitude of 1. Therefore, Eq. (6) can be expressed as:

$$R_{CCF}(\tau) = E[s_1(t)s_2(t+\tau)] = \frac{1}{N}\sum_{i=0}^{N-1}\sum_{j=0}^{N-1} d_j d_i' \Lambda_{T_{SC}}[\tau - (j-i)T_{SC}]. \tag{8}$$

Equation (8) is the auto-correlation function of the BOC modulation signal when the two shape code vectors d and d' are the same. The shape code vectors of the autocorrelation functions of BOCc (1, 1) and BOCs (1, 1) respectively are $d = [1\ \ -1\ -1\ \ 1\ ]_4$ and $d = [1\ \ -1\ ]_2$.

3 Sub-correlation Combination Technique

From the shape-code vector proposed in the previous section, we can see that the shape code vectors of the auto-correlation functions of BOCc (1, 1) is $d = [1\ -1\ -1\ \ 1\ ]_4$, which splits the shape code vector that is d into four shape code vectors: d_0, d_1, d_2 and d_3, as shown below:

$$\begin{cases} d_0 = [\ 1\ 0\ 0\ \ 0\ ]_4 \\ d_1 = [0\ \ -1\ 0\ 0]_4. \\ d_2 = [0\ 0\ \ -1\ 0]_4 \\ d_3 = [0\ 0\ 0\ \ 1\ ]_4 \end{cases} \tag{9}$$

According to the shape code vector in Eq. (9), the BOCc (1, 1) modulation signal is split into four sub-signal waveforms as shown in Fig. 2.

As shown in Fig. 2, the BOCc (1, 1) modulation signal is obtained by the d modulating the pseudo-random code, d_0, d_1, d_2 and d_3 respectively modulate the pseudo-random code to obtain the sub-signal waveforms $s_{boc,0}(t)$, $s_{boc,1}(t)$, $s_{boc,2}(t)$ and $s_{boc,3}(t)$. Therefore, the sub-signal waveform and the received signal correlation function are defined as sub-correlation functions.

According to the definition of the sub-correlation function, the auto-correlation function of BOCc (1, 1) can be expressed as:

$$R = \sum_{i=0}^{3} R_i. \tag{10}$$

Combining Eq. (8), R_i, that is, the sub-correlation function can be simplified as:

$$R_i = \frac{1}{N} \sum H_k(d, d(i)) \Lambda_{T_{SC}}(\tau - kT_{SC}), \tag{11}$$

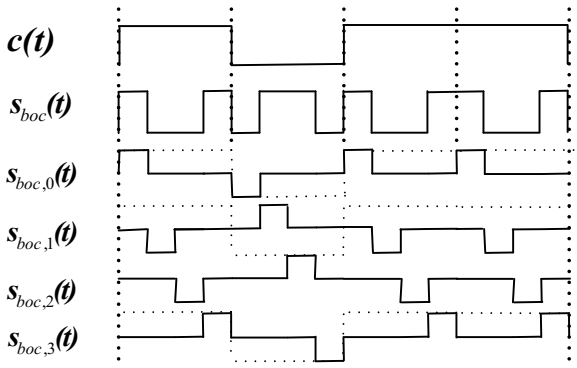

Fig. 2 Modulation signal and decompositions of BOCc (1, 1)

H_k is a set including the shape code vector d and sub-signal shape codes $\boldsymbol{d(i)}$. The subscript of H_k, that is, K is the difference between the two shape codes, and the summation symbol represents the sum of all the components in the set. For example, when the sub-functions of BOCc (1, 1) are R_0, $d = [1\ -1\ -1\ \ 1\ ]_4$ and $d0 = [\ 1\ 0\ 0\ \ 0\ ]_4$, then the set H_0 is:

$$H_0 = \begin{Bmatrix} d_0d0_0 & d_1d0_0 & d_2d0_0 & d_3d0_0 \\ d_0d0_1 & d_1d0_1 & d_2d0_1 & d_3d0_1 \\ d_0d0_2 & d_1d0_2 & d_2d0_2 & d_3d0_2 \\ d_0d0_3 & d_1d0_3 & d_2d0_3 & d_3d0_3 \end{Bmatrix} = \begin{Bmatrix} 1 & -1 & -1 & 1 \\ 0 & 0 & 0 & 0 \\ 0 & 0 & 0 & 0 \\ 0 & 0 & 0 & 0 \end{Bmatrix}. \tag{12}$$

Multiply that shape code combination with the corresponding triangular function to get $d_0d0_0 \cdot \Lambda_{T_{SC}}$, $d_1d0_0 \cdot \Lambda_{T_{SC}}(\tau - T_{SC})$, $d_2d0_0 \cdot \Lambda_{T_{SC}}(\tau - 2T_{SC})$, and $d_3d0_0 \cdot \Lambda_{T_{SC}}(\tau - 3T_{SC})$. The sub-correlation function R_0 is obtained by adding the above. In the same way, the set of shape codes of other sub-related function is as follows:

$$H_1 = \begin{Bmatrix} 0 & 0\,0 & 0 \\ -1 & 1\ 1 & -1 \\ 0 & 0\,0 & 0 \\ 0 & 0\,0 & 0 \end{Bmatrix} \quad H_2 = \begin{Bmatrix} 0 & 0\,0 & 0 \\ 0 & 0\,0 & 0 \\ -1 & 1\ 1 & -1 \\ 0 & 0\,0 & 0 \end{Bmatrix}$$

$$H_3 = \begin{Bmatrix} 0 & 0 & 0 & 0 \\ 0 & 0 & 0 & 0 \\ 0 & 0 & 0 & 0 \\ 1 & -1 & -1 & 1 \end{Bmatrix}. \tag{13}$$

According to Eqs. (12) and (13), the auto-correlation and the sub-correlation function of BOCc (1, 1) are shown in Fig. 3.

Figure 3 shows the auto-correlation and sub-correlation functions of BOCc (1, 1). The sum of all sub-correlation functions is an auto-correlation function. In addition, it can be found that R_0 and R_3 are symmetric about the origin, and the combination of the two above yields $C1$. Similarly, R_1 and R_2 combine to obtain $C2$, as shown in Fig. 4.

From Fig. 4, it can be seen that the graphs $C1$ and $C2$ are symmetrical about the origin. When the code phase is ± 0.25, ± 0.5 and ± 0.75, the peak correlation value of the combined pattern of the sub-functions of BOCc (1, 1) is equal, and it corresponds to two peaks at 0 chips, which will eliminate ambiguity.

Reconstruct the graphs $C1$ and $C2$ according to the following rules:

$$R = |R_{C1}| + |R_{C2}| - |R_{C1} - R_{C2}|, \tag{14}$$

where R is the correlation function obtained by the reconstruction.

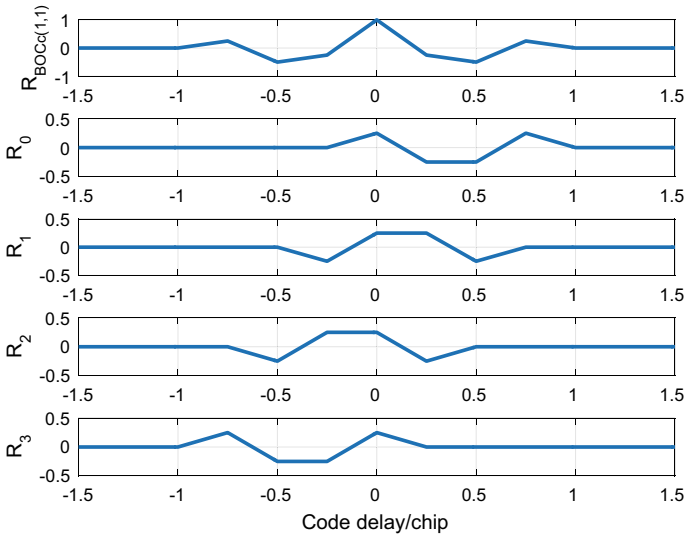

Fig. 3 Auto-correlation and sub-correlation functions of BOCc (1, 1)

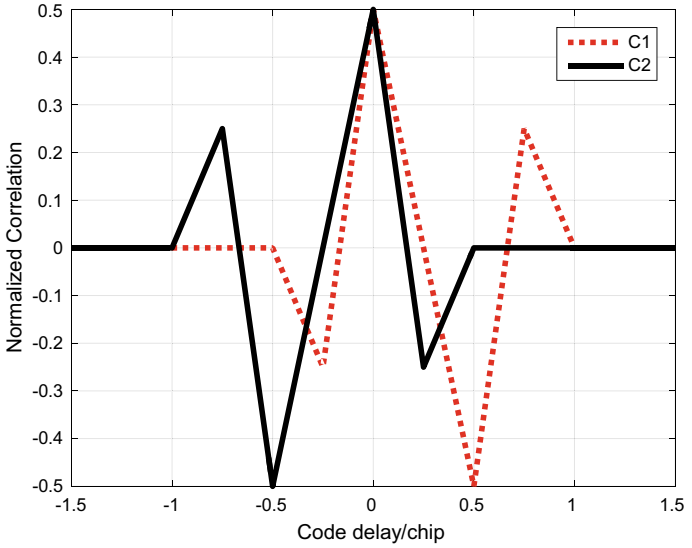

Fig. 4 Combination of sub-correlation functions of BOCc (1, 1)

4 Performance Analysis

4.1 Detection Probability Comparison Simulation

Compared with the BOC signal tracking process, BOC signal acquisition is a process of continuously comparing the detection statistics and detection thresholds of the non-coherent integrator output. The detection statistic is the auto-correlation value or amplitude squared value output from the correlator. The detection probability P_{d} is an important parameter for detecting the capture performance. Non-coherent detection statistics for traditional capture schemes can be expressed as:

$$T = \sum_{j=1}^{M} (I_j^2 + Q_j^2). \tag{15}$$

In Eq. (15),

$$\begin{cases} I_j = \sqrt{T_s C/N_0}\,\mathrm{sin}\,c(\pi \Delta f_D T_s) R(\Delta\tau)\cos(\Delta\varphi) + N_{i,j} \\ Q_j = \sqrt{T_s C/N_0}\,\mathrm{sin}\,c(\pi \Delta f_D T_s) R(\Delta\tau)\sin(\Delta\varphi) + N_{q,j} \end{cases}, \tag{16}$$

where M is the non-coherent integration accumulative times, T_s is the coherent integration time, C/N_0 is the carrier-to-noise ratio, Δf_D, $\Delta\tau$ and $\Delta\varphi$ are the Doppler frequency error, code phase error and carrier phase error respectively, $R(\Delta\tau)$ represents the local chip and Received signal correlation function, $N_{i,j}$ and $N_{q,j}$ are Gaussian white noise with a mean value of 0 and a unilateral power spectrum of N_0.

When the received signal is aligned with the locally generated chip, Eq. (15) is taken into Eq. (16), and the detection statistic at this time is:

$$\begin{aligned} T = \sum_{j=1}^{M} \Big[&(\sqrt{T_s C/N_0}\,\mathrm{sin}\,c(\pi \Delta f_D T_s) R(\Delta\tau)\cos(\Delta\varphi) + N_{i,j})^2 \\ &+ (\sqrt{T_s C/N_0}\,\mathrm{sin}\,c(\pi \Delta f_D T_s) R(\Delta\tau)\sin(\Delta\varphi) + N_{q,j})^2 \Big]. \end{aligned} \tag{17}$$

In this case, T follows the non-center $2M$ distribution with degree of freedom χ^2. Non-central parameters are:

$$\zeta^2 = M T_s C/N_0\,\mathrm{sin}\,c^2(\pi \Delta f_D T_s) R^2(\Delta\tau). \tag{18}$$

Assuming the probability density is $P_T(x)$, the detection probability P_d is:

$$P_d = \int_V^{+\infty} P_T(x)dx, \tag{19}$$

where V is the detection threshold, it can be obtained based on the given false alarm rate P_{fa}. From Eqs. (17) to (18), it can be seen that the statistical detection amount can only be maximized when the code phase error $\Delta\tau$ is close to zero.

The in-phase and quadrature operations of the local generated two waveforms $S_1(t)$, $S_2(t)$ and the received signal can be expressed as:

$$\begin{cases} I_{1,j} = \sqrt{T_s C/N_0}\,\mathrm{sin}\,c(\pi\Delta f_D T_s)R_1(\Delta\tau)\cos(\Delta\varphi) + N_{1,i,j} \\ Q_{1,j} = \sqrt{T_s C/N_0}\,\mathrm{sin}\,c(\pi\Delta f_D T_s)R_1(\Delta\tau)\sin(\Delta\varphi) + N_{1,q,j} \\ I_{2,j} = \sqrt{T_s C/N_0}\,\mathrm{sin}\,c(\pi\Delta f_D T_s)R_2(\Delta\tau)\cos(\Delta\varphi) + N_{2,i,j} \\ Q_{2,j} = \sqrt{T_s C/N_0}\,\mathrm{sin}\,c(\pi\Delta f_D T_s)R_2(\Delta\tau)\sin(\Delta\varphi) + N_{2,q,j} \end{cases}, \tag{20}$$

where $I_{1,j}$ and $Q_{1,j}$ represent the in-phase and quadrature branch outputs of the local generated signal $S_1(t)$ and the received BOC signal correlator respectively. Since the noise is Gaussian white noise, $I_{1,j}(I_{1,j})$ and $Q_{1,j}(Q_{1,j})$ are irrelevant. In addition, $I_{1,j}(Q_{1,j})$ and $I_{2,j}(Q_{2,j})$ are also irrelevant. It is only necessary to prove that noise $N_{1,i,j}$ and $N_{2,i,j}$ is not related.

$$\begin{aligned} E[N_{1,i,j}\cdot N_{2,i,j}] &= \tfrac{1}{T_C}\int_0^{T_C} n(t)\cdot s_1(t+\tau)dt \cdot \int_0^{T_C} n(v)\cdot s_2(v+\tau)dv \\ &= \tfrac{N_0}{T^2}\int_0^{T_p} s_1(t)s_2(t+\tau) = \tfrac{N_0}{T^2}R_{12} \end{aligned}. \tag{21}$$

In Eq. (21), R_{12} is a two-way local code cross-correlation function. According to the designed two-way local code shape code vector, the cross-correlation function is 0, so it is proved that $N_{1,i,j}$ and $N_{2,i,j}$ is not related.

Combine the detection statistic formula in Eq. (15) and the combined correlation function rule, the detection statistic T_1 of the new method is:

$$T_1 = \sum_{j=1}^{M}\begin{bmatrix} (\left|I_{1,j}+I_{2,j}\right| - \left|I_{1,j}-I_{2,j}\right|)^2 + \\ (\left|Q_{1,j}+Q_{2,j}\right| - \left|Q_{1,j}-Q_{2,j}\right|)^2 \end{bmatrix}. \tag{22}$$

Because $I_{1,j}(Q_{1,j})$ and $I_{2,j}(Q_{2,j})$ are not related, they can be reduced to:

$$T_1 = \sum_{j=1}^{M}\left[2(I_{1,j}^2 + Q_{1,j}^2) + 2(I_{2,j}^2 + Q_{2,j}^2)\right], \tag{23}$$

since both $\sum_{j=1}^{M}(I_{1,j}^2 + Q_{1,j}^2)$ and $\sum_{j=1}^{M}(I_{2,j}^2 + Q_{2,j}^2)$ obey non-central χ^2 distributions with degree of freedom $2M$, their non-central parameters are:

$$\begin{cases} \zeta_e^2 = 2MT_sC/N_0 \sin c^2(\pi \Delta f_D T_s) R_1^2(\Delta\tau) \\ \zeta_o^2 = 2MT_sC/N_0 \sin c^2(\pi \Delta f_D T_s) R_2^2(\Delta\tau) \end{cases} . \tag{24}$$

The Monte Carlo method simulates the detection probability comparison of BOCs (1, 1) and BOCc (1, 1) under different capture methods. Where the probability of false alarms is $P_{fa} = 10^{-6}$, the cumulative number of times is M = 10, and 20,000 statistics are performed as follows.

As can be seen from the Figs. 5 and 6, for the BOCs (1, 1) signal, the detection probability of the combined correlation function method is significantly better than that of the ASPeCT and BPSK-LIKE methods. The combined correlation function can achieve a capture probability of more than 0.9 at 37 dBHz, while ASPeCT and BPSK-LIKE needs to reach 40 dBHz to get the same effect, so the sensitivity of the combined correlation function is increased by 3 dBHz. The sensitivity of the BOCc (1,1) signal sub-function combination correlation function method has a 1 dBHZ decrease compared to BPSK-LIKE, when the number of accumulations increases to M = 10, it can obtain the same performance as BPSK-LIKE.

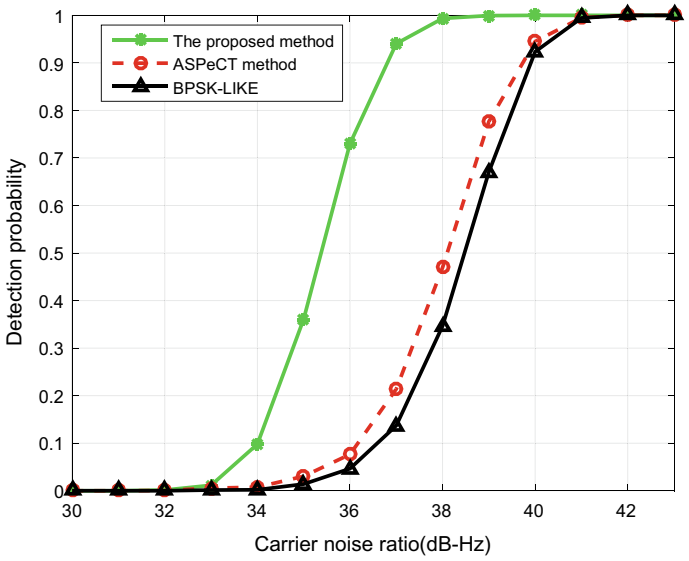

Fig. 5 BOCs (1, 1) signal detection probability

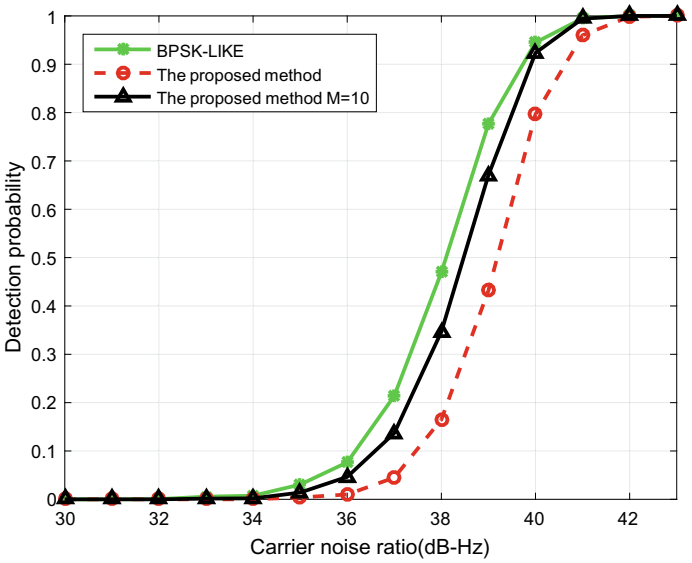

Fig. 6 BOCc (1, 1) signal detection probability

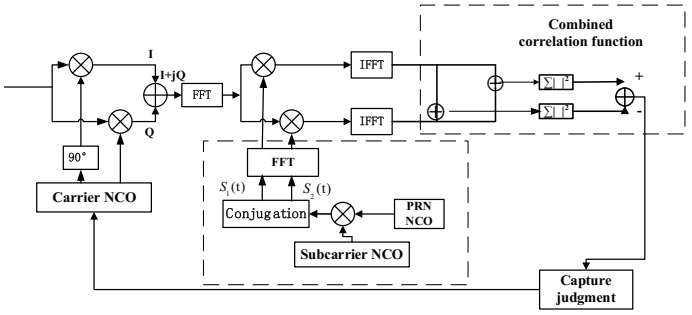

Fig. 7 The correlation-combination method schematic

4.2 Algorithm Computation Analysis

Assume that both the data length and the non-coherent accumulation time are L points and in condition that the correlation between the local code waveform and the received signal has been obtained when it is implemented, different capture methods are shown in Table 1. From the table, it can be seen that, in order to remove the influence of multi-peaks, the amount of computation that generates two local codes locally will increase appropriately compared to the traditional BPSK-LIKE and ASPECT. The amount of computation generated by multiplexing the 4-way local code of the correlator is the same as that of the conventional BPSK-LIKE. Figure 7 shows the block diagram of the combined correlation method.

Table 1 Comparison calculation between three algorithms

Number	Algorithm name	Multiplication/times	Additions/times
1	BPSK-LIKE	2L	2L-1
2	ASPeCT	5L	4L-1
3	Sub function combination to generate 2 local codes	5L	6L-1
4	Sub function combination to generate 4 local codes	2L	2L-1

5 Conclusions

This paper presents an unambiguous acquisition method that combines sub-correlation functions. Using the shape code to obtain mathematic expression of autocorrelation of BOC signal and each sub-correlation. Simulations of detection probabilities show that for BOCs (1,1) signals, the detection sensitivity of the sub-correlation function method is 3 dBHz higher than that of the classic ASPeCT algorithm, and for the BOCc (1,1) signal, there is a similar detection probability to the BPSK-LIKE. To make the algorithm proposed applicable to B1C signal receivers of BeiDou 3G navigation systems in the future, a lot of simulation and improvement still need to be done.

Acknowledgements This work was supported by the National Natural Science Foundation of China (61561016, 11603041), Guangxi Information Science Experiment Center funded project, Department of Science and Technology of Guangxi Zhuang Autonomous Region (AC16380014, AA17202048, AA17202033), the basic ability promotion project of young and middle-aged teachers in Universities of Guangxi province (ky2016YB164).

References

1. Serikawa, S., Lu, H.: Underwater Image Dehazing Using Joint Trilateral Filter. Pergamon Press, Inc. (2014)
2. Lu, H., Li, Y., Mu, S., et al.: Motor anomaly detection for unmanned aerial vehicles using reinforcement learning. IEEE Internet Things J. **PP**(99), 1–1 (2017)
3. Lu, H., Li, Y., Chen, M., et al.: Brain Intelligence: go beyond artificial intelligence. Mob. Netw. Appl. **23**(2), 368–375 (2017)

4. Lu, H., Li, B., Zhu, J., et al.: Wound intensity correction and segmentation with convolutional neural networks. Concurr. Comput. Pract. Exp. **29**(6) (2016)
5. Lu, H., Li, Y., Uemura, T., et al.: Low illumination underwater light field images reconstruction using deep convolutional neural networks. Futur. Gener. Comput. Syst. **82** (2018)
6. Burian, A., Lohan, E.S., Renfors, M.: BPSK-like methods for hybrid-search acquisition of galileo signals. In: Proceedings of IEEE ICC, June, pp. 5211–5216 (2006)
7. Lohan, E.S.: Statistical analysis of BPSK-like techniques for the acquisition of Galileo signals. J. Aerosp. Comput. Inf. Commun. **3**(5), 234–243 (2006)
8. Fishman, P., Betz J.W.: Predicting performance of direct acquisition for the M-code signal. In: Proceedings of ION NMT, pp. 574–582 (2000)
9. Yao, Z., Lu, M.Q.: Unambiguous sine-phase binary offset carrier modulated signal acquisition technique. IEEE Trans. Wirel. Commun. Lett. **9**(2), 577–580 (2010)
10. Ward, P.W.: A design technique to remove the correlation ambiguity in binary offset carrier (BOC) spread spectrum signal, pp. 146–155. ION Press, Albuquerque, NM, USA (2003)
11. Zhang, X.X., Cheng, Y.W., Guo C.J.: A novel blur-less acquisition algorithm for BOC (1, 1). In: China Satellite Navigation Academic Annual Meeting (2017)
12. Ji, Y.F., Liu, Y., Zhen, W.M., et al.: An unambiguous acquisition algorithm based on unit correlation for BOC (n, n) signal. IEICE Trans. Commun. **8 (**2017)
13. Zhang, H.L., Ba, X.H., Chen, J., et al.: The unambiguous acquisition technology for BOC (m, n) signals. Aeronaut. Acta **38**(4), 217–226 (2017)
14. Cao, X.L., Guo, C.J.: A new unambiguity acquisition algorithm for BOC (n, n) signal. Glob. Position. Syst. **41**(6), 1–5 (2016)
15. Hu, G.Y., Zhao, T.L., Chen, S., et al.: An unambiguity and direct acquisition algorithm of BOC signal. Electron. Technol. Appl. **39**(12), 122–125 (2013)

Occluded Face Recognition by Identity-Preserving Inpainting

Chenyu Li, Shiming Ge, Yingying Hua, Haolin Liu and Xin Jin

Abstract Occluded face recognition, which has an attractive application in the visual analysis field, is challenged by the missing cues due to heavy occlusions. Recently, several face inpainting methods based on generative adversarial networks (GANs) fill in the occluded parts by generating images fitting the real image distributions. They can lead to a visually natural result and satisfy human perception. However, these methods fail to capture the identity attributes, thus the inpainted faces may be recognized at a low accuracy by machine. To enable the convergence of human perception and machine perception, this paper proposes an Identity Preserving Generative Adversary Networks (IP-GANs) to jointly inpaint and recognize occluded faces. The IP-GANs consists of an inpainting network for regressing missing facial parts, a global-local discriminative network for guiding the inpainted face to the real conditional distribution, a parsing network for enhancing structure consistence and an identity network for recovering missing identity cues. Especially, the novel identity network suppresses the identity diffusion by constraining the feature consistence from the early subnetwork of a well-trained face recognition network between the inpainted face and its corresponding ground-true. In this way, it regularizes the inpaintor, enforcing the generated faces to preserve identity attributes. Experimental results prove the proposed IP-GANs capable of dealing with varieties of occlusions and producing photorealistic and identity-preserving results, promoting occluded face recognition performance.

Keywords Image inpainting · Occluded face recognition · Generative adversarial networks (GANs) · Identity preserving

C. Li · S. Ge (✉) · Y. Hua · H. Liu
Institute of Information Engineering, Chinese Academy of Sciences, Beijing, China
e-mail: geshiming@iie.ac.cn

C. Li · Y. Hua · H. Liu
School of Cyber Security, University of Chinese Academy of Sciences, Beijing, China

X. Jin
Department of Cyber Security, Beijing Electronic Science and Technology Institute, Beijing, China

H. Lu (ed.), *Cognitive Internet of Things: Frameworks, Tools and Applications*, Studies in Computational Intelligence 810,
https://doi.org/10.1007/978-3-030-04946-1_41

1 Introduction

With the rapid development of deep learning in intelligent image recognition, face recognition has achieved impressive accuracy under un-occluded conditions. However in wild scenarios, it is common to encounter occlusions. Occlusions caused by facial accessories, objects in front of the faces, extreme illumination, self-occlusion or poor image quality exist everywhere, which results in sharp drop in recognition accuracy. Occlusion has become one of the strongest hinderance of face recognition in the wild.

Existing occluded face recognition methods mainly depend on partial feature extraction [12], inpainting [2] or sparse representation [21]. They had good performance in handling light occluded faces but were difficult to work effectively under heavy occlusions. Recently, with the help of deep generative models, face inpainting or completion approaches [5, 7, 14] have achieved remarkable improvements. These approaches are capable of extracting high-level context features and generating photorealistic results, making them a feasible fit for occluded face recognition. In general, they mainly aim to obtain consistent looking, neglecting to capture the identity attributes. This leads to a gap of recognition accuracy compared to the ground truth, though winning the occluded one.

In this work, we devise a novel model named Identity Preserving Generative Adversarial Networks (IP-GANs) to improve occluded face recognition. The networks consist of an inpainting network for generating the missing contents, local-global discriminators and a semantic parsing network are incorporated to urge the inpainted result to be photorealistic, and an identity network is introduced to ensure the correct diffusion of identity information along the border. In this way, the inpainting network is forced to narrow the distance with ground truth in both pixel and feature subspaces. Toward this end, occluded face inpainting and recognition can be jointly solved.

Our main contributions can be summarized as three folds:

- We propose a novel model named Identity Preservation Generative Adversarial Networks (IP-GANs) for photorealistic and identity preserving face completion, under the circumstance where large region of contents are missing.
- We propose an identity network to suppress the identity diffusion, enabling the convergence of human and machine perception.
- We conduct qualitative and quantitative experiments to show the strength of IP-GANs to generate photorealistic and identity-preserving completed faces.

2 Related Work

2.1 Image Inpainting

Since the concept of digital image inpainting was introduced by Bertalmio et al. [1], many approaches have been proposed in this field. Early inpainting approaches based

on information diffusion and texture synthesis exhibited fine performance when missing region is relatively small, but blurring when missing region is large. Exemplar-based methods applied texture synthesis by seeking similar patches as reference, maybe perfectly fitting background completing task. But when completing objects with unique textures like faces, things get tough. In the last few years, as deep models, GANs especially, have made remarkable progress in image generation [15], enhancement [16], cross-modal retrival [23], widely applied in fields including safety [11], medical [9] and so on, the field of image inpainting also witness an evolution. In [22], Xie et al. first applied deep networks into image denoising and reconstruction tasks. Gaining knowledge from big data, the model could handle inpainting problems more flexibly than traditional ones. However when it comes to cases where large region of contents are missing, higher semantic knowledge is needed. Pathak et al. [14] proposed context encoder to learn feature representation to capture both appearance and semantics by introducing adversary loss. Iizuka et al. [5] employed two discriminators to jointly enforce global and local consistency. In their approach, adversary training allows generators to better learn the real image distribution, therefore leading to a visually natural result. Wang et al. [20] employed perceptual loss to increase semantic similarity. Targeting at GAN based networks' huge scale and resulting high training and executing cost, some approaches aimed at fast and efficient inpainting, by introducing new structure of deep models, such as fully connected networks, dilated convolution layers [24]. Some researchers also made effort to simulate the way human learn [10].

2.2 Occluded Face Recognition

Existing occluded face recognition approaches can be divided into two types: representation-based and reconstruction-based. The "representation" idea aims to represent the occluded face directly by decreasing or excluding the influence of missing regions and tapping the useable information hidden in remaining pixels. Zhang et al. [26] introduced Local Gabor Binary Patterns (LGBP) to form face representation, then estimated the probability of occlusion by using KullbackLeibler divergence of the LGBP features between the local region and the non-occluded local region. In [12], Oh et al. proposed selective local non-negative matrix factorization to segment the image into multiple patches and detect the unoccluded parts first, and then map them into local non-negative matrix factorization space and perform the matching. However, they are not as convenient to execute as they sound. There still lies challenges like weights setting, especially when missing area is large.

Different from the "representation" idea, the "reconstruction" idea utilizes the redundancy of image data instead by recognizing after completing. Deng et al. [2] proposed exemplar-based graph Laplace algorithm to complete occluded faces. In this way, the approach can use completed faces to boost recognition accuracy. It performs well when similar appearance and expression can be found in the library. However, the type and shape of the occlusions are unenumerable and unpredictable

in real scenarios, which limits its applications. More recently, novel methods based on sparse representation and deep learning were proposed. Zhang et al. [25] proposed DeMeshNet to enforce pixel as well as feature level similarity between input Mesh-Faces and output inpainted faces. It can recover the missing contents with little pixel difference, greatly benefiting recognition task at the same time. While it can only deal with small occluded region, the model proposed in [7] can perform remarkable face completion when a large part of image content is missing, and to some extent increase the identity matching accuracy.

3 Identity Preserving GANs

It is a natural idea to apply state-of-the-art inpainting methods to help promote occluded face recognition performance. Intuitively, an ideal image inpainting model which could truly benefit occluded face recognition should follow two rules: photorealistic and identity preserving. Inspired by that, we propose IP-GANs to meet these two rules for occluded face recognition, which consist of five networks (as shown in Fig. 1), including: an inpainting network, global and local discriminate networks, a parsing network and an identity network. The inpainting network acts as generator, while the global and local discriminate networks play for the discriminator. Moreover, the parsing network and the identity network are used to regularize the generator by enforcing the semantic and identity consistencies, respectively.

3.1 Generator for Inpainting

The inpainting network takes a face image with missing regions (generally filled with random noises) as input and generate a photorealistic and identity-preserving completed face image. Let $\mathbf{x}$ and $\mathbf{y}$ denote the face image with size $m \times n$ to be

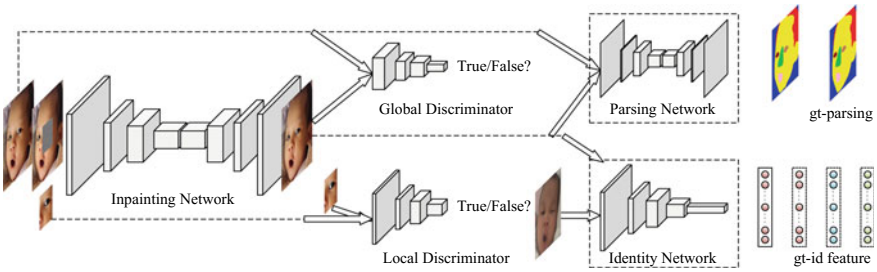

Fig. 1 The structure of IP-GANs. They consist of five networks: an inpainting network acting as the generator, two discriminate networks as the discriminator, a parsing network for facial harmony, and an identity network for recovering identity cues

inpainted and the complete ground truth, respectively. The binary mask $\mathbf{M}$ with the same size as $\mathbf{x}$ is used to label the missing region, marking with 1 and 0 for inside and outside the missing region, respectively. Then, the generator takes $\mathbf{x}$ and $\mathbf{M}$ as input and is defined as $\mathcal{G}(\mathbf{x}, \mathbf{M})$. Following traditional GANs [3], the reconstruction loss could be defined with mean square error (MSE) between the inpainted image $\mathbf{x}$ and the ground truth $\mathbf{y}$:

$$\mathcal{L}_{rec} = \frac{1}{mn} \|\mathcal{G}(\mathbf{x}, \mathbf{M}) - \mathbf{y}\|^2 \tag{1}$$

where $\| * \|$ is ℓ_2 norm operator. In this way, MSE loss can benefit the stability during training although it tends to bring blurring.

The architecture follows an encoder-decoder framework. It first maps the input image into a hidden feature space, then reconstructs it based on the feature representation. Following [7], we use the architecture from "conv1" to "pool3" of the VGG-19 network [17], stack two more convolution layers and one more pooling layer on top of that, and add a fully-connected layer after that as the encoder. The decoder is symmetric to the encoder with unpooling layers accordingly.

3.2 Discriminators in Global and Local

Inspired by recent success of inpainting using GANs [5, 7], we adopt two discriminate networks to preserve global and local structures, respectively. Toward this end, the global discriminator takes the whole image as input, while the local discriminator uses only the inpainted region. During the training, the discriminators learn to identify whether input images are real or fake. Contextual information from local and global regions compensate each other, eventually reaching a balance between global consistency and local details. Two discriminators regularize the inpainting network via local and global adversary loss by solving a min-max optimization problem:

$$\mathcal{L}_{D_i} = \min_{\mathcal{G}} \max_{\mathcal{D}_i} \mathbb{E}[\log \mathcal{D}_i(\mathbf{y}) + \log(1 - \mathcal{D}_i(\mathcal{G}(\mathbf{x}, \mathbf{M})))], i \in \{g, l\} \tag{2}$$

where $\mathcal{D}_i$ is the global discriminator when $i = g$ and the local discriminator when $i = l$. At each iteration, the generator and discriminator are alternatively optimized and updated.

The local and global discriminate networks follow the similar architecture, except that the input is the inpainted region and entire image respectively. The architecture is similar to that in DCGAN [15]. It consists of ten convolutional layers and a single fully-connected layer.

3.3 Regularizers for Semantic and Identity

Semantic Regularization. As Fig. 2e shows, introduction of the two discriminators enable the inpainting network to generate realistic face components. However we noted that the generated contents sometimes lack certain consistency with existing parts in size and shape, leading to unnatural expression. Same to [7], we adopt a semantic parsing network to encourage facial harmony. The parsing network functions as a multi-class classifier and assigns a label to every pixel, semantically segmenting the image into 11 parts representing eyes, mouth etc. The parsing network is pre-trained on Helen [5] dataset, which contains 2,330 images, labeled by [18]. The parsing loss is defined as the pixel-wise softmax loss:

$$\mathcal{L}_p = -\frac{1}{mn}\sum_{i=1}^{mn}\log\left(\frac{e^{f_i^{l_i}}}{\sum_{j=1}^{k} e^{f_i^j}}\right) \tag{3}$$

where k is the number of classes, f_i denotes the feature vector of the ith sample and f_i^j denotes the predicted probability of the ith sample belonging to class j, and l_i is the ground true class label.

Identity Regularization. Recent researches have found deep networks to be fragile when facing adversarial examples, which are indistinguishable to human eyes while causing a sharp drop in performance of networks [19]. Inpainting, as an image preprocess method, should provide convenience for later high-level tasks like recognition. Toward this end, both visual and identity information need rightly diffuse into the region to complete. Existing methods tend to neglect the huge divergence between human and machine perception. During the inpainting process, identity information diffuse into the inpainted region with less restraint, leaving a gap of recognition accuracy between the inpainted face images and the ground truths. In order to truly benefit recognition performance, we introduce a novel identity network to narrow the gap in feature space. We use the VGGFace [13] and extract the identity feature representations from its $fc7$ layer. We enforce the effective diffusion of identity information by demanding the features to be as close to the ground truth as possible. Different from perceptual loss, we use another two images with same identity to further restrain the diffusion. We define a corresponding identity content loss $\mathcal{L}_{ip}$ as the ℓ_1 distance between features of inpainted face and realistic face, formulated as below:

$$\mathcal{L}_{ip} = \frac{1}{3}\sum_{i=1}^{3}\left|f_{\mathcal{G}(\mathbf{x},\mathbf{M})} - f_{Y_i}\right| \tag{4}$$

where $|*|$ is ℓ_1 norm operator, $f_{\mathcal{G}(\mathbf{x},\mathbf{M})}$ and f_y denotes the feature representation of the completed face and realistic face respectively, Y_i the ground truth $\mathbf{y}$ when $i = 1$, and images with same identity when $i = 2, 3$.

3.4 Total Loss

Intergrating the terms above, the total loss function can be formulated as

$$\mathcal{L} = \mathcal{L}_{rec} + \lambda_{D_l}\mathcal{L}_{D_l} + \lambda_{D_g}\mathcal{L}_{D_g} + \lambda_p\mathcal{L}_p + \lambda_{ip}\mathcal{L}_{ip} \tag{5}$$

where λ_{D_l}, λ_{D_g}, λ_p and λ_{ip} are weights, the losses $\mathcal{L}_{rec}$, $\mathcal{L}_{D_l}$, $\mathcal{L}_{D_g}$, $\mathcal{L}_p$ and $\mathcal{L}_{ip}$ are defined in Eqs. 1, 2, 3 and 4, respectively. The optimization is implemented in Caffe [6] with ADAM algorithm.

4 Experiment

4.1 Dataset

We use the CelebA [8] dataset to train our model. It consists of 202,599 face images covering 10,177 celebrities. Each image is aligned and cropped, via similarity transform based on the two eyes and mouth. As the provided images are rectangle, we do simple cropping and resize them into 128×128 pixels. We follow the standard split with 162,770 images for training and 19,867 for validation. As our aim is to improve the recognition performance, we apply the LFW [4] dataset for testing. As one of the most authoritative dataset for face verification in the unconstrained environment, the LFW dataset consists of 13,323 images of 5,749 identities. To show justice, we apply the same process as in CelebA dataset to prepare the data. We set the mask size to be 64×64 for training. To prevent over-fitting and improve the generalization ability of the model, we do data augmentation that includes flipping, shift and rotation ($\pm 15°$). During the training, the size of the mask is fixed but the position is random, preventing the model from latching on certain contents only.

4.2 Implementation Details

The masked region of the image is pre-filled with random noise before inputting into the generator. In this experiment, we set $\lambda_{D_l} = \lambda_{D_g} = 300$, $\lambda_p = 0.05$ and $\lambda_{ip} = 2 \times 10^5$, other hyper parameters like learning rate refer to [15].

During the training, joint optimization of the generator and two discriminators brings great instability. To settle this, we split the training process into three stages and gradually increase the difficulty. At the first stage, only reconstruction loss is used. Then at the second stage, we finetune the model with local adversary loss. Finally we introduce the global adversary loss, the parsing loss and the identity loss. Each stage serves as a pre-training for the next one, allowing more efficient and stable training. When training with adversary loss, we further split it into two

phases to ensure stable training. At the local and global adversary stage, we fixed the generator and train the discriminator for some time to initiate, then jointly train the generator and discriminators.

4.3 Qualitative Results

First we investigate the influence of different regularization terms, by only use incomplete combination of them and make comparations. The completion results by models of different stages are present in Fig. 2, where the models are trained with $\mathbf{S}_1$: $\{\mathcal{L}_{rec}\}$, $\mathbf{S}_2$: $\{\mathcal{L}_{rec}, \mathcal{L}_{D_l}\}$, $\mathbf{S}_3$: $\{\mathcal{L}_{rec}, \mathcal{L}_{D_l}, \mathcal{L}_{D_g}\}$, $\mathbf{S}_4$: $\{\mathcal{L}_{rec}, \mathcal{L}_{D_l}, \mathcal{L}_{D_g}, \mathcal{L}_p\}$, respectively. As Fig. 2 shows, first at the reconstruction stage, the generator reconstruct the general shape of facial components, though blurry. More details are restored as local adversary loss is invited, which greatly help the realism. The global adversary loss then make some adjustment to keep consistency around the borders of region to inpaint. On top of that, the semantic parsing loss refines the synthesised content to keep in harmony with existing contents. Finally, the identity-preserving term further refines the image, narrowing the gap in feature space, therefore truly benefiting the field of occluded face recognition.

Figure 3 shows our completion results on LFW dataset. It is worth noting that in the second and third column at (II) row, given different definition of mask, the model presents different inpainting accordingly. This proves our model capable of utilize semantic context and do intelligent inpainting.

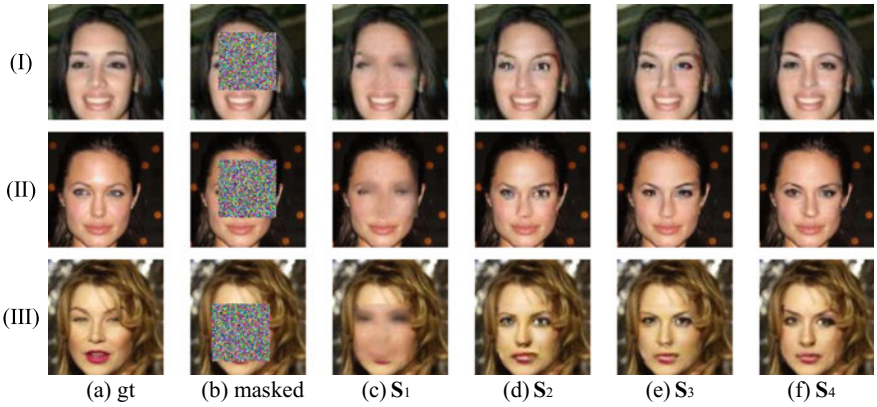

Fig. 2 Completion results under different settings of our models. The first two column are original images and masked input. The others are completion results of models trained with $\mathbf{S}_1$: $\{\mathcal{L}_{rec}\}$, $\mathbf{S}_2$: $\{\mathcal{L}_{rec}, \mathcal{L}_{D_l}\}$, $\mathbf{S}_3$: $\{\mathcal{L}_{rec}, \mathcal{L}_{D_l}, \mathcal{L}_{D_g}\}$, $\mathbf{S}_4$: $\{\mathcal{L}_{rec}, \mathcal{L}_{D_l}, \mathcal{L}_{D_g}, \mathcal{L}_p\}$, from left to right

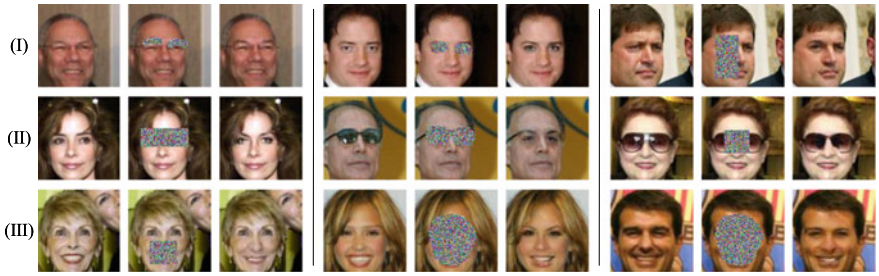

Fig. 3 Inpainting results with irregular mask. In each panel, from left to right: ground truth, masked face, faces completed by IP-GANs

4.4 Quantitative Results

Beyond the subjective visual results, we further perform quantitative evaluation using metrics with PSNR and SSIM (Structural Similarity Index) following [7, 14]. PSNR directly measures the pixel-level difference between two pictures, and SSIM measures the similarity between images from a global structural view. Moreover, the accuracy is applied for evaluating the performance of occluded face recognition. These three metrics are computed between every completed image and its corresponding original one. The results are shown in Table 1.

5 Conclusion

In this work, we propose a novel Identity Preserving GANs (IP-GANs) for occluded face recognition tasks. The model can successfully synthesize semantically valid and visually plausible contents for the missing facial key parts from random noise and greatly promote recognition performance. Thorough experiments show that our model is capable of handling occlusions with varieties of shapes and sizes, providing general and effective solution for occluded face recognition.

Table 1 Quantitative results of un-inpainted face images, face images inpainted by GFC [7] and the our proposed models trained with different loss setting. Specifically, model $\mathbf{S}_{1-4}$ are trained with $\mathbf{S}_1$: $\{\mathcal{L}_{rec}\}$, $\mathbf{S}_2$: $\{\mathcal{L}_{rec}, \mathcal{L}_{D_l}\}$, $\mathbf{S}_3$: $\{\mathcal{L}_{rec}, \mathcal{L}_{D_l}, \mathcal{L}_{D_g}\}$, $\mathbf{S}_4$: $\{\mathcal{L}_{rec}, \mathcal{L}_{D_l}, \mathcal{L}_{D_g}, \mathcal{L}_p\}$, and the final IP-GANs $\mathbf{S}_5$: $\{\mathcal{L}_{rec}, \mathcal{L}_{D_l}, \mathcal{L}_{D_g}, \mathcal{L}_p, \mathcal{L}_{ip}\}$

Metrics	Un-inpainted	GFC [7]	S_1	S_2	S_3	S_4	S_5
SSIM	0.7285	0.9384	0.9335	0.9337	0.9405	0.9408	0.9442
PSNR (dB)	5.3952	18.088	16.9467	17.2232	18.7169	18.7346	19.301
Accuracy	0.7998	0.8417	0.819	0.8335	0.842	0.844	0.855

Acknowledgements This work is supported in part by the National Natural Science Foundation of China (61772513 & 61402463), the National Key Research and Development Plan (2016YFC0801005) and the International Cooperation Project of Institute of Information Engineering, Chinese Academy of Sciences (Y7Z0511101). Shiming Ge is also supported by Youth Innovation Promotion Association, CAS.

References

1. Bertalmio, M., Sapiro, G., Caselles, V., Ballester, C.: Image inpainting. In: Proceedings of SIGGRAPH, vol. 4, no. 9, pp. 417–424 (2005)
2. Deng, Y., Dai, Q., Zhang, Z.: Graph Laplace for occluded face completion and recognition. IEEE Trans. Image Process. Publ. IEEE Signal Process. Soc. **20**(8), 2329–2338 (2011)
3. Goodfellow, I.J., Pouget-Abadie, J., Mirza, M., Xu, B., Warde-Farley, D., Ozair, S., Courville, A., Bengio, Y.: Generative adversarial nets. In: International Conference on Neural Information Processing Systems, pp. 2672–2680 (2014)
4. Huang, G.B., Ramesh, M., Berg, T., Learned-Miller, E.: Labeled faces in the wild: a database for studying face recognition in unconstrained environments. Technical Report 07-49, University of Massachusetts, Amherst (October 2007)
5. Ishikawa, H., Ishikawa, H., Ishikawa, H.: Globally and locally consistent image completion. ACM (2017)
6. Jia, Y., Shelhamer, E., Donahue, J., et al.: Caffe: convolutional architecture for fast feature embedding (2014). arXiv:1408.5093
7. Li, Y., Liu, S., Yang, J., Yang, M.H.: Generative face completion. In: The IEEE Conference on Computer Vision and Pattern Recognition (CVPR), July 2017
8. Liu, Z., Luo, P., Wang, X., Tang, X.: Deep learning face attributes in the wild. In: IEEE International Conference on Computer Vision, pp. 3730–3738 (2015)
9. Lu, H., Li, B., Zhu, J., Li, Y., Li, Y., Xu, X., He, L., Li, X., Li, J., Serikawa, S.: Wound intensity correction and segmentation with convolutional neural networks. Concur. Comput. Pract. Exp. **29**(6) (2016)
10. Lu, H., Li, Y., Chen, M., Kim, H., Serikawa, S.: Brain intelligence: go beyond artificial intelligence. Mob. Netw. Appl. **23**(2), 368–375 (2017)
11. Lu, H., Li, Y., Mu, S., Wang, D., Kim, H., Serikawa, S.: Motor anomaly detection for unmanned aerial vehicles using reinforcement learning. IEEE Internet Things J **5**(4), 2315–2322 (2018)
12. Oh, H.J., Lee, K.M., Sang, U.L.: Occlusion invariant face recognition using selective local non-negative matrix factorization basis images. Image Vis. Comput. **26**(11), 1515–1523 (2008)
13. Parkhi, O.M., Vedaldi, A., Zisserman, A.: Deep face recognition. In: British Machine Vision Conference (2015)
14. Pathak, D., Krahenbuhl, P., Donahue, J., Darrell, T., Efros, A.A.: Context encoders: feature learning by inpainting. In: The IEEE Conference on Computer Vision and Pattern Recognition (CVPR), pp. 2536–2544 (2016)
15. Radford, A., Metz, L., Chintala, S.: Unsupervised representation learning with deep convolutional generative adversarial networks. CoRR (2015). arXiv:1511.06434
16. Serikawa, S., Lu, H.: Underwater image dehazing using joint trilateral filter. Pergamon Press, Inc. (2014)
17. Simonyan, K., Zisserman, A.: Very deep convolutional networks for large-scale image recognition. CoRR (2014). arXiv:1409.1556
18. Smith, B.M., Zhang, L., Brandt, J., Lin, Z., Yang, J.: Exemplar-based face parsing. In: IEEE Conference on Computer Vision and Pattern Recognition, pp. 3484–3491 (2013)
19. Szegedy, C., Zaremba, W., Sutskever, I., Bruna, J., Erhan, D., Goodfellow, I., Fergus, R.: Intriguing properties of neural networks. Computer Science (2013)

20. Wang, C., Xu, C., Wanga, C., Tao, D.: Perceptual adversarial networks for image-to-image transformation. IEEE Trans. Image Process. **27**(8), 4066–4079 (2018)
21. Wright, J., Ganesh, A., Zhou, Z., Wagner, A., Ma, Y.: Demo: robust face recognition via sparse representation. In: IEEE International Conference on Automatic Face & Gesture Recognition, pp. 1–2 (2009)
22. Xie, J., Xu, L., Chen, E.: Image denoising and inpainting with deep neural networks. In: International Conference on Neural Information Processing Systems, pp. 341–349 (2012)
23. Xu, X., He, L., Lu, H., Gao, L., Ji, Y.: Deep adversarial metric learning for cross-modal retrieval. In: World Wide Web-internet & Web Information Systems, pp. 1–16 (2018)
24. Yu, J., Lin, Z., Yang, J., Shen, X., Lu, X., Huang, T.S.: Generative image inpainting with contextual attention. CoRR (2018). arXiv:1801.07892
25. Zhang, S., He, R., Sun, Z., Tan, T.: Demeshnet: blind face inpainting for deep meshface verification. IEEE Trans. Inf. Forensics Secur. **13**(3), 637–647 (2017)
26. Zhang, W., Shan, S., Chen, X., Gao, W.: Local Gabor binary patterns based on Kullback–Leibler divergence for partially occluded face recognition. IEEE Signal Process. Lett. **14**(11), 875–878 (2007)

Batch Dictionary Learning with Augmented Orthogonal Matching Pursuit

Ping He, Baichuan Fan, Xiaohua Xu, Yali Liang, Yuan Lou, Zhijun Zhang and Xincheng Chang

Abstract Dictionary learning is often incorporated in classification method, which can obtain a new representation under the learned dictionary to achieve better classification performance. In this paper, we propose a novel Batch Dictionary Learning model with augmented orthogonal matching pursuit classification. Batch Dictionary Learning model is capable of improving the dictionary by removing the redundancy of over-complete dictionary, thus the learned optimal dictionary is more suitable for classification. To solve the optimization target, we improve the traditional orthogonal matching pursuit (OMP) algorithm and propose an augmented orthogonal matching pursuit algorithm (AOMP) to solve the objective function. Superior experimental results demonstrate that our proposed model outperform the other state-of-the-art classification algorithms on real-world dataset.

Keywords Classification · Sparse learning · Dictionary learning
Sparse representation

1 Introduction

Dictionary learning is a promising method that emerges in recent years, which is especially adept in dealing with small number of sample and reducing data redundancy. By far, different classification methods have been proposed based on dictionary learning [1–3]. However, in the existing research of dictionary learning, dictionary is set as the whole training data, thus the size of the dictionary is large. This limitation can be overcome by learning a self-adapting dictionary, and K-SVD [3–5] is an effective dictionary learning method and has been successfully applied in medical diagnosis [6–8].

P. He · B. Fan · X. Xu (✉) · Y. Liang · Y. Lou · Z. Zhang · X. Chang
Department of Computer Science, Yangzhou University, Yangzhou, China
e-mail: arterx@gmail.com

H. Lu (ed.), *Cognitive Internet of Things: Frameworks, Tools and Applications*, Studies in Computational Intelligence 810,
https://doi.org/10.1007/978-3-030-04946-1_42

We propose a novel *Batch Dictionary Learning* (BDL) model on the basis of K-SVD in this paper, which reduces the times of performing SVD and removes the redundancy of over-complete dictionary by using a batch updating strategy. Moreover, we propose an augmented orthogonal matching pursuit (AOMP) algorithm to solve the optimization problem of BDL model. After the dictionary is learned, we classify samples with a similarity-based classification method. To evaluate the performance of our proposed model, we compared our model with some state-of-the-art classification algorithms on real-world datasets by classification accuracy. Promising experimental results demonstrate the effectiveness and efficiency of our method.

The rest of this paper is organized as follows: Sect. 2 introduces the K-SVD algorithm. Section 3 describes the Batch Dictionary Learning model as well as AOMP algorithm, which is used to solve the objective function. Section 4 compares the proposed method with some state-of-the-art classification methods on real-world gene expression datasets. Section 5 gives a conclusion.

2 K-SVD

K-SVD aims to find an optimal dictionary $\mathbf{D} \in \mathbb{R}^{m\times K}$ and the corresponding sparse representation $\mathbf{X} \in \mathbb{R}^{K\times n}$ to approximate the data matrix $\Phi \in \mathbb{R}^{m\times n}$.

$$\min_{\mathbf{D},\mathbf{X}} \|\Phi - \mathbf{D}\mathbf{X}\|_F^2 \text{ s.t.} \forall i,\ \|\boldsymbol{x}_i\|_0 \leq T_0 \tag{1}$$

where $\boldsymbol{x}_i$ is the i-th column vector of $\mathbf{X}$, the constraint is to ensure the sparsity of the new representations.

K-SVD algorithm alternatively updates the factors in turn since the optimization problems is non-convex. When updating sparse code, K-SVD keeps the dictionary $\mathbf{D}$ fixed and obtains $\mathbf{X}$ by solving following problem:

$$\min_{x_i} \|\Phi_i - \mathbf{D}\boldsymbol{x}_i\|_2^2 \text{ s.t.} \forall i,\ \|\boldsymbol{x}_i\|_0 \leq T_0 \tag{2}$$

When updating the dictionary, K-SVD fixes the representation matrix $\mathbf{X}$, and only updates the k-th column $\boldsymbol{d}_k$ of the dictionary D. We set the k-th row of $\mathbf{X}$ as $\boldsymbol{x}^k$, which is to be multiplied by $\boldsymbol{d}_k$, thus the objective function is

$$\|\Phi - \mathbf{D}\mathbf{X}\|_F^2 = \left\|\Phi - \sum_{i=1}^{K} \boldsymbol{d}_i\, \boldsymbol{x}^i\right\|_F^2 = \left\|(\Phi - \sum_{i\neq k} \boldsymbol{d}_i\, \boldsymbol{x}^i) - \boldsymbol{d}_k\, \boldsymbol{x}^k\right\|_F^2 = \left\|\boldsymbol{E}_k - \boldsymbol{d}_k\, \boldsymbol{x}^k\right\|_F^2 \tag{3}$$

3 Proposed Model

We develop a Batch Dictionary Learning model on the basis of K-SVD, which can reduce the computational cost of performing SVD and remove the redundancy of dictionary. The proposed model generally updates the dictionary as follows.

First, we rearrange the order of row vectors in $\mathbf{X}$ according to the index of nonzero elements in a row and rearrange the order of column vectors in $\mathbf{D}$ accordingly. In essence, we divide the rows in $\mathbf{X}$ and the columns in $\mathbf{D}$ into C groups. Then, we use τ to denote the index after rearrangement, and use τ_i to denote the indexes belong to the i-th group.

Second, we update the dictionary $\mathbf{D}$ in a batch mode, instead of updating one column each time:

$$\|\Phi - \mathbf{DX}\|_F^2 = \left\|(\Phi - \sum_{i \neq c} \boldsymbol{d}_{\tau_i} \boldsymbol{x}^{\tau_i}) - \boldsymbol{d}_{\tau_c} \boldsymbol{x}^{\tau_c}\right\|_F^2 = \left\|\mathbf{E}_{\tau_c} - \boldsymbol{d}_{\tau_c} \boldsymbol{x}^{\tau_c}\right\|_F^2 \tag{4}$$

In order to fix the position of nonzero elements, we perform SVD on $\mathbf{E}_{\tau_c}^R$, which only keeps the nonzero positions of inner product of $\boldsymbol{d}_{\tau_c}$ and $\boldsymbol{x}^{\tau_c}$ in $\mathbf{E}_{\tau_c}$, then update $\boldsymbol{d}_{\tau_c}$ and $\boldsymbol{x}^{\tau_c}$ by:

$$\boldsymbol{d}_{\tau_c} = \boldsymbol{u}_1, \boldsymbol{x}^{\tau_c} = \boldsymbol{\sigma}_1 \boldsymbol{v}_1^T \tag{5}$$

For the dictionary update stage of the proposed method, we propose an augmented orthogonal matching pursuit algorithm, i.e., AOMP, to solve the problem $\min_{\boldsymbol{a}} \|\boldsymbol{a}\|_1$, s.t.$\boldsymbol{y} = \mathbf{D}\boldsymbol{a}$. AOMP is developed on the basis of OMP. The difference between two algorithms is that in each iteration AOMP selects multiple vectors as candidate optimal vectors, instead of only one vector.

Assume that h is the number of candidate vectors selected in an iteration, we sort the absolute inner product between the dictionary and the residual in descending order,

$$[\boldsymbol{p}, \boldsymbol{j}] = \text{sort}(\left|\mathbf{D}^T \boldsymbol{r}\right|, \text{'descend'}) \tag{6}$$

where $\boldsymbol{p}$ is the n-dimensional vector after sorting, $\boldsymbol{j}$ is the vector of corresponding index. While OMP selects the vector corresponding to max value in $\boldsymbol{p}$, AOMP selects the first h vectors in $\mathbf{D}$ whose sum of values in $\boldsymbol{p}$ is larger than a threshold $\lambda \sum \boldsymbol{p}$, where $\lambda \in [0, 1]$ is a specified weight:

$$\min_h \sum_{t=1}^{h} \boldsymbol{p}_t > \lambda \sum \boldsymbol{p} \tag{7}$$

Then these h vectors are added to the index set V. With the index set V, we can update $\boldsymbol{a}$ by $\boldsymbol{a} = (\mathbf{D}_V^T \mathbf{D}_V)^{-1} \mathbf{D}_V^T \boldsymbol{y}$ until convergence.

With the proposed AOMP algorithm, we can compute the sparse representation $\boldsymbol{a}$ of an arbitrary test data $\boldsymbol{y}$ is the sparse representation under the dictionary $\mathbf{D}$. Assume that the number of the training sample in the i-th class is n_i, we use $\mathbf{X}^{(i)} = [\boldsymbol{x}_1^{(i)}, \ldots, \boldsymbol{x}_{n_i}^{(i)}]$ to denote the sparse representation of training samples under $\mathbf{D}$. Then, we can obtain the mean sparse representation of the training samples in the i-th class:

$$\overline{X^{(i)}} = \frac{1}{n_i} \sum_{j=1}^{n_i} \boldsymbol{x}_j^{(i)} \tag{8}$$

Finally, we assign the test data to the class that has the highest absolute cosine similarity between $\boldsymbol{a}$ and $\mathbf{X}^{(i)}$.

4 Experiments

We evaluate the performance of our model on the task of classification in comparison with three classic classification methods, including Linear SVM, C4.5 algorithm and KNN (K nearest neighbors) with K set to the half number of classes, on two real-world gene expression datasets, i.e., SRBCT and Brain. SRBCT dataset contains gene expression level of 2308 genes from 83 patients with 4 subtype tumors and Brain dataset contains gene expression level of 5920 gens from 90 patients with 5 different brain diseases.

During the experiments, we use the one-versus-rest cross validation, i.e. choosing one sample as test sample and the rest as training samples. We change the test sample in turn to compute the average classification accuracy of each algorithm. For each algorithm, we first reduce the dimension of datasets to 4, 8, 16, 32 and 64 dimensions with SVD.

According to Tables 1 and 2, it is obvious that our model is capable of producing as high classification accuracy as SVM when dimension is reduced to an appropriate dimension. Meanwhile, results show that BDL model costs much less computational time than the state-of-the-art SVM and C4.5, and is even comparable to KNN. In generation, Batch Dictionary Learning model outperform the other classic classification algorithms, and the time cost is relatively low. The comparison of these algorithms demonstrates the effectiveness as well as efficiency of our proposed BDL model.

Table 1 The classification accuracy on SRBCT

Methods	Dimensions				
	4	8	16	32	64
BDL	0.8072	0.9518	**0.9759**	0.9477	**0.9639**
SVM	**0.8795**	**0.9759**	0.9639	**0.9639**	0.9518
C4.5	0.7470	0.8193	0.8193	0.8072	0.7831
KNN	0.7590	0.8916	0.8554	0.8554	0.8675

Table 2 The classification accuracy on Brain

Methods	Dimensions				
	4	8	16	32	64
BDL	0.7111	0.7656	**0.8111**	**0.8222**	**0.8556**
SVM	**0.8111**	**0.7889**	**0.8111**	0.8000	0.8111
C4.5	0.7333	0.7111	0.6667	0.6889	0.6667
KNN	0.7556	0.7333	0.7667	0.7222	0.7444

5 Conclusion

We propose a Batch Dictionary Learning model to solve the classification problem in this paper. BDL model improves the K-SVD algorithm by using a batch strategy to update the dictionary. To solve the optimization problem, we propose a new optimization method AOMP based on OMP, and classify the samples using a similarity based method.

Superior experimental results show that BDL model achieves higher classification accuracy and relatively less time cost than the state-of-the-art classifiers when datasets are reduced to an appropriate dimension.

Acknowledgements This research was supported in part by the Chinese National Natural Science Foundation under Grant nos. 61402395, 61472343 and 61502412, Natural Science Foundation of Jiangsu Province under contracts BK20140492, BK20151314, Jiangsu overseas research and training program for university prominent young and middle-aged teachers and presidents, Jiangsu government scholarship funding.

References

1. Donoho, D.L.: Compressed sensing. J. IEEE Trans. Inf. Theory **52**(4), 1289–1306 (2006)
2. Engan, K., Aase, S.O., Husoy, J.H.: Method of optimal directions for frame design. In: Proceedings of 1999 IEEE International Conference on Acoustics, Speech, and Signal Processing, vol. 5, pp. 2443–2446. IEEE (1999)
3. Aharon, M., Elad, M., Bruckstein, A.M.: The K-SVD: an algorithm for designing of overcomplete dictionaries for sparse representations. IEEE Trans. Image Process. **54**, 4311–4322 (2006)
4. Aharon, M., Elad, M., Bruckstein, A.: K-SVD: design of dictionaries for sparse representation. In: Proceedings of SPARS, vol. 5, pp. 9–12 (2005)
5. Bruckstein, A.M., Donoho, D.L., Elad, M.: From sparse solutions of systems of equations to sparse modeling of signals and images. SIAM Rev. **51**, 34–81 (2009)
6. Farouk, R.M., Elsayed, M., Aly, M.: Medical image denoising based on log-Gabor wavelet dictionary and K-SVD algorithm. Int. J. Comput. Appl. **141**(2016)
7. Yang, J., Zhang, X., Peng, W., et al.: A novel regularized K-SVD dictionary learning based medical image super-resolution algorithm. Multimed. Tools Appl. **75**, 13107–13120 (2016)
8. Chen, J., Liu, S., Huang, M., et al.: Dictionary learning for MRI denoising based on modified K-SVD. J. Imaging Sci. Technol. 61: 30505-1–30505-10 (2017)

A Skin Lesion Segmentation Method Based on Saliency and Adaptive Thresholding in Wavelet Domain

Kai Hu, Si Liu, Yuan Zhang, Chunhong Cao, Fen Xiao, Wei Huang and Xieping Gao

Abstract Segmentation is the essential requirement in automated computer-aided diagnosis (CAD) of skin diseases. In this paper, we propose an unsupervised skin lesion segmentation method to challenge the difficulties existing in the dermoscopy images such as low contrast, border indistinct, and skin lesion is close to the boundary. Our method combines the enhanced fusion saliency with adaptive thresholding based on wavelet transform to get the lesion regions. Firstly, the saliency map increases the contract of the skin lesion and healthy skin, and then an adaptive thresholding method based on wavelet transform is used to obtain more accurate lesion regions. Experiments on dermoscopy images demonstrate the effectiveness of the proposed method over several state-of-the-art methods in terms of quantitative results and visual effects.

Keywords Saliency map · Adaptive thresholding · Wavelet transform
Dermoscopy images · Segmentation

1 Introduction

According to the World Health Organization, one out of every three cancers diagnosed is the skin cancer [1]. And the incidence of skin cancer continues to annually escalate [1]. Melanoma, as one of the deadliest skin cancers which is reported a high cure

K. Hu (✉) · S. Liu · Y. Zhang · C. Cao · F. Xiao · X. Gao
Key Laboratory of Intelligent Computing and Information Processing
of Ministry of Education, Xiangtan University, Xiangtan 411105, China
e-mail: kaihu@xtu.edu.cn

K. Hu
Postdoctoral Research Station for Mechanics,
Xiangtan University, Xiangtan 411105, China

W. Huang
Department of Radiology, The First Hospital
of Changsha, Changsha 410005, China

H. Lu (ed.), *Cognitive Internet of Things: Frameworks, Tools and Applications*, Studies in Computational Intelligence 810,
https://doi.org/10.1007/978-3-030-04946-1_43

rate on condition it diagnosed in early stages [2, 3]. Dermoscopy is a non-invasive image diagnosis technique for the in vivo observation of pigmented skin lesions in dermatology [4, 5]. However, it needs a great deal of experience from dermatologists to apply this tool for improving diagnostic accuracy. Therefore, it is necessary to develop an automated and efficient noninvasive computer-aided diagnosis (CAD) system [6–8] to assist dermatologists for the diagnosis of skin diseases.

In general, the CAD system of the skin lesion includes the following steps [6]: image pre-processing, segmentation of skin lesions, dermoscopy feature extraction, and classification. Among them, the effective segmentation of skin lesions will boost the accuracy of the subsequent steps and plays an important role in the whole CAD system.

In the past few years, a large variety of approaches such as histogram thresholding [9], region-based method [10, 11], and active contour model [12] have shown their significant merits for the segmentation of skin lesions. Histogram thresholding is effective to segment the images with high contrast between skin lesions with healthy skin. The region-based method has poor performance in segmenting the images with variegated color. And the active contour model is sensitive with the fuzzy borders. Therefore, due to the complexity of dermoscopy images [13], the accurate segmentation of skin lesions remains challenging.

The saliency detection model detects visually significant areas or objects by mimicking the mechanisms of human visual and cognitive systems [5, 14–16], can develop high contrast, unit color and clear borders between skin lesions with healthy skin. Therefore, the lesion segmentation based on the saliency detection has been received an increasing attention in recent years. Ahn et al. [5] employed the superpixel segmentation algorithm to segment the image into several superpixels and created the background template by measuring the boundary connectivity of each superpixel [17]. Then, they used the sparse coding method to construct the saliency map [3]. This method obtained a better result by using the structural, color, and spatial location cues, but the construction of the saliency map didn't consider the other useful information like brightness. Fan et al. [13] proposed a novel saliency map by combining both of brightness and color saliency map. Their color saliency map used the quantized image to quicken up the saliency calculating process [13]. In the meantime, it means that they reduced the contrast between the skin lesions with healthy skin. Hence, some lesions maybe recognize wrongly according to their hypothesis [3].

To solve the preceding issues, we introduce a hybrid dermoscopy image segmentation framework, which consists of an image enhancement based on fusion saliency and an adaptive thresholding segmentation based on wavelet transform. Our segmentation method firstly characterizes the image contrast in different regions to obtain the saliency map. Then, we employ an adaptive thresholding strategy based on wavelet transform to obtain the segmentation of skin lesions. On the side, it is an unsupervised method which does not exist any training process. The proposed method was evaluated on the PH2 dataset, and the results have shown that it performed better than several state-of-the-art methods.

2 Method

Compared to surrounding regions, the skin lesions can be considered a salient object in dermoscopy images by color and brightness. Hence, we use the saliency map to enhance lesion regions and then the adaptive thresholding based on wavelet transform is improved to accurately separate the lesion area from the healthy skin. The flowchart of the proposed segmentation method is shown in Fig. 1.

2.1 Preprocessing

The visual artifact like skin hairs will influence the performance of the segmentation approach, so the algorithm of Lee et al. is utilized to exclude this artifact [18].

2.2 Image Enhancement Based on Fusion Saliency Map

Color saliency map. As mentioned in [19], the saliency method is the first application for segmenting skin lesion in dermoscopy images [5]. And they extended their previous work to solve the situation that skin lesions touch the image boundaries. In this paper, like the work of Ahn et al. [5], the color saliency map is obtained by the following steps:

- We partition the dermoscopy image into some superpixels and measure the boundary connectivity [17] of each superpixel to construct the background template.
- The saliency map is created via the sparse reconstruction error which compared the error value with the background template and then we apply the Context-based error propagation for further optimize the saliency map [5].
- We use a multi-scale framework to integrate superpixel level saliency map to pixel level saliency map.

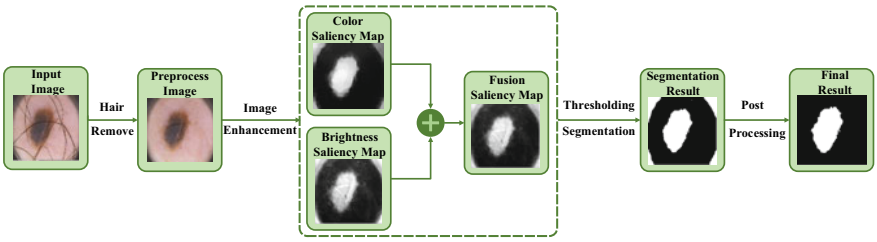

Fig. 1 The flowchart of the proposed segmentation method

Brightness saliency map. Inspired by Fan et al. in [13] used boundary prior and brightness prior to construct the brightness saliency map, we herein utilize the RGB color space of dermoscopy images for segmenting the skin lesion from healthy skin. And then we find that the image has better contract between lesion and healthy skin in the blue channel. Therefore, blue component is used for further processing, which can show better segmentation result as other channels.

The brightness I_B is represented as the blue component of three channels in RGB images. Similar to the design of brightness saliency map in [13], we can easily obtain the average brightness values of boundary patches [13], which marked as $m_1, m_2, \ldots, m_N$. At the same time, the average brightness values quantify the contribution of boundary patches to the brightness saliency map, which is used to avoid the situation that those boundary patches belonging to skin lesions have a great influence on the composition of the saliency map [13]. In other words, it measures the patch located in healthy skin areas has weight than skin lesions [13], the weighting ω_i for ith patch satisfies the following formula:

$$\omega_i = m_i \Big/ \sum_{j=1}^{N} m_j, \quad i = 1, 2, 3, \ldots, N. \tag{1}$$

In the case of brightness prior, when the brightness value of pixels higher than the mean value of boundary patches that on behalf of healthy skin, the saliency value of the pixels is zero. Hence, we defined the following formula for the generation of the brightness saliency map by ith boundary patch:

$$S_{Bi}(j) = \begin{cases} m_i - I_B(j), & m_i > I_B(j). \\ 0, & m_i \le I_B(j). \end{cases} \tag{2}$$

where $j = 1, 2, \ldots, N_p$, N_p is the number of pixels in the input image, and m_i is the mean of the ith boundary prior patch.

The final brightness saliency map is accomplished by calculating the following formula:

$$S_B(j) = \sum_{i=1}^{N} \omega_i S_{Bi}(j), \quad j = 1, 2, \ldots, N_p. \tag{3}$$

Fusion saliency map. The saliency values of healthy skin pixels in color and brightness saliency maps tend to be close to zero, and the high saliency value belongs to the skin lesions. For the purpose of enhancing the lesion regions, we fused the color saliency map and brightness saliency map by the following strategy.

$$Fusion\,saliency = \alpha \times saliency_C + \beta \times saliency_B, \ \alpha + \beta = 1. \tag{4}$$

where α and β denote the minimum of error evaluation metric which are obtained by grid search method. In our experiments, α and β are set as 0.32 and 0.68, respectively. The fusion saliency map is effective to suppress the backgrounds and enhance the objects.

2.3 Adaptive Thresholding Segmentation Based on Wavelet Transform

The skin lesion and healthy skin have high contract in the fusion saliency map. And the histograms of the fusion saliency map present bimodal distribution. Therefore, the adaptive thresholding method based on wavelet transform can be utilized to effectively divide the saliency map into the lesion and background region. The approximation subimages of the fusion map are obtained by two times Cohen-Daubechies-Feauveau-biorthogonal (bior1.1). According to Zhang and Desai [20], the gray-level probability density function (PDF) approaches to Gaussian distribution after wavelet transform. Let $P_s(t)$ and $P_l(t)$ indicate the PDFs of the skin and the lesion, they can be computed as

$$P_s(t) = \frac{1}{\sqrt{2\pi}\sigma_1}\exp\left\{-\frac{(t-\bar{t}_1)^2}{2\sigma_1^2}\right\}$$
$$P_l(t) = \frac{1}{\sqrt{2\pi}\sigma_2}\exp\left\{-\frac{(t-\bar{t}_2)^2}{2\sigma_2^2}\right\},\ \bar{t}_2 > \bar{t}_1. \tag{5}$$

where t denotes the pixel value, $\bar{t}_1$ and $\bar{t}_2$ are the means of the skin and the lesion of the image, σ_1 and σ_2 indicate the standard deviations of the skin and the lesion, respectively.

The priori probabilities of the skin and the lesion in the image I_f are presented as $P(S)$ and $P(L)$. Let $P_f(t)$ be the PDF of the image I_f, and it can be calculated as

$$P_f(t) = P(S)P_s(t) + P(L)P_l(t) \tag{6}$$

When the Bayes threshold λ_1 [21] satisfies $P(S)P_s(\lambda_1) = P(L)P_l(\lambda_1)$, we can get the segmentation by a process of pixel classify using the following formula

$$Binary(u, v) = \begin{cases} 0,\ I_f(u, v) < \lambda_1. \\ 1,\ I_f(u, v) \geq \lambda_1. \end{cases} \tag{7}$$

where (u, v) indicates the pixel location and $I_f(u, v)$ indicates the pixel value of (u, v). In general, the Bayes threshold λ_1 cannot be calculated since $P_s(t)$, $P_l(t)$, and the priori probability of each class are unknown [21]. However, Zhang and Desai have proved that λ_1 can be approximated by a global local minima which removed the fluctuations after wavelet transform on the PDF. Hence, we use two times Cohen-Daubechies-Feauveau-biorthogonal (bior6.8) to smooth the curve. And then, the global local minima can be found as the adaptive global threshold to achieve the lesion segmentation.

2.4 Postprocessing

Usually, it is easy to observe that the lesion regions contain more than one connected region. However, we only maintain one lesion region which closes to the center of image as our final segmentation result. Therefore, the following postprocessing steps are performed to obtain the final segmentation. Firstly, the hole filling and morphological close operations are used to fill the small holes and isolated islands. Secondly, a Gaussian mask is used to weigh the closeness of connected regions against the center of image [22]. After the connected areas multiply with the Gaussian mask, the largest area is selected as the final segmentation result.

3 Experimental Results

3.1 Dataset

We evaluated the proposed segmentation method on PH2 dataset [23] that had an extensive popularity in the area of dermoscopy image analysis. This dataset consists of 200 dermoscopy images and their corresponding ground truth images. These images are 8-bit RGB color images with a resolution of 768×560 pixels [24].

3.2 Performance Evaluation Metrics and Parameter Setting

A variety of evaluation indicators were used to measure the effectiveness of the segmentation approach. These evaluation metrics are Precision, Error, Recall, Dice Similarity Coefficient (DSC), XOR, and Hammoude Distance (HM). When the higher values of Precision, Recall, and DSC, and lower values of HM, Error, and XOR, the better performance of the segmentation method.

In the experiments, we used the same parameter settings of Ahn et al. did in [5] and Fan et al. did in [13] to respectively construct the color saliency map and brightness saliency map.

3.3 Results

Blue channel selection. We generated the gray-level PDF of input image in R, G and B channels. From Fig. 2, it can be found that the blue channel is more discriminate than other two channels for describing the skin lesion from healthy skin. Therefore, we used the blue color channel for the segmentation of skin lesions.

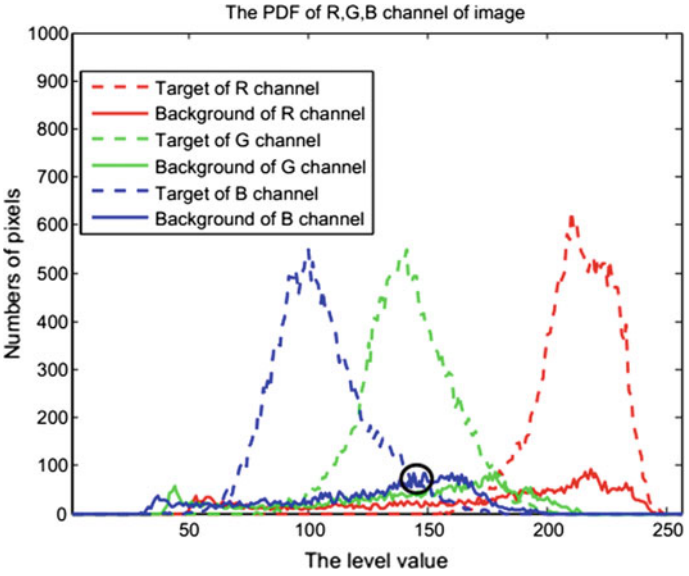

Fig. 2 The example for the selection of blue color channel

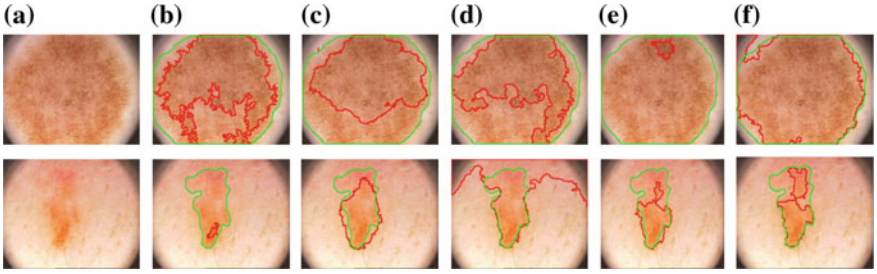

Fig. 3 Comparison of visual effects for the different segmentation methods. **a** Original images. Segmentation results by **b** Otsu [25], **c** SSLS [19], **d** RSSLS [5], **e** Fan et al. [13], and **f** the proposed method. The green and red contours represent the ground truth and the segmentation results, respectively

Comparison with the state-of-the-art methods. In this paper, we compared the proposed method with several state-of-the-art methods, which are named Otsu [25], SSLS [19], RSSLS [5], and Fan et al. [13]. Figure 3 shows the visual effects of the segmentation results.

Table 1 presents the average value of evaluation metrics on PH2 dataset. For Otsu, SSLS and Fan methods, we used the results reported in the paper [13]. Compared with other methods, our method has a better balance between precision with recall. And the other outstanding evaluation metrics also show that our method outperformed than others.

Table 1 Comparison of the proposed method with state-of-the-art methods on the PH2 dataset

Methods	Precision	Recall	Error	DSC	HM	XOR
Otsu [25]	96.37	73.45	11.45	81.33	–	–
SSLS [19]	91.53	83.17	9.88	85.30	–	–
RSSLS [5]	–	–	–	91.05	15.49	16.46
Fan et al. [13]	**96.78**	87.03	6.40	89.35	–	–
Proposed	91.34	**94.24**	**5.34**	**92.19**	**13.86**	**15.87**

The bold font indicates the best result

4 Conclusion

In this paper, we proposed an unsupervised method for the segmentation of dermoscopy images, which combined fusion saliency map with adaptive thresholding based on wavelet transform. We developed an enhanced saliency which fused color saliency and brightness saliency to increase the contrast between skin lesions and healthy skin. Since the histograms of fusion saliency map presented bimodal distribution, we used the adaptive thresholding method based on wavelet transform to effectively segment skin lesions. The results have shown that our method outperformed several state-of-the-art methods.

Acknowledgements This work was supported by the National Natural Science Foundation of China under Grants no. 61802328 and 61771415, and the Cernet Innovation Project under Grant no. NGII20170702.

References

1. Navarro, F., Escudero-Vinolo, M., Bescos, J.: Accurate segmentation and registration of skin lesion images to evaluate lesion change. IEEE J. Biomed. Health Inform. (99), 1 (2018)
2. Stewart, B.W., Wild, C.P.: World Cancer Report 2014, p. 953. World Health Organization (2014)
3. Jahanifar, M., Tajeddin, N.Z., Asl, B.M., Gooya, A., et al.: Supervised saliency map driven segmentation of lesions in dermoscopic images. IEEE J. Biomed. Health Inform. (2018)
4. Silveira, M., Nascimento, J.C., Marques, J.S., et al.: Comparison of segmentation methods for melanoma diagnosis in dermoscopy images. IEEE J. Sel. Top. Signal Process. **3**(1), 35–45 (2009)
5. Ahn, E., Kim, J., Bi, L., et al.: Saliency-based lesion segmentation via background detection in dermoscopic images. IEEE J. Biomed. Health Inform. **21**(6), 1685–1693 (2017)
6. Pathan, S., Prabhu, K.G., Siddalingaswamy, P.C.: Techniques and algorithms for computer aided diagnosis of pigmented skin lesions—a review. Biomed. Signal Process. Control **39**, 237–262 (2018)
7. Lu, H., Li, B., Zhu, J., et al.: Wound intensity correction and segmentation with convolutional neural networks. Concurr. Comput. Pract. Exp. **29**(6), e3927 (2017)
8. Xu, X., He, L., Lu, H., et al.: Deep adversarial metric learning for cross-modal retrieval. In: World Wide Web, pp. 1–16 (2018)

9. Yüksel, M.E., Borlu, M.: Accurate segmentation of dermoscopic images by image thresholding based on type-2 fuzzy logic. IEEE Trans. Fuzzy Syst. **17**(4), 976–982 (2009)
10. Emre Celebi, M., Kingravi, H.A., Iyatomi, H., et al.: Border detection in dermoscopy images using statistical region merging. Ski. Res. Technol. **14**(3), 347–353 (2008)
11. Serikawa, S., Lu, H.: Underwater image dehazing using joint trilateral filter. Comput. Electr. Eng. **40**(1), 41–50 (2014)
12. Kasmi, R., Mokrani, K., Rader, R.K., et al.: Biologically inspired skin lesion segmentation using a geodesic active contour technique. Ski. Res. Technol. **22**(2), 208–222 (2016)
13. Fan, H., Xie, F., Li, Y., et al.: Automatic segmentation of dermoscopy images using saliency combined with Otsu threshold. Comput. Biol. Med. **85**, 75–85 (2017)
14. Cheng, M.M., Mitra, N.J., Huang, X., et al.: Global contrast based salient region detection. IEEE Trans. Pattern Anal. Mach. Intell. **37**(3), 569–582 (2015)
15. Lu, H., Li, Y., Mu, S., et al.: Motor anomaly detection for unmanned aerial vehicles using reinforcement learning. IEEE Internet Things J. (2017)
16. Lu, H., Li, Y., Chen, M., et al.: Brain intelligence: go beyond artificial intelligence. Mob. Netw. Appl. **23**(2), 368–375 (2018)
17. Zhu, W., Liang, S., Wei, Y., et al.: Saliency optimization from robust background detection. In: Proceedings of the IEEE Conference on Computer Vision and Pattern Recognition, pp. 2814–2821 (2014)
18. Lee, T., Ng, V., Gallagher, R., et al.: Dullrazor®: a software approach to hair removal from images. Comput. Biol. Med. **27**(6), 533–543 (1997)
19. Ahn, E., Bi, L., Jung, Y.H., et al.: Automated saliency-based lesion segmentation in dermoscopic images. In: 2015 37th Annual International Conference of the IEEE Engineering in Medicine and Biology Society (EMBC), pp. 3009–3012. IEEE (2015)
20. Zhang, X.P., Desai, M.D.: Segmentation of bright targets using wavelets and adaptive thresholding. IEEE Trans. Image Process. **10**(7), 1020–1030 (2001)
21. Hu, K., Gao, X., Li, F.: Detection of suspicious lesions by adaptive thresholding based on multiresolution analysis in mammograms. IEEE Trans. Instrum. Meas. **60**(2), 462–472 (2011)
22. Flores, E., Scharcanski, J.: Segmentation of melanocytic skin lesions using feature learning and dictionaries. Expert Syst. Appl. **56**, 300–309 (2016)
23. Mendonça, T., Ferreira, P.M., Marques, J.S., et al.: PH 2-A dermoscopic image database for research and benchmarking. In: 2013 35th Annual International Conference of the IEEE Engineering in Medicine and Biology Society (EMBC), pp. 5437–5440. IEEE (2013)
24. Abuzaghleh, O., Barkana, B.D., Faezipour, M.: Noninvasive real-time automated skin lesion analysis system for melanoma early detection and prevention. IEEE J. Transl. Eng. Health Med. **3**, 1–12 (2015)
25. Otsu, N.: A threshold selection method from gray-level histograms. IEEE Trans. Syst., Man, Cybern. **9**(1), 62–66 (1979)

Chinese Medical Question Answer Matching with Stack-CNN

Yuteng Zhang, Wenpeng Lu, Weihua Ou, Ruoyu Zhang, Xu Zhang and Shutong Yue

Abstract Question and answer matching in Chinese medical science is a challenging problem, which requires an effective text semantic representation. In recent years, deep learning has achieved brilliant achievements in natural language processing field, which is utilized to capture various semantic features. In this paper, we propose a neural network, i.e., stack-CNN, to address question answer matching, which stacks multiple convolutional neural networks to capture the high-level semantic information from the low-level n-gram features. Substantial experiments on a real-world dataset show that our proposed model significantly outperforms a variety of strong baselines.

Keywords Chinese medical question answering · Question answer matching Stack-CNN · Convolutional neural network

1 Introduction

This paper mainly discusses Chinese medical question and answer (QA) matching, which can be briefly described as selecting the most relevant answer from all candidate answers for a target question. Aiming at the problem, the early machine learning methods rely on the manually constructed features [1], including lexical, syntactic and grammatical features, e.g., BM25, edit distance and TF-IDF. With the manual features, some classifiers, e.g., KNN, Bayesian and SVM, judge the

Y. Zhang · W. Lu (✉) · R. Zhang · X. Zhang · S. Yue
School of Computer Science and Technology, QiLu University of Technology (Shandong Academy of Sciences), Jinan, China
e-mail: lwp@qlu.edu.cn

Y. Zhang
e-mail: zhangyuteng1029@163.com

W. Ou
School of Big Data and Computer Science, Guizhou Normal University, Guiyang, China
e-mail: ouweihuahust@gmail.com

H. Lu (ed.), *Cognitive Internet of Things: Frameworks, Tools and Applications*, Studies in Computational Intelligence 810,
https://doi.org/10.1007/978-3-030-04946-1_44

matching relationship between question and answer pairs [2]. These models with manually constructed features belong to shallow machine learning, which rely heavily on the quality of feature extraction with poor generalization ability for different data. More importantly, these models cannot effectively extract the high-level semantic features of sentences on the data.

In recent years, deep learning has become more and more powerful and popular. The core problem of medical QA matching is to calculate the correlation degree between questions and answers, and select the right answer based on the relevance. This is very similar with the task of text similarity, where deep learning is popular to model the text. Convolutional neural network has been applied in the text classification tasks and show excellent performance [3]. In [4], Johnson and Zhang design a model with convolutional neural network to classify short text, achieving outstanding results. In [5], Xiang et al. propose an attention-based neural network architecture that supports multiple input formats to learn key information in QA pairs. In [6], Zhang et al. develop a framework for solving Chinese QA matching, which achieves good results on the cMedQA dataset. However, the existing methods utilize only one single neural network structure, which can capture only one-side low-level features while missing some more intrinsic high-level features.

Aiming at the problem, we design a novel neural network, i.e., stack-CNN, which stacks multiple convolutional neural networks to capture the high-level features from the low-level ones. The experimental results on cMedQA dataset show that our stack-CNN significantly outperforms the existing methods on medical QA task.

2 Related Work

Previous works on QA matching usually rely on feature engineering, linguistic tools, or external resources. For example, Williams et al. utilize regular expressions to extract candidate answers from the collected paragraphs [7]. Wang and Lemon design a confidence-based approach to calculate the similarity between a question and candidate answer [8]. Yih et al. utilize a knowledge base to model events and entities, by which the answers are inferred [9]. The above works suffer from one drawback: as all of them need to construct features manually, it is difficult for them to consider all-side relationships between QA pairs.

Recently, deep learning has shown valuable in passage-level QA matching task. Abacha et al. propose a general convolutional neural network-based framework for solving QA tasks [10]. Severyn and Moschitti demonstrate the effectiveness of vector representation of questions and answers using a multi-layer convolutional neural network [11]. Yu et al. [12] apply a deep convolutional neural network to model sentences and use the model to identify answers for questions in QA dataset. Though the above methods achieve good performance, all of them are single neural network architecture, which can only capture one-side feature while missing some intrinsic high-level features.

3 Proposed Model

3.1 Framework of the Proposed Model

In the QA matching task, given a question q and a set of candidate answers $C = \{a_1, a_2, \ldots, a_p\}$. The goal of the task is to select the correct answer $a^+ \in C$ for the question q from the set of candidate questions. Given a QA pair (q, a) containing a question q and a candidate answer a, our proposed method first represents q and a as fixed-length embeddings e_q and e_a, and then computes its cosine similarity to judge the right answer.

Figure 1 shows the framework of our model. In the first step, in the embedding layer, the model converts the questions and answers to an embedding matrix. Each character in the question and answer is represented with a fixed-length vector. In the second step, in the stack-CNN layer, the questions and answers are handled with the stack-CNN module, which capture the high-level semantic features from the low-level n-gram features and generate embedding representations of QA pairs. In the final step, the cosine similarity of embeddings of QA pair is computed to select the right answer. The previous two layers of the model utilize the *Siamese* structure [13], which has two identical subnets that can handle both questions and answers.

As shown in Fig. 1, in embedding layer, according to a pre-trained word embeddings, each word w in input QA pair is represented with a fixed-length word vector $e^w \in \mathbb{R}^d$. Word embeddings is a matrix, whose rows represent words and columns represent their features $E \in \mathbb{R}^{|V| \times d}$, where $|V|$ indicates the word number in the corpus, d is the dimension of word embeddings. Given an QA pair (q, a), where the question q contains m tokens, the answer a contains l tokens, handled by the embedding layer, the question q and the answer a become $q^{emb} = \{e^{w_1}, e^{w_2}, \ldots, e^{w_m}\}$ and $a^{emb} = \{e^{w_1}, e^{w_2}, \ldots, e^{w_l}\}$. In stack-CNN layer, the outputs of embedding layer are

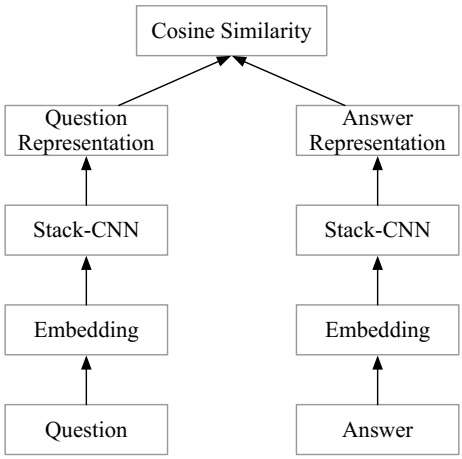

Fig. 1 Framework of our proposed method

convoluted to capture the complex n-gram and high-level semantic information. 1-max pooling is utilized to extract the most important feature and generate the embedding representation of QA pairs, that is, e_q and e_a. In output layer, the cosine similarity of embedding representation is computed to recommend the suitable answers for the target question.

3.2 Stack-CNN

The core module of the proposed framework in the former section is stack-CNN, which stacks convolution kernels of different sizes, where the layers are interdependent each other and the output of the lower layer as the input to the higher layer, as is shown in Fig. 2.

Given a question character sequence $q^{emb} = (e^{w_1}, e^{w_2}, \ldots, e^{w_m})$, each column contains a vector e^{w_m}, m represents the m characters in the question sequence. The formula for the convolution with c filters over the question q is:

$$Q = f(W \circ q^{emb} + b) \tag{1}$$

where each column in question embedding $Q \in \mathbb{R}^{c \times m}$ contains features extracted in a context window around the i-th word of q. $f(\cdot)$ is the activation function, and $W \circ q^{emb}$ indicates the element-wise multiplication of W with each element in q^{emb}. The matrix W and the vector b are the parameters that need to be learned. The number c of convolution kernels and the size k of context windows are hyper-parameters, which need to be adjusted manually.

Similar to the above steps, for the processing of the answer sequence a^{emb}, we use the same W and b to generate the semantic representation of the answer $A \in \mathbb{R}^{c \times l}$. The formula for the convolution operation is:

$$A = f(W \circ a^{emb} + b) \tag{2}$$

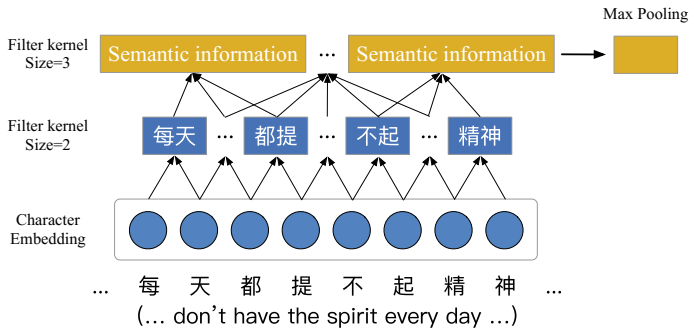

Fig. 2 Network architecture of stack-CNN

For example, if we want to design a 2-stack-CNN network, it has two different convolution kernels, and the size of the convolution kernel is: c_1, c_2. First, we use the c_1 convolution kernel to extract features at the n-gram level to get the output O^{c_1}. Then, we use the c_2 convolution kernel to do a convolution operation on O^{c_1} to get the output O^{c_2}.

3.3 Ranking Loss

In our proposed method, given a question q_i, its right answer is written as a_i^+, the wrong answer is written as a_i^-. Our objective is to maximize the result $sim(q_i, a_i^+)$ of q_i and a_i^+, minimize the result $sim(q_i, a_i^-)$ of q_i and a_i^-. Therefore, we use the following max-margin loss [14] to optimize the ranking order over pairs:

$$L = max(0, margin - sim(q_i, a_i^+) + sim(q_i, a_i^i)) \tag{3}$$

where $margin$ is a hyperparameter that needs to be adjusted based on actual data.

4 Experiment and Result

In order to evaluate the performance of the model, we conduct a comparison experiment with baselines on the cMedQA dataset [6]. Experiments show that our model is at the leading level. We implemented the models using PyTorch.

4.1 Dataset and Evaluation Metric

The Chinese medical question and answers dataset (cMedQA) is constructed by Zhang et al. [6], where QA pairs are chosen from some real-world online health and wellness communities, such as DingXiangYuan[1] and XunYiWenYao[2]. The dataset consists of 101,743 QA pairs, where the sentences have been splitted into individual characters [15]. The vocabulary has a total of 4979 tokens.

We use the top-k accuracy (ACC@k) as the measure to evaluate the performance of the methods [6]. In this paper, the top-1 accuracy is used as a metric to evaluate the result of the model.

[1] http://dxy.com.

[2] http://www.xywy.com.

4.2 Baselines

The following relevant and representative state-of-the-art methods are used as baselines to evaluate our method.

- **Random Selection**: randomly select an answer from the candidate answers as the correct answer.
- **Matching**: choose the matching answer according to the number of similar characters between QA pair [6].
- **BM25**: BM25 (Best Matching) is a ranking function in information retrieval (IR), which has been used in QA matching [6, 16].
- **singleCNN**: similar to the framework in Sect. 3.1, the stack-CNN layer uses only one convolution kernel to process the questions and answers.

4.3 Experimental Parameters

In the embedding layer of our model, we used pre-trained embedding as the initial value of the layer and adjusted it in training. We share the weight of the embedding layer of questions and answers. We use pre-trained Chinese character vectors from Chinese-Word-Vectors,[3] [17] whose dimension is 300. Stack-CNN architectures use filters of size (2, 3) with 500 feature maps.

4.4 Results

Table 1 shows the results of our model with all baselings on ACC@1. The performance of stack-CNN is the highest, which demonstrate an approximate 86.82, 43.61, 1.09% improvement over Matching, BM25, singleCNN on the cMedQA test dataset. The results demonstrate that our model stack-CNN is superior to all baseline models, which means that it can capture and model complex relationships and high-level information between question and answer pairs.

Comparing the rows from A to D, the performance of row D, that is singleCNN, is significantly higher than those of rows A, B, and C, which demonstrates that deep neural networks are more suitable to model the relationships of QA pairs than the traditional machine learning methods.

Both D and E are neural network-based methods. The results of stack-CNN are higher than that of singleCNN. This is because the stack-CNN can capture more fine-grained information, including complex n-gram relationship or high-level semantic information.

[3] https://github.com/Embedding/Chinese-Word-Vectors.

Table 1 ACC@1 results of the models

	Model	Dev (%)	Test (%)
A	Random selection	01.00	01.00
B	Matching	33.65	34.90
C	BM25	44.80	45.40
D	singleCNN	**64.05**	64.50
E	stack-CNN	63.50	**65.20**

5 Conclusion

Different from the existing methods, which rely on manually constructed features or capture only one-side relationship between QA pairs, we propose a deep learning model to address QA matching, that is stack-CNN, to capture n-gram relationships and high-level semantic features of QA pairs. Extensive experiments show that our method outperforms the existing state-of-the-art baseline methods. Our future work is to consider the importance of different words or characters and enhance the current method with attention mechanism to capture the interaction of keyword or specific features between QA pairs.

Acknowledgements The research work is supported by the National Nature Science Foundation of China under Grant No. 61502259 and No. 61762021, Natural Science Foundation of Guizhou Province under Grant No. 2017[1130], Key Subjects Construction of Guizhou Province under Grant No. ZDXK[2016]8 and Natural Science Foundation of Shandong Province under Grant No. ZR2017MF056.

References

1. Wang, M., Manning, C.D.: Probabilistic tree-edit models with structured latent variables for textual entailment and question answering, pp. 1164–1172. Association for Computational Linguistics (2010)
2. Yao, X., Van Durme, B., Callison-Burch, C., Clark, P.: Answer extraction as sequence tagging with tree edit distance. In: Proceedings of the 2013 Conference of the North American Chapter of the Association for Computational Linguistics: Human Language Technologies, pp. 858–867 (2013)
3. Zhang, D., Wang, D.: Relation classification via recurrent neural network (2015). arXiv:1508.01006
4. Johnson, R., Zhang, T.: Effective use of word order for text categorization with convolutional neural networks (2014). arXiv:1412.1058
5. Xiang, Y., Chen, Q., Wang, X., Qin, Y.: Answer selection in community question answering via attentive neural networks. IEEE Signal Process. Lett. **24**(4), 505–509 (2017)
6. Zhang, S., Zhang, X., Wang, H., Cheng, J., Li, P., Ding, Z.: Chinese medical question answer matching using end-to-end character-level multi-scale CNNs. Appl. Sci. **7**(8), 767 (2017)
7. Williams, J.D.: Young, S.: Partially observable Markov decision processes for spoken dialog systems. Comput. Speech Lang. **21**(2), 393–422 (2007)

8. Wang, Z., Lemon, O.: A simple and generic belief tracking mechanism for the dialog state tracking challenge: on the believability of observed information. In: Proceedings of the SIGDIAL 2013 Conference, pp. 423–432 (2013)
9. Yih, W.-T., Chang, M.-W., Meek, C., Pastusiak, A.: Question answering using enhanced lexical semantic models. In: Proceedings of the 51st Annual Meeting of the Association for Computational Linguistics (Volume 1: Long Papers), vol. 1, pp. 1744–1753 (2013)
10. Abacha, A.B., Zweigenbaum, P.: Medical question answering: translating medical questions into SPARQL queries. In: Proceedings of the 2nd ACM SIGHIT International Health Informatics Symposium, pp. 41–50. ACM (2012)
11. Severyn, A., Moschitti, A.: Automatic feature engineering for answer selection and extraction. In: Proceedings of the 2013 Conference on Empirical Methods in Natural Language Processing, pp. 458–467 (2013)
12. Yu, L., Hermann, K.M., Blunsom, P., Pulman,S.: Deep learning for answer sentence selection (2014). arXiv:1412.1632
13. Bromley, J., Guyon, I., LeCun, Y., Säckinger, E., Shah, R.: Signature verification using a "siamese" time delay neural network. In: Advances in Neural Information Processing Systems, pp. 737–744 (1994)
14. LeCun, Y., Chopra, S., Hadsell, R., Ranzato, M., Huang, F.: A tutorial on energy-based learning. Predicting Structured Data, vol. 1 (2006)
15. Zhang, M., Zhang, Y., Che, W., Liu, T.: Character-level Chinese dependency parsing. In: Proceedings of the 52nd Annual Meeting of the Association for Computational Linguistics (Volume 1: Long Papers), vol. 1, pp. 1326–1336 (2014)
16. Wang, B., Niu, J., Ma, L., Zhang, Y., Zhang, L., Li, J., Zhang, P., Song, D.: A Chinese question answering approach integrating count-based and embedding-based features. Natural Language Understanding and Intelligent Applications, pp. 934–941. Springer (2016)
17. Li, S., Zhao, Z., Hu, R., Li, W., Liu, T., Du, X.: Analogical reasoning on Chinese morphological and semantic relations (2018). arXiv:1805.06504

Semantics Consistent Adversarial Cross-Modal Retrieval

Ruisheng Xuan, Weihua Ou, Quan Zhou, Yongfeng Cao, Hua Yang, Xiangguang Xiong and Fangming Ruan

Abstract Cross-modal retrieval returns the relevant results from the other modalities given a query from one modality. The main challenge of cross-modal retrieval is the "heterogeneity gap" amongst modalities, because different modalities have different distributions and representations. Therefore, the similarity of different modalities can not be measured directly. In this paper, we propose a semantics consistent adversarial cross-modal retrieval approach, which learns a semantics consistent representation for different modalities with same semantic category. Specifically, we encourage the class center of different modalities with same semantic label to be as close as possible, and also minimize the distances between the samples and the class center with same semantic label from different modalities. Comprehensive experiments on Wikipedia dataset are conducted and the experimental results show the efficiency and effectiveness of our approach in cross-modal retrieval.

Keywords Cross-modal retrieval · Adversarial learning · Semantics consistent Common subspace · Media gap

R. Xuan · W. Ou (✉) · Y. Cao · H. Yang · X. Xiong · F. Ruan
School of Big Data and Computer Science, Guizhou Normal University, Guiyang, People's Republic of China
e-mail: ouweihuahust@gmail.com

Q. Zhou
National Engineering Research Center of Communications and Networking, Nanjing University of Posts & Telecommunications, Nanjing, People's Republic of China

Q. Zhou
State Key Laboratory for Novel Software Technology, Nanjing University, Nanjing, People's Republic of China

H. Lu (ed.), *Cognitive Internet of Things: Frameworks, Tools and Applications*, Studies in Computational Intelligence 810,
https://doi.org/10.1007/978-3-030-04946-1_45

1 Introduction

In the past decades, different types of multimedia data have been increasing and accumulated explosively, such as image, text, video and audio. Those different modal data are often utilized to describe the same events or topics. For example, image and textual descriptions usually coexist in a web page to illustrate an event or a topic. Naturally, there have been semantically correlated from content and shared a certain level of semantic consistency. Therefore, there is a growing demand to effectively retrieve relevant information across different modalities given a query from one modality [1]. However, they have different distributions and representations, and exhibit heterogeneous properties, which makes it difficult for traditional single-modal retrieval method [2, 3].

Cross-modal retrieval aims to return the relevant information across other modalities given a query from one modality, which can satisfy this demand. The main challenge in cross-modal retrieval is the similarity of different modalities cannot be measured directly, which is also referred as "media gap" problem [4–8]. An intuitive idea for this problem is to map different modalities into a common semantic space, in which the similarity can be measured. Based on this idea, many methods have been proposed during in the past years [1, 9–15]. According to the differences of the model, existing methods can be roughly divided into traditional method and deep neural network method. Traditional methods [16–19] mainly consider to learn different mapping matrices for different modalities and project them into one common subspace. The representative work is the Canonical Correlation Analysis (CCA) [20], which maximizes the projection correlation of different modalities. Different from the linear projector that the traditional methods learned, deep neural network can learn more complex map via multilayer network across different modalities and achieved the state-of-the-art performances in cross-modal retrieval [18, 21–23].

Recently, deep convolutional neural networks [24, 25] and the Generative Adversarial Networks (GANs) [26, 27] have been utilized to learn the common representation for cross-modal retrieval by modeling the joint distribution over the heterogeneous data of different modalities. Different from single modality, the GANs is mainly utilized to establish correlation on the heterogeneous data of different modalities for the common representation generation. For example, Wang et al. [27] proposed an Adversarial Cross-Modal Retrieval (ACMR) method by seeking an effective common subspace considering the underlying cross-modal semantic structure of different modalities. To learn a more discriminative common representation, Peng et al. [28] proposed Cross-Modal Generative Adversarial Networks (CM-GANs) for common representation learning. Different from ACMR, CM-GANs proposed the weight-sharing constraint in the generative model and constructed intra-modality and inter-modality discrimination term. Although those methods show promising performance in cross-modal retrieval, they do not consider semantics consistency in their model, which has been demonstrated important in cross-modal retrieval.

In this paper, we propose Semantics Consistent Adversarial Cross-Modal Retrieval (SC-ACMR), which ensures the representations in common space to be semantically

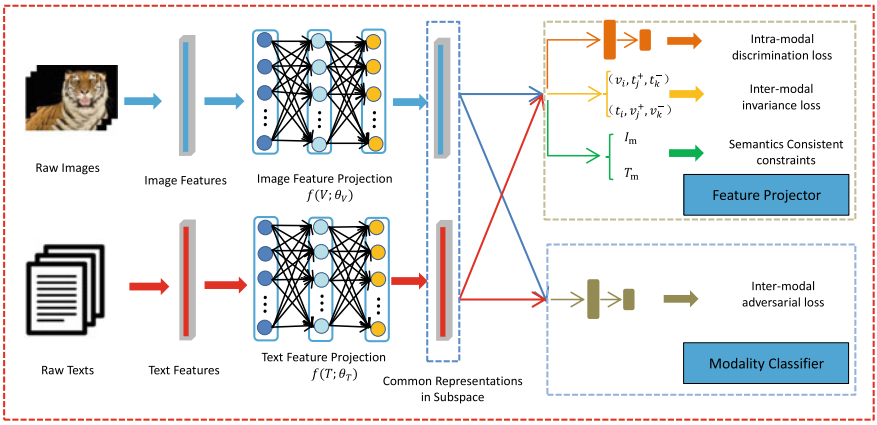

Fig. 1 The flowchart of the proposed SC-ACMR, which consists of the feature projector and modality classifier. The feature projector is to learn a complex map, while modality classifier encourages representation to be modality-invariant

consistent with same semantic label from different modalities. Figure 1 shows the framework, which consists of a feature projector and a modality classifier under the generative adversarial framework. The feature projector is to generate modality-invariant embedding of texts and images into a common subspace. The modality classifier is to detect the modality of an instance from the feature projection. The key idea of our approach is inspired by [27]. Different from ACMR [27], we consider sufficiently the semantics consistency from three aspects as follows: (1) the intra-class distances was minimized for the same semantic category in the same modality; (2) the distances between the class center of one modality and the samples from the other modality with same semantic category was minimized; (3) the inter-class center distances between different modalities with same semantic category was minimized. After that, more compact semantic consistency representation can be obtained.

The contributions of our approach are two-folds: (1) In the feature projector, we propose a semantics consistent constraints, which ensures to learn more compact semantic representations; (2) Compared with most competitive models, our method achieves the state-of-art results on Wikipedia dataset.

2 Our Approach

In this section, we first briefly review the adversarial cross-modal retrieval, then elaborate on the details of the objective function and optimization for our approach.

2.1 ACMR

Given a set of n instances of image-text pairs $\mathbf{X} = \{\mathbf{X}_i = [\mathbf{v}_i, \mathbf{t}_i]\}_{i=1}^{n}$, where $\mathbf{v}_i \in \mathbb{R}^{d_v}$ is an image feature vector with dimension d_v, and $\mathbf{t}_i \in \mathbb{R}^{d_t}$ is a text feature vector with dimension d_t, usually $d_v \neq d_t$. For each instance $\mathbf{X}_i$, a semantic label vector $\mathbf{l}_i = \{l_{i1}, l_{i2}, ..., l_{ik}\} \in \mathbb{R}^k$ is assigned, where k is the total number of semantic category. If the ith instance belongs to the jth semantic category, then $l_{ij} = 1$, otherwise $l_{ij} = 0$. For all the instances in $\mathbf{X}$, the image feature matrix, text feature matrix and label matrix can be denoted as $\mathbf{V} = \{\mathbf{v}_1, \mathbf{v}_2, ..., \mathbf{v}_n\} \in \mathbb{R}^{d_v \times n}$, $\mathbf{T} = \{\mathbf{t}_1, \mathbf{t}_2, ..., \mathbf{t}_n\} \in \mathbb{R}^{d_t \times n}$, $\mathbf{L} = \{\mathbf{l}_1, \mathbf{l}_2, ..., \mathbf{l}_n\} \in \mathbb{R}^{k \times n}$, respectively.

The objective function of ACMR includes adversarial loss $\mathcal{L}_{adv}(\theta_D)$ and embedding loss $\mathcal{L}_{emb}(\theta_V, \theta_T, \theta_{imd})$. Specifically, the adversarial loss is below:

$$\mathcal{L}_{adv}(\theta_D) = -\frac{1}{n_s}\sum_{i=1}^{n_s}(\mathbf{m}_i \cdot (\log D(\mathbf{v}_i; \theta_D) + \log(1 - D(\mathbf{t}_i; \theta_D)))) \tag{1}$$

where, $\mathbf{m}_i$ is the ground-truth modality label for each instance, expressed as one-hot vector, while $D(\cdot; \theta_D)$ is the generated modality probability per item of the instance $\mathbf{X}_i$, n_s is the mini-batch size.

The embedding loss includes label prediction loss $\mathcal{L}_{imi}$ and structural preservation loss $\mathcal{L}_{imd}$. The formulation is below

$$\mathcal{L}_{emb}(\theta_V, \theta_T, \theta_{imd}) = \alpha \cdot \mathcal{L}_{imi} + \beta \cdot \mathcal{L}_{imd} \tag{2}$$

where $\mathcal{L}_{imd}(\theta_{imd}) = -\frac{1}{n_s}\sum_{i=1}^{n_s}(\mathbf{I}_i \cdot (\log \hat{p}(\mathbf{v}_i) + \log \hat{p}(\mathbf{t}_i)))$ and $\hat{p}(\cdot)$ is the generated probability distribution per item (image or text) of the instance $\mathbf{X}_i$, and θ_{imd} is the classifier parameters.

The structure preservation loss $\mathcal{L}_{imi}$ includes two parts and the formulation is shown below

$$\mathcal{L}_{imi}(\theta_V, \theta_T) = \mathcal{L}_{imi,V}(\theta_V) + \mathcal{L}_{imi,T}(\theta_T) \tag{3}$$

where,

$$\mathcal{L}_{imi,V}(\theta_V) = \sum_{i,j,k}(\ell_2(\mathbf{v}_i, \mathbf{t}_j^+) + \lambda \cdot \max(0, \mu - \ell_2(\mathbf{v}_i, \mathbf{t}_k^-))) \tag{4}$$

$$\mathcal{L}_{imi,T}(\theta_T) = \sum_{i,j,k}(\ell_2(\mathbf{t}_i, \mathbf{v}_j^+) + \lambda \cdot \max(0, \mu - \ell_2(\mathbf{t}_i, \mathbf{v}_k^-))) \tag{5}$$

Here, $\{(\mathbf{v}_i, \mathbf{t}_j^+, \mathbf{t}_k^-)\}_i$ and $\{(\mathbf{t}_i, \mathbf{v}_j^+, \mathbf{v}_k^-)\}_i$ are the triplet samples set for each semantic label, $\ell_2(\cdot)$ is the 2-norm.

2.2 SC-ACMR

To measure the similarity of different modalities, we aims at learning a common semantic space S, in which the text features and image features can be projected to by $S_T = f_T(\mathbf{T}; \theta_T)$, and $S_V = f_V(\mathbf{V}; \theta_V)$. Here, f_T and f_V are the mapping functions, $S_T \in \mathbb{R}^{p \times n}$ and $S_V \in \mathbb{R}^{p \times n}$ are the transformed features of text and image, respectively.

To ensure semantics to be consistent from different modalities with same semantic category, we propose a semantics consistency regularization term. Specifically, for image modality features $\mathbf{V} = \{\mathbf{v}_1, \mathbf{v}_2, ..., \mathbf{v}_n\}$, and text modality features $\mathbf{T} = \{\mathbf{t}_1, \mathbf{t}_2, ..., \mathbf{t}_n\}$, we compute their class center $\mathbf{C}^v = \{\mathbf{c}_1^v, ..., \mathbf{c}_k^v\}$ and $\mathbf{C}^t = \{\mathbf{c}_1^t, ..., \mathbf{c}_k^t\}$, respectively, here

$$\mathbf{c}_j^v = \frac{1}{n_j} \sum_{i=1}^{n_j} \mathbf{v}_j^i, \qquad \mathbf{c}_j^t = \frac{1}{n_j} \sum_{i=1}^{n_j} \mathbf{t}_j^i, \qquad j = 1, 2, \ldots, k \tag{6}$$

As shown in Fig. 2, the intra-class distances in each modality is minimized and the formulation is presented in d_1. For the same semantic category from different modalities, the distances of class center is minimized and the formulation is shown in d_2. To effectively model the relationship between different modalities, the distances between the class center and the samples from the other modality with same semantic category are minimized and their formulations are shown in d_3 and d_4.

$$d_1 = \frac{1}{k} \sum_{j=1}^{k} \left[\frac{1}{n_j} \sum_{i=1}^{n_j} \left(\|\mathbf{c}_j^v - \mathbf{v}_j^i\|_2 + \|\mathbf{c}_j^t - \mathbf{t}_j^i\|_2 \right) \right], \quad d_2 = \frac{1}{k} \sum_{j=1}^{k} \|\mathbf{c}_j^t - \mathbf{c}_j^v\|_2 \tag{7}$$

$$d_3 = \frac{1}{k} \sum_{j=1}^{k} \left(\frac{1}{n_j} \sum_{i=1}^{n_j} \|\mathbf{c}_j^v - \mathbf{t}_j^i\|_2 \right), \quad d_4 = \frac{1}{k} \sum_{j=1}^{k} \left(\frac{1}{n_j} \sum_{i=1}^{n_j} \|\mathbf{c}_j^t - \mathbf{v}_j^i\|_2 \right) \tag{8}$$

Thus, the semantics consistency regularization term can be formulated as follows:

$$\mathcal{L}_{reg} = d_1 + d_2 + d_3 + d_4 \tag{9}$$

Combined with the formula (2), we get the embedding loss for SC-ACMR as follows:

$$\mathcal{L}_{emb}(\theta_V, \theta_T, \theta_{imd}) = \alpha \cdot \mathcal{L}_{imi} + \beta \cdot \mathcal{L}_{imd} + \gamma \cdot \mathcal{L}_{reg} \tag{10}$$

Here, α, β and γ are super parameters, which balances the importance of different parts. Compared to ACMR, we defined a new embedding loss, which sufficiently considers the semantics consistency.

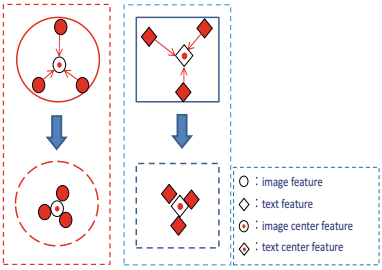

(a) For each modality, minimizing the intraclass distances

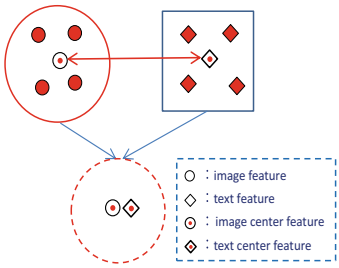

(b) For different modalities, minimizing the inter-class center distances with same semantic label

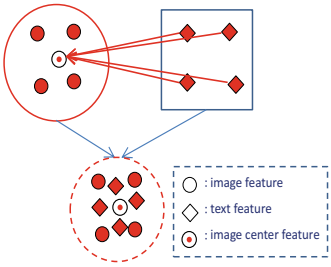

(c) For each class center, minimizing the distances between the center and the samples from the other modality with same semantic label

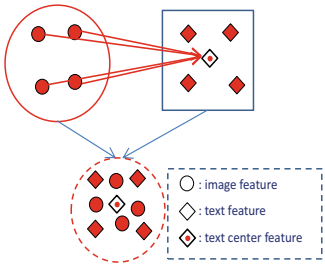

(d) For each class center, minimizing the distances between the center and the samples from the other modality with same semantic label

Fig. 2 The motivation of semantics consistent adversarial cross-modal retrieval. Different shape represents different modality, while the same color represents same semantic category

2.3 Optimization

According to the generative adversarial mechanism, the training process of optimal feature representation runs as a minimax game of two sub-processes [26]:

$$(\hat{\theta}_V, \hat{\theta}_T, \hat{\theta}_{imd}) = \arg\min_{(\theta_V, \theta_T, \theta_{imd})}(\mathcal{L}_{emb}(\theta_V, \theta_T, \theta_{imd}) - \mathcal{L}_{adv}(\hat{\theta}_D)) \tag{11}$$

$$\hat{\theta}_D = \arg\max_{\theta_D}(\mathcal{L}_{emb}(\hat{\theta}_V, \hat{\theta}_T, \hat{\theta}_{imd}) - \mathcal{L}_{adv}(\theta_D)) \tag{12}$$

Similar to [27], the whole algorithm is presented as below.

Algorithm 1 Pseudocode of the proposed SC-ACMR

Require: Image features matrix $\mathbf{V} = \{\mathbf{v}_1, \mathbf{v}_2, ..., \mathbf{v}_n\} \in \mathbb{R}^{d_v \times n}$, text feature matrix $\mathbf{T} = \{\mathbf{t}_1, \mathbf{t}_2, ..., \mathbf{t}_n\} \in \mathbb{R}^{d_t \times n}$, and label matrix $\mathbf{L} = \{\mathbf{l}_1, \mathbf{l}_2, ..., \mathbf{l}_n\} \in \mathbb{R}^{k \times n}$, parameters s, α, β, γ, minibatch size n_s for each iteration.
Ensure:
for s steps **do**
  Update parameters of feature projectors θ_V, θ_T and θ_{imd} by descending their stochastic gradients:
  $\theta_V \leftarrow \theta_V - \mu \cdot \nabla_{\theta_V} \frac{1}{n_s}(\mathcal{L}_{emb} - \mathcal{L}_{adv})$
  $\theta_T \leftarrow \theta_T - \mu \cdot \nabla_{\theta_T} \frac{1}{n_s}(\mathcal{L}_{emb} - \mathcal{L}_{adv})$
  $\theta_{imd} \leftarrow \theta_{imd} - \mu \cdot \nabla_{\theta_{imd}} \frac{1}{n_s}(\mathcal{L}_{emb} - \mathcal{L}_{adv})$
end for
Update parameters of modality classifier by ascending its stochastic gradeints through gradient reversal layer:
$\theta_D \leftarrow \theta_D + \mu \cdot \lambda \cdot \nabla_{\theta_D} \frac{1}{n_s}(\mathcal{L}_{emb} - \mathcal{L}_{adv})$
Return learned representations in common subspace: $f_V(V)$ and $f_T(T)$

3 Experiment and Results Analysis

To validate our approach, we conducted experiments on Wikipedia dataset, which is widely used for cross-modal retrieval. Specifically, the Wikipedia dataset consists of 10 categories, 2866 instances (image and text pairs). Among them, 1300 image-text pairs are randomly selected for training, and the rest of 1566 image-text pairs are selected for testing. The image feature is 128d SIFT and 4096d VGG, while the text feature is 10d LDA and 3000d BOW.

Baselines. To show the effectiveness of our method, we selected following methods as baselines for comparison: (1) CCA [20], CCA-3V [29], LCFS [30], JRL [31] and JFSSL [32], which are traditional cross-modal retrieval methods; and (2) Multimodal-DBN [33], Bimodal-AE [34], Corr-AE [35], and ACMR [27], which are DNN-based cross-modal retrieval methods.

Implementation details During the training process, the size of each batch is 64, the model parameters α, β, γ are set by grid search, respectively. For our method, all the experiments are implemented on 4-core CPUs with 3.4 GHz, 8 GB memory, and GeForce GTX 1070 GPUs.

Overall Results The experimental results are shown in Table 1. From that, we can see that the performances of image-to-text are better than that of text-to-image for all the methods. The performances of Multimodal-DBN, bimodal-AE and Corr-AE are worse than the other traditional methods for two tasks. This might be the data is not enough for the training of deep networks. ACMR and SC-ACMR obtained better results than other traditional methods and DNN-based methods. Compared to ACMR, our SC-ACMR obtained the state-of-the-art performances on this dataset.

To further show the advantages, we visualized the distribution of the learned representations for SC-ACMR and ACMR on the Wikipedia dataset using t-SNE [36]. Specifically, five categories are selected from the total ten categories and 1566 test samples. The visualization of the low-dimensional representation learned by ACMR and SC-ACMR are shown in Fig. 3. From Fig. 3b, c, we can see that our approach obtained more compact semantics representation than that of ACMR, especially for

Table 1 Comparison of the cross-modal retrieval performance on the Wikipedia dataset

Methods	Img2Txt	Txt2Img	Avg
CCA [20]	0.267	0.222	0.245
CCA-3V [29]	0.437	0.383	0.410
LCFS [30]	0.455	0.398	0.427
JRL [31]	0.453	0.400	0.426
JFSSL [32]	0.428	0.396	0.412
Multimodal-DBN [33]	0.204	0.183	0.194
Bimodal-AE [34]	0.314	0.290	0.302
Corr-AE [35]	0.402	0.395	0.398
ACMR [27]	0.619	0.489	0.546
SC-ACMR (Proposed)	0.622	0.498	0.560

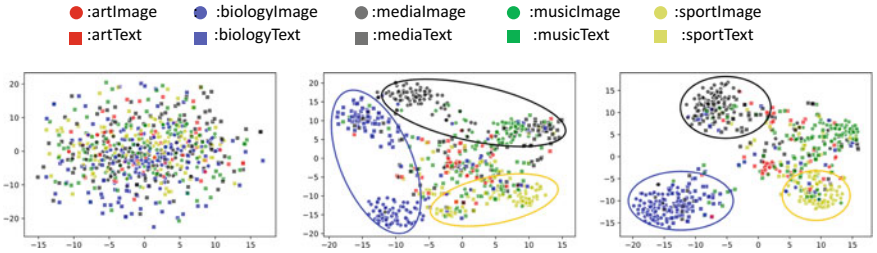

(b) Original data (c) ACMR method (d) SC-ACMR method

Fig. 3 t-SNE visualization for five semantic categories in the Wikipedia dataset. Different color represents different semantic category, and different shape represents different modalities

the biology, medical and sports semantics category, which are marked with blue color, black color and yellow color, respectively.

4 Conclusions

In this paper, we propose a semantics consistency adversarial cross-modal retrieval method, which sufficiently considers the semantics consistency from different modalities. Compared with existing methods, our proposed method achieved better retrieved results and obtained more compact semantics representations. In the future, we would like to improve upon the performances by encouraging the distances of different semantics categories.

Acknowledgements Weihua Ou is the corresponding author of this paper. This work was partly supported by the National Natural Science Foundation of China (Grant No. 61762021, 61876093, 61402122, 61881240048), Natural Science Foundation of Guizhou Province (Grant No. [2017] 1130), the 2014 Ph.D. Recruitment Program of Guizhou Normal University, Foundation of Guizhou Educational Department (KY[2016]027), HIRP Open 2018 Project of Huawei, the Natural Science Foundation of Educational Commission of Guizhou Province under Grant No. [2015]434, Guizhou Province Innovation Talents Team of Electrostatic and Electromagnetic Protection (No. QKHP-TRC[2017]5653), Key Subjects Construction of Guizhou Province (ZDXK[2016]8).

References

1. Rasiwasia, N., Costa Pereira, J., Coviello, E., Doyle, G., Lanckriet, G.R., Levy, R., Vasconcelos, N.: A new approach to cross-modal multimedia retrieval. In: International Conference on Multimedia, pp. 251–260 (2010)
2. Datta, R., Joshi, D., Li, J., Wang, J.Z.: Image retrieval: ideas, influences, and trends of the new age. ACM Comput. Surv. **40**(2), 1–60 (2008)
3. Smeulders, A.W.M., Worring, M., Santini, S., Gupta, A., Jain, R.: Content-based image retrieval at the end of the early years. IEEE Trans. Pattern Anal. Mach. Intell. **22**(12), 1349–1380 (2000)
4. Lu, H., Li, B., Zhu, J., Li, Y., Li, Y., Xu, X., He, L., Li, X., Li, J., Serikawa, S.: Wound intensity correction and segmentation with convolutional neural networks. Concurr. Comput. Pract. Exp. (2017). https://doi.org/10.1002/cpe.3927
5. Huimin, L., Li, Y., Chen, M., Kim, H., Serikawa, S.: Brain intelligence: go beyond artificial intelligence. Mob. Netw. Appl. **23**(2), 368–375 (2018)
6. Peng, Y., Huang, X., Zhao, Y.: An overview of cross-media retrieval: concepts, methodologies, benchmarks and challenges. IEEE Trans. Circuits Syst. Video Technol. 1–14 (2017)
7. Serikawa, S., Huimin, L.: Underwater image dehazing using joint trilateral filter. Comput. Electr. Eng. **40**(1), 41–50 (2014)
8. Wang, K., Yin, Q., Wang, W., Wu, S., Wang, L.: A comprehensive survey on cross-modal retrieval. CoRR (2016). arXiv:1607.06215
9. Cao, Y., Long, M., Wang, J., Yang, Q., Yu, P.S.: Deep visual semantic hashing for cross-modal retrieval. In: ACM SIGKDD International Conference on Knowledge Discovery and Data Mining, pp. 1445–1454 (2016)
10. Deng, C., Chen, Z., Liu, X., Gao, X., Tao, D.: Triplet-based deep hashing network for cross-modal retrieval. IEEE Trans. Image Process. **27**(8), 3893–3903 (2018)
11. Kang, C., Xiang, S., Liao, S., Changsheng, X., Pan, C.: Learning consistent feature representation for cross-modal multimedia retrieval. IEEE Trans. Multimed. **17**(3), 370–381 (2015)
12. Lu, H., Li, Y., Mu, S., Wang, D., Kim, H., Serikawa, S.: Motor anomaly detection for unmanned aerial vehicles using reinforcement learning. IEEE Internet Things J. (2018). https://doi.org/10.1109/JIOT.2017.2737479
13. Lu, H., Li, Y., Uemura, T., Kim, H., Serikawa, S.: Low illumination underwater light field images reconstruction using deep convolutional neural networks. Future Gen. Comput. Syst. (2018). https://doi.org/10.1016/j.future.2018.01.001
14. Tang, X., Yang, Y., Deng, C., Gao, X.: Coupled dictionary learning with common label alignment for cross-modal retrieval. IEEE Trans. Multimed. **18**(2), 208–218 (2016)
15. Wei, Y., Zhao, Y., Canyi, L., Wei, S., Liu, L., Zhu, Z., Yan, S.: Cross-modal retrieval with cnn visual features: a new baseline. IEEE Trans. Cybern. **47**(2), 449–460 (2016)
16. Li, X., Liu, Q., He, Z., Wang, H., Zhang, C., Chen, W.-S.: A multi-view model for visual tracking via correlation filters. Knowl. Based Syst. **113**, 88–99 (2016)
17. Lin, Z., Ding, G., Hu, M., Wang, J.: Semantics-preserving hashing for cross-view retrieval. In: Proceedings of Computer Vision and Pattern Recognition, pp. 3864–3872 (2015)

18. Ou, M., Cui, P., Wang, F., Wang, J., Zhu, W., Yang, S.: Comparing apples to oranges: a scalable solution with heterogeneous hashing. In: Proceedings of the 19th SIGKDD International Conference on Knowledge Discovery and Data Mining, pp. 230–238 (2013)
19. Zhen,Y., Yeung, D.Y.: Co-regularized hashing for multimodal data. Neural Inf. Process. Syst. **2**, 1376–1384 (2012)
20. Hardoon, D.R., Szedmak, S., Shawetaylor, J.: Canonical correlation analysis: an overview with application to learning methods. Neural Comput. **16**(12), 2639–2664 (2004)
21. Jiang, Q., Li, W.: Deep cross-modal hashing. In: Proceedings of Computer Vision and Pattern Recognition, pp. 3270–3278 (2017)
22. Fei, W., Xinyan, L., Song, J., Yan, S., Zhang, Z.M., Yong, R., Zhuang, Y.: Learning of multimodal representations with random walks on the click graph. IEEE Trans. Image Process **25**(2), 630–642 (2015)
23. Zhang, H., Yang, Y., Luan, H., Yang, S., Chua, T.S.: Start from scratch: Towards automatically identifying, modeling, and naming visual attributes. In: ACM International Conference on Multimedia, pp. 187–196 (2014)
24. Liu, Q., Xiaohuan, L., He, Z., Zhang, C., Chen, W.-S.: Deep convolutional neural networks for thermal infrared object tracking. Knowl. Based Syst. **134**, 189–198 (2017)
25. Xu, X., He, L., Lu, H., Gao, L., Ji, Y.: Deep adversarial metric learning for cross-modal retrieval. In: World Wide Web (2018). https://doi.org/10.1007/s11280-018-0541-x
26. Goodfellow, I.J., Pouget-Abadie, J., Mirza, M., Xu, B., Warde-Farley, D., Ozair, S., Courville, A., Bengio, Y.: Generative adversarial nets. In: International Conference on Neural Information Processing Systems, pp. 2672–2680 (2014)
27. Wang, B., Yang, Y., Xu, X., Hanjalic, A., Shen, H.T.: Adversarial cross-modal retrieval. In: ACM on Multimedia Conference, pp. 154–162 (2017)
28. Peng, Y., Qi, J., Yuan, Y.: CM-GANs: cross-modal generative adversarial networks for common representation learning (2017). arXiv:1710.05106
29. Gong, Y., Ke, Q., Isard, M., Lazebnik, S.: A multi-view embedding space for modeling internet images, tags, and their semantics. Int. J. Comput. Vis. **106**(2), 210–233 (2014)
30. Wang, K., He, R., Wang, W., Wang, L., Tan, T.: Learning coupled feature spaces for cross-modal matching. In: Proceedings of the IEEE International Conference on Computer Vision, pp. 2088–2095 (2013)
31. Zhai, X., Peng, Y., Xiao, J.: Learning cross-media joint representation with sparse and semisupervised regularization. IEEE Trans. Circuits Syst. Video Technol. **24**(6), 965–978 (2014)
32. Wang, K., He, R., Wang, L., Wang, W., Tan, T.: Joint feature selection and subspace learning for cross-modal retrieval. IEEE Trans. Pattern Anal. Mach. Intell. **38**(10), 2010–2023 (2016)
33. Srivastava, N., Salakhutdinov, R.: Learning representations for multimodal data with deep belief nets. In: ICML Workshop, p. 79 (2012)
34. Ngiam, J., Khosla, A., Kim, M., Nam, J., Lee, H., Ng, A.Y.: Multimodal deep learning. In: Proceedings of the 28th International Conference on Machine Learning (ICML), pp. 689–696 (2011)
35. Feng, F., Wang, X., Li, R.: Cross-modal retrieval with correspondence autoencoder. In: Proceedings of the 22nd ACM International Conference on Multimedia, pp. 7–16 (2014)
36. van der Maaten, L., Hinton, G.: Visualizing data using t-SNE. J. Mach. Learn. Res. **9**(11), 2579–2605 (2008)

Domain Adaptation for Semantic Segmentation with Conditional Random Field

Yuze Sun, Xiaofu Wu, Quan Zhou and Suofei Zhang

Abstract Fully-convolutional neural networks (CNNs) for semantic segmentation dramatically improve performance using end-to-end learning on whole images in a supervised manner. The success of CNNs for semantic segmentation depends heavily on the pixel-level ground truth, which is labor-intensive in general. To partially solve this problem, domain adaptation techniques have been adapted to the two similar tasks for semantic segmentation, one of which is fully-labelled, while the other is unlabelled. Based on the adversarial learning method for domain adaptation in the context of semantic segmentation (AdaptSegNet), this paper proposes to employ the conditional random field (CRF) to refine the output of the segmentation network before domain adaptation. The proposed system fully integrates CRF model with CNNs, making it possible to train the whole system end-to-end with the usual backpropagation algorithm. Extensive experiments demonstrate the effectiveness of our framework under various domain adaptation settings, including synthetic-to-real scenarios.

Keywords Semantic segmentation · Adaptation domain · CRF

1 Introduction

Semantic segmentation aims to assign each pixel of an image to a semantic category label, e.g., person, car, road or tree. It not only plays an important role in computer vision and pattern recognition, but also facilitates some real-world applications, such as autonomous driving [1] and image editing. Recently, methods based on convolutional neural networks (CNNs) [2–4] have achieved significant progress in semantic segmentation [5–7]. These methods, however, rely heavily on the dense pixel-level labels, which often entail prohibitively high labor cost. Due to the high labor cost

Y. Sun · X. Wu (✉) · Q. Zhou · S. Zhang
National Engineering Research Center of Communications and Networking,
Nanjing University of Posts & Telecommunications, Nanjing, People's Republic of China
e-mail: xfuwu@njupt.edu.cn

H. Lu (ed.), *Cognitive Internet of Things: Frameworks, Tools and Applications*, Studies in Computational Intelligence 810,
https://doi.org/10.1007/978-3-030-04946-1_46

of pixel-wise annotated ground truth, there has been great interest for the usage of domain-adaptation for semantic segmentation. With domain adaptation, it requires to construct large-scale synthetic datasets with annotations, e.g., GTA5 [8] and SYNTHIA [9]. Then, one can adapt the model trained on synthetic data to real world datasets, such as Cityscapes [10]. In previous literature, the adaptive structured output space for semantic segmentation (AdaptSegNet) has been proposed based on the generative adversarial network (GAN) [11], which introduces a domain adaptation method for pixel-level semantic segmentation via adversarial learning. The work demonstrates that the adaptation in the output (segmentation) space can effectively align scene layouts and local contexts between source and target images.

However, there are significant challenges in adapting CNNs, which are often designed for high level computer vision tasks such as object detection and recognition. Firstly, traditional CNNs have convolutional filters with large receptive fields and hence produce coarse outputs when restructured to produce pixel-level labels [10, 12]. Presence of max-pooling layers further increases the coarseness of the outputs. As for domain adaptation, it can result in non-sharp boundaries and blob-like shapes, leading to the drop of segmentation performance. Secondly, CNNs lack smoothness constraints that encourage label agreement between pixels with similar appearances consistency and neighborhood spatial relationships. Lacking of such smoothness constraints may result in poor object delineation and small spurious regions in the segmentation outputs [8, 13]. For semantic segmentation, conditional random field (CRF) can pose further local constraints among pixels, which can lead to improve performance in the supervised settings. In this paper, we propose to employ CRF to refine the outputs of the segmentation network before domain adaptation based on the AdaptSegNet. The proposed system fully integrates CRF model with CNNs, making it possible to train the whole system end-to-end with the usual back-propagation algorithms. Our method is composed of two steps, as shown in Fig. 1. In the first step, the fully-labeled source domain is used to train segmentation network and the results are refined by CRF. Thereafter, the trained segmentation network and CRF

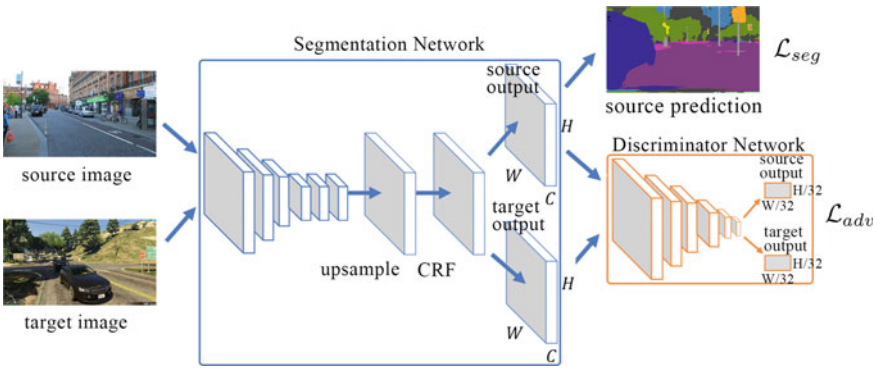

Fig. 1 The pipeline of our whole method

are employed to produce the segmentation estimations for target domain. To make target predictions closer to the source ones, in the second step, we employ adversarial learning to confuse a domain classifier, which can distinguish whether the segmentation network outputs come from source domain or target domain. We use GTA5 to Cityscapes and SYNTHIA to Cityscapes to evaluate our approach, the experience results demonstrate the effectiveness of our method.

2 Method

In this section, we first elaborate on the details of subcomponents of our system, including segmentation network with CRF, and discriminator network. Then, we introduce how to train the whole framework using different loss functions.

To begin with, we first formulate the adaptation tasks containing two loss functions from both modules:

$$\mathcal{L}(I_s, I_t) = \mathcal{L}_{seg}(I_s) + \lambda \mathcal{L}_{adv}(I_t) \tag{1}$$

where $\mathcal{L}_{seg}$ is the cross-entropy loss using ground truth annotations in the source domain, and $\mathcal{L}_{adv}(I_t)$ is the adversarial loss that adapts predicted segmentations of target images to the distribution of source predictions, λ is the weight used to balance two losses, and always sets as 0.001 following.

2.1 Segmentation Network

We build upon a good baseline model to achieve high-quality segmentation results [7]. Specifically, this paper employs the DeepLab-v2 [7] framework with ResNet-101 [14] model pre-trained on ImageNet [15] as the baseline network. However, we do not use the multi-scale fusion strategy [7] due to the memory issue. Similar to the recent work on semantic segmentation [7], we remove the last classification layer and modify the stride of the last two convolution layers from 2 to 1, making the resolution of the output feature maps 1/8 times with respect to the original input image size. To enlarge the receptive field, we apply dilated convolution layers in conv4 and conv5 layers with a stride of 2 and 4, respectively. After the last layer, we use the Atrous Spatial Pyramid Pooling (ASPP) [7] as the final classifier. Finally, we apply an up-sampling layer along with the softmax output to match the size of the input image. Table 1 illustrates the details of hyper parameter setting to construct the segmentation network, where h and w are the width and hight of input source images. Noting that the output of the segmentation network is input to the CRF module for further processing.

Table 1 Details of hyper parameter setting of segmentation network

Layer name	Output size	Network size
conv1	$\frac{h}{2} \times \frac{w}{2}$	7×7, 64, stride 2
conv2_x	$\frac{h}{4} \times \frac{w}{4}$	3×3 max pool, stride 2 $\begin{bmatrix} 1 \times 1, & 64 \\ 3 \times 3, & 64 \\ 1 \times 1, & 256 \end{bmatrix} \times 3$
conv3_x	$\frac{h}{8} \times \frac{w}{8}$	$\begin{bmatrix} 1 \times 1, & 128 \\ 3 \times 3, & 128 \\ 1 \times 1, & 512 \end{bmatrix} \times 4$
conv4_x	$\frac{h}{8} \times \frac{w}{8}$	$\begin{bmatrix} 1 \times 1, & 256 \\ 3 \times 3, & 256 \\ 1 \times 1, & 1024 \end{bmatrix} \times 23$
conv5_x	$\frac{h}{8} \times \frac{w}{8}$	$\begin{bmatrix} 1 \times 1, & 512 \\ 3 \times 3, & 512 \\ 1 \times 1, & 2048 \end{bmatrix} \times 3$
Upsample	$h \times w$	Bilinear interpolation
CRF	$h \times w$	CRF as RNN

The implementation of fully-connected CRFs [15] as layers rely on applying Gaussian and bilateral filters for approximate mean-field inference. The parameters of the final combined CNN-CRF network are learned end-to-end, using back-propagation [16] to minimise the structured loss which captures the contextual information of the pixel-level labelling. Given the CRF softmax output $Y_s \in \mathcal{R}^{H \times W \times C}$, H and W are the width and height of input source images, and C indicates the number of categories, the loss of segmentation network with CRF is defined as a cross-entropy loss:

$$\mathcal{L}_{seg}(I_s) = -\sum_{h,w} \sum_{c} L_s^{(h,w,c)} log(Y_s^{(h,w,c)}) \tag{2}$$

where c indicates the number of categories, L_s is the pixel-level annotated ground truth for the source images.

2.2 *Discriminator Network*

For the discriminator network, we employ an architecture similar to but use all fully-convolutional layers to retain the spatial information. The network consists of 5 convolution layers with kernel 4×4 and stride of 2, where the channel numbers are {64, 128, 256, 512, 1}, respectively. Except for the last layer, each convolutional layer is followed by a leaky ReLU [8] parameterized by 0.2. An up-sampling layer is

Table 2 Details of hyper parameter setting of discriminator network

Layer name	Output size	Network size
conv1	$\frac{h}{2} \times \frac{w}{2}$	4×4, 64, stride 2
conv2	$\frac{h}{4} \times \frac{w}{4}$	4×4, 128, stride 2
conv3	$\frac{h}{8} \times \frac{w}{8}$	4×4, 256, stride 2
conv4	$\frac{h}{16} \times \frac{w}{16}$	4×4, 512, stride 2
conv5	$\frac{h}{32} \times \frac{w}{32}$	4×4, 1, stride 2

followed to the last convolution layer for rescaling the output to the size of the input. We do not use any batch-normalization layers [17] as we train the discriminator with the segmentation network using a small batch size. Table 2 illustrates the details of hyper parameter setting to construct the discriminator network.

We first describe the training objective for the discriminator, the CRF softmax output Y from source domain and target domain is the input to the discriminator, which employs the cross-entropy loss $\mathcal{L}_D$ for classifying if the input image is from the source domain or the target domain, $Y_s, Y_t \in \mathcal{R}^{H \times W \times C}$, H and W are the width and hight of input source images, and C indicates the number of categories of the output domains, the adversarial loss mentioned next paragraph will base on it.

$$\mathcal{L}_D(I_s, I_t) = -\sum_{h,w} log(D(Y_s)^{(h,w,1)}) + log(D(Y_t)^{(h,w,0)}) \tag{3}$$

where $D(Y_s)$ and $D(Y_t)$ denote the output of the discriminator network from source domain and target domain, respectively. This loss is only designed to optimize the parameters of the discriminator network.

In addition, for any image I_t in the target domain, we fed it into the segmentation network and obtain the prediction Y_t without any labels. To discriminate the feature between source domain and target domain, the adversarial loss $\mathcal{L}_{adv}$ is defined as:

$$\mathcal{L}_{adv}(I_t) = -\sum_{h,w} log(D(Y_t)^{(h,w,1)}) \tag{4}$$

With adversarial learning, it should maximize the probability of target predictions being considered as source predictions. This loss is only designed to optimize the parameters of the segmentation network.

2.3 Training

Jointly optimizing Eqs. (2)–(4) is very difficult, we thus resort to an iterative, EM-like strategy to alternately optimize segmentation network $\mathcal{G}$ and discriminator network $\mathcal{D}$, simultaneously. The whole iterations are repeated until convergence is reached. Mathematically, each iteration repeats the following optimized problem:

$$\begin{cases} \min\limits_{\mathcal{D}} \mathcal{L}_D(I_s, I_t), \\ \min\limits_{\mathcal{G}} \mathcal{L}(I_s, I_t). \end{cases} \tag{5}$$

where $\mathcal{L}_D$ and $\mathcal{L}$ are defined in Eq. (3) and Eq. (1), respectively. The ultimate goal is to minimize the segmentation loss in $\mathcal{G}$ for source images, while maximizing the probability of target predictions being considered as source predictions.

2.3.1 Update $\mathcal{D}$

With alternate optimization approach, we always assume that $\mathcal{G}$ is fixed when updating $\mathcal{D}$. Then, the problem of Eq. (5) can be simplified as:

$$\min_{\mathcal{D}} \mathcal{L}_D(I_s, I_t) \tag{6}$$

For the target image I_t, we obtain the $\mathcal{G}$ output Y_t, and pass it along with Y_s to the $\mathcal{D}$ for optimizing $\mathcal{L}_D$ in Eq. (3), which only optimize the parameters for the $\mathcal{D}$ with the learning rate parameterized by 2.5×10^{-4}.

2.3.2 Updating $\mathcal{G}$

Now, $\mathcal{D}$ is fixed, and Eq. (5) can be written as:

$$\min_{\mathcal{G}} \left(\mathcal{L}_{seg}(I_s) + \lambda \mathcal{L}_{adv}(I_t)\right) \tag{7}$$

We forward the source image I_s to optimize the $\mathcal{G}$ for $\mathcal{L}_{seg}$ in Eq. (2) and obtain the output Y_s. Next, we try to make the discriminator consider the target predictions as the source predictions, by computing the adversarial loss $\mathcal{L}_{adv}$ in Eq. (4), which only optimize the parameters for the $\mathcal{G}$ with the learning rate parameterized by 1×10^{-4}.

3 Experiments

3.1 Dataset

We employ GTA5 and SYNTHIA-RAND-CITYSCAPES datasets as two source domains, and adapt the trained model into target domain: Cityscapes dataset.

The GTA5 dataset. It consists of 24966 images with the resolution of 1914×1052 synthesized from the video games based on the city of Los Angeles [8]. The ground truth annotations are compatible with the Cityscapes dataset [10] that contains 19 categories. Following [18], we use the full set of GTA5 and adapt the model to the Cityscapes training set with 2975 images. During testing, we evaluate on the Cityscapes validation set with 500 images.

The SYNTHIA-RAND-CITYSCAPES dataset. To adapt from the SYNTHIA to Cityscapes datasets, we use the SYNTHIA-RAND-CITYSCAPES [9] set as the source domain which contains 9400 images compatible with the cityscapes annotated classes. Similar to [1], we evaluate images on the Cityscapes validation set with 13 classes.

3.2 Overall Results

3.2.1 GTA5 to Cityscapes

The performance of domain-adapted sematic segmentation with or without CRF are shown in Table 3. For both approaches, the baseline model is trained using ResNet-101-based architectures. Clearly, our method performs favorably against the algorithm without CRF. The changes for $\mathcal{L}_{adv}$ in the whole iteration process are shown in Fig. 2, where red solid line is the training without CRF, and the blue solid line is ours. We note that CRF can help to fool the discriminator and increase the probability of the target prediction being considered as the source prediction. Figure 3 presents some results for adapted segmentation. We note that for big vehicle objects such as truck and bus sign, they are better to adapt. As for domain adaptation for semantic segmentation, CRF-RNN is helpful for distinguishing the objects with big regular outline.

3.2.2 SYNTHIA to Cityscapes

Table 4 shows evaluational results of the proposed algorithm to adapt SYNTHIA to Cityscapes dataset. The experimental results suggest that CRF-RNN can help the adapt structured output space for semantic segmentation. Similar with the adaption

Table 3 The results of adaption from GTA5 to Cityscapes

Method	Road	Sidewalk	Building	Wall	Fence	Pole	Light	Sign	Veg	Terrain	Sky	Person	Rider	Car	Truck	Bus	Train	mbike	Bicycle	mIoU
FCN in the wild	70.4	32.4	62.1	14.9	5.4	10.9	14.2	2.7	79.2	21.3	64.6	44.1	4.2	70.4	8.0	7.3	0.0	3.5	0.0	27.1
Cross-city	83.3	38.3	76.4	20.6	16.5	22.2	26.2	**21.9**	80.4	28.7	65.7	49.4	4.2	74.6	16.0	26.6	2.0	8.0	0.0	34.8
AdaptSegNet	86.3	22.1	80.4	21.6	24.6	25.2	33.6	15.3	82.6	30.5	76.2	57.1	27.6	77.5	24.7	36.2	1.5	29.0	21.2	40.7
Ours	87.7	21.2	81.4	27.3	27.3	21.6	32.6	15.4	84	37.2	76.7	54.9	28.2	**84.7**	**35.4**	**48.4**	0.9	26.0	10.0	**41.9**

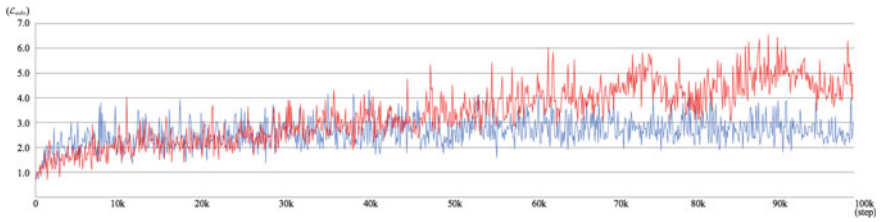

Fig. 2 Changes for $\mathcal{L}_{adv}$ in the whole iteration process, red solid line is the training without CRF, blue solid line is ours

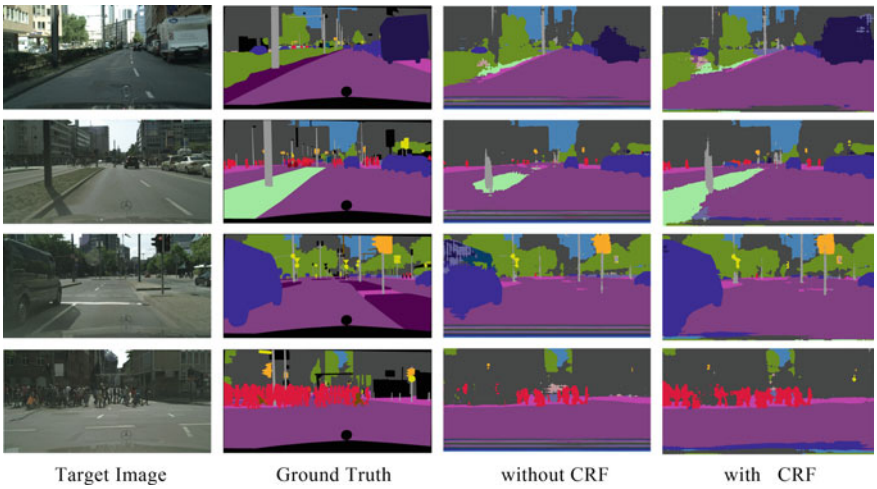

Fig. 3 Example results of adapted segmentation for GTA5-to-Cityscapes. For each target image, we show results without CRF and with CRF

from GTA5 to Cityspaces, our model performs better in semantic segmentation for bus, which can enhance the accuracy of the objects with big regular outline.

4 Conclusion and Future Work

In this paper, we employed CRF-RNN to adapt structured output space for semantic segmentation. We tackled the end-to-end model with CRF via adversarial learning in the output space. In particular, the accuracy of the objects with big regular outline could be improved with the help of CRF-RNN. We have shown the superiority of our approach over existing methods on two large scale datasets, demonstrating the generality and scalability of our training procedure. As future work, we would like to extend this approach to evaluate CRF-RNN in other domain-adaptation approaches for semantic segmentation.

Table 4 The results of adaption from SYNTHIA to Cityscapes

Method	Road	Sidewalk	Building	Light	Sign	Veg	Sky	Person	Rider	Car	Bus	mbike	Bicycle	mIoU
FCN in the wild	11.5	19.6	30.8	0.1	11.7	42.3	68.7	51.2	3.8	54.0	3.2	0.2	0.6	22.9
Cross-city	62.7	25.6	78.3	1.2	5.4	81.3	81.0	37.4	6.4	63.5	16.1	1.2	4.6	35.7
AdaptSegNet	80.1	42.3	74.1	4.6	6.8	74.3	81.4	52.1	19.7	69.6	31.1	20.2	30.3	45.1
Ours	84.1	39.1	72.9	4.9	10.0	73.2	79.8	55.1	21.2	71.1	45.2	19.1	28.6	46.4

Acknowledgements This work was partly supported the National Natural Science Foundation of China (Grant No. 61881240048, 61701252, 61876093, BK20181393), and HIRP Open 2018 Project of Huawei.

References

1. Geiger, A., Lenz, P., Urtasun, R.: Are we ready for autonomous driving? The KITTI vision benchmark suite. In: Proceedings of CVPR (2012)
2. Serikawaa, S., Huimin, L.: Underwater image dehazing using joint trilateral filter. Comput. Electr. Eng. **40**(1), 41–50 (2014)
3. Lu, H., Li, Y., Mu, S., Wang, D., Kim, H., Serikawa, S.: Motor anomaly detection for unmanned aerial vehicles using reinforcement learning. IEEE Internet Things J. (2017). https://doi.org/10.1109/JIOT.2017.2737479
4. Lu, H., Li, Y., Chen, M., Kim, H., Serikawa, S.: Brain intelligence: go beyond artificial intelligence. Mob. Netw. Appl. 1–8 (2017)
5. Lu, H., Li, B., Zhu, J., Li, Y., Li, Y., Xu, X., He, L., Li, X., Li, J., Serikawa, S.: Wound intensity correction and segmentation with convolutional neural networks. Concurr. Comput. Pract. Exp. (2017). https://doi.org/10.1002/cpe.3927
6. Lu, H., Li, Y., Uemura, T., Kim, H., Serikawa, S.: Low illumination underwater light field images reconstruction using deep convolutional neural networks. Future Gen. Comput. Syst. (2018). https://doi.org/10.1016/j.future.2018.01.001
7. Chen, L.-C., Papandreou, G., Kokkinos, I., Murphy, K., Yuille, A.L.: Deeplab: semantic image segmentation with deep convolutional nets, atrous convolution, and fully connected CRFs. CoRR arXiv:1606.00915
8. Richter, S.R., Vineet, V., Roth, S., Koltun, V.: Playing for data: ground truth from computer games. In: Proceedings of ECCV (2016)
9. Ros, G., Sellart, L., Materzynska, J., Vazquez, D., Lopez, A.: The SYNTHIA dataset: a large collection of synthetic images for semantic segmentation of urban scenes. In: Proceedings of CVPR (2016)
10. Cordts, M., Omran, M., Ramos, S., Rehfeld, T., Enzweiler, M., Benenson, R., Franke, U., Roth, S., Schiele, B.: The cityscapes dataset for semantic urban scene understanding. In: Proceedings of CVPR (2016)
11. Goodfellow, I., Pouget-Abadie, J., Mirza, M., Xu, B., Warde-Farley, D., Ozair, S., Courville, A., Bengio, Y.: Generative adversarial nets. In: Proceedings of NIPS (2014)
12. Kingma, D.P., Ba, J.: Adam: a method for stochastic optimization. In: Proceedings of ICLR (2015)
13. Hong, S., Noh, H., Han, B.: Decoupled deep neural network for semi-supervised semantic segmentation. In: Proceedings of NIPS (2015)
14. He, K., Zhang, X., Ren, S., Sun, J.: Deep residual learning for image recognition. In: Proceedings of CVPR (2016)
15. Hoffman, J., Tzeng, E., Park, T., Zhu, J.-Y., Isola, P., Saenko, K., Efros, A.A., Darrell, T.: CyCADA: cycle-consistent adversarial domain adaptation. CoRR (2017). arXiv:1711.03213
16. Khoreva, A., Benenson, R., Hosang, J., Hein, M., Schiele, B.: Simple does it: weakly supervised instance and semantic segmentation. In: Proceedings of CVPR (2017)
17. Ioffe, S., Szegedy, C.: Batch normalization: accelerating deep network training by reducing internal covariate shift. In: Proceedings of ICML (2015)
18. Hoffman, J., Wang, D., Yu, F., Darrell, T.: FCNs in the wild: pixel-level adversarial and constraint-based adaptation. CoRR (2016). arXiv:1612.02649

Human Detection in Crowded Situations by Combining Stereo Depth and Deeply-Learned Models

Csaba Beleznai, Daniel Steininger and Elisabeth Broneder

Abstract Human detection in crowded situations represents a challenging task in many practically relevant scenarios. In this paper we propose a passive stereo depth based human detection scheme employing a hierarchically-structured tree of learned shape templates for delineating clusters corresponding to humans. In order to enhance the specificity of the depth-based detection approach towards humans, we also incorporate a visual object recognition modality in form of a deeply-trained model. We propose a simple way to combine the depth and appearance modalities to better cope with complex effects such as heavily occluded and small-sized humans, and clutter. Obtained results are analyzed in terms of improvements and shortcomings introduced by the individual detection modalities. Our proposed combination achieves a good accuracy at a decent computational speed in difficult scenarios exhibiting crowded situations. Hence in our view, the presented concepts represent a detection scheme of practical relevance.

Keywords Human detection · Detection in a crowd · Prior shape model
Mean shift clustering · Semantic segmentation · Stereo vision · Occupancy map
Video surveillance

1 Introduction

Computer vision based analysis of humans in crowded scenes has been receiving increasing amount of attention in the recent years. Learned representations of the human appearance, especially in form of deep distributed representations [16], offer

C. Beleznai (✉) · D. Steininger
Center for Vision, Automation & Control, AIT Austrian Institute of Technology, Vienna, Austria
e-mail: csaba.beleznai@ait.ac.at

E. Broneder
Center for Digital Safety & Security, AIT Austrian Institute of Technology, Vienna, Austria

H. Lu (ed.), *Cognitive Internet of Things: Frameworks, Tools and Applications*, Studies in Computational Intelligence 810,
https://doi.org/10.1007/978-3-030-04946-1_47

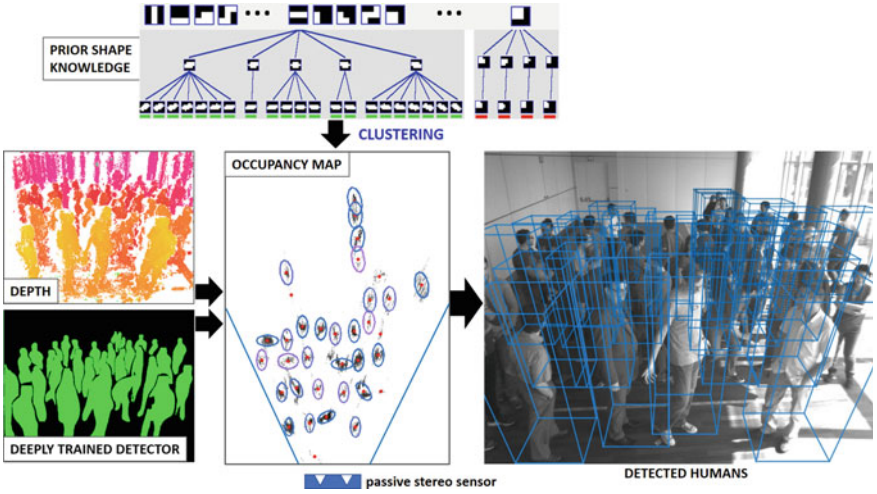

Fig. 1 Our proposed detection scheme combining the input modalities of depth data and a deeply trained detector. An occupancy map representation is used to combine individual responses, which are clustered using prior, structure-specific knowledge on the expected shape of clusters

significant accuracy improvements given their enhanced specificity and invariance properties. Such representational advantages accomplish significant accuracy gains in cases where many humans mutually interact within a spatially confined space, inducing challenging situations such as a high degree of dynamic occlusions, clutter and greatly varying size of the humans.

Human detection from depth data has been another promising approach to tackle many of these issues, for example in the fields of robotics and intelligent vehicles [2, 7, 15, 17]. Depth information greatly facilitates the spatial delineation and depth ordering of detection hypotheses, thus greatly mitigating the complexity of object detection under heavy occlusions. However, an often-encountered problem is a rapid degradation of the depth data quality (accuracy, missing data, noise) with increasing object-to-sensor distances. Consequently, the analysis of fine details (occlusions, small-sized humans) becomes highly challenging at greater distances.

Motivated by these open issues and the recent emergence of reliable appearance based recognition, we strive to combine the two detection modalities such that accurate delineation and detection of occluding humans also farther from the camera becomes feasible. Figure 1 displays our combined detection scheme, where a spatial accumulation in form of an *occupancy map* is used to combine and delineate detection responses. Local grouping within the two-dimensional occupancy map is a key step towards generating consistent object hypotheses. In case of weak detection responses, background clutter and noise, knowledge associated with prior structural information—such as the expected shape of the local distribution—can help to recover weak evidence. The challenge arises from the fact that the distributions to be analyzed are multi-structured: multiple spatially extended patterns might exist at different locations, orientations and scales, thus rendering a robust and

computationally efficient clustering and spatial delineation a challenge. To cope with these problems, we employ a coarse-to-fine organized binary shape codebook to evaluate the local distribution around a density maximum in terms of a best matching shape. This clustering step requires only a coarse initial scale estimate, and capable to adapt to varying size, orientation and location. The proposed vision system achieves a relatively fast run-time performance when taking into account that two detection modalities and clustering are performed on the same computing unit.

2 Related Work

During the last two decades much research has been carried out to improve the accuracy of human detection and to extend its operational domain into increasingly complex scenarios. In this process employed representations of appearance and shape have played a key role.

Appearance-based detection: Recent years have demonstrated a shift from handcrafted representations to end-to-end learned recognition systems employing deep distributed representations. The Integral Channel Features [6], DPM [8] and LDCF [21] detectors are some well-performing detection algorithms of the former type. Modern detection schemes based on Deep Convolutional Neural Networks have demonstrated significant improvement on common benchmarks, however at the expense of significantly higher computational costs. Fast and Faster R-CNN [9, 20] and Mask R-CNN [10] are typical examples for such advanced detection concepts. Dense pixel-wise classification in form of semantic segmentation [4, 22] also represents a detection concept which offers enhanced algorithmic capabilities to outline thin or small-sized objects. A recent comprehensive review on the state-of-the-art of pedestrian detection [23] provides an in-depth comparison and analysis of limitations for many modern techniques.

Depth-based detection: Information in depth data inherently offers ways to lower the ambiguity associated with occlusions and depth ordering. Low-cost active RGB-D sensors [15], passive stereo vision [18] or Lidar sensors [2] provide spatial information with increasingly larger ranges, and representations often rely on occupancy maps or 3d point clouds. To further enhance the range and the robustness with respect to occlusions, fusion of several modalities, such as RGB-D, Lidar and appearance-based detection [7, 13, 14] can be used.

Delineation and clustering: Generating object hypotheses by delineating consistent maxima in a probabilistic map is a relevant task in computer vision. Often, a weakly constrained structural prior in form of a local maximum search is employed. Non-maximum suppression is a common way to address this task. A greedy maximum search scheme [19]. Mean Shift [5] and its scale adaptive variants [3] represent a similar strategy as they are simple non-parametric ways to locate density maxima and to characterize their spatial extent by determining the so-called basin of attraction [5] or estimating the local covariance.

Our detection approach uses information from stereo depth as the primary modality, however, we propose a simple combination with detection outputs from modern deeply learned detectors. The motivation behind the combination is twofold. On one hand we aim to enhance weak detection responses, commonly encountered upon poor object visibilities. On the other hand, the combination also seeks to suppress noisy structures within two-dimensional distributions, not corresponding to true detection responses. To support the object delineation task, we employ a patch-based hierarchical structure representation. Given a learned set of possible shapes (encoded as binary shapes), our clustering technique can better cope with weak and noisy signals within the heavily multi-modal two-dimensional distribution of an occupancy map.

3 Methodology

In this section we describe the overall scheme of our detection algorithm, characterize the input data and explain the individual algorithms in detail.

The main motivation behind the proposed combined processing scheme stems from the fact that multiple visual inputs of complementary nature are sought to improve weak or ambiguous detection responses while suppressing noise. Our framework uses visual input from a trinocular stereo setup consisting of three monochrome cameras, where a stereo disparity image is computed for each of the three stereo baselines, and combined into one disparity image. We use an in-house developed sensor with a baseline of 40 cm between the two extremal cameras. The monochrome cameras are board-level industrial cameras of 2 Megapixel with a GigE interface. During rectification the images are resampled to 900×720 pixels with 8 bit quantization. The stereo matching process outputs disparity data alongside with rectified intensity images, congruent to the disparity image. Disparity information is computed via a pyramidal implementation of a Census-based stereo matching algorithm [11].

The disparity data is used to estimate a dominant ground plane. We adopt a well-known estimation scheme based on vertical disparity statistics [12], exploiting that the computed disparity d exhibits a linear dependence from the image coordinates. Accordingly, we accumulate the vertical disparity statistics for the entire image, and robust statistics is used to find the dominant linear structure. The robustly estimated ground plane parameters allow for a depth-aware combination of detection responses for both depth and appearance-based detection schemes on the 3d ground plane. Disparity data is converted to depth and a perpendicular projection onto the 3d ground plane is computed. This projection results in a *occupancy map* representation, further denoted as O. The occupancy map is analyzed by our clustering scheme encoding prior shape information.

Integration of deep convolutional neural network detector: We select two detectors for evaluating an integration: Deep Layer Aggregation (DLA) [22] and Mask R-CNN [10]. In order to combine the output of a deeply trained human detector with an occupancy map, we proceed in the following steps. First, we generate a binary mask from the deep human detector's output (see Fig. 1). DLA generates a seman-

tic segmentation map, and Mask R-CNN generates instance segmentations. For the latter we use its output as a segmentation map without instance information. We use the generated binary mask and the given depth information to project the detection response onto the 3d ground plane and to generate an occupancy map O_d from the detection responses as well. In order to combine the two modalities, we perform a mixing between the two occupancy maps:

$$O = (1 - \alpha) O_D + \alpha O_d, \tag{1}$$

where O_D represents the occupancy map from depth data only. α is a mixing factor, defined in the range of [0, 1]. $\alpha = 1$ uses information from a deeply trained detector, while employing the depth information to spatially index the occupancy map. In the other extremal case of $\alpha = 0$, only depth information is used for detection. The motivation behind the proposed mixing is to strive to preserve weak signals while discarding those of noise origin.

Shape learning for clustering: Using an extension of our previous work [1], we learn a structured representation of binary shapes from a set of annotated positive and negative samples. An illustration of the learning process is depicted in Fig. 2. In the learning step, first we derive a pool of local binary shapes at multiple resolutions from annotated data. We annotated 4000 positive samples (image patches containing valid clusters) in the occupancy map data. Annotation consisted of a bounding box and a definition of a circumscribing elliptic shape. By applying additional image transforms (flipping, random rotation around the patch center), we generated 30,000 positive samples in total. The same number of negative samples were generated from local patterns which do not represent humans (noisy regions, non-centered objects). We center on each training sample (positive and negative alike) a $n_i \times n_i$ grid G, with

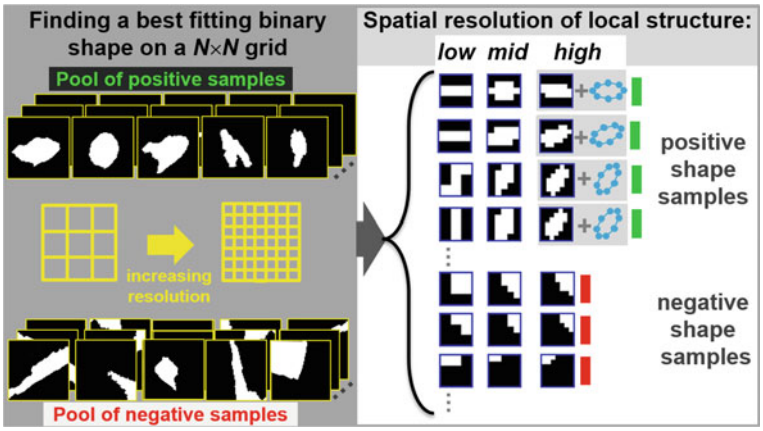

Fig. 2 Illustration explaining the construction of the structured shape representation encoding and discriminating shapes between two shape classes. The left side shows the grid-based fitting of best matching shapes. The right side displays the obtained class-specific binary shapes at different resolutions

multiple resolutions (in our case $n_1 = 3, n_2 = 5$ and $n_3 = 7$). At each resolution i we generate a binary shape $\mathbf{l}_i$, represented as a vector of label values at each cell position C of the grid G. The obtained pool of binary signatures can be easily quantized by binning. Since low-resolution structures are simplified variants for many mid- and high-resolution shapes, therefore binning generates a tree-like hierarchy. The low-resolution layer represents prototypical shapes, while higher resolutions encode more detailed and specific structures. We denote the obtained shape tree as the *binary shape codebook*.

During cluster delineation we can use this previously learnt codebook to quickly look up the best-matching shape for the underlying distribution, and to estimate its class label (human vs. not human). First, we perform a Mean Shift mode-seeking [5] to locate local density maxima at a scale s. At each potential human candidate location, we carry out the same subdivision scheme of the analysis window as performed in the learning step. At the given location in the occupancy map O we evaluate following density measure using the learnt codebook:

$$D_i\,(l_i \mid O\,) = \frac{1}{A_F} \sum_{\{x,y \in C \mid l=1\,\}} O(x, y) \; - \\ \frac{1}{A_B} \sum_{\{x,y \in C \mid l=0\,\}} O(x, y), \tag{2}$$

where A_F and A_B denote the binary foreground/background areas within a cell C of the local grid, respectively. l_j are the cell labels (1-foreground, 0-background). The above equation can be evaluated very efficiently by means integral images since area-sum computations are involved. As illustrated in Fig. 3, a given mode location

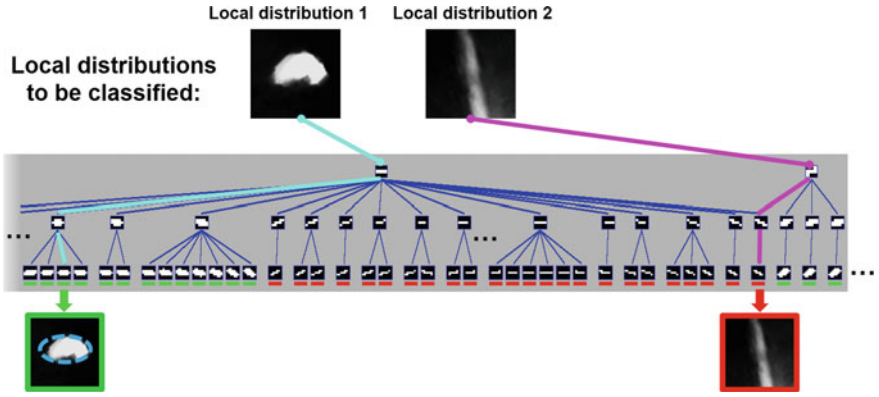

Fig. 3 Illustration showing the analysis (delineation, classification) of two local distributions in the occupancy map. Given the previously learnt structured shape codebook and the cost function of Eq. 1, the best matching structures and their label (green—human, red—noise) are quickly inferred at each resolution level

(centered on a local distribution) is evaluated first at a coarse level, then at finer details, based on the structural dependencies defined in the structured codebook. The best matching codebook entry at resolution i maximizes the density within the hypothesized foreground region, while minimizing the density in the hypothesized background region:

$$l_i^* = \arg\max_l \; D_i\left(l_i \,|O\right). \tag{3}$$

Evaluating the above measure at each resolution in the shape tree guides the selection towards the best matching high resolution candidate at the leaf-node of the tree. The stored class information (valid vs. noise) and the polygonal contour information can be used to delineate the underlying local distribution.

4 Results and Discussion

In this section we demonstrate and discuss our experiments and results on our proposed detection scheme.

Data sets and their characteristics: In order to quantitatively evaluate our detection scheme, we annotated 56,214 human instances in four datasets, consisting of 2000 frames. Humans occluded more than 90% were not annotated. All four scenarios have a similar camera look-down angle and observe an area of about 10 m $\times$ 15 m (width $\times$ depth). To gauge the complexity of the detection task we analyzed the annotations with respect to object visibilities (occlusion rates) and the distribution of human size in the images. Figure 4 show the corresponding analysis results. Occlusions were computed between bounding boxes, therefore (although heavily occluded objects were not annotated) also 100% occlusions are possible. As it can be seen from the typical annotations and the statistics, the scenarios represent a dense crowd, where primarily the high occlusion rates pose a challenge. Half of the annotated humans is occluded more than 50%.

Results: Quantitative analysis was performed in terms of a Precision-Recall characterization, employing a bounding-box overlap criterion (between annotations and back-projected bounding boxes). Furthermore, a one-to-one match between the results and annotations was enforced. Precision is referred to how many delineated humans are relevant and equals to $\frac{tp}{tp+fp}$. Recall is referred to what fraction of the relevant clusters was found and equals to $\frac{tp}{tp+fn}$. tp, fp and fn are the number of true, false and missed cluster delineations, respectively. Table 1 displays the obtained quantitative results for all experiments. As it can be seen from the qualitative and quantitative results, detection via depth information only suffers from occasional false positives, typically induced by vertical structures (pillars, walls). Depth-based detection performs often well in highly occluded situations where learned detectors start to fail. It is also visible, that the DLA [22] segmentation offers poor quality in our scenarios, exhibiting a high miss rate for occlusions, and also producing false

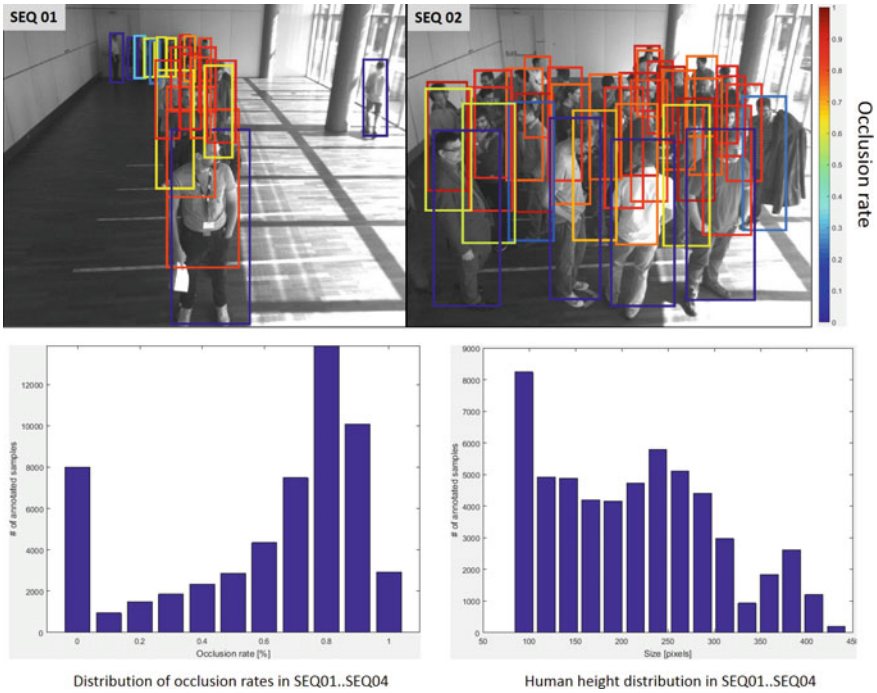

Fig. 4 Top row: annotations shown for two of our test sequences. Annotations are color-coded by their occlusion rates (0—unoccluded, 1—fully occluded). Bottom row: aggregated occlusion and size statistics from all of our four test sequences

alarms. Therefore, a depth-DLA combination does not introduce improvements, and a mixing favoring nearly entirely the depth modality is obtained. On the other hand, Mask R-CNN represents a high-quality detection modality [10], yielding a high recall, and producing false alarms in different situations than depth-based detection (Fig. 5). Surprisingly, the combination depth + Mask R-CNN does not achieve a significant gain. It seems that the mapping of Mask R-CNN responses via the depth data is not always optimal (Fig. 6). If only few pixels with valid depth are defined for an object, even a strong Mask R-CNN response becomes weak after the mapping. A direct mapping from the image space via the learned ground plane might be another option to be explored.

Table 1 Obtained quantitative results for using the individual and combined modalities, from all test sequences SEQ01-SEQ04. D denotes the usage of depth data

Performance measure	D	DLA	Mask R-CNN	D + DLA	D + Mask R-CNN
Recall (R)	0.82	0.72	0.83	0.81	0.84
Precision (P)	0.84	0.81	0.93	0.83	0.92
F-measure (F)	0.83	0.76	**0.88**	0.82	**0.88**

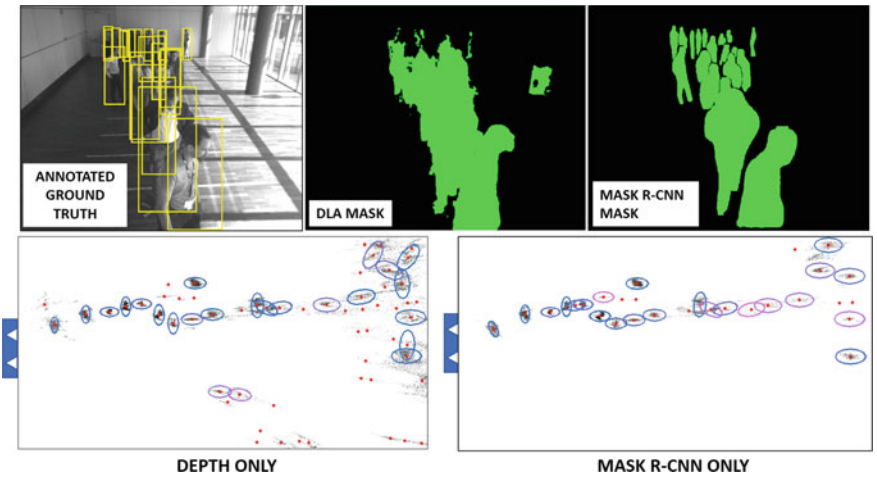

Fig. 5 Top row: annotations and the corresponding DLA [22] and Mask-RCNN [10] segmentations for a selected frame of SEQ01. Bottom row: occupancy maps with overlaid clusters for depth-only and Mask R-CNN-only detection modalities

Fig. 6 Sample detection results shown for the four test sequences using an optimum combination between depth and learned human detectors

Run-time performance: Our proposed approach exhibits following run-time characteristics: Depth based detection (including stereo depth computation and clustering) runs at 6 fps (CPU-only) on a modern PC. Combinations with the DLA and Mask R-CNN detectors run at 0.5 fps and 4 fps, respectively. In these cases, appearance-based detection is performed on a GPU hardware (NVIDIA Titan X). Cluster delineation (measured separately) runs at about 65 fps on the CPU.

5 Conclusions

We present a human detection scheme combining two detection modalities in form of stereo depth and a deeply trained human detector. We target complex scenarios with high people densities, exhibiting frequent occlusions. We solve the human detection problem as an occupancy map clustering task. For a fast two-dimensional cluster delineation we employ a coarse-to-fine shape codebook to enforce prior shape information upon analyzing a local distribution. We demonstrate for some selected scenarios that the combination of complementing detection modalities improves the detection accuracy in crowded situations.

Acknowledgements The authors thank both the Austrian Federal Ministry for Transport, Innovation and Technology as well as the Austrian Research Promotion Agency (FFG) for co-funding the research project "LEAL" (FFG Nr. 850218) within the National Research Development Programme KIRAS Austria.

References

1. Beleznai, C., Zweng, A., Netousek, T., Birchbauer, J.A.: Multi-resolution binary shape tree for efficient 2D clustering. In: 3rd IAPR Asian Conference on Pattern Recognition, pp. 569–573 (2015)
2. Beyer, L., Hermans, A., Linder, T., Arras, K.O., Leibe, B.: Deep person detection in 2D range data (2018). arXiv:1804.02463
3. Bradski, G.R.: Computer vision face tracking for use in a perceptual user interface. Intel Technol. J. (Q2), 15 (1998)
4. Bulò, S.R., Neuhold, G., Kontschieder, P.: Loss max-pooling for semantic image segmentation. In: Proceedings of CVPR, pp. 7082–7091. IEEE Computer Society (2017)
5. Comaniciu, D., Meer, P.: Mean shift: a robust approach toward feature space analysis. IEEE Trans. PAMI **24**, 603–619 (2002)
6. Dollár, P., Tu, Z., Perona, P., Belongie, S.: Integral channel features. In: Proceedings of BMVC, pp. 91.1–91.11 (2009)
7. Engelmann, F., Stückler, J., Leibe, B.: Joint object pose estimation and shape reconstruction in urban street scenes using 3D shape priors. In: Proceedings of the German Conference on Pattern Recognition (GCPR) (2016)
8. Felzenszwalb, P., Mcallester, D., Ramanan, D.: A discriminatively trained, multiscale, deformable part model. In: Proceedings of Computer Vision and Pattern Recognition (CVPR) (2008)

9. Girshick, R.: Fast R-CNN. In: Proceedings of IEEE International Conference on Computer Vision (ICCV), pp. 1440–1448 (2015)
10. He, K., Gkioxari, G., Dollár, P., Girshick, R.B.: Mask R-CNN. In: IEEE International Conference on Computer Vision, ICCV 2017, pp. 2980–2988 (2017)
11. Humenberger, M., Zinner, C., Weber, M., Kubinger, W., Vincze, M.: A fast stereo matching algorithm suitable for embedded real-time systems. Comput. Vis. Image Underst. **114**(11), 1180–1202 (2010)
12. Krotosky, S., Trivedi, M.M.: A comparison of color and infrared stereo approaches to pedestrian detection. In: 2007 IEEE Intelligent Vehicles Symposium, pp. 81–86 (2007)
13. Linder, T., Arras, K.O.: Multi-model hypothesis tracking of groups of people in RGB-D data. In: 17th International Conference on Information Fusion, FUSION, pp. 1–7 (2014)
14. Linder, T., Breuers, S., Leibe, B., Arras, K.O.: On multi-modal people tracking from mobile platforms in very crowded and dynamic environments. IEEE International Conference on Robotics and Automation (ICRA), pp. 5512–5519 (2016)
15. Liu, H., Luo, J., Wu, P., Xie, S., Li, H.: People detection and tracking using RGB-D cameras for mobile robots. Int. J. Adv. Robot. Syst. **13**(5), 1–8 (2016)
16. Lu, H., Li, Y., Chen, M., Kim, H., Serikawa, S.: Brain intelligence: go beyond artificial intelligence. Mob. Netw. Appl. (2017)
17. Lu, H., Li, Y., Uemura, T., Kim, H., Serikawa, S.: Low illumination underwater light field images reconstruction using deep convolutional neural networks. Future Gen. Comput. Syst. **82**, 142–148 (2018)
18. Muñoz Salinas, R., Aguirre, E., García-Silvente, M.: People detection and tracking using stereo vision and color. Image Vis. Comput. **25**(6), 995–1007 (2007)
19. Neubeck, A., Van Gool, L.: Efficient non-maximum suppression. In: Proceedings of International Conference on Pattern Recognition, vol 3, pp. 850–855 (2006)
20. Ren, S., He, K., Girshick, R., Sun, J.: Faster R-CNN: towards real-time object detection with region proposal networks. In: Proceedings of Advances in Neural Information Processing Systems, vol. 28, pp. 91–99 (2015)
21. Woonhyun, N., Dollár, P., Hee Han, J.: Local decorrelation for improved pedestrian detection. In: Proceedings of NIPS (2014)
22. Yu, F., Wang, D., Darrell, T.: Deep layer aggregation. In: Proceedings of CVPR. IEEE Computer Society (2018)
23. Zhang, S., Benenson, R., Omran, M., Hosang, J., Schiele, B.: Towards reaching human performance in pedestrian detection. IEEE Trans. Pattern Anal. Mach. Intell. **40**(4), 973–986 (2018)

Small Object Tracking in High Density Crowd Scenes

Yujie Li and Shinya Takahashi

Abstract In recent years, computer vision for automatically identification and tracking of animals has evolved into a popular tool for quantifying behavior. Honeybees are a popular model for learning and memory, so tracking of honeybees within a colony is a particularly task due to dense populations, similar target appearance and a significant portion of the colony frequently leaving the hive. In this paper we present a detection method based on improved three-frame difference method and VIBE algorithm and one tracking method based on Kalman filtering for honeybees tracking. We evaluate the performance of the proposed methods on datasets which contains videos with crowd honeybee colony. The experimental results show that the proposed method performs good performance in detection and tracking.

Keywords Target detection · Object tracking · Kalman filter

1 Introduction

Computer vision uses computers to simulate human visual mechanism thereby understand external information, and as an interdisciplinary subject. It includes the knowledge of computer science, mathematics, engineering, physics, biology, neuroscience etc. In recent years, it has been the fundamental research in the field of artificial intelligence. As one of the important researches in this field, target detection and tracking combine image processing, pattern recognition, and automatic control, are the common setting for solving the problems. It also has a wide range of applications in the fields of intelligent transportation, video conferencing, image retrieval, and robot navigation.

Y. Li (✉) · S. Takahashi
Department of Electronics Engineering and Computer Science,
Fukuoka University, Fukuoka, Japan
e-mail: yzyjli@fukuoka-u.ac.jp

S. Takahashi
e-mail: takahasi@tl.fukuoka-u.ac.jp

H. Lu (ed.), *Cognitive Internet of Things: Frameworks, Tools and Applications*, Studies in Computational Intelligence 810,
https://doi.org/10.1007/978-3-030-04946-1_48

Multiple targets video detection and tracking from video data refers to finding and extracting targets with real-time in a sequence of video, and obtaining the trajectories of these targets according to the edges, local motions, and gray levels, then providing data for the next step of target recognition, motion analysis and other processing [1]. At present, the target detection methods without a priori knowledge can be classified as background subtraction method [2], optical flow method [3] and inter-frame difference algorithm [4]. The main principle of the inter-frame difference algorithm is to perform differential operation between adjacent two frames or three frames in the video sequence, then extract the target by threshold. The algorithm has good real-time performance, but it is impossible to extract all the relevant feature pixels completely, and the same target may be split into multiple parts, so the accuracy of detection is affected. The optical flow method detects targets by utilizing relationship between velocity and grayscale between two frames. However, the algorithm is very sensitive to light and low in real-time. The background subtraction method is the most widely used target detection algorithm. Firstly, it establishes a suitable background model, and performs a difference operation between the current frame image and the background model, then determine the foreground region in the light of corresponding criteria. Background modeling methods include multi-frame averaging, mixed Gaussian background modeling, pixel value clustering, and VIBE algorithm etc. Among them, the VIBE method is widely used due to its simple algorithm and fast calculation speed, the algorithm also has some shortcomings. Such as, when multiple targets are stuck together, they will be mistakenly divided into one target.

The target tracking means the prediction of the future location of a dynamical system based on its estimates and measurements. There are a lot of methods for tracking. For example, [5] describes the target by as SIFT features, and uses the Euclidean distance to track the moving target by matching criterion, but when the target is completely occluded and reappears When it leads to tracking failure. This approach is called; region-based tracking method and some improved methods such as Mean-shift tracking algorithm [6], Camshift tracking algorithm [7] are proposed. However, these methods are very time consuming when the range of the target candidate area is large, so this method is very time consuming, the efficient is very low. On the other hand, a gradient climbing technique and an isocontour slicing approach for high density homogeneous targets is proposed to analyse honeybee ethology. However, tracking of honeybees within a colony is an especially hard task due to dense populations, similarity of target appearance, and a frequently location changes, and so on.

In this paper, an improved detection and tracking methods are proposed for multiple small objects tracking in high density crowd scene. This paper is organized as follows, in Sect. 2 of this paper, the improved target detection and tracking method is proposed. Firstly, the improved VIBE algorithm with improved three-frame difference method is used to effectively extract the targets. In Sect. 3, the Kalman filter is used for multiple targets tracking. In Sect. 4, the experimental results on tracking multiple moving objects with a honeybee dataset [12] is reported to demonstrate the effectiveness of the proposed approach.

2 Detection of Multiple Targets

2.1 Preprocessing of Improved Three-Frames Subtraction

Comparing two images at different times in the same background, the common method is to do differential operations, and then obtain the motion information of the object based on the difference results. The inter-frame difference [4] is a method of finding a difference operation on adjacent two frames of images in a video sequence, and then to obtain a target region by threshold. The principle is as following:

$$\boldsymbol{g}(x, y) = \begin{cases} 1, |f_k(x, y) - f_{k-1}(x, y)| \geq Thr \\ 0, |f_k(x, y) - f_{k-1}(x, y)| < Thr \end{cases} \tag{1}$$

where Thr is a threshold. If Thr is too large, the detected target will have a large loss, if T is too small, it will be have a lot of noise. In order to improve these shortcomings, a three-frame difference method is proposed. The three-frame difference method firstly do a difference operation on the current frame and the previous frame, then performs a difference operation on the next frame and the current frame, and do logical conjunction operations on the results, finally do segmentation. Thereby the target is extracted. Let a video sequence, $f_{k-1}(x, y)$, $f_k(x, y)$, $f_{k+1}(x, y)$ are continuous three frames of images, we can obtain the position of the target by following formula.

$$\boldsymbol{g}_1(x, y) = f_k(x, y) - f_{k-1}(x, y) \tag{2}$$

$$\boldsymbol{g}_2(x, y) = f_{k+1}(x, y) - f_k(x, y) \tag{3}$$

$$G(x, y) = \boldsymbol{g}_1(x, y) \otimes \boldsymbol{g}_2(x, y) = \begin{cases} 1, & \boldsymbol{g}_1(x, y) \,\&\, \boldsymbol{g}_2(x, y) \neq 0 \\ 0, & others \end{cases} \tag{4}$$

This method has some improvements, but sometimes it is not possible to completely detect the target regions. Therefore, in this paper we combine edge extraction and contour filling based on it. There are many algorithms that can implement edge extraction. For example, the sobel operator with small complexity, but it is not accurate; the Roberts operator is weak of noise; the canny operator completely extracts the edge information through the double threshold. Therefore, in this paper, the canny operator is used for edge detection. First, the number of pre-processing frames n is set, s is the step size of frame, and k is current frame, applying the traditional three-frame difference method to the frame of $f_{k-s}(x, y), f_k(x, y), f_{k+s}(x, y)$. After the difference operation, the threshold segmentation and the logical conjunction operation, the result *res1* is obtained; next do edge-extracted for k, at the same time, the results of the two differences are expanded, and then respectively perform the logical

conjunction operation on the results of the edge extraction, two results are obtained, and then obtain *res2* which do logical disjunction for the two results. Finally, obtain *res3* which do logical disjunction with *res1*.

2.2 Improved VIBE Based Target Detection

The VIBE method [8, 9] initializes the background model using the first frame of an image. Next, it compares the pixels of the current image with the background model, thereby determines whether the current pixel is the background through setting a threshold. Finally, it randomly updates a historical value of the pixel in the background model and a historical value of the neighboring pixel when the pixel is of background. However, when the first frame of image contains targets, it will cause "ghost". That is because the target is incorrectly initialized to the background. Although ghosts can be eliminated by updating the background model in subsequent frames, this process is particularly slow, simultaneously due to the ghost, if there is a target passing through the ghost area, the accuracy of target detection will be reduced. The improved three-frame difference method proposed in Sect. 2.1 is with small computation, and less sensitive to scene changes such as light. It also has strong adaptability and does not produce ghost. Therefore, in this paper we use VIBE method which uses the pre-processing results mentioned in Sect. 1 as the real background.

Start from the Ith frame. The steps of target detection are as follows.

(a) Construct background model. Construct n background samples with preprocessing results.
(b) Foreground detection. Calculate the Euclidean distance of the corresponding pixel in each background sample and the image, then set a threshold, if at least two results are less than the threshold, the pixel is determined as the background, and go to step (c). Otherwise it is in foreground.
(c) Update the background. If the current pixel is the background pixel, the background update factor q is set, that is, the background is randomly updated as a probability of $1/q$.
At the same time, a certain pixel in the eight neighborhoods of the pixel is updated with the same probability.

3 Tracking of Multiple Targets

A goal of block matching is to find the moving vector. And it is substitution at the block locations from a current frame to it with a reference frame. Generally, the method that there is a block is performed by following three components: Block determination, searching and matching (Fig. 1).

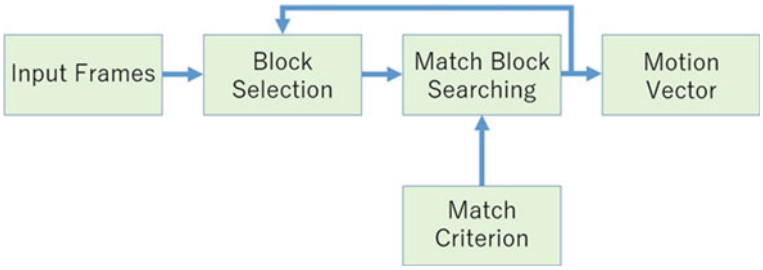

Fig. 1 Flowchart of block matching for moving objects detection

The following steps are performed:

Step 1: Set the initialize motion vector as 0, and set the best match value to a dissimilarity value of the block in the current frame and the reference frame. If the best match value is lower than the threshold, then search stops. Otherwise, go to Step 2.

Step 2: The best match is the minimum of the current best match value and the dissimilarity values of the eight neighboring blocks in the reference frame. A new best match value is determined in this step, and the corresponding motion vector is obtained accordingly.

Step 3: If the step size is larger than 1, then halve the step size and return to Step 2. Otherwise, return the motion vector

3.1 Kalman Filtering

The time interval of adjacent frames is very short and the motion state of the target changes little, so the target can be considered to be moving at a uniform speed. The Kalman filter (KF) [10, 11] is a recursive estimator whose basic principle is to give the predicted value x_{k+1} at time k + 1 which is with the minimal mean square error through the value x_k. It is described by a prediction equation (5) and an observation equation (6). Prediction is to update the state equation as the next measurement is obtained, observation is to correct the measurement from sensors according to the measurement equation. Each Kalman filter is defined as;

$$x_{k+1} = \mathrm{A}x_k + B \tag{5}$$

$$z_{k+1} = \mathrm{H}x_{k+1} + C \tag{6}$$

where $x = \left[p_x \ p_y \ v_x \ v_y \right]^T$

$$\mathrm{A} = \begin{bmatrix} 1 & 0 & T & 0 \\ 0 & 1 & 0 & T \\ 0 & 0 & 1 & 0 \\ 0 & 0 & 0 & 1 \end{bmatrix}, \quad \mathrm{H} = \begin{bmatrix} 1 & 0 & 0 & 0 \\ 0 & 1 & 0 & 0 \end{bmatrix} \tag{7}$$

where p_x, p_y are the center position of x-axis and y-axis. v_x, v_y are the velocity of x-axis and y-axis. Matrix A represents the transition matrix and matrix H is the measurement matrix. T is the time interval between two frames. B and C are the system noises and measurement noise.

The loop of the Kalman filter uses a feedback control system to estimate the motion state. The process is divided into two steps, prediction and correction. The prediction obtains the priori estimate by using the current state and the next state with error covariance. The correction obtains a posteriori estimate by considering the value of new actual observation and a priori estimate.

4 Experimental Results

In this paper, we test our algorithms in a honeybee dataset [12]. The experimental results are summarized in two groups, detection of moving objects with VIBE algorithm and object tracking with Kalman filtering.

4.1 Detection of Objects

We have used the frame subtraction technique described in Sect. 2 to obtain initial motion vectors from the image sequences. Figure 2 shows the bees detections using VIBE algorithm. From this figure, the region of interest (ROI) of bees can be detected, however, because of the non-uniform illumination and the background of honeycomb, the over segmentation is caused.

Fig. 2 VIBE algorithm based object segmentation

4.2 *Tracking of Multiple Moving Objects*

We have implemented the proposed Kalman filtering approach and tested the method on several moving objects with complex motion patterns. In this part, we reported some tracking results on the bee dataset. Experimental results are shown in Figs. 3, 4 and 5. Figure 3 shows the detection from the movement of bees. Figure 3b shows the tracking result.

In Fig. 4, the multiple bees were tracked by VIBE segmentation and Kalman filtering. The result showed that because of the over segmentation in the step of

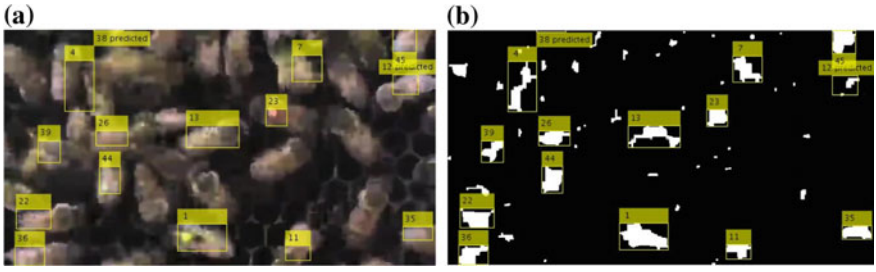

Fig. 3 Sample tracking results on the bee dataset: **a** input video frame; **b** tracking of detected bees

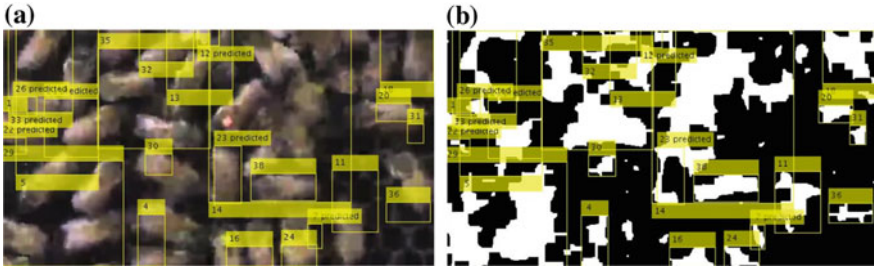

Fig. 4 Detection and tracking of multiple moving bees: **a** input video frame; **b** tracking of detected objects

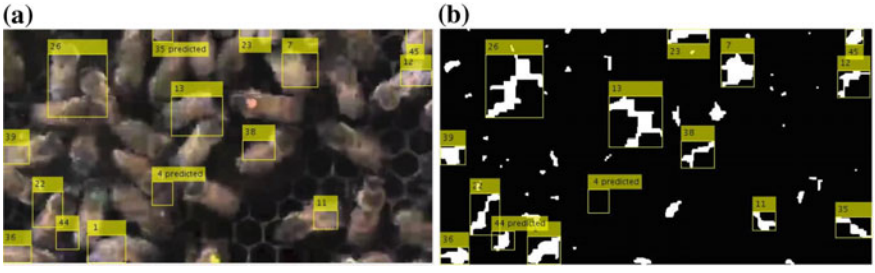

Fig. 5 Detection and tracking of multiple moving bees: **a** input video frame; **b** tracking of detected objects

VIBE segmentation, there caused some mis-tracking with Kalman tracking. Some overlapped bees were assumed as the merged one object, such as object No. 35 in the Fig. 4, contains 5 bees. As a result, even the merged one object can be detected, but it cannot be used for single bee tracking. So, for the tracking of a single bee and drawing the trajectory of the bee, there are many problems with the proposed method.

In Fig. 5, only the moving bees were detected in the result. The proposed method showed the effectiveness of tracking some moving bees. From the above experiments, it is expected that the proposed method is useful to track multiple objects in the real-world.

5 Conclusion

In this paper, we presented an improved three-frame difference method and VIBE algorithm and tracking method which is based on Kalman filtering for honey bees tracking in high density crowed scenes. The experimental results show the effectiveness of the proposed method in honeybee dataset [12]. However, in practical, because of high similarity between the targets and background, we need to develop new algorithms to detect the bees. Meanwhile, we will also use the deep learning based tracking methods to improve the accuracy of the tracking in future.

Acknowledgements This work was supported by Research Fund of SKL of Ocean Engineering in Shanghai Jiaotong University (1315; 1510), Research Fund of SKL of Marine Geology in Tongji University (MGK1608).

References

1. Li, G., Zeng, R., Lin, L.: Moving target detection in video monitoring system. In: Proceeding of the 6th World Congress on Intelligent Control and Automation, pp. 9778–9781 (2006)
2. Elgammal, A., Duraiswami, R.: Background and foreground modelling using nonparametric kernel density estimation for visual surveillance. In: Proceedings of IEEE, pp. 1151–1163 (2002)
3. Ohta, N., Kanatani, K.: Moving object detection from optical flow without empirical thresholds. IEICE Trans. Inf. Syst. **E81-D**(2), 243–245 (1998)
4. Shi, J., Tomasi, C.: Good features to track. In: Proceedings of IEEE Conference on Computer Vision and Pattern Recognition (1994)
5. Lowe, D.: Object recognition from local scale-invariant features. In: Proceedings of the International Conference on Computer Vision ICCV, Corfu, pp. 1150–1157 (1999)
6. Comaniciu, D., Ramesh, V., Meer, P.: Real-time tracking of non-rigid objects using mean shift. In: Proceedings of CVPR, pp. 142–151 (2000)
7. Allen, J.G., Xu, R.Y.D.: Object tracking using Camshift algorithm and multiple quantized feature spaces. In: Proceedings of Pan-Sydney Area Workshop on Visual Information Processing VIP 2003, pp. 1–5 (2003)
8. Barnich, O., Van Droogenbroeck, M.: VIBE: a universal background subtraction algorithm for video sequences. IEEE Trans. Image Process. **20**(6), 1709–1724 (2011)

9. Van Droogenbroeck, M., Paquot, O.: Background subtraction: experiments and improvements for VIBE. In: Computer Vision and Pattern Recognition Workshops (CVPRW), pp. 32–37 (2012)
10. Kalman, R.E.: A new approach to linear filtering nonlinear systems. J. Basic Eng. 35–45 (1960)
11. Welch, G., Bishop, G.: An introduction to the Kalman filter. In: Proceedings of SIGGRAPH, pp. 19–24 (2001)
12. Poiesi, F., Cavallaro, A.: Tracking multiple high-density homogeneous targets. IEEE Trans. Circuits Syst. Video Technol. **25**(4), 623–637 (2014)

DeepEye: A Dedicated Camera for Deep-Sea Tripod Observation Systems

Huimin Lu, Yujie Li, Hyoungseop Kim and Seiichi Serikawa

Abstract The deep-sea tripod systems are designed and built at the U.S. Geological Survey (USGS) Pacific Coastal and Marine Science Center (PCMSC) in Santa Cruz, California. They are recovered in late September 2014 after spending about half a year collecting data on the floor of the South China Sea. The deep-sea tripod systems are named as Free-Ascending Tripod (FAT), are deployed at 2,100 m water depth—roughly 10 times as deep as most tripods dedicated to measuring currents and sediment movement at the seafloor. Deployment at this unusual depth was made possible by the tripod's ability to rise by itself to the surface rather than being pulled up by a line. Instruments mounted on the tripod took bottom photographs and measured such variables as water temperature, current velocity, and suspended-sediment concentration. FAT is used to better understand how and where deep-seafloor sediment moves and accumulates. Besides of this, we also use them to study the deep-sea biology. The obtained the images from the camera, the biology animals are hardly to be distinguished. In this project, we are concerned to use novel underwater imaging technologies for recovering the deep-sea scene.

Keywords Underwater camera · Deep-sea tripod · South China Sea

1 Introduction

Ocean observations [1] are being developed and deployed by scientists, researchers and institutions around the world oceans for monitoring the status of ocean. Some observatories are cabled, For example, the Ocean Networks Canada Observatory [2], contains VENUS and NEPTUNE Canada cabled networks. It enables real-time

H. Lu (✉) · H. Kim · S. Serikawa
Kyushu Institute of Technology, Fukuoka, Japan
e-mail: luhuimin@ieee.org

Y. Li
Fukuoka University, Fukuoka, Japan
e-mail: yzyjli@gmail.com

H. Lu (ed.), *Cognitive Internet of Things: Frameworks, Tools and Applications*, Studies in Computational Intelligence 810,
https://doi.org/10.1007/978-3-030-04946-1_49

interactive experiments, for measuring ocean health, ecosystems, resources, natural hazards and marine conservation. Some observatories are moored or made up of surface buoys, such as National Oceanic and Atmospheric Administration (NOAA) Ocean Climate Observation System [3]. The observations near the equator are of particular important to climate. Besides of monitoring the air-water exchange of heat and water, the moored buoys provide platforms for instrumentation to measure the air-water exchange of carbon dioxide in the tropics. Some observatories are remote sensed, such as Japanese Ocean Flux Data Sets with Use of Remote Sensing Observation [4]. It is used for monitoring the changes of heat, water and momentum with atmosphere at ocean surface.

Interestingly, there are some excellent systems for ocean observing, such as Global Ocean Observing System proposed by Henry. Stommel Woods Hole Oceanographic Institution (WHOI) [5]. More than 30 countries are joined in this program. However, until now this system also has some drawbacks. First, the system is not fully built-out because of funding issues. Second, most of subsystems are not at full operational capacity. Many of them are funded through research programs rather than operational. Third, deep ocean (under 2000 m) is very under-sampled-issue of technology and cost.

2 Methods

Figure 1 shows the location of captured images by the dedicated camera. Size of the image is 5184×3456 pixels. Figure 2 shows the free-ascending tripod for observing the bottom of the South China Sea. The image Fig. 2b was captured on May 5, 2014. The water depth is about 1900 m. We utilize the Housing for the dedicated CANON EOS 70D MarkII camera and take underwater blue-green LED light for imaging. The distance between the camera and sea bottom is about 1.53 m. Because of using a single blue-green deep sea LED lighting, the illumination is inhomogeneous. Meanwhile, the captured images contain some floating sediments and color distortion. Hence, we need to take the proposed descattering [6] method and pre-processing method [7, 8] to remove the haze-like objects. Furthermore, deep sea blue-green LED light has the limitation of wavelength. The real underwater scene cannot illuminate as well as on the land. Consequently, we need to use the camera spectral response function and illumination characteristics in water to recover the scene color [9, 10]. The processing steps of this camera is: firstly, we need to know the illumination characteristics and camera spectral response function. After that, we take the proposed color correction method for color reconstruction in Fig. 3.

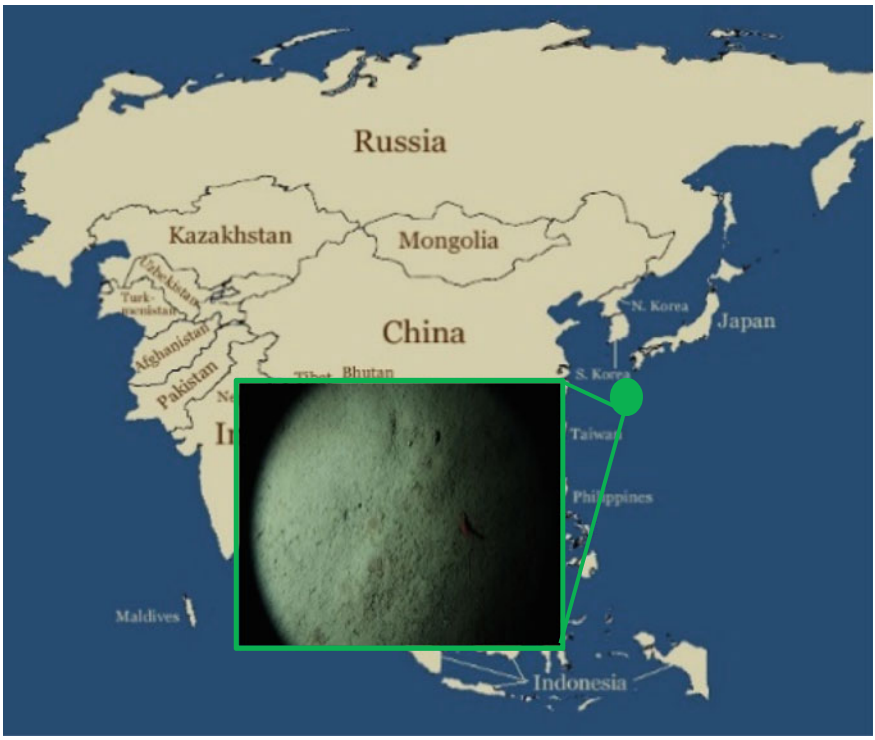

Fig. 1 Captured image at the northeastern South China Sea of China

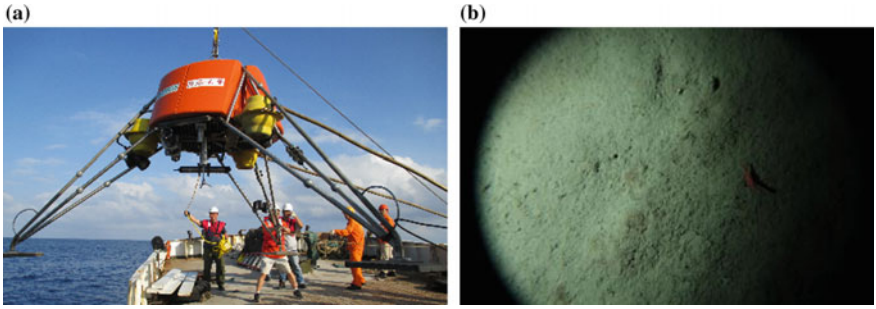

Fig. 2 Free-ascending tripod for the seafloor observation in the South China Sea. **a** Loading the equipment. **b** Captured deep sea image

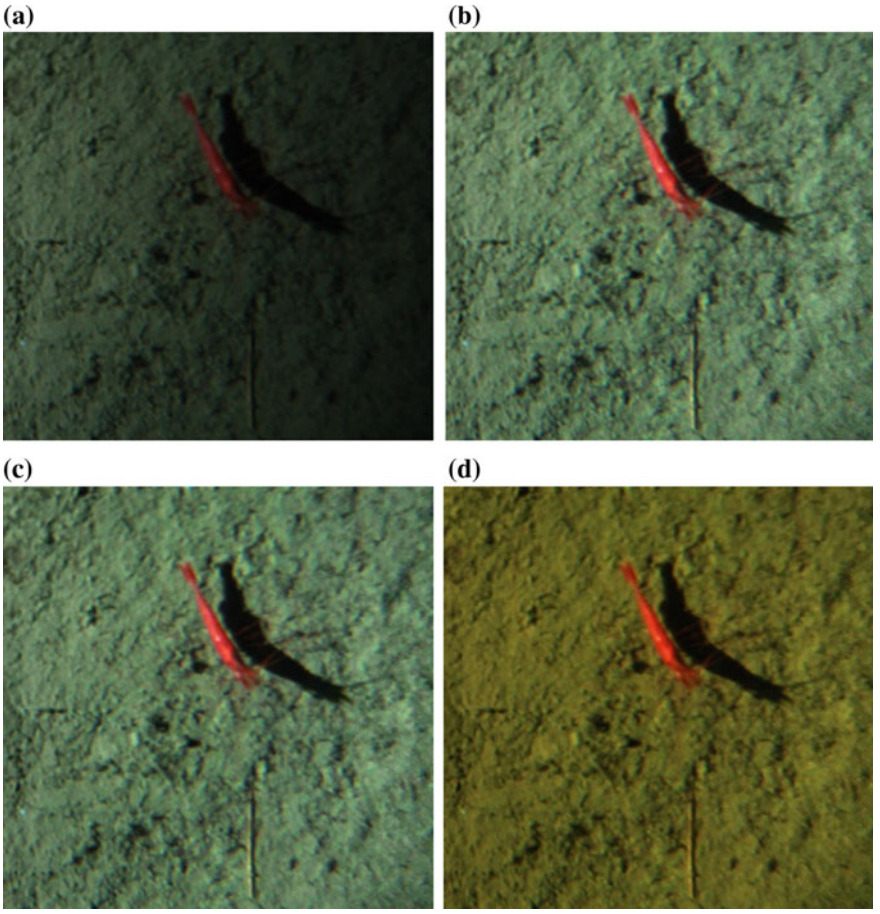

Fig. 3 Summary of the proposed approach for recovering the color of deepsea image. **a** Cropped initial image (1122 × 1106 p). **b** Result after descattering. **c** Result after BM3D denoising. **d** Result after color correction

3 Results

We also test the proposed method with the images of real-world, deep-sea observation systems. The image used was captured by the Free-Ascending Tripod (FAT), which was built at the U.S. Geological Survey (USGS) Pacific Coastal and Marine Science Center (PCMSC) in Santa Cruz, California and is used to monitor in situ sediment movement. FAT was recovered in late September 2014 after spending about half a year collecting data on the floor of the northeastern South China Sea (SCS). The enhanced images are characterized by a reduced noised level with better exposure in dark regions and improved global contrast, by which the finest details and edges are significantly enhanced, demonstrating the effectiveness of proposed method [11–15].

4 Conclusion

In this paper, we built a dedicated camera and a corresponding image processing technologies for in-suit deep sea observing in the South China Sea. The proposed device can improve the quality of deep-sea images well. It can remove the unwanted particles, can correct the non-uniform illumination as well as recover the real scene color, and super resolving the images. Water tank experiments and sea water experiments demonstrate that the proposed system performs better. The proposed methods are suitable for ocean observing.

Acknowledgements This work was supported by Leading Initiative for Excellent Young Researcher of Ministry of Education, Culture, Sports, Science and Technology-Japan (16809746), Grants-in-Aid for Scientific Research of JSPS (17K14694), Research Fund of State Key Laboratory of Marine Geology in Tongji University (MGK1803), Research Fund of State Key Laboratory of Ocean Engineering in Shanghai Jiaotong University (1510; 1315), Research Fund of The Telecommunications Advancement Foundation, Fundamental Research Developing Association for Shipbuilding and Offshore, Japan-China Scientific Cooperation Program (6171101454), International Exchange Program of National Institute of Information and Communications (NICT), and Collaboration Program of National Institute of Informatics (NII).

References

1. Ocean Observations. http://en.wikipedia.org/wiki/ocean_observations
2. Ocean Networks Canada. http://www.oceannetworks.ca/
3. NOAA Ocean Climate Observation Program. http://www.oco.noaa.gov/
4. Japanese Ocean Flux Data Sets with Use of Remote Sensing Observation. http://dtsv.scc.u-tokai.ac.jp/j-ofuro/
5. Woods Hole Oceanographic Institution. http://www.whoi.edu/
6. Serikawa, S., Lu, H.: Underwater image dehazing using joint trilateral filter. Comput. Electr. Eng. **40**(1), 41–50 (2014)
7. Lu, H., Li, Y., Zhang, Y., Chen, M., Serikawa, S., Kim, H.: Underwater optical image processing: a comprehensive review. Mob. Netw. Appl. 1–8 (2017)
8. Lu, H., Li, Y., Uemura, T., Ge, Z., Xu, X., He, L., Serikawa, S., Kim, H.: FDCNet: filtering deep convolutional network for marine organism classification. Multimed. Tools Appl. 1–14 (2017)
9. Lu, H., Li, Y., Nakashima, S., Kim, H., Serikawa, S.: Underwater image super-resolution by descattering and fusion. IEEE Access **5**, 670–679 (2017)
10. Li, Y., Lu, H., Li, J., Li, X., Li, Y., Serikawa, S.: Underwater image de-scattering and classification by deep neural network. Comput. Electr. Eng. **54**, 68–77 (2016)
11. Lu, H., Li, B., Zhu, J., Li, Y., Li, Y., Xu, X., He, L., Li, X., Li, J., Serikawa, S.: Wound intensity correction and segmentation with convolutional neural networks. Concurr. Comput.: Pract. Exp. **27**(9), 1–10 (2017)
12. Lu, H., Li, Y., Nakashima, S., Serikawa, S.: Turbidity underwater image restoration using spectral properties and light compensation. IEICE Trans. Inf. Syst. **99**(1), 219–227 (2016)
13. Lu, H., Li, Y., Zhang, L., Serikawa, S.: Contrast enhancement for images in turbid water. JOSA **32**(5), 886–893 (2015)
14. Li, Y., Lu, H., Zhang, L., Li, J., Serikawa, S.: Real-time visualization system for deep-sea surveying. Math. Probl. Eng. 1–10 (2014)
15. Lu, H., Zhang, L., Serikawa, S.: Maximum local energy: an effective approach for multisensor image fusion in beyond wavelet transform domain. Comput. Math Appl. **64**(5), 996–1003 (2012)

Hyperspectral Images Segmentation Using Active Contour Model for Underwater Mineral Detection

Huimin Lu, Yinqiang Zheng, Kazuhiro Hatano, Yujie Li, Shota Nakashima and Hyoungseop Kim

Abstract In this paper, we design a novel underwater hyperspectral imaging technique for deep-sea mining detection. The spectral sensitivity peaks are in the region of the visible spectrum, 580, 650, 720, 800 nm. In addition, to the underwater objects recognition, because of the physical properties of the medium, the captured images are distorted seriously by scattering, absorption and noise effect. Scattering is caused by large suspended particles, such as in turbid water, which contains abundant particles, algae, and dissolved organic compounds. In order to resolve these problems of recognizing mineral accurately, fast and effectively, an identifying and classifying algorithm is proposed in this paper. We take the following steps: firstly, through image preprocessing, hyperspectral images are gained by using denoising, smoothness, image erosion. After that, we segment the cells by the method of the modified active contour method. These methods are designed for real-time execution on limited-memory platforms, and are suitable for detecting underwater objects in practice. The Initial results are presented and experiments demonstrate the effectiveness of the proposed imaging system.

Keywords Underwater hyperspectral imaging · Mineral detection
Image processing

H. Lu (✉) · K. Hatano · H. Kim
Kyushu Institute of Technology, Kitakyushu, Japan
e-mail: dr.huimin.lu@ieee.org

Y. Zheng
National Institute of Informatics, Tokyo, Japan
e-mail: yqzheng@nii.ac.jp

Y. Li
Fukuoka University, Fukuoka, Japan
e-mail: yzyjli@fukuoka-u.ac.jp

S. Nakashima
Yamaguchi University, Ube, Japan
e-mail: s-naka@yamaguchi-u.ac.jp

H. Lu (ed.), *Cognitive Internet of Things: Frameworks, Tools and Applications*, Studies in Computational Intelligence 810,
https://doi.org/10.1007/978-3-030-04946-1_50

1 Introduction

Many researchers have developed techniques to restore and enhance underwater images. Schechner et al. [1] exploited a polarization filter to compensate for visibility degradation. Bazeille et al. [2] proposed an image preprocessing pipeline for enhancing images in turbid water. Fattal designed a graphic-theory-based independent-component analysis model to estimate the synthetic transmission and shading for recovering clean images [3]. Nicholas et al. [4] improved the dark channel prior and used the graph-cut method instead of soft matting to refine the depth transmission. Hou et al. [5] combined a point spread function and modulation transfer function to reduce the effects of blurring. Ouyang et al. [6] proposed bilateral filtering based on an image deconvolution method. Ancuti et al. [7] used an exposed fusion method in a turbid medium to reconstruct a clear image. However, most recent methods have several drawbacks that reduce their practical applicability. First, imaging equipment is difficult to use in practice (e.g., a range-gated laser imaging system, which is rarely applied in practice [6]). Second, it is difficult to process multiple input images [1] (e.g., different polarization images or different exposed images). Third, nonphysical approaches are not suitable for underwater images [2, 4, 5, 7] because they ignore the imaging environment. Fourth, manual operation is needed in processing, which leads to a lack of intelligence [3]. The most critical drawback is that almost all of the aforementioned methods cannot process high-turbidity underwater images. Therefore, we propose a physical model-based near-infrared lighting and white lighting fused method in high-turbidity water.

2 Related Works

The system is composed of an Olympus microscope, a Panasonic color camera, a color image acquisition card and a computer. The smears of bone marrow cells are captured by the optical microscope and then converted into a computer image through a CCD camera. Subsequently, the images are transmitted to the acquisition card and converted to digital images for computer processing, storage, display, printing and so on.

2.1 Eliminate the Background of the Original Image

The influence of illuminance in the original image may affect the final processing results; therefore, to modify the whole image, smoothness and denoising are necessary. Using the subtraction method in the original image and the background, one can effectively eliminate the uneven background. This is defined as

$$g_i(x, y) = f_i(x, y) - h(x, y) + k \tag{1}$$

where $g_i(x, y)$ is the image after processing, $f_i(x, y)$ is the original image, $h(x, y)$ is the background, and k is the correction conference.

2.2 Principles of Denoising by Using Morphology

The basic operations of mathematical morphology include dilation, erosion, opening and closing [8]. Based on the type of the prepared image and requirement, mathematical morphology can also be divided into binary morphology, gray morphology and color morphology. The basic operations in gray morphology are introduced as follows.

Assuming that $f(x, y)$ expresses the input image, $b(x, y)$ is the structure element. D_f and D_b are the definition domain of the image $f(x, y)$ and the structure element $b(x, y)$. The expression of the gray dilation is

$$(f \oplus b)(s, t) = \max\left\{f(s - x, t - y) - b(x, y) | (s - x), (t - y) \in D_f; (x, y) \in D_b\right\} \tag{2}$$

The expression of the gray erosion is

$$(f \Theta b)(s, t) = \min\left\{f(s + x, t + y) - b(x, y) | (s + x), (t + y) \in D_f; (x, y) \in D_b\right\} \tag{3}$$

The opening and closing operations of the gray image have the same form as the corresponding operations of the binary image.

The opening operation carries out simple corrosion on image f with structure element b and then carries out the dilation operation on the previous result with b. However, the closing operation is opposite to the opening operation. It carries out simple dilation on image f with structure element b and then carries out the erosion operation on the previous result with structure element b.

The expression of the opening operation is

$$f \circ b = (f \Theta b) \oplus b \tag{4}$$

The expression of the closing operation is

$$f \bullet b = (f \oplus b) \Theta b \tag{5}$$

The opening operation is often used to remove less bright detail relative to the size of the structure elements and keeps the whole gray level and the bright large-area relatively invariable at the same time. The closed operation is often used to remove the dark detail part in the image but to keep the relatively bright part unaffected.

Image denoising is a fundamental part of image preprocessing. It removes interference in images to extract useful information in complicated images. Although a series of traditional filtering methods can obtain good effects on denoising, some useful image information is simultaneously lost. For instance, the image border will be blurred when accompanied by denoising. Denoising based on morphology uses the structure element to handle the image, to extract useful information and to reserve the border information well.

3 Improved Active Contour Model

Chan and Vese proposed a method (CV) based on the Mumford-Shah model and the level set method. Set an image $u_0(x, y)$. Let us give the curve $C = \partial w$, with $w \subset \Omega$ as an open subset and two unknown constants c_1 and c_2. Denoting $\Omega_1 = w$,$\Omega_2 = \Omega \backslash w$, the energy function is

$$E^{CV}(c_1, c_2, C) = \mu \cdot Length(C) + \nu \cdot Area(inside(C)) + \lambda_1 \int_{\Omega_1 = w} |u_0 - c_1|^2 dxdy + \lambda_2 \int_{\Omega_2 = \Omega \backslash w} |u_0 - c_2|^2 dxdy \quad (6)$$

where $\mu \geq 0, \nu \geq 0, \lambda_1, \lambda_2 > 0$ are fixed parameters. In almost all calculations, we fix $\lambda_1 = \lambda_2 = 1$ and $\nu = 0$. If and only if curve C is on the boundary of the homogeneity area, the above function obtains a minimum value. Set ϕ as the level set function. Then, the energy $E^{CV}(c_1, c_2, \phi)$ can be written as

$$E^{CV}(c_1, c_2, \phi) = \mu \int_{\Omega} \delta(\phi)|\nabla\phi| dxdy + \nu \int_{\Omega} H(\phi) dxdy + \lambda_1 \int_{\Omega} |u_0 - c_1|^2 H(\phi) dxdy + \lambda_2 \int_{\Omega} |u_0 - c_2|^2 (1 - H(\phi)) dxdy \quad (7)$$

Keeping ϕ fixed and minimizing the energy $E^{CV}(c_1, c_2, \phi)$ with respect to the constants c_1 and c_2, we can obtain the following formulas with $C = \{(x, y)|\phi(x, y) = 0\}$

$$c_1 = \frac{\int_{\Omega} u_0(x, y) H(\phi(x, y)) dxdy}{\int_{\Omega} H(\phi(x, y)) dxdy} \quad c_2 = \frac{\int_{\Omega} u_0(x, y)(1 - H(\phi(x, y))) dxdy}{\int_{\Omega} (1 - H(\phi(x, y))) dxdy}$$
$$\frac{\partial \phi}{\partial t} = \delta(\phi)\left[\mu \nabla\left(\frac{\nabla\phi}{|\nabla\phi|}\right) - \nu - \lambda_1 (u_0 - c_1)^2 + \lambda_2 (u_0 - c_2)^2\right] \quad (8)$$

where the Heaviside function $H(z) = \begin{cases} 1 & z \geq 0 \\ 0 & z < 0 \end{cases}$. $\delta_\varepsilon(z) = \frac{dH(z)}{dz}$ is the Dirac function. In practice, $H_\varepsilon(z) = \frac{1}{2}(1 + \frac{2}{\pi} \arctan(\frac{z}{\varepsilon}))$ and $\delta_\varepsilon(z) = \frac{1}{\pi} \cdot \frac{\varepsilon}{\varepsilon^2 + z^2}$, where ε is constant.

We briefly introduce the multiphase piecewise constant active contour model without edges [9, 10] in image processing. Let us write the energy for $n=4$ phases or classes that use $m=2$ level set functions ($n=2^m$). Set the level set functions $\phi_i (1 \leq i \leq m)$ to implicitly express the curves C_i. Then, we obtain the energy function

$$\begin{aligned} F_4(c, \Phi) = & \int_\Omega (u_0 - c_{11})^2 H(\phi_1) H(\phi_2) dxdy \\ & + \int_\Omega (u_0 - c_{10})^2 H(\phi_1)(1 - H(\phi_2)) dxdy \\ & + \int_\Omega (u_0 - c_{01})^2 (1 - H(\phi_1)) H(\phi_2) dxdy \\ & + \int_\Omega (u_0 - c_{00})^2 (1 - H(\phi_1))(1 - H(\phi_2)) dxdy \\ & + \nu \int_\Omega |\nabla H(\phi_1)| + \nu \int_\Omega |\nabla H(\phi_2)| \end{aligned} \tag{9}$$

where $c = (c_{11}, c_{10}, c_{01}, c_{00})$ is a constant vector and $\Phi = (\phi_1, \phi_2)$. Then, minimizing the energy functional $F_4(c, \Phi)$ with respect to ϕ_i, we derive the gradient descent flow,

$$\begin{aligned} \frac{\partial \phi_1}{\partial t} = & \delta_\varepsilon(\phi_1) \{ \nu div\left(\frac{\nabla \phi_1}{|\phi_1|}\right) - [\left((u_0 - c_{11})^2 - (u_0 - c_{01})^2\right) H(\phi_2) \\ & + \left((u_0 - c_{10})^2 - (u_0 - c_{00})^2\right)(1 - H(\phi_2))] \} \\ \frac{\partial \phi_2}{\partial t} = & \delta_\varepsilon(\phi_2) \{ \nu div\left(\frac{\nabla \phi_2}{|\phi_2|}\right) - [\left((u_0 - c_{11})^2 - (u_0 - c_{10})^2\right) H(\phi_1) \\ & + \left((u_0 - c_{01})^2 - (u_0 - c_{00})^2\right)(1 - H(\phi_1))] \} \end{aligned} \tag{10}$$

where the constants functions $c_{11}, c_{10}, c_{01}, c_{00}$ are denoted respectively as

$$\begin{aligned} c_{11}(\Phi) &= \frac{\int_\Omega u_0 H_\varepsilon(\phi_1) H_\varepsilon(\phi_2) dxdy}{\int_\Omega H_\varepsilon(\phi_1) H_\varepsilon(\phi_2) dxdy} \\ c_{10}(\Phi) &= \frac{\int_\Omega u_0 H_\varepsilon(\phi_1)(1 - H_\varepsilon(\phi_2)) dxdy}{\int_\Omega H_\varepsilon(\phi_1)(1 - H_\varepsilon(\phi_2)) dxdy} \\ c_{01}(\Phi) &= \frac{\int_\Omega u_0 (1 - H_\varepsilon(\phi_1)) H_\varepsilon(\phi_2) dxdy}{\int_\Omega (1 - H_\varepsilon(\phi_1)) H_\varepsilon(\phi_2) dxdy} \\ c_{00}(\Phi) &= \frac{\int_\Omega u_0 (1 - H_\varepsilon(\phi_1))(1 - H_\varepsilon(\phi_2)) dxdy}{\int_\Omega (1 - H_\varepsilon(\phi_1))(1 - H_\varepsilon(\phi_2)) dxdy} \end{aligned} \tag{11}$$

where the Heaviside function $H(z) = \begin{cases} 1 & z \geq 0 \\ 0 & z < 0 \end{cases}$. $\delta(z) = \frac{dH(z)}{dz}$ is the Dirac measurement ($\delta_\varepsilon(x) = H_\varepsilon^{'}(x)$). In function (10), $\lambda_1 = \lambda_2 = 1$.

In this study, we use a semi-implicit additive operator splitting (AOS) [11] method rather than explicit schemes to implement discrete level set processing. The basic idea of the AOS scheme is to split the *m-dimensional* spatial operator into a set of *one-dimensional* space discretizations that can be efficiently solved with the Gaussian elimination algorithm named the *Thomas Algorithm*.

To simplify the form of function (7), $\frac{\partial \phi}{\partial t} = \delta_\varepsilon(\phi) div(\frac{\nabla \phi}{|\nabla \phi|})$ can be written by the semi-implicit AOS scheme [12] as

$$\phi_i^{n+1} = \phi_i^n + \tau \delta(\phi_i) \sum_{j \in N(i)} \frac{2}{(|\nabla \phi|)_i^n + (|\nabla \phi|)_j^n} (\phi_j^{n+1} - \phi_i^{n+1}) \tag{12}$$

Note that by evaluating only image positions with $|\nabla \phi|_i \neq 0$, the denominator in this scheme cannot vanish. In matrix-vector notation this becomes

$$\phi^{n+1} = \phi^n + \tau \left(\sum_{l \in \{x,y\}} A_l(\phi^n) \right) \phi^{n+1} \tag{13}$$

where A_l describes the interaction in the l direction. x and y represent the *x-direction* and *y-direction* (2D), respectively. With the definition of $A_l(\phi^n) = a_{ij}(\phi^n)$, and $a_{ij}(\phi^n)$ can be expressed as

$$a_{ij} = \begin{cases} \delta(\phi_i) \frac{2}{(|\nabla \varphi|)_i^n + (|\nabla \varphi|)_j^n}, & j \in N_l(i) \\ 0, & else \\ -\delta(\phi_i) \frac{2}{(|\nabla \varphi|)_i^n + (|\nabla \varphi|)_j^n}, & i = j \end{cases} \tag{14}$$

According to the above equations, formulation (13) can be re-expressed as

$$\phi^{n+1} = \frac{1}{2} \sum_{l \in \{x,y\}} \left(I - 2\tau A_l(\phi^n) \right)^{-1} \phi^n \tag{15}$$

Thus, combining with formulation (11), formulation (10) can finally be written as

$$\begin{aligned} \phi_1^{n+1} = |\nabla \phi_1^n| \Bigg\{ & \frac{1}{2} \sum_{l=1}^{2} \left(I - 2\tau \mu A_l(\phi_1^n) \right)^{-1} \\ & \times \left[\phi_1^n - \left(u_0 - \tfrac{c_{11}+c_{01}}{2} \right) H(\phi_2^n) + \left(u_0 - \tfrac{c_{10}+c_{00}}{2} \right) \left(1 - H(\phi_2^n) \right) \right] \Bigg\} \\ \phi_2^{n+1} = |\nabla \phi_2^n| \Bigg\{ & \frac{1}{2} \sum_{l=1}^{2} \left(I - 2\tau \mu A_l(\phi_2^n) \right)^{-1} \\ & \times \left[\phi_2^n - \left(u_0 - \tfrac{c_{11}+c_{10}}{2} \right) H(\phi_1^n) + \left(u_0 - \tfrac{c_{01}+c_{00}}{2} \right) \left(1 - H(\phi_1^n) \right) \right] \Bigg\} \end{aligned} \tag{16}$$

4 Experimental Results

The performance of the proposed algorithm is evaluated both objectively and subjectively utilizing ground-truth color patches. The computer used is equipped with Windows 8 and an Intel Core i7 (2.0 GHz) processor with 4 GB RAM [11]. The captured image used the Spectral Devices Inc. hyperspectral camera shown in Fig. 1.

Figure 1 shows the captured grayscale multispectral images with different bands. Figure 2 shows the segmentation results from the proposed ACM method. To evaluate the accuracy of Fig. 2, we created the ground truth image by hand. Figure 3 shows the fused images in Fig. 2 and the ground truth image. The correct region is an image in which the intersection over union (IoU) with the true box exceeds the threshold in

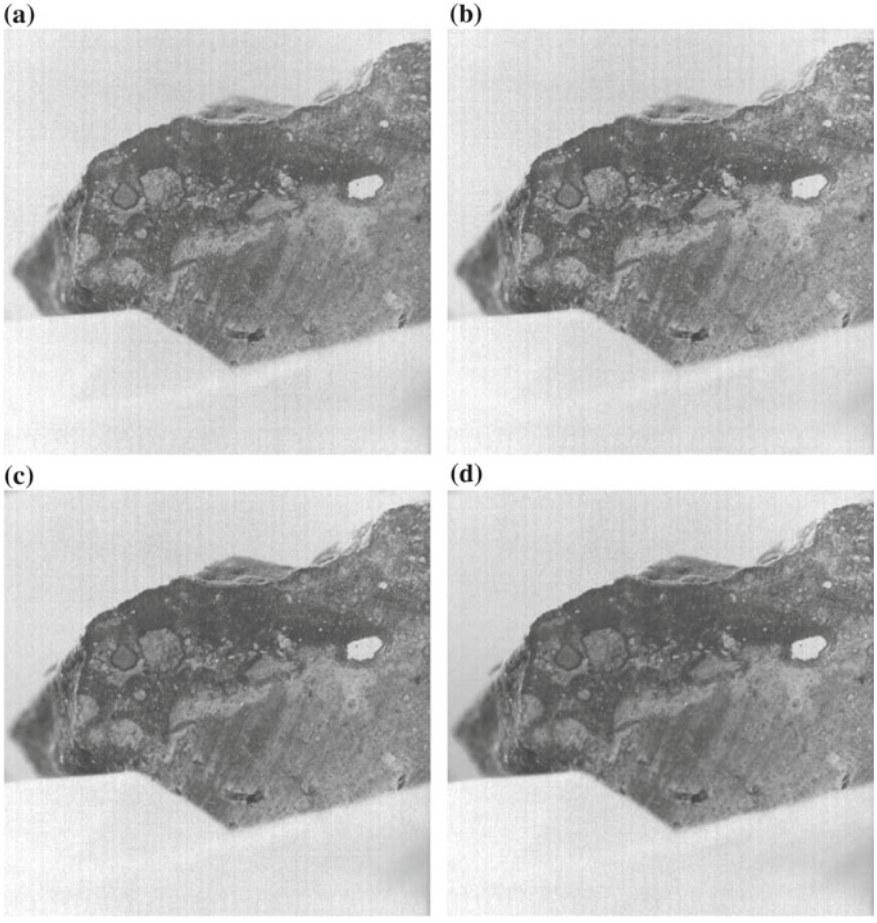

Fig. 1 Multispectral images captured by a multispectral camera. **a** 580 nm; **b** 650 nm; **c** 720 nm; **d** 800 nm

the detected boxes. When the true region number is 0, the detection rate is 0 if there are result regions, and it is 1 if there are no overlaps. From Table 1, we find that the 650 nm image performs well in recognizing minerals.

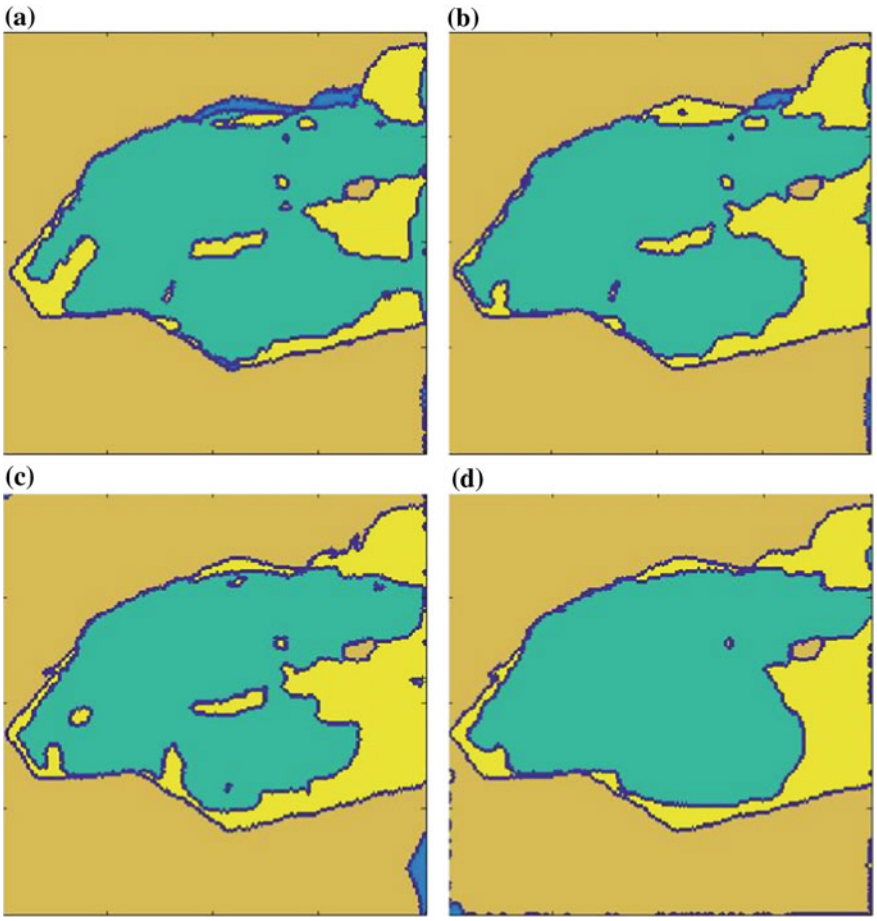

Fig. 2 Segmentation results of the proposed method. **a** 580 nm; **b** 650 nm; **c** 720 nm; **d** 800 nm

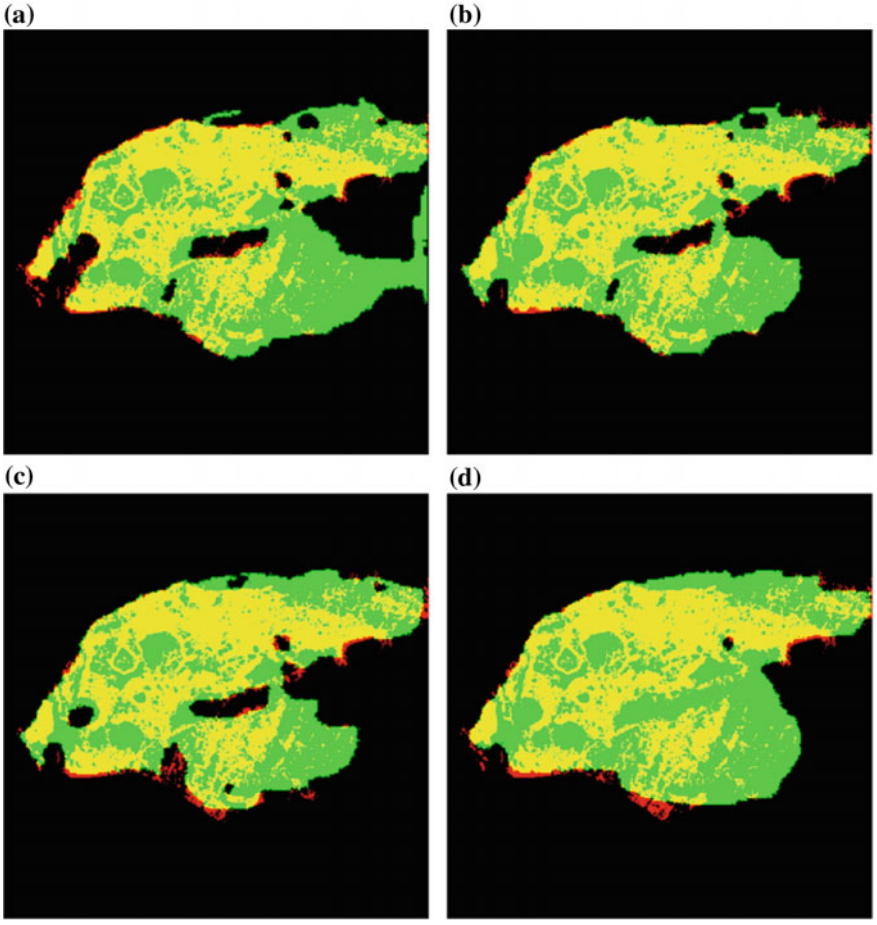

Fig. 3 Fused results with the ground truth image

Table 1 IoU result of different bands

	580 nm	650 nm	720 nm	800 nm
IoU	0.60002	0.66124	0.65515	0.62340

5 Conclusion

In this paper, we have explored and successfully implemented novel multispectral image segmentation in clean water. The proposed modified active contour method can segment the low-contrast images well. These methods are designed for real-time execution on limited-memory platforms and are suitable for detecting underwater objects in practice. The initial results are presented, and experiments demonstrate that 650 nm is the best band for detection. In the future, we will consider experiments in high-turbidity water and other methods for mineral detection.

Acknowledgements This work was supported by Leading Initiative for Excellent Young Researcher (LEADER) of MEXT-Japan (16809746), Grants-in-Aid for Scientific Research of JSPS (17K14694), Research Fund of SKL of Ocean Engineering in Shanghai Jiaotong University (1315; 1510), Research Fund of SKL of Marine Geology in Tongji University (MGK1608), Research Fund of The Telecommunications Advancement Foundation, Open Collaborative Research Program at National Institute of Informatics Japan (NII), Japan-China Scientific Cooperation Program (6171101454), and International Exchange Program of National Institute of Information and Communications (NICT), and Fundamental Research Developing Association for Shipbuilding and Offshore.

References

1. Schechner, Y.Y., Karpel, N.: Recovery of underwater visibility and structure by polarization analysis. IEEE J. Ocean. Eng. **30**(3), 570–587 (2005)
2. Bazeille, S., Quidu, I., Jaulin, L., Malkasse, J.P.: Automatic underwater image pre-processing. In: Proceedings of Caracterisation Du Milieu Marin (CMM'06), pp. 1–8 (2006)
3. Fattal, R.: Single image dehazing. ACM Trans. Gr. **27**(3), 1–8 (2008)
4. Nicholas, C.-B., Anush, M., Eustice, R.M.: Initial results in underwater single image dehazing. In: Proceedings of IEEE OCEANS 2010, pp. 1–8 (2010)
5. Hou, W., Gray, D.J., Weidemann, A.D., Fournier, G.R., Forand, J.L.: Automated underwater image restoration and retrieval of related optical properties. In: Proceedings of IEEE International Symposium of Geoscience and Remote Sensing, pp. 1889–1892 (2007)
6. Ouyang, B., Dalgleish, F.R., Caimi, F.M., Vuorenkoski, A.K., Giddings, T.E., Shirron, J.J.: Image enhancement for underwater pulsed laser line scan imaging system. In: Proceedings of SPIE **8372**, 83720R (2012)
7. Ancuti, C., Ancuti, C.O., Haber, T., Bekaert, P.: Enhancing underwater images and videos by fusion. In: Proceedings of IEEE Conference on Computer Vision and Pattern Recognition (CVPR '12), pp. 81–88 (2012)
8. Tang, X., Lin, X., He, L.: Research on automatic recognition system for leucocyte image. J. Biomed. Eng. **24**(6), 1250–1255 (2007)
9. Yujie, L., Huimin, L., Lifeng, Z., Shiyuan, Y., Seiichi, S.: A new image segmentation method based on improved fast implicit level set scheme in X/γ-ray inspection system. Appl. Mech. Mater. **103**, 705–710 (2012)
10. Huimin, L., Lifeng, Z., Seiichi, S.: Maximum local energy: an effective approach for image fusion in beyond wavelet transform domain. Comput. Math Appl. **64**(5), 996–1003 (2012)
11. Weickert, J., Kuhne, G.: Fast methods for implicit active contour models. Lect. Notes Comput. Sci. **2449**, 43–58 (2003)
12. Huimin, L., Lifeng, Z., Seiichi, S.: (2010) A method for infrared image segment based on sharp frequency localized contourlet transform and morphology. In: Proceeding of IEEE International Conference on Intelligent Control and Inform Processing, pp. 79–82 (2010)